MICROPOROUS MATERIALS FOR HYDROGEN STORAGE

by

STEVEN PAUL TEDDS

A thesis submitted to
The University of Birmingham
for the degree of
DOCTOR OF PHILOSOPHY

School of Metallurgy and Materials
College of Engineering and Physical Sciences
University of Birmingham
December 2010

Synopsis

Microporous materials (with pores of less than 2 nm in diameter) have attracted considerable attention due to the variety of applications in which they can be used, including heterogeneous catalysis, gas purification, gas separation and gas storage. Physisorption of molecular hydrogen offers several advantages over chemical absorption, namely, fast kinetics and complete reversibility. The overall aim of this work was to investigate the potential of microporous materials for hydrogen storage, with particular attention given to a relatively new class of material (synthesised by our partners at the Universities of Cardiff and Manchester): microporous polymers. This was performed by measuring pressure-composition-temperature isotherms, and determining the enthalpy of adsorption, which is a crucial property as it indicates the strength of the adsorbate-adsorbent interaction and thus the temperature and pressure at which sorption occurs.

This study utilised a newly developed liquid nitrogen cryostat to measure pressure-composition-temperature isotherms over multiple temperatures from 77 to 137 K, for a range of well-known porous materials including activated carbons, zeolites and MOFs. Two empirical equations, Sips and Tóth, were used in addition to a multi-parameter Virial type thermal equation to fit adsorption curves, in order to calculate the enthalpy of adsorption for all materials as a function of hydrogen adsorption. The empirical equations allow for the hydrogen adsorption to be extrapolated to higher pressures, and also for the saturation values to be determined. A review of the different techniques is given in this study.

Porous polymers offer an attractive combination of properties, which may make them suitable as hydrogen storage materials, including: low intrinsic density (as they are only composed of light elements such as C, H, N, O, and do not include metal ions); chemical homogeneity; and thin pore walls. A series of microporous polymers were synthesised with the aim of maximising the available surface area, whilst optimising the pore size to increase the enthalpy of adsorption.

Generally the polymers of intrinsic microporosity were seen to adhere to Chahine's rule, which predicts a linear correlation of hydrogen adsorption capacity, at 77 K, with surface area (1 wt.% per 500 $m^2 g^{-1}$).

Using different monomers the gas adsorption properties could be tailored. This was particularly apparent in the series of network PIMs based on the triptycene monomers that possess different alkyl groups attached to their bridgehead positions. The PIMs exhibit a sloping adsorption and pronounced hysteresis in the nitrogen isotherms, which is possibly due to the swelling of the porous structure.

Of all of the materials measured in this investigation, IRMOF-1 and Cu-BTC exhibited the largest gravimetric storage capacities of 4.86 and 4.50 wt.% at 77 K and 15 bar, respectively. The largest for a microporous polymer was 3.26 wt.% at 77 K and 15 bar, for the methyl triptycene-based PIM. Treatment of PIM-1 with supercritical carbon dioxide led to a 24% increase in the gravimetric hydrogen storage capacity at 77 K and 20 bar.

The enthalpy of adsorption was found to vary, as a function of hydrogen uptake, depending on the number of temperatures used. At low hydrogen coverage, the enthalpy of adsorption was found to follow a general trend with pore size, with higher enthalpies of adsorption exhibited by materials with smaller pore sizes. However, both zeolite NaX and Cu-BTC exhibited higher enthalpies of adsorption than may have been expected by the effect of pore size alone. This is likely to be due to the influence from electrostatic forces within these materials. Of all of the materials measured, the triptycene-based macromolecule PIM exhibited the highest enthalpy of adsorption with the Tóth and Virial type thermal equation giving 10.6 and 9.8 kJ mol^{-1}, respectively, at 0.02 wt.%.

Materials that exhibit higher enthalpy of adsorption values have been shown to retain more of their hydrogen capacity with increasing temperature. Previous literature studies have suggested that an adsorption enthalpy of around 20 kJ mol^{-1} would be required to make a porous material suitable to use at ambient temperatures, as is required for a practical hydrogen storage system. A large apparent surface area and accessible pore volume are required for an adsorbent to achieve high hydrogen storage densities. The findings in this investigation suggest that there is a trade-off between gas sorption capacity and enthalpy of adsorption where dispersive van der Waals interactions dominate adsorption. It is unlikely that the optimal enthalpy of adsorption will be achieved by simply reducing the pore size of the material.

Acknowledgments

Firstly I would like to thank Dr. David Book for his supervision over the course of my PhD studies. He has been an enormous help and has always been available with lots of enthusiastic ideas. The help I received from Dr. Allan Walton in teaching me how to use the lab equipment (especially the Intelligent Gravimetric Analyser - IGA), and also with constructive comments and criticisms has also been extremely useful.

I would like to thank the other members of the Hydrogen Materials Group, especially Dr. Dan Reed for help with equipment in the Hydrogen lab. Dr. Phil Chater for help with many things, but in particular the XRD analysis and crystallographic drawing programs, Chekcell and Vesta. Thanks to Dr. Rupert Millard, without whom the Virial analysis may never have happened.

Thanks to Professor Neil B. McKeown, Dr. Bader S. Ghanem and Dr. Kadhum J. Msayib and the rest of McKeown research group down at the University of Cardiff for spending long hours in the lab synthesising organic polymers. Thanks to Professor Peter M. Budd and Nhamo Chaukura at the University of Manchester for their help and especially their work on pore size measurements.

Thanks to Dr. Darren Broom for always replying to my continuous stream of questions via email, and for the immensely helpful discussions and advice throughout my PhD.

The support of my family; my mother, father and older brother Mark, has been invaluable in helping me to complete my studies. I would also like to acknowledge the support and love of Rachel, whom has put up with my endless moaning about my PhD and who has spent so much time waiting for me to finish.

Lastly, without the support of funding from the EPSRC it would not have been possible for me to even contemplate doing further study after my undergraduate degree, so I would like to thank them for providing the means.

Table of Contents

Chapter 1

THE HYDROGEN ECONOMY

1.1. Introduction

The need for an alternative to fossil fuels is escalating due to the increasing problem of global warming and climate change; not to mention worries over energy security and adverse health effects. Little more than a decade ago, many scientists still put climate change down to conjecture; however current consequences of anthropogenic climate change are already being observed. Most notable are the disappearance of the Arctic ice and glaciers, increased forest fires, heat waves that are being observed by Europeans and recent vast flooding across the world.

1.2. The Hydrogen Energy System

A new Hydrogen Economy presents a clear and comprehensive case for moving the world away from the destructive nature of the fossil fuel era and toward a new energy regime. Hydrogen is merely an energy carrier, but has the potential to replace fossil fuels[1] as it can be produced renewably and used without increasing greenhouse gas emissions. However, several challenges have to be overcome before a Hydrogen Economy can become a reality, namely production, storage, delivery, and utilisation. A simple schematic of how a hydrogen life cycle might look (based upon a renewable source of energy) is displayed in Figure 1.1.

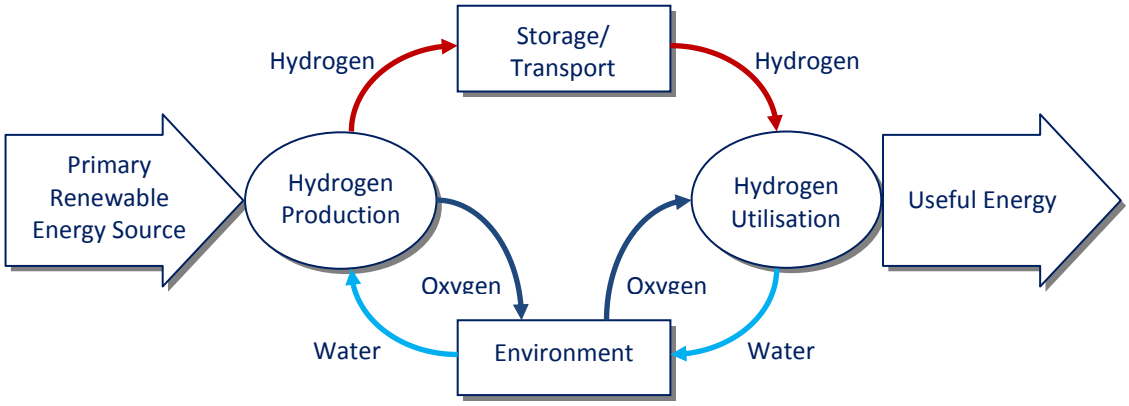

Figure 1.1 - Hydrogen life cycle from a renewable energy source.[2]

1.2.1. Hydrogen Production

Hydrogen is the most abundant element in the universe, however, on Earth it almost always exists as a compound. Most of the hydrogen produced today is manufactured by the cracking of hydrocarbons, steam reforming of natural gas, or the partial oxidation of light hydrocarbons, which produce greenhouse gases.[3] It is possible to produce hydrogen by electrolysing water without producing CO_2 but a renewable source of energy is required, such as wind or solar energy for a zero carbon footprint. The process is also still relatively expensive. Biological production is also an attractive method, as biomass is deemed to be a renewable energy source. Biomass such as agricultural waste contains a significant amount of hydrogen that can be harvested.

1.2.1.1. Primary Fuels

Hydrogen can be steam reformed (or extracted) from natural gas or other light hydrocarbons. The process involves two endothermic steps to make four parts hydrogen from one part methane and two parts water. The first stage is performed at 850 °C and 35 bar with the aid of a catalyst. The second stage can be split in to two steps; which occur at 350 and 200 °C, respectively.[4]

Stage 1: $$CH_4 + H_2O \rightarrow 3\,H_2 + CO \quad (1.1)$$

Stage 2: $$CO + H_2O \rightarrow H_2 + CO_2 \quad (1.2)$$

A relatively inexpensive and efficient process, this can be made more efficient if the waste heat were to be harvested.[2] The latest report from the United States DOE indicates that the process is *ca.* 70% efficient, based on the lower heating value (LHV) of hydrogen.[5] Producing hydrogen from primary fuels has one main disadvantage; the carbon contained in the fossil fuel will be released to the atmosphere as CO_2. Although, the carbon dioxide could be removed through carbon-sequestration.[6] Natural gas is not the ultimate answer to a new hydrogen economy as it is a finite resource, but could well be a transitional solution.

1.2.1.2. Electrolysis

In 1874, Jules Verne, recognised the finite supply of coal and suggested that "water will be the coal of the future" as could hydrogen be produced by the electrolysis of water.[7]

$$H_2O \rightarrow H_2 + \tfrac{1}{2} O_2 \qquad (1.3)$$

Water is extremely abundant and in virtually infinite supply. The cleavage of water into its constituent molecules is endothermic, and in order to produce significant amounts of hydrogen a relatively large amount of energy is required. Current low-temperature electrolysis systems are *ca*. 62% efficient, based on the LHV of hydrogen.[5,8] Ideally, the energy source will be abundant in supply and also environmentally friendly. By coupling a renewable energy source (like solar or wind) to an electrolyser, it is possible to produce and store hydrogen, which can then be used to compensate for the intermittency of the electricity supply. Hydrogen could be stored when there is less energy demand and utilised when the energy demand is greater than the renewable energy source can supply.[9]

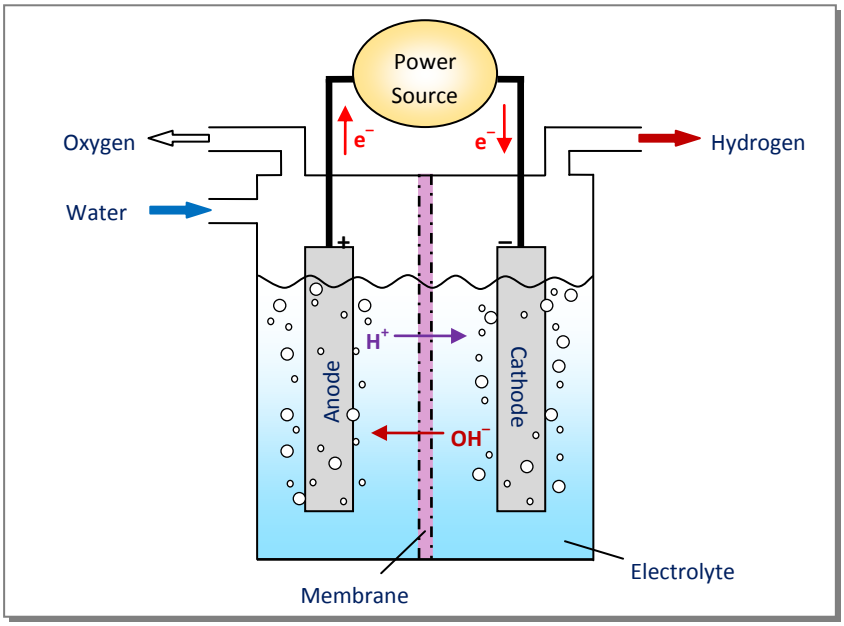

Figure 1.2 - Schematic of a typical electrolysis cell.

1.2.1.3. Biological Production

Most biomass sources like wood chip and agricultural waste contain significant quantities of hydrogen. Gasification is the heating of organic materials when heated (around 700 °C) in a controlled atmosphere;

the biomass can be converted to a synthetic gas which consists primarily of carbon monoxide, carbon dioxide and hydrogen. As a renewable resource, biomass has the advantage of being of low environmental impact in comparison to fossil fuels. On a large scale, gasification of biomass is an attractive option since useful by-products such as ethanol and acetate are also produced.[10] However, the United States Department of Energy (DOE) report that the cost of producing hydrogen by direct gasification of lignocellulosic biomass is about 3 times more than using steam reformation of natural gas.[4,11] Additionally the hydrogen content of lignocellulosic biomass is only 6 to 6.5 wt.%, compared to almost 25 wt.% in natural gas.[12] The process also has a relatively low efficiency, *ca*. 35% based on the lower heating value (LHV) of hydrogen.[5]

Other biological processes involve fermentation and photosynthesis.[13] However, the biological production of hydrogen does have a significant drawback as it has a particularly low yield.

1.2.2. Hydrogen Distribution and Delivery

1.2.2.1. Onsite

With the onsite production of hydrogen, no major distribution or delivery problems need to be considered; it can be stored as a compressed gas, a liquid or within a solid-state storage material at the point of production. Gaseous hydrogen can then be distributed to the point of use via a pipeline.

1.2.2.2. National Infrastructure

Most developed countries like the United Kingdom rely on an infrastructure of pipelines for natural gas in order to heat homes and cook meals. Hydrogen could also be transported using pipelines from the place of production to the place of use. New hydrogen pipelines are made from steel. To avoid problems with hydrogen embrittlement, the steel contains low amounts of carbon and manganese, *ca*. 1 to 1.2 and 0.2 wt.%, respectively. These low concentrations affect the yield strength (< 290 MPa) of the steel and consequently restrict the operating pressure to < 100 bar, with typical pressures of 40 to 60 bar being used. However, research into fibre-reinforced polymer steel pipelines suggests that pressures of 70 to 250 bar could be used as they are impermeable to hydrogen.[14]

In some countries, namely, the United States, Germany, Italy and Japan, industries use a network of pipelines to distribute hydrogen.[10] Moreover, a site in Teesside, in the North East of England produced up to 100,000 tonnes of hydrogen in 2005 and operated a twenty-one mile pipeline, in addition to storing hydrogen underground in salt caverns.[14,15]

Currently in the U.K., the majority of hydrogen is distributed in a compressed gaseous form by cylinders as there are no hydrogen liquefaction plants in the U.K.[14] In other countries, hydrogen is also transported by large pressure vessels and in liquefied form by tankers and pipelines. To ease the technical and logistical problems of changing over to a hydrogen economy, it could be possible to adapt the existing network of natural gas pipelines to distribute a mixture of hydrogen and natural gas, followed by the separation of hydrogen.[5,14]

1.2.3. Hydrogen Utilisation

The energy carried by hydrogen is typically utilised using one of two methods. Hydrogen can be burnt in an internal combustion engine to produce kinetic energy or used in a fuel cell to produce electricity.

1.2.3.1. Combustion

Like many other fuels, hydrogen can be burned, in a simple oxidation reaction with the production of water. However, small amounts of unwanted by-products such as nitrous oxides can also be formed. The amount of NO_x formed depends upon: the air to fuel ratio, the engine compression ratio, the engine speed, the ignition timing and whether thermal dilution is utilised. Slight amounts of carbon monoxide or carbon dioxide can also form if traces of oil seep into the combustion chamber. Hydrogen internal combustion engines are typically designed to operate at elevated air to fuel ratios in order to reduce the amount of NO_x produced in the exhaust gas stream. As with traditional petrol engines, the efficiency of transforming chemical energy, through thermal energy, and into kinetic energy is limited by the Carnot efficiency.[16] Current petrol engines can be converted to run on hydrogen by injecting hydrogen through a specialised spark plug. However, this is not deemed to be a sustainable solution due to the energy inefficiencies associated with current petrol engines.[17]

1.2.3.2. Fuel Cells

A fuel cell combines hydrogen with oxygen from the air with the only by-product being water. Fuel cells use the reverse electrochemical reaction to the electrolysis of water. Oxygen (from the air) can be recombined with hydrogen to produce water and electricity. There are many different types of fuels cells, which are categorised by the type of electrolyte used and the operating temperature. The fuel cells used for on-board vehicular use will most likely be the proton exchange membrane (PEM) fuel cell, which has undergone significant developments in recent years. A schematic of a PEM fuel cell is shown in Figure 1.3. In PEM fuel cells, hydrogen is delivered to the anode, where it is split into protons and electrons. The electrons flow around the circuit, providing electricity, whilst the protons travel across a polymer membrane to the cathode. At the cathode, an intake of air provides oxygen, which recombines with the protons and electrons to produce water. These are the most common type of fuel cells and have a relatively low operating temperature of 50 to 80 °C with an efficiency of *ca*. 60%.[16] However, if some of the waste heat is re-used, the efficiency can be as high as 80%. PEM fuel cells typically operate at between 1 and 3 bar.[5,14,18]

Unfortunately, PEM fuel cells are poisoned by impurities such as carbon monoxide. Vehicles require several fuel cells combined in a stack in order for them to be able to produce enough electricity to power an electric motor. Several challenges still remain in this area including, cost reduction (precious metals are used on the membranes), reliability and poisoning resistance. Unlike the combustion process, the efficiency of the electrochemical process can be as high as 60% as it is not limited by the Carnot efficiency.[16]

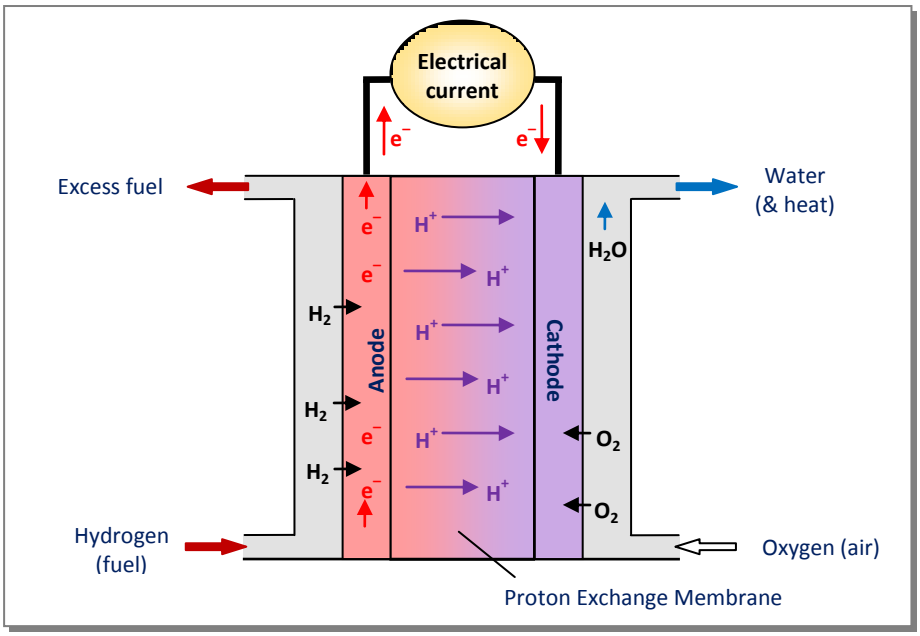

Figure 1.3 - Schematic of a PEM fuel cell.

1.2.4. Hydrogen Storage

One of the biggest issues with hydrogen is its storage for mobile applications. Hydrogen is the lightest and smallest element and confining hydrogen in to a small space is very difficult. At room temperature and atmospheric pressure, 1 kg of hydrogen gas occupies a volume of 11 m^3. Therefore the problem of hydrogen storage is essentially one of gas compression. There are in fact several ways in which this can be performed, including gas compression, liquefaction of hydrogen, or storage within solid-state materials. The latter involves the repulsion of the hydrogen molecules by interaction with another material by physical or chemical means.[3] This work concentrates on the storage of molecular hydrogen within the structure of microporous materials.

Chapter 2

OVERVIEW OF HYDROGEN STORAGE

2.1. Introduction

Hydrogen storage has been identified as one of the key barriers to a hydrogen economy. The storage solution must be economical, secure, safe and convenient. Designers of a practical hydrogen storage system would need to consider volume, weight, safety and cost as well as the reversibility of uptake and release rate of hydrogen to and from the system.

The requirements for hydrogen storage systems differ depending upon the end use. For instance, for mobile applications, such as vehicles, a lightweight system is critical. However, for large stationary application, such as filling stations, the weight of the system is not so important. The United States DOE has set targets for on-board hydrogen storage systems for light-duty vehicles such as cars and small trucks. For these targets, there are two important hydrogen energy density properties; gravimetric density and volumetric density. For the gravimetric storage density of a material, the weight percent capacity (wt.%) is the most frequently quoted quantity. The weight percentage of an adsorbed gas, is the total weight of the system, including the weight of the gas. At this point it is also important to note that the gravimetric target is that for the complete storage system (i.e. inclusive of the weight of any container that will hold the solid-state hydrogen storage material, any valves, regulators, piping, mounting brackets, insulation, added cooling, and/or other components).

Table 2.1 shows several different targets for hydrogen storage systems. In 2009, the United States DOE reviewed their targets with consideration to the current results of worldwide scientific research. The consequence of the review was to reduce the targets to a more realistic level.

All of the targets in Table 2.1 are set for a vehicle range greater than 300 miles (483 km); they are based on the lower heating value of hydrogen; and unless otherwise stated, they are for both fuel cells and internal combustion engines.

Table 2.1 - U.S. Department of Energy hydrogen storage system targets.[19,20]

Target	Units	2007	2010 (old)	2010 (new)	2015 (old)	2015 (new)	ultimate
System gravimetric density	[wt.%] (kWh kg^{-1})	[4.5] (1.5)	[6.0] (2.0)	[4.5] (1.5)	[9.0] (3.0)	[5.5] (1.8)	[7.5] (2.5)
System volumetric density	[kg m^{-3}] (kWh L^{-1})	[36] (1.2)	[45] (1.5)	[28] (0.9)	[81] (2.7)	[40] (1.3)	[70] (2.3)
System filling time (5 kg)	[minute] (kg H_2 $minute^{-1}$)	[10] (0.5)	[3] (1.66)	[4.2] (1.2)	[2.5] (2.0)	[3.3] (1.5)	[2.5] (2.0)
System cost	[$/kg$H_2$] ($kWh$_{net}$)	[200] (6.0)	[133] (4.0)	TBD	[67] (2.0)	TBD	TBD
Delivery Pressure, minimum acceptable, [FC][a], (ICE)[b]	bar absolute	[8] (10)	[4] (35)	[4] (35)	[3] (35)	[3] (35)	[3] (35)

[a] FC = Fuel Cell, [b] ICE = Internal Combustion Engine.

For hydride materials, the volumetric storage density is based upon the number of hydrogen atoms that can be accommodated per unit volume in the host structure.[21] However, an adsorbent has to take into account the volume occupied by the solid, as well as the pore volume (the volume that would be occupied by hydrogen gas if there were no gas-solid interactions) and the excess adsorption. For stationary applications the gravimetric and volumetric storage density is less important than for mobile applications. Figure 2.1 demonstrates the volume occupied by several common hydrogen storage methods in comparison to the size of a hatchback car. The same weight of gaseous hydrogen at room temperature and pressure would occupy almost 45,000 litres; equivalent to a balloon around 4.4 metres in diameter.[17]

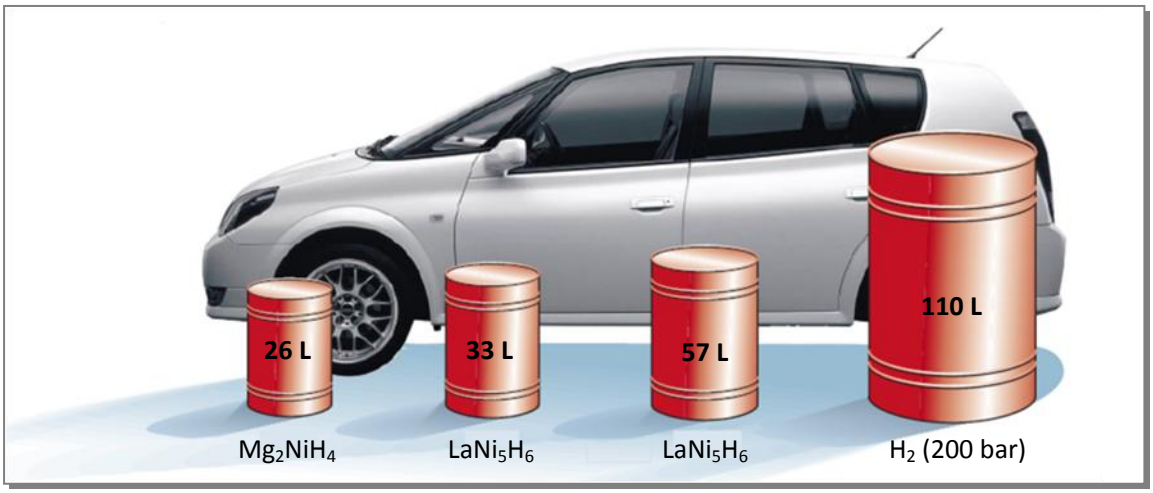

Figure 2.1 - Volume of 4 kg of hydrogen in different storage mediums, with size relative to a car.[16]

Table 2.1 contains targets for system cost which were based on the value of the U.S.$ in 2003. The target refers to the total projected cost for the whole on-board hydrogen storage system, including all hardware and storage media, along with the cost of any replacement part of the system within 15 years or 150,000 miles. Currently, these targets are being reviewed by the United States DOE and are still to be decided upon. However, whilst it is believed that a vehicle fuelled by hydrogen may not become as low cost as current commercial vehicles, social benefits and increased efficiencies are hoped to justify the targets. Any new hydrogen storage technology should be affordable and have low maintenance costs throughout the span of the system lifetime. The targets for system filling are based upon 5 kg of hydrogen. With respect to solid-state materials the target refers to rehydriding. Therefore requiring a material with fast kinetics. Ideally, the system should also work at (least close to) ambient temperatures whilst operating at the required delivery pressures. It also stands to reason that a new on-board hydrogen technology would need to fulfil strict safety criteria with regard to collisions including penetration and punctures of storage tanks.

2.2. Storage Methods

There are several ways in which hydrogen can be stored; each method has its own advantages and disadvantages. In 2004, Züttel[3] described six main categories for hydrogen storage (see Table 2.2); the first two use conventional hydrogen storage techniques, the third process is a type of hydrogen generation and the last three are solid-state hydrogen storage techniques.

The conventional hydrogen storage methods have distinct disadvantages; as both methods require a significant energy input and have serious safety implications. Figure 2.2 shows the volumetric and gravimetric densities of some solid-state storage materials alongside the conventional storage methods.

Table 2.2 - Comparison of the gravimetric density, ρ_m, volumetric density, ρ_v, operating temperature, T, and pressure, p, for the six basic hydrogen storage methods.[3,22,23]

Storage Method	ρ_m (wt.%)	ρ_v (kg H_2 m^{-3})	T (°C)	p (bar)	Advantages / Disadvantages
Compressed hydrogen	13	<40	25	350-800	Extreme pressures
Liquid hydrogen	tank size dependent	70.8	-252	1	Extreme temperatures and problem of "boil-off"
Chemical reaction with water	<40	>150	25	1	Complicated and directly reversible
Metal hydrides - chemisorption	<7	150	<300	1	Low wt.% values due to heavy metals (e.g. $LaNi_5$)
Complex hydrides	<18	150	<650	1 for desorption & 350 for sorption	Desorption needs elevated temperature. Sorption needs high pressures, in excess of 80 bar (e.g. $NaBH_4$)
Adsorbed hydrogen - physisorption	1-8	20	-80	100	Fully reversible but low temperature

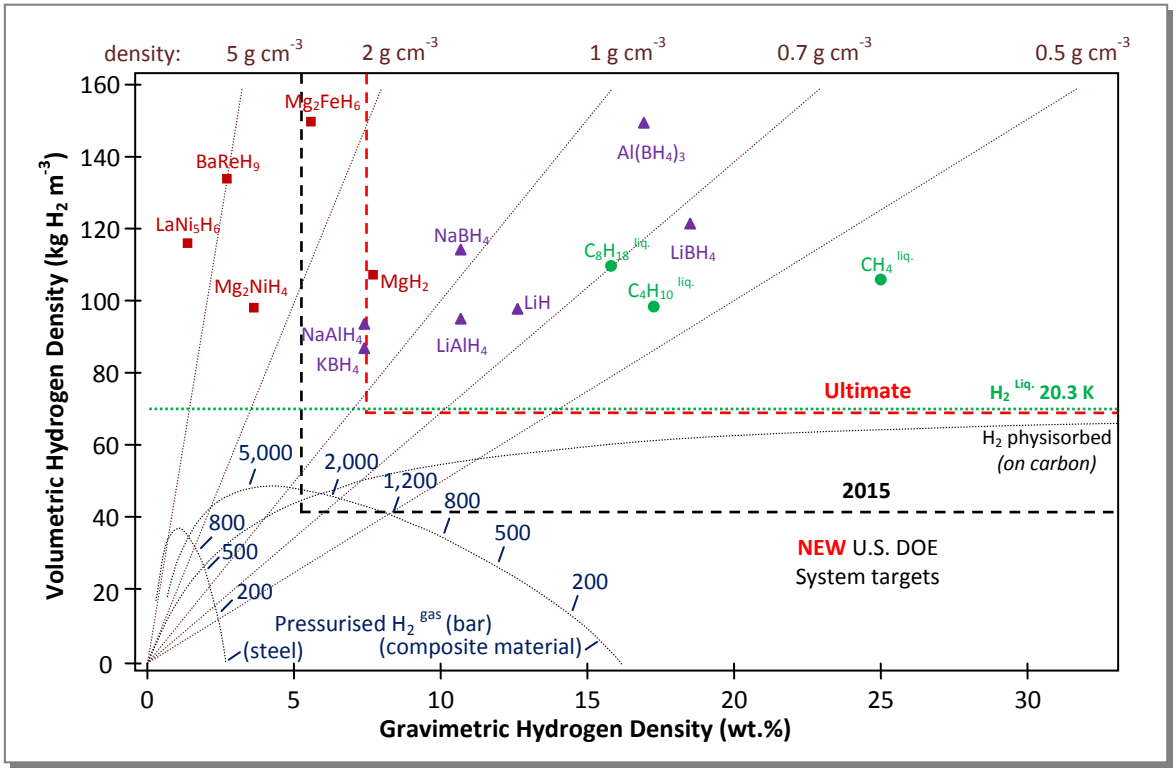

Figure 2.2 - Volumetric and gravimetric hydrogen density of some selected hydrogen storage materials. Modified from reference [22].

2.2.1. Conventional Hydrogen Storage

2.2.1.1. Compressed Hydrogen

Compressed gas is currently the most common form of hydrogen storage.[22] Typically, cylinders are made from steel and used at an operating pressure of 200 bar. They are limited to approximately 350 bar. However, lightweight composite cylinders have operating pressures up to 800 bar, where hydrogen has a volumetric density of 36 kg m^{-3}, approximately half that of liquid hydrogen (at its boiling point). Figure 2.2 illustrates the differences in energy density that can be achieved by using a lightweight composite material instead of steel.

Storage tank materials need to have very high tensile strength, a low density and must not react with hydrogen or allow hydrogen to diffuse in to it. The amount of energy used to compress hydrogen gas depends on what pressure it is being compressed from and to, as well as the method using for the gas compression. The ideal (isothermal) compression of hydrogen from 1 to 800 bar requires 2.21 kWh kg^{-1} of energy, which is *ca*. 5% of the energy content in hydrogen.[22,24] In a real process, the work consumption is significantly higher because compression is not isothermal. In fact, adiabatic compression requires over 16% of the energy content in hydrogen.[22,24]

2.2.1.2. Liquid Hydrogen

Liquid hydrogen must be stored below its low critical temperature (33 K) and pressure (13 bar); typically it is stored at its boiling point (20.3 K).[3,25] The volumetric density of liquid hydrogen is almost twice that of compressed hydrogen gas at 70.8 kg m^{-3}.

Significant disadvantages of storing hydrogen as a liquid are boil-off and the relatively large amount of energy required for the liquefaction. The liquefaction process typically requires 30% of the lower heating value.[5] However, boil-off losses are reduced when large-scale storage vessels are used due to the small surface-to-volume ratio, as the evaporation rate decreases as the size of the storage tank increases.[22,26]

2.2.1.3. Storage via Chemical Reaction with Water

Hydrogen can be generated as a result of the reaction of metals and chemical compounds with water. The most common experiment, seen in many chemistry classes, is the reaction between sodium metal and water, where the surface of the floating sodium reacts to produce hydrogen gas and sodium hydroxide. The reaction is not easily reversible, but metallic sodium can be formed by reducing NaOH in a solar furnace. The hydrogen produced reacts with oxygen in the furnace to produce water, which is then recycled to generate more hydrogen gas. This gives sodium a gravimetric density of 3.0 wt.% and if lithium is used in the same process, it has a gravimetric density of 6.3 wt.%.[3] The reversibility of these reactions is however a problem, particularly in controlling the thermal reduction of the compound back to the original metal.[22]

2.2.2. Solid-State Storage

Solid-state storage has become a large research field with vast numbers of materials under investigation. No material currently meets all of the targets set out by the United States DOE for mobile storage systems. Reactivity and the temperature either for significant hydrogen release or hydrogen sorption are two distinct problems. However even those materials that do not suffer from either or both of those problems simply has an inadequate hydrogen storage capacity. Figure 2.3 displays the observed hydrogen storage capacities for some well-known materials as a function of the temperature for significant hydrogen release and hydrogen sorption. The newly revised United States DOE systems targets are indicated by the dashed area.

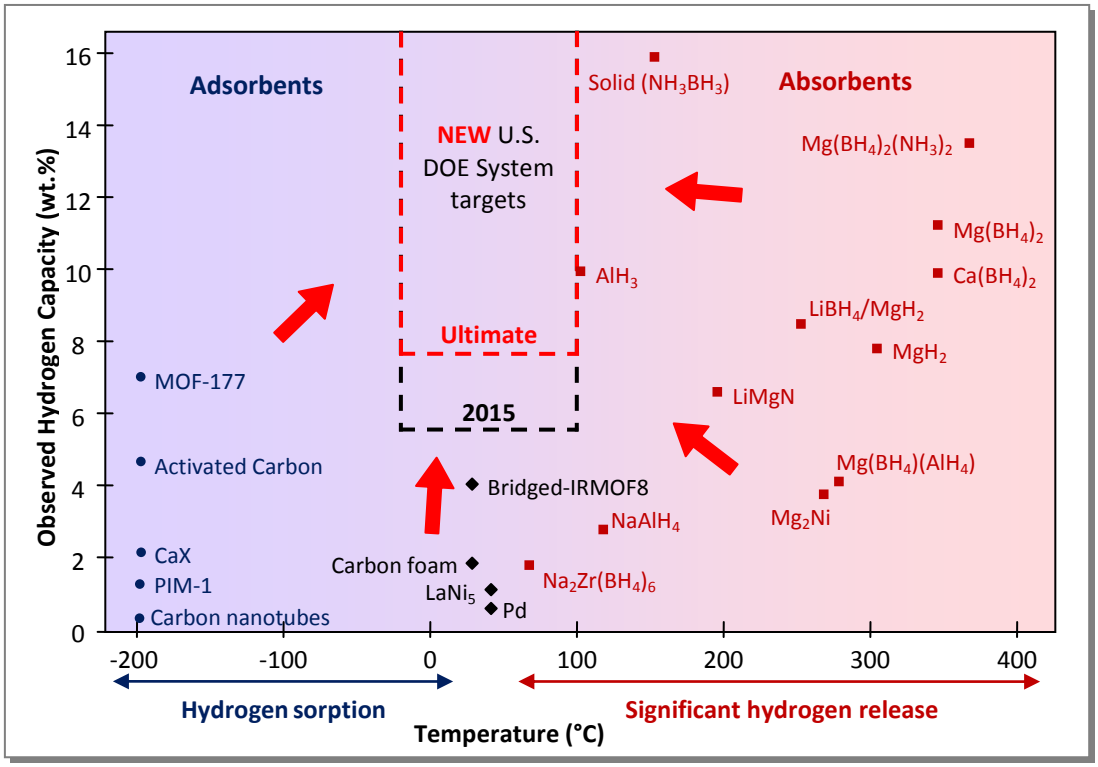

Figure 2.3 - Observed hydrogen storage capacity against temperature for some solid-state hydrogen materials. Modified from reference [20].

2.2.2.4. Chemical Storage

2.2.2.4.1. Metal Hydrides

Hydrogen reacts with metals and their alloys to form hydrides (typically at elevated temperatures). Molecular hydrogen is initially physisorbed onto the surface of the metal. The hydrogen molecule then dissociates, allowing atomic hydrogen to migrate across the surface. Diffusion into local interstitial sites creates a solid-solution (α-phase). The enthalpy of solution becomes negative with increasing hydrogen pressure/concentration. The formation of the α-phase therefore becomes increasingly exothermic. Eventually it becomes more energetically favourable for the hydrogen to be concentrated locally in comparison to being randomly distributed throughout the metal, therefore the nucleation and growth of the β-phase occurs. The two phases co-exist until the increasing hydrogen concentration results in a complete transformation from the α-phase to the β-phase. The process is illustrated in Figure 2.4.

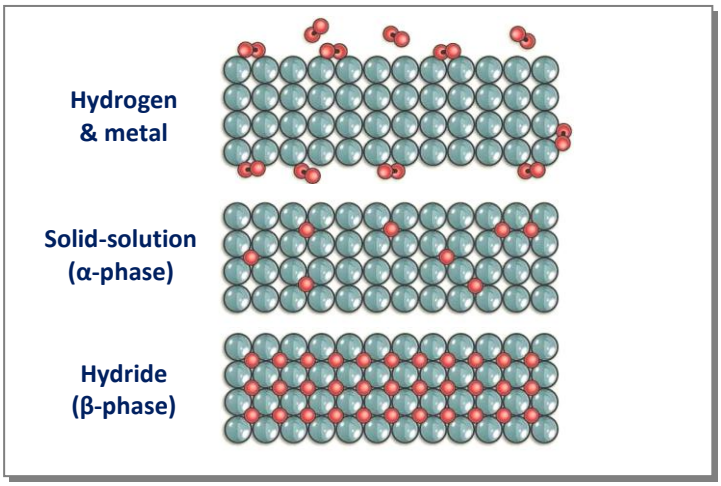

Figure 2.4 - Illustration of the interaction of hydrogen gas with a metal at different stages of the conversion to a metal hydride.[17]

The hydrogen storage properties of metal hydrides can be derived from pressure-composition isotherms (PCT curves). A PCT curve is a measure of equilibrium pressure against hydrogen concentration of a closed system (at a constant temperature). Initially only the α-phase forms and the hydrogen concentration increases as the equilibrium pressure increases. As the hydrogen atoms diffuse through the metal, forming the β-phase, the hydrogen concentration continues to rise, however a plateau is observed in the equilibrium pressure. Here the α- and β-phases are in co-existence. The plateau continues until the transformation from the α-phase to the β-phase is complete. For some systems it is possible to reach additional plateaus at even higher hydrogen pressures. Figure 2.5 shows an arbitrary (ideal) PCT curve of a metal hydride system. It also shows that the plateau occurs at higher pressures with greater temperatures. In fact, the plateau pressure is strongly dependant up on temperature and is related to the change in both enthalpy and entropy.

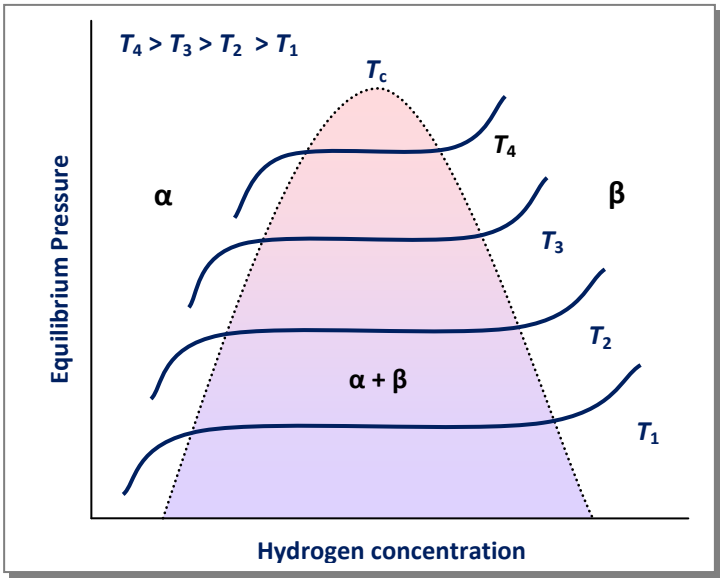

Figure 2.5 - Arbitrary ideal pressure-composition isotherms of a metal hydride system showing the phases that occur during the formation of the hydride.[16]

Many of these compounds exist in multiphase systems and show relatively large deviations from their ideal stoichiometry (MH_n, n = 1, 2, 3). Alloys containing various ratios of metals to hydrogen have been intensely investigated. The alloys usually contain an element with a high affinity for hydrogen (denoted as the A metal) and an element with a low affinity of hydrogen (denoted as the B metal). The former is capable of forming a stable binary hydride, whereas the latter is not; however it helps catalyse the dissociation of hydrogen.[22] Element A is typically a transition, rare-earth or alkaline-earth metal such as La, Ti, Zr, and Mg with the B element being different combinations of 3d atoms, namely, V, Cr, Mn and Fe. The discovery of hydrogen absorption by $LaNi_5$[27] and FeTi[28] and their alloys have relatively large volumetric storage capacities, however, their low gravimetric capacities (*ca*. 2 wt.%) meant they were not suitable for on-board automotive applications.[29] Nevertheless, metal hydrides have been used for stationary and marine applications such as boats and submarines.[30] In both instances the weight is not a problem. In fact in the latter, the weight is actually an advantage, where the initial ballast is removed and the metal hydride is positioned in its place.

Magnesium shows considerable potential as an on-board hydrogen storage material due to its low cost, good reversibility during cycling and its theoretical maximum storage capacity of 7.66 wt.%. It also has a

low plateau pressure of around 1 bar.[31] However, the operating temperature is too high for an on-board PEM fuel cell (which is around 80 °C). MgH_2 has a high enthalpy of formation (76 kJ mol^{-1}) which makes it typical high temperature metal hydride, with a desorption temperature of 300 °C. The thermodynamics of the Mg/MgH_2 system can be altered by alloying with other elements such as Ni. However this affects the storage capacity as the Ni is non-hydriding. Extensive research has been undertaken to try to improve the hydrogen storage kinetics for absorbing and desorbing hydrogen in magnesium hydrides. High velocity ball milling significantly increases the sorption kinetics by reducing the particle size and hence increasing the accessible surface area. Catalysts such as, V_2O_5 or NbO_5 have been found to reduce the charging time to less than two minutes by dissociating hydrogen at the surface at 250 °C.[32,33]

2.2.2.4.2. Complex Hydrides

Complex hydrides typically involve light-weight elements from Groups 1, 2 and 3 of the Periodic Table. They differ from metal hydrides as they form ionic or covalent compounds upon hydrogen absorption. Tetrahedral complex anions such as $[BH_4]^-$ and $[AlH_4]^-$ are often formed with cations such as B or Na.

Complex hydrides release and absorb hydrogen through a series of decomposition and recombination reactions. Some have shown extremely high volumetric and gravimetric hydrogen densities, $LiBH_4$ has the highest (18.5 wt.%).[34] However, the mechanism is not directly reversible. $LiBH_4$ desorbs three of the four hydrogen atoms up on melting at 280 °C and decomposes in to LiH and B, see equation (2.1).[23] This represents a gravimetric hydrogen storage capacity of 13.8 wt.%, and has an enthalpy of reaction of 67 kJ mol^{-1}.[35]

$$LiBH_4 \rightarrow LiH + B + 1\frac{1}{2}\,H_2 \quad (13.8\ \text{wt.\%}) \qquad (2.1)$$

A significant disadvantage is the extreme temperature and pressure required for the recombination of $LiBH_4$ from the elements (600 °C and 350 bar).[36] Another disadvantage for the borohydride systems stems from the volatility of borane, which is often produced upon decomposition as well as hydrogen, causing significant reductions in storage capabilities.

Despite the problems associated with the boron hydrides as previously mentioned, their high hydrogen content means that they are still being vigorously investigated. The addition of MgH_2 (including 2 to 3 mol% $TiCl_3$) to $LiBH_4$ enabled the system to reversibly store 8 to 10 wt.% hydrogen at temperatures of 315 to 400 °C.[35] In this process the $LiBH_4$ is be destabilised by the formation of MgB_2, which also stabilises the dehydrogenated state,[35] however the process has slow kinetics.[31]

The decomposition of $NaAlH_4$ occurs in three steps. The first two provide a reversible hydrogen content of 5.6 wt.% at 60 °C and 20 bar (see equations (2.2) and (2.3)).[22,37,38] The third step increases the hydrogen capacity to 7.6 wt.%, however this requires 270 °C and *ca*. 150 bar.[22,39]

$$3\ NaAlH_4 \rightarrow Na_3AlH_6 + 2\ Al + 3\ H_2 \qquad (2.2)$$

$$Na_3AlH_6 \rightarrow 3\ NaH + Al + 1½\ H_2 \qquad (2.3)$$

Unfortunately the kinetics were relatively slow, although Bogdanovic *et al*. showed that this could be improved by Ti-doping.[37,38] High desorption temperatures are typical of the alanates, and this was also the case for $LiAlH_4$, which was capable of desorbing 10.5 wt.%.[38] However like $NaAlH_4$, the decomposition of $LiAlH_4$ occurs in the same three step process. The first two provide a reversible hydrogen content of 7.9 wt.% at 220 °C and atmospheric pressure.[40]

2.2.2.4.3. Hydrocarbons

It has long been known that hydrogen is stored in, and liberated from, hydrocarbons. The hydrogenation and dehydrogenation of cyclic hydrocarbons such as benzene/cyclohexane, toluene/methylcyclohexane, or naphthalene/decalin, have reasonably high storage capacities: cyclohexane, 7.1 wt.% and 55.5 kg m^{-3}; methylcyclohexane, 6.2 wt.% and 47.0 kg m^{-3}; and decalin, 7.2 wt.% and 64.9 kg m^{-3}. However, complete dehydrogenation requires high temperatures, *ca*. 300 °C, and re-hydrogenation of the aromatic hydrocarbon cannot be performed '*in-situ*'.[34,41]

Hydrogen can also be liberated from hydrocarbons by steam reformation (equation (2.4)) or partial oxidation ((equation (2.5)) or a combination of both, called autothermal reformation. These produce hydrogen in addition to carbon monoxide or carbon dioxide.

$$C_nH_{2n+2} + n\,H_2O \rightarrow n\,CO + (n+1)\,H_2 \quad (2.4)$$

$$C_nH_{2n+2} + n\,O_2 \rightarrow n\,CO_2 + (n+1)\,H_2 \quad (2.5)$$

Steam reformation produces higher efficiencies (70 to 80%) compared to autothermal reforming or partial oxidation (40 to 50%). However, it is more endothermic and therefore requires more heating to be supplied from an external source, which is a disadvantage. The steam reformation process also has long start-up times in comparison to partial oxidation.[34] Studies have shown that a combination of the three processes, steam reforming, autothermal reforming and then partial oxidation can increase fuel processing efficiencies.[42,43]

Methanol can be reformed at lower operating temperatures compared to other hydrocarbons (approximately 250 to 300 °C) with a higher hydrogen yield.[44] This lead to the development of fuel cell vehicles, such as the Necar III by Mercedes, which contains a methanol fuel processor for the hydrogen supply.[45] Methanol can also be injected directly in to a methanol fuel cell producing a less complicated system.[46]

2.2.2.5. Physical Storage

2.2.2.5.1. Physisorption

Physisorption is also known as physical adsorption; which is where a layer of gas, liquid or solid forms on a surface or within the pores of a solid material. It offers several advantages over chemical absorption of hydrogen, namely, fast kinetics and complete reversibility. This type of storage utilises the weak van der Waals interactions between hydrogen molecules and the surface of the material. Only a very small amount of energy (< 10 kJ mol^{-1}) is involved both in the adsorption and desorption of hydrogen. These low adsorption enthalpies means that low temperatures (*ca*. 80 K) and relatively high pressures (*ca*. 100 bar) are required for significant hydrogen uptake.

Relatively low density materials (for example metal-organic frameworks) can store more than 8 wt.%, although volumetric storage capacities are typically low (*ca*. 30 kg m^{-3}).[47] There are a large number of porous (high surface area) materials that have been investigated as potential hydrogen storage materials

including, carbon nanotubes, various types of carbons soot, activated carbons, zeolites, metal-organic frameworks (MOF) and porous polymers. These materials demonstrate relatively high internal (or external) surface area. They can be ordered (for example, zeolites and MOFs) or disordered structures (for example, activated carbons and porous polymers).

The theory of gas adsorption in porous materials is covered in Chapter 3. An introduction to hydrogen storage in porous materials will be discussed afterwards in Chapter 4.

2.3. Aims and Objectives

The overall aim of this work was to investigate the potential of microporous materials for hydrogen storage, with particular attention given to microporous polymers.

The first objective was to determine the accuracy of the gas sorption equipment as there have been many inaccurate reports of high hydrogen storage capacities. This was to be performed using a standard commercial microporous carbon material that was provided as part of a round-robin test by the E.C. Framework 6 NESSHY (Novel Efficient Solid Storage for Hydrogen) project. The results were compared to those found by other E.U. participants and a discussion of this is given in this report.

The enthalpy of hydrogen is a crucial property to calculate as this value indicates the strength of the adsorbate-adsorbent interaction and thus the temperature and pressure at which sorption occurs. There are several ways in which these measurements can be performed and in the way the data is interpreted. One of the aims of this thesis was to provide a review of some of these techniques.

The isosteric enthalpies of adsorption for hydrogen in porous materials are typically calculated using data generated for just two temperatures, 77 and 87 K. By using several temperatures it should be possible to more accurately calculate a value for the enthalpy of adsorption and provide vital information on the usable hydrogen capacity of the materials over a range of temperatures. One of the aims of this project was to compare the enthalpies of adsorption calculated using two temperatures (77 and 87 K) to those generated at several temperatures between 77 and 137 K. A newly developed liquid nitrogen cryostat was

installed during this project and used to measure pressure composition isotherms over this temperature range for several well known porous materials including activated carbons, zeolites and MOFs.

As the pressure composition isotherms are not measured at perfectly spaced intervals of hydrogen uptake, it is necessary to either fit the experimental isotherm to a function or attempt to interpolate the appropriate value of hydrogen uptake between the data points. An aim of this work was to compare some of the available techniques used to fit hydrogen isotherms; and a discussion of the findings is presented in this thesis.

Porous polymers offer an attractive combination of properties which may make them suitable as hydrogen storage materials including; low intrinsic density (as they are only composed of light elements such as C, H, N, O, and do not include metal ions), chemical homogeneity and thin pore walls. The Polymers of Intrinsic Microporosity (PIMs) used in this project were synthesised at the University of Cardiff as part of a joint EPSRC project (EP/D074312/1) on polymer-based hydrogen storage materials. One of the aims of this project was to fully characterise the gas sorption properties of these novel materials. A series of microporous polymers were synthesised with the aim of maximising the available surface area, whilst optimising the pore size to increase the enthalpy of adsorption.

This report attempts to relate the hydrogen adsorption characteristics, such as the enthalpy of adsorption and usable capacity, for all the materials presented, to the physical properties of each material; for example, surface area and pore size. A discussion is presented on how the different materials may be more or less suitable for use in a practical storage system depending upon the working pressure and temperature of the device.

Chapter 3

GAS ADSORPTION BY POROUS MATERIALS

3.1. Introduction

It has long been known that solid materials can take up vast quantities of gas. Quantitative gas uptake was first reported in the 18th Century, when gas was expelled from charcoal upon heating and taken up again on cooling. It was also found that the amount of gas uptake was dependent upon the gas itself.[48] When a gas penetrates the structure of a solid the phenomenon is termed absorption. In contrast, when a gas condenses onto an available surface of a solid the term given is adsorption. Commonly used terminology relating to the gas and the solid are given to be the adsorbate and the adsorbent, respectively. This chapter outlines the mechanisms behind gas adsorption by porous materials.

3.2. Gas Adsorption

If a molecule approaches a solid surface, it experiences a mixture of both attractive and repulsive intermolecular forces; physisorption occurs once these forces become balanced. These dispersive interactions are caused by changes of the charge distributions. When there are molecules already adsorbed to the surface (or inside a pore), both the adsorbent-adsorbate and adsorbate-adsorbate interactions are involved. As more and more molecules become adsorbed to the surface, the adsorption energy becomes increasingly complicated.

On approaching the surface, the dispersive attractive interactions decrease with r^{-6}, and the short-range repulsion decreases with r^{-m}, where r is equal to distance and m is usually given the value 12. The total (Lennard-Jones) potential energy, ε, between two isolated atoms, is therefore represented by:

$$\varepsilon(r) = Br^{-12} - Cr^{-6} \qquad (3.1)$$

Where B is an empirical constant, and C is a constant which can be expressed in terms of the polarizabilities of the adsorptive and the adsorbent.[49] In order to apply these interactions to the

adsorption of a gas on a solid; the solid surface must be considered as individual atoms (or ions) and the gas as isolated gas molecules, this can then be summarised by equation (3.2).

$$\varphi_i(z) = \sum_j \varepsilon_{ij}\left(r_{ij}\right) \qquad (3.2)$$

Here, r_{ij} is the distance between the molecule, i in the gas phase and j is the centre of the atom. The potential energy, $\varphi_i(z)$ of the gas molecule is expressed as a function of distance. After the rapid decrease in potential energy with distance, a balance between attractive and repulsive forces is established at a point z_e.[50] Here the potential energy is at a minimum as represented in Figure 3.1.

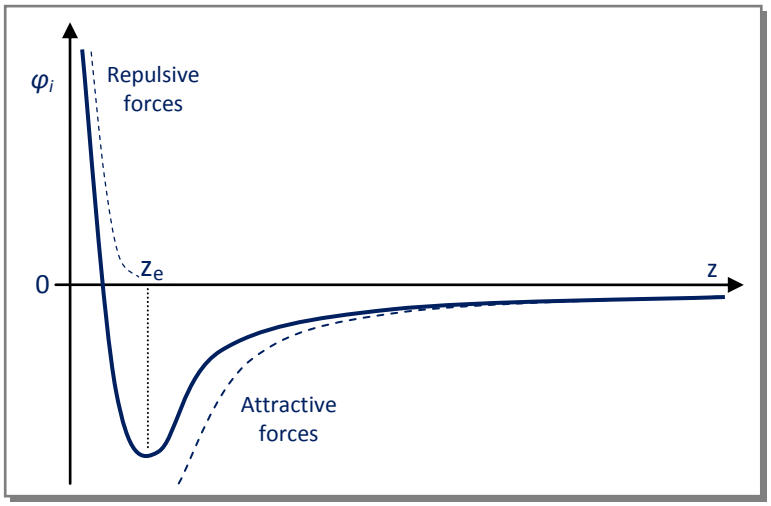

Figure 3.1 - Potential energy, φ_i, of a molecule versus its distance, z, from the adsorbing surface.[50]

In small pores the interaction energy is influenced by more than one plane surface. Though different materials have pores of various shapes and sizes, typically pores are either taken to be slit-shaped or cylindrical, in which case the pore width is a measure of the distance between the two sides and the diameter of the cylinder, respectively.[51,52] It was deduced that ratio between the size of the adsorbate molecule and pore size was the important parameter.[48,52] In Figure 3.2 (a), (b) and (c) refer to different values of the ratio d/r_0 for the slit-shaped pore; where d is the half-width of the slit and r_0 is the collision radius of the molecule.

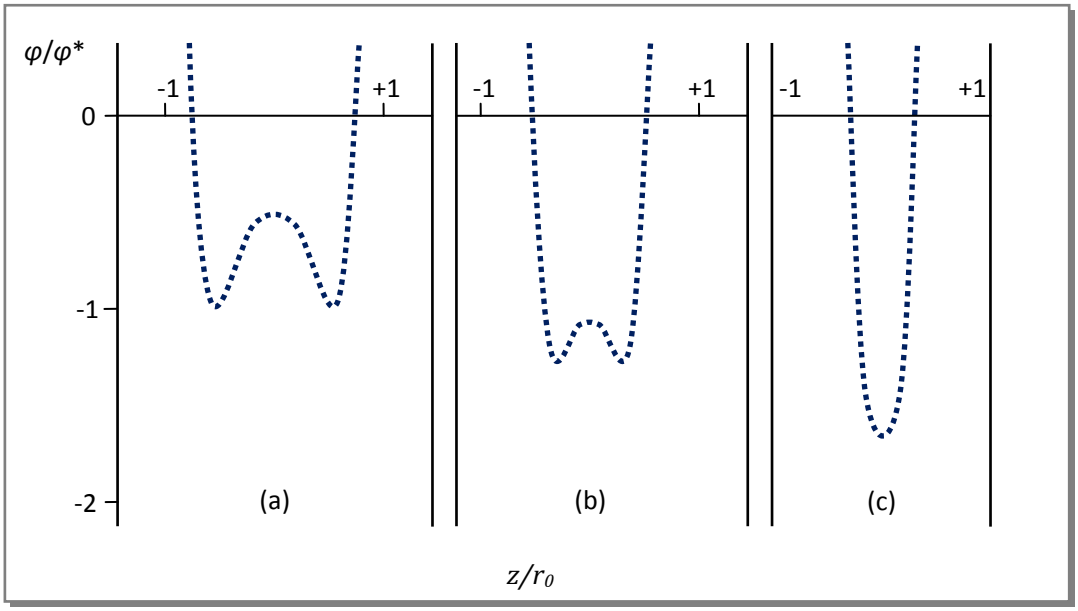

Figure 3.2 - Interaction potential of a molecule in a microporous material. Plot of φ/φ^* against z/r_0 for different values of d/r_0.[52]

The three curves show the interaction potential, φ of an adsorbate molecule with its distance from the middle of the slit (from within the pore). Here, φ^* is the interaction potential of a molecule with one plane surface, and it corresponds to the point of minimum energy z_e, as shown in Figure 3.1.[52] For smaller d/r_0 values the potential energy produces a single minima of increased depth and sharpened curvature, indicating an optimum pore width for adsorption in microporous materials, this is seen in (c) in Figure 3.2.[52,53]

The individual pores within any porous material may vary greatly in both size and shape. As mentioned above, the width, *w,* of a pore is of particular interest; this is the diameter in cylindrical pores and the distance between two sides in a slit-shaped pore. In 1960, Dubinin proposed that the porous materials could be classified according to their average pore width.[54] This pore size classification was based on the characteristic adsorption effects shown in each range. They were later adopted by the International Union of Pure and Applied Chemistry,[55] as shown in Table 3.1.

Table 3.1 - Classification of pores based on pore width, w.

Pore type	Pore width, *w*
Micropores	< 20 Å (2 nm)
Mesopores	20 to 500 Å (2 to 50 nm)
Macropores	> 500 Å (50 nm)

3.3. Adsorption Isotherm

The amount of gas taken up by a solid is dependent on the temperature, T the pressure, p of the gas, and the properties of the solid and gas themselves. If n is the quantity of the adsorbed gas, expressed in moles per gram of solid, then:

$$n = f(p, T, gas, solid) \tag{3.3}$$

For a given gas on a particular solid at a constant temperature, this becomes:

$$n = f(p)_{T,gas,solid} \tag{3.4}$$

By plotting the amount of gas adsorbed on an absorbent versus the pressure (or concentration) of a gas at fixed temperatures results in an adsorption isotherm. The International Union of Pure and Applied Chemistry (IUPAC) define six different types of isotherms, which can be seen in Figure 3.3. The first five types (I to V) of the classification were originally proposed by Brunauer, Deming, Deming and Teller, as the BDDT classification,[56] with type VI being later proposed by Sing *et al.*[48,57]

Type I isotherms are characteristic of physisorption of gases onto 'microporous' solids, whilst type II isotherms are characteristic of physisorption of gases onto 'non-porous' solids. Type IV isotherms are typical for mesoporous solids. An important characteristic is the increase in volume adsorbed at higher relative pressure (p/p_0) of the adsorbate as a result of the filling and emptying of pores by capillary condensation. Types III and IV may arise from the adsorption of either polar or non-polar molecules if the interaction between adsorbate and adsorbent is relatively weak. They are much less common than those of the other three types. Type VI isotherms occur as a result of layer-by-layer adsorption on well-defined, uniform solids.

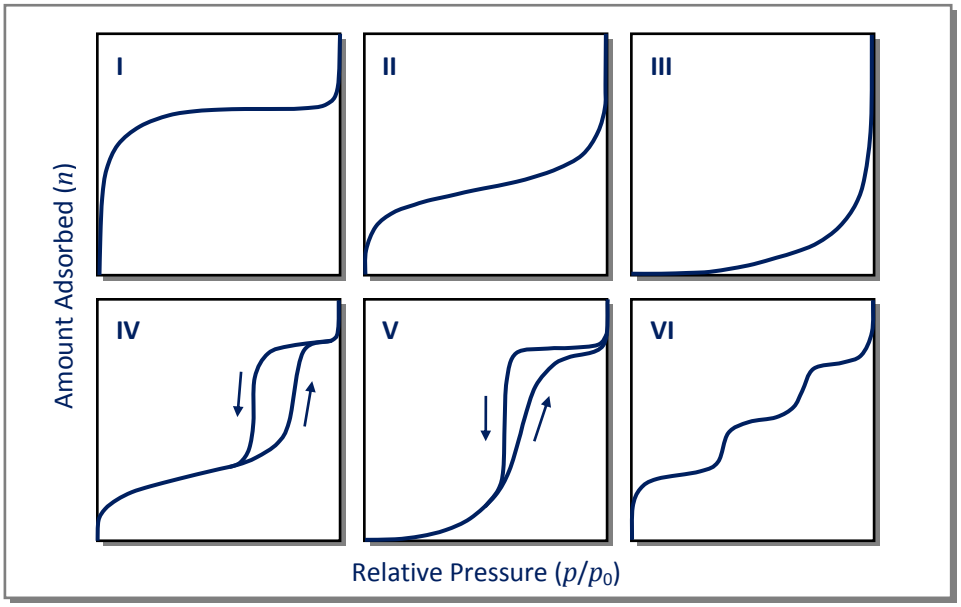

Figure 3.3 - The six main types of gas adsorption isotherms, according to the IUPAC classification.[50]

Type I isotherms display a steep initial increase (at low relative pressures) and approach a limiting value as $p/p_0 \rightarrow 1$, indicated by a horizontal plateau region, corresponding to complete surface coverage and micropore filling. The fraction of the surface covered is commonly expressed by, θ. A closer proximity of the side walls leads to a significantly greater interaction potential in microporous materials than those with wider pore systems; this is seen in isothermal measurements, in which the amount of an adsorbed gas is increased at a given relative pressure.[48]

3.3.1. Henry's Law

The simplest interpretation of adsorption isotherms stems from Henry's Law, which was originally formulated in 1803 by William Henry. It stated that the weight of a gas dissolved by a liquid is proportional to the pressure of the gas upon the liquid. From this came equation (3.5)

$$n = k_{\mathrm{H}} p \qquad (3.5)$$

where n is used to represent the amount of gas adsorbed, p is the equilibrium pressure and k_{H} is Henry's law constant.[58,59] With physisorption of gases on a solid surface, Henry's law is applicable at very low relative pressures, where adsorption increases linearly with increasing pressure. The equilibrium pressure up to which Henry's law applies depends on the gas, the temperature and the solid. This proportionality

enables the Henry's law constant to be determined by plotting ln(p/n) versus n, which should yield a straight line where n approaches zero. The intercept of such a plot can be designated ξ, which subsequently gives the Henry's law constant to be equal to exp($-\xi$).

$$k_{\mathrm{H}} = exp(-\xi) \tag{3.6}$$

Further research found that surface heterogeneity and microporosity lead to curvature of adsorption isotherms, even at very low pressures.[50] Henry's law constant, depends on the potential energy of adsorption, φ according to equation (3.7).

$$k_{\mathrm{H}} = \frac{V_{\mathrm{P}}}{RT} * \left[exp\left(-\frac{\varphi}{k_{\mathrm{B}}T}\right) - 1 \right] \tag{3.7}$$

where, V_p is the accessible pore volume.

3.3.2. Freundlich

The Freundlich isotherm[60] was the first of what was to become a long list of empirical isotherms. It became so named after Herbert Freundlich widely used the equation from 1906[61,62] and later proposed that it could be applied to physisorption isotherms on microporous adsorbents in 1926[50] with the form:

$$n = kp^{1/m} \tag{3.8}$$

where k and m are constants (m > 1); n is the amount of gas adsorbed and p is the equilibrium pressure of the gas. The validity of equation (3.8) can be tested by taking logarithms, as shown in equation (3.9), to create a linear plot of ln(n) versus ln(p); the constants k and m are determined from the intercept ln(k) and the gradient (1/m) of the line, respectively.

$$ln(n) = ln(k) + \frac{1}{m} ln\,(p) \tag{3.9}$$

The valid pressure range for the Freundlich equation varies with the adsorbate-adsorbent combination. However, the equation typically shows poor agreement at high pressures and low temperatures; the limitations are partly due to the fact that the equation does not form a horizontal plateau, and therefore does not provide a limiting value of n as $p \to \infty$. The equation also does not reduce to Henry's Law as $p \to 0$.[63]

3.3.3. Langmuir Theory

The original derivation of the Langmuir equation[64] was to become of great historical importance. It was based upon kinetics and made several assumptions:

- the adsorbent contained an array of equivalent and independent adsorption sites, N^s;
- each site is only capable of holding one adsorbate molecule; and,
- there are no interactions between molecules adsorbed on neighbouring sites

The fraction of occupied sites, θ is given by equation (3.10).

$$\theta = \frac{N}{N^s} \tag{3.10}$$

where N is the amount of occupied adsorption sites. Using alternative nomenclature to equation (3.10), the fractional coverage can also be shown in the form:

$$\theta = \frac{n}{n_m} \tag{3.11}$$

Where n, is the specific amount of gas adsorbed, and n_m corresponds to the maximum possible amount of gas adsorbed and is equal to the monolayer capacity (when θ is equal to 1). The fraction of occupied sites is given by the well-known Langmuir isotherm equation.

$$\theta = \frac{bp}{(1 + bp)} \tag{3.12}$$

where p is the equilibrium pressure, and b is the adsorption coefficient, which is exponentially related to the positive value of the adsorption energy, E:

$$b = K\ exp(E/RT) \tag{3.13}$$

Where K is the pre-exponential factor equal to the ratio of adsorption and desorption coefficients, and in general terms can be simply referred to as an equilibrium constant; R is the ideal gas constant and T is the temperature.

At low surface coverage, equation (3.12) reduces to Henry's law, and at high surface coverage, $\theta \to 1$, creating a plateau. By rearranging the terms in the equation, it can be transformed in to a linear form:

$$^{p}/_{n} = {}^{1}/_{n_m b} + {}^{p}/_{n_m} \quad (3.14)$$

A plot of p/n against p, allows for the maximum adsorption capacity, n_m to be obtained from the gradient of the straight line plot.

The weakest points to the Langmuir theory stem from the assumptions of uniform site energies and that no interactions occur between the adsorbed molecules.

The fractional coverage can also be expressed as a function of the chemical potential of the gas, μ and of the adsorption potential, ε in the Fermi-Dirac[65,66] form:

$$\theta = \frac{1}{1 + exp\left(\frac{\varepsilon - \mu}{k_B T}\right)} \quad (3.15)$$

Where k_B is the Boltzmann constant. Equation (3.15) is equivalent to:

$$\varepsilon = k_B T \, ln\left(\frac{1}{\theta} - 1\right) + \mu \quad (3.16)$$

For an ideal gas, the expression of the chemical potential depends on the standard chemical potential, μ^0 at the measured temperature and on the pressure as shown in equation (3.17).

$$\mu = \mu^0 + k_B T \, ln(p/p^0) \quad (3.17)$$

Here, p^0 corresponds to the standard pressure. The validity of this equation can be determined by plotting μ against ln(p/p^0). The chemical potential is calculated from the tabulated values of the enthalpy and the entropy of the gas.[67]

Where there is more than a single adsorption potential due to different types of adsorption sites, equation (3.15) would not produce a good fit of the data. For example, where there are known to be two distinct adsorption sites it might be more applicable to apply a double langmuir isotherm[65] in the form:

$$\theta = a\frac{1}{1 + exp\left(\frac{\varepsilon_1 - \mu}{k_B T}\right)} + (1 - a)\frac{1}{1 + exp\left(\frac{\varepsilon_2 - \mu}{k_B T}\right)} \quad (3.18)$$

where, a and (1-a) are the fractions of the available sites with adsorption energies of ε_1 and ε_2, respectively.

3.3.4. Sips (Langmuir-Freundlich)

Sips proposed an equation that combined the Freundlich equation with the Langmuir equation,[68,69] which produced a finite limit when the pressure became sufficiently high.

$$n = n_m * \frac{(kp)^{1/\mathrm{m}}}{1 + (kp)^{1/\mathrm{m}}} \qquad (3.19)$$

where n and n_m are the amount of moles adsorbed (at a given pressure) and the amount of moles adsorbed at saturation, respectively, p is the pressure and k and m are constants. The constant m is often regarded as the heterogeneity factor,[70] with values greater than 1 indicating a heterogeneous system. Values close to (or exactly) 1 indicate a material with relatively homogenous binding sites.[62] In this case, the Sips model is reduced to the Langmuir equation as shown by equation (3.12). The Sips equation is believed to give a more accurate fit over a larger pressure regime than the standard Langmuir or Freundlich equations, thus resulting in a more accurate prediction of the quantity of hydrogen adsorbed at saturation. However, it does suffer from the same disadvantage as the Freundlich equation: it does not reduce to Henry's Law as $p \to 0$.[71,72]

3.3.5. Tóth

Although it was originally proposed for monolayer adsorption by Tóth,[59,73] it is believed to give a more extensive range of fit when applied to Type I isotherms;[62] the Tóth equation has the advantage that it appears to satisfy the two end limits of the isotherm, $p \to 0$ and $p \to \infty$.

$$n = n_m * \left(\frac{(kp)^m}{1 + (kp)^m} \right)^{1/m} \qquad (3.20)$$

where the parameters are the same as for the Sips equation in section 3.3.4. The parameters k and m are specific for adsorbent-adsorbate pairs, and here m is less than 1.[63] Again, m is said to characterise the system heterogeneity; and when it is equal to 1, the Tóth equation reduces to the Langmuir equation as shown by equation (3.12). Vast data sets for hydrocarbons on Nuxit-al charcoal were well described by the Tóth equation,[63] and due to its simplicity and correct behaviour at both low and high pressures, it is

often the first choice equation for fitting isotherm data for several different adsorbates on activated carbons and zeolites.[63,72,74-78]

3.3.6. Potential Theory Isotherm Equations

Workers such as Pierce, Wiley and Smith began to postulate the mechanism of pore filling in 1949,[48,79] but it was Dubinin who was to become the pioneer in the concept of micropore filling.[48,80,81] Dubinin examined the physisorption data in terms of the Polanyi potential theory of adsorption, which gave a temperature independent 'characteristic curve'.[50,82] Dubinin and Radushkevich used this to propose the simple functional relationship that was later to be known as the Dubinin-Radushkevich (DR) equation (see section 3.3.6.1). This was to form the basis of the Theory of Volume Filling of Micropores (TVFM).[83,84] Dubinin and Radushkevich adapted the earlier Polanyi theory of adsorption,[82] redefining the adsorption potential, A as the differential molar work of adsorption in the expression:

$$A = RT\ ln\left(\frac{p_s}{p}\right) \qquad (3.21)$$

where R is the ideal gas constant and p_s is the saturation vapour pressure of the adsorbate. The adsorption of supercritical gases does however pose a problem. In this region, the gas does not saturate to form a liquid, regardless of the temperature and pressure. Unfortunately, hydrogen adsorption measurements, for porous materials, are typically performed at 77 K, which is in the supercritical region. The critical point for hydrogen is 32.97 K and 1.29 MPa (12.9 bar). In sub-critical conditions, p_s is a definite physical parameter; the point at which there is a phase change between a gas and a liquid. At the saturation vapour pressure, the pores (of a porous material) will become filled with the bulk liquid phase. As there will not actually be a physical saturation vapour pressure above the critical temperature, then using a "pseudo saturation vapour pressure" might be the best option in order to define a reference pressure, despite it having no physical meaning. The saturation vapour pressure for supercritical adsorbents can be defined by the relationship of measurement temperature to the critical point, along with the parameter γ, which is dependent on the adsorbent-adsorbate system.[85,86]

$$p_s = (T/T_c)^{\gamma} p_c \qquad (3.22)$$

The expression (3.21) gives the maximum differential molar work A, needed to transport one mole of the adsorbate from the gas or liquid phase to a surface of an infinitely large amount of adsorbent at a given temperature T, and an equilibrium partial pressure p, of the adsorbate. The differential molar work A, is also equal to the negative change of Gibbs free energy of adsorption:

$$A = -\Delta G \qquad (3.23)$$

All theories, prior to the work of Dubinin (1975)[84], described physical adsorption onto a flat surface of one or more successive adsorption layers. In the TVFM however, where the pore diameter is comparable to the size of the gas molecule, the process of adsorption involves the volume filling of micropores rather than the layer-by-layer adsorption on the sides of the pore walls.[48] Thus, the plateau of the Type I isotherm represents the filling of the pores by a process similar to but not identical with capillary condensation (which occurs in mesoporous adsorbents and exhibit Type IV isotherms). This gave the adsorbate a similar density to that of a liquid and provided the basis of the Dubinin series of equations.

3.3.6.1. Dubinin-Radushkevich

In 1947, Dubinin and Radushkevich proposed an equation for the low and medium pressures of the adsorption isotherm, in order to estimate the micropore volume of a homogenous microporous material.[83]

$$W = W_0 exp\left[-\frac{A}{\beta E_0}\right]^2 \qquad (3.24)$$

where W_0 is the micropore volume; W is the volume that has been filled when at the pressure relative to the saturation vapour pressure; A is as presented in equations (3.21) and (3.23); E_0 is the characteristic adsorption energy; and β is a similarity (affinity) coefficient (which is the ratio of characteristic free energy of adsorption between the test and reference adsorbate). Benzene was typically used as the reference adsorbate, where β is equal to 1.[48,87]

3.3.6.2. Dubinin-Astakhov

Dubinin and Astakhov[88] later proposed a more general equation to estimate the micropore volume, with the empirical parameter, n which is said to describe the surface heterogeneity of the adsorbent.[63]

$$W = W_0 exp\left[-\frac{A}{\beta E_0}\right]^n \quad (3.25)$$

Intermediate values $2 > n > 1$ are used to describe materials with large micropores, whilst values of 2 are used for materials with particularly small micropores (notably molecular sieves).[62] Values from 2 to 6 are often seen for materials with very fine micropores, with the 'best' values for n, typically being non-integers. The exponent n manifests from the width of the energy distribution and therefore qualitatively at least is connected to the pore size distribution;[89] the use of the Dubinin-Astakhov equation for predicting pore size distribution is discussed in section 3.4.1. It must also be noted that the value of n may also depend on the temperature and the range of the temperatures used.[50]

3.4. Pore Size Distribution

A fundamental problem with the characterisation of porous adsorbent materials is the quantitative estimation of pore size distribution. The Kelvin equation can be used for mesoporous adsorbents that give a Type IV isotherm, and applies to the area of the isotherm that is associated with capillary condensation.[48] Nitrogen adsorption isotherms are typically used as this also allows for surface area analysis to be performed simultaneously (see section 3.5). Several procedures for estimating the pore size distribution using nitrogen isotherms were proposed in the period between 1945 and 1970.[50,90] Of those classical methods proposed, the Barrett, Joyner, and Halenda (BJH) method[91] still remains popular.[50]

3.4.1. Dubinin-Astakhov

In section 3.3.6.2, the Dubinin-Astakhov equation (see equation (3.25) was described for estimating the pore volume of the adsorbent. It was also mentioned that the exponent n reflects the width of the energy distribution and therefore, qualitatively at least, this value has a bearing on the pore size distribution.[89] Cerofolini postulated that a heterogeneous surface comprises of homogeneous 'patches', and that an

overall isotherm that describes the complete adsorptive system is related to a local isotherm for the patches and a distribution of adsorptive energies.[89] Stoeckli showed that the semi-empirical basis of VFM theory (which is based on equation (3.25) by Dubinin and Astakhov) has a reasonable theoretical basis if a variational technique called the condensation approximation is applied to the isotherm.[89,92] Stoeckli suggested that if the local isotherm θ_l is the Langmuir type, and overall isotherm θ_t of the DR type

$$\theta_t = exp\left(-B\left(RT\ ln\frac{p_m}{p}\right)^2\right) \tag{3.26}$$

corresponds to the energy distribution

$$\chi_c(\epsilon) = 2B(\epsilon - \epsilon_0)\ exp(-B(\epsilon - \epsilon_0)^2) \tag{3.27}$$

where, as a consequence of condensation approximation[92]

$$\epsilon - \epsilon_0 = RT\ ln\left(\frac{p_m}{p}\right) \tag{3.28}$$

The condensation pressure p_m corresponds to the sites of minimum adsorption energy ϵ_0, however, in the generalisation of this technique, p_m, is assumed to be equal to that of the saturation pressure p_s, and therefore ϵ–ϵ_0 is also equal to the negative differential molar work of adsorption (A) and the change in the Gibbs free energy (ΔG).[92] The generalisation of the condensation approximation method leads to the following approximate energy distributions associated with the DA equation (3.25)[93]

$$\chi_c(\epsilon) = n\frac{(\epsilon - \epsilon_0)^{n-1}}{(\beta E_0)^n} exp\left(-\left(\frac{(\epsilon - \epsilon_0)}{\beta E_0}\right)^n\right) \tag{3.29}$$

If the repulsion forces are neglected, the simplest approximation to relate the energy distribution to pore radius assumes an adsorption potential of the form[94]

$$A = D/z^3 \tag{3.30}$$

where D is the dispersion interaction energy for the gas-solid and z is the pore radius. Substitution of equation (3.30) into equation (3.25), and then differentiation with respect to z, leads to an approximate pore size distribution.[93-95]

$$\frac{\delta(W/W_0)}{\delta z} = 3n\left(\frac{D}{\beta E_0}\right)^n z^{-(3n+1)} exp\left(-\left(\frac{D}{\beta E_0}\right)^n z^{-3n}\right) \tag{3.31}$$

Equation (3.31) is the derivative of the characteristic curve (as mentioned in section 3.3.6) with respect to the pore size assuming a given function for the adsorption potential (which in turn is a function of relative pressure as shown in equation (3.21)). If the adsorbed amount increases at a lower adsorption potential due to smaller pore sizes, then its derivative as a function of pore size will give a plot of the pore size distribution. No uptake at low relative pressures (i.e. low adsorption potential), indicates that there are no small pores, and therefore $d(W/W_0)/dr$ is equal to zero. As the uptake increases, the adsorption potential will also increase until it reaches values that correspond to the expected uptake for that particular pore size; subsequently the derivative will in turn increase in proportion with the number of pores of that size. Once the adsorption has saturated, the relative pressure (adsorption potential) will be too high for even the largest micropores and therefore it is assumed that all of the micropores have been filled; consequently $d(W/W_0)/dr$ will decrease to zero again.

3.4.2. Horváth-Kawazoe

It was discussed earlier that if a molecule approaches a solid surface, it experiences a mixture of both attractive and repulsive intermolecular forces. The energy profile for a two isolated atoms was given in equation (3.1), for the energy profile of a adsorbate molecule within a pore, the Lennard-Jones 6-12 potential can be given in the form[59]

$$\varepsilon(z) = 4\varepsilon^* \left[(\sigma/z)^{12} - (\sigma/z)^6\right] \qquad (3.32)$$

where z is the distance between the centres of two atoms, ε*is the depth of the potential energy well and here σ is the distance at which $\varepsilon(z)$ = 0, i.e. the distance from a surface atom at zero interaction energy. The interaction energy of an adsorbate molecule with a single infinite-layer plane of adsorbent molecules is given as[59,96]

$$\varepsilon(z) = \frac{N_a A_a}{2\sigma^4}\left[-\frac{\sigma^4}{z} + \frac{\sigma^{10}}{z}\right] \qquad (3.33)$$

Where N_a is the number of adsorbate molecules per unit area, and A_a is a dispersion constant. Equation (3.33) can be extended to apply to two parallel infinite lattice planes[52]

$$\varepsilon(z) = \frac{N_a A_a}{2\sigma^4}\left[-\frac{\sigma^4}{z} + \frac{\sigma^{10}}{z} - \frac{\sigma^4}{(l-z)} + \frac{\sigma^{10}}{(l-z)}\right] \quad (3.34)$$

where l is the distance between nuclei on either side of the two parallel infinite lattice planes at zero-interaction energy. Horváth and Kawazoe then took this expression and used it to propose that the potential is increased by the interaction of adsorbate molecules within the pores giving the expression[59,90,97]

$$\varepsilon(z) = \frac{N_a A_a + N_A A_A}{2\sigma^4}\left[-\frac{\sigma^4}{z} + \frac{\sigma^{10}}{z} - \frac{\sigma^4}{(l-z)} + \frac{\sigma^{10}}{(l-z)}\right] \quad (3.35)$$

where N_A is the number of adsorbent molecules per unit area, and A_A is a dispersion constant.

The Horváth-Kawazoe (H-K) expression included the additional interaction by adding an adsorbate dispersion term ($N_A A_A$) to the numerator of the depth of the potential energy minimum ($N_a/2\sigma^4$).[90] The numerator ($N_a A_a + N_A A_A$) in equation (3.35) is often denoted as the interaction parameter (I.P.),[98] and in many software applications it is inputted by the user from a table of calculated values from the literature. Equation (3.35) was originally developed to calculate the micropore size distribution of slit-shaped pores in molecular-sieve carbons, from adsorption isotherms. Despite being known to be flawed, the method is still popular and in wide use. The H-K expansion assumes that the (slit-shaped) pore is filled with adsorbate molecules and so incorporates adsorbate-adsorbate-adsorbent interactions in addition to that of the adsorbate-adsorbent interaction. However, no comprehensible justification has been found in the literature for this inclusion.[90] Horváth and Kawazoe derived an expression, which described the free energy change of a system upon adsorption in terms of gas-phase pressure

$$RT\ ln\left(\frac{p}{p_0}\right) = U_0 + P_a \quad (3.36)$$

where U_0 is the expression for adsorbent-adsorbate interactions, and P_a is the implicit function of the adsorbate-adsorbate-adsorbent interactions.[97] The right hand side of equation (3.36) is then a function of the pore geometry and dimension, which is related to the relative pressure of the adsorbate.[90] Equation (3.35) consists of two parts, the first considers the adsorbate-adsorbent interactions ($N_a A_a/2\sigma^4$), and when multiplied by the expressions in the parentheses, corresponds to (U_0/L), the second part

considers the adsorbate-adsorbate interactions ($N_A A_A/2\sigma^4$) and corresponds to (P_a/L); where L is Avogadro's constant.[97] Taking this in to account, Horváth and Kawazoe proposed the equation

$$RT\ ln\left(\frac{p}{p_0}\right) = L\left[\frac{N_a A_a + N_A A_A}{\sigma^4\ (l - 2d_0)}\right] * \left[\frac{\sigma^4}{3(l-d_0)^3} - \frac{\sigma^{10}}{9(l-d_0)^9} - \frac{\sigma^4}{3(d_0)^3} + \frac{\sigma^{10}}{9(d_0)^9}\right] \quad (3.37)$$

where

$$d_0 = \frac{d_a + d_A}{2} \quad (3.38)$$

and d_a is the diameter of the adsorbate molecule, and d_A is the diameter of the adsorbent molecule.[59,90] The pore size distribution can then be calculated by using different values for the pore width ($l - d_A$) with the measured relative pressure, from which the amount adsorbed can be plotted directly against pore width.[63]

One problem with the theory is the requirement for micropores to be either full or empty according to whether the pressure of the adsorptive is greater or less than the value characteristic of a particular micropore size, which is known to be an improbable situation. This is not expected to be true, instead the micropore will undergo a 'filling' at a particular relative pressure.[98-101] Another problem is the incorrect assumption that the adsorbed phase behaves thermodynamically as a two-dimensional ideal gas.[59,98]

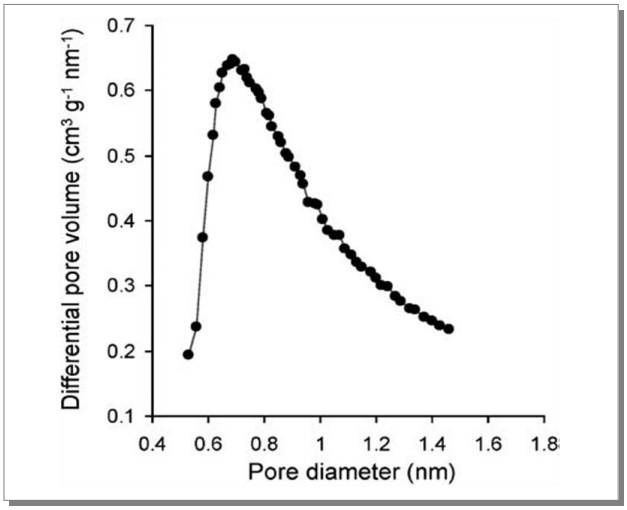

Figure 3.4 - Micropore size distribution for a hypercrosslinked polymer calculated by the Horváth–Kawazoe method (carbon-slit pore model).[102]

The original Horváth-Kawazoe equation was based on slit-shaped pores. Saito and Foley (S-F)[103] extended the equation to cylindrical-shaped pores, with the hope that it would be more applicable to microporous

materials such as zeolites. As with the H-K model, Saito and Foley based their work on that done by Everett and Powell,[52] but used a cylindrical potential. Cheng and Yang[104,105] extended the H-K and S-F equations further still to incorporate spherical pores, with particular interest towards the cavities in zeolites. The Cheng and Yang (C-Y) expression is believed to correct for the nonlinearity of the isotherm, which was not accounted for in the original H-K equation.[98] In the C-Y model, it is assumed that the pore cavity wall consists of a single layer of adsorbent atoms and is spherical in shape.

3.5. Surface Area

The surface area per unit mass is termed the specific surface area (SSA) of solids and is typically given the units $m^2\ g^{-1}$. There are several methods for calculating the specific surface area of microporous materials, here we will consider two that are commonly reported in the literature, BET and Langmuir. The two methods for evaluating the specific surface areas often produce quite different values. One possible explanation for this is that the BET method only considers physical adsorption in the form of a monolayer, whereas the Langmuir method, takes data directly from the isotherm, which would therefore include any pores within a solid material.

3.5.1. Langmuir

Langmuir theory was described in section 3.3.3. The Langmuir equation is often more applicable to chemisorption situations rather than physisorption situations due to the first assumption that gases form a single monolayer on a solid.[98] However, the equation is often applied to physisorption isotherms of type I, which is typically seen with microporous adsorbents, where due to a high adsorption potential, differentiation between pore filling and monolayer coverage is not possible.[106] Equation (3.14) shows the Langmuir equation in its linear form, where p/n plotted against p gives $1/n_m$ and $1/n_{\mathrm{m}}b$ as the gradient of the straight line plot and the intercept of the y-axis, respectively.

The amount of gas adsorbed when the surface is saturated (expressed in moles of adsorbate per gramme of adsorbent) can then be used in conjunction with the cross-sectional area of one adsorbate molecule, σ, to calculate the Langmuir surface area, S_L.[48,50,98]

$$S_{\mathrm{L}} = n_m \, L \, \sigma \qquad (3.39)$$

3.5.2. Brunauer, Emmett and Teller (BET) Theory

The BET equation was first derived by Brunauer, Emmett and Teller with a kinetic related argument,[107] which was based on the original Langmuir theory.[62] The three authors generalised the Langmuir theory and incorporated the concept of multilayer adsorption,[98] with the assumption that the Langmuir isotherm can be applied to every adsorption layer.

There are two stages in using the BET method for evaluating the SSA from physisorption isotherm data. The BET plot needs to be constructed by plotting $(p/p_0)/[n(1\text{-}p/p_0)]$ against (p/p_0), which should yield a straight line in the region of $0.05 \leq p/p_0 \leq 0.35$ according the BET equation[48,50,62,98,106]

$$\frac{p/p_0}{n(1-p/p_0)} = \frac{1}{n_m C} + \frac{C-1}{n_m C}\,(p/p_0) \qquad (3.40)$$

where the gradient of the graph is $(C - 1)n_{\mathrm{m}}C$, and the intercept is $1/n_{\mathrm{m}}C$. By solving the two simultaneous equations, n_{m} and C can be obtained.[50] The value of C in its simplest terms is[48,50,98]

$$C = \exp\left(\frac{q_1 - q_L}{RT}\right) \qquad (3.41)$$

where q_1 is the enthalpy of adsorption for the first layer, and q_{L} is the enthalpy of liquefaction, thus making $(q_1 - q_{\mathrm{L}})$ the net enthalpy of adsorption.[48] The BET surface area S_{B}, can then be calculated from the simple relation[48]

$$S_{\mathrm{B}} = n_m \, L \, \sigma \qquad (3.42)$$

where the symbols are described above. Equation (3.42) is effectively the same as equation (3.39); the difference that allows these two equations to calculate the Langmuir and BET specific surface areas comes from the linear plot, which defines n_m, the monolayer capacity.

The BET method for assessing the specific surface area is widely known to be essentially erroneous when looking at microporous materials.[108,109] However, it is also a widely used tool in the literature for comparison of these types of materials.

3.6. Hydrogen Storage Capacity

The most frequently quoted quantity, in terms of hydrogen storage applications, is the weight percent capacity (wt.%). The definition for the weight percent capacity (or the gravimetric storage density) of a material differs between hydrogen absorbents and adsorbents. The definition is more clearly defined in the case of the absorbents. However, the definitions of wt.% for both absorbents and adsorbents exhibit associated uncertainties as a result of the uncertainties in defining both the sample volume and sample density.

3.6.1. Hydrogen Absorption

The gravimetric storage capacity of a hydrogen-absorbing material, where the hydrogen becomes stored in the bulk of the material (as with metal hydrides); is typically calculated from the ratio of the mass of hydrogen stored within the metal (or compound) to the combined mass of the host material and the hydrogen.[110] Therefore, the storage capacity is given as

$$wt.\% = \left(\frac{{}^{H}/_{M} * M_{\mathrm{H}}}{M_{\mathrm{HOST}} + {}^{H}/_{M} * M_{\mathrm{H}}} * 100\% \right) \qquad (3.43)$$

Where H/M is equal to the hydrogen-to-metal/material host atom ratio, M_{H} is the molar mass of hydrogen and M_{HOST} is the molar mass of the host material (or metal).[111]

With an absorbent such as a metal or complex hydride, the volumetric storage capacity is based on the number of hydrogen atoms that can be accommodated by the structure of the host material either by residing in interstitial sites or chemically bonding to the host structure.

3.6.2. Hydrogen Adsorption

Defining the total amount of adsorbed hydrogen is somewhat more difficult and requires the inclusion of the excess adsorption. Therefore it is not possible to use equation (3.44)) for adsorbent materials, instead an equivalent calculation is[112]

$$wt.\% = \left(\frac{n_{\mathrm{e}} M_{\mathrm{H}}}{n_{\mathrm{HOST}} M_{\mathrm{HOST}} + n_{\mathrm{e}} M_{\mathrm{H}}} * 100\%\right) \qquad (3.44)$$

where n_{e} is the excess adsorption in moles and n_{HOST} is the total number of moles of the host material in the sample, M_{H} is the molar mass of hydrogen and M_{HOST} is the molar mass of the host material. A typical unit for the excess adsorption is the number of moles of adsorbate per unit mass of adsorbent, for example, mol g^{-1}, as recommended by IUPAC.[57] The gravimetric uptake can also be expressed in terms of the adsorbate mass and adsorbate volume per gramme of adsorbent material, mg g^{-1} and cm^3 (STP) g^{-1}, respectively. At this point it is important to note that the gravimetric storage capacity when expressed as adsorbate volume (at STP) is not the volumetric uptake, instead it is simply an alternative use of units for a mole of adsorbate.

With adsorbent materials, the volumetric storage capacity must include the volume of the solid structure as well as the volume of the pores, and the volume of the surface excess adsorption. It is important to note here that the volume of the pores refers to the volume accessible to hydrogen gas if there were no gas-solid interactions. Therefore, in order to calculate the volumetric storage capacity, knowledge of the bulk density is required. The *bulk density* is defined as the ratio of the mass to the volume occupied by the sample including all internal pore and interparticle void space, while the *tap density* is essentially the same, but is determined after the container holding the material is tapped in a specific manner to allow more efficient packing of the bed.[106] These are important in the assessment of the performance of materials in storage applications because they represent two effective definitions of the density of a real solid-state storage system bed.[113,114] This provides units for the volumetric storage capacity in kilogrammes of hydrogen per cubic metre of material (kg H_2 m^{-3}), or grammes per litre (g L^{-1}).

Techniques such as pycnometry result in the *apparent density* which is calculated using the skeletal volume observed by the chosen characterisation fluid, *e.g.* helium. The *true density* is the ratio of the mass to the volume occupied by the sample excluding both open and closed pores, while the *envelope* or *geometric density* is the ratio of the mass to the volume occupied by the sample including all internal pore space. For the buoyancy effect and dead-space volume corrections (see section 3.7), it is the skeletal density that is important. The *skeletal density* is the ratio of the mass to the volume occupied by the sample excluding the volume of any open pores.[106]

3.6.2.1. Excess, Absolute and Total Adsorption

The measured quantity in a volumetric or gravimetric hydrogen adsorption measurement is the *excess adsorption*, also known as the *surface excess*, the *Gibbs excess* or the G*ibbsian surface* excess.[115,116] This surface excess quantity is the difference between the actual amount of adsorbate present in the adsorbed layer and that which would be present in the layer if it had the same density as the bulk gas phase, at the particular measurement temperature and pressure.[50,111,115,117,118] Figure 3.5 shows a schematic for the surface excess, which is represented as region (a) in the lower part of the diagram. In addition, Figure 3.5 shows an illustration for the volumes of the solid V_{solid} the adsorbed layer V_{a} and the bulk gas phase V_{f}. The volume of the adsorbed layer is defined as being the volume between the solid surface (i.e. where $\mathrm{X} = 0$) and the boundary at distance $\mathrm{X_a}$ from the solid surface. The hollow circles are those attributed to the region (b + c), whereas the filled circles indicate gas molecules that are attributed to the surface excess region (a).

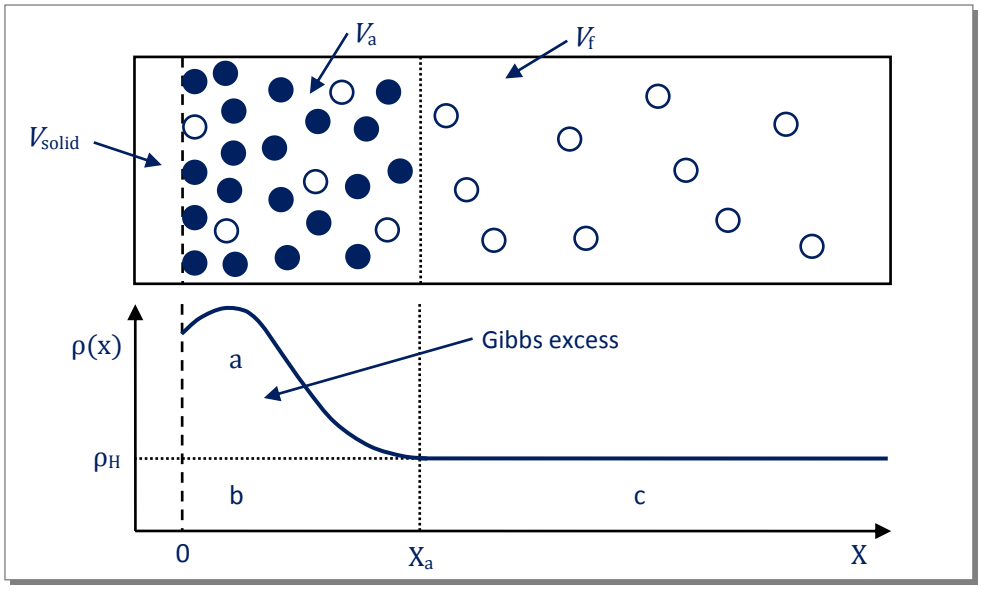

Figure 3.5 - A schematic diagram illustrating the concept of the Gibbs excess (a) and the total (absolute) adsorbed (a + b) quantities. The total amount of fluid (gas) present in the syste is equal to regions a + b + c.[111,118]

The important difficulty with comparing measured experimental data with theoretically calculated or modelled adsorbed quantities, comes from the latter being expressed as the absolute (or total) adsorption; shown as region (a + b) in Figure 3.5. Therefore a comparison requires the conversion of theoretical gas sorption capacities (i.e. absolute adsorption) into measured sorption capacities (i.e. excess adsorption), or vice versa.[111] The conversion requires an assumption regarding the state of the adsorbed layer at sub- or supercritical temperatures. In general, it is assumed that the adsorbate has the same density as the bulk liquid phase at sub-critical temperatures; however, this is not necessarily applicable at supercritical temperatures as with the typical measurement regimes for hydrogen adsorption. The measured excess is related to the total adsorbed amount by the relationship

$$m_e = m_a - \rho_H V_a \qquad (3.45)$$

where m_e is the excess mass adsorbed, m_a is the total mass adsorbed and ρ_H is the density of hydrogen.[85,119,120] The measured excess is determined with reference to a non-adsorbing system (e.g. usually established using helium, a gas that has negligible adsorption).[111,119] The density of hydrogen can be calculated from

$$\rho_H = {}^{p}/_{ZRT} \qquad (3.46)$$

where p is pressure, R is the gas constant, T is temperature Z is the compressibility, which can be obtained from the NIST Chemistry WebBook[25,121] and REFPROP Database.[122] When the pressure becomes very low, region (b) will also become very small and becomes negligible in comparison to region (a); in this instance the mass of the total adsorbed quantity is approximately equal to the excess adsorbed quantity. Conversely, when the pressure becomes very large, region (b) becomes very large in comparison to region (a), as illustrated in Figure 3.6. If the pressure is greatly increased, it is possible for the surface excess amount to fall to zero; and at even higher pressures still, the excess can become negative.[111,118]

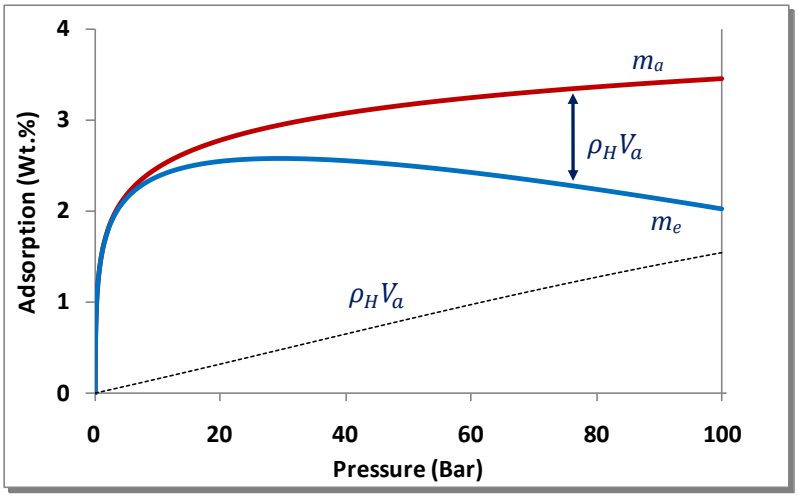

Figure 3.6 - Example of excess (-) and absolute (-) hydrogen uptake 77 K. The dashed line represents the density of hydrogen of compressed hydrogen over the given pressure range at this temperature multiplied by the volume of the adsorbed phase.

To calculate the total adsorbed amount of hydrogen from the measured excess we use a rearrangement of equation (3.45)

$$m_a = m_e + \rho_H V_a \qquad (3.47)$$

The conversion between the measured excess adsorption and the absolute amount adsorbed requires knowledge of the volume of the adsorbed phase; however, this cannot be measured experimentally and is therefore not known.[123,124] Where a monolayer is being considered, the adsorbed phase can be assumed to be a simple 2-dimensional layer of adsorbate molecules of known cross-sectional area and thickness. However, with microporous materials this is not the case; instead the adsorbate phase is a volume that

may be fragmented in a similar way to the pore network (or solid structure).[111] One assumption that is typically used is to assume that[118,124]

$$V_a = V_p \tag{3.48}$$

where V_P is the estimated, theoretical, or independently measured pore volume.[111,117] The assumption itself does however provide further problems in that it assumes the thickness of the adsorbed layer remains constant with increasing pressure therefore an increased concentration of hydrogen. Even the accurate determination of the pore volume of the material is not simple.[125] Some adsorbents such as activated carbons or microporous polymers are more susceptible to errors due to their amorphous and non-crystalline pore structure. Whereas, crystalline adsorbents, such as MOFs and zeolites, the structures are more clearly defined, and therefore the assumption has greater validity.[111]

In an attempt to remove the uncertainty behind the unknown volume of the adsorbed mass, a different equation can be found by derivation of equation (3.47) (see Appendix D) which is based on the simple equation of mass, volume and density

$$V_a = \frac{m_a}{\rho_a} \tag{3.49}$$

Using this method however, leads to another assumption, which is that of the density of the adsorbed phase ρ_a.[85,120,126]

$$m_a = \frac{m_e}{(1 - \rho_B/\rho_a)} \tag{3.50}$$

where m_a is the mass of the absolute adsorption, m_e is the mass of excess adsorption, ρ_B is the bulk gas phase density. This assumption is in itself somewhat problematic in the fact that the density of the adsorbed phase is also unknown. Typically the mean adsorbate phase density $\langle \rho_a \rangle$ is approximated to be equal to the liquid density ρ_{liq}[71,111,124,127,128]

$$\langle \rho_a \rangle = \rho_{liq} \tag{3.51}$$

Or

$$\langle \rho_a \rangle = \frac{\rho_{liq}^b}{exp[\alpha(T - T_b)]} \tag{3.52}$$

where ρ_{liq}^{b} is the liquid density at the boiling temperature T_b (0.0708 g cm^{-3})[71,127] and α is the thermal expansion coefficient of a superheated liquid.[111,124] Other assumptions over the density of the adsorbed phase include the layer density being equal to the critical density of hydrogen ρ_c[111,124]

$$\langle \rho_a \rangle = \rho_c \tag{3.53}$$

or being equal to the density of hydrogen at the triple point (0.077 g cm^{-3}).[71,128]

The van der Waals approximation is given as[111,124]

$$\langle \rho_a \rangle = \frac{M}{b'} = \frac{MRT_c}{8p_c} \tag{3.54}$$

where b' is the van der Waals constant, M is the molar mass, R is the gas constant, T_c is the critical temperature and p_c is the critical pressure. In this constant density approximation, ρ_H is expressed in terms of fugacity f

$$\rho_H = {}^{Mf}/_{RT} \tag{3.55}$$

Which enables the total (or absolute) adsorption to be defined as a function of fugacity

$$m_a(f) = m_e(f) + \left(\frac{Mf}{RT}\right)\left(\frac{m_a}{\langle \rho_a \rangle}\right) \tag{3.56}$$

Hence,

$$m_a = \frac{m_e(f)}{\left(1 - \frac{Mf}{RT\langle \rho_a \rangle}\right)} \tag{3.57}$$

There are two constant volume approximations, the first was given by equation (3.48) were the volume of the adsorbed phase was given to be equal to the accessible pore volume. The other constant volume method, is also given the term, the effective thickness approximation[111,124,126]

$$V_a = 2\sigma S \tag{3.58}$$

where σ is the molecular diameter of the adsorbate and S is the specific surface area of the host material. In both approximations, the density of the bulk gas is multiplied by a constant volume and this becomes the difference that separates the total adsorption from the measured excess.

3.6.3. Isosteric Enthalpy of Adsorption

The adsorption of a gas onto a solid is an exothermic process with positive entropy and negative enthalpy. The magnitude and variation of the enthalpy of adsorption as a function of coverage can reveal information concerning the bonding to the surface. It is commonly referred to as the isosteric enthalpy of adsorption and can be derived from the condition of the phase equilibrium between the ambient gas phase and the adsorbed phase. The phase equilibrium stems from the equal balance of the chemical potentials of these two phases.[59] The isosteric enthalpy of adsorption can be obtained from the analysis of pressure composition isotherms at multiple temperatures using several different approaches, however, it is most commonly calculated by using a form of the Clausius-Clapeyron equation[58,129,130]:

$$Q_{st} = RT^2 \left[\frac{\delta \ln p}{\delta T}\right]_n \qquad (3.59)$$

When calculating the isosteric enthalpy of adsorption it is important that only adsorbate-adsorbent interactions are taken into account. This is opposed to the inclusion of any adsorbate-adsorbate interactions that would occur at increased fractional coverages. Therefore, only the low pressure region of the isotherm will represent a characteristic adsorbate-adsorbent system.[58]

Typically just two temperatures are used; that of liquid nitrogen (77.3 K) and either that of liquid argon (87.3 K) or room temperature. There are few examples that use several different temperatures in order to calculate the isosteric enthalpy of adsorption of a porous material, despite the potential increase in accuracy that multiple temperatures would provide.[118,131]

3.6.3.2. Clausius-Clapeyron

The application of the Clausius-Clapeyron equation is widely used in calculating the isosteric enthalpy of adsorption. It relates the effects of adsorption enthalpy to the temperature dependence of the adsorption isotherm. The equation makes two assumptions[130], which are reasonable at low pressures:

1. the bulk gas phase is considered ideal; and
2. the adsorbed phase volume is neglected.

However, they may not be true at higher pressures. Derivations from the Langmuir equation yield a form of the Clausius-Clapeyron equation (3.61); by considering Henry's Law an equation relating pressure to the enthalpy of adsorption can be given as[59,120]:

$$\frac{d \ln p}{d T} = \frac{\Delta H_0}{RT^2} \qquad (3.60)$$

By applying equation (3.60) to two isotherms at different temperatures it becomes:

$$ln\left(\frac{p_1}{p_2}\right) = \frac{\Delta H_0}{R}\left(\frac{1}{T_1} - \frac{1}{T_2}\right) \qquad (3.61)$$

which can be rearranged to give:

$$\Delta H_0 = -\frac{R\, T_1\, T_2}{T_2 - T_1}.ln\left(\frac{p_2}{p_1}\right) \qquad (3.62)$$

where T_n is the temperature for isotherm n; p_1 and p_2 are pressures at T_1 and T_2 for an equal fractional coverage.

3.6.3.3. Virial

3.6.3.3.1. Virial Type Expansion Equation

Relatively low quantities of gas adsorption can be expressed by the following form of the virial equation[128,132,133]:

$$ln(n/p) = A_0 + A_1 n + A_2 n^2 + \ldots \qquad (3.63)$$

where n is the amount of gas adsorbed at a pressure, p and A_0, A_1, etc, are virial coefficients. The equation is applicable to the low coverage region of the adsorption isotherm, where only adsorbate-adsorbent interactions occur, which is important for calculating isosteric enthalpies of adsorption. Another advantage would be that the application of the virial equation is not restricted to particular mechanisms or systems. The first virial coefficient, A_0, is related to the Henry's law constant, k_H,[133] by the equation:

$$k_H = \exp(A_0) \qquad (3.64)$$

This relationship indicates the dependence of k_H on the interaction between the adsorbed gas molecules and the adsorbent surface.[133] Adsorbate-adsorbent interactions are shown in the equation by the first virial coefficient, A_0, with the second virial coefficient, A_1, reflecting the adsorbate-adsorbate interactions.

It is generally appreciated that higher virial coefficients (A_2, and above) are negligible when considering conditions of low fractional coverage[128]; therefore reducing equation (3.63) to the following:

$$ln(n/p) = A_0 + A_1 n \quad (3.65)$$

A plot of $ln(n/p)$ versus n is linear and allows for the first virial coefficient to be obtained from the intercept, which subsequently allows for Henry's Law constant to be calculated by using equation (3.64). The Henry's Law constant can be used via the same method as previously described in section 3.6.3.2 using the van't Hoff equation, (3.61).

3.6.3.3.2. Virial Type Thermal Equation

A virial-type expression of the following form can be used to fit the isothermal data for a given material at different temperatures[118,134-136]:

$$\ln p = \ln n + \frac{1}{T}\sum_{i=0}^{m} a_i n^i + \sum_{i=0}^{n} b_i n^i \quad (3.66)$$

where n is the amount adsorbed, p is the pressure, T is the temperature, a_i and b_i are empirical parameters. The equation includes terms m and n, the values of which represent the number of coefficients required to adequately describe the isotherms and therefore have a direct impact upon the accuracy of the fit. This means the greater the number of terms the more accurate the fit will be to the experimental data; however, it is unreasonable to automatically suggest large numbers of terms. Therefore, it is typical to allow the fitting expression to be run, gradually increasing the values of m and n until the contribution of additional a and b coefficients is deemed to be statistically insignificant toward the overall fit.

The resulting virial coefficients a_0 through to a_m are then used to calculate the isosteric enthalpy of adsorption, Q_{st}, as a function of coverage using the following equation[118,135,136]:

$$Q_{st} = -R\sum_{i=0}^{m} a_i n^i \quad (3.67)$$

3.6.4. Extended Empirical Isotherm Equations

Recently it has been suggested that empirical isotherms equations such as the Sips and Tóth equations can be combined with equation (3.45) and used to estimate the pore volume (as well as the maximum total hydrogen uptake).[121] The Sips equation is extended to become

$$n = n_m \left[\frac{(kp)^{1/m}}{1 + (kp)^{1/m}} \right] - \rho_B V_P \qquad (3.68)$$

where all of the parameters have the same meaning as previously described, and the Tóth equation becomes

$$n = n_m \left[\left(\frac{(kp)^m}{1 + (kp)^m} \right)^{1/m} \right] - \rho_B V_P \qquad (3.69)$$

The extended empirical equations can then be applied to the measured surface excess isotherms; and by using the parameters obtained from fitting the data, the equation can be extrapolated to higher pressures and therefore be used to predict the downturn of the excess adsorption.

3.7. Gas Sorption Measurements

Gas sorption measurements can be divided in to static and dynamic as well as volumetric and gravimetric methods. The static and dynamic methods refer to whether or not the sorption or desorption of gas from the sample is allowed to reach equilibrium at any point. For instance temperature-programmed desorption (TPD) and thermogravimetric analysis (TGA) operate with a flow of gas but can also be carried out with temperature steps (static) or with a continuous temperature ramp at a set rate (dynamic).

For porous materials, the hydrogen storage capacity is typically performed with a static technique, at a constant temperature, with steps in pressure. This technique is said to be isothermal. However, some workers such as Zhao *et al*. have found useful results from holding a constant pressure and slowly increasing the temperature (0.3 K minute^{-1}), from 77 K to room temperature, which is referred to as being isobaric.[128]

The majority of reports in the literature utilise the volumetric method with Sievert's type apparatus. A simple schematic is displayed in Figure 3.7. This basic setup illustrates how the gas uptake of the sample can be determined using two cells of known volume and a calibrated pressure transducer. Initially, gas is set to a pressure in the reference cell (V_{ref}) with the valve (V_3) between this and the sample cell (V_{cell}) closed. As the volume of the two cells are precisely known, the pressure drop as a result of opening valve (V_3) can be calculated. After the pressure between the two cells equilibrates, the decrease in pressure is converted in to a quantity of gas. The equilibrium gas concentration can be then plotted against pressure.

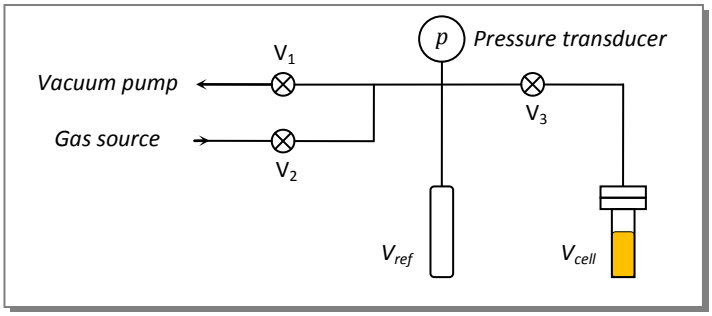

Figure 3.7 - Simple schematic of a volumetric Sievert's apparatus.[137]

The gravimetric techniques relies on the weight change of the sample material during sorption and desorption of gases.[138] Before the gas sorption measurement, the weight of the sample is determined by placing it on one side of a symmetric microbalance, with an inert counter-weight material on the opposite side. The measurement is then typically performed isothermally, with small increments at low pressures. Often the increment size is increased as the pressure is increased to reduce the number of points recorded and time taken to the complete the measurement. At each pressure step, it is important to establish equilibrium before taking the mass reading. Buoyancy corrections need to be taken into consideration, which become more significant at high pressures particularly with samples of low density. More details regarding the gravimetric setup used in this work is presented in Chapter 5.

3.7.1. Errors in Gas Sorption Measurements

Many potential sources of error exist for gas sorption measurements. Experimentalists must be aware of these sources of error in order to achieve reproducible results. The accuracy of measuring hydrogen

storage capacities came to prominence after controversial results were reported for carbon nanostructures at room temperature. Dillon *et al*. reported between 5 to 10 wt.% for single walled carbon nanotubes (mixed with carbon soot) at just 0.4 bar,[139] Chen *et al*. reported 20 wt.% in carbon nanotubes at 1 bar[140] and Chambers *et al*. reported hydrogen storage capacities greater than 60 wt.% in graphite nanofibres at 120 bar and room temperature.[16,110,141] A review by Larkim-Darkim *et al*. questioned many of the high hydrogen storage capacities in carbon nanostructures reported at the time.[142] Yang found the results reported by Chen *et al*. were not reproducible using 'dry hydrogen' and concluded that the results were most likely a consequence of moisture contamination of the hydrogen gas supply.[143]

Presented here are some general sources of error that are relevant to both volumetric and gravimetric methods.

Calibration of various sections of any instrument is an obvious requirement before performing any measurement. In addition to this, the following section discusses further considerations that need to be made when performing gas sorption measurements. Most issues, such as ensuring equilibrium is reached and samples being fully degassed, affect both volumetric and gravimetric techniques and are discussed in conjunction below. Those that only affect the individual technique, such as accumulative errors and buoyancy correction, are discussed separately in relation to the relevant method.

The ability to accurately monitor and control temperature at any given pressure is an important aspect for gas sorption measurements. Generally, temperatures that are further from ambient cause more problems due to temperature gradients throughout the apparatus. This is particularly important for the volumetric system where the dosing volume and reactor volume are at different temperatures during the isothermal measurements. The thermal gradient between the sample and the rest of the apparatus needs to be included in sorption calculations.[144] Many of the hydrogen adsorption measurements are performed at cryogenic (liquid nitrogen) temperatures, where the IUPAC guidelines suggest that volumes of 'appreciable' amounts of gas should be regulated to within ±0.1 °C, but also that the entire apparatus is 'maintained at reasonably constant temperature'.[57,144] Few systems measure the actual temperature of sample material during a gas sorption measurement. The volumetric method offers the advantage of

being able to have the temperature sensor in contact with the sample container during measurements. However, for the gravimetric method it can only be in the vicinity of the sample.[57,144]

The obvious consideration for small sample sizes is that the instrument used has a great enough sensitivity. Poirier *et al*. compared volumetric and gravimetric techniques on small samples (3 to 25 mg) of palladium absorption using 1 bar hydrogen at 295 K. They found their volumetrically determined hydrogen uptake correlated with sample size, with smaller samples giving higher hydrogen uptake. However, their gravimetrically determined data did not correlate.[138] Rouquérol *et al*. discussed the importance of sample size in relation to microporous adsorbents. They concluded that for high surface area materials (> 500 $m^2 g^{-1}$), care needs to be taken not to reduce the sample size too much: they recommend that sample sizes < 50 mg should be avoided.[50] In essence, the appropriate sample size should be selected based upon the sensitivity of the equipment being used.

Robens *et al.* reported the significant effects of sample storage and preparation from round-robin tests using candidate high surface area reference materials.[145] Therefore, care should be taken over the reproducibility of results obtained from materials that have been stored differently.[144] Avraham *et al*. investigated the sensitivity of a microporous carbon compared to the conditions in which it was stored.[146] Kaye *et al*. showed that MOF-5 suffered irreversible structural changes on exposure to air. They demonstrated that synthesis and constant storage in an inert atmosphere significantly improved the hydrogen storage capacity of the material.[147]

Before any sorption measurements are performed on a material, both the material and the apparatus must be degassed. The extent to which degassing is performed will depend on the material and the analysis required. The thermal stability of the sample and the strength of binding of solvents and/or gas molecules will govern the temperature and the length of time in which degassing is performed. Guidelines from IUPAC suggest that for surface area and porosity measurements a high vacuum level of 10 mPa (10^{-4} mbar) is suggested as a satisfactory residual pressure. It also suggests that ultra high vacuums of around 1 μPa (10^{-8} mbar) may be enough to cause irreversible changes in surface structure. Some porous

materials (such as MOFs) are known to require the presence of solvents or some gas molecules to maintain the porous 3-dimensional structure, which collapses upon their removal.

It is important to note that for the purpose of degassing it is the pressure immediately above the sample that is important and not the pressure that is necessarily measured or achieved by the vacuum system. For instance, in the IGA-001 system (Hiden Isochema Ltd.), the pressure at the sample is expected to be around two orders of magnitude higher than at the turbomolecular pump.

The optimum temperature for degassing can be determined by thermogravimetric analysis or by trial and error experiments using different degassing conditions of time and temperature.[148] Figure 3.8 displays the effect of using three different temperatures for degassing: too low; too high; and the optimum temperature.

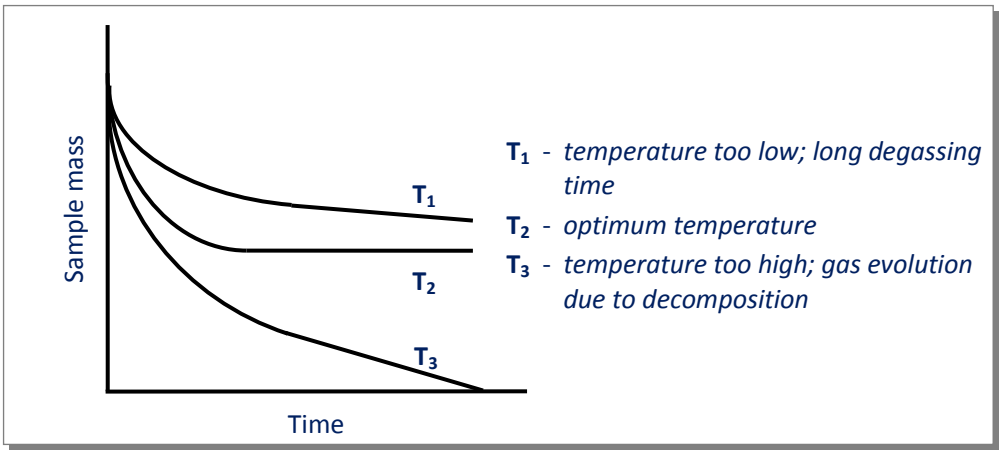

Figure 3.8 - Thermogravimetric control of degassing.[148]

Unfortunately, for porous materials the optimum temperature for degassing is very rarely achieved as there always appears to be some mass loss, even after extensive degassing at the highest possible temperature (without affecting the structure). This poses problems in determining the 'dry mass' of a material, particularly when performing several measurements at different temperatures. The sample requires degassing between each run in hydrogen and the dry mass recorded for each degassing procedure and subsequent isothermal measurement.

The situation is considerably worse for volumetric methods where the mass of the sample cannot be accurately monitored during the degassing procedure and therefore an alternative method must be used to determine the degassed mass of the sample. Typically the sample may be degassed prior to loading in the measurement equipment and then inertly loaded, or degassed inside the measurement equipment and then inertly unloaded before using an appropriate method to determine the 'dry mass' of the sample.

The sample and the equipment must be in thermal equilibrium before beginning a sorption measurement. It is also important to ensure that sufficient time is allowed for an equilibrium to be reached throughout the sample at given pressures.[50] In microporous materials, molecular hydrogen has to diffuse through the entire porous network until an equilibrium is reached. Due to the reasonably fast kinetics associated with physisorption, this typically occurs relatively quickly once the desired pressure has been reached. Equilibrium time for microporous materials are typically between 5 to 20 minutes. This can be measured either by the change in mass of the material or by a change in pressure (as previously mentioned) for the gravimetric and volumetric techniques, respectively; and can be analysed by the kinetic uptake at any particular sorption step. Sorption isotherms are made up of several kinetic traces at a series of pressures at a constant temperature (see Figure 3.9).

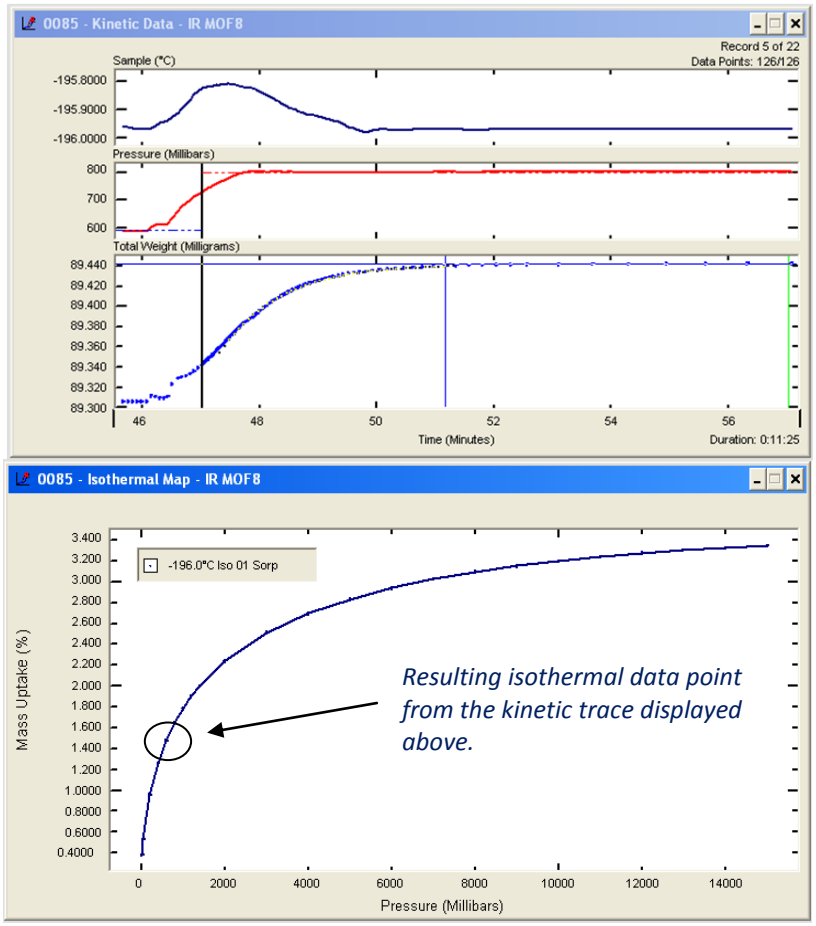

Figure 3.9 - Example of an individual kinetic trace (top) and the resulting adsorption isotherm (bottom) performed by the IGA at 77 K.

3.7.1.4. Volumetric

For volumetric measurements, the error in the accuracy of the pressure measurement device needs to be small enough to make it negligible in comparison to the expected pressure drop as a result of hydrogen adsorption (increase in the case of desorption), for any given sample size. This is also important for gravimetric devices, but is less critical for the overall gas sorption isotherms. It may therefore be necessary to equip both types of equipment with multiple pressure barometers, which are accurate in different pressure regimes within the pressure range of the equipment.

The volumetric method suffers from accumulative errors that may be introduced from the determination of the quantity of gas (in a single aliquot) from any number of sources. Many potential sources of error have already been mentioned but the obvious ones include the pressure measurement, temperature

measurement or gradient considerations, an inaccurate description of the hydrogen compressibility at higher pressures, the volume calibration and gas leaks.

Gas leaks that originate from connections in the pipe-work or from manual valves should be apparent from initial leak tests. Leaks internally through automated valves can often be observed by assessing the shape of an isotherm from relatively well-understood materials, or by kinetic traces not reaching equilibrium. Small gas leaks in a volumetric system can be mistaken as sorption by the sample material, although as mentioned this should be apparent from non-equilibrium conditions.[149]

The compressibility of hydrogen becomes significantly more important as the pressure increases. In the volumetric method, the uptake of hydrogen is calculated using the real gas law ($pV = nZRT$) where p is the pressure, V is the volume, n is the number of moles, Z is the gas compressibility factor, R is the universal gas constant and T is the temperature. The compressibility factor must be accurately described and applied to the experimental data, otherwise errors are introduced, which accumulate with increasing pressure. An appropriate equation of state (EOS) needs to be selected for each gas, temperature and pressure range. However, the correct choice is not straightforward.[144] Zhou and Zhou performed hydrogen adsorption measurements on 5A-zeolite and concluded that the Soave-Redlich-Kwong (SRK) and Benedict-Webb-Rubin (BWR) equations were suitable candidates to determine the compressibility factor of hydrogen for the use in the adsorption measurements.[150] The NIST Chemistry WebBook[25] (and REFPROP Database[122]) used a 32-term modified BWR EOS which can describe the behaviour of hydrogen down to around 14 K. However, the latest version of REFPROP uses a 14-term Helmholtz energy EOS, developed by Leachman *et al*.[151] Figure 3.10 shows the change in the compressibility of hydrogen as a function of pressure at a few different sub-ambient temperatures.

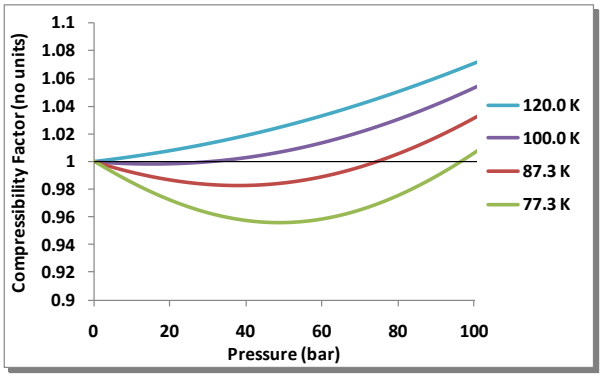

Figure 3.10 - Compressibility of hydrogen gas against pressure as determined by the modified 32-term Benedict-Webb-Rubin (BWR) equation of state. Produced from the NIST Chemistry WebBook.[25]

3.7.1.5. Gravimetric

In the gravimetric method, the dry sample mass is used as a reference point to determine each uptake value. Therefore each point in the isotherm is independent from the previous point, and hence not subject to accumulative errors.

The corrections required for the gravimetric techniques (particularly the buoyancy correction) are often believed to result in a significant source of error if incorrectly calculated.[111,144,149] The buoyancy correction is equivalent to dead space volume corrections in volumetric data, which account for the space occupied by the sample in the apparatus. An error in the buoyancy calculation is most commonly caused as a result of incorrectly determining the density of the sample material. The apparent change in weight Δw, upon gas sorption is expressed by IUPAC[57] as

$$\Delta w = w - w_0 = \left[m_e - \frac{V_s}{V_a}\right] M \qquad (3.70)$$

Where w is the apparent equilibrium weight after gas adsorption, w_0 is the weight of the sample in vacuum (the dry mass), m_e is the apparent gas adsorption (the Gibbs excess), V_s is the volume occupied by the sample (determined from an accurate density determination), V_a is the molar volume of the adsorbate (for example, hydrogen), and M is the molar mass of adsorbate. Equation (3.70) rearranges to

$$m_e = \frac{\Delta w}{M} + \frac{V_s}{V_a} \qquad (3.71)$$

where V_s/V_a is the buoyancy correction.[57] The change in volume (and weight) associated with sorption causes displacement of the gas inside the chamber (following Archimedes' principle). The volume and density of each component inside the chamber (including the sample, the sample holder, the microbalance counterweights and hangdowns) as well as the density of the gas affects the amount gas that is displaced. Determination of the amount of gas displaced therefore requires a summation of the masses and densities of each component and the density of the gas at the relevant temperature and pressure. This phenomenon can also be used for the determination of the sample density using a non-adsorbing gas and the subsequent change in weight with pressure. The amount of buoyancy correction also depends upon the density of the sample, with lower density samples requiring more correction as a result of the buoyancy effect.[111,144]

The size of the buoyancy correction does not significantly increase with increasing pressure (or temperature) if the bulk gas phase gas remains at a constant density. The changes in gas density (as a result of the compressibility of a real gas and temperature) gives rise to increasingly significant buoyancy corrections with increasing pressure, as the upward force deviates from linearity.[111,144]

Yang showed that gas purity was extremely important when performing hydrogen sorption measurements.[143] The comparable weight of impurities such as water makes an enormous difference in gravimetric techniques. Gas lines can introduce significant levels of impurities and it is therefore often important to add sufficient filtration to gas lines (such as liquid nitrogen traps), especially if the gas bottle is not directly attached to the equipment.[149] Broom recommended that the hydrogen purity should be > 99.999%.[144] Although, only using a hydrogen purity of 99.995%, Langmi investigated the effect of using a liquid nitrogen trap on the hydrogen inlet when measuring MWNTs at RT and 12 bar on a gravimetric system. An increase of 2 wt.% was observed when the liquid nitrogen trap was not used. Using a mass spectrometer, it was possible to identify the presence of water. This test was performed with only 30 bar hydrogen remaining in the gas cylinder.[152]

Additionally the shape of individual kinetic traces can also be used to give an indication of the adsorption of impurities such as water. This may be observed as a slow near-linear rise in mass.

Gas purity of other gases such as helium are also important for determining accurate hydrogen storage capacities. For instance, helium is used for the density determination and dead space volume calibrations, where it is assumed that helium is a non-adsorbing gas.[115,153,154]

Chapter 4

INTRODUCTION TO POROUS MATERIALS

4.1. Introduction

A report of 5.3 wt.% hydrogen at 40 bar and 77 K, for an activated carbon, by Chahine and Bose[155] in 1994 is believed to have sparked considerable research on hydrogen storage. Further reports in the late 1990's made sizeable claims of high hydrogen storage capacities in carbon nanotubes and fibres at room temperature (see Figure 4.1).[141]

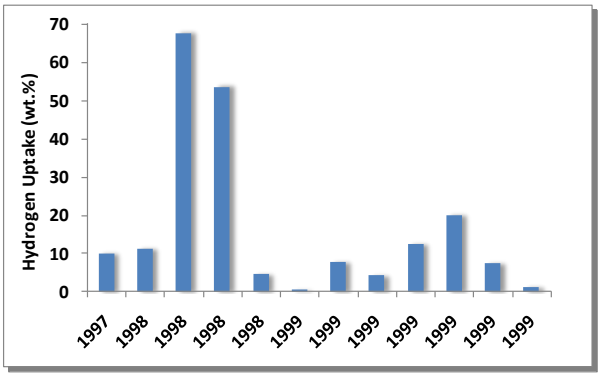

Figure 4.1 - Summary of some of the room temperature hydrogen storage capacities reported in the late 1990's.[66,139-141,156-160]

Physisorption of molecular hydrogen has been shown to correlate with surface area at intermediate pressures.[71,111,127,161,162] It therefore stands to reason that materials with large surface areas and low densities would be good for hydrogen storage applications.[161] Figure 4.2 displays the hydrogen uptake (at 10 bar and 77 K) against BET surface area for some carbon-based materials.

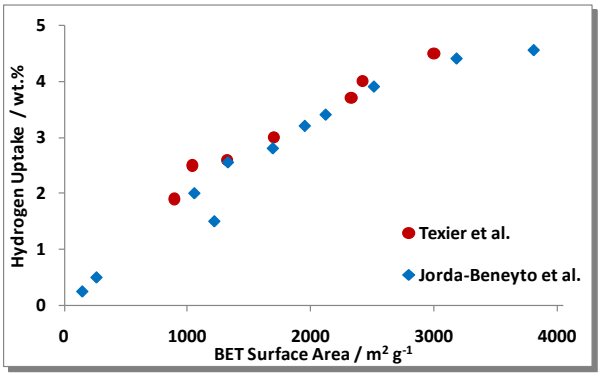

Figure 4.2 - The variation of hydrogen uptake at 10 bar and 77 K with BET surface area for activated carbons: Texier et al.[163], Jordá-Beneyto et al.[164], and carbon nanotubes: Jordá-Beneyto et al.[164]

Over the last twenty years, a large variety of materials have been reported as potential hydrogen storage materials including activated carbons, zeolites, framework materials and certain types of porous polymers. This chapter provides a review of the hydrogen storage properties of these materials.

4.2. Carbons

Elemental carbon atoms can form a variety of structures; generally these materials have sp^2-hybridised carbon atoms bonded to 3 other carbon atoms, and form six-membered rings.[165] The way in which the rings are arranged determines the differences in the materials. There are several known structures of carbon in the literature that have been considered for hydrogen storage, for example, carbon soots, carbon nanofibres, single-walled and multi-walled nanotubes, and activated carbons. Essentially carbon materials can be divided into two groups: those in which their six-membered rings form irregular structures, as in activated carbons, and those which have long-range order and therefore have regular structures, as in carbon nanotubes.

4.2.1. Carbon Nanotubes

Carbon nanotubes (CNTs) were accidentally discovered during research on fullerenes,[166] and were first described as 'helical microtubules of graphitic carbon'. They consist of graphite sheets rolled up into a cylindrical shape.[167] There are two types of carbon nanotube: those that form with a single wall (SWNT) and those that form multi-walls (MWNT).

SWNTs have inner diameters reported to be as low as 0.7 nm[165,168] and can range up to several nm. The lengths of the SWNT can significantly vary but typically lie in the range of 10 to 100 μm.[167] MWNTs consist of graphene sheets wrapped up to form a series of concentric cylindrical shells.[165] The number of shells can vary from 2 to more than 100 and they mutually interact via van der Waals intermolecular forces,[169] with the separation between adjacent shells being around 0.3 nm.[165,167]

Dillon *et al*. reported some of the first hydrogen uptake measurements on SWNTs. They suggested SWNTs could hold around 5 to 10 wt.% of hydrogen at room temperature.[139] This was based on a brief hydrogen

desorption experiment where the sample showed a hydrogen capacity of 0.01 wt.%; and through examination of a TEM micrograph, it was estimated that only 0.1 to 0.2 wt.% of the sample was occupied by SWNT. They assumed that the remainder of the sample had no influence on hydrogen uptake, and multiplied the hydrogen capacity accordingly to arrive at 5 to 10 wt.%.[139] Continuing research prompted many publications, with several authors claiming high hydrogen storage levels as shown in Figure 4.1 above.[170,171] However, the high hydrogen storage capacities could not be reproduced by other workers[172] and in recent years, values of < 1.2 wt.%[147,173-179] have been reported at room temperature. The low energy associated with the physisorption of hydrogen into porous materials means that low temperatures are required for significant hydrogen uptake. Table 4.1 shows a brief summary of some more recently reported properties and hydrogen uptake of some carbon nanotubes at 77 K. The quantity of hydrogen that could be adsorbed was found to be related to the specific surface area of the material.[180] This lead to increased interest being shown in other carbon materials, which had the potential to show large surface areas, such as activated carbons.

Table 4.1 - Brief summary of reported properties and hydrogen uptake of various carbon nanotubes.

Material	Surface Area / $m^2 g^{-1}$	Pore Volume / $cm^3 g^{-1}$	Conditions		Hydrogen Uptake / wt.%	Ref.
			p / bar	*T* / K		
SWCNT	780	0.12	1	77	0.8	[181]
A-SWCNT	1300	0.25	1	77	1.8	[181]
A-MNWT	1220	0.46	1	77	0.9	[164]
			10	77	1.5	[164]

Surface areas obtained from BET and t-method for reference [181] and [164], respectively.

4.2.2. Activated Carbons

It has been shown that synthetic graphite has very little surface area and is essentially non-porous.[182] However, by processing carbonaceous materials, porous structures with large internal surface areas, known as activated carbons (AC) have been developed. A wide range of applications already utilise ACs, with purification (of water and different gases) being one of the main uses. Other uses such as metal extraction, sewage treatment and in medicine for treating poisonings, mean that the ACs are already made in large quantities. The relative low cost and abundance of the raw material is one of the main advantages for using ACs in so many applications.[183]

ACs mainly consist of carbon, although they do also contain non-carbonaceous additives depending on the origin of the carbon-rich starting material, which includes, coal, peat, wood, fruit stones, nut-shells (and coconut shells) as well as some synthetic organic polymers.[183,184] These provide the ACs with non-carbonaceous additives such as mineral substances like oxides, minor quantities of sulphates, carbonates and other compounds such as Na, K, Ca, Mg, Fe and Al. The preparation of activated carbons typically requires two steps; carbonization and activation. Some workers such as Tam and Antal also used an oxidising intermediate step called oxygenation.[185] Carbonization involves heating to high temperatures (typically in the region of 600 to 800 °C) to remove volatile matter.[186,187] The carbon-rich product is then activated with steam (or CO_2) at atmospheric pressure and temperatures around 800 to 1000 °C.[188,189]

Activated carbons have microcrystalline structures that are often similar to graphite. However, unlike pure graphite, ACs contain disorder, which depends upon its precursor and treatment.[190] ACs often take the shape of distorted three-dimensional arrays of incomplete graphene sheets. It therefore would not be unreasonable to see ACs as being defective, however, it is these defects that give this class of materials a high degree of porosity and a wide of range pore sizes (with reports from as low as 0.3 nm).[190-193] Factors that govern the adsorptive properties of ACs and hence made them potential hydrogen storage materials.[182,194]

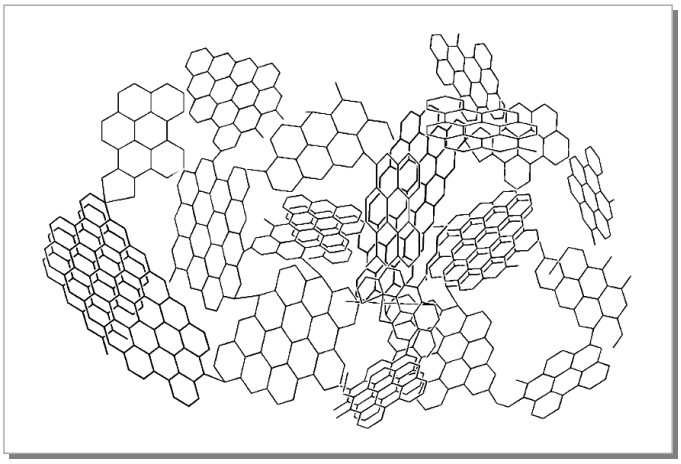

Figure 4.3 - A simplified representation of an activated carbon material.[195]

One of the first reported investigations into hydrogen adsorption on activated carbons, used carbon produced from coconut shells. The work was reported to show a maximum excess gravimetric hydrogen

storage density of 2.0 wt.% at 77 K and 25 bar.[171] Norit produced a large range of activated carbons, with surface areas over 2000 $m^2 g^{-1}$, some of which were reported to give hydrogen uptakes as high as 238 ml (STP) g^{-1} (2.14 wt.%) at 1 bar and 77 K.[182] Another activated carbon material with a surface area of 2564 $m^2 g^{-1}$ and average pore diameter of 1.2 nm, was fitted with the Fermi–Dirac (Single Langmuir) isotherm[65], to give a unique site energy of -56 ± 10 meV (-5.4 kJ mol^{-1}). It was also shown to give a maximum hydrogen uptake of 4.5 wt.% at 77 K and 40 bar.[196]

4.2.2.6. Templated Carbons

Chemical vapour deposition (CVD) has been used to make porous carbon materials. In this process, a flow of nitrogen gas, mixed with a carbon precursor is passed through a thermally stable zeolite. The thermal decomposition of the carbon precursor in a zeolite results in pyrolytic carbon forming in the channel.[197] The carbon/zeolite mixture is washed with an appropriate acid in order to remove the zeolite framework.[197,198] Advances were made with these types of materials, when two zeolite β templates were used with acetonitrile (as the carbon precursor) at 800 or 850 °C.[198] Hydrogen storage capacities of 6.0 and 6.9 wt.% were reported at 20 bar and 77 K, with BET surface areas of 3189 and 3150 $m^2 g^{-1}$, respectively. The pore size distributions of these materials were dominated by pores in the range 0.6 to 0.8 nm.[198] Some also show a 'kink' in the nitrogen desorption trace which could indicate two distinct pore sizes.[198-201] Hydrogen capacities for the (zeolite) starting materials were not reported, however, a 4-fold increase in surface area was observed.[198]

Su *et al*. obtained template carbons with high surfaces areas (up to 3683 $m^2 g^{-1}$) by using an ammonium form of zeolite-Y (NH_4Y) as the template and 2-furanmethanol as the carbon precursor. Interestingly, these materials did not show a 'kink' in the nitrogen desorption despite showing theoretical (Density Functional Theory - DFT) calculations of multiple pore sizes with an average of 1.5 nm.[202] Unfortunately, these materials were not subject to hydrogen storage measurements. Table 4.2 shows a summary of reported properties of selected activated carbons. Unfortunately, much of the early research did not consider the enthalpy of adsorption and pore volume, two properties which have been shown to be

important in defining hydrogen storage capacity in the relative low-pressure and high-pressure regimes, respectively.

Table 4.2 - Summary of reported properties and hydrogen uptake of various activated carbon materials.

Material	BET Surface Area / $m^2 g^{-1}$	Pore Volume / $cm^3 g^{-1}$	Hydrogen Uptake			Q_{st} / kJ mol^{-1}	Ref.
			p / bar	*T* / K	/ wt.%		
Synthetic Graphite	7	0.04	1.0	77	0	-	[182]
AC Norit SX 1	922	0.67	1.0	77	1.51	-	[182]
PICACTIF-SC	1700	-	1.0	77	1.9	-	[163]
			10	77	3.0		[163]
AC (AX-21)	2421	-	1.0	77	2.4	-	[163]
			10	77	4.0		[163]
	2800		35	77	5.3	6.4	[203]
Norit R0.8	1320	-	1.0	77	1.6	-	[163]
	1384	1.95	20	77	2.9	5.0	[191]
CB850h	3150	1.79	20	77	6.9	8.2	[198]
CA800	2191	0.75	20	77	3.0	-	[198]
Activated Carbon I	2564	-	40	77	4.5	5.4	[196]

4.3. Zeolites

The first zeolites were found as naturally occurring minerals and more recently, are typically formed by hydrothermal synthesis.[152,204,205] They have several uses including: molecular sieves, adsorbents, drying agents, catalysts, ion exchangers and water softeners.[206,207] Zeolites form a large family of aluminosilicate materials, with over 150 different zeolite structures being reported.[207-209] Unlike activated carbons, they have very ordered structures. Depending on the assembly of their tetrahedral building units and framework type they can also be microporous. Their structures are based upon $[SiO_4]^{4-}$ and $[AlO_4]^{5-}$ tetrahedral units that link together to give anionic networks in which each oxygen of a given tetrahedron is shared between this tetrahedron and one of four others. Thus forming bent oxygen bridges and which form the primary building units. These primary units then form cages of various sizes, and these are termed secondary units. The anionic skeleton of zeolites is penetrated by channels giving a honeycomb-like structure, see Figure 4.4.[206,207]

The additional negative charge created by the presence of aluminium (in place of silicon), is electronically neutralised by the presence of cations (typically metals), which sit in the centre of the tetrahedral units.

Water is also typically present in order to fulfil coordination requirements. Zeolites have the general formula:

$$M_{x/n}[(AlO_2)_x(SiO_2)_y].mH_2O$$

where cations, M, of a valence equal to n, neutralise the negative charge of the zeolite framework.[206,207] The cations are exchangeable, Langmi *et al*. performed a systematic investigation of hydrogen storage in zeolites.[152,204,205] Zeolites NaA, NaX, NaY and NaCsRho were used as starting materials for the ion-exchange process. They concluded that calcium-exchanged zeolite X had the greatest excess gravimetric hydrogen storage capacity; 2.19 wt.% at 15 bar and 77 K, with a BET surface area of 669 $m^2 g^{-1}$. NaX and NaY had the highest uptake from the starting materials and were found to adsorb 1.79 and 1.81 wt.%, respectively, at 15 bar and 77 K.[152,204] Zeolites typically exhibit reasonably good volumetric capacities (31 kg H_2 m^{-3} for CaX) relative to their low gravimetric storage capacities, which is caused by the relatively large concentration of metal ions.[152,204]

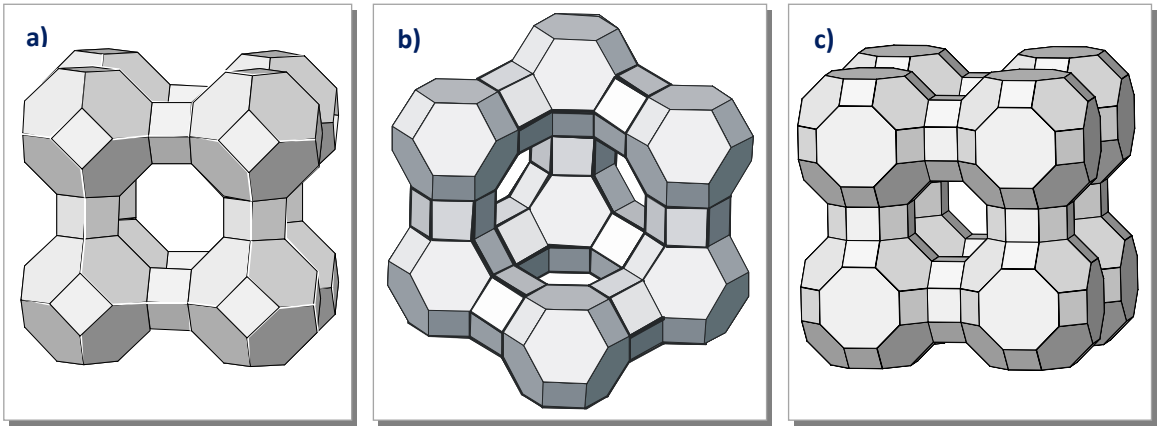

Figure 4.4 - Framework structures of a) zeolite A; b) zeolite X and Y; and c) zeolite RHO.[152,205]

Diameters of the central open cages range from 0.66 to 1.18 nm which can give them an aperture of around 0.74 nm in diameter for zeolite NaX as can be seen in Table 4.3.[152,204-207] For zeolites A, X, and Y, the diameter of the β cage is too small for the kinetic diameter of the hydrogen molecule (0.29 nm),[210,211] and therefore does not participate in the physical adsorption of hydrogen. Therefore the α cage and the supercage, for the A and X or Y zeolites are responsible for hydrogen uptake, respectively. The NaA zeolite exhibited considerable hydrogen uptake at 77 K and 15 bar despite not adsorbing nitrogen at 77 K and hence not displaying a BET surface area (see

Table 4.4). This phenomenon is probably a consequence of the kinetic diameter of the two molecules, which is 0.29 and 0.36 nm, respectively.[210,211]

Table 4.3 - Structural characteristics of zeolites A, X, Y and RHO determined by X-ray and neutron crystallographic techniques.[152,205-207,209]

Zeolite Type	Cage Type	Pore Aperture Diameter / nm	Pore Size / nm
A	β	0.22	0.66
	α	0.41	1.14
X or Y	β	0.22	0.65
	supercage	0.74	1.18
Rho	α	0.36	1.10

Zeolite Rho lacks any β-cages, thus meaning that it relies upon α-cages for hydrogen uptake. However, the hydrogen uptake by zeolite Rho was found to be insignificant. This was believed to be a consequence of Cs^+ ions (from the starting material, NaCsRho) remaining after the ion-exchange and effectively blocking the adsorption sites within the α-cages.[152,205] This effect was confirmed by the CdRho zeolite, which was made as a result of ion exchange with NaCsRho. Two samples of the CdRho zeolite exhibited BET surface areas of 90 and 138 $m^2 g^{-1}$, respectively. Energy Dispersive X-ray (EDX) analysis confirmed that the two materials had undergone different degrees of ion exchange (67 and 83%, respectively). This lead to the first CdRho product containing three times more Cs^+ ions, which consequently exhibited a greater blocking effect.[152]

Table 4.4 - Summary of reported BET surface area (using nitrogen adsorption at 77 K) and hydrogen uptake (at 77 K and 15 bar) of some Group I and II ion-exchanged zeolites A, X, Y and Rho.

Zeolite	BET Surface Area / $m^2\ g^{-1}$	Hydrogen Uptake / wt.%	Reference
LiA	1.26	0.1	[152]
NaA	N/A	1.54	[152,204,205]
MgA	410	1.09	[152,205]
CaA	565	1.89	[152,204]
LiX	742	2.17	[152]
NaX	662	1.79	[152,204,205]
MgX	597	1.62	[152,204,205]
CaX	669	2.19	[152,204]
LiY	738	1.80	[152]
NaY	725	1.81	[152,204]
MgY	670	1.76	[152,204]
CaY	684	1.82	[152,204]
NaCsRho	3	0.00	[152,205]
CdRho	138	0.08	[152,205]

Li and Wu measured the hydrogen adsorption in NaX at temperatures around the critical point.[212] However, their excess hydrogen storage capacity at 20 bar and 80 K, was only *ca*. 1.2 wt.%. They used nitrogen adsorption and the spherical model of the H-K equation to produce a pore size distribution with a mean pore size of 1.2 nm.[212] They also calculated total and micropore volumes to be 0.34 and 0.26 $cm^3\ g^{-1}$, respectively, using the *t*-plot method. The authors calculated a value of 4.4 kJ mol^{-1}, by using the low-pressure region of adsorption isotherms to create a plot of ln$p$ against $1/T$ according to the Clausius-Clapeyron equation.[212] This was in line with workers, such as Jhung *et al*.[213], and within the typical range for hydrogen adsorption in zeolites (4 to 10 kJ mol^{-1}).[212] Stéphanie-Victoire *et al*. used a gravimetric technique, between 77 and 120 K, to measure the hydrogen uptake and subsequently determine the enthalpy of adsorption for NaY. The authors reported values of 10.7 kJ mol^{-1} at low coverage which decreased to 6.2 kJ mol^{-1} after 10 hydrogen molecules had been adsorbed into each cavity.[214]

The isosteric enthalpy of adsorption has also been determined using variable temperature infrared (VTIR) spectroscopy. Values as high as 18.2 kJ mol^{-1} have been reported for (Mg,Na)-Y Zeolite, with the Mg^{2+} ions being attributed to the high binding energies.[215,216] This is compared to 15.0 kJ mol^{-1} in (Ca,Na)-Y,[217]

which contains the larger divalent Ca^{2+} ion. For zeolites the charge-to-volume ratio was found to be important for the electrostatic interactions, which increase as univalent exchangeable cations are replaced by divalent and trivalent ones. For a particular zeolite type, hydrogen interaction would be expected to be stronger for zeolites containing extraframework cations with larger charge-to-volume ratio.[218] In fact, Kazansky *et al*. reported from IR spectroscopy that the rotation of hydrogen molecules adsorbed in LiX were substantially hindered, whereas in CsX they were almost free.[219]

4.4. Metal-Organic Framework (MOF) Materials

Carbon-based crystalline and porous structures similar to those of zeolites have long been sort after. Framework materials can be used for a variety of applications, including heterogeneous catalysis, gas purification, gas separation and gas storage.[208,220-222]

Under the general theme 'Framework materials', many compounds are often given the term MOF (Metal-Organic Framework). Framework materials are actually broken down into different categories, such as: IRMOF (Isoreticular Metal-Organic Frameworks), MOP (Metal-Organic Polyhedra), ZIF (Zeolitic Imidazole Frameworks), PMOF (Porous Metal-Organic Frameworks), and MMOF (Microporous Metal-Organic Frameworks, Magnetic Metal-Organic Frameworks or Mixed Metal Organic Frameworks) as well as others. In addition to this list, CP (Coordination Polymers), and PCP (Porous Coordination Polymers) are also sometimes included. However, it is generally now excepted that these two latter categories are distinguished from general 'MOF' materials.[223]

MOF materials are formed by coordinate bonds from multidentate ligands (such as 1,4-benzenedicarboxylate) to metal centres (such as ZnO_4 tetrahedra), which can have extensive open-framework structures allowing for the inclusion of guest species. The guest specie is usually a solvent and would generally be a direct result of the synthesis process. MOFs exist as an extensive network of metal-oxygen bonds with carboxylate ligands, which offers excellent robustness even after the removal of the solvent. The ligand linkages differ both in functionality of pendant groups, and in length. Simply varying these ligand linkages enabled researchers to 'design' MOF materials in a process that was to become

"reticular chemistry". Using the same inorganic secondary building unit and by simply changing the ditopic organic linkers researchers were able to produce a variety of materials with the same structural topology but differing in pore size and functionality. The Isoreticular series of MOFs was the first of this kind, some of the organic linkers used in forming this series are illustrated in Figure 4.5.[224,225]

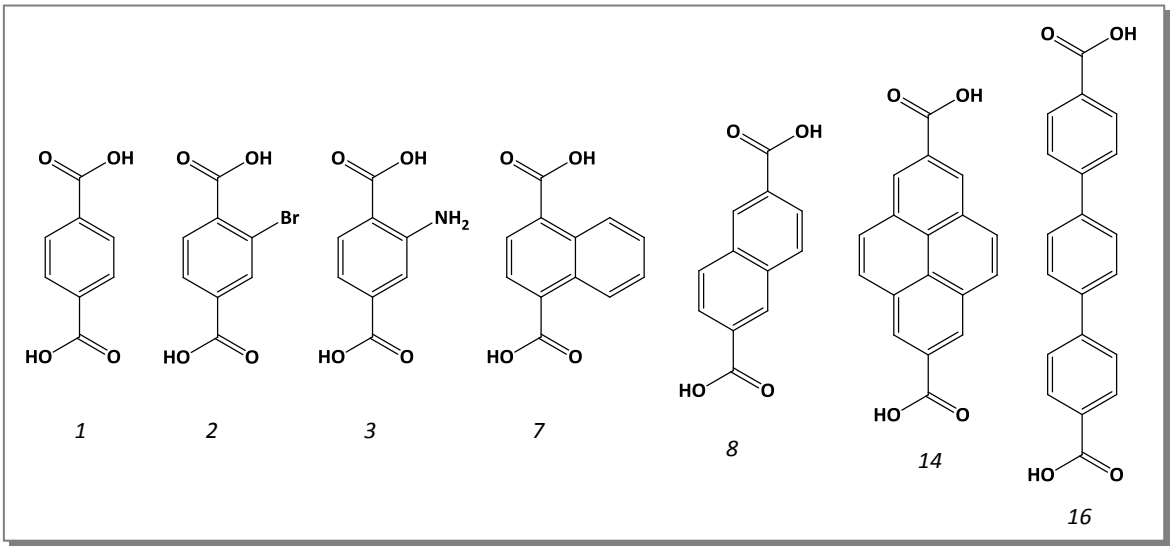

Figure 4.5 - Example of dicarboxylic acid linkers used in forming IRMOFs. Here the linkers used form IRMOF- 1, 2, 3, 7, 8, 14 and 16, labelled respectively.[225]

4.4.1. Carboxylate-based Framework Materials

IRMOF-1 is based on the cubic carboxylate framework Zn_4O(1,4-benzenedicarboxylate)$_3$ and was one of the first of these materials to be studied for hydrogen storage applications;[226] it was originally given the alternative name of MOF-5.[225] The porous structure of MOF-5 is illustrated in Figure 4.6.

Carboxylate-based framework materials form the majority of reported MOFs. Commercial availability and high-yielding synthetic routes of these carboxylate-based ligands are likely reasons for their high number. Carboxylic acids are also attractive as framework-forming reagents because their high acidity (*p*Ka of *ca*. 4) allows facile *in situ* deprotonation, which is presumably related to the full reversibility of the metal-carboxylate bond under mild conditions. Together this provides further suggestions for the high proportion of carboxylate-based framework materials.[161]

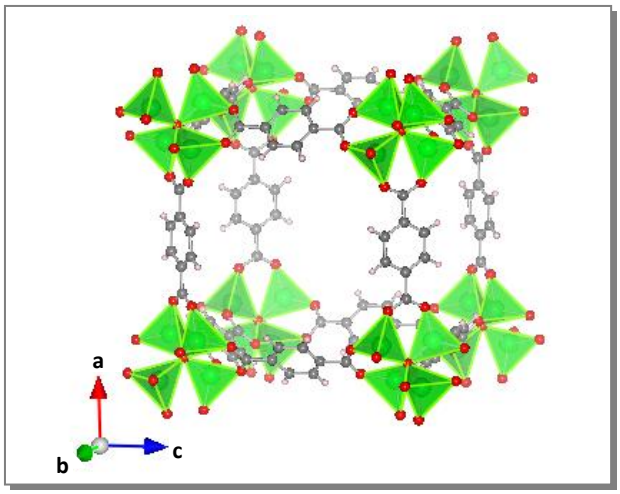

Figure 4.6 - Isoreticular MOF-1 (MOF-5) with four Zn_4O tetrahedra (green), which give an octahedral subunit at each corner of the cubic cell (Zn, green; O, red; C, grey; H, pink). Reconstructed using data from the following reference [227].

Since the structure was first reported, the compound has undergone rigorous research due to its high thermal stability and the wide variation in adsorption data that it seemed to produce with BET and langmuir apparent surface areas; ranging from 572 to 3800 $m^2 g^{-1}$ and 1014 to 4400 $m^2 g^{-1}$, respectively.[47,134,147,226,228-232] Initial reports presented an excess gravimetric uptake of 1.3 wt.% at 1 bar[134] and 5.1 wt.% at 50 bar and 77 K.[228] However, these differences were later attributed to the preparation and handling of the material; specifically, the partial decomposition of the framework, (which was observed using powder X-ray diffraction after just a few minutes) and the incomplete evacuation of the porous network.[147,233] The ability to protect the sample from exposure to air and water (during and after synthesis in an inert atmosphere) coupled with complete activation provided an excess gravimetric hydrogen uptake of 7.1 wt.% and 40 bar at 77 K.[147] At 100 bar, it showed a total gravimetric hydrogen uptake of 10.0 wt.%, corresponding to a volumetric storage density of 66 kg m^{-3} (see Figure 4.7).[147] Subsequently, the importance of the complete removal of any solvents and other gas molecules, by activation, before performing hydrogen measurements became apparent.

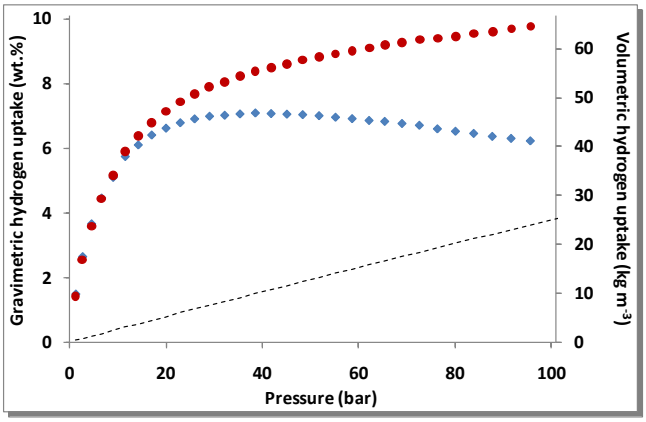

Figure 4.7 - Excess (♦) and absolute (●) hydrogen adsorption for MOF-5 at 77 K.[147] The density of compressed hydrogen (at 77 K) multiplied by the pore volume is indicated by the dashed line, over the given pressure range.

Whilst MOF-5 is still one of the best cryogenic storage materials available, its performance at ambient temperature is poor as a result of the relatively low enthalpy of adsorption. In fact, its excess hydrogen capacity at 298 K and 100 bar is merely 0.57 wt.%, which corresponds to a total uptake of 1.47 wt.% and a volumetric storage capacity of 8.8 kg m^{-3}.[147] This volumetric storage density is not much more than pure hydrogen gas under the same conditions (7.7 kg m^{-3}).[234]

Isosteric enthalpy of adsorption values have been reported ranging from 2.2 to 7.7 kJ mol^{-1}.[117,228,230,235-238] Saha *et al*. proposed particularly low enthalpies of adsorption (between 2.2 and 2.6 kJ mol^{-1}) using the Clausius-Clapeyron method. Additionally they used the H-K method to determine a median pore size of 0.86 nm and a cumulative pore volume of 1.39 cm^3 g^{-1}.[235] However, these did not match the values that were first reported by Rowsell *et al*. who stated MOF-5 has a aperture window size of 0.78 nm, then has (spherical) pore sizes of 1.21 and 1.52 nm, with a pore volume of 1.19 cm^3 g^{-1}.[134,227,237] Sillar *et al*. found the strongest site specific hydrogen interaction energy to be 7.1 kJ mol^{-1}, and the lowest to be 4.1 kJ mol^{-1}.[236]

Bordiga *et al*. performed IR spectroscopy at 15 K, in addition to *ab initio* calculations, to show that the adsorptive properties in IRMOF-1 were mainly a result of dispersive interactions with the internal pore walls (*ca*. 3.5 kJ mol^{-1}). However, they did observe some weak electrostatic interactions, which they associated with clusters of Zn_4O_{13}. The authors reported a binding energy of 7.4 kJ mol^{-1}, for the hydrogen adsorption to these sites.[239]

The gravimetric hydrogen storage density in metal-organic framework materials is influenced by the mass of metal ions within the structure. It is logical to make use of light metal ions, for example, Be^{2+}, Mg^{2+}, Ca^{2+}, and Al^{3+}. However, despite this, there are only a few reported MOF materials containing such ions, presumably due to synthesis difficulties. Indeed there is only one reported porous beryllium-containing framework[240] and no calcium-based frameworks that have demonstrated any microporosity.[161] The first structurally characterised MOF to be based on upon beryllium contains saddle-shaped ring units, which are composed of tetrahedrally coordinated Be^{2+} ions. Low-pressure nitrogen adsorption measurements, performed at 77 K, provided BET and Langmuir surface areas of 4030 and 4400 $m^2 g^{-1}$, respectively. Low-pressure hydrogen adsorption measurements at 77 K revealed a gradual rise in uptake and reached values of 1.6 wt.% at 1 bar, which yielded an isosteric enthalpy of adsorption of 5.5 kJ mol^{-1}. The excess hydrogen storage capacity of the $Be_{12}(OH)_{12}(BTB)_4$ framework* continues to rise to 6.0 wt.% at 20 bar and to a total value of 9.2 wt.% at 100 bar, which equates to 43 kg m^{-3}.[240] Framework materials containing magnesium[241] or aluminium ions are rare; however, they do at least adsorb hydrogen at cryogenic temperatures. Unfortunately, all magnesium-based frameworks only exhibit relatively low surface areas and consequently the highest hydrogen uptake observed is 0.78 wt.% at 1 bar and 77 K. This was achieved by $Mg_3(NDC)_3$*, which has a Langmuir surface area of just 520 $m^2 g^{-1}$.[242] Just two aluminium-based frameworks have been reported for hydrogen storage:[238,243] of which the highest uptake is 3.8 wt.% at 16 bar and 77 K for Al(OH)(BDC)*, MIL-53(Al), which is structurally analogous to Cr(OH)(BDC), MIL-53(Cr). The chromium-based MOF exhibits just 3.1 wt.% under the same conditions as its counterpart material. This is despite their structural similarities including; free apertures of 0.84 and 0.85 nm, BET and Langmuir surface areas of 1020 and 1026 $m^2 g^{-1}$ and 1590 and 1500 $m^2 g^{-1}$; and pore volumes of 0.59 and 0.56 $cm^3 g^{-1}$, respectively.[161,173,238] Other noteworthy chromium-based frameworks include $Cr_3OF(BTC)_2$* and $Cr_3OF(BDC)_3$ which have been given the names MIL-100 and MIL-101, respectively. The latter framework exhibits BET and Langmuir surface areas of 4100 and 5900 $m^2 g^{-1}$, this in conjunction with a

* BTB = 1,3,5-benzenetribenzoate; NDC = 2,6-napthalenedicarboxylate; BDC = 1,4-benzenedicarboxylate; BTC = 1,3,5-benzenetricarboxylate.

pore volume of 1.9 $cm^3 g^{-1}$ gives an excess gravimetric hydrogen storage capacity of 6.1 wt.% at 80 bar and 77 K. This remarkable material not only offers a relatively high surface area and pore volume but it has also been reported to have an isosteric enthalpy of adsorption of 10 $kJ\,mol^{-1}$ at low coverage measured directly by microcalorimetric experiments.[173,238,244,245] $Cr_3OF(BDC)_3$ contains the same organic linker (1,4-benzenedicarboxylate) as the aforementioned $Zn_4O(BDC)_3$, the former however encompasses oxo-centred triangular clusters.[243]

Transition metal-carboxylate frameworks have attracted the most interest, where much of the focus has been on 3d divalent ions such as Zn^{2+} and Cu^{2+}. $Zn_4O(BTB)_2$ (MOF-177) was the subject of independent verification due to its exceptionally high gravimetric uptake of 7.5 wt.% at 80 bar and 77 K.[47,118] However, in MOF-177 (as shown in Figure 4.8) the tetrahedral $[Zn_4O]^{6+}$ units are linked via large triangular tricarboxylate ligands, resulting in particularly large pores; and as a consequence shows a relatively low volumetric storage capacity, just 32 $kg\,m^{-3}$ relative to its gravimetric capacity, under the same conditions.[47,118,246] The low crystallographic density (0.43 $g\,cm^{-3}$) is also a result of the pore volume (1.69 $cm^3 g^{-1}$), which can accommodate a sphere with a diameter of 1.18 nm.[118] The large pore volume of MOF-177 leads to a total gravimetric uptake of 11.4 wt.% and volumetric uptake of 48 $kg\,m^{-3}$.[118] $Zn_4O(BTB)_2$ also has one of the largest reported surface areas, with BET and Langmuir calculations giving as high as 4750 and 5640 $m^2 g^{-1}$, respectively.[47,118]

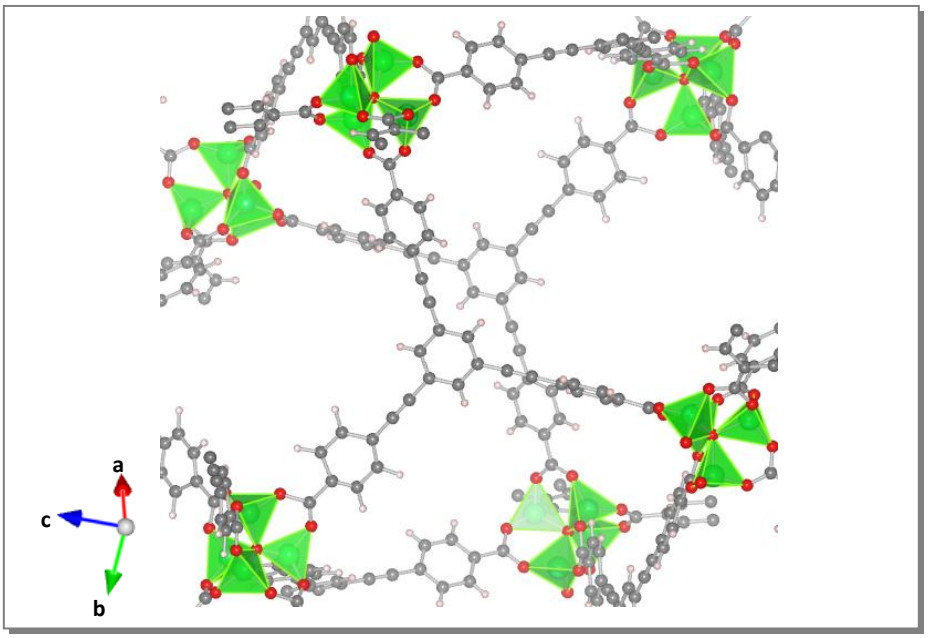

Figure 4.8 - MOF-177, with six central Zn_4O tetrahedra (green), forming the edge of the pore (Zn, green; O, red; C, grey; H, pink). Reconstructed using data from reference [247].

One of the highest reported gravimetric uptakes at 20 bar and 77 K is the Cu^{2+}-containing framework Cu_2(qptc), which features paddlewheel-type clusters. This compound demonstrated a BET surface area of just 2932 $m^2\,g^{-1}$, however it also produced an excess gravimetric hydrogen uptake of 6.1 wt.% and a volumetric capacity of 41.1 $kg\,m^{-3}$. At 1 bar and 77 K, this material exhibited an excess uptake of 2.24 wt.%.[248] Cu_2(qptc)* has a pore volume of 1.14 $cm^3\,g^{-1}$, which is similar to that of MOF-5. Another notable Cu^{2+}-containing compound is $Cu_3(BTC)_2$ (commonly named HKUST-1 or Cu-BTC), which consists of $Cu_2(O_2CR)_4$ paddlewheels (where R is an aromatic ring) with dimeric cupric tetracarboxylate units.[249] Twelve carboxylate oxygen atoms from the two BTC ligands bind to four coordination sites for each of the three Cu^{2+} ions.[250] Each Cu^{2+} ion is also coordinated by a water molecule in axial position, which can be removed in vacuum or by heating.[161] The structure of Cu-BTC (shown in Figure 4.9) consists of main channels of a square cross-section of *ca*. 0.98 nm in diameter and tetrahedral side pockets with a diameter of *ca*. 0.5 nm which are connected to the main channels by a triangular window of 0.35 nm in diameter.[161,228,250]

* qptc = quarterphenyl-3,3’’’5,5’’’-tetracarboxylate.

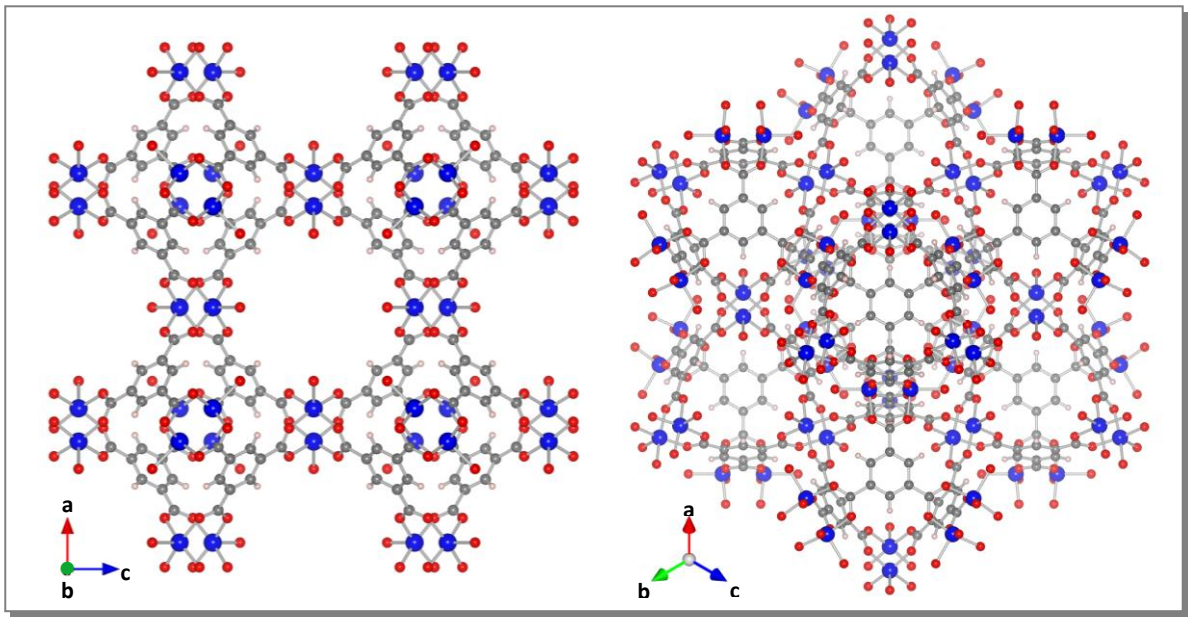

Figure 4.9 - Cu-BTC unit cell looking along the 100 and 111 directions (left and right, respectively). (Cu, blue; O, red; C, grey; H, white). Reconstructed using data from references [249].

Using variable-temperature infrared spectroscopy and powder neutron diffraction this MOF material was one of the first that was shown to bind hydrogen to exposed metal sites at low temperatures.[251,252] The exposed metal sites increase the adsorbate-adsorbent interaction energy[253], which for this material was reported to be as high as 6.8 kJ mol^{-1}.[134] This is also seen by the relatively steep gradient of the hydrogen isotherm at 77 K. The material exhibits a gravimetric hydrogen capacity of 2.5 wt.% at 1 bar,[134] which rises to 3.6 wt.% at just 10 bar.[254] This is despite the comparatively moderate specific surface areas of 1507 and 2175 $m^2 g^{-1}$, for the BET and Langmuir calculations respectively, and a pore volume of 0.75 $cm^3 g^{-1}$.[134]

4.4.2. Heterocyclic Azolate-based Framework Materials

Tetrazolate is a five-membered heterocyclic ring with four adjacent nitrogen atoms (see Figure 4.10), and is a functional analogue of the carboxylate group. Additionally, the similarity between the tetrazolates and the carboxylate extends to their coordination chemistry, with structural analogues existing in the literature. For example, $Zn_3(BDT)_3$ and $Cu[(Cu_4Cl)(ttpm)_2]_2$* are structurally equivalent to $Zn_2(BDC)_3$ and

* ttpm = tetrakis(4-tetrazolylphenyl)methane.

$Cd_4(TCPM)_2$,*[255] respectively. The two tetrazolate-based frameworks exhibit a hydrogen capacity of 1.46 and 2.8 wt.%, respectively, at 1 bar and 77 K.[256,257]

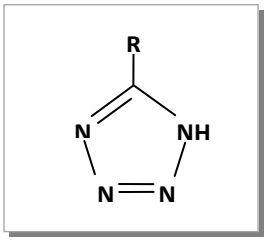

Figure 4.10 - Basic tetrazole ring which is incorporated in to different organic linkers forming heterocyclic azolate-based frameworks.

Unfortunately, there have been no reported hydrogen sorption measurements for these carboxylate-based analogues and furthermore there have been no published comparisons of tetrazolate-carboxylate framework analogues for hydrogen storage.[161]

Differences do however exist; whilst carboxylate ligands are typically bidentate, the tetrazolate ligand is able to use all four nitrogen atoms for metal coordination. This facilitates additional structural possibilities that are not achievable with the equivalent carboxylate group. Both types of framework materials are sensitive to moisture, however, whilst the carboxylate-based frameworks are generally quite thermally stable the tetrazolate-based frameworks are not. This brings about the problem of complete outgassing (and activation). Indeed, most tetrazolate-based frameworks begin to collapse above 200 °C.[161] Unfortunately, the temperature instability and moisture sensitivity, somewhat renders these tetrazolate-based frameworks as unsuitable hydrogen storage materials. However, replacing the tetrazole units with five-membered azole rings, such as, triazole, pyrazole or imidazole, could reduce the effect of these issues. For instance, Co(BDP)* is structurally analogous to Cu(BDT)*, but whereas Cu(BDT) is not thermally stable and does not significantly adsorb hydrogen,[256] Co(BDP) is stable up to 400 °C and has a hydrogen storage capacity of 3.1 wt.% at 30 bar and 77 K (with a Langmuir surface area of 2670 $m^2 g^{-1}$ and a pore volume of 0.93 $cm^3 g^{-1}$).[258] A linear BET plot cannot be created from the nitrogen adsorption isotherm of Co(BDP) due to unusual adsorption steps (see Figure 4.11). The step behaviour is typically attributed to

* TCPM = tetrakis(4-carboxyphenyl)methane; BDP = 1,4-bezenedipyrazolate; BDT = 1,4-benzeneditetrazolate.

adsorption on energetically homogeneous surfaces, multiple adsorbent-adsorbate interaction energies, or various structural phase transitions occurring at different adsorbate pressures.[48,258-261] The hydrogen sorption isotherms also exhibit unusual behaviour for a microporous material. In fact, below 20 bar, at 77 K, it adsorbs almost no hydrogen at all, but then exhibits a sharp rise in uptake. This is accompanied by significant desorption only occurring below 15 bar, which gives a broad hysteresis as displayed in Figure 4.11. An effect which is more commonly seen in metal-hydride compounds, when pressure is plotted against uptake.[258] The effect for this porous material is thought to be as a result of a structural change, where at low pressures the porous channels are thought to be in a collapsed state, which are then re-opened with an increase in pressure.[210,238,258,262]

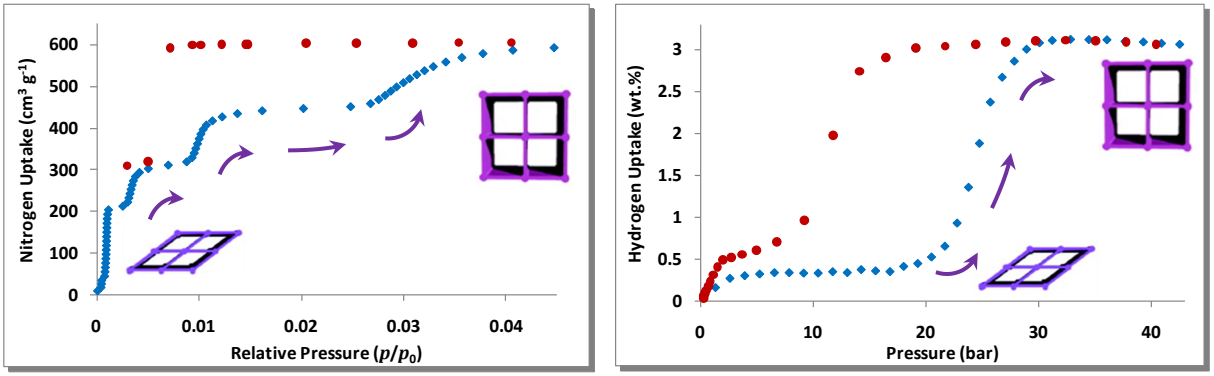

Figure 4.11 - Nitrogen (left) and Hydrogen (right) adsorption (♦) and desorption (●) isotherms for Co(BDP) at 77 K. [258]

4.4.2.7. Zeolitic Imidazolate-based Framework (ZIF) Materials

Despite the wide variety and diversity of structures shown by MOF materials, the relative lack of zeolite-like structures prompted additional research. In silicate structures, the Si-O-Si bond angle is typically around 145 °. The organic carboxylate linkers offer great flexibility resulting in various different structures, however it is a property that also leads to the lack of an ideal bond angle that is required for rigid bonding between metal centres. The imidazole molecule has been shown to hold a bond angle of 144 ° between nitrogen atoms.[263] Zeolitic Imidazole Frameworks (ZIFs), are a class of MOFs, in which metal atoms such as Zn are linked through nitrogen atoms by ditopic imidazolate ($C_3N_2H_3^-$ = Im) or functionalized Im links to form neutral framework materials.[264] The use of a bivalent metal also gives a distinct resemblance to the SiO_2 units that are present in zeolites.[263] These give very robust metal-organic frameworks, several of

which have been shown to have high chemical and thermal stabilities; including concentrated basic solutions and temperatures in excess of 350 °C.[208]

A vast number of imidazolate-based frameworks have been reported in the literature[117,208,224,264-268], however, there have been very few reports that include hydrogen storage data. Among these, the highest capacity measured is by $Zn(MeIm)_2$ (ZIF-8), which showed 1.3 wt.% at 1 bar, and 3.3 wt.% at 30 bar and 77 K;[117] with a specific surface area of 1630 and 1810 $m^2 g^{-1}$ for the BET and Langmuir methods, respectively. These values are greater than any reported zeolite. The report also included a micropore volume of 0.636 $cm^3 g^{-1}$ for the ZIF-8 material.[208] The isosteric enthalpy of adsorption was calculated using a Clausius-Clapeyron equation to be *ca*. 4.8 kJ mol^{-1}.[117] The hydrogen uptake capacity for a similar ZIF material, $Zn(PhIm)_2$ (ZIF-11) has been reported as being 1.37 wt.% at 1 bar. Figure 4.12 illustrates the unit cells for the ZIF-8 and ZIF-11 materials. The only other comparable data for these two ZIFs are some structural characteristics from single crystal X-ray diffraction, which can be seen in Table 4.5.

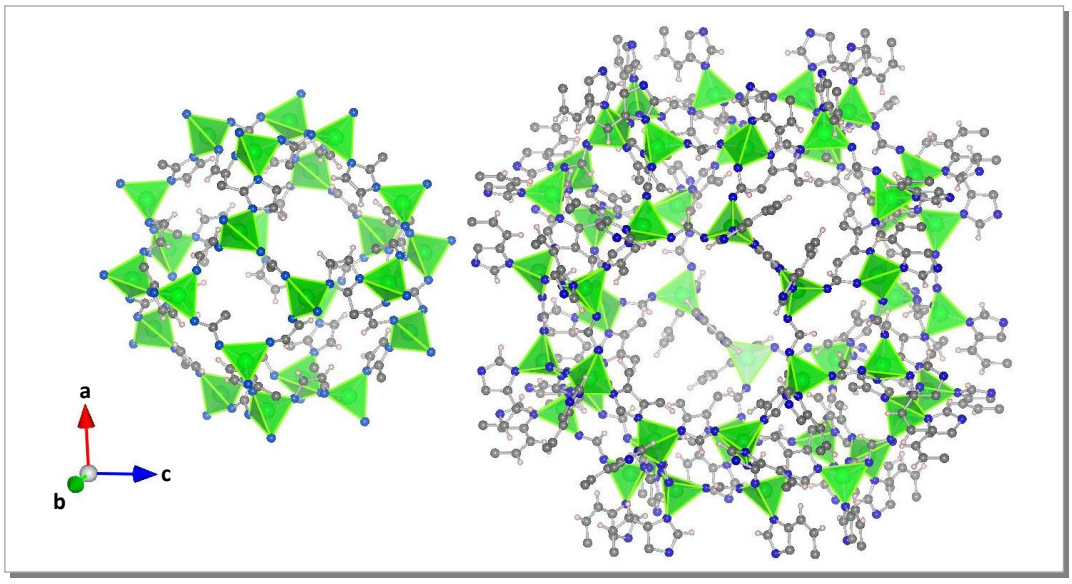

Figure 4.12 - Unit cells for ZIF-8 (left) and ZIF-11 (right), showing ZnN_4 tetrahedra (green) linked by MeIm and PhIm for ZIF-8 and ZIF-11, respectively, (Zn, green; N, blue; C, grey; H, white). Reconstructed using data from reference [208].

The increased pore size, lower surface area and smaller pore volume, would lead to an estimation of lower isosteric enthalpy of adsorption as well as a decreased hydrogen uptake capacity. Interestingly however, whilst the decrease in hydrogen uptake was observed at higher pressures, the excess hydrogen

isotherm up 1 bar shows greater initial excess hydrogen uptake for ZIF-11. This likely to be as a result of the protruding benzene side rings (benzimidazolate units) in the PhIm links or due to the marginally smaller diameter of the pore aperture, which will give favourable hydrogen adsorption sites.[208]

Table 4.5 - Structural characteristics of ZIF-8 and ZIF-11 calculated from single crystal x-ray analysis. [208]

Material	Pore Aperture Diameter / nm	Pore Size / nm	Surface Area / $m^2 g^{-1}$	Pore Volume / $cm^3 g^{-1}$
ZIF-8	0.34	1.16	1947	0.66
ZIF-11	0.30	1.46	1676	0.58

4.4.3. Mixed-Ligand/Functionality Systems

Whilst designing a system that contains both tetrazolate and carboxylate ligands is somewhat challenging due to their different metal-binding functionalities; obtaining such a material could address the thermal stability problems of the tetrazolate-based frameworks.[161] Nouar *et al*. reported an example of such a framework, $Cu_6O(tzi)_3(NO_3)$, which exhibits a BET and Langmuir surface area of 2847 and 3223 $m^2 g^{-1}$, respectively, and a gravimetric hydrogen storage capacity of 2.4 wt.% at 1 bar and 77 K.[269] The framework contains two carboxylate groups and a tetrazolate ring; within which, each Cu^{2+} ion offers two exposed coordination sites and three different cage sizes with "spherical" diameters of 2.0, 1.3 and 1.2 nm. These result in an isosteric enthalpy of adsorption of 9.5 kJ mol^{-1}, dropping to 4.7 kJ mol^{-1} from 0.1 to 1.5 wt.%; Unfortunately, the method used for calculating this was not reported.[269]

4.4.4. Metal-Cyanide Framework Materials

Prussian Blue is often considered as the first synthetic coordination compound and has since been extensively studied due to its diverse magnetic and electronic properties.[270,271] Kaye *et al*. investigated dehydrated Prussian Blue analogues of the formula $M_3[Co(CN)_6]_2$ (where M = Mn, Fe, Co, Ni, Cu, Zn). They form a cubic structure and contain open M coordination sites, which lie in the pore walls.[271] Whilst the Mn-based framework showed the greatest BET surface area at 870 $m^2 g^{-1}$, it was the Cu-based framework that exhibited the greatest hydrogen uptake at 1.2 bar and 77 K, at 1.8 wt.% (and 25 kg m^{-3}). The isosteric enthalpies of adsorption (determined using a variant of the Clausius-Clapeyron equation) ranged from *ca*.

7.4 to 5.8 kJ mol^{-1} at the lowest reported hydrogen uptake value (0.4 wt.%).[272]Prussian Blue itself had an enthalpy of adsorption of 7.6 kJ mol^{-1} at 0.3 wt.% hydrogen uptake[273] and a pore size of *ca*. 0.5 nm.[270]

The relatively short cyanide bridge leads to quite dense frameworks and low surface areas. Thus meaning that this type of frameworks are unlikely to exhibit substantial hydrogen storage capacities at elevated pressures, despite reasonable uptake values in the low-pressure regime.[161]

4.4.5. Covalent Organic Framework (COF) Materials

Covalent organic frameworks are the first 3-periodic crystalline structures that do not contain metal ions. Instead they were solely held together by strong covalent bonds. The absence of any (typically weaker) metal-ligand bonds offers greater thermal and chemical stability in comparison to their metal-containing counterparts. COFs were not simply defined as organic polymers however, due to their similarities to MOFs. They are crystalline with a well defined macromolecular structure, in addition to a highly porous network and large surface areas.[274]

Despite the extraordinary total gravimetric capacities that have been predicted for some COF materials (21 wt.% for COF-105 and 20 wt.% for COF-108) their volumetric capacities are not expected to exceed 50 kg m^{-3}, at 100 bar and 77 K.[275] This appears to be a direct result of the low material weight, and hence low density. Excess gravimetric capacities have also been simulated to be greater than 10 wt.% at 100 bar and 77 K, for COF-108.[276]

Of the COFs that have been successfully synthesised and consequently measured by Furukawa and Yaghi, $C_{25}H_{24}B_4O_8$, COF-102 and $C_{24}H_{24}B_4O_8Si$, COF-103 have shown the largest hydrogen storage capacities of 7.2 and 7.1 excess wt.% at 35 bar and 77 K; but no volumetric capacities were reported. These two materials exhibited BET and Langmuir surface areas of 3620 and 3530 $m^2 g^{-1}$, and 4650 and 4630 $m^2 g^{-1}$, respectively; with pore volumes of 1.55 and 1.54 $cm^3 g^{-1}$, respectively.[277]

Table 4.6 - Brief summary of reported properties and saturation hydrogen uptakes at 77 K in COFs.[277]

Material	Pore Size / nm	Surface Area / $m^2 g^{-1}$		Pore Volume / $cm^3 g^{-1}$	Hydrogen Uptake / wt.%	Q_{st} / kJ mol^{-1}
		BET	Langmuir			
COF-1	0.9	750	970	0.30	1.5	6.2
COF-5	2.7	1670	1990	1.07	3.6	6.0
COF-102	1.2	3620	4650	1.55	7.2	3.9
COF-103	1.2	3530	4630	1.54	7.1	4.4

4.5. Porous Polymers

Davankov *et al*. patented the synthesis of hypercrosslinked polystyrene networks in the 1970s.[278] However it was only within the last decade that polymers have been considered for hydrogen storage via physisorption. This was because most polymers possess sufficient conformational flexibility and rotational freedom to fill space efficiently, and are not microporous (containing pores of less than 2 nm in size). Porous polymers possess attributes such as crosslinking networks or spiro-centres, which give rigidity. Porous polymers may offer an attractive combination of properties including low intrinsic density (as they are only composed of light elements; C, H, N, O, which is a real advantage over Metal-Organic Framework materials), chemical homogeneity (an advantage over activated carbons), thermal and chemical stability and synthetic reproducibility.[127,279-281]

4.5.1. Hypercrosslinked Polymers

Microporosity can also be obtained within amorphous organic materials, as demonstrated by hypercrosslinked polymers. The synthesis leads to a solvent-swollen rigid polymer network. An extensive system of chemical crosslinks means the polymer network does not collapse after the removal of the solvent, but instead provides an open microporous structure.[282-286] 'Davankov-type'[287] resins[283-285,287-289] are perhaps the most well-studied type of hypercrosslinked polymers and are prepared by cross-linking polystyrenic networks, and have been shown to exhibit BET surface areas greater than 2000 $m^2 g^{-1}$.[289,290]

Hypercrosslinked polystyrene was synthesised by the polymerisation of vinyl benzyl chloride by a Friedel-Crafts post-crosslinking reaction in dichloroethane at 80 °C using $FeCl_3$ as the catalyst. The product was

reported to have BET and Langmuir surface areas of 1466 and 2138 $m^2 g^{-1}$, respectively, and a micropore volume of 0.48 $cm^3 g^{-1}$; and also gave a gravimetric hydrogen uptake of 1.27 wt.% at 1 bar and 3.04 wt.% at 15 bar and 77 K.[102]

Wood *et al*. used an alternative route to produce microporous organic polymers based on the step growth polycondensation of dichloroxylene and other bischloromethyl monomers.[284] This produced materials with BET and Langmuir surface areas of around 1900 and 3000 $m^2 g^{-1}$, respectively. The *p*-DCX/BCMBP hypercrosslinked polymer had the largest surface area and saw hydrogen uptake of 1.61 and 3.68 wt.% at 1 and 15 bar, respectively at 77 K.[290] The p-DCX/ BCMBP polymer was reported to have a median pore width of 0.89 nm and exhibited isosteric enthalpies of adsorption in the range 6.2 to 7.5 kJ mol^{-1} using the Clausius-Clapeyron equation.[290]

Germain *et al*. reported a range of hypercrosslinked polyanilines. They all had relatively low BET surface areas, with the highest being 632 $m^2 g^{-1}$. The same material exhibited a hydrogen storage capacity of 2.2 wt.% at 30 bar and 77 K; and an isosteric enthalpy of adsorption of 7.5 kJ mol^{-1} (determined using the van't Hoff equation, from the 77 and 87 K isotherms).[291] Some of the other hypercrosslinked polyanilines reported in the same investigation produced higher isosteric enthalpies of adsorption, the highest of which was 9.3 kJ mol^{-1}.[291]

In a separate investigation Germain *et al*. reported several nanoporous polymer networks of aromatic rings. Again they all exhibited low BET surface areas, the highest being just 316 $m^2 g^{-1}$, resulting in a hydrogen uptake of 0.85 wt.% at 1.2 bar and 77 K. The authors claim that four of the nanoporous polymers possess unusually high initial enthalpies of adsorption of hydrogen reaching values ranging from 10 to 18 kJ mol^{-1} (determined using the van't Hoff equation, from the 77 and 87 K isotherms).[292] Unfortunately pore sizes were not reported in either of the investigations described here by Germain *et al*.

Yuan *et al*. reported four porous organic polymers (POP) with BET surface areas up 1246 $m^2 g^{-1}$ (for POP-3) and pore sizes distributions in the range 0.8 to 0.9 nm (using the H-K method). POP-3 displayed the greatest hydrogen uptake of the four POPs, 3.0 wt.% at 60 bar and 77 K. POP-4 exhibited the highest

enthalpy of adsorption of 9 kJ mol^{-1} at *ca*. 0.05 wt.%, with all four materials producing values in the range of 4.5 to 6.5 at 1.5 wt.%.[293]

4.5.2. Polymers of Intrinsic Microporosity (PIMs)

PIMs are termed "intrinsic" as they arise solely from their molecular structures and they are not dependent on the thermal or processing history of the material.[294] Monomers that have restricted rotation about a covalent bond or spiro-centre (i.e. a single tetrahedral carbon atom shared by two rings) are deemed to have a "site-of-contortion". Polymers which are synthesised without a "site-of-contortion" are likely to be linear and thus be able to pack efficiently,[281] they could also then be insoluble and non-porous.[295] In view of this, PIMs have no rotational freedom within the polymer backbone, instead they have a randomly contorted molecular structure. They have no single carbon-carbon bonds but do have spiro-centres along the backbone at regular intervals. These spiro-centres introduce a sharp bend into the chain, which results in an inflexible but contorted polymer molecule. It is this high rigidity combined with the randomly contorted shape, which prevents an efficient packing of the macromolecules within the solid state; this then gives rise to the microporosity of PIMs.[294-296]

Prior to this investigation being started, there was a limited amount of work that had been carried out on PIMs. PIM-1 was the first of a series of soluble PIMs that exhibited BET surface areas up to around 850 m^2g^{-1},[294] with hydrogen uptake values 1.04 and 1.40 wt.% at 1 bar and 15 bar, respectively at 77 K,[296] with a total pore volume of 0.78 cm^3 g^{-1}.[294] Weber *et al*. observed a similar BET surface area of 875 m^2 g^{-1}, however their reported total pore volume was somewhat lower (0.52 cm^3 g^{-1}), this probably as a result of this value being determined at p/p_0 = 0.9.[297]

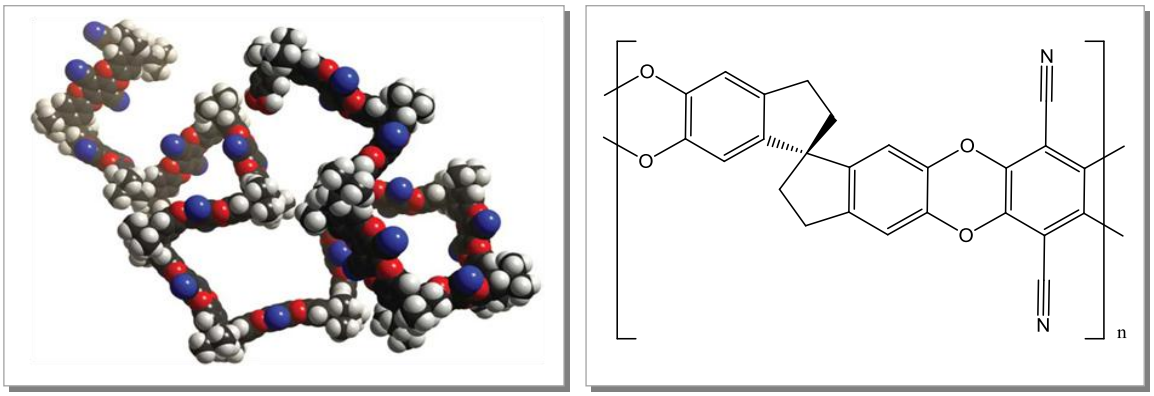

Figure 4.13 - Molecular model (left) and chemical structure (right) of PIM-1. [295]

Later insoluble network-PIMs were synthesised based on larger monomer units, namely the HATN-, CTC- and Porph-PIMs.[298] The CTC-PIM was designed to possess enhanced ultramicroporosity due to the incorporation of bowl-shaped cyclotricatechylene subunits.[296] These showed improvements, but it was an additional network-PIM that incorporated the triptycene subunit that showed the highest BET surface area and hydrogen uptake; 1.65 and 2.71 wt.% at 1 and 10 bar, respectively, at 77 K.[281,296,299] All of the PIMs show pore size distributions in the micropore region (< 2 nm), however, due to their amorphicity definitive pore sizes cannot be stated.[281]

These improved results for hydrogen uptake in PIMs as well as the potential advantages over activated carbons, zeolite and MOFs led to the investigation of these materials in this project.

4.6. Isosteric Enthalpy of Adsorption

The isosteric enthalpy of adsorption gives an indication of the binding strength of the hydrogen molecules to the adsorbent material. High enthalpies of adsorption not only increase the rate at which hydrogen is adsorbed with increasing pressure, but they also result in a greater hydrogen capacity (and hence greater usable hydrogen storage capacity) at higher temperatures. Therefore, increasing the enthalpies of adsorption would lessen the requirement to significantly cool a physisorption-based hydrogen storage system. Typically, porous materials exhibit isosteric enthalpies of adsorption in the range 4 to 7 kJ mol^{-1}. However an increase of around 3- to 5-fold would be required in order to achieve the calculated optimum values of 20 kJ mol^{-1} in order to have significant hydrogen uptake at room temperature.[161]

As described in the previous chapter there are several methods for calculating the isosteric enthalpy of adsorption. Each method provides slightly different value. Additionally the same method can produce different values depending on the number of isotherms and data points used. It has also been shown by multiple authors that the adsorbate-adsorbent interaction changes as a function of the amount of adsorbate (i.e. hydrogen uptake). This means that when the isosteric enthalpy of adsorption is reported, it is imperative that it is stated in conjunction with a value for hydrogen uptake. Average values for the isosteric enthalpy of adsorption (as reported by Schmitz *et al.*[191]) are therefore somewhat meaningless; as such a value would depend up on the range of hydrogen uptake from which it was calculated. Furthermore, using data points that are influenced by adsorbate-adsorbate interactions should also be avoided. However, this is extremely difficult as it not known when these begin to occur (at a significant level).

Many reports of the isosteric enthalpy of adsorption as a function of hydrogen uptake seem to suffer from extreme errors.[191,300] These problems are most obviously seen when using the Clausius-Clapeyron equation in conjunction with a van't Hoff plot. For example, the isosteric heat adsorption plot versus surface coverage displayed in Figure 4.14 contains various 'steps'. The steps occur as a result of using a different number of data points (i.e. isotherms and temperatures). This issue is discussed in more detail with comparison to results obtained from a round-robin test in Chapter 6.

Additionally, if the enthalpy of adsorption is plotted as function of fractional (surface) coverage further problems can occur. Here this is typically caused by the error in calculating the saturation point, which is seen most notably when trying to 'normalise' all the hydrogen isotherms to a single saturation pressure. The surface coverage in the plot of isosteric enthalpy of adsorption displayed in Figure 4.14 was calculated by assuming the saturation point was at 20 bar (the maximum pressure that was capable of being measured). This means that attempts to compare materials against each other, using surface (or fractional) coverage, are enormously dependant up on the methods used to calculate the saturation uptake.[191,300] Therefore this thesis will not contain any results plotted against surface (or fractional) coverage.

Additionally, using too few data points (or isotherms) in conjunction with the van't Hoff plot typically results in values with large errors. This may be the reason behind the unusually high values reported by Germain *et al*.[292]

In comparison to the number of published reports on the physisorption of hydrogen at cryogenic temperatures, in recent years, there have been relatively few investigations using multiple isotherms at various temperatures in order to calculate the isosteric enthalpy of adsorption.[85,117,119,191,203,213,300-303]

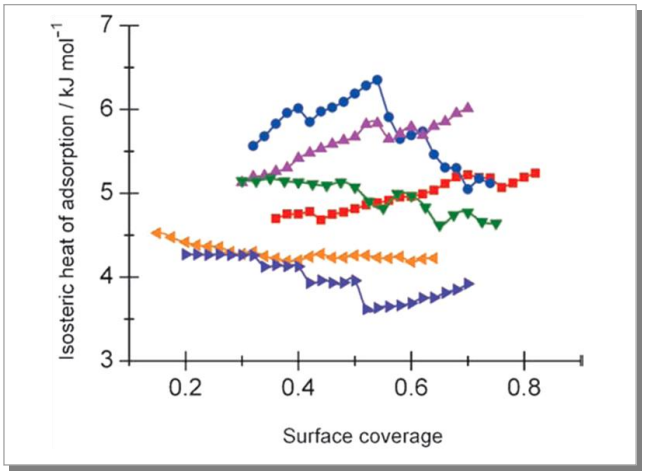

Figure 4.14 - Isosteric enthalpy of adsorption against 'surface coverage' for some microporous materials. Carbons: Takeda 4A (●) and Norit R0.8 (■); MOFs: MIL-53 (▲), Cu-BTC (▼),MIL-101 (◀), and MOF-5 (▶).[191]See Reference for more details.

Experimental isotherms also have the problem of being measured at spaced intervals of pressure, and not perfectly spaced intervals of hydrogen adsorption. Therefore, it is necessary to either interpolate an approximate value of hydrogen uptake between data points, or to fit the isotherm to some function.[63,304,305] Several authors have used various fitting functions in conjunction with multiple temperatures in order to more accurately deduce isosteric enthalpies of adsorption as a function of hydrogen uptake.[71,85,119,301,302,306] However, the majority of these used a modified version of the DA equation on the excess isotherm data. Using this method they appear to underestimate the isosteric enthalpies of adsorption. Poirier *et al*. measured the hydrogen adsorption in MOF-5, at five temperatures ranging from 77 to 98 K, up to 30 bar (60 bar for 77 K). Poirier *et al*. used a Dubinin-Astakhov type equation to fit the isotherm data, which wasn't originally derived for the adsorption of supercritical gases and it is not believed to reduce to Henry's Law.[78]

They reported a near zero coverage enthalpy of adsorption at 2.9 kJ mol^{-1} which decreases to < 1 kJ mol^{-1} at around 3.7 wt.%.[85,302] It is important to mention that the MOF-5 material measured by Poirier *et al*. showed a maximum excess hydrogen uptake of 3.9 wt.% at 30 bar and 77 K[85,302] compared to the 7.1 wt.% at 40 bar and 77 K observed by Kaye *et al*.[147] as mentioned above. Zhou *et al*. measured the hydrogen adsorption in MOF-5, using multiple temperatures between 40 and 125 K (at various pressures). They used the Clausius-Clapeyron equation to calculate an isosteric enthalpy of adsorption of 4.8 kJ mol^{-1} at near zero coverage decreasing to < 4.0 kJ mol^{-1} by 2 wt.%. The workers reported significant errors in the low-pressure region, in addition to errors incorporated by extrapolation of data back to zero gas adsorption. They also performed their calculations on the excess adsorption isotherms instead of the absolute isotherm data. Similar results were reported by Schmitz *et al*. for MOF-5 and can be observed in Figure 4.14.[191]

Bordiga *et al*. performed infra-red spectroscopy on MOF-5 in order to determine the enthalpy of hydrogen adsorption. They found that the main adsorption site had a enthalpy of 3.5 kJ mol^{-1}, however they also found two defect sites which had higher enthalpies of adsorption *ca*. 7.4 kJ mol^{-1}.[239] The isosteric enthalpy of adsorption may also be determined calorimetrically.[307]

Panella *et al*. used Thermal Desorption Spectroscopy (TDS) also named Thermal Programmed Desorption (TPD) to characterize the energy of adsorbate molecules on surfaces, and in pores.[300,308,309] With the relatively weak interaction energies associated with the physisorption of hydrogen, the authors found it necessary to cool the samples down to 20 K and observe the desorption of hydrogen, using mass spectrometry, on heating the sample (at 0.1 K s^{-1}) in a vacuum 10^{-5} Pa. They observed that desorption occurred below 77 K for all porous materials.[300,308,309] Panella *et al*. observed a sharp desorption peak at *ca.* 25 K in all desorption spectra, independent of the material. This was suggested to be the result of liquid hydrogen.[308] The temperatures at which peaks of hydrogen desorption occurred was related to the enthalpy of hydrogen adsorption. With the number of desorption peaks correlating with the number of different distinct pore sizes.[300,308] However, calculating a numerical value for the enthalpy of hydrogen adsorption is not possible via TDS.

4.6.1. Exposed Metal Sites

Cu-BTC is a neutrally charged metal-organic framework,[250] however, partial charges, either positive or negative, can provide a material with increased binding of the hydrogen molecules through the dipole-induced dipole interactions.[310,311] To achieve the optimal isosteric enthalpy of adsorption of around 20 kJ mol^{-1},[161] it might seem logical to utilise the interaction between the Li^+ cation and the hydrogen molecule, which has been measured in the gas phase to have a binding energy of 27 kJ mol^{-1} (albeit with a substantial potential error).[312] However, it also known that this seemingly ideal binding energy it not carried in to any porous material, in fact, the energy is said to be quenched, resulting in a significantly lower hydrogen binding energy. This is seen with $Li_2Zn_3[Fe(CN)_6]_2.H_2O$, which exhibits an isosteric enthalpy of adsorption of 7.9 kJ mol^{-1}.[313] It is therefore presumed that a metal cation with a greater charge, such as Mg^{2+}, or a divalent transition metal cation, or maybe even Al^{3+} may provide better isosteric enthalpies of adsorption as a result of coordinatively-unsaturated metal binding sites.[161,252] For example, a material utilising this is $Mn_3[(Mn_4Cl)_3(BTT)_8]_2$,* which contains open Mn^{2+} coordination sites, exhibits an isosteric enthalpy of adsorption of 10.1 kJ mol^{-1} at zero coverage.[136] Further investigation, by powder neutron diffraction, in to the bound-hydrogen of this material found that the Mn-D_2 interaction was very strong, resulting in a distance of just 2.3 nm, which is significantly less than the typical distance of physisorbed hydrogen (> 0.3 nm) as seen for MOF-5.[314] This reduced metal-hydrogen distance aids the packing of the hydrogen molecules within pores and so despite only having a BET surface area of 2100 $m^2 g^{-1}$, $Mn_3[(Mn_4Cl)_3(BTT)_8]_2$ exhibits an total volumetric storage capacity of 60 kg m^{-3}. The excess and total gravimetric hydrogen uptake is 5.1 and 6.9 wt.%, respectively.[136] One of the highest reported isosteric enthalpies of adsorption for hydrogen in a MOF material was for $Zn_3(BDC)_3[Cu(pyen)]$*, which gave 12.3 kJ mol^{-1} at zero coverage. This high enthalpy value is thought to be result of the strong adsorption on open Cu^{2+} sites.[315]

* BTT = 1,3,5-benzenetristetrazolate; pyen = conjugate base of 5-methyl-4-oxo-1,4-dihydro-pyridine-3-carbaldehyde.

4.6.2. Catenation/Interpenetration

As previously mentioned in relation to MOF-177, frameworks with extremely large pores have poor hydrogen volumetric storage capacities. However, if a material were to have a large micropore volume that was made up of small pores, then it could have a high isosteric enthalpy of adsorption in addition to a high surface area.[316] Framework interpenetration is one way of reducing the size of large voids. Just one example was found in the literature, whereby both catenated and non-catenated forms of the same framework, $Cu_3(tatb)_2$* (see Table 4.7). The catenated form (PCN-6) was activated at 50 °C, and was found to adsorb 1.9 wt.% at 1 bar and 77 K.[317]

Whereas the non-catenated form (PCN-6') adsorbed significantly less, just 1.35 wt.% under the same conditions; however, after activation at 150 °C, the non-catenated framework exhibited 1.62 wt.% at 1 bar and 77 K.[318]

Table 4.7 - A comparison of a catenated and non-catenated form of the same framework.[317,318]

$Cu_3(tatb)_4$	Langmuir Surface Area / $m^2\ g^{-1}$	Pore Volume / $cm^3\ g^{-1}$	Hydrogen Capacity	
			/ wt.%	/ kg m^{-3}
Catenated (PCN-6)	3800	1.453	1.90	9.19
Non-catenated (PCN-6')	2700	1.045	1.35	3.94

4.6.3. Spillover

Hydrogen spillover involves the dissociative chemisorption of hydrogen molecules on to a metal particle followed by the subsequent migration of the hydrogen atoms and into the bulk material (as illustrated in Figure 4.15).[319-326] The phenomenon is claimed to be reversible, assuming no irreversible hydrogenation reactions occur, with the hydrogen atoms subsequently recombining to form molecular gas. If the metal surfaces are dispersed throughout a porous material, it is believed that the diffusion of hydrogen atoms (as a result of spillover) can significantly improve the hydrogen storage capacity at ambient temperatures. However, this can only occur if the adsorbate-adsorbent interaction and packing density is greater for hydrogen atoms than for molecular hydrogen.[326-328]

* tatb = 4,4',4''-*s*-triazine-2,4,6-triyltribenzoate.

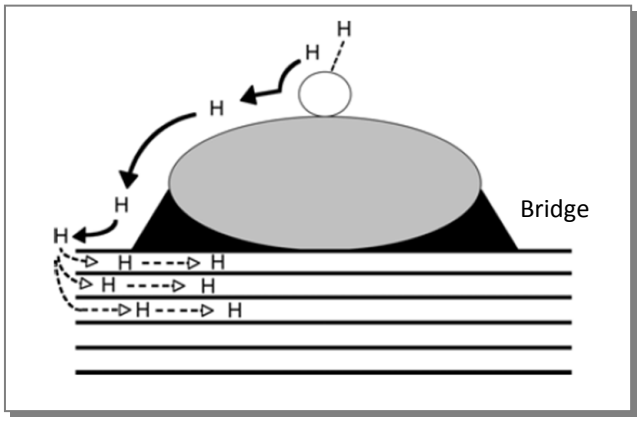

Figure 4.15 - Illustration of the proposed hydrogen spillover mechanism.[326]

The spillover phenomenon has been used on a number of different types of porous materials, including SWNTs and MWNTs,[329-331] graphite nanofibres,[330,332] mesoporous silica,[333] activated carbons,[334,335] zeolites,[336] MOFs,[337-340] and COFs.[341] The spillover effect was reported to have been accountable for the greater than two-fold increase that was observed in hydrogen storage capacity at 298 K and 100 bar, for a mechanically milled mixture of Pt/C catalyst, consisting of 50 mg of 20 wt.% platinum nanoparticles on activated carbon. This improvement was also found to not simply be a sum of uptake by the two separate storage systems. For many of the framework materials, powder X-ray diffraction patterns were also run before and after the 'bridging' treatment in order to confirm that the original crystallinity of the framework was preserved.[161] Many materials have shown reversibility through two (or more) cycles. However, no reports have shown high hydrogen capacities in continuous cycles. A possible reason being the relatively slow kinetics. The kinetics for the hydrogen spillover mechanism was proposed to be subject to the slow diffusion of the hydrogen atoms, after the initial fast dissociation, and it was believed to be the rate determining step.[327] A comparison of the hydrogen storage properties of MOFs, pure and bridged to Pt/C catalyst is shown in Table 4.8.

Table 4.8 - Comparison of the hydrogen storage properties of MOFs, pure and bridged to Pt/C catalyst. Bridged sample: 10 wt.% Pt/C (containing 5% Pt), 10 wt.% carbon bridges, and 80 wt.% MOF. [47,118,134,173,177,246,277,327,341]

MOF	Pure sample					Bridged sample	
	Surface Area / $m^2 g^{-1}$		Hydrogen Uptake / wt.%		Q_{st} / kJ mol^{-1}	Hydrogen Uptake / wt.%	Q_{st} / kJ mol^{-1}
	BET	Langmuir	77 K, 1 bar	298 K, 100 bar		298 K, 100 bar	
IRMOF-8	1466	1818	1.48	0.40	6.1	2.2	21
COF-1	750	970	1.28	0.26	6.2	0.7	7
Cu-BTC	1507	2175	2.27	0.35	6.8	1.1	9
MIL-101	4100	5900	1.80	0.43	10.0	1.5	13
MOF-177	4630	5250	1.23	0.62	4.4	1.5	10

4.7. Hydrogen Storage Systems

Ahluwalia and Peng recently reported a hydrogen storage tank using activated carbon material.[342] The carbon fibre tank had a tensile strength of 2550 MPa, with system weight and volume of 30 kg and 25 litres, respectively. A schematic of the on-board cryogenic adsorption system is shown in Figure 4.16. The AX-21 carbon material has a bulk and skeletal density of 0.3 and 2.3 g cm^{-3}, respectively. The authors reported a specific surface area of 2800 $m^2 g^{-1}$, but did not specify the method used to calculate the value. An excess hydrogen storage capacity of 5.4 wt.% at 77 K and 40 bar led to a system gravimetric capacity of 4.5 wt.% at *ca*. 300 bar and 100 K. However only *ca*. 80% of this storage capacity is usable when reducing the system pressure to 8 bar (the pressure at which the system operates).

The storage tank had a maximum capacity of 5.6 kg of recoverable hydrogen at 350 bar and 100 K, which could be refuelled in just over 11 minutes after being completely discharged to 8 bar. The temperature of the storage system was maintained using an off-board feed of liquid nitrogen produced by air liquefaction and separation. The quantity of liquid nitrogen required to simply maintain the storage temperature of 100 K was not reported. However, during the hydrogen refuelling process the authors reported that 10.9 kg of liquid nitrogen was required for every kilogramme of hydrogen, which equates to 4.5 MJ kg^{-1} H_2.[342]

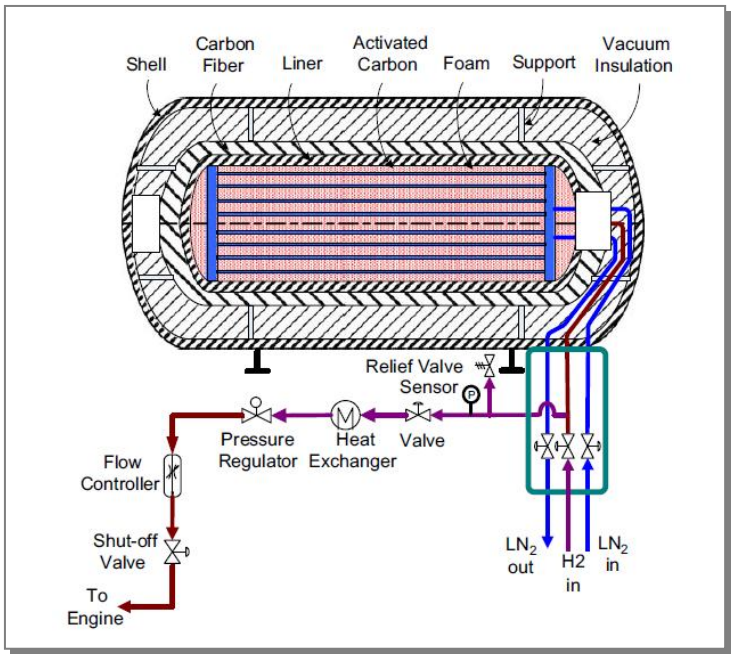

Figure 4.16 - Schematic of the on-board cryogenic adsorption system reported by Ahluwalia and Peng.[342]

4.8. Microporous Materials Review

The relationships between hydrogen adsorption and porous structure characteristics are complex. Hydrogen storage capacities have previously been shown to relate to the surface area and temperature on CNTs.[180] This was later also found to be true for other materials and was seen to be generally applicable to low-temperature physisorption of hydrogen in porous materials. Other properties such as total pore volume[196] or micropore volume also have a significant influence on the hydrogen adsorption.[127]

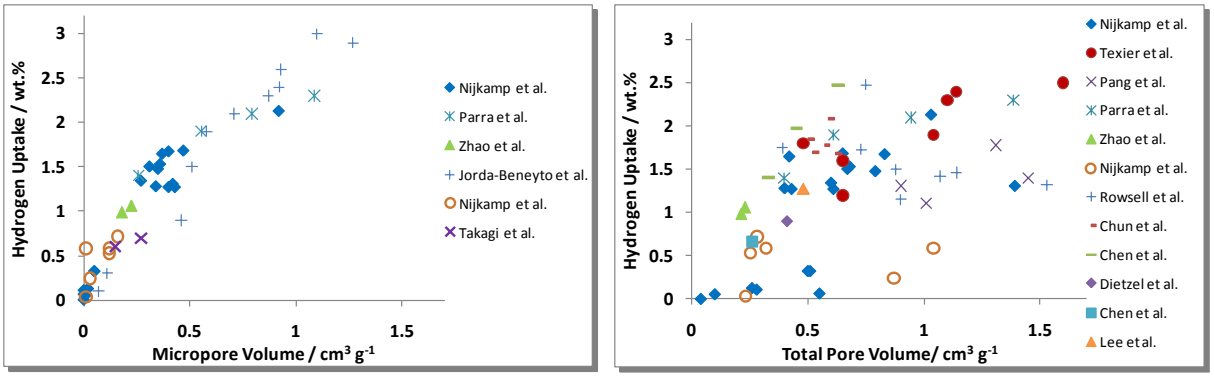

Figure 4.17 - The variation of hydrogen uptake at 1 bar and 77 K with the micropore (left) and total volume (right) area for some porous adsorbents. Micropore volume: activated carbons by NiJkamp et al.[343], Zhao et al.[132] and Jordá-Beneyto et al.[164]; carbon nanotubes by Parra et al.[344] and Jordá-Beneyto et al.[164] and zeolites by NiJkamp et al.[343] and Takagi et al.[181]. Total pore volume: activated carbons by NiJkamp et al.[341], Texier et al.[163] and Zhao et al.[132]; carbon nanotubes by Pang et al.[345] and Parra et al.[344]; zeolites by NiJkamp et al.[343] and MOFs by Rowsell et al.[134], Chun et al.[346], Chen et al.[315,347], Dietzel et al.[348] and Lee et al.[102]

Some selected data can be seen in Figure 4.18 for the hydrogen uptake in carbon adsorbents at 10 bar at 77 K. A correlation can be observed between the hydrogen storage capacity and specific surface area and micropore volume under these conditions. The scattering of the data observed could be attributed to an uncertainty in the measurements of the apparent specific surface area using the BET model and the comparison of data measured from different laboratories, or indeed to the applicability of the BET method to microporous adsorbents.[108,109] Nevertheless, there is a general linear trend for all porous materials. These results show that, independently of texture, structure and composition, the specific surface area is a very important property in determining high gravimetric hydrogen storage capacities. For this reason, quick BET measurements are often performed in order to determine the potential of a microporous material to be a successful hydrogen storage material.

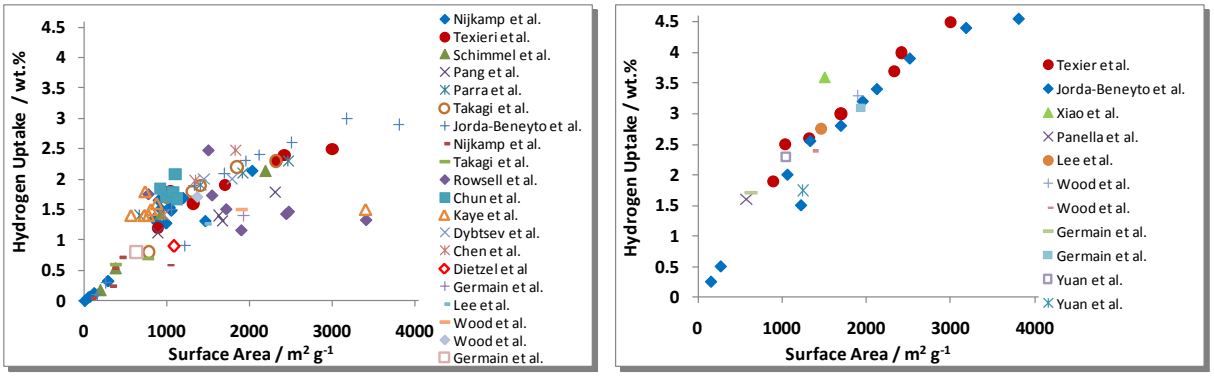

Figure 4.18 - The variation of hydrogen uptake at 1 (left) and 10 bar (right) and 77 K with BET surface area for some porous adsorbents. 1 bar: activated carbons by NiJkamp et al.[343], Texier et al.[163] and Zhao et al.[132] carbon nanotubes by Schimmel et al.[349,350], Pang et al.[345], Parra et al.[344] and Jordá-Beneyto et al.[164]; zeolites by NiJkamp et al.[343] and Takagi et al.[181]; MOFs by Rowsell et al.[134], Chun et al.[346], Kaye et al.[272], Dybtsev et al.[229], Chen et al.[315,347] and Dietzel et al.[348]; porous polymers by Germain et al.[291,351], Lee et al.[102] and Wood et al.[290,352]. 10 bar: activated carbons by Texier et al.[163] and Jorda-Beneyto et al.[164]; carbon nanotubes by Jordá-Beneyto et al.[164]; MOFs: Xiao et al.[254] and Panella et al.[231]; porous polymers: Germain et al.[291,351], Lee et al.[102], Wood et al.[290,352] and Yuan et al.[293,353]

These observed correlations indicate that the structural characteristics of porous materials are of greater importance than surface interactions. Adsorbents with large pore volumes do not automatically have significantly high hydrogen storage capacities. Increased hydrogen uptake in the low-pressure region requires greater adsorption potential, as brought about by narrow pores. Whereas, large pores, or more accurately large pore volumes, bring about increased hydrogen uptake in the high-pressure region. Therefore, there is an important compromise that must be addressed when 'designing' (and synthesising) porous materials.[127] Additionally, there is also some evidence that suggests the density of the adsorbed hydrogen phase decreases with increasing pore size,[248] and this is complemented by the adsorbate-adsorbent contribution decreasing with increasing adsorbate density.[354]

MOFs have been shown to exhibit the highest hydrogen uptake of all porous materials reported in literature owing to their high specific surface area. The maximum amount of hydrogen uptake is limited by the adsorbate density, adsorbent pore structure and the subsequent pore volume being available in narrow pores. Porous materials with high surface area and with 'thin-walls' leading to moderate/low density will provide the highest storage density on a volumetric basis.[127]

In recent literature, both the surface area and pore volume have been deemed to be of great significance in the hydrogen uptake of a porous adsorbent. Theoretical studies using Grand Canonical Monte Carlo

simulations[355] were performed to predict adsorption isotherms for hydrogen in a series of MOFs up to high pressures. Frost *et al*. revealed the existence of three adsorption regimes[355]: at low pressure the hydrogen uptake correlates with the enthalpy of adsorption; at intermediate pressure, uptake correlates with the surface area; and at the highest pressures, uptake correlates with the accessible pore volume. Frost *et al*. suggest that the low pressure region is in the order of 0.1 bar, intermediate pressure is in the order of 30 bar and high pressure at around 120 bar.[355] The workers indicated that it would not be reasonable to assume that the adsorbate layer thickness remains constant with increasing pressure, therefore suggesting that the pore volume approximation is more applicable (in reference to those materials studied). This conclusion is reinforced by the increasing difference (with increasing pressure) between the surface excess and the absolute amount of hydrogen adsorbed, where the pore volume appears to dominate the absolute adsorption.[111,355]

Chapter 5

EXPERIMENTAL

5.1. Introduction

This chapter provides an overview of the experimental procedures, techniques and equipment employed in this work. It is broadly divided into: (1) Characterisation Techniques (powder X-ray diffraction, infrared and Raman spectroscopy, thermogravimetric analysis, differential scanning calorimetry and helium pycnometry); (2) Gas Sorption Measurements (hydrogen storage measurements, surface area analysis, and pore size analysis and (3); Material Processing.

5.2. Characterisation Techniques

5.2.1. X-ray Diffraction

A Bruker D8 advance spectrometer was used for all powder X-ray diffraction measurements using CuKα radiation with a Göbel Mirror. This gives an appropriate absorption coefficient and minimises the white radiation, cutting out other sharp peaks leaving coherent focused light, Kα (λ = 1.5406 Å). The diffraction pattern is collected as intensity versus a scattering angle, θ multiplied by 2. The scattering angle is measured by using Vantec position sensitive detector (PSD) between 5 and 70 2θ.

Simple powder X-ray diffraction was performed using a 7 position multi-changer, with samples loaded inertly into a Kapton dome-shaped, air-tight, sample holder via an argon filled glovebox.

In-situ powder X-ray diffraction was performed using an Anton Parr XRK900 cell under flowing helium at a pressure of 1.5 bar (gauge pressure). A flow rate of 100 ml min^{-1} was used. Samples were inertly loaded into the cell, inside an argon-filled glovebox. The *in-situ* diffraction patterns were recorded isothermally, i.e. at a single (constant) temperature before heating to the next set point.

Diffraction occurs when Bragg's Law is satisfied:

$$n\lambda = 2d\ sin\theta \qquad (5.1)$$

Where the x-ray wavelength is λ, d relates to the lattice spacings, n is an integer value and θ is the angle of the incident and scattered wave. Chekcell was used to determine the lattice parameters and to compare observed and calculated 2θ positions. Space groups were obtained from the literature.

5.2.2. Infrared Spectroscopy

Infrared spectroscopy was used to confirm the effectiveness of the degassing procedure in the PIM materials. Infrared activity stems from changes in the dipole moment within a molecule. These changes occur as a result of the movement of the bonds. Bonds naturally vibrate. Within a molecule these bonds can vibrate more intensely by absorbing infra-red radiation. Symmetric stretches, ν_1, symmetric bends, ν_2, antisymmetric stretches, ν_3, are the causes for the three most common observed bands in an IR spectrum. Polyatomic molecules are likely to show several peaks in an IR spectrum, most of which will appear in the "fingerprint" region between 1000 and 1550 cm^{-1}. The functional groups from alcohols (O-H), carbonyls (C=O) and carboxylic acids (C=O and O-H) are (normally) easily identifiable using IR spectroscopy. These allow for additional bonds due to oxidation or the adsorption of water to be characterised. Starting materials and synthesis reagents can also be identified.

Infrared spectroscopy was performed using a Thermo Nicolet 8600 Fourier transform Infrared (FTIR) spectrometer fitted with a Specac 'Golden Gate' ATR attachment allowing the inert transfer of samples from within an argon-filled glovebox. Prior to the measurements the system was purged with dry oxygen free nitrogen to reduce the background signals from water and carbon dioxide. Each spectrum was a result of 100 scans at a resolution of 4 cm^{-1}.

5.2.3. Raman Spectroscopy

Raman spectroscopy was used to compliment the infrared spectroscopy and to see whether any noticeable differences could be found between PIM samples. The technique was also used to confirm the lack of C=O, O-H and N-H groups within the materials. Raman activity stems from changes in the polarizability within a molecule. The Raman effect occurs when the laser excites a molecule from its

ground state to an excited energy level. Upon relaxation, the molecules emit a phonon to a an excited energy level (and hence leaves the molecule in a different rotational or vibrational state). The energy difference between the ground state and the 'new' state leads to shift in frequency. If the new state is above the ground state, it is known as a Stokes shift. If the new state is below the original energy level, it is known as Anti-Stokes shift. If the molecule falls back to the same state, Rayleigh scattering is observed. This is typically of much greater intensity than either of the Raman scatterings, but is removed with use of filters.

The laser is focused on the sample, and the emitted light is channel back through the objective where a holographic notch filter removes all phonons with a shift of ±100 cm^{-1}, hence also removing any Rayleigh scattering. The remaining phonons are then focused and separated using a series of lenses, and a grating before being detected by charge coupled device (CCD). Raman spectroscopy was performed using a Renishaw InVia reflex using a 785 nm laser with a grating of 1200 lines per mm.

The samples exhibit varying amounts of fluorescence. This was manually removed as part of the baseline correction. A disproportionate degree of fluorescence to signal observed when using shorter wavelengths meant that variable wavelength Raman spectroscopy could not be performed.

5.2.4. Thermogravimetric Analysis

Thermogravimetric Analysis (TGA) was performed in order to monitor the decomposition characteristics of materials. This information was used to obtain the necessary degassing temperatures prior to gas sorption measurements.

A Netzsch 209 system was used to perform TGA, which is simply a measurement of sample mass as a function of temperature. In this system, the sample is mounted on top of the thermocouple inside the furnace. The thermocouple is directly attached to a (top-loaded) microbalance, which accurately records the sample weight to a resolution of 0.1 μg. Samples of approximately 10 mg, are measured in an alumina (Al_2O_3) crucible. A baseline measurement was performed with an empty alumina crucible using the same conditions to account for any buoyancy effects on the sample during the measurement. A heating rate of

2 °C min^{-1} was used for all samples. TGA measurements were performed with argon gas flow of 40 ml $minute^{-1}$. This ensures that any desorbed gasses are carried out of the system.

5.2.5. Differential Scanning Calorimetry

A DSC (Netzsch 204 HP) was used to assess the thermodynamics of various reactions. The technique utilises the temperature difference between a sample and an inert reference material. The two materials are housed in the same enclosure and therefore are subjected to identical pressures and temperatures. Samples of around 5 mg are measured in an aluminium crucible. Samples were subjected to a heating rate of 2 °C min^{-1}, with a dynamic argon flow of 100 ml min^{-1}, at a pressure of 3 bar.

Temperature differences between the sample and the reference material arise from changes in enthalpy or heat capacity of the sample. The system is calibrated by measuring the melting points of five metal standards (In, Bi, Sn, Pb, and Zn), which are spread throughout the temperature range of the DSC equipment; this enables the temperature difference to be related to the enthalpy change in the sample. Baseline measurements are also performed, using the exact conditions to be used in the measurement, to account for any background between the empty sample and reference crucibles, which are both made of aluminium.

5.2.6. Helium Pycnometry

The densities of all porous samples were assessed using helium pyconometry (Micromeritics AccuPyc II 1340), for the purpose of buoyancy correction in the gravimetric analysis (see Chapter 3). The system is housed inside an argon-filled glovebox, to enable the loading of air-sensitive samples. Ultra-pure helium (Air Products, BIPs; 99.99996%), was used as the measurement gas.

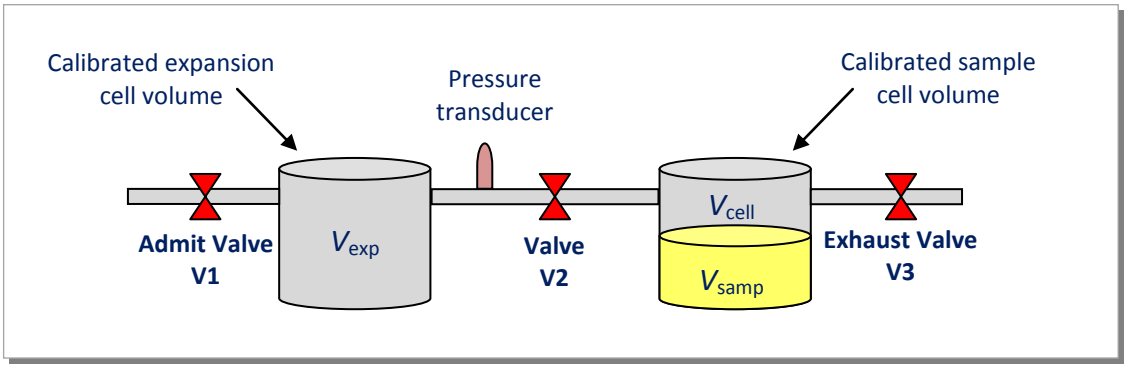

Figure 5.1 - Simplified schematic of the pycnometer system (Micromeritics AccuPyc II 1340).

The system uses a gas displacement technique to measure the volume of the sample chamber. It uses the observed pressure upon filling the expansion chamber (V_{exp}). After the pressure equilibrates (P_1), valve (V2) is opened and allows gas to flow into the sample chamber (V_{cell}), which then also reaches an equilibrium pressure (P_2). Using known volumes of both chambers allows the system to calculate the volume of the sample using equation (5.2).

$$V_{sample} = V_{cell} - V_{exp}\left(\frac{P_1}{P_2} - 1\right) \qquad (5.2)$$

The system typically uses a 1 cm^3 sample chamber, however, the chamber can be adapted to a volume of 0.1 cm^3 with the use of an additional stainless steel insert. This was used where only very small quantities of sample were available. Calibration of the sample cell volume (and subsequently the expansion cell volume) is achieved with the use of a stainless steel ball of known precise volume. Before running each sample the chambers were purged thirty times with helium gas. Afterwards, fifty measurements were taken, with average values being used, along with standard deviations being noted. The system relies upon the manual input of the sample mass for the calculation of the sample density. This is measured using a balance, with an accuracy of ±0.1 mg, which is also situated inside the argon-filled glovebox.

5.3. Gas Sorption Measurements

5.3.1. Gravimetric Technique

Two constant-pressure TGA systems, known as Intelligent Gravimetric Analysers (IGAs) were used to monitor the hydrogen sorption characteristics of a range of porous materials. The IGA is a pressure

controlled thermogravimetric balance supplied by Hiden Isochema Ltd. It has a bottom-loading balance, connected to a galvanometer, which detects deflections on a balance head as a voltage, this is then converted into a mass. Typical sample sizes are approximately 100 mg and the microbalance has a long term stability of ±1 μg, with a weighing resolution of 0.2 μg.

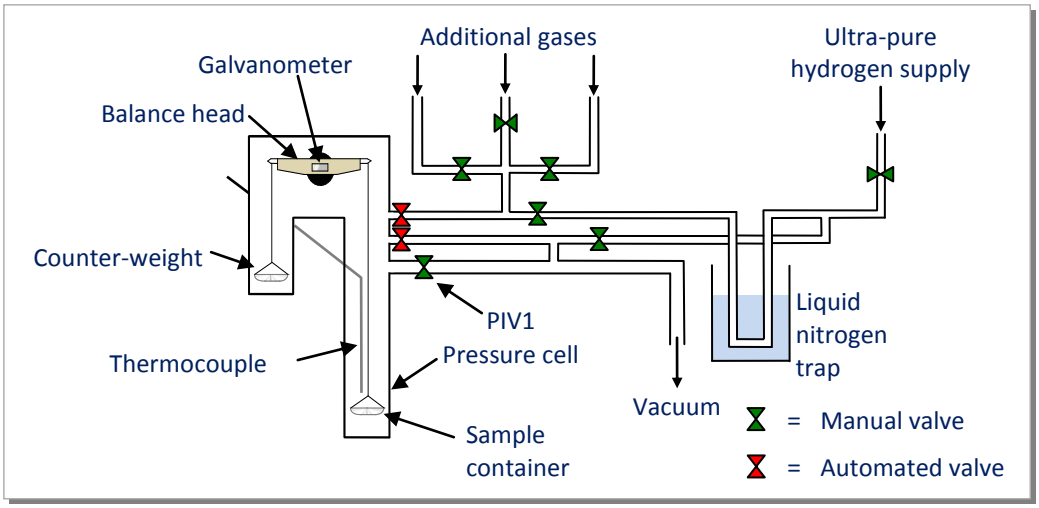

Figure 5.2 - Schematic of an Intelligent Gravimetric Analyser (IGA) setup with input gases and liquid nitrogen trap.

The balance is housed inside a pressure vessel in which it is possible to control the gas pressure from 20 bar down to 10^{-7} mbar (which is likely to be *ca.* $10^{-4}/10^{-5}$ mbar at the sample). The resolution of the pressure barometer is ±0.02% of the range. The temperature of the sample can be controlled from 500 °C down to 77 K. The balance head is maintained at a constant 45 °C to comply with IUPAC guidelines (as mentioned in section 3.7.1). Ultra-pure hydrogen (Air Products, BIPs; 99.99996%), was used as the measurement gas. This was passed through a liquid nitrogen trap to capture any further impurities in the gas supply. Additionally, the last 40 bar of the hydrogen from the gas cylinder was not used due to the increased relative concentration of impurities.

Initially, real-time kinetics were monitored using a 'chart recorder' which plots pressure, temperature and mass versus time. On a typical run, samples were loaded in air (although they could be loaded inertly, if necessary). Samples were initially degassed in ultra-high vacuum (UHV) for around 1000 minutes at temperatures ranging from 50 to 415 °C depending on the structural stability of each sample. At which point the mass is assessed for stability, and further outgassing continues if required. The level of the UHV

has a significant influence, which can be increased by the use of wider bore pipes and a more direct route from the vacuum pump to the sample. This is done by operating a manual valve (labelled PIV1 in Figure 5.2). The temperature for which each material was degassed at was obtained using TGA measurements. The degassed "dry mass" is assumed to be the mass of the sample without impurities. The dry mass is recorded in vacuum after cooling to room temperature. Typical impurities include the solvents that were used during synthesis; such as dimethylformamide (DMF) or water; which is often adsorbed from the atmosphere. Sorption isotherms are made up of several kinetic traces at a series of pressures at a constant temperature. At each pressure step the mass is monitored versus time. The IGA system continuously calculates an asymptote mass based on the sorption curve, with minimum and maximum equilibrium times of 10 and 20 minutes. Where the sorption curve lies within set tolerances (typically 98.5%) of the calculated asymptote, the system moves on to the next pressure step (unless the maximum equilibrium time is reached first).

The temperature of the reaction vessel is controlled during the isotherms either by submersion in liquid nitrogen or liquid argon (77 or 87 K, respectively), or by a cryofurnace system (which is discussed below). This IGA is also fitted with a liquid nitrogen cryostat, which allows for isotherms to be measured at temperatures ranging from *ca*. 82 K up to 773 K (500 °C). In conjunction with Hiden Isochema, three generations of cryostat have been designed and tested to maximise cooling efficiency and temperature stability during this project. The cryofurnace is detachable from the reaction vessel, so that submerged liquid nitrogen (77 K) measurements can be performed. At present only temperatures as low as 82 K are possible using the cryofurnace.

The cryofurnace is compromised of a helically wound pipe that circulates liquid nitrogen, intertwined with a resistively heated element. By varying the amount of power to the element and changing the flow rate of liquid nitrogen it is possible to control temperature between 82 and 773 K (500 °C). The cryostat relies on a proportional-integral-derivative (PID) controller to regulate the amount of power and thus the heat produced by the heating element. By changing the design of the cryostat and by refining the PID

parameters it has been possible to achieve a temperature stability of 0.10 K over a temperature range of 82 to 170 K at varying pressures.

Unfortunately, this furnace is controlled by the sample thermocouple (inside the chamber). This causes a problem when using it to degas samples in UHV. Due to the problems with conducting heat through a 'vacuum', the sample temperature tends to 'over-shoot' above the set temperature as the furnace inputs too much power, before the sample temperature reaches the set point. Oscillation can occur if this is followed by the furnace inputting too little power, and so on. This can be minimised by adjusting the PID controls. The standard furnace controls the temperature through an external thermocouple and so does not suffer from the same problem. Instead a small temperature lag occurs which can be accounted for.

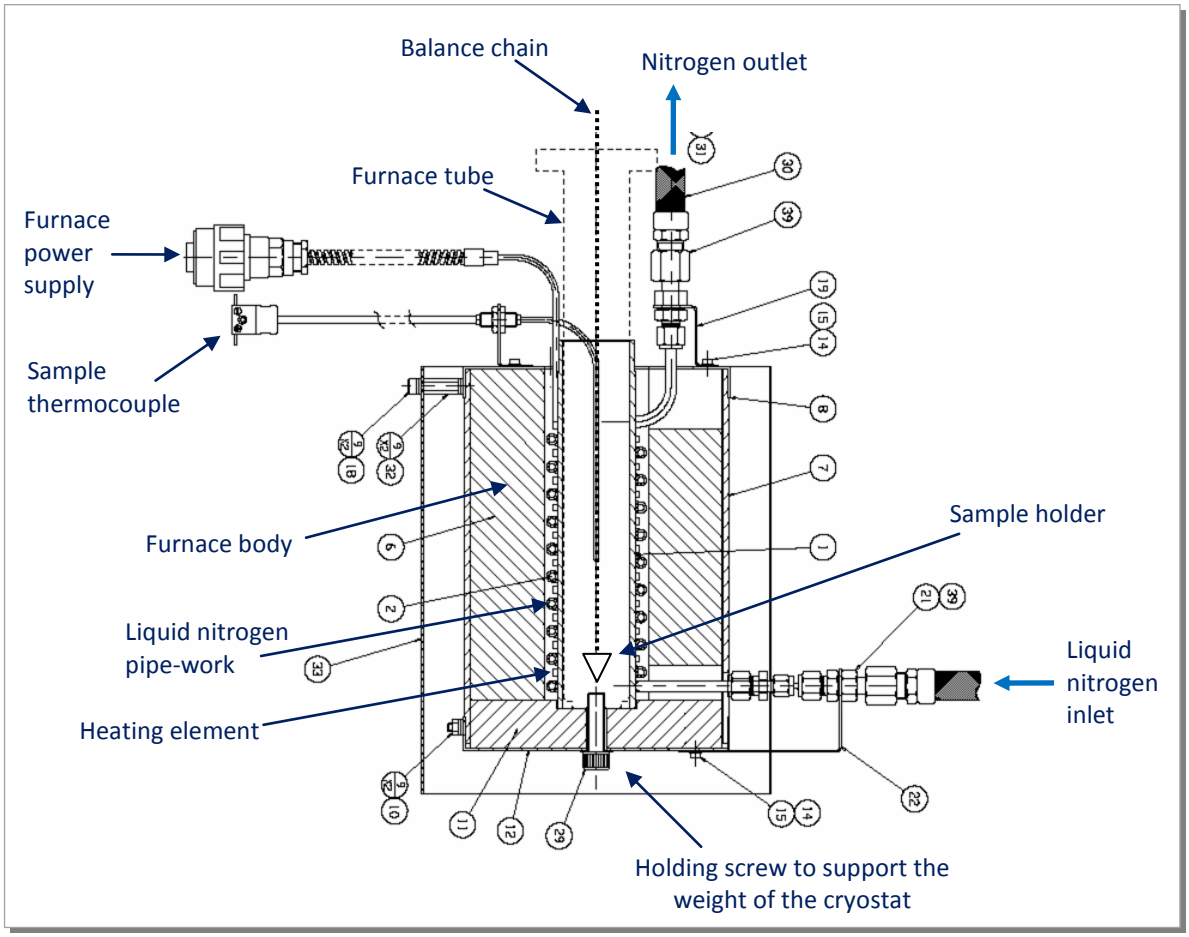

Figure 5.3 - Detailed drawing of the 3rd generation Hiden Cryofurnace system.

5.3.2. Volumetric Technique

Volumetric nitrogen sorption measurements were performed in order to investigate the apparent surface area and the pore size distribution of the PIM materials. Crystallographic data was used for the pore sizes of the framework materials.

The nitrogen adsorption measurements were performed on samples that had been previously degassed using ultra high vacuum (10^{-6} mbar) at 50 to 120 °C for 8 to 16 hours to remove residual solvent and other potential adsorbates. Basic volumetric nitrogen sorption studies were performed on the PIM materials at 77 K using a Beckman Coulter 3100 Surface Area Analyzer at the University of Cardiff. Apparent surface areas were calculated from nitrogen adsorption data by the multi-point Brunauer–Emmet–Teller (BET) and Langmuir methods for the PIMs as described in Chapter 3. The cross-sectional area per nitrogen molecule at 77 K was taken as 0.162 nm^2.[356]

Low-pressure nitrogen sorption data, suitable for modelling micropore size distribution, was obtained using an Accelerated Surface Area and Porosimetry (ASAP) 2020 system (Micromeritics Instrument Corporation). Helium was used for the free space determination, after nitrogen sorption analysis, both at 77 K and at ambient temperature. Apparent micropore distributions were calculated from nitrogen adsorption data by the Horváth-Kawazoe method assuming a slit-pore geometry and the original HK carbon-graphite interaction potential,[97] as described in Chapter 3.

5.4. Material Processing

5.4.1. Conditioning with Carbon Dioxide

Some of the PIMs were subjected to an additional activation technique, where the sample was exposed to a pressure of carbon dioxide in order to remove adsorbed species such as solvents. Subcritical carbon dioxide conditioning measurements were performed using the IGA system. After the degassing of the PIM sample, a relatively high pressure (*ca*. 18 bar) of carbon dioxide was admitted in to the chamber at room temperature. This was left for several days before the chamber was evacuated and a typical hydrogen isotherm measurement was performed at 77 K.

Supercritical carbon dioxide conditioning was performed at 100 °C and 100 bar for 2 hours before being immediately transferred to the IGA system to perform hydrogen sorption measurements at 77 K. The apparatus used to submit the samples to supercritical CO_2 is displayed in Figure 5.4. The apparatus is situated in the Chemical Engineering Department, at the University of Birmingham.

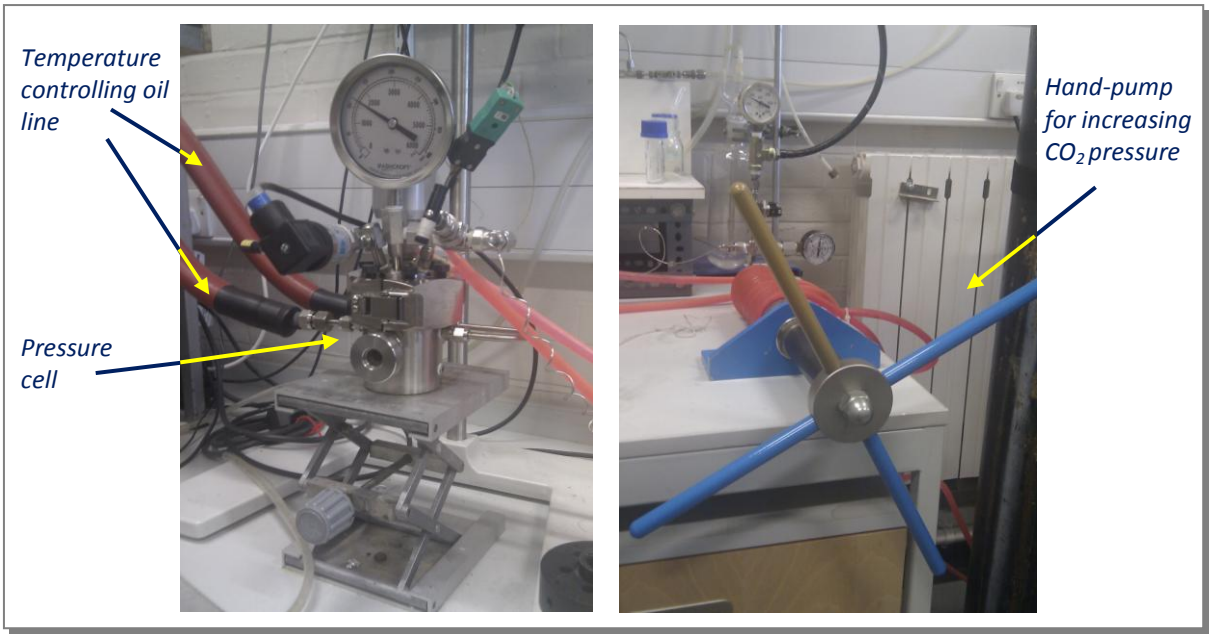

Figure 5.4 - Photographs of the apparatus used for submitting samples to supercritical carbon dioxide situated in the Chemical Engineering Department, University of Birmingham. (Left) pressure cell with connection for the flow of heated oil for temperature control. (Right) Hand-pump for increasing the CO_2 pressure.

Chapter 6

POROUS CARBONS

6.1. Introduction

During the course of this work, a commercial microporous carbon material (Takeda CMS 4A) was provided by the E.C. Framework 6 NESSHY (Novel Efficient Solid Storage for Hydrogen) project[357], in order to determine the variability in hydrogen adsorption measurements of porous samples across many European laboratories. Participants of the inter-laboratory test measured pressure composition isotherms for hydrogen adsorption and desorption at 77 K and room temperature. An assessment of the enthalpy of adsorption was also required for partners who were able to perform isotherm measurements in a low temperature range.

6.2. Porous Carbon (Takeda 4A CMS)

Takeda CMS 4A is a commercial carbon molecular sieve material from Takeda Chem. Ind. Japan, which has been shown to be microporous.[358] The material was selected for a number of reasons. Firstly, there have been many discrepancies in the literature with regard to the hydrogen storage capacities of carbon materials in which the material density plays a significant role; therefore the organisation thought that a material with a relatively low skeletal density should be chosen (in addition to other representative solid-state storage materials, such as sodium alanate and milled magnesium). Secondly, it was decided to use a low hydrogen storage capacity material that was relatively unknown to the 'hydrogen storage community' as such materials are more difficult to measure accurately. Batch homogeneity and commercial availability along with an available pre-treatment also played a part in the selection of this material. Finally, the Takeda 4A material was one of four materials that had already been the subject of a round-robin test on the textural characteristics of porous solids by gas adsorption.[359] The test provided apparent surface area and pore volume for the material as measured by a range of laboratories.

6.2.1. Structure and Characterisation

Scanning electron microscopy showed individual particle dimensions ranging from 1 to 5 μm,[360] which were compressed in to the form of cylindrical extruded pellets. The pellets were approximately 2 mm in diameter (and *ca*. 2 to 4 mm in length). The material is known to not be permanently affected by exposure to air and therefore could be degassed (using appropriate conditions) prior to sorption measurements.[360]

6.2.1.1. Pycnometry

The skeletal density was determined using the Hiden IGA system using helium buoyancy scans at room temperature up to 18 bar. 150.2 mg of the material was measured to displace a volume of 0.08802 cm^3 giving a skeletal density of 1.695 g cm^{-3}.

Of the fourteen participants in the round-robin test, only six reported measured values for the skeletal density of the carbon material. These six results ranged from 0.2 to 2.0 g cm^{-3} (excluding the extremely low value of 0.2 g cm^{-3}, the lowest reported measured density was 1.7 g cm^{-3}, which was our own reported value). The very lowest value was also neglected by the test organisers in their statistical calculations for being too far from the other values. Two partners reported values using helium pycnometry measurements, these were 1.72 and 2.0 g cm^{-3}, respectively. The three other participants that later show good correlation for the hydrogen uptake at 77 K, each use a different method for determining the density of the material: helium pycnometry, volumetric and gravimetric; values from these three partners were 1.72, 1.82, 2.0 g cm^{-3}, respectively.

6.2.2. Gas Adsorption

6.2.2.2. Nitrogen

Grande *et al*. and Zlotea *et al*. reported that the carbon material had an apparent surface area and micropore volume of 423 ± 20 $m^2 g^{-1}$ and 0.17 ± 0.1 $cm^3 g^{-1}$, respectively.[360,361] These were determined by applying the BET and DR methods to the nitrogen isotherms at 77 K. The micropore volume was also reported using carbon dioxide adsorption isotherms at 297 K to give the same value.[360,361]

However, a previous round-robin test aimed at determining the correct textural characteristics of porous solids reported an apparent surface area of 389 ± 37 $m^2 g^{-1}$. The same report also included micropore volumes as determined by nitrogen adsorption at 77 K and carbon dioxide adsorption at 273 K, which produced 0.14 to 0.17 and 0.22 to 0.27 $cm^3 g^{-1}$, respectively. The authors reported the use of immersion calorimetry to determine the pore size distribution of the subject materials. For the Takeda 4A carbon material the PSD was found to be narrow with very narrow pores. In fact, they found that cyclohexane (with a kinetic diameter of 0.48 nm) was not able to access the pores in the material, suggesting that the Takeda 4A material has pores < 0.4 nm in diameter. These results were also published by Krutyeva *et al*. (a member of that round-robin test).[191,361] For comparison, the same carbon molecular sieve 4A material was synthesised by Bergbau–Forschung, which is reported to have pores between 0.3 and 0.5 nm.[359,361]

6.2.2.3. Hydrogen

The outgassing procedure was provided by the test organisers and was followed as closely as possible. Approximately 132 mg of the sample was heated to 110 °C for 24 hours followed by 250 °C for 4 hours under a vacuum (1×10^{-6} mbar) resulting in a 3% loss in mass. The test organisers requested that the material be degassed in vacuum of 1×10^{-3} Pa (or better): the Hiden IGA is capable of 1×10^{-7} mbar. After which the sample was not exposed to air before the hydrogen adsorption measurements. The hydrogen gas purity used was 99.99996% and was supplied by Air Products. This was passed through a zeolite and liquid nitrogen trap to capture any further impurities in the gas supply.

6.2.2.4. Excess Adsorption

Eleven partners of the round-robin test showed results for measurements at 77 K for the activated carbon.[360] The results ranged from 1.2 to 2 wt.% up to 20 bar at 77 K, and had increasing dispersion with increasing pressure. The curve shapes of the isotherms also differed significantly, which increased with pressure. Of the eleven partners, six groups performed static volumetric measurements, four performed static gravimetric measurements, and one performed dynamic volumetric measurements. The results can be split in to four groups. The first group contained two static volumetric methods and two gravimetric

methods, one of which was our own. Each of the four participants that fell into this group, reported a hydrogen uptake of 1.4 ± 0.1 wt.% up to 10 bar.

The second group consisted of two volumetric instruments from the same laboratory. Both instruments saw an uptake of 1.1 wt.% at 1 and 5 bar respectively. The third group contains each partner that observed hydrogen uptake greater than that of the first group. Each member of the third group used a different technique: volumetric; dynamic volumetric; or gravimetric. The partner using the volumetric method (shown as red circles in Figure 6.1) reported data that was comparable to the first group at 5 bar. However, the isotherm continued to rise linearly with increasing pressure. The linear rise of the isotherm suggests that experimental errors, such as a gas leak or impurities in the hydrogen gas, occurred. The second member of this group (shown as orange triangles in Figure 6.1) is a dynamic volumetric method using a hydrogen flow rate of 50 ml min^{-1}. However, multiple measurements using different flow rates did not produce consistent results, indicating an error in the experimental procedure, as the change in flow rate should not influence the hydrogen uptake.[57] The third member of this group (shown as light blue diamonds in Figure 6.1) used a gravimetric method. The high uptake values were suggested to be due to contamination and adsorption of impurities as result of a combination of low-purity hydrogen and no additional filters.

The last remaining group of results in the round-robin test contain two members. Both members reported hydrogen uptake values lower than those in the first group. The first of these two participants (shown as purple pentagons in Figure 6.1) used a gravimetric method. The low uptake and continual rise in adsorption could not be explained by the test organisers or participant. The partner did not report the hydrogen purity used and this could explain the continuing adsorption after the initial steep rise at low pressures. However, impurities would have resulted in higher uptake values than were seen by the partners in the first group. This partner did not determine the density of the carbon material, instead they assumed the materials had a skeletal density equal to that of pure carbon (2.2 g cm^{-3}),[360] however, an incorrect density, that is too high creates a 'downward curve' in place of a horizontal plateau. The partner did report that they used a minimum equilibrium time of five minutes: depending on the actual system used, this could mean that the equilibrium was not achieved before moving on to the next pressure

increment. For example, the Hiden IGA system requires each kinetic trace to lie within a set percentage of the calculated asymptote before progressing to the next pressure step. Therefore, having a low minimum equilibrium time and low required percentage fit of the asymptote could lead to the type of isotherm reported by this partner. The organiser also suggested possible errors in dry mass along with surface poisoning as possible explanations. The second participant of this final group used a volumetric instrument and reported an isotherm of an unusual shape with very few data points. The participant used an extremely short minimum equilibrium time (1.6 minutes). This, along with the large chamber volume of 40 cm^3 (relative to the sample volume, *ca*. 0.4 cm^3) could explain the low uptake and inconsistent shape of the isotherm. Although, a final plateau at 1.4 wt.% was achieved above 30 bar.[360]

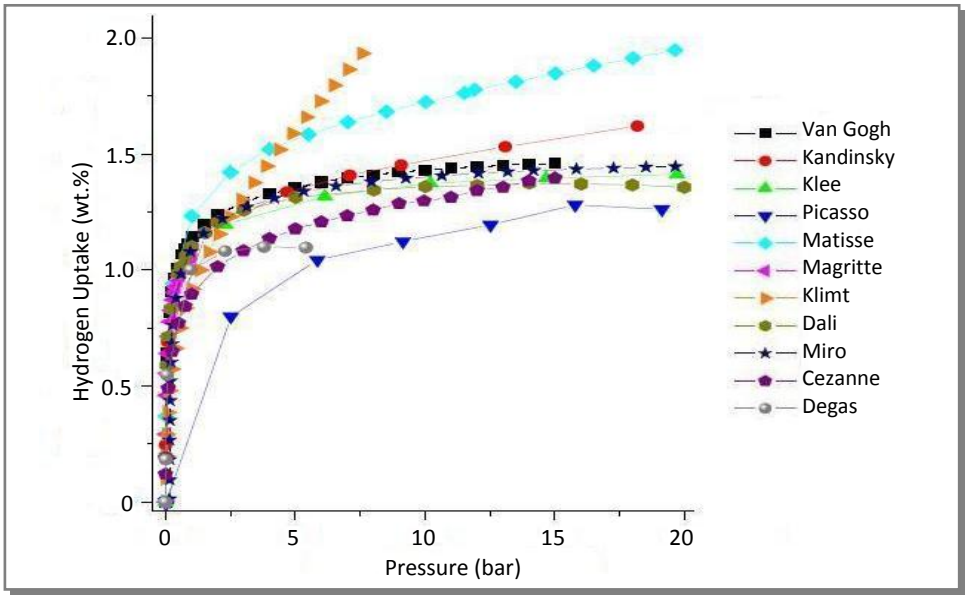

Figure 6.1 - A comparison of the adsorption isotherms for the eleven partners of a round-robin test that measured the Takeda CMS 4A porous carbon at 77 K. Code names for the different partners are used to maintain anonymity. The Van Gogh plot (■) illustrates results described in this work.[360]

The four participants in the first group not only demonstrated similar adsorption isotherms, but also showed consistencies for other measurements such as the density determination. Additionally, they reported similar experimental conditions such as degassing pressure, equilibration times and hydrogen gas purity. Thus, the very low variability between the four isotherms together with the diversity of originating laboratories and instrumentation allowed the organisers to conclude that a coincidental agreement of results could be excluded.

After submitting the results to the round-robin test organisers, the carbon material was measured using helium pycnometry. The pycnometry system is housed inside the argon-filled glovebox to allow for degassed samples to be run without exposure to air. The outgassed material (387.0 mg) was measured giving a volume of 0.18(1) cm^3. This gave a skeletal density of 2.15(1) g cm^{-3}. The difference between this value and that previously determined using the Hiden IGA, led to a recalibration of the system using a evacuated quartz bulb of known density. Subsequently, the Takeda 4A porous carbon was measured again on a IGA system. The material displaced a volume of 0.0592 cm^3 giving a skeletal density of 2.16 g cm^{-3}. This second value from the IGA is close that of the helium pycnometry. With this correlation between two techniques and also considering the density measured by other laboratories only helium pycnometry was performed for the remaining materials.

It can be seen in Figure 6.1 that our result is slightly higher than some of the other groups. Using a higher density in the buoyancy correction results in an adsorption isotherm at a slightly lower hydrogen uptake, and also adjusts the shape of the excess isotherm at higher pressures. A higher density stops an excess isotherm from continually rising (or having a very gentle rise until much higher pressures). The adjusted 77 K adsorption and desorption excess hydrogen isotherm is displayed in Figure 6.2.

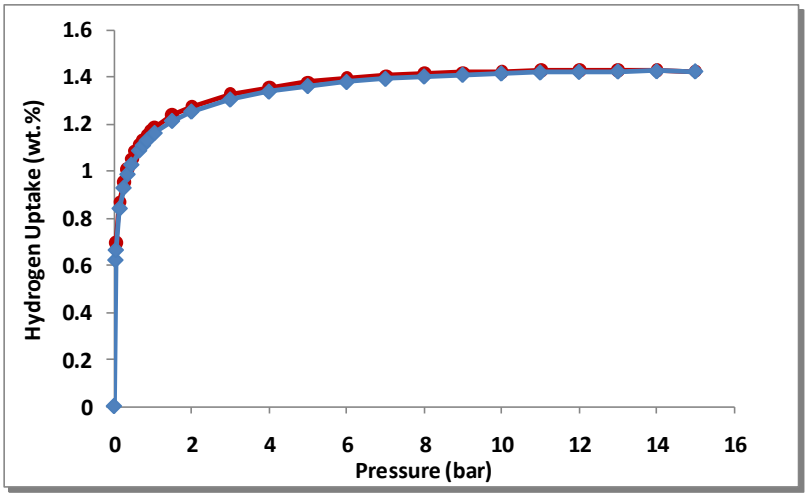

Figure 6.2 - Excess gravimetric hydrogen adsorption (♦) and desorption (●) at 77 K, up to 15 bar, for the Takeda 4A porous carbon.

The excess gravimetric hydrogen storage capacity at a variety of temperatures is presented in Figure 6.3. The Takeda CMS 4A porous carbon exhibited an excess hydrogen uptake of 1.42 wt.% and 0.07 wt.% at 15 bar and 77 K and room temperature, respectively. The decrease in hydrogen uptake with increasing

temperature is characteristic of porous materials. This is illustrated by plotting hydrogen uptake at different pressures against temperature, also shown in Figure 6.3.

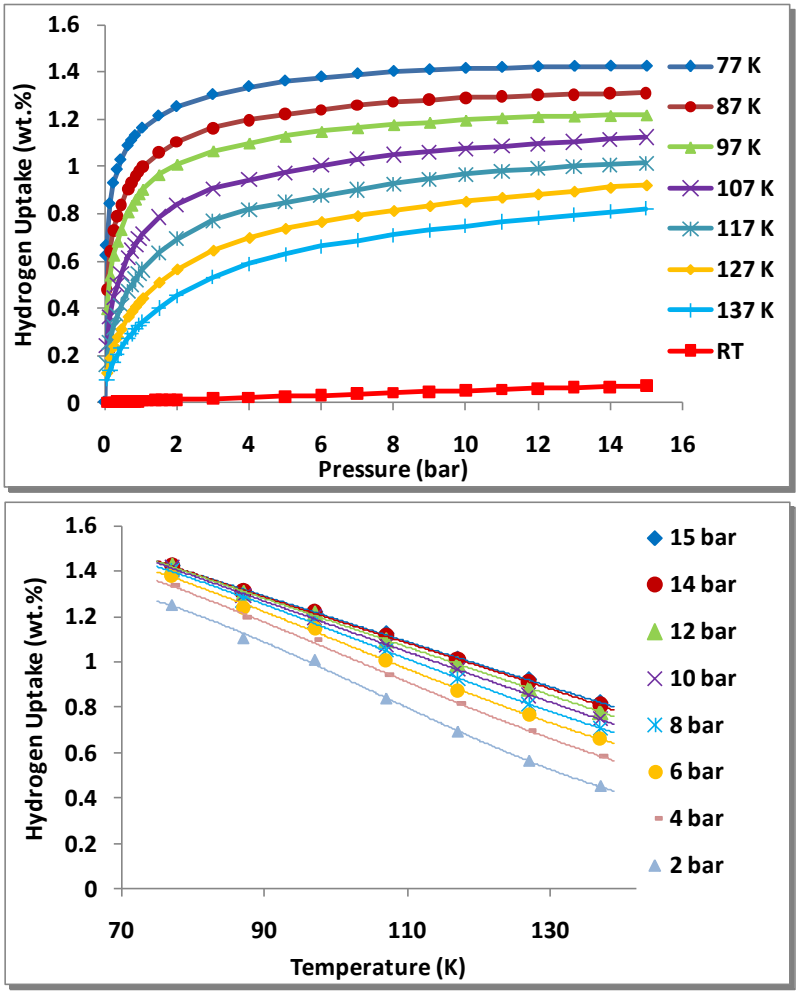

Figure 6.3 - (Top) Variable temperature excess gravimetric hydrogen isotherms for the Takeda 4A porous carbon sample. (Bottom) Excess gravimetric hydrogen uptake against temperature at varying pressures.

6.2.2.5. Absolute Adsorption

As discussed in Chapter 3, the conversion between the measured excess adsorption and the absolute amount adsorbed requires knowledge of the volume of the adsorbed phase;[121,123,124] however, this cannot be measured experimentally and is therefore not known.[123,124]

Richard *et al*.[123] and others[118,121,161] utilise equation (3.47) and make the assumption that the adsorbed phase volume is simply equal to the pore volume. In order to eliminate the associated problems with making this assumption, the density of the adsorbed phase is used instead (as shown in equation (3.50) and is set to be equal to that of hydrogen at the triple point (0.077 g cm^{-3}).[128] A comparison between different expressions can be seen in Appendix D. The closeness of the different methods suggests that

using the density of hydrogen at the triple point is valid and is also not subject to the potential error associated with the adsorbed phase volume. Therefore, this method has been used in all subsequent calculations of the absolute adsorption.

The difference between the excess and absolute adsorption at 77 K is presented in Figure 6.4. The Takeda CMS 4A activated carbon exhibited an absolute hydrogen uptake of 1.55 wt.% and 0.07 wt.% at 15 bar and 77 K and room temperature, respectively.

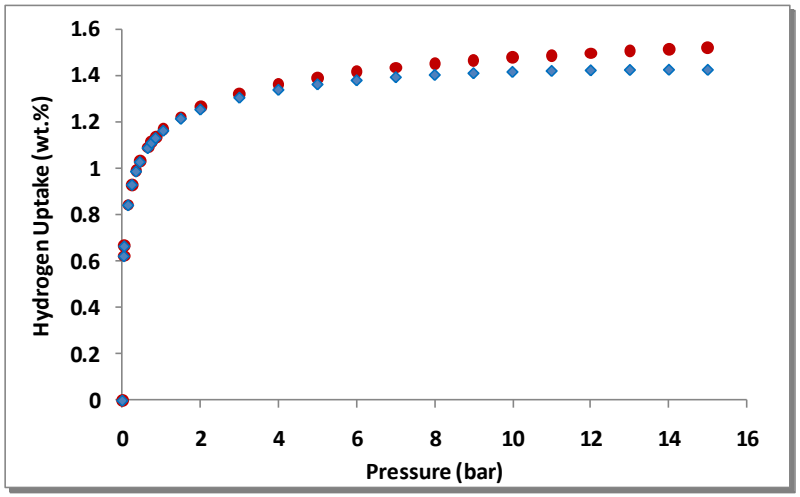

Figure 6.4 - Difference between excess (♦) and absolute (●) hydrogen uptake (wt.%) against pressure (bar) at 77 K, for the Takeda 4A porous carbon, using the adsorbed phase density equal to that of hydrogen at the triple point.

6.2.2.5.3. Empirical Isotherm Equations

The Sips and Tóth empirical isotherm equations were applied to the absolute adsorption isotherm at each temperature using the Levenberg-Marquardt algorithm that is used to search for the coefficient values that minimize chi-square (a form of nonlinear, least-squares fitting).[72,362] Both equations appear to produce a good fit for the 77 K isotherm, but residual plots illustrate the differences between the data and the fitted model, as shown in Figure 6.5. It is important to note that in the residual plots displayed in Figure 6.5 (and throughout this thesis) the central horizontal line represents the fitting model and the symbols show how close the data lies to each model.

An acceptable fit of the isotherm model to the experimental data is that 99% of the residuals lie within $\pm$ 0.02.[125] The residuals for both models were within $\pm$ 0.005 wt.%, and therefore indicate an excellent fit. The Tóth model appears to stick closer to the absolute isotherm from *ca*. 1 to 10 bar, before beginning

to veer away at higher pressures. The two models produce fairly significant differences in their predicted saturation uptakes, which are 1.87 ± 0.005 and 2.06 ± 0.01 wt.%, for the Sips and Tóth models, respectively at 77 K.

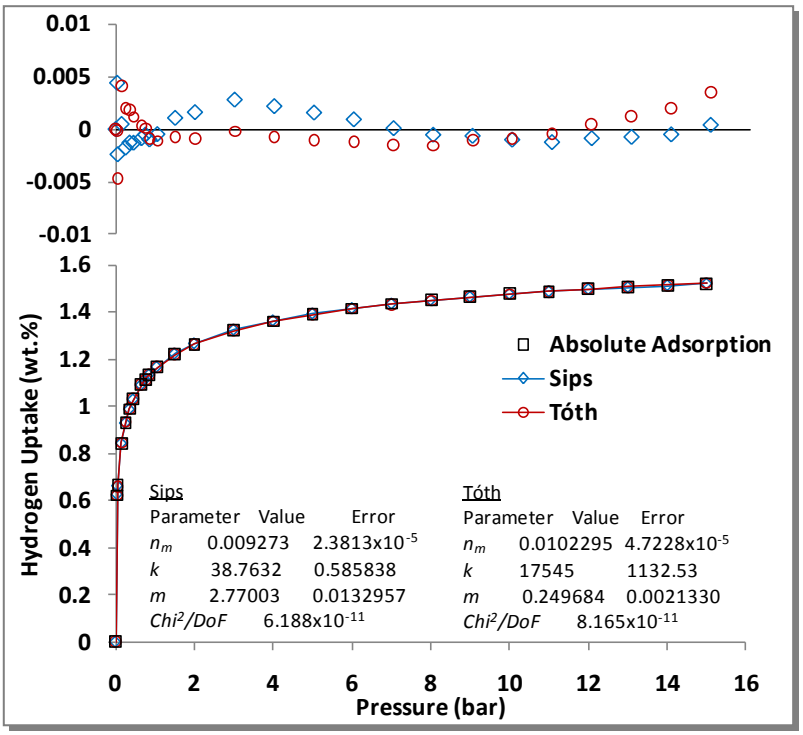

Figure 6.5 - Fitted Sips (◊) and Tóth (○) equations to the absolute hydrogen uptake versus pressure at 77 K up to 15 bar, for the Takeda 4A porous carbon. Residual plots can be seen at the top.

6.2.2.5.4. Enthalpy of Adsorption

6.2.2.5.4.1. Clausius-Clapeyron

The organisers of the round-robin test requested that the isosteric enthalpy of adsorption to be calculated by plotting ln(p) against $1/T$ at particular hydrogen uptake values. Originally for the purpose of the test, this was performed by manually reading-off uptakes values as accurately as possible from the excess isotherms.

Two other laboratories from the round-robin test were also able to produce plots of enthalpy of adsorption versus hydrogen uptake at multiple temperatures. These partners showed enthalpy of adsorption values between 5.5 and 6.5 kJ mol^{-1} from 30 to 55% coverage and then decrease from 6.5 to 5 kJ mol^{-1} between 55 and 80% coverage.[191] However, the isosteric enthalpy of adsorption determined from the isotherms measured in our laboratory showed a decrease from 7.5 to 6.5 kJ mol^{-1} between 40%

and 55% coverage. These higher values are more consistent with the theory that the adsorbate-adsorbent interaction decreases with increasing adsorbate concentration.

Fitting a function, the absolute adsorption isotherm allows for precise values for uptake and pressure to be determined. Figure 6.6 shows the isosteric enthalpy of adsorption for the Takeda CMS 4A material as determined using the hydrogen uptake values from the two fitted models (Sips and Tóth) at 77 and 87 K. It is difficult to select up to what value of hydrogen uptake to calculate the isosteric enthalpy of adsorption. Ideally the low-pressure regime should be used in an attempt to ensure that only adsorbate-adsorbent interactions are being considered (without being influenced by adsorbate-adsorbate interactions). Throughout this work the isosteric enthalpy of adsorption will be consistently displayed up to 0.8 wt.% (4.0 mmol g^{-1}). For the carbon material, these levels of absolute hydrogen uptake correspond to at *ca*. 0.15 and 0.45 bar at 77 and 87 K, respectively.

The analysis shows particularly high enthalpies of adsorption for a microporous material, with a value of 15.8 and 10.2 kJ mol^{-1}, at the near zero coverage of 0.02 wt.% of hydrogen, for the Sips and Tóth fits, respectively. The enthalpies of adsorption decrease sharply with increasing hydrogen uptake, with the two models both giving 5.8 kJ mol^{-1}, at 0.8 wt.%. Furukawa *et al*. previously observed a similar difference between two isosteric enthalpy of adsorption curves, when comparing the use of the Sips (Langmuir-Freundlich) model and a Virial-type thermal equation. These workers believed the viral fit to be more accurate and claimed that the Sips fit provided an overestimation of the enthalpy of adsorption due to a poor fit of the isotherm at low coverage.[118]

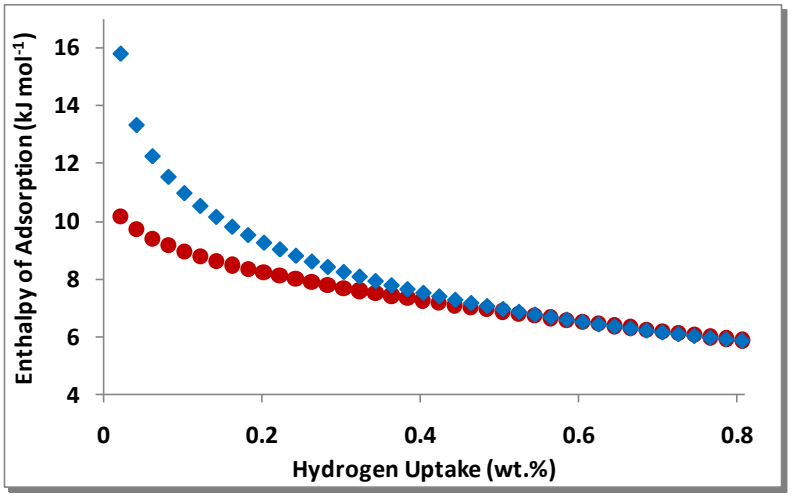

Figure 6.6 - Comparison of the Clausius-Clapeyron equation (in conjunction with Sips (♦) and Tóth (●) equations fitted to the 77 and 87 K absolute isotherms), for the Takeda 4A porous carbon.

Using the isothermal data from multiple isotherms at different temperatures it is believed that a more accurate plot for the enthalpy of adsorption versus hydrogen uptake can be determined. However, inaccuracies can result when taking the ln(p) against 1/T; often data is ignored in the steep and flat regions of the isotherm due to the fear of relatively high errors.[191] This means that often isotherms at lower temperatures are discounted at low pressures, which is illustrated by the van't Hoff plot in Figure 6.7. However, failing to take a consistent number of isotherms into consideration when calculating the isosteric enthalpy of adsorption results in a worse error. This is in addition to trying to calculate the enthalpy of hydrogen interaction with the surface of material when the interaction itself is influenced by the presence of hydrogen that is already adsorbed on the surface. This is a typical problem when isosteric enthalpies of adsorption have been previously reported. Therefore, caution should be exercised to reported adsorption enthalpies that are not in the low pressure regime as is the case with many publications.[191,228,300]

Using a different number of isotherms to calculate the enthalpy of adsorption (at different values of hydrogen uptake) can result in 'steps' being observed in the resulting plot (see Figure 6.7, bottom).[191] These errors are illustrated in Figure 6.7, where each region of the isosteric enthalpy of adsorption can be directly related to the number of data points used in each van't Hoff plot, and each vertical set of data points corresponds to an isotherm at a different temperature. In Figure 6.7, region A can be seen to include six van't Hoff plots (each containing three data points, i.e. using three isotherms at different

temperatures)) and subsequently results in six values for the enthalpy of adsorption. While, region B includes seven van't Hoff plots (each containing 4 data points) and subsequently results in six values for enthalpy of adsorption. This difference causes a 'step' between region A and region B. In the example shown in Figure 6.7, this problem occurs throughout the plot of isosteric enthalpy of adsorption against hydrogen uptake (or surface coverage, as is displayed), resulting in several steps in the subsequent regions. These errors could be avoided by using fitted data as these can easily be extrapolated and/or interpolated.[71]

Moreover, some systems are only capable of measuring from a vacuum up to atmospheric pressure and in the case of most microporous hydrogen storage materials this low-pressure range should be used for calculating the isosteric enthalpy of adsorption.

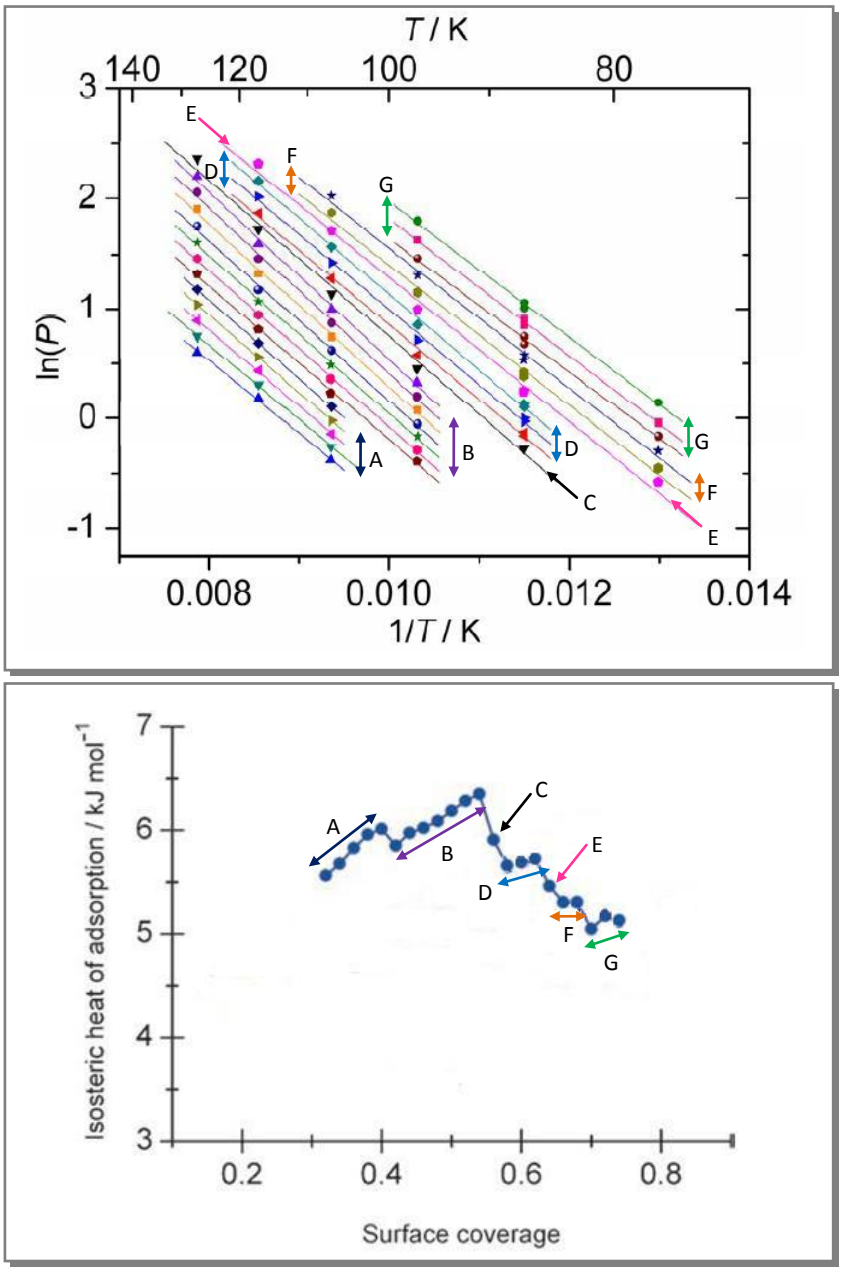

Figure 6.7 - Van't Hoff plot (top) and isosteric enthalpy of adsorption (bottom) of the Takeda 4A porous carbon. Taken from the literature to illustrate the direct relationship between the number of data points in van't Hoff plot and the 'steps' that can occur in the isosteric enthalpy of adsorption versus hydrogen uptake.[191]

Some researchers report hydrogen uptake as a fraction of complete surface coverage (fractional coverage). This however can result in very poor comparisons being made between materials, depending on how the complete coverage is determined. For high surface area materials, complete surface coverage is never reached at 77 K (or at higher temperatures). Therefore the complete surface coverage (or complete pore filling) can never be accurately determined where it occurs dramatically above experimental pressures. Schmitz *et al*. attempted to normalise the hydrogen isotherms from different

materials in order to compare the different curve shapes. This was performed by assuming that complete coverage occurred at 20 bar,[191] which has certainly been proven to be incorrect for some high surface area microporous materials.[147]

Additionally, due to hydrogen being supercritical in the typical temperature range in which potential storage materials are measured, the hydrogen will never condense in the bulk gas phase regardless of pressure. For this reason hydrogen isotherms can never be plotted using relative pressure, as is typically reported for nitrogen isotherms (and other gases such as carbon dioxide). However, despite this researchers have attempted to use so-called pseudo-saturation pressures (using equation 3.22) in order to display data as relative pressure, as discussed previously in Chapter 3.[85,86,119,302]

To combat the inaccuracies of taking a different number of isotherms and manually interpreting the pressure at which a particular hydrogen uptake value is reached; the Sips and Tóth models were fitted to the absolute isotherms at each measured temperature for the Takeda 4A porous carbon sample. The fitted data was then used to create a plot of ln(p) against $1/T$ (see Figure 6.8) and subsequently determine isosteric enthalpies of adsorption against hydrogen uptake using a consistent number of isotherms (see Figure 6.9). The errors presented in Figure 6.9 are equal to the standard deviation of each individual van't Hoff plot. The enthalpy of adsorption was only calculated for hydrogen uptake up to 0.8 wt.% in order for it to be consistent when making comparisons using different methods (and between different materials). Figure 6.9 presents a direct comparison between fitting the same absolute isotherm with two different models. A very similar difference is observed between the two isosteric enthalpy of adsorption curves produced from the two fitting models, using several isotherms at different temperatures, as was seen previously when using just 77 and 87 K isotherms.

The analysis shows particularly high enthalpies of adsorption for a microporous material, with a value of 12.3 and 8.6 kJ mol^{-1}, at the near zero coverage of 0.02 wt.% of hydrogen, for the Sips and Tóth fits, respectively. The enthalpies of adsorption decrease sharply with increasing hydrogen uptake, with the two models giving 6.7 and 6.8 kJ mol^{-1}, respectively, at 0.8 wt.%. Consequently, using various temperatures is shown to alter the shape of the enthalpy of adsorption curve, with the enthalpy of

adsorption decreasing at low coverage and very slightly increasing it at higher coverage, thus reducing the dramatic gradient of the curve.

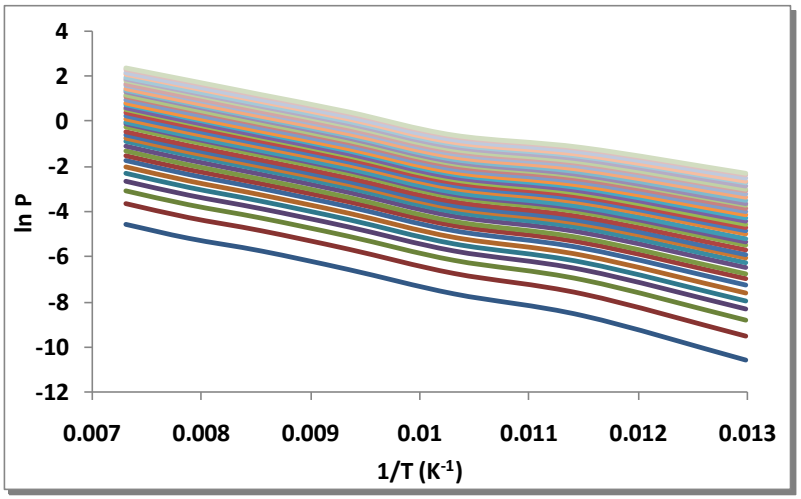

Figure 6.8 - Example of the van't Hoff plot used to determine the isosteric enthalpy of adsorption for the Takeda 4A porous carbon. This example uses the Tóth model from 77 to 137 K in 10 K steps. Hydrogen uptake values of 0.1 to 4.0 mmol g^{-1} were taken in 0.1 mmol g^{-1} steps, which corresponds to ca. 0.02 to 0.8 wt.% in 0.02 wt.% steps.

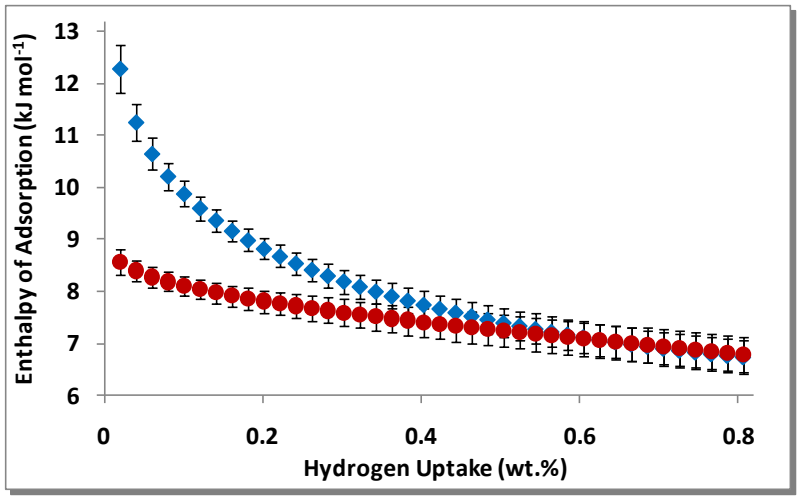

Figure 6.9 - Enthalpy of adsorption versus hydrogen uptake for the Takeda 4A porous carbon. Using the Sips (♦) and Tóth (●) models to fit the absolute isotherms and then the Clausius-Clapeyron equation and van't Hoff plot to determine the enthalpy of adsorption.

6.2.2.5.4.2. Virial Type Expansion Equation

Figure 6.10 shows the virial plots for the hydrogen adsorption on the Takeda 4A porous carbon at 77 to 137 K, in 10 K steps). The plots are taken to be linear at pressures ≥ 0.15 bar to *ca.* 1 bar, allowing the determination of A_0 and A_1 values from the intercepts and gradients respectively (values are given in Table 6.1). The gradient from the plot of A_0 against $1/T$ (see Figure 6.10) produced an isosteric enthalpy of adsorption of 8.1 ± 0.3 kJ mol^{-1}. The Henry's law constant (which is related to the first virial parameter

($K_H = \exp(A_0)$) is seen to decrease with increasing temperature, which indicates a decrease in adsorbate-adsorbent interaction with increasing temperature. The second virial parameter appears to increase from 77 to 117 K, which suggests stronger adsorbate-adsorbate interactions occur at 117 K compared to 77 K. This decrease to less negative values from 117 to 137 K indicates weaker adsorbate-adsorbate interactions.

Table 6.1 - Henry's law constant and virial Parameters A_0 and A_1 for hydrogen adsorption on Takeda 4A porous carbon at various temperatures (from 77 to 137 K, in 10 K steps). The errors shown are equal to one standard deviation.

Temperature **K**	k_H **mol g^{-1} Pa^{-1}**	A_0 **ln(mol g^{-1} Pa^{-1})**	A_1 **g mol^{-1}**
77	1.92E-05	-10.86 ± 0.04	-1010.66 ± 8.67
87	3.19E-06	-12.66 ± 0.01	-851.81 ± 2.43
97	1.40E-06	-13.48 ± 0.04	-780.22 ± 11.02
107	4.47E-07	-14.62 ± 0.04	-734.81 ± 12.16
117	1.98E-07	-15.44 ± 0.02	-720.91 ± 9.11
127	1.27E-07	-15.88 ± 0.04	-838.19 ± 25.44
137	7.02E-08	-16.47 ± 0.04	-877.97 ± 27.871

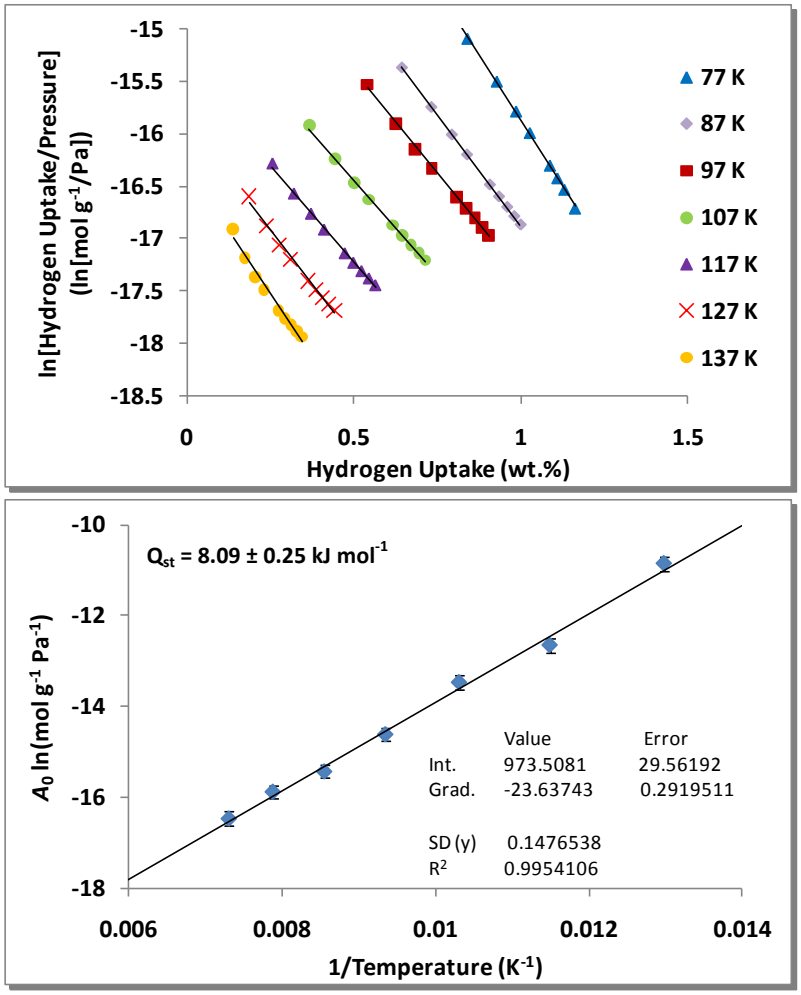

Figure 6.10 - (Top) Virial plots for the absolute adsorption of hydrogen on the Takeda 4A porous carbon and (bottom) the variation of virial parameter, A_0 with 1/T (from 77 to 137 K, in 10 K steps).

6.2.2.5.4.3. Virial Type Thermal Equation

Equation (3.66) was used to fit the 77 and 87 K isotherms simultaneously (see Figure 6.10). The equation has no limit to the number of coefficients that can be included; previous researchers have found that values of $m \leq 6$ and $n \leq 3$, were enough to appreciably reduce the χ^2 goodness-of-fit for their range of microporous MOF materials.[134] The isosteric enthalpy of adsorption was subsequently calculated according to equation (3.67), as a function of hydrogen uptake as shown in Figure 6.12. The analysis gives an isosteric enthalpy of adsorption at zero coverage for the Takeda 4A porous carbon of 10.1 kJ mol^{-1}, which subsequently decreases sharply with increasing hydrogen uptake.

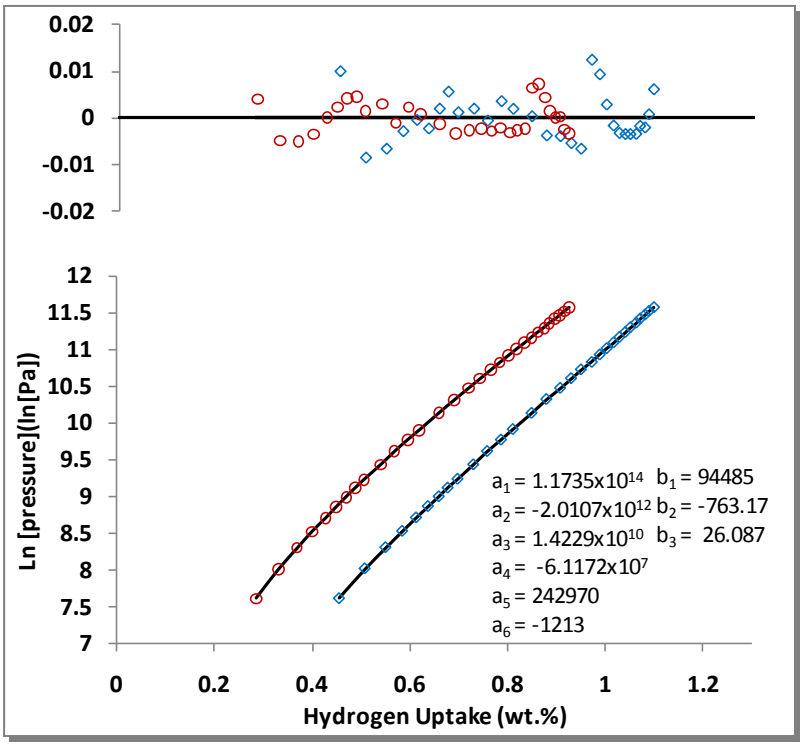

Figure 6.11 - Hydrogen adsorption isotherms at 77 (◊) and 87 K (○) for the Takeda 4A carbon material up to 15 bar. Data is shown by open shapes, while virial plots are shown by solid lines. Residual plots can be seen at the top.

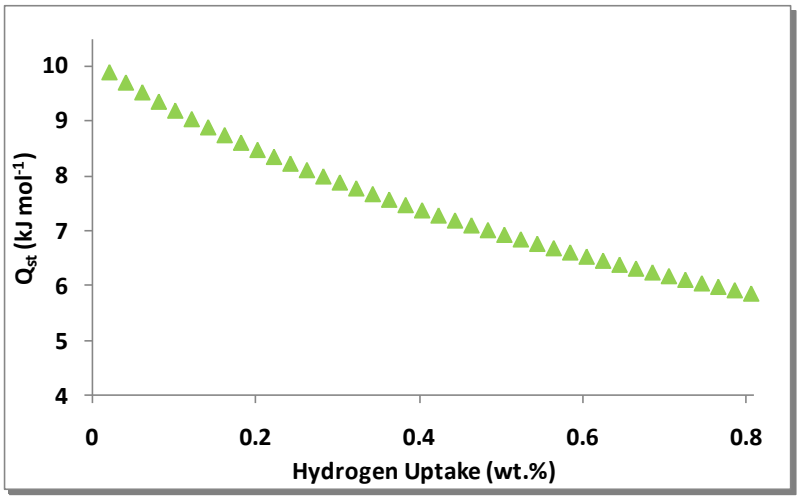

Figure 6.12 - Isosteric enthalpy of adsorption for the carbon Takeda 4A as a function of hydrogen uptake as determined using the virial type thermal equation and data from 77 and 87 K.

Figure 6.13 displays the comparison between the isosteric enthalpy of adsorption determined using the Clausius-Clapeyron equation after fitting with the Sips and Tóth equations and that determined by the virial equation (as shown in Figure 6.12). When using just two temperatures (77 and 87 K) the Sips model appears to overestimate the enthalpy of adsorption at low coverage. This was also observed by Furukawa *et al*. with MOF-177.[118] However the Tóth and Virial fits produce plots that almost overlap, although the

Tóth model appears to show more curvature in the dependence of isosteric enthalpy of adsorption with hydrogen uptake. The three models show consistent enthalpy of adsorption values from 0.5 wt.%. In fact, both the Sips and Tóth models give a value of 6.2 kJ mol^{-1} at 0.8 wt.%, with the virial equation yielding 5.9 kJ mol^{-1} at the same coverage. The virial equation (using 77 and 87 K) did not produce such a close fit to either of the curves produced by the Clausius-Clapeyron equation and Sips and Tóth models with multiple temperatures (see Figure 6.13).

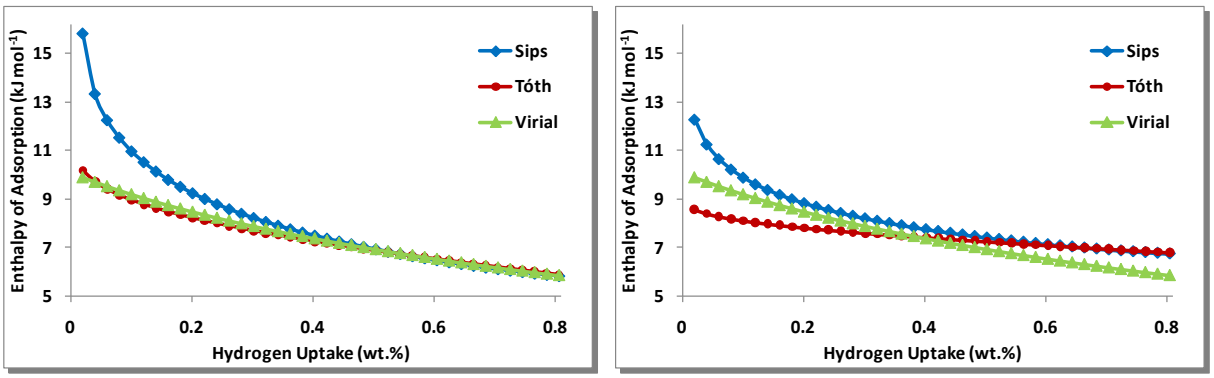

Figure 6.13 - Comparison of the isosteric enthalpy of adsorption for Takeda 4A porous carbon, as a function of hydrogen uptake determined by fitting the Sips and Tóth equations and Virial thermal type equation. Sips and Tóth plots utilise two temperatures, 77 and 87 K (left) and multiple temperatures (right). The virial thermal type equation utilises two temperatures; 77 and 87 K in both plots.

6.2.2.5.4.4. Extended Empirical Isotherm Equation

The extended Tóth equation (3.69) was used fit the excess hydrogen isotherms for the porous carbon material at 77 and 87 K. The excess hydrogen adsorption prediction shown in Figure 6.14 gives a pore volume of 0.253 and 0.257 $cm^3 g^{-1}$, respectively for the 77 and 87 K data. Zlotea *et al*. reported a micropore volume of 0.17 $cm^3 g^{-1}$.[360,361,363] Additionally, the results of the round-robin test reported by Silvestre-Albero *et al*. gave micropore volumes (using nitrogen adsorption at 77 K) in the range 0.14 to 0.17 $cm^3 g^{-1}$ and mesopore volumes in the range 0.00 to 0.11 $cm^3 g^{-1}$.[359]

A significant downturn is observed in the predicted excess adsorption isotherm which is consistent with the theory of the Gibbs excess (as discussed in Chapter 3) and that illustrated by Furukawa *et al*. in relation to MOF-177.[118] However, the prediction suggests that the porous carbon material has already reached its maximum excess hydrogen adsorption by 15 bar at both 77 and 87 K. Whilst this appears to be

consistent with the other measurements preformed as part of the round-robin exercise the predicted downturn at higher pressures is more severe than observed by the other partners.

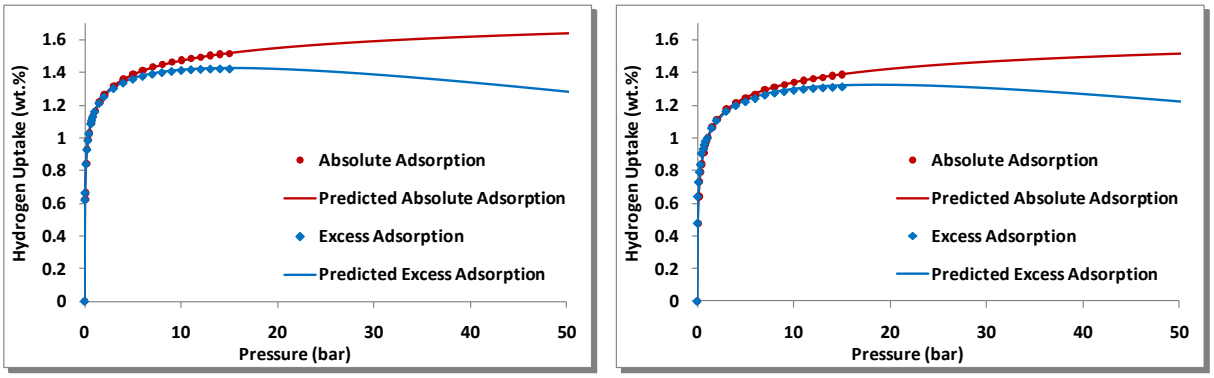

Figure 6.14 - Predicted excess and absolute adsorption at 77 (left) and 87 K (right) up to 50 bar. The predicted excess uses the extended Tóth equation, whereas the absolute prediction uses the usual Tóth model.

6.3. Chapter Summary

The objective of this chapter was to demonstrate the relative accuracy of the thermogravimetric gas sorption equipment (IGA) that is used throughout this work. The excess hydrogen adsorption of a porous carbon material with a low surface area was used as the subject material. The differences found between the different laboratories were discussed with respect to the possible errors in gas sorption measurements that can occur. The excess gravimetric hydrogen adsorption isotherm at 77 K determined by the IGA sufficiently matched the isotherms produced by other groups.

As part of the round-robin exercise, the isosteric enthalpy of adsorption was required to be 'manually' calculated from the excess adsorption isotherm. This was shown to produce inconsistent results. Additionally, fundamental errors were demonstrated when taking inconsistent numbers of adsorption isotherms to calculate the isosteric enthalpy of adsorption.

This chapter introduced the outcome of fitting absolute hydrogen isotherms (rather than excess) in order to more accurately determine the dependence of the isosteric enthalpy of adsorption as a function of hydrogen adsorption. The Tóth and virial fitting models were found to produce relatively similar curves, whilst the Sips model appeared to overestimate the enthalpy of adsorption at low coverage, possibly to due to poor fitting in the low-pressure region. The relatively high enthalpy of adsorption values at low coverage reported here are more consistent with the small pore size than has been found by previous

workers. The steep decrease in the isosteric enthalpy of adsorption as a function of hydrogen uptake also correlates with distribution of pore sizes (in comparison to that expected to be exhibited by a crystalline material with a single pore size).

Chapter 7

ZEOLITES

7.1. Introduction

Langmi carried out a systematic investigation of the hydrogen adsorption properties of a wide range of zeolite materials, at three different temperatures (at the University of Birmingham in 2004).[152,204,205] The zeolites that were synthesised by Langmi were available to be used in this work; NaX was included here due to the high purity of the sample that was synthesised. Zeolites themselves are typically very crystalline, well characterised and particularly robust, which are all good qualities that lead to the inclusion of a zeolite in this study.

7.2. Zeolite NaX

The NaX zeolite material was synthesised by Langmi *et al*. for previous studies within the University of Birmingham (School of Metallurgy and Materials, and the School of Chemistry).[152,204,205] NaX is the parent zeolite X, where the sodium content is equal to the aluminium content and has the formula $Na_{76}[(AlO_2)_{76}(SiO_2)_{116}]$.

7.2.1. Structure and Characterisation

NaX has the faujsite (FAU) structure, which is one of over 150 different zeolite structures. The FAU structure consists of sodalite cages linked by double 6 rings and has the space group Fd3m (number 227). The International Zeolite Association (IZA) report the lattice parameter for Zeolite X to be 2.48 to 2.50 nm. Langmi previously reported that scanning electron microscopy showed well-defined crystals in the size range approximately 1 to 3 μm.[152] NaX like most zeolites is known to have a strong affinity to water. Moisture originally adsorbed from the atmosphere is known to be desorbed from the material upon degassing (using appropriate conditions) without altering the structure.

7.2.1.1. XRD

Figure 7.1 displays the room temperature powder XRD pattern for Zeolite NaX. Chekcell was used in order to compare the observed peak positions to those calculated from the space group and lattice parameter reported for the zeolite structure by Olson (see Appendix A).[364] Chekcell was also used to refine the zero point error, and determine hkl values and a refined lattice parameter of 25.025(4) Å. The XRD pattern shows an excellent match with the expected structure derived from single crystal data, which was used to give a lattice parameter of 25.099(5) Å.[364]

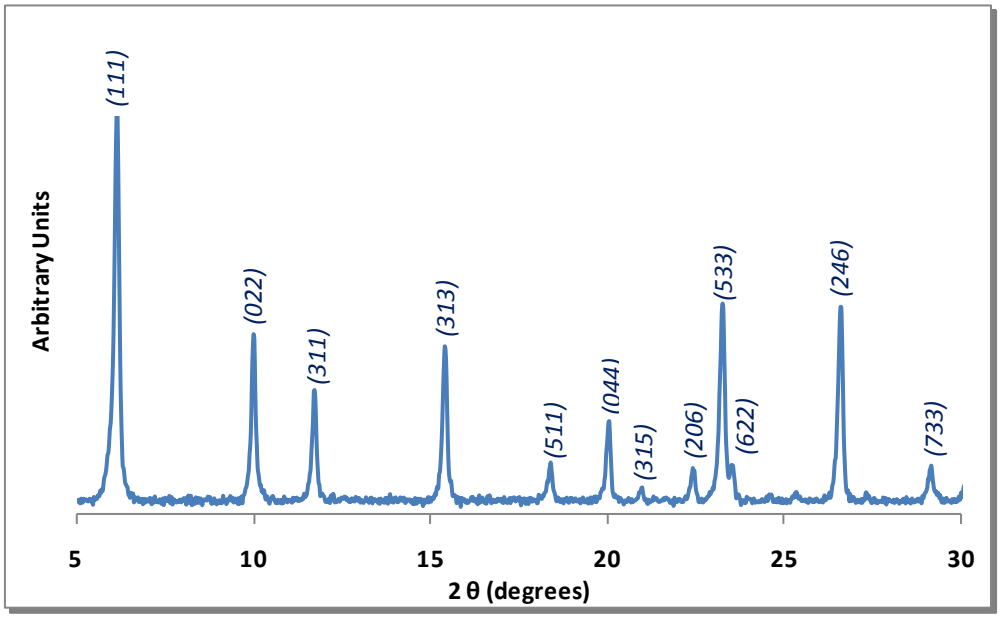

Figure 7.1 - Powder X-ray diffraction pattern for NaX using the multi-changer (at RT) and Göebel Mirror.

7.2.1.2. TGA

Thermogravimetric analysis (TGA) of NaX was performed on both the TGA and IGA systems. The TGA measurements provide a guide for determining an appropriate degassing temperature (before gas sorption measurements). The TGA was performed in a flow of argon gas (at 2 °C min^{-1}) from room temperature up to 600 °C, as displayed in Figure 7.2. The sample mass decreased immediately with increasing temperature, with significant mass loss starting at around 200 °C and almost completely finishing by 415 °C with a mass loss of 9.8%. A further 0.4% loss in mass is observed up to 600 °C. Joshi *et al*. reported TGA of NaX with a heating rate of 10 K $minute^{-1}$; as a result they saw significant mass loss

immediately with increasing temperature. The authors reported that complete dehydration of NaX was achieved by 700 K (427 °C), with a mass loss of *ca*. 25%.[365]

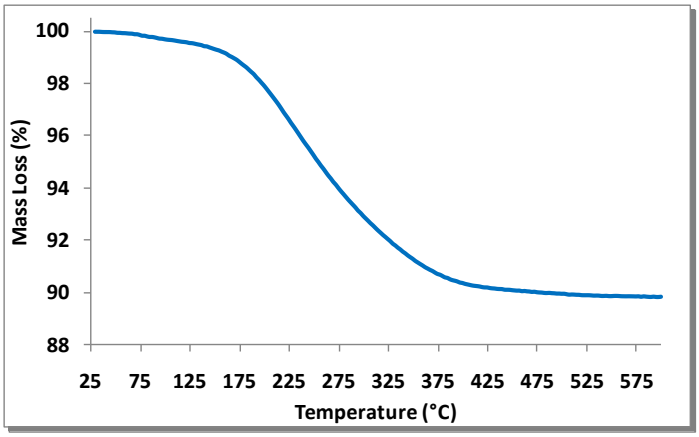

Figure 7.2 - TGA of Zeolite NaX, from RT to 600 °C at 2 °C min^{-1}. A mass loss of 10.2% was observed. TGA was performed with a flow of argon gas at 40 ml min^{-1}.

The thermogravimetric analysis performed on the IGA differs (from the typical TGA) as it utilises UHV rather than a flow of argon gas. This allows for samples to be degassed at lower temperatures. In this case we can see that the UHV is important for the degassing of NaX, as solely heating the materials (as seen in Figure 7.2) does not completely evacuate the zeolite framework.

Typically, porous materials have been shown to lose a substantial amount of mass during the initial evacuation (at room temperature). The effect of increasing the UHV level is observed by a sudden decrease in mass as a result of opening of the PIV1 valve. This is illustrated in Figure 7.3. Substantial mass loss (18.0%) was observed at room temperature with a further 6.5% lost on increasing the temperature up to *ca*. 200 °C. After degassing up to 415 °C, only another 0.1% was lost after 900 minutes. A total mass of *ca*. 25% was observed, which was in good agreement with that reported by Joshi *et al*.[365]

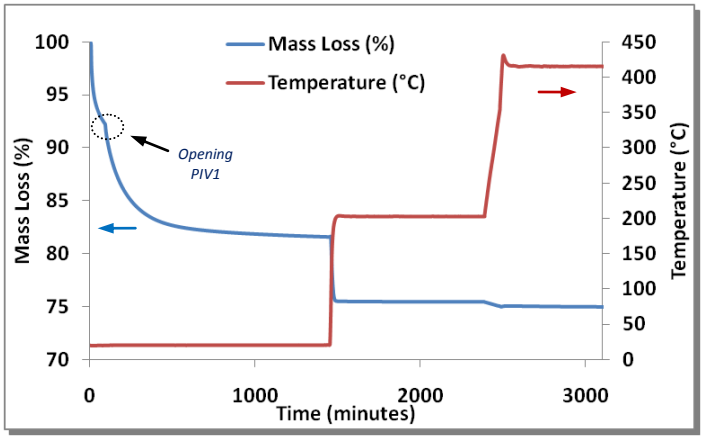

Figure 7.3 - Degassing profile for NaX measured on a Hiden IGA-001. A mass loss of ca. 25% was observed up to ca. 415 °C in UHV.

7.2.2. Gas Adsorption

7.2.2.3. Nitrogen

Figure 7.4 displays the nitrogen adsorption isotherm for zeolite NaX at 77 K from a relative pressure of 0.01 to 1. NaX showed reasonable nitrogen uptake (almost 200 $cm^3\ g^{-1}$ STP) at low relative pressures ($p/p_0 < 0.1$), which is consistent with microporous materials. Very little adsorption occurs above $p/p_0 = 0.1$ making it characteristically close to Langmuir type adsorption. This implied that the nitrogen isotherm for the zeolite material was Type I in the IUPAC classification. Figure 7.4 shows the resulting BET plot from p/p_0 of 0.06 to 0.2, where the plot was taken to be linear from which an apparent BET surface area of 662.3 ± 13.7 $m^2\ g^{-1}$ was calculated. According to equation (3.14), a Langmuir surface area of 867.5 ± 3.5 $m^2\ g^{-1}$ was calculated from the same region of p/p_0. A complete least squares curve fitting routine was performed in order to calculate both surface area values.

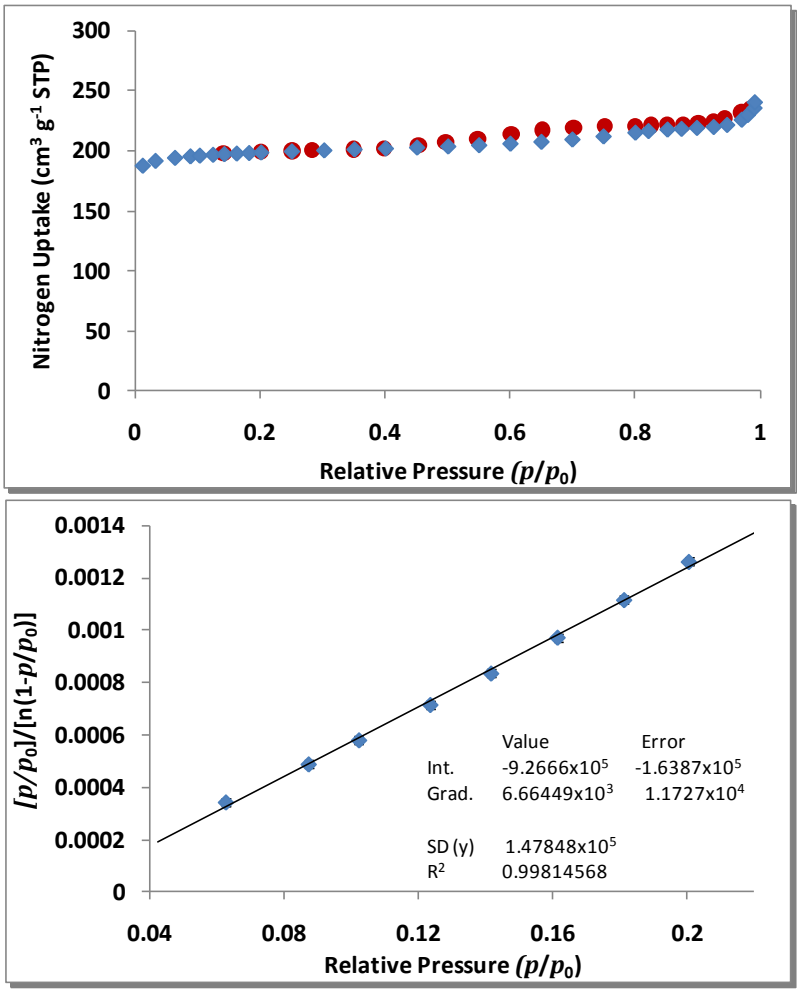

Figure 7.4 - (Top) Nitrogen adsorption (♦) and desorption (●) isotherm from a relative pressure of 0.01 to 1, at 77 K. (Bottom) BET plot for NaX taken from the region between 0.06 and 0.2 p/p_0, which was taken to be linear.

7.2.2.4. Hydrogen

The NaX zeolite material was outgassed at 200 °C for around 800 minutes and then at *ca*. 415 °C for a further 900 minutes under a vacuum (1 x 10^{-6} mbar). The NaX material was still losing mass at the rate of 0.4 μg min^{-1}. As shown above, a mass loss of *ca*. 25% was observed which was in good agreement with that reported by Joshi *et al*.[365]

7.2.2.4.1. Excess Adsorption

Helium pycnometry was performed on the degassed NaX zeolite material, giving a skeletal density of 2.50(4) g cm^{-3}. Figure 7.5 displays the excess gravimetric hydrogen adsorption isotherms for multiple temperatures up to 20 bar. The 77 and 87 K isotherms are measured by submersion in liquid nitrogen and

argon, respectively; the 97 to 237 K isotherms are measured using the Hiden Cryofurnace. No hysteresis was observed for any of the measured isotherms, which is typical of a microporous material. At 77 K the NaX material displayed a hydrogen uptake of 2.14 wt.% at 20 bar and 2.12 wt.% at 15 bar. This is compared to 1.42 wt.% exhibited by Takeda 4A porous carbon at the latter temperature and pressure. The higher hydrogen storage capacity for NaX is consistent with the higher apparent BET surface area. The temperature dependence of NaX is illustrated in Figure 7.5. The plot of excess hydrogen uptake against temperature shows a decrease in storage capacity, which is typical of porous materials with *ca*. 45% of the storage capacity being lost from 77 to 137 K at 15 bar.

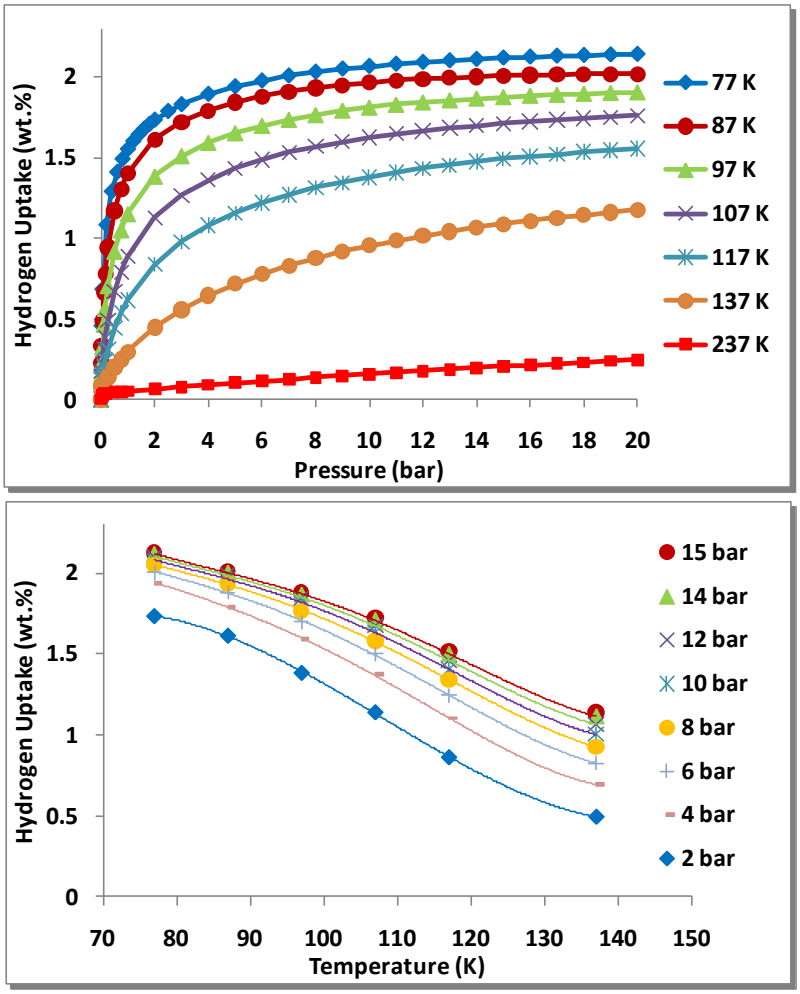

Figure 7.5 - (Top) Variable temperature excess gravimetric isotherms for the NaX Zeolite up to 20 bar. The 77 and 87 K isotherms are measured using submersion by liquid nitrogen and argon, respectively; the 97 to 137 K and 237 K isotherms are measured using the Hiden Cryofurnace. (Bottom) Excess gravimetric hydrogen uptake against temperature at various pressures.

The conversion between the measured excess adsorption and the absolute amount adsorbed utilises equation (3.50) and assumes that the density of the adsorbed phase equal to that of hydrogen at the triple point (0.077 g cm^{-3}). The zeolite NaX exhibited an excess and absolute hydrogen uptake of 2.07 and 2.26 wt.% at 20 bar and 77 K, respectively (see Appendix B).

The geometric density of NaX can be estimated using the measured skeletal density (2.50 g cm^{-3}) and the pore volume (0.36 cm^3 g^{-1}).[366,367] This can then be used to calculate a (theoretical) volumetric storage capacity. For NaX this gave a geometric density of 1.31 g cm^{-3} and an excess and absolute volumetric capacity of 27.3 and 29.8 kg m^{-3} at 20 bar and 77 K, which is consistent with values reported by Langmi *et al*.[152,204] However, the interparticle void space would also need to be considered if a true volumetric capacity were to be determined.

7.2.2.4.2. The Langmuir Isotherm

The Langmuir plot for NaX can be seen in the Figure 7.6. The graph is taken to be linear from 2 to 12 bar, which enables it to be used for calculating maximum amount adsorbed, n_m; this would be consistent with a plateau in absolute hydrogen adsorption isotherms. The analysis predicts that NaX will have a maximum hydrogen uptake of 12.06(8) mmol g^{-1}, which equates to 2.43(2) wt.%. Using the pore volume of 0.36 cm g^{-1}[162,366,367], at saturation the adsorbate phase density is estimated to be 0.067 g cm^{-3}, slightly less than that of liquid hydrogen.

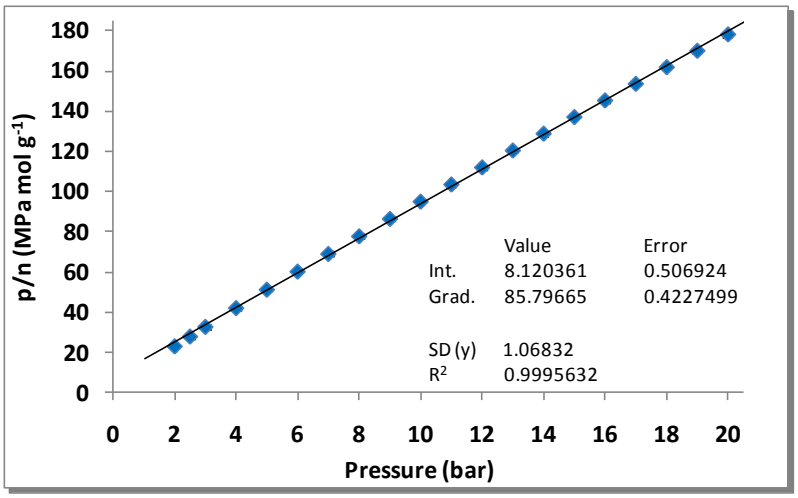

Figure 7.6 - Linearised Langmuir plots for the hydrogen adsorption of NaX at 77 K from 2 to 20 bar.

7.2.2.4.3. Empirical Isotherm Equations

The Sips and Tóth empirical isotherm equations were applied to the absolute adsorption isotherm at each temperature. Both equations appear to produce a good fit for the 77 K isotherm, but residual plots illustrate the differences between the data and the fitted model, as shown in Figure 7.7. The residual plots indicate that the two equations produce an excellent fit to the absolute adsorption (at 77 K) of NaX, with both models being within ± 0.04. The Tóth model appears to stick closer to the absolute isotherm from *ca*. 0.5 to 20 bar. The two models produce fairly significant differences in their predicted saturation uptakes, which are 2.83 ± 0.04 and 3.28 ± 0.05 wt.%, for the Sips and Tóth models, respectively at 77 K.

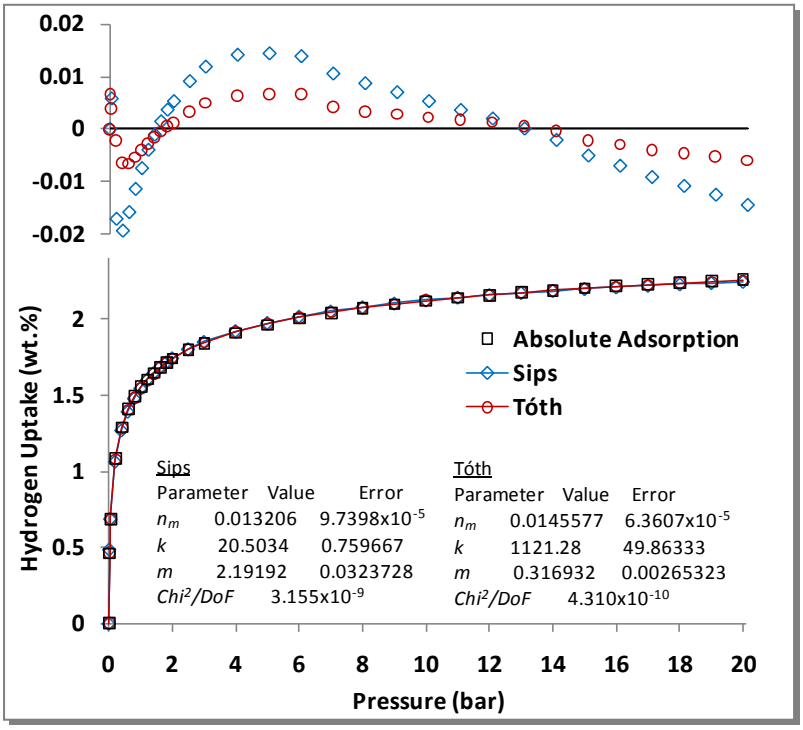

Figure 7.7 - Fitted Sips and Tóth equations to the absolute hydrogen uptake of NaX versus pressure at 77 K up to 20 bar. Residual plots can be seen at the top.

7.2.2.5. Enthalpy of Adsorption

7.2.2.5.1. Clausius-Clapeyron

The Clausius-Clapeyron equation was used in conjunction with both the Sips and Tóth equations along with the 77 and 87 K absolute hydrogen isotherms, in order to give an enthalpy of hydrogen adsorption as

a function of hydrogen uptake (see Figure 7.8). The enthalpy of adsorption is calculated up to 0.8 wt.% as explained in section 6.2.2.5.4. The analysis shows the reasonably high enthalpies of adsorption for a microporous material, with a value of 15.6 and 10.3 kJ mol^{-1}, at the near zero coverage of 0.02 wt.% of hydrogen, for the Sips and Tóth fits, respectively. The enthalpies of adsorption decrease sharply with increasing hydrogen uptake, giving 7.1 and 7.0 kJ mol^{-1}, at 0.8 wt.%, respectively for the two models.

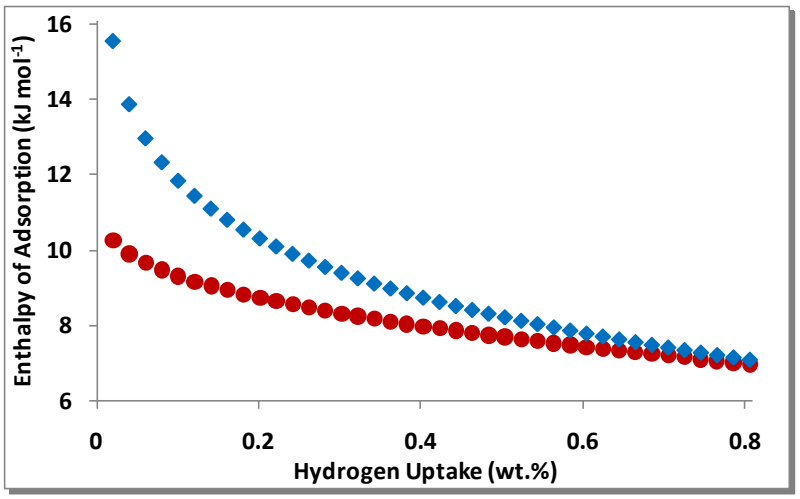

Figure 7.8 - Comparison of the Clausius-Clapeyron equation (in conjunction with Sips (♦) and Tóth (●) equations fitted to the 77 and 87 K absolute isotherms) for NaX.

The absolute isotherms for NaX, at various temperatures, for were fitted to both the Sips and Tóth models. The resulting fitted data was plotted as ln(p) against $1/T$ to produce van't Hoff plots at regular intervals of hydrogen uptake. The gradient of each line was taken, and converted in to a value for the enthalpy of adsorption for that specific amount of hydrogen uptake. Figure 7.9 shows the resulting enthalpy of adsorption against hydrogen uptake, for both the Sips and Tóth fitted models. The standard deviation in the van't Hoff plots were also converted to a value for enthalpy of adsorption, and subsequently used as the error at each specific amount of hydrogen uptake. This analysis showed enthalpies of adsorption of 10.1 and 7.4 kJ mol^{-1} at the near zero coverage of 0.02 wt.% for the Sips and Tóth models, respectively. The latter is comparable to that reported by Rowsell *et al*. for zeolite 13 X.[134] Figure 7.10 compares the use of the two different models.

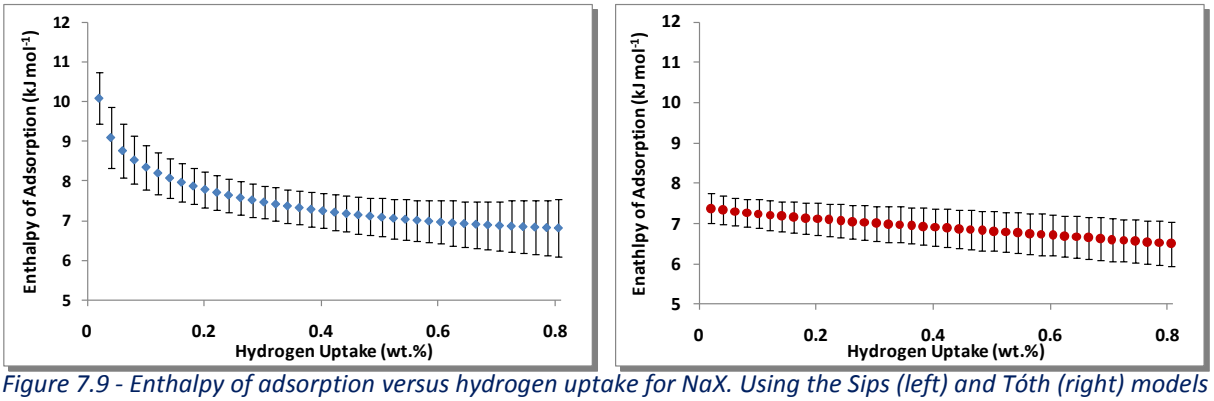

Figure 7.9 - Enthalpy of adsorption versus hydrogen uptake for NaX. Using the Sips (left) and Tóth (right) models to fit the absolute isotherms (at 77 and 87 to 117 K, in 10 K steps, and 137 K). The Clausius-Clapeyron Equation and van't Hoff plot were then used to determine the enthalpy of adsorption.

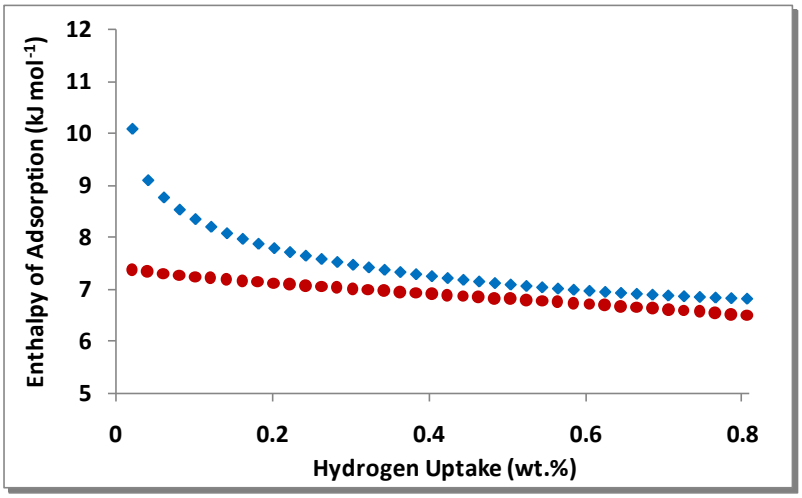

Figure 7.10 - Comparison of the enthalpy of adsorption versus hydrogen uptake for NaX. Using the Sips (♦) and Tóth (●) models as shown in Figure 7.9.

7.2.2.5.2. Virial Type Expansion Equation

Figure 7.11 shows the virial plots for the hydrogen adsorption on NaX at 77 to 137 K, in 10 K steps. The plots are taken to be linear at pressures ≥ 0.5 bar to *ca.* 5 bar, allowing the A_0 and A_1 values to be determined from the intercepts and gradients respectively, the values for which can be seen in Table 7.1. The gradient from the plot of A_0 against $1/T$ (see Figure 7.11) produced an isosteric enthalpy of adsorption of 8.6 ± 0.3 kJ mol^{-1}. The Henry's law constant (which is related to the first virial parameter ($K_H = \exp(A_0)$) is seen to decrease with increasing temperature, which indicates a decrease in adsorbate-adsorbent interaction with in increasing temperature. The second virial parameter is generally seen to

decrease to less negative values with increasing temperature, thus indicating weaker adsorbate-adsorbate interactions.

Table 7.1 - Henry's law constant and virial parameters A_0 and A_1 for hydrogen adsorption on NaX zeolite series at various temperatures (77 and 87 to 117 K, in 10 K steps, and 137 K). The errors shown are equal to one standard deviation.

Temperature K	k_H mol g^{-1} Pa^{-1}	A_0 ln(mol g^{-1} Pa^{-1})	A_1 g mol^{-1}
77	8.95E-06	-11.62 ± 0.08	-617.37 ± 9.78
87	2.58E-06	-12.87 ± 0.12	-523.82 ± 15.53
97	7.30E-07	-14.13 ± 0.07	-448.13 ± 10.00
107	2.44E-07	-15.23 ± 0.03	-388.74 ± 5.21
117	9.41E-08	-16.18 ± 0.02	-359.71 ± 4.52
137	2.47E-08	-17.52 ± 0.03	-348.14 ± 11.06

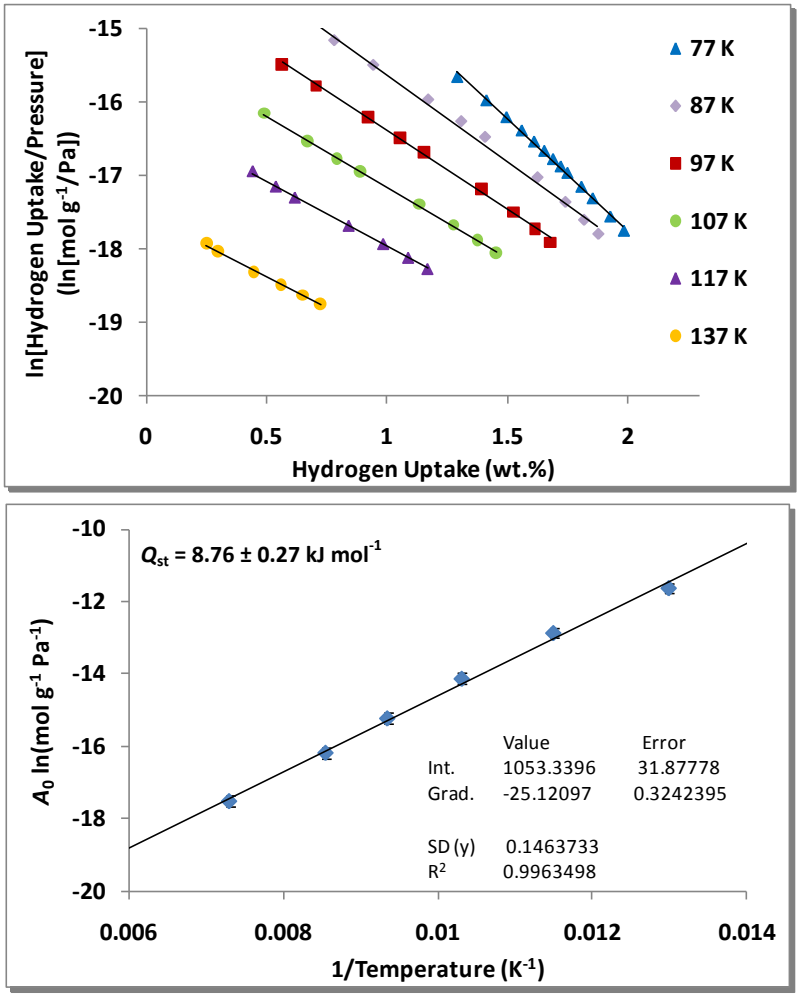

Figure 7.11 - (Top) Virial plots for the absolute adsorption of hydrogen on NaX and (bottom) the variation of virial parameter, A_0 with 1/T for NaX (from 77 and 87 to 117 K, in 10 K steps, and 137 K).

7.2.2.5.3. Virial Type Thermal Equation

Equation (3.66) was used to fit the 77 and 87 K isotherms simultaneously (see Figure 7.12). The equation has no limit to the number of coefficients that can be included; previous researchers have found that values of $m \leq 6$ and $n \leq 3$, were enough to appreciably reduce the χ^2 goodness-of-fit for their range of microporous MOF materials.[134] The isosteric enthalpy of adsorption was subsequently calculated according to equation (3.67), as a function of hydrogen uptake (which can be seen in Figure 7.13). The analysis produces an isosteric enthalpy of adsorption at zero coverage for NaX zeolite of 9.2 kJ mol^{-1}. It decreases sharply (and almost linearly) with hydrogen uptake up to 20 bar. Interestingly, at a hydrogen uptake of 0.8 wt.%, the enthalpy of adsorption is 7.2 kJ mol^{-1}, just 0.1 and 0.2 kJ mol^{-1} greater than the Sips and Tóth models, respectively, at the same hydrogen uptake.

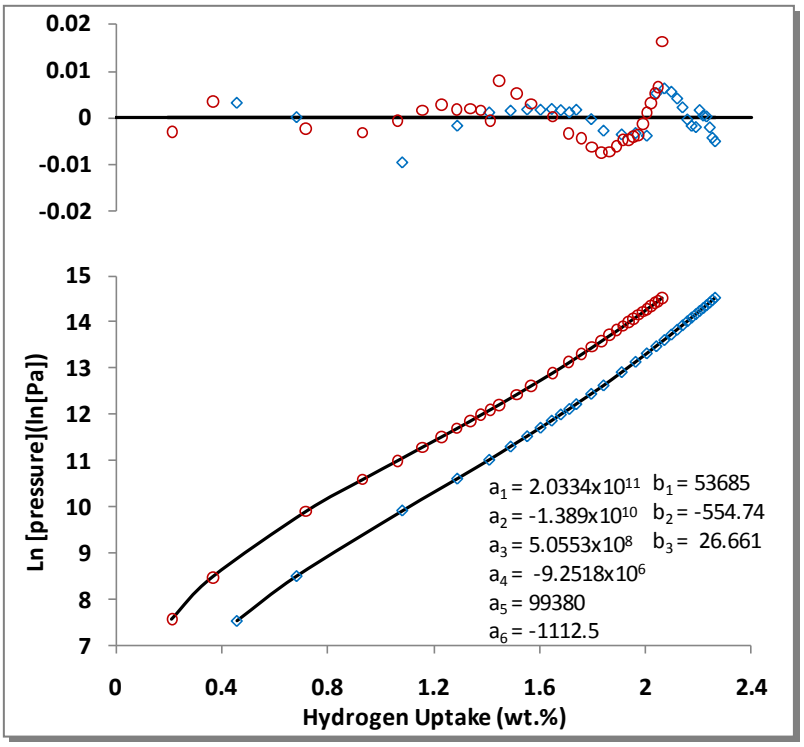

Figure 7.12 - Hydrogen adsorption isotherms at 77 (◊) and 87 K (○) for NaX to 20 bar. Data is shown by open shapes, while virial plots are shown by solid lines. Residual plots can be seen at the top.

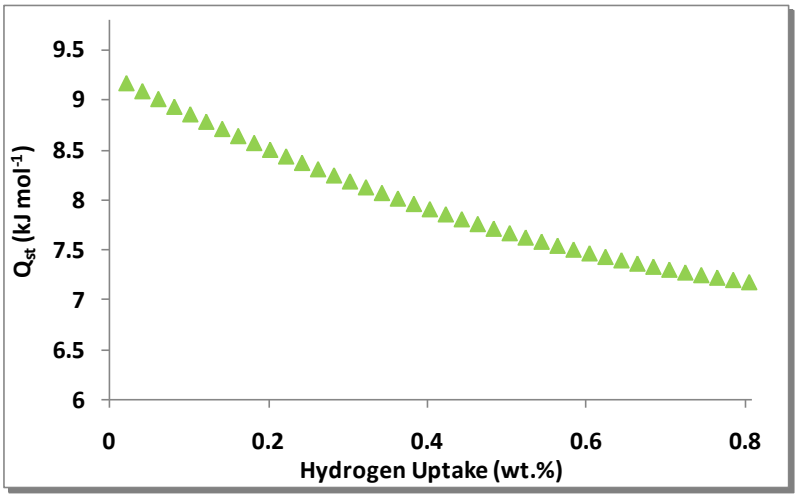

Figure 7.13 - Isosteric enthalpy of adsorption for the NaX as a function of hydrogen uptake as determined using the virial type thermal equation and data from 77 and 87 K.

Figure 7.14 displays a comparison for the previously determined enthalpies of adsorption with the virial type thermal equation. Using two temperatures, all three fitting models produced similar values at 0.8 wt.%. As with the porous carbon material in the previous chapter, the virial curve shows reasonable correlation with the Tóth model. However, the two curves do span further apart at low coverage, with *ca*. 1.1 kJmol^{-1} difference at 0.02 wt.%. In contrast, the virial method (using just two temperatures) lies significantly above the curve produced by the multiple temperature (Clausius-Clapeyron) method.

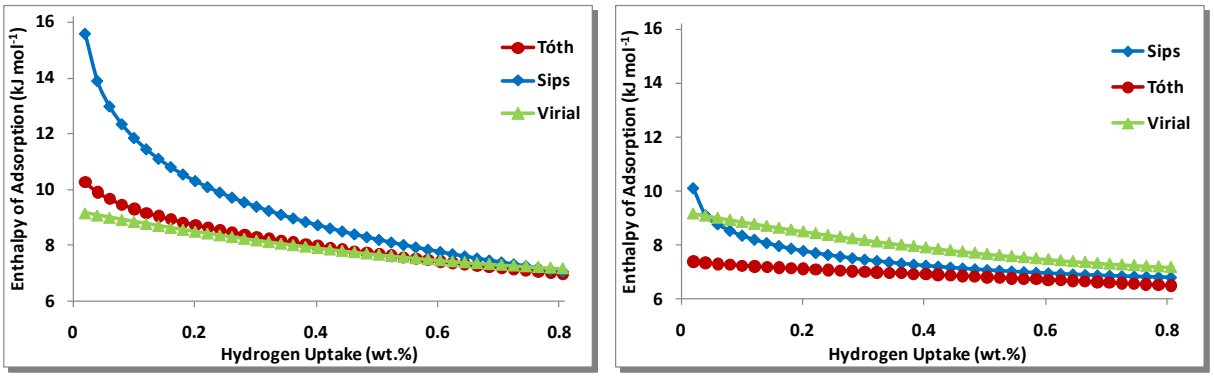

Figure 7.14 - Comparison of the isosteric enthalpy of adsorption for NaX as a function of hydrogen uptake determined by fitting the Sips and Tóth equations and Virial thermal type equation. Sips and Tóth plots utilise two temperatures, 77 and 87 K (left) and multiple temperatures (right). The Virial thermal type equation utilises two temperatures; 77 and 87 K in both plots.

All of the enthalpy of adsorption values were much greater than that observed by Li and Wu (4.4 kJ mol^{-1}), although the values are still within the range that they claimed to be typical of zeolites.[212] The low enthalpy of adsorption values reported by Li and Wu may be a result of their relatively low hydrogen

uptake. They reported *ca*. 1.2 wt.% at 20 bar and 80 K using a volumetric system, this is in contrast to the results from this work, where 1.2 wt.% (excess) was observed at 0.3 and 0.95 bar at 77 and 87 K, respectively. Their low uptake may have been a result of their chosen degassing conditions, just 4 hours in a vacuum at 350 °C. Additionally, they also reported the use of a relatively low hydrogen purity (99.99%), when compared to the 99.99996% purity hydrogen (used in conjunction with a liquid nitrogen trap), used in this work.

The diameter of free aperture in NaX is known to be 0.74 nm; however, the diameter of the supercage is 1.18 nm. This indicates that the relatively high enthalpy of adsorption observed here for the NaX should be lower. However, in addition to dispersive (van der Waals) interactions, the hydrogen molecules in zeolite materials are influenced by the presence of electrostatic interactions created by the cations within the framework. These induce polarisation of the hydrogen molecules and hence a higher energy interaction.[368] The electrostatic forces are increased by the presence of divalent and trivalent cations in the place of univalent cations, thus suggesting that a zeolite with a high charge-to-volume ratio would also have a high enthalpy of adsorption.[152]

7.2.2.6. Extended Empirical Excess Isotherm Equation

The extended Tóth equation (3.69) was used to fit the excess hydrogen isotherms for the porous carbon material at 77 and 87 K. The excess hydrogen adsorption prediction shown in Figure 7.15 gives a pore volume of 0.348 and 0.343 $cm^3 g^{-1}$, respectively for the 77 and 87 K data. This is consistent with the reported total pore volume of 0.34 $cm^3 g^{-1}$ by Li and Wu[212] and very close to that reported by Joshi *et al*. (0.35 $cm^3 g^{-1}$)[365] Kelly and Fuller (0.352 $cm^3 g^{-1}$)[369], Breck and Chahine and Bose (0.36 $cm^3 g^{-1}$)[162,366]

As with the Takeda 4A porous carbon, the predicted excess adsorption curves show a considerable downturn. The predicted excess adsorption at 77 K displays a slightly greater downturn than the prediction at 87 K. This is consistent with the reported excess adsorption at higher pressures using other frameworks materials.[117]

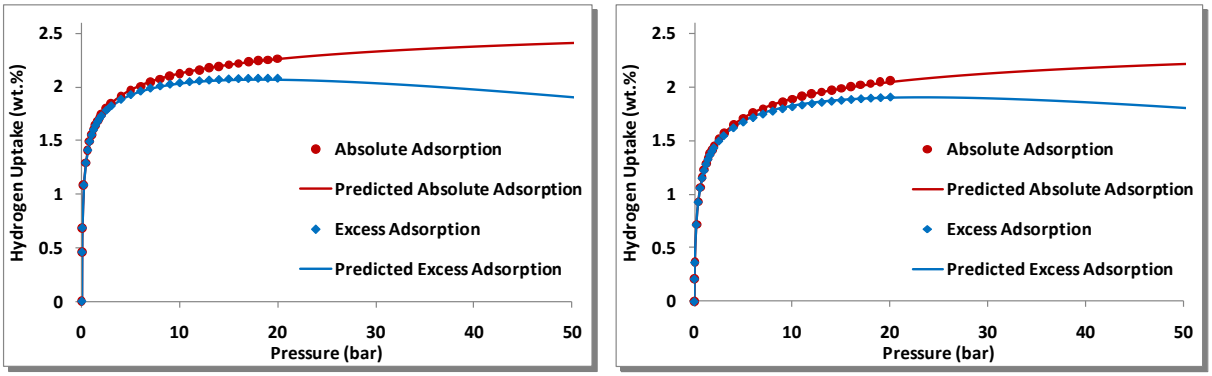

Figure 7.15 - Predicted excess and absolute adsorption at 77 (left) and 87 K (right) up to 50 bar. The predicted excess uses the extended Tóth equation, whereas the absolute prediction uses the Tóth model (as shown previously in this chapter).

7.3. Chapter Summary

This chapter describes the hydrogen storage properties of a NaX zeolite. The analysis of this well-characterised material will be used as a means of comparison with other porous materials (i.e. MOFs and PIMs). The material exhibited an excess gravimetric hydrogen adsorption uptake of 1.55 wt.% at 1 bar and 77 K and 2.14 wt.% at 20 bar. The relatively high hydrogen uptake below 1 bar and the lack of further significant hydrogen uptake between 1 and 20 bar, is a direct outcome of the high enthalpy of adsorption and low apparent surface area, respectively.

The enthalpy of adsorption was determined as a function of the absolute hydrogen uptake using pressure composition isotherms at two temperatures (77 and 87 K) after fitting with the Sips and Tóth equations. These were compared to the enthalpy of adsorption curve produced by fitting the multiparameter Virial type thermal equation, where good correlation between the Tóth and Virial curves was observed. After fitting each adsorption isotherm with the Sips and Tóth equations, the Clausius-Clapeyron equation was used in the form of a van't Hoff plot in order to determine the isosteric enthalpy of adsorption, as function of multiple temperatures, at regularly spaced values of hydrogen uptake. The resulting isosteric enthalpy of adsorption curve was found to be lower by approximately 5 and 3 kJ mol^{-1}, at the low coverage value of 0.02 wt.%, for the Sips and Tóth models, respectively, but only *ca*. 0.3 and 0.5 kJ mol^{-1} at 0.8 wt.%.

The extended Tóth equation was also fitted to the 77 and 87 K excess hydrogen isotherm to predict the excess adsorption at higher pressures. The analysis also produced pore volumes with good correlation to values reported in the literature.

Chapter 8

METAL-ORGANIC FRAMEWORKS

8.1. Introduction

Two metal-organic framework materials (IRMOF-1 and Cu-BTC) were obtained due to their uniform and well-characterised structures. These two materials also had high surface areas which resulted in some of the highest hydrogen storage capacities for porous materials at 77 K. The effect of the exposed metal sites in the Cu-BTC, on the enthalpy of adsorption as a function of hydrogen adsorption, was investigated. Several fitting methods have been employed to calculate the isosteric enthalpy of adsorption using just two temperatures (77 and 87 K), and is compared to using multiple temperatures.

8.2. IRMOF-1 (MOF-5)

IRMOF-1 is the first of an extensive family of Isoreticular MOFs based on the cubic carboxylate framework. Several different synthetic methods have been reported for the formation of IRMOF-1.[147,224-226,235,370-373] Unfortunately, as previously mentioned in Chapter 4, there were also several different reported values for hydrogen uptake. In this section, the hydrogen storage capacity of IRMOF-1 samples from two different sources has been investigated.

Collaboration with a research group in the Department of Chemistry at Soongsil University, Seoul (South Korea), provided approximately 200 mg of IRMOF-1 in the form of a white powder. The sample is thought to have been synthesised using the conventional solvothermal method, utilising the reaction between metal ion salts and organic linkers.[374] The second source was provided by the chemical company, BASF as a larger batch of small white crystals via Hirscher *et al.* at the Max Planck Institute in Stuttgart, Germany.[228] These were synthesised using an electrochemical technique.[373]

8.2.1. Structure and Characterisation

IRMOF-1 is MOFs based on the cubic carboxylate framework with tetrahedral Zn_4O units in each corner with 1,4-benzenedicarboxylate$_3$ as the organic linker. Rowsell *et al*. reported the structure to have an aperture window size of 0.78 nm, with two different (spherical) pore sizes of 1.21 and 1.52 nm, with a pore volume of 1.19 $cm^3\ g^{-1}$.[134,227,237]

The two different sized pores are caused by the rotation of the dicarboxylate ligand. The rotation of organic linker is reported to alternate from perpendicular or parallel to the centre of the cavity. The alternating linker causes the two different pores as is illustrated in Figure 8.2. Crystallographic data from Li *et al*., Rowsell and Yaghi indicates that IRMOF-1 has the space group Fm-3m and has a lattice parameter of 25.894(4) Å.[227,375]

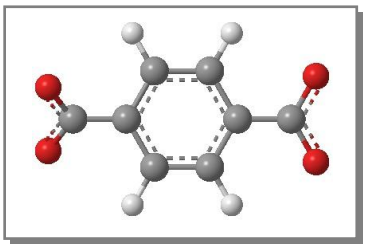

Figure 8.1 - 1,4-benzenedicarboxylate (BDC) organic ligand, (O, red; C, grey; and H, white).

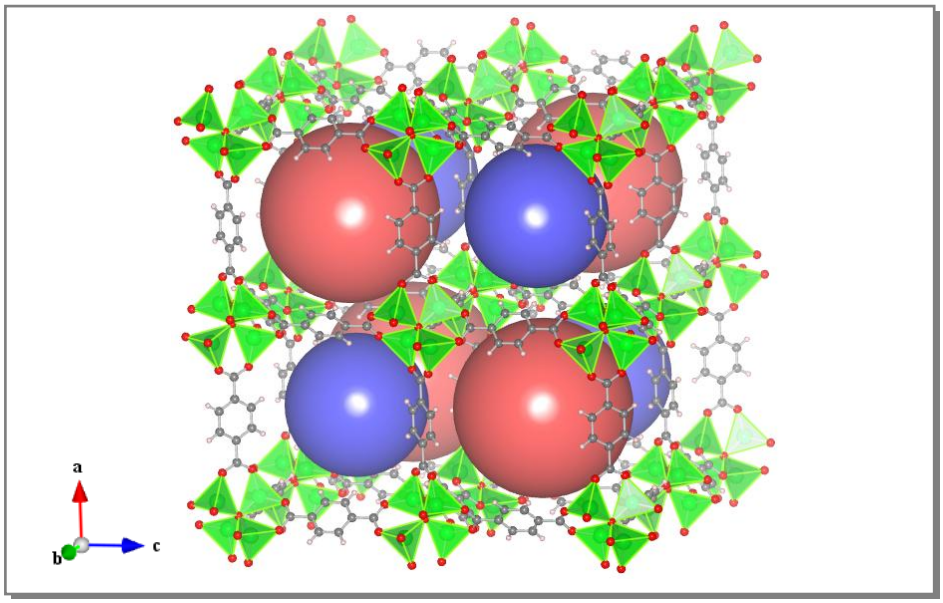

Figure 8.2 - Illustration of the IRMOF-1 pore structure proposed by Li et al., Rowsell and Yaghi. [227,375] *The blue balls represent the smaller cavities (1.2 nm) and the red balls, the larger pores (1.5 nm) with slightly different dimensions due to different orientation of the framework.*

8.2.1.1. XRD

Despite the known robustness of IRMOF-1, Kaye *et al*. reported demonstrated a change in structure on exposure to air due to moisture.[147] Figure 8.3 displays the powder XRD pattern that was collected from the IRMOF-1 material (provided by BASF) at 30 °C under an argon atmosphere. Chekcell was used in order to compare the observed peak positions to those calculated from the space group and lattice parameter reported for the ideal structure by Li *et al*., Rowsell and Yaghi (see Table A.2, in Appendix A).[227,375] Chekcell was also used to refine the zero point error, and determine hkl values and a refined lattice parameter of 25.811(2) Å. The XRD pattern shows an excellent match with the expected structure derived from single crystal data.[375]

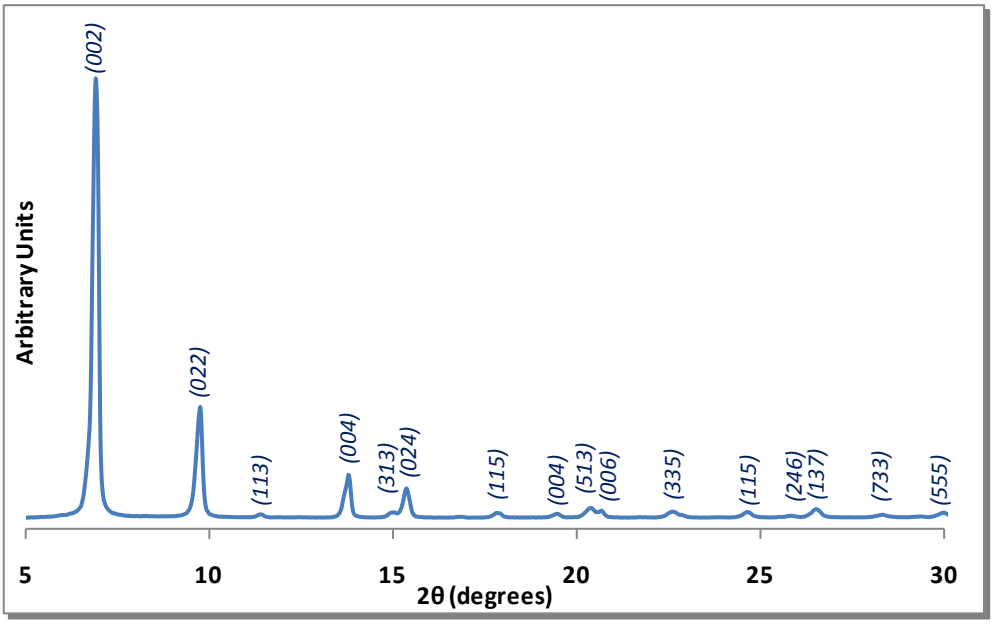

Figure 8.3 - Powder X-ray diffraction pattern for MOF-5 (BASF) at 30 °C using the Anton Parr Cell with hkl assignments above each peak.

Figure 8.4 shows another XRD pattern for the IRMOF-1 (BASF) material after exposure to air for 48 hours. The pattern did not match original XRD pattern from the inertly loaded material. A strong peak was observed at 8.8 2θ which was not previously present and was not part of the calculated pattern. Additional peaks were also observed at 15.6 and 17.6 2θ. This is consistent with findings by Huang *et al.*[376] and Kaye *et al*.[147] Kaye *et al*. observed the appearance of this peak after just ten minutes in air and which became dominant after 24 hours.[147] Kaye *et al*. suggested that the decomposed compound was

isostructural to $Zn_3(OH)_2(BDC)_2.2DEF$ (MOF-69C).[147] This has a monoclinic structure with $P2_1/n$ space group. Rosi *et al*. reported lattice parameters of a = 17.664, b = 14.848, c = 18.129 Å, α = 90, β = 112.140, and γ = 90.[377] Chekcell was used to compare the XRD pattern of the IRMOF-1 material after exposure to air with the structure of MOF-69C (see Table A.3, in Appendix A). Three peaks did not correlate to the monoclinic structure, two of which could be identified to be the 002 and 022 planes from the pure cubic structure at 6.8 and 9.7 2θ, respectively in IRMOF-1. The refined lattice parameters produced by Chekcell were a = 17.59(3), b = 14.81(2), c = 18.00(3) Å and β = 111.69(1) °. The peaks that were not part of the new phase were not included in the lattice parameter refinement. There were also two peaks (marked ◆) that did not match either the original IRMOF-1 or the MOF-69C XRD pattern, these require further investigation to determine their origin.

It is worth noting that Kaye *et al*. also exposed their IRMOF-1 material to dry O_2 and anhydrous organic solvents such as methanol, DMF, or DMSO, none of which affected the material in the same manner as air.[147]

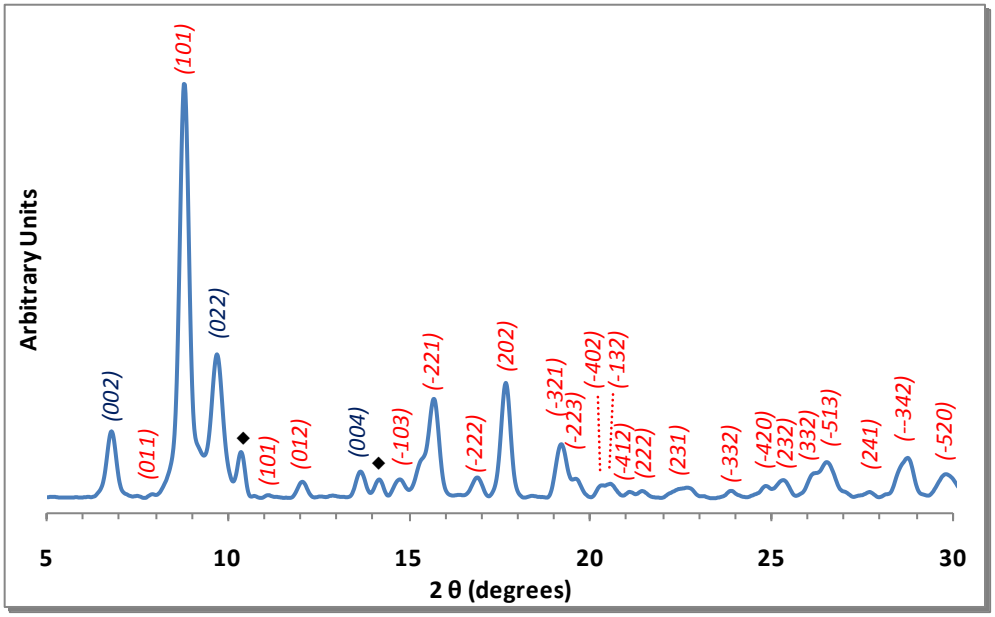

Figure 8.4 - Powder X-ray diffraction pattern for MOF-5 (BASF) using the Göebel Mirror (at RT) and after expoaure to air for 48 hours. hkl assignments for the monoclinic structure are shown in red and those matched to the cubic structure are shown in blue.

In order to determine whether the observed deviation from the ideal structure could be reversed using thermal activation, a variable temperature powder XRD pattern was collected from room temperature up

to 380 °C. This temperature was determined to be the highest possible activation temperature as it remained below the thermal decomposition temperature (*ca*. 390 °C) determined using TGA (see Figure 8.5). The XRD patterns not only showed that the heating cannot reverse the structural effect caused by exposure to air, but also displayed reduced thermal stability compared to the pure IRMOF-1 material. This is illustrated by the loss of the 101 plane peak. The same in-situ experiment was also performed on an IRMOF-1 sample that had not been exposed to air. The multiple powder XRD patterns recorded with increasing temperature confirmed the thermal stability by not displaying any significant changes in relative peak intensity.

8.2.1.2. TGA

Thermogravimetric analysis (TGA) of IRMOF-1 was performed to provide a guide for determining an appropriate degassing temperature (before gas sorption measurements). The TGA was performed in a flow of argon gas (at 2 °C min^{-1}) from room temperature up to 600 °C, as shown in Figure 8.5. The sample mass decreased immediately with increasing temperature and then levelled off from *ca*. 200 °C, where a mass loss of 5.2% was observed. A further 0.5% mass loss occurred up to 250 °C. The mass began to drop again by *ca*. 300 °C before the thermal decomposition at around 390 °C. A 46.4% decrease in mass was observed when the temperature reached 600 °C. This is consistent with that found by Calleja *et al*.[378]

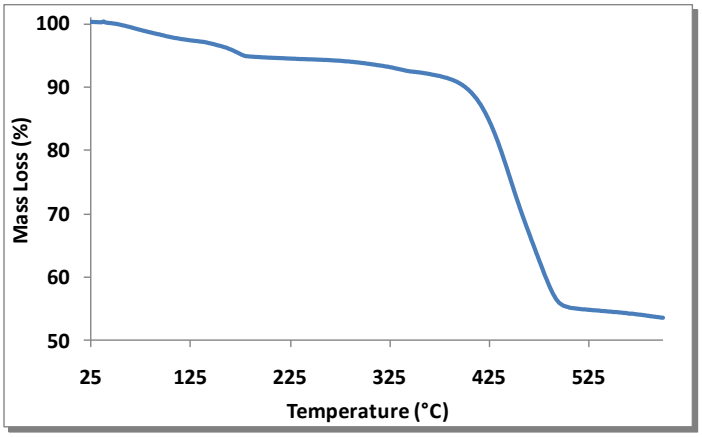

Figure 8.5 - TGA of IRMOF-1 (BASF), from RT to 600 °C at 2 °C min^{-1}. A mass loss of 5.7% was observed up to 250 °C. TGA was performed with a flow of argon gas at 40 ml min^{-1}.

The degassing profile for the IRMOF-1 (BASF) presented in Figure 8.6. From the TGA displayed in Figure 8.5, IRMOF-1 (BASF) was degassed on the IGA at 250 °C in UHV. A total mass loss of 5.1% was observed after *ca*. 1000 minutes at 250 °C and UHV. After degassing up to 250 °C, only another 0.1% was lost after 900 minutes.

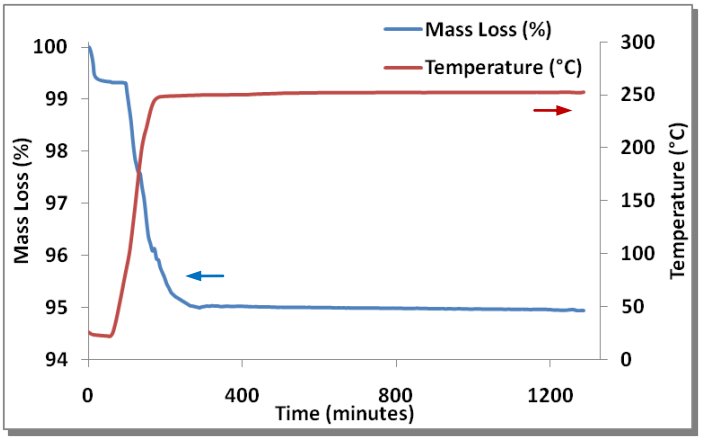

Figure 8.6 - Degassing profile for IRMOF-1 (BASF), measured on a Hiden IGA-001. A mass loss of ca. 5.1% was observed up to ca. 250 °C in UHV.

8.2.2. Gas Adsorption

8.2.2.1. Nitrogen

There have been several reports in the literature, including nitrogen sorption data (at 77 K), that assess the apparent surface area of IRMOF-1. As mentioned before, the research group of Hirscher was provided with a sample of the same batch of BASF IRMOF-1. The BET and Langmuir surface area that they reported was 2296 and 3840 $m^2 g^{-1}$, respectively.[228] The surface area of the Korean IRMOF-1 sample is unknown but is expected to be much lower as the hydrogen uptake was significantly lower (see Figure 8.7), thus indicating that the BET surface area can be substantially affected by the synthesis method and also by the evacuation/activation of the material.

8.2.2.2. Hydrogen

Both IRMOF-1 materials were degassed at 250 °C for *ca*. 1000 minutes under a vacuum (1×10^{-6} mbar). The Korean IRMOF-1 material displayed a relatively large mass loss of 33.2%, whilst the BASF material only had a mass loss of 4.7%. This large difference is likely be due to the synthetic procedure, with the

small-scale laboratory process used by the Korean group likely to have left substantial quantities of residual solvent in the porous structure of the material.

8.2.2.2.1. Excess Adsorption

Helium pyconometry was performed on the degassed IRMOF-1 (BASF) material, giving a skeletal density of 1.97(5) g cm^{-3}, which is comparable to previously reported values.[117,231,379] The excess gravimetric isotherms measured at 77 K gave 2.7 wt.% hydrogen at 15 bar for the Korean sample, compared to 4.8 wt.% hydrogen for the BASF IRMOF-1 at the same pressure and temperature (see Figure 8.7). Panella and Hirscher[231] used a solvothermal technique reported by Huang *et al.*[376] to synthesize IRMOF-1 and also reported relatively low hydrogen uptake (1.6 wt.%) at 10 bar and 77 K, and a low BET surface area (572 m^2 g^{-1}). Another notable difference between the two isotherms was the initial steepness in hydrogen uptake. The Korean material exhibited a much sharper rise in hydrogen uptake in the low pressure region suggesting that its structure has a greater affinity for molecular hydrogen, and hence a higher enthalpy of adsorption. No hysteresis was observed between the adsorption and desorption isotherms for either of the IRMOF-1 materials, which is typical of a microporous material.

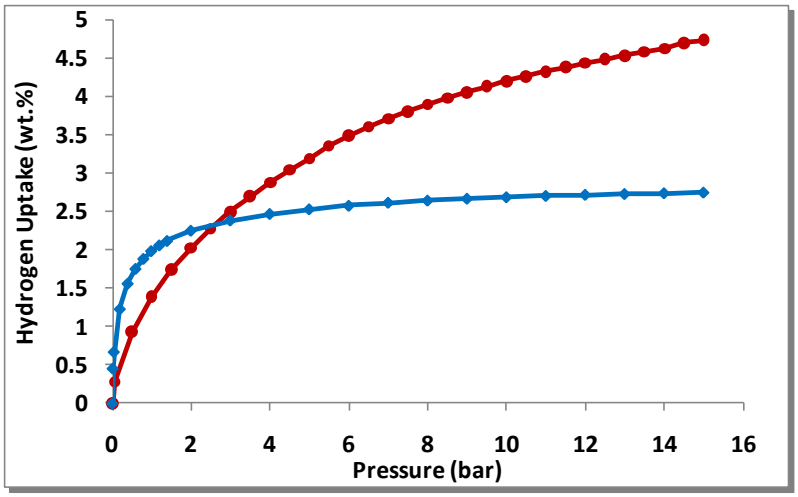

Figure 8.7 - Comparison of the excess gravimetric hydrogen isotherms for the Korean (♦) and BASF (●) IRMOF-1 samples at 77 K up to 15 bar.

The significantly greater hydrogen storage capacity of the BASF material meant that it was chosen for further variable temperature analysis. The excess gravimetric hydrogen storage capacity at a variety of

temperatures is presented in Figure 8.8. The characteristic decrease in hydrogen uptake with increasing temperature was observed (similar to both the activated carbon and the zeolite). This is illustrated by plotting hydrogen uptake at different pressures against temperature, also shown in Figure 8.8.

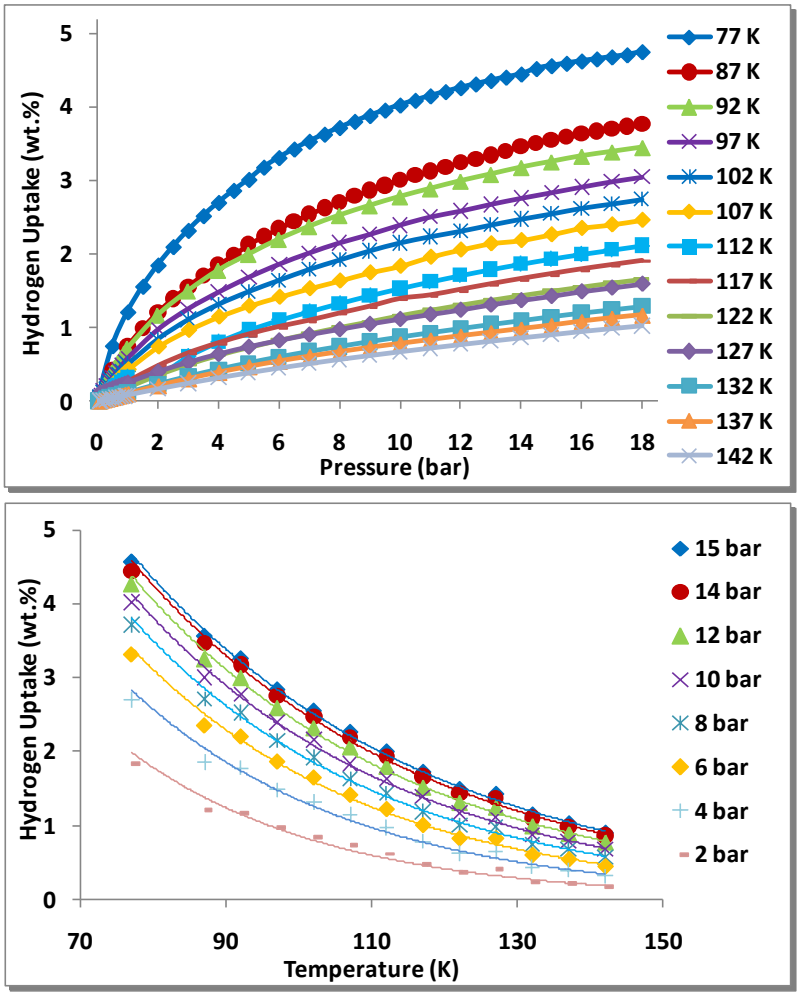

Figure 8.8 - (Top) Excess gravimetric hydrogen isotherms up to 18 bar at various temperatures for IRMOF-1 (BASF). The 77 and 87 K isotherms are measured using submersion by liquid nitrogen and argon, respectively; the 92 to 142 K isotherms are measured using the Hiden Cryofurnace. (Bottom) Excess gravimetric hydrogen uptake against temperature at various pressures.

8.2.2.2.2. Absolute Adsorption

The conversion between the measured excess adsorption and the absolute amount adsorbed utilises equation (3.50) and assumes the density of the adsorbed phase is equal to liquid hydrogen (0.077 g cm^{-3}), see section 3.6.2.1. Figure 8.9 shows the difference in the excess and absolute adsorption at 77 K for the IRMOF-1 (BASF) material, which exhibited an absolute hydrogen uptake of 5.37 wt.% at 18 bar and 77 K.

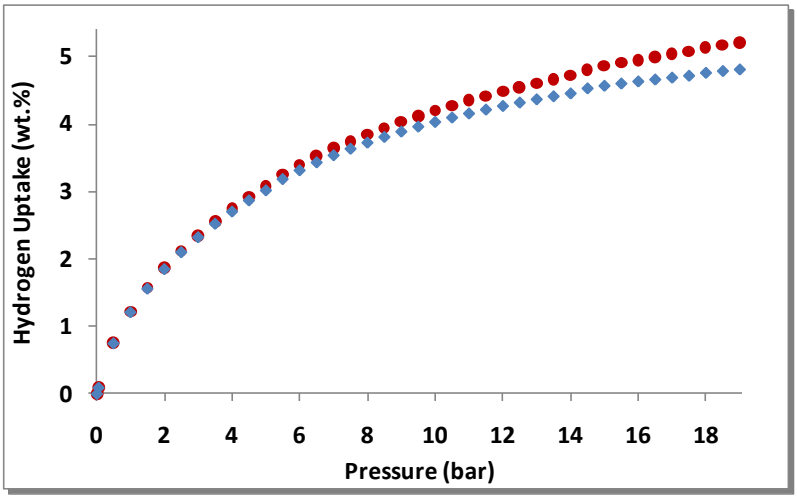

Figure 8.9 - Excess (♦) and absolute (●) hydrogen uptake (wt.%) against pressure (bar) at 77 K, using the adsorbed phase density equal to that of hydrogen at the triple point.

8.2.2.2.3. The Langmuir Isotherm

The Langmuir plot for IRMOF-1 (BASF) is shown in Figure 8.10. The graph is taken to be linear from 2 to 20 bar, which enables it to be used for calculating the maximum amount adsorbed, n_m. The analysis predicts that IRMOF-1 (BASF) will have a maximum hydrogen uptake of 33.9(3) mmol g^{-1}, *ca*. 6.85(5) wt.%, which considerably higher than the saturation value of 5.1 wt.% reported by Panella *et al*. at 77 K.[228] A possible reason for this difference is that fact that Panella *et al*. fitted the Langmuir equation to the excess adsorption isotherm rather than the absolute adsorption.

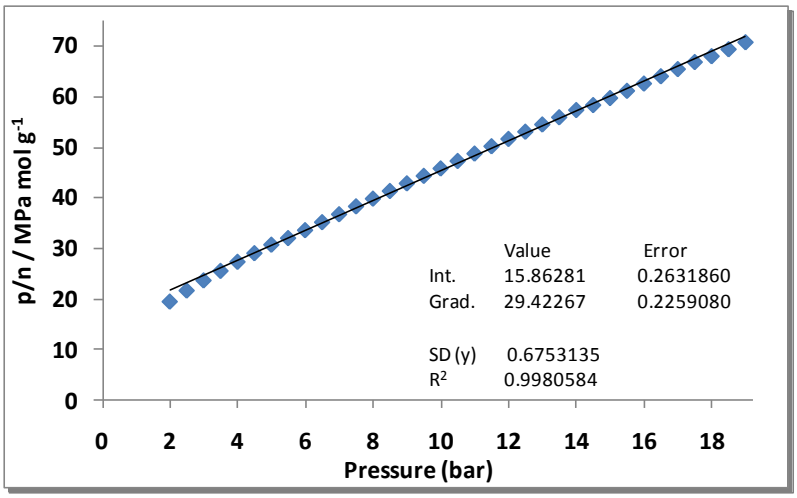

Figure 8.10 - Linearised Langmuir plot for the absolute hydrogen adsorption of the IRMOF-1 (BASF) at 77 K.

8.2.2.2.4. Empirical Isotherm Equations

The Sips and Tóth empirical isotherm equations were applied to the absolute adsorption isotherm for IRMOF-1 (BASF), at each measured temperature. Both equations appear to produce good fits for the 77 K isotherm, but residual plots illustrate the differences between the data and the fitted model as shown in Figure 8.11. The residual plots indicate that the two equations produce a good fit to the absolute adsorption (at 77 K) of IRMOF-1 from *ca*. 1 to 10 bar, with both models being within ±0.005. Below this pressure, both models lie considerably below the absolute adsorption. The two models produce very significant differences in their predicted saturation uptakes, which are 9.3(2) and 12.4(7) wt.%, for the Sips and Tóth models, respectively at 77 K.

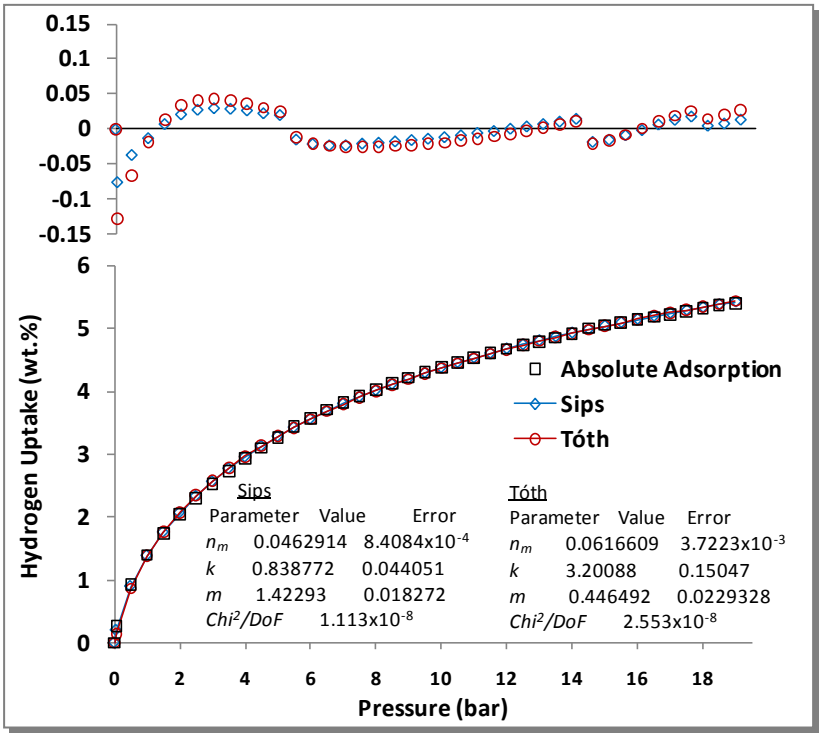

Figure 8.11 - Fitted Sips and Tóth equations to the absolute hydrogen uptake versus pressure at 77 K up to 19 bar. Residual plots are shown at the top of the figure.

8.2.2.2.5. Enthalpy of Adsorption

8.2.2.2.5.1. Clausius-Clapeyron

The Clausius-Clapeyron equation was used in conjunction with both the Sips and Tóth equations along with the 77 and 87 K absolute hydrogen isotherms in order to derive a figure for the enthalpy of hydrogen

adsorption as a function of hydrogen uptake. The enthalpy of adsorption is calculated up to 0.8 wt.% as explained in section 6.2.2.5.4. The analysis displayed in Figure 8.12 indicates reasonably high enthalpies of adsorption for a microporous material, with a value of 7.80 and 5.46 kJ mol^{-1}, at the near zero coverage of 0.02 wt.% of hydrogen, for the Sips and Tóth fits, respectively. The enthalpies of adsorption calculated using the Sips fit decreases sharply with increasing hydrogen uptake coming close to the curve produced from the Tóth fit. At higher hydrogen uptake (*ca*. 4 wt.%) the two curves overlap and give values of *ca*. 4.3 kJ mol^{-1}.

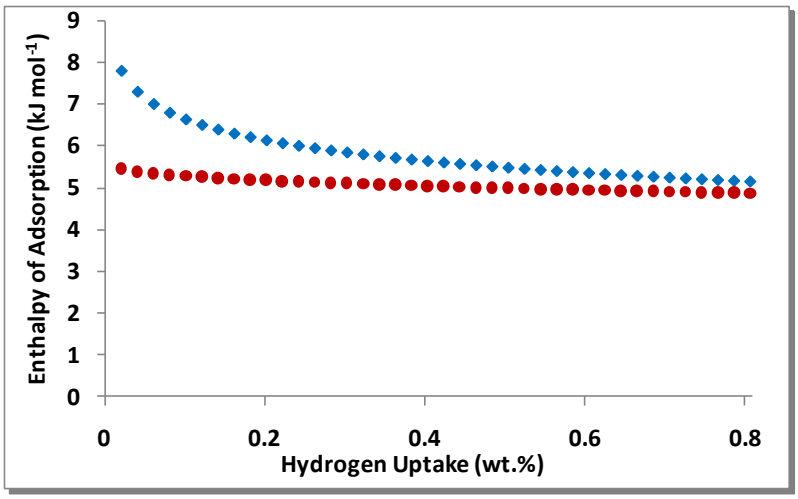

Figure 8.12 - Comparison of the enthalpy of adsorption versus hydrogen uptake for IRMOF-1, calculated using Clausius-Clapeyron equation (in conjunction with Sips (♦) and Tóth (●) equations fitted to the 77 and 87 K absolute isotherms).

The absolute isotherms, at various temperatures, for IRMOF-1 (BASF) were fitted to both the Sips and Tóth models. The resulting fitted data was plotted as ln(p) against 1/T to produce van't Hoff plots at regular intervals of hydrogen uptake. The gradient of each line was taken, and converted in to a value for the enthalpy of adsorption for that specific amount of hydrogen uptake. Figure 8.13 shows the resulting enthalpy of adsorption against hydrogen uptake, for both the Sips and Tóth fitted models. The standard deviation in the van't Hoff plots were also converted to a value for enthalpy of adsorption, and subsequently used as the error at each specific amount of hydrogen uptake. This analysis showed a heat adsorption of 6.6 and 4.5 kJ mol^{-1} at a near zero coverage of 0.02 wt.% for the Sips and Tóth models, respectively.

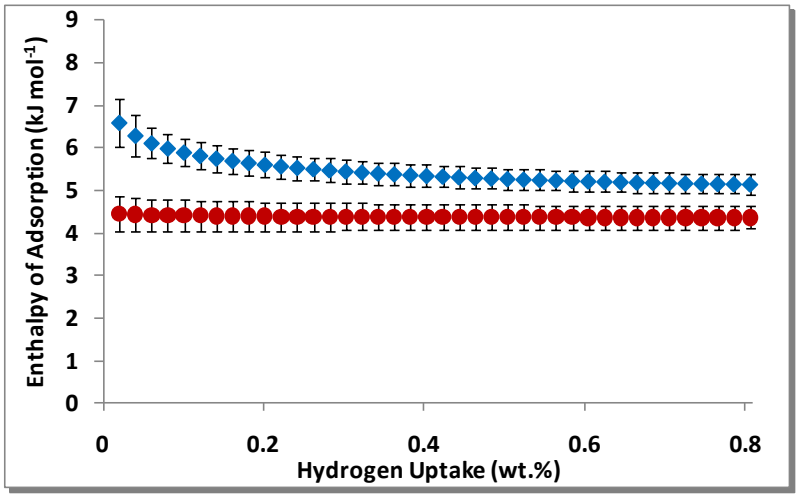

Figure 8.13 - Enthalpy of adsorption versus hydrogen uptake for IRMOF-1 (BASF). Using the Sips (♦) and Tóth (●) models to fit the absolute isotherms (at 77 and 87 to 137 K, at 5 K steps). The Clausius-Clapeyron Equation and van't Hoff plot were then used to determine the enthalpy of adsorption.

8.2.2.2.6. Virial Type Expansion Equation

Figure 8.14 shows the virial plots for hydrogen adsorption on IRMOF-1 (BASF) at 77 and 87 and then up to 142 K, in 5 K steps). The plots are taken to be linear at pressures ≥ 2 bar, allowing for the determination of A_0 and A_1 values from the intercepts and gradients respectively, the values for which can be seen in Table 8.1. The gradient from the plot of A_0 against $1/T$ (see Figure 8.14) produced an isosteric enthalpy of adsorption of 4.5(2) kJ mol^{-1}. The Henry's law constant (which is related to the first virial parameter (K_H=exp(A_0)) is seen to decrease with increasing temperature, which indicates a decrease in adsorbate-adsorbent interaction with increasing temperature. The second virial parameter is generally seen to decrease to less negative values with increasing temperature, thus indicating weaker adsorbate-adsorbate interactions. This is with the exception of 77 K, where the A1 parameter indicates a similar adsorbate-adsorbate interaction as at 102 K. The virial graphs in Figure 8.14 shows that the 87 K plot overlaps with the 92 K plot. The van't Hoff plot (also in Figure 8.14), indicates that the 87 K data point falls significantly far from the line of best fit. If this point is assumed to be anomalous and therefore removed, the resulting isosteric enthalpy of adsorption is 4.7(2) kJ mol^{-1}, which lies within the error stated above (inclusive of the anomalous data point).

Table 8.1 - Henry's law constant and Virial parameters A_0 and A_1 for hydrogen adsorption on IRMOF-1 (BASF) series at various temperatures (77 and 87 to 142 K, in 5 K steps). The errors shown are equal to one standard deviation.

Temperature K	k_H mol g^{-1} Pa^{-1}	A_0 ln(mol g^{-1} Pa^{-1})	A_1 g mol^{-1}
77	2.21E-07	-15.32 ± 0.03	-103.04 ± 1.18
87	6.14E-08	-16.61 ± 0.01	-84.17 ± 0.28
92	5.66E-08	-16.69 ± 0.02	-92.13 ± 1.86
97	4.43E-08	-16.93 ± 0.02	-99.41 ± 2.12
102	3.65E-08	-17.12 ± 0.02	-104.65 ± 2.44
107	3.23E-08	-17.25 ± 0.01	-130.51 ± 1.14
112	2.70E-08	-17.43 ± 0.02	-136.99 ± 3.45
117	1.89E-08	-17.78 ± 0.02	-138.75 ± 3.92
122	1.56E-08	-17.98 ± 0.03	-151.79 ± 7.31
127	1.08E-08	-18.34 ± 0.01	-129.42 ± 1.69
132	9.53E-09	-18.47 ± 0.02	-130.67 ± 4.05
137	8.95E-09	-18.53 ± 0.02	-152.82 ± 4.39
142	6.59E-09	-18.84 ± 0.02	-126.44 ± 4.97

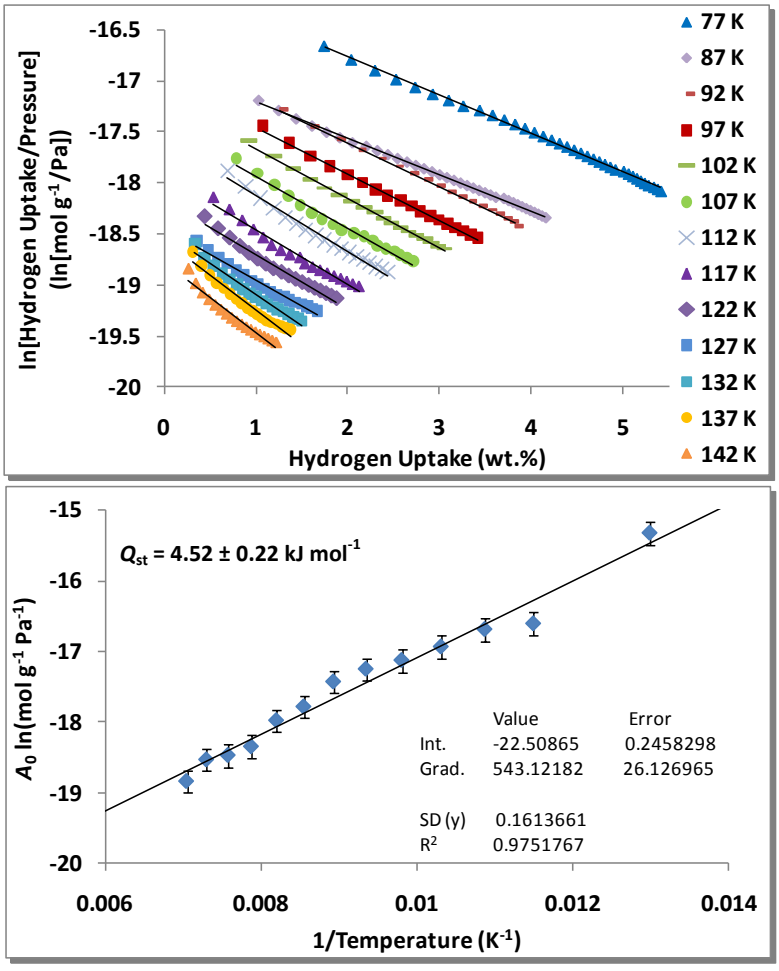

Figure 8.14 - (Top) Virial plots for the absolute adsorption of hydrogen on MOF-5 (BASF) and (bottom) the variation of virial parameter, A_0 with 1/T for IRMOF-1 (BASF), (from 77 and 87 to 142 K, in 5 K steps).

8.2.2.2.7. Virial Type Thermal Equation

Equation (3.66) was used to fit the 77 and 87 K isotherms simultaneously (see Figure 8.15). The equation has no limit to the number of coefficients that can be included, but previous researchers have found that values of $m \leq 6$ and $n \leq 3$, were enough to appreciably reduce the χ^2 goodness-of-fit for their range of microporous MOF materials.[147] The isosteric enthalpy of adsorption was subsequently calculated according to equation (3.67), as a function of hydrogen uptake, which is displayed in Figure 8.16. The analysis produces an isosteric enthalpy of adsorption at zero coverage for IRMOF-1 of 6.4 kJ mol^{-1}. It decreases almost linearly with hydrogen uptake up to 0.8 wt.%, where the enthalpy of adsorption was 5.4 kJ mol^{-1}.

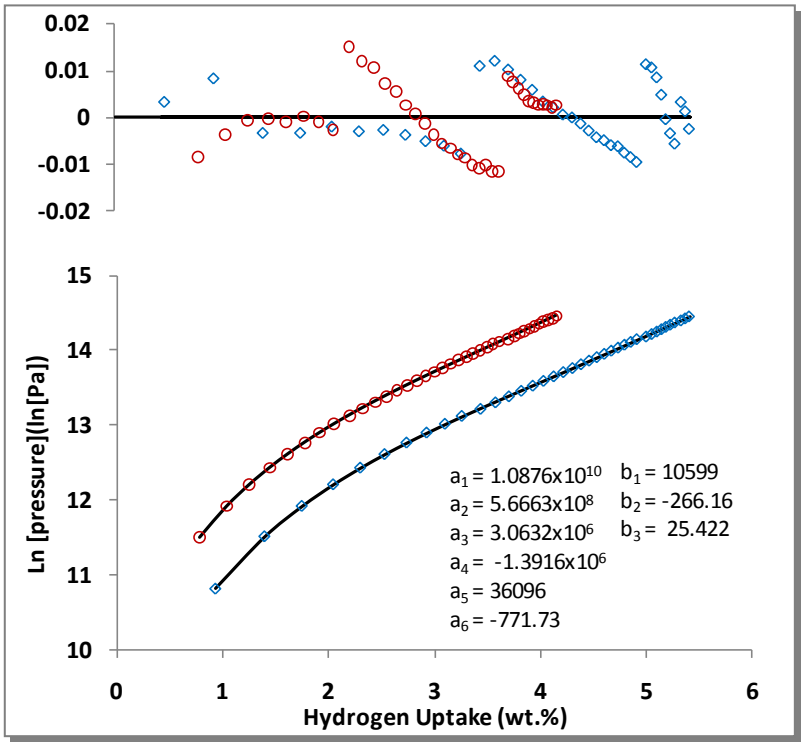

Figure 8.15 - Hydrogen adsorption isotherms at 77 (◊) and 87 K (○) for IRMOF-1 (BASF) to 20 bar. Data is shown by open shapes, virial plots are shown by solid lines. Residual plots are shown at the top of the figure.

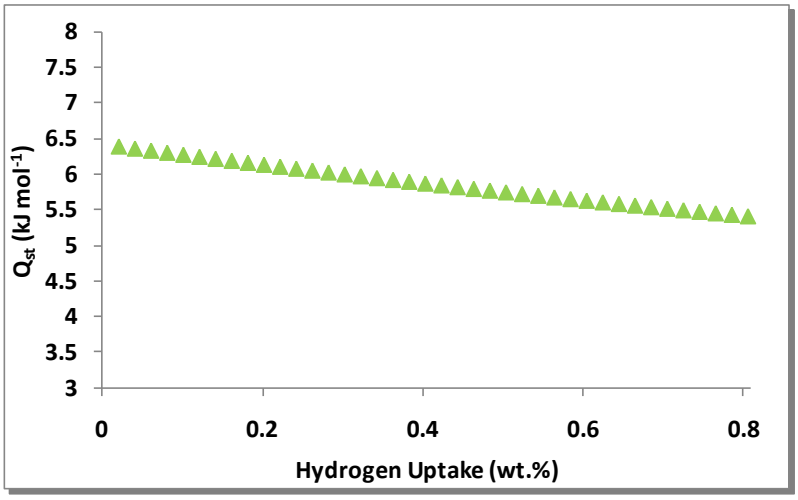

Figure 8.16 - Isosteric enthalpy of adsorption for IRMOF-1 (BASF) as a function of hydrogen uptake. Calculated using the Virial type thermal equation and two isotherms at 77 and 87 K.

Figure 8.17 displays a comparison between the enthalpies of adsorption calculated using the Clausius-Clapeyron equation and that determined using the virial type thermal equation. A relatively large spread is observed from the three models. All three lie between the range of values previously reported (2.2 to 7.7 kJ mol^{-1}),[117,228,230,235-238] however the Sips model does increase above this value at 0.02 wt.%, using two temperatures (77 and 87 K). The enthalpy of adsorption curves displayed here appear to show average values around those reported by Sillar *et al*. who found the strongest site specific hydrogen interaction energy to be 7.1 kJ mol^{-1}, and the lowest to be 4.1 kJ mol^{-1}.[236]

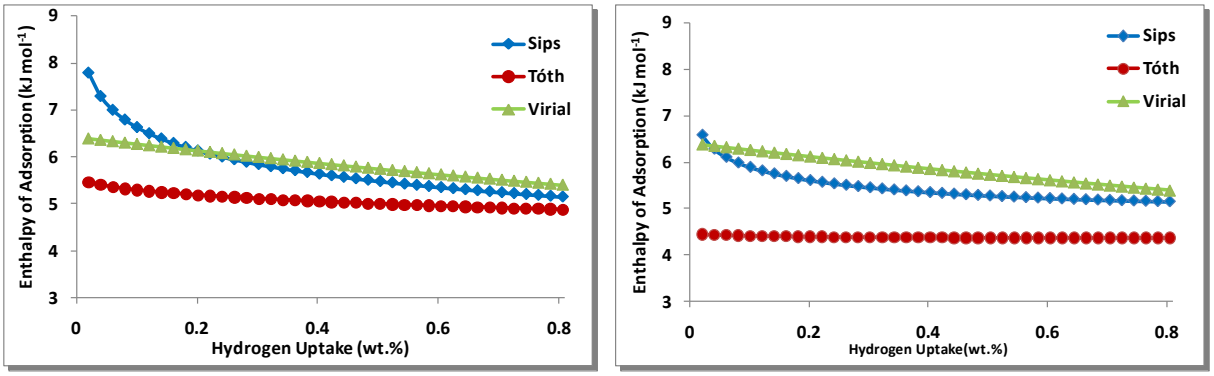

Figure 8.17 - A comparison of the isosteric enthalpy of adsorption for IRMOF-1 (BASF) as a function of hydrogen uptake using different fitting methods. Only 77 and 87 K data was used for three models on the left whereas multiple temperatures were used for the Sips and Tóth models on the right.

In addition, these are also consistent with Bordiga *et al*. who performed IR spectroscopy at 15 K in addition to ab initio calculations to show that the adsorptive properties in IRMOF-1 were mainly a result

of dispersive interactions with the internal pore walls (*ca*. 3.5 kJ mol^{-1}), but also found a binding energy of 7.4 kJ mol^{-1}, for the hydrogen adsorption to clusters of Zn_4O_{13}.[239]

Sillar *et al*. and Rowsell *et al*. described four different adsorption sites with 26 sites in total within each formula unit ($Zn_4O(BDC)_3$). This is made up of four α-sites (cup-site), four β-sites (ZnO_3-site), twelve γ-sites (ZnO_2-site) and six linker-sites.[227,236] Sillar *et al*. performed an ab initio study using density functional theory to calculate adsorption enthalpies of 7.1, 4.1, 4.6 and 4.3 kJ mol^{-1}, for each site respectively, at 1 bar and 77 K. With this in mind, the enthalpy of adsorption values of approximately 4.5 kJ mol^{-1}, as demonstrated here by the multiple temperature Clausius-Clapeyron (Tóth) and Virial type expansion equations, are in good agreement. Additionally, the average enthalpy of adsorption value (considering the values reported by Sillar *et al*. and the number of adsorption sites) should be in the region of 4.8 kJ mol^{-1}, which is the average enthalpy of adsorption observed using the Clausius-Clapeyron (Tóth) with just the 77 and 87 K isotherms.[236]

8.2.2.3. Extended Empirical Isotherm Equations

The extended Tóth equation (3.69) was used fit the excess hydrogen isotherms for the BASF IRMOF-1 material at 77 and 87 K. The excess hydrogen adsorption prediction shown in Figure 8.18 gives a pore volume of 1.19 and 1.23 $cm^3\ g^{-1}$, respectively for the 77 and 87 K data. This shows good agreement with the reported total pore volume of 1.19 $cm^3\ g^{-1}$.[134,173,177]

As with both the carbon material and zeolite materials, the predicted excess adsorption begins to exhibit a downturn in the 77 K isotherm. However, in the 87 K isotherm no downturn was observed up to 50 bar. The excess adsorption for both temperatures is consistent with the isotherms reported by Panella *et al*.[228]

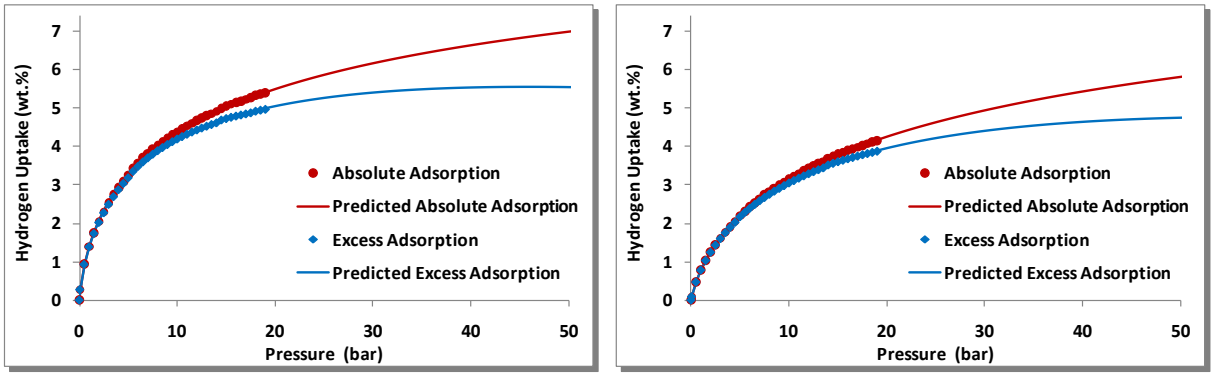

Figure 8.18 - Extended Empirical Tóth equation used to fit to the excess hydrogen uptake for IRMOF-1 up to 19 bar, and the subsequent prediction up to 50 bar, at 77 K.

8.3. Cu-BTC MOF

In addition to IRMOF-1, BASF provided a sample of the Cu^{2+}-containing MOF material, Cu-BTC, which was also synthesised using an electrochemical technique.[373] This material hosts exposed metal sites that are capable of coordinating to adsorbate molecules such as hydrogen. The increased binding strength of these sites should provide this material with a higher isosteric enthalpy of adsorption in comparison to other materials with a similar pore size.

8.3.1. Structure and Characterisation

$Cu_3(BTC)_2(H_2O)_3$ or Cu-BTC consists of $Cu_2(COO)_4$ paddle-wheels with copper dimers as four connectors and benzene-1,3,5-tricarboxylate as three connectors in a cubic framework. Twelve carboxylate oxygen atoms from the two BTC ligands bind to four coordination sites for each of the three Cu^{2+} ions.[250] Each Cu^{2+} ion is also coordinated by a water molecule in axial position, which can be removed in vacuum or by heating,[161] which results in a colour change (turquoise to deep purple).[134] The structure of the Cu-BTC MOF was previously illustrated in Figure 4.9.

Different reports in the literature provide different structural dimensions for the material. Some workers such as Panella *et al*. state that the main channels of a square cross-section are *ca*. 0.98 nm in diameter and tetrahedral side pockets with a diameter of *ca*. 0.5 nm which are connected to the main channels by a triangular window of 0.35 nm in diameter.[161,250] Crystallographic data from Chui *et al*. indicates that Cu-BTC has the space group Fm-3m and has a lattice parameter of 26.343(5) Å.[249]

However, Rowsell *et al*. describe the structure as being similar to the IRMOF series with three mutually perpendicular arrays of channels which intersect at cavities that are 1.32 and 1.11 nm in diameter, with pore apertures of 0.69 nm. The exposed metal sites are described as pointing inwards to the larger pores. The structure also has secondary pores of 0.69 nm in diameter that are accessible through windows of 0.41 nm.[134]

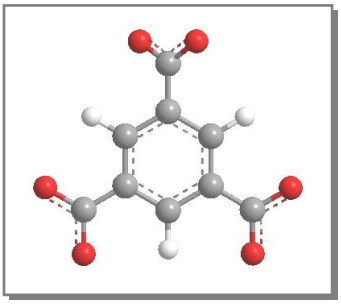

Figure 8.19 - Benzene-1,3,5-tricarboxylate (BTC) organic ligand, (O, red; C, grey; and H, white).

8.3.1.1. XRD

Figure 8.20 displays the powder XRD pattern that was collected from the Cu-BTC material at room temperature. Chekcell was used in order to compare the observed peak positions to those calculated from the space group and lattice parameter reported for the ideal structure by Chui *et al*. (see Table A.3, in Appendix A). Chekcell was also used to refine the zero point error, and determine hkl values and a refined lattice parameter of 26.293(6) Å. The XRD pattern shows an excellent match with the expected structure derived from single crystal data by Chui *et al*.[249] and that calculated by Schlichte *et al*.[380]

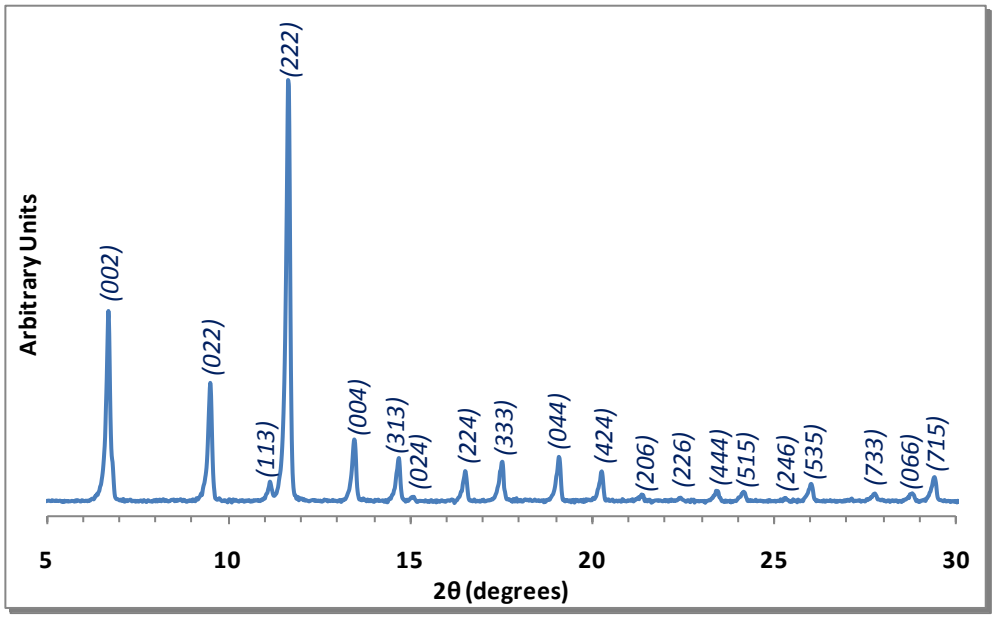

Figure 8.20 - Powder X-ray diffraction pattern for Cu-BTC using the multi-changer (at RT) and Göebel Mirror.

8.3.1.2. TGA

TGA of Cu-BTC was performed to provide a guide for determining an appropriate degassing temperature (before gas sorption measurements). The TGA was performed in a flow of argon gas (at 2 °C min^{-1}) from room temperature up to 600 °C, as displayed in Figure 8.21. The sample mass decreased immediately with increasing temperature and then levelled off from *ca.* 200 °C, where a mass loss of 3.2% was observed. A further 0.7% loss in mass occurred by 300 °C where thermal decomposition began leading to a final 46.5% decrease in mass by 600 °C. The TGA of Cu-BTC shows that it is less thermally stable than IRMOF-1. Excellent correlation was observed between the TGA of the degassed BASF Cu-BTC material and that produced by Schlichte *et al*.[380] and that reported by Li and Yang.[341]

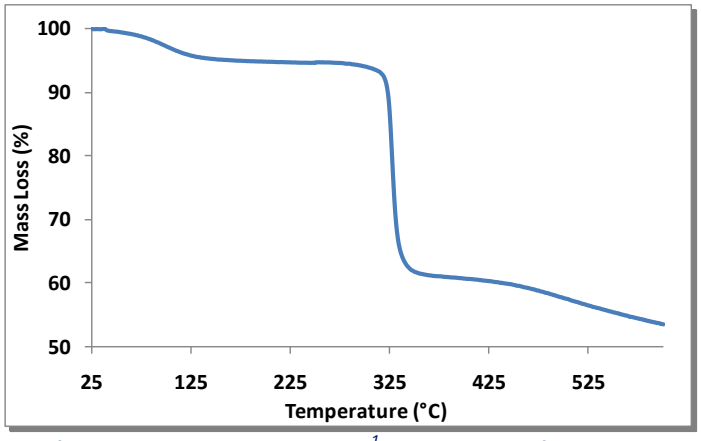

Figure 8.21 - TGA of Cu-BTC from RT to 600 °C at 2 °C min^{-1}. A mass loss of 3.2% was observed up to 200 °C. TGA was performed with a flow of argon gas at 40 ml min^{-1}.

The degassing profile for Cu-BTC presented in Figure 8.22. From the TGA displayed in Figure 8.21, Cu-BTC was degassed at 200 °C. After degassing up to 200 °C for *ca*. 1500 minutes, the sample exhibited a mass loss of *ca*. 14.0%, at which point the sample was still losing mass at a rate of 0.006% per hour, which was *ca*. 0.01 mg, for the Cu-BTC sample.

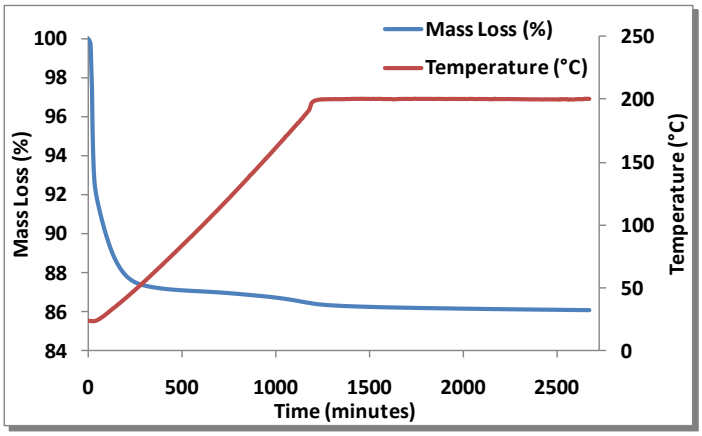

Figure 8.22 - Degassing profile for Cu-BTC *measured on a Hiden IGA-001. A mass loss of ca. 14.0% was observed up to ca. 250 °C in UHV.*

8.3.2. Gas Adsorption

8.3.2.1. Nitrogen

There have been several reports including nitrogen sorption data (at 77 K) in order to assess the apparent surface area of Cu-BTC in the literature. As mentioned earlier, the research group of Hirscher (Max Planck

Institute, Stuttgart) was given a sample of the same batch of BASF Cu-BTC. They reported BET and Langmuir surface area values of 1154 and 1958 $m^2 g^{-1}$, respectively.[228]

8.3.2.2. Hydrogen

The Cu-BTC MOF material was outgassed at 200 °C for *ca*. 1500 minutes under a vacuum (1 x 10^{-6} mbar). After degassing the material had a total mass loss of 14.0%. It is worth noting that *ca*. 8% of this mass loss occurred at room temperature during the evacuation of the sample chamber, and approximately a further 4.5% was lost below 50 °C (whilst the sample was being heated up to 200 °C).

8.3.2.2.1. Excess Adsorption

Helium pyconometry was performed on the degassed Cu-BTC material giving a skeletal density of 1.94(8) g cm^{-3}, which is comparable to previously reported values.[379] Figure 8.21 displays the excess gravimetric hydrogen adsorption isotherms for multiple temperatures up to 16 bar. The 77 and 87 K isotherms were measured by submersing the reaction vessel in liquid nitrogen and argon, respectively; the 92 to 132 K isotherms were measured using the Hiden Cryofurnace. No hysteresis was observed for any of the measured isotherms, this is typical of a microporous material. At 77 K the Cu-BTC MOF material displayed a hydrogen uptake of 4.25 wt.% at 16 bar. This is compared to 4.81 wt.% exhibited by IRMOF-1 at the same temperature and pressure. The lower hydrogen storage capacity for Cu-BTC is consistent with the lower apparent BET surface area. The excess adsorption isotherms also appear to rise more steeply at relatively low pressures (less than 1 bar), suggesting that the material exhibits a greater affinity for hydrogen compared to IRMOF-1. The temperature dependence of Cu-BTC is illustrated in Figure 8.23. The plot of excess hydrogen uptake against temperature shows a sharp decrease in storage capacity which is typical of porous materials with over 50% of the storage capacity being lost from 77 to 132 K at 15 bar. Despite attempts to repeat the measurement at 97 K, the plot highlights the isotherm at this temperature as being potentially erroneous. Indeed, it can be seen in Figure 8.23 that the isotherm at this temperature is not evenly spaced between the isotherms at 92 and 102 K. Therefore it may be sensible to eliminate the

isotherm at this temperature from any multiple temperature analysis conducted to calculate the isosteric enthalpy of adsorption.

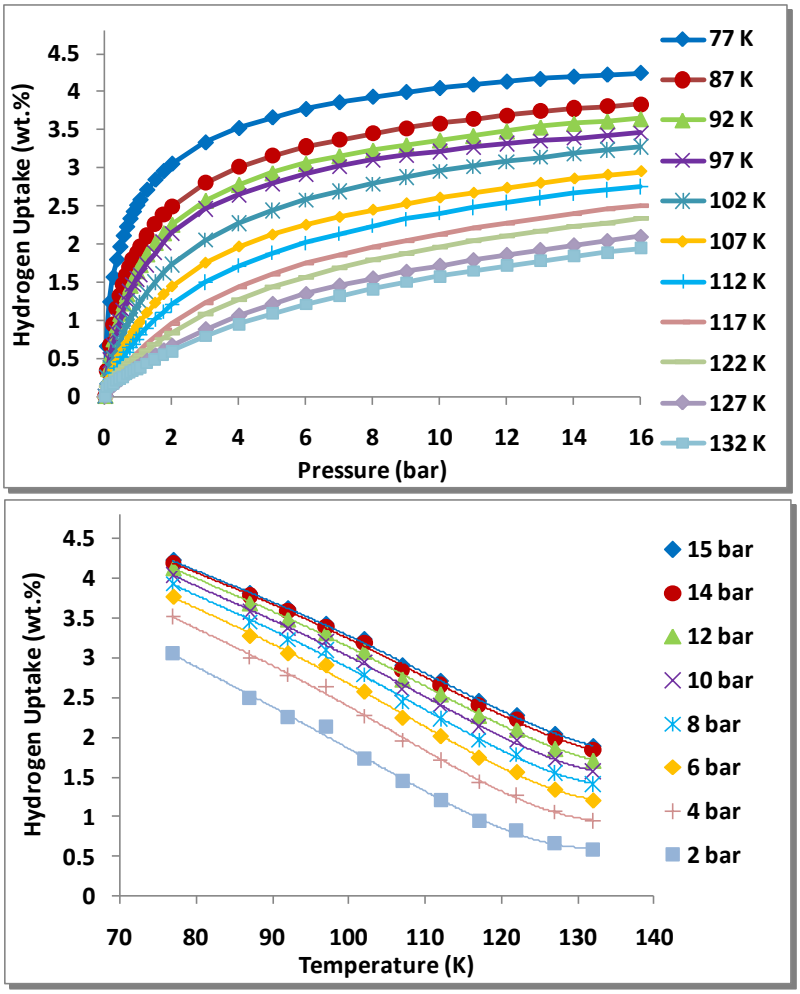

Figure 8.23 - (Top) Excess hydrogen isotherms up to 16 bar at various temperatures. The 77 and 87 K isotherms are measured using submersion by liquid nitrogen and argon, respectively; the 92 to 132 K isotherms are measured using the Hiden Cryofurnace. (Bottom) Gravimetric excess hydrogen uptake against temperature at various pressures.

8.3.2.2.2. Absolute Adsorption

The conversion between the measured excess adsorption and the absolute amount adsorbed utilises equation (3.50) and assumes that the density of the adsorbed phase is equal to that of hydrogen at the triple point (0.077 g cm^{-3}), see section 3.6.2.1. The Cu-BTC (BASF) material exhibited an excess and absolute hydrogen uptake of 4.25 and 4.55 wt.% at 16 bar and 77 K, respectively.

8.3.2.3. The Langmuir Isotherm

The Langmuir plot for Cu-BTC can be seen in the Figure 8.24. The graph is taken to be linear from 2 to 16 bar, which allows it to be used to calculate the maximum amount adsorbed, n_m. The analysis predicts that Cu-BTC will have a maximum hydrogen uptake of 24.4(2) mmol g^{-1}, which equates to 4.92(4) wt.%. Several authors reported an excess gravimetric hydrogen uptake for Cu-BTC is 3.6 wt.% at 77 K using a variety of pressures.[191,228,254]

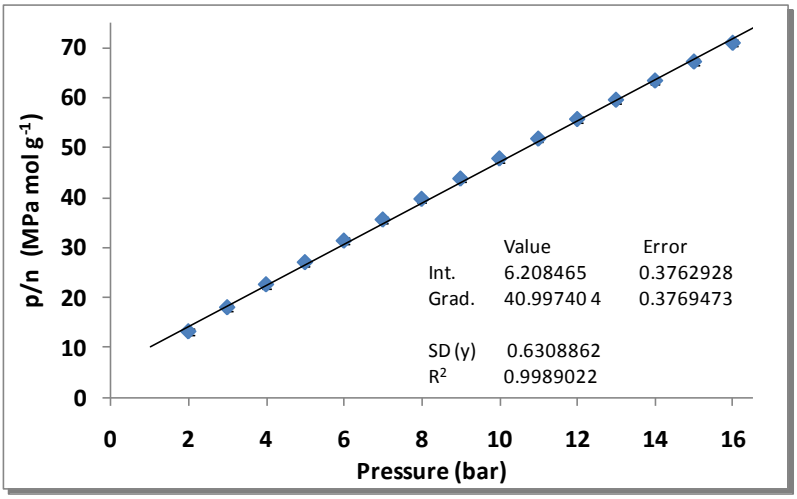

Figure 8.24 - Linearised Langmuir plots for the hydrogen adsorption of the Cu-BTC at 77 K.

8.3.2.4. Empirical Isotherm Equations

The Sips and Tóth empirical isotherm equations were applied to the absolute adsorption isotherm for Cu-BTC, at each measured temperature. Both equations appear to produce good fits for the 77 K isotherm, but residual plots illustrate the differences between the data and the fitted model as shown in Figure 8.25. The residual plots indicate that the Tóth equation can fit the absolute adsorption isotherm slightly better than the Sips equation, particularly at relatively low pressures. This is probably due to the Tóth equation reducing to Henry's Law as $p \rightarrow 0$. Above *ca*. 0.1 bar both models lie within $\pm$0.005 wt.% of the absolute hydrogen adsorption. The closer fit provided by the Tóth equation is also seen by the χ^2 goodness-of-fit values, which are 5.5 and 1.2 x10^{-7}, respectively for the Sips and Tóth functions. The two models produce very significant differences in their predicted saturation uptakes, which are 5.77(8) and 6.69(8) wt.%, for the Sips and Tóth models, respectively at 77 K.

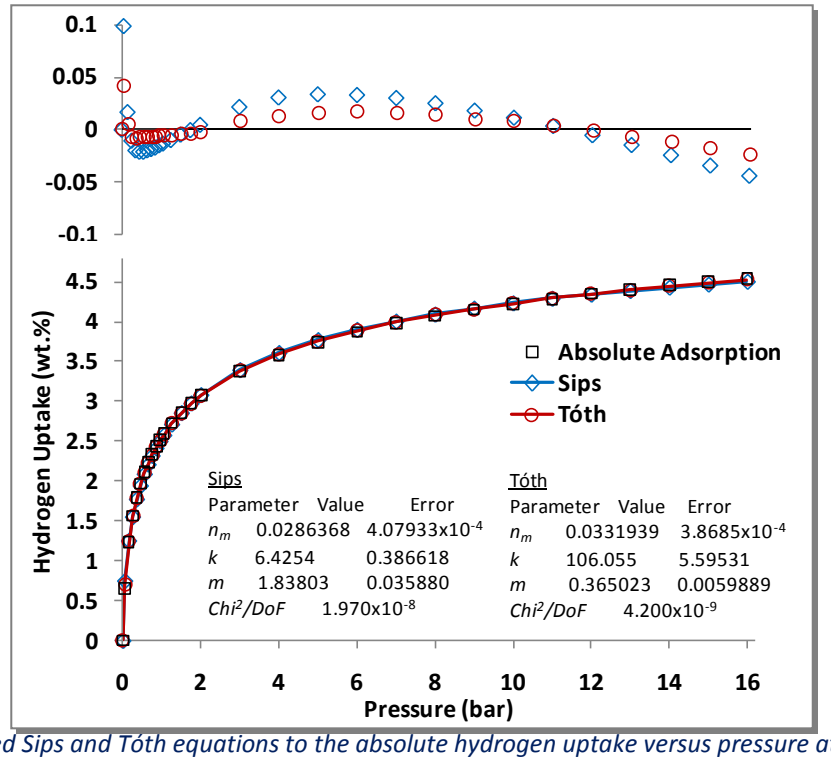

Figure 8.25 - Fitted Sips and Tóth equations to the absolute hydrogen uptake versus pressure at 77 K up to 16 bar for Cu-BTC. Residual plots are shown at the top of the figure.

8.3.2.5. Enthalpy of Adsorption

8.3.2.5.1. Clausius-Clapeyron

The Clausius-Clapeyron equation was used in conjunction with both the Sips and Tóth equations along with the 77 and 87 K absolute hydrogen isotherms in order to give an enthalpy of hydrogen adsorption as a function of hydrogen uptake (see Figure 8.26). The enthalpy of adsorption is calculated up to 0.8 wt.% as explained in section 6.2.2.5.4. The analysis demonstrates reasonably high enthalpies of adsorption for a microporous material, with values of 14.2 and 9.0 kJ mol^{-1}, at the near zero coverage of 0.02 wt.% of hydrogen, for the Sips and Tóth fits, respectively. The enthalpies of adsorption decrease sharply with increasing hydrogen uptake, with the two models giving 6.6 and 6.1 kJ mol^{-1}, at 0.8 wt.%. Beyond that, both models indicate that the isosteric enthalpy of adsorption falls to less than 4.0 kJ mol^{-1} at hydrogen uptake values greater than 3.0 wt.%. The isosteric enthalpy of adsorption for Cu-BTC is much higher than for IRMOF-1, as was previously observed in the literature by Rowsell *et al.*[134] This is also to be expected due to the smaller pore size of Cu-BTC in comparison to IRMOF-1. This is in addition to the exposed metal sites present in Cu-BTC to which hydrogen can bind at low pressures.

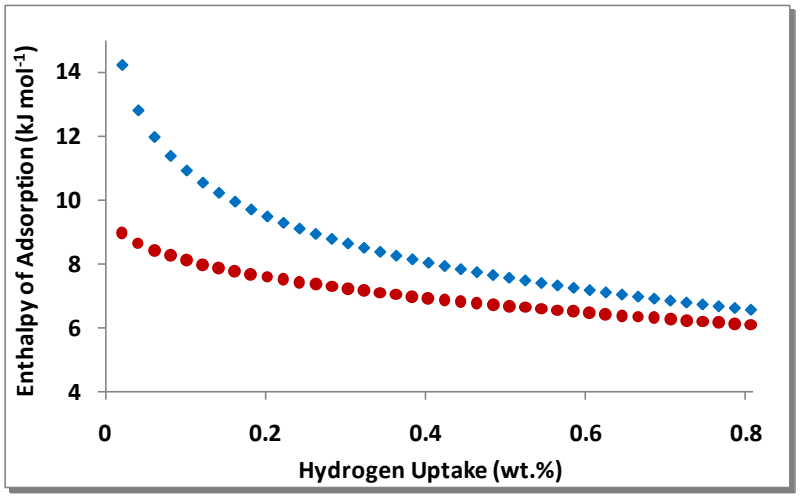

Figure 8.26 - Comparison of the enthalpy of adsorption versus hydrogen uptake for Cu-BTC, calculated using Clausius-Clapeyron equation (in conjunction with Sips (♦) and Tóth (●) equations fitted to the 77 and 87 K absolute isotherms).

The absolute isotherms, at various temperatures, for Cu-BTC were fitted to both the Sips and Tóth models. The resulting fitted data was plotted as $\ln(p)$ against $1/T$ to produce van't Hoff plots at regular intervals of hydrogen uptake. The gradient of each line was taken, and converted in to a value for the enthalpy of adsorption for that specific amount of hydrogen uptake. Figure 8.27 shows the resulting enthalpy of adsorption against hydrogen uptake, for both the Sips and Tóth fitted models. The standard deviation in the van't Hoff plots were also converted to a value for enthalpy of adsorption, and subsequently used as the error at each specific amount of hydrogen uptake. This analysis showed heat adsorption of 9.0 and 6.6 kJ mol^{-1} at the near zero coverage of 0.02 wt.% for the Sips and Tóth models, respectively.

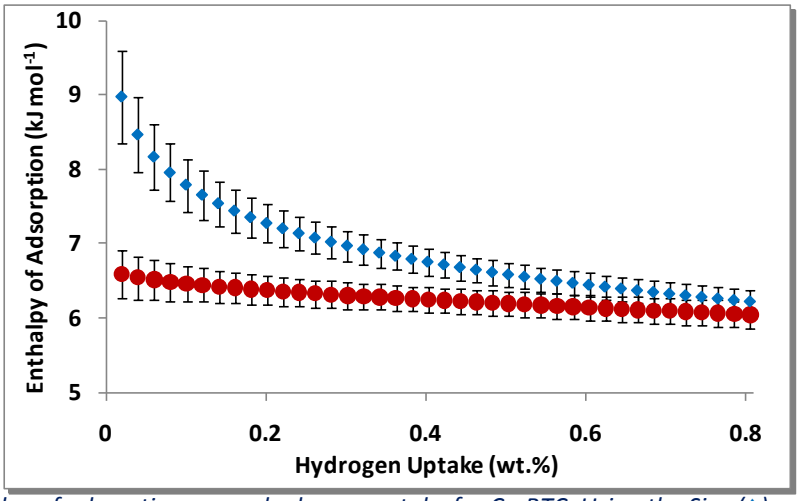

Figure 8.27 - Enthalpy of adsorption versus hydrogen uptake for Cu-BTC. Using the Sips (♦) and Tóth (●) models to fit the absolute isotherms (at 77 and 87 to 132 K, at 5 K steps). The Clausius-Clapeyron equation and van't Hoff plot were then used to determine the enthalpy of adsorption.

8.3.2.5.2. Virial Type Expansion Equation

Figure 8.28 shows the virial plots for the hydrogen adsorption on Cu-BTC at 77 K and then 87 to 132 K, in 5 K steps). The plots are taken to be linear at pressures ≥ 0.8 bar to *ca.* 4 bar, allowing for the determination of A_0 and A_1 values from the intercepts and gradients respectively, using linear regression. The values for which can be seen in Table 8.2. The gradient from the plot of A_0 against $1/T$ (see Figure 8.28) produced an isosteric enthalpy of adsorption of 6.4(2) kJ mol^{-1}. The Henry's law constant (which is related to the first virial parameter (K_H=exp(A_0)) is seen to decrease with increasing temperature, which indicates a decrease in adsorbate-adsorbent interaction with in increasing temperature. No real trend can be seen in the second virial parameter in the pressure range used above.

Table 8.2 - Henry's law constant and Virial parameters A_0 and A_1 for hydrogen adsorption on Cu-BTC at various temperatures (77 K and then 87 to 132 K, in 5 K steps). The errors shown are equal to one standard deviation.

Temperature K	k_H mol g^{-1} Pa^{-1}	A_0 ln(mol g^{-1} Pa^{-1})	A_1 g mol^{-1}
77	1.45E-06	-13.45 ± 0.02	-192.86 ± 1.80
87	3.85E-07	-14.77 ± 0.01	-145.28 ± 1.25
92	2.41E-07	-15.24 ± 0.02	-127.31 ± 1.88
97	2.15E-07	-15.35 ± 0.03	-129.84 ± 4.18
102	1.26E-07	-15.88 ± 0.01	-124.92 ± 0.74
107	7.68E-08	-16.38 ± 0.01	-104.54 ± 1.11
112	6.01E-08	-16.63 ± 0.01	-116.34 ± 0.76
117	4.24E-08	-16.98 ± 0.01	-131.91 ± 5.46
122	3.85E-08	-17.07 ± 0.02	-154.50 ± 6.32
127	2.40E-08	-17.54 ± 0.01	-112.63 ± 2.41
132	2.16E-08	-17.65 ± 0.01	-124.96 ± 2.28

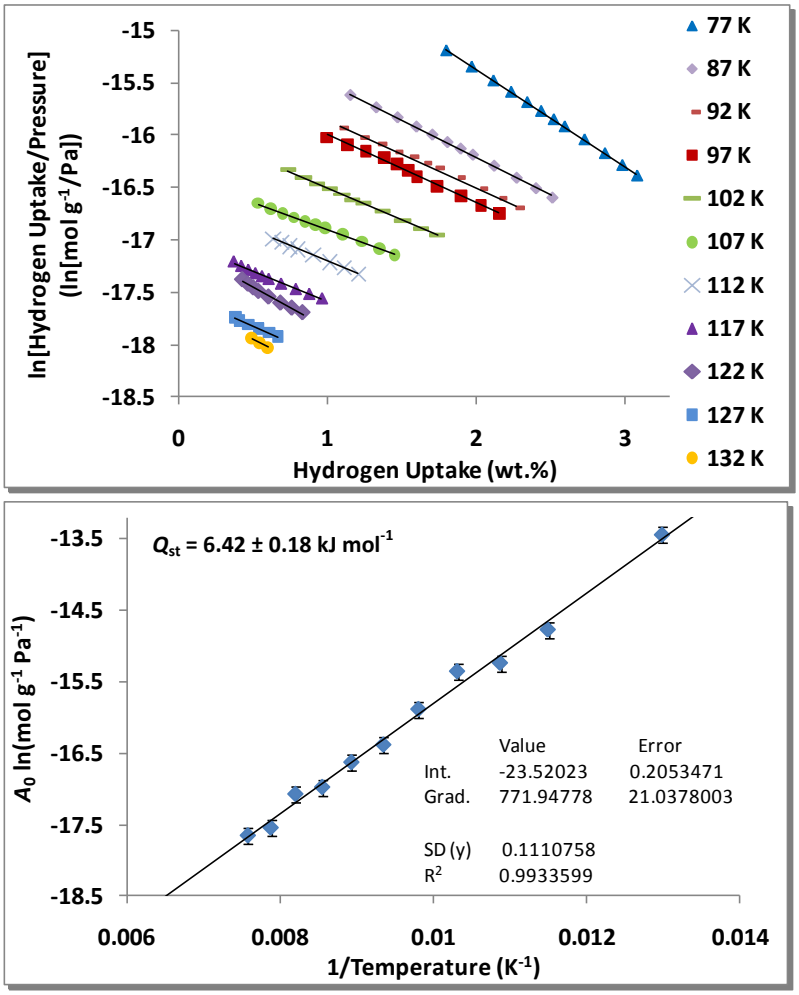

Figure 8.28 - (Top) Virial plots for the absolute adsorption of hydrogen on Cu-BTC and (bottom) the variation of virial parameter, A_0 with 1/T for Cu-BTC (from 77 K and then 87 to 132 K, in 5 K steps).

8.3.2.5.3. Virial Type Thermal Equation

Equation (3.66) was used to fit the 77 and 87 K isotherms simultaneously (see Figure 8.29). The equation has no limit to the number of coefficients that can be included, previous researchers have found that values of $m \leq 6$ and $n \leq 3$, were enough to appreciably reduce the χ^2 goodness-of-fit for their range of microporous MOF materials.[134] The isosteric enthalpy of adsorption was subsequently calculated according to equation (3.67), as a function of hydrogen uptake is displayed in Figure 8.30. The analysis produces an isosteric enthalpy of adsorption at zero coverage of 7.2 kJ mol^{-1}, which decreases to 5.9 kJ mol^{-1} by 0.8 wt.%. This is similar to that observed by Rowsell *et al*. (*ca*. 6.8 kJ mol^{-1}) using the same technique.[134]

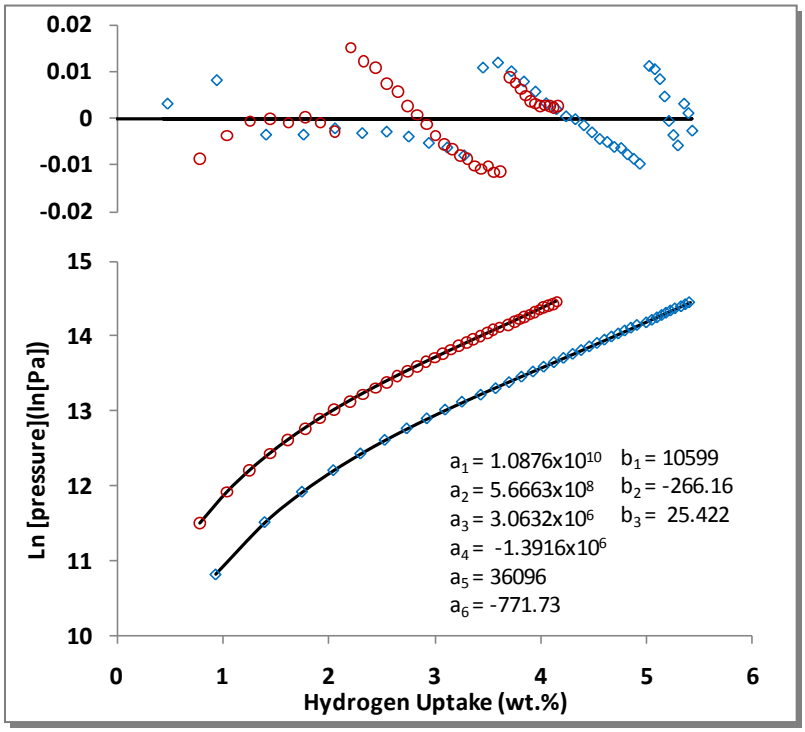

Figure 8.29 - Hydrogen adsorption isotherms at 77 (◊) and 87 K (○) for Cu-BTC to 16 bar. Data is shown by open shapes, virial plots are shown by solid lines. Residual plots are shown at the top of the figure.

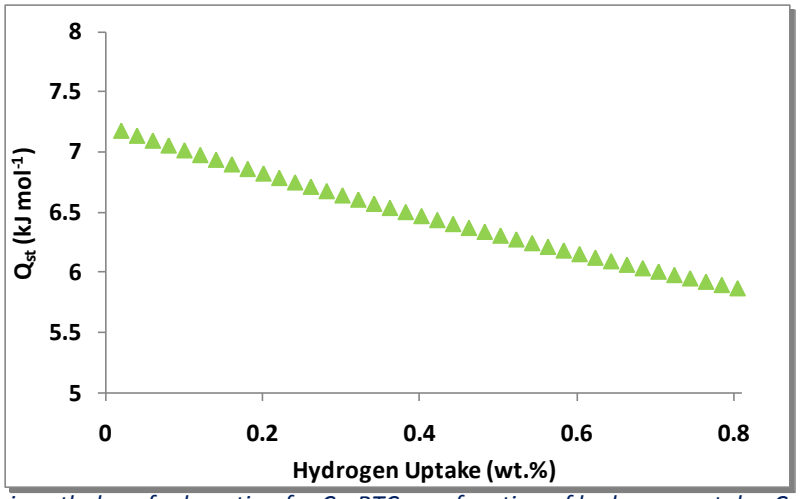

Figure 8.30 - Isosteric enthalpy of adsorption for Cu-BTC as a function of hydrogen uptake. Calculated using the Virial type thermal equation and two isotherms at 77 and 87 K.

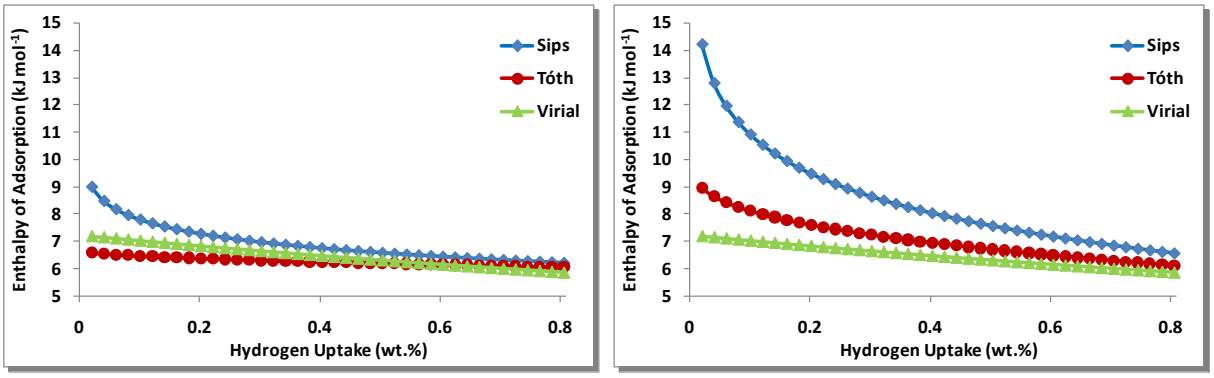

Figure 8.31 - A comparison of the isosteric enthalpy of adsorption for Cu-BTC as a function of hydrogen uptake using different fitting methods. Only 77 and 87 K data was used for three models on the left, whereas multiple temperatures were used for the Sips and Tóth models on the right.

The increased enthalpy of adsorption observed for Cu-BTC in comparison to IRMOF-1 could be a result of stronger hydrogen binding to the smaller pores of Cu-BTC or that hydrogen has a greater interaction with the $Cu_2(O_2C\text{-})_4$ cluster compared to $Zn_4O(O_2C\text{-})_6$. A comparison between the virial type thermal equation of the two MOF materials (using 77 and 87 K) is shown in Figure 8.32.

Rowsell *et al*. compared both IRMOF-1 and Cu-BTC to the interpenetrated IRMOF-11. They used the Virial type thermal equation to determine enthalpies of adsorption values for the three MOFs to be 4.8, 6.8 and 9.1 kJ mol^{-1}, respectively, at low coverage. The authors concluded that high values determined for IRMOF-11 were a result of its catenation, which provides small pores (*ca*. 0.87 nm in diameter). As both IRMOF-1 and Cu-BTC mainly consist of larger pores of a similar size (1.21 and 1.52 nm and 1.11 and

1.32 nm, respectively), the authors stated that the differences between the IRMOF-1 and Cu-BTC were expected to be a result of the exposed metal sites, and not to stronger hydrogen binding in the smaller pores in Cu-BTC.

The trends in enthalpy of adsorption (as a function of hydrogen uptake) for the two materials investigated, agree very well with those reported by Rowsell *et al*.[134], suggesting that the structures were similar to those reported by Rowsell *et al*.[134], with the increased enthalpy of adsorption observed being a result of stronger hydrogen interaction with the $Cu_2(O_2C\text{-})_4$ cluster compared to $Zn_4O(O_2C\text{-})_6$.

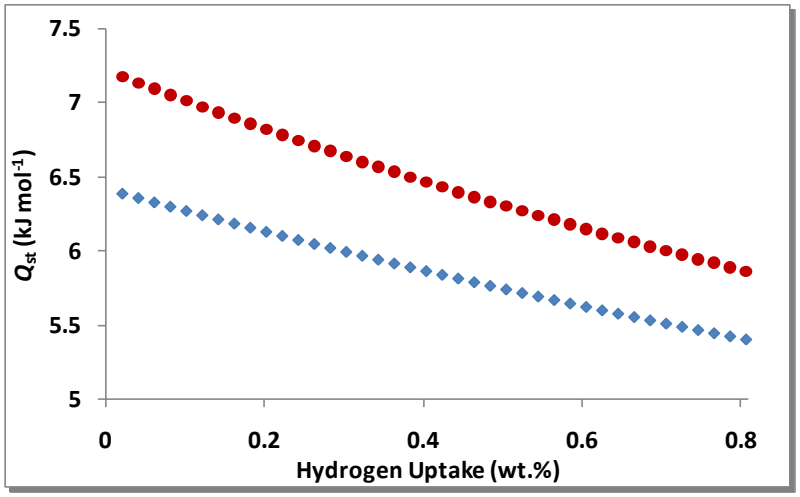

Figure 8.32 - Isosteric enthalpy of adsorption for IRMOF-1 (♦) and Cu-BTC (●) as a function of hydrogen uptake calculated using the Virial type thermal equation and two isotherms at 77 and 87 K.

8.3.2.6. Extended Empirical Isotherm Equations

The extended Tóth equation (3.69) was used to fit the excess hydrogen isotherms for Cu-BTC at 77 and 87 K. The excess hydrogen adsorption prediction shown in Figure 8.33 gives a pore volume of 0.738 $cm^3\ g^{-1}$ for the 77 K data. The Levenberg-Marquardt algorithm that is used to search for the coefficient values that minimize chi-square (a form of nonlinear, least-squares fitting)[72,362], unfortunately reduces the unknown pore volume to unrealistic values for the 87 K excess isotherm. Therefore, for the 87 K excess data displayed in Figure 8.33, the pore volume was constrained to 0.75 $cm^3\ g^{-1}$ as was reported by Rowsell and Yaghi.[134] The reason why the fitting did not work with an unknown pore volume is not entirely known, however it is expected to be a consequence of two combined factors. The hydrogen uptake was not recorded at a high enough pressure for the 87 K data, and this caused a lack of significant

enough curvature to the isotherm in order for the nonlinear, least-squares fitting method to find a local minimum within the constraints (0.2 to 2 $cm^3 g^{-1}$) of a reasonable pore volume.

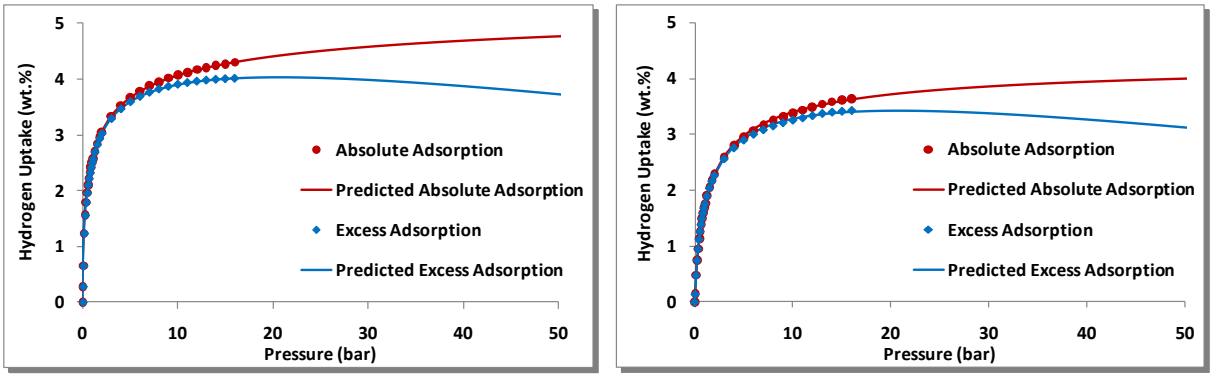

Figure 8.33 - Predicted excess and absolute adsorption at 77 (left) and 87 K (right) up to 50 bar for Cu-BTC. The predicted excess uses the extended Tóth equation, whereas the absolute prediction uses the Tóth model (as shown previously in this chapter).

8.4. Chapter Summary

This chapter describes the hydrogen storage properties of two metal organic framework materials; IRMOF-1 and Cu-BTC. The impact on the hydrogen storage properties of different synthetic methods, was illustrated by the difference in excess hydrogen adsorption at 77 K for two samples of IRMOF-1. The IRMOF-1 sample produced by BASF showed a greater uptake and so led to this being used throughout the remainder of this study; this was in addition to Cu-BTC which was also supplied by BASF.

At low pressures, the Cu-BTC material exhibited a greater affinity for hydrogen at 77 K; this was shown by the relatively steep adsorption in comparison to IRMOF-1. However, due to the greater surface area and pore volume of IRMOF-1, the hydrogen uptake increases to higher values compared to Cu-BTC, with the two materials exhibiting 4.81 and 4.25 wt.%, for IRMOF-1 and Cu-BTC, respectively at 16 bar and 77 K.

Using several different fitting methods, the isosteric enthalpy of adsorption was shown to be higher for Cu-BTC than for IRMOF-1 with the Virial type expansion equation giving 6.42 and 4.52 kJ mol^{-1}, respectively. Similar values (6.59 and 4.45 kJ mol^{-1}) using the Clausius-Clapeyron equation were also found for the two MOF materials at 0.02 wt.% after each isotherm (at each temperature) was fitted using the Tóth equation.

The isosteric enthalpy of adsorption determined using multiple temperatures has been shown to be consistently lower than when only using the 77 and 87 K absolute isotherms. It is not clear yet whether this is a function of temperature dependence of the isosteric enthalpy of adsorption or whether simply using more isotherms at different temperatures results in greater accuracy. The isosteric enthalpy of adsorption for the Cu-BTC was higher than IRMOF-1 as a result of the exposed metal sites, which point inwards to the larger pores.

The extended Tóth equation was also fitted to the 77 and 87 K excess hydrogen isotherms to predict the excess adsorption at higher pressures. The analysis also produced pore volumes with reasonable correlation to reported values in the literature by Rowsell *et al*.[134] and Xiao *et al*.[254]

Chapter 9

POLYMERS OF INTRINSIC MICROPOROSITY

9.1. Introduction

Polymers of Intrinsic Microporosity (PIMs) were synthesised at the University of Cardiff as part of a joint EPRSC project (EP/D074312/1) on polymer-based hydrogen storage materials. The gas adsorption properties of these materials were characterised and assessed at the University of Manchester and the University of Birmingham as part of this work.

This study starts with the first of series of polymers (PIM-1) and progresses through the challenge of increasing the accessible surface area and creating a more open structure whilst maintaining ultramicroporosity within the PIMs. Basic analysis of surface area was performed using nitrogen adsorption at 77 K, and excess hydrogen isotherms (at 77 and 87 K) were measured for all materials. The enthalpy of adsorption was calculated in various ways for all of the PIMs. Variable temperature analysis (hydrogen uptake) was also performed on the material that exhibited the largest hydrogen uptake at 77 K. Low relative pressure nitrogen adsorption (at 77 K) isotherms were recorded in order to determine pore size distributions. These are then discussed in relation to the enthalpy of adsorption values.

9.2. General PIM Synthesis

The general PIM synthesis is displayed in Figure 9.1, the required fused-ring linkage is formed using a double aromatic nucleophilic substitution (dibenzodioxane formation) between a 1,2-dihydroaryl- (catechol) and 1,2-difluoro- (1,2-dichloro-) aryl unit containing monomers. The reaction typically uses potassium carbonate (K_2CO_3) and dimethylformamide (DMF) and an elevated temperature of *ca*. 60 to 150 °C.

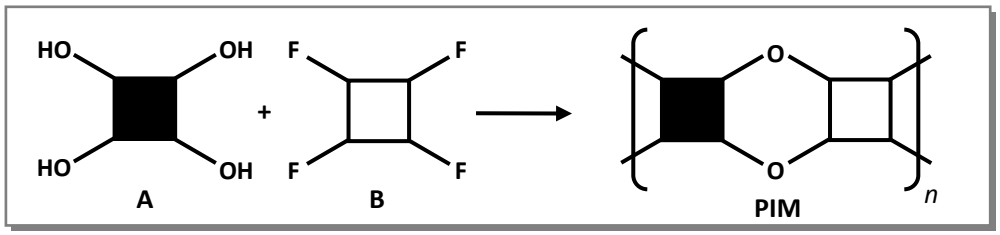

Figure 9.1 - General PIM reaction occurs via base-mediated aromatic nucleophilic substitution to form rigid linkages between rigid 1,2-dihydroaryl- (catechol) and 1,2-difluoro- (1,2-dichloro-) aryl unit containing monomers, A and B respectively.

In the schematic shown in Figure 9.1, both the A and B monomers have functionality equal to 2. Therefore, they both have two binding sites available to participate in the dibenzodioxane formation where each pair of adjacent hydroxyl groups or fluorines count as a single functional group.[280] If two planar monomers are reacted together then a non-porous material is produced. However, if at least one of the monomers is rigid with a "site of contortion" then microporosity results. To obtain an insoluble network polymer, the average functionality (f_{av}) of the monomer combination should be greater than two ($f_{av} > 2$).

9.3. PIM-1

Microporous polymers were originally studied for their catalytic and adsorption behaviour.[298] PIM-1 was the first in a series of soluble PIMs that showed relatively high specific surface area, and was one of just a few PIMs in the literature.[294] The University of Manchester a provided relatively large quantity (*ca*. 15 g) of the material to allow many different forms of analysis to be performed. A film was also cast from the same batch; this allowed us to assess differences in gas adsorption properties as well as its ability to act as a gas separation membrane.

9.3.1. Structure and Characterisation

As with the general PIM reaction as mentioned previously, PIM-1 is synthesised from a catechol and 1,2-difluoro- aryl unit containing monomers as shown in Figure 9.2. Monomers 5,5′,6,6′-tetrahydroxy-3,3,3′,3′-tetramethyl-1,1′-spirobisindane (A1) and 2,3,5,6-tetrafluoroterephthalonitrile (B1) react via a

dibenzodioxane formation when mixed with K_2CO_3 and DMF at 60 °C for 48 hours. Note that the B1 monomer is also known as 1,4-dicyanotetrafluorobenzene.

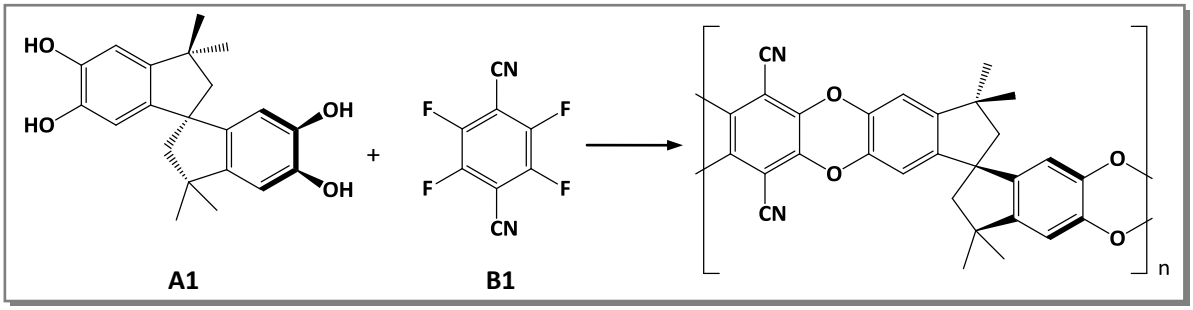

Figure 9.2 - Formation of the soluble PIM-1 from 5,5´,6,6´-tetrahydroxy-3,3,3´,3´-tetramethyl-1,1´-spirobisindane (A1) plus 2,3,5,6-tetrafluoroterephthalonitrile (B1) monomer. Reagents and conditions: K_2CO_3, DMF, 60 °C and 48 h.

PIM-1 is bright yellow, and is typically precipitated out from the reaction as a very fine amorphous powder. All of the PIMs studied in this work demonstrated a very similar morphology under electron microscopy, with particle sizes in the region of 3 to 5 microns (see Figure 9.3). Due to the non-conductive nature of the PIMs, it was necessary to coat the material with a thin layer of gold to avoid the discharge effect of the electron beam. The images were taken using FEI STRATA Dual Beam 235, by Hossein Ostadi in the group of Micro-Engineering and Nano-Technology, University of Birmingham. An accelerating voltage of 5.0 kV was used in secondary electron mode. Figure 9.3 displays the SEM image of the (gold-coated) PIM-1 powder.

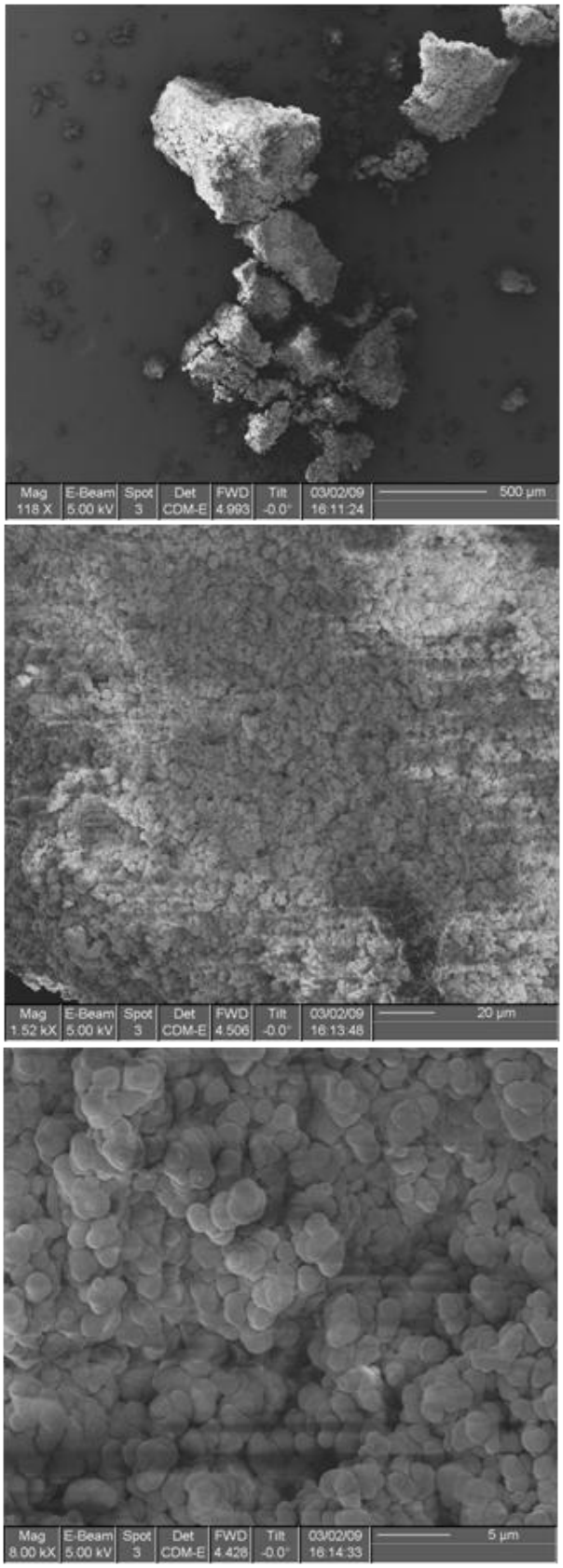

Figure 9.3 - SEM secondary electron images of (gold coated) PIM-1 powder using FEI STRATA Dual Beam 235.

9.3.1.1. TGA

Thermogravimetric analysis (TGA) of the PIM-1 powder was performed on both the TGA and IGA systems. The TGA measurements provide a guide for determining an appropriate degassing temperature (before gas sorption measurements). The TGA was performed in a flow of argon gas (at 2 °C min^{-1}) from room temperature up to 400 °C, as displayed in Figure 9.4. The sample mass decreased immediately with increasing temperature, with a mass loss of 5.5% up to 150 °C. A further 0.4% loss in mass is observed up to 400 °C, but thermal decomposition was not observed, which is consistent with Budd *et al.*[294] Differential scanning calorimetry (DSC) was performed confirming the lack of a glass transition temperature or melting point up to 400 °C. The observed changes in the DSC are as a result of less relative power being required to heat the material due to mass loss.

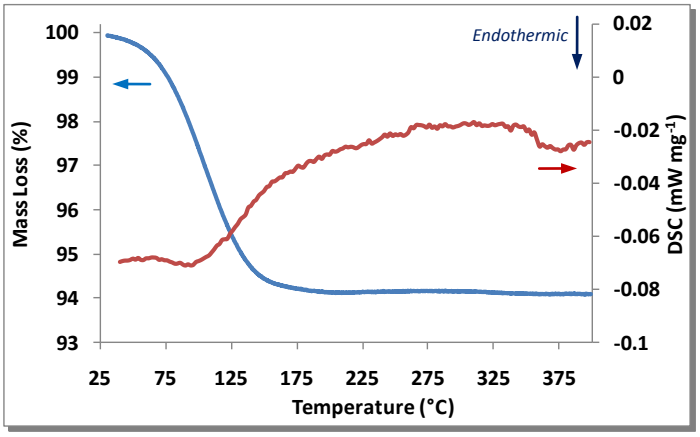

Figure 9.4 - TGA-DSC of PIM-1 powder, from RT to 400 °C at 2 °C min^{-1}. A mass loss of 5.91% was observed. TGA was performed with a flow of argon gas at 40 ml min^{-1}, DSC was performed at a dynamic argon pressure of 3 bar (with a flow of 100 ml min^{-1}).

The thermogravimetric analysis performed on the IGA differs (from the typical TGA) as it utilises a UHV rather than a flow of argon gas, enabling samples to be degassed at lower temperatures. Using the IGA, a mass loss of 5.98% was observed up to 100 °C (in a UHV of *ca*. 10^{-6} mbar), see Figure 9.5. The mass loss is typically associated by the removal of solvents that were used during synthesis, in this case dimethylformamide (DMF).

Typically, porous materials have been shown to lose a substantial amount of mass during the initial evacuation (at room temperature). The level of the UHV has a significant influence (as mentioned in Chapter 5), which can be increased by the use of wider bore pipes and a more direct route from the

vacuum pump to the sample. This effect is observed in the degassing of PIM-1, where the sudden decrease in mass, at around 180 minutes, is a result of opening the PIV1 valve on the IGA.

Figure 9.5 illustrates the importance of finding the optimum degassing temperature. No mass loss was observed upon heating the PIM-1 sample in UHV up to 120 °C. The temperature was then increased every 200 minutes in 20 °C steps up to 220 °C. In fact no mass loss was observed at 160 °C, and only 1 μg was lost during the 200 minute period at 180 °C. However this then tripled during the 200 °C period to 3 μg and further increased (to 7.8 μg) during the period at 220 °C.

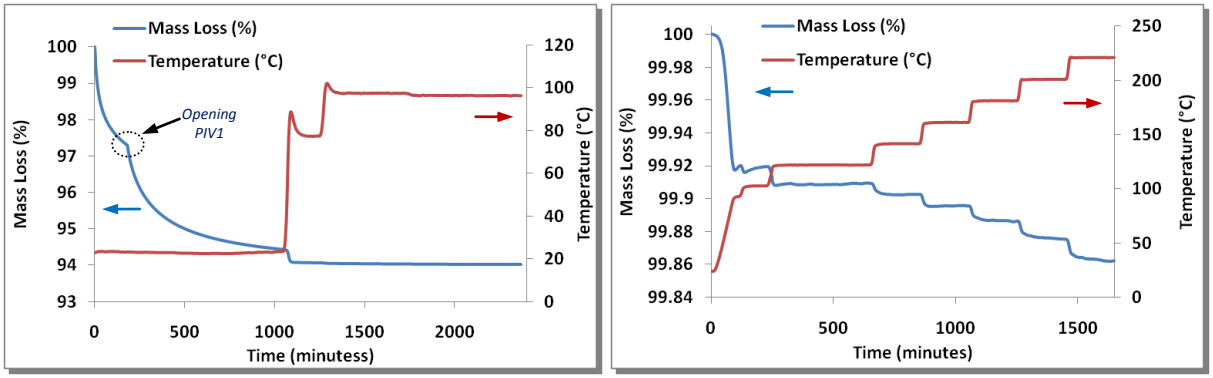

Figure 9.5 - (Left) Degassing profile for PIM-1 powder, measured on a Hiden IGA-001. A mass loss of ca. 5.98% was observed up to ca. 98 °C at UHV. Note that the sudden drop in mass at ca. 180 minutes is due to opening of the valve PIV1 on the IGA system and the temperature 'overshoot' is caused by the set-up of the cryo-furnace, which is discussed in Chapter 5. (Right) Stepped increases in temperature demonstrate the optimum degassing temperature with UHV.

9.3.1.2. Infrared Spectroscopy

Many porous materials are made in solution before being subsequently precipitated-out. This typically leads to the inclusion of solvents within the structure of the materials. One of the reagents used to synthesise PIMs is DMF, the structure of which shown in Figure 9.6. Despite DMF having a boiling point of 153 °C, it is known to be desorbed from porous samples in the temperature range of 25 to 200 °C.[381] This can be seen in the thermogravimetric analysis of PIM-1, where significant mass loss is observed from room temperature up to around 150 °C, as was shown in Figure 9.4.

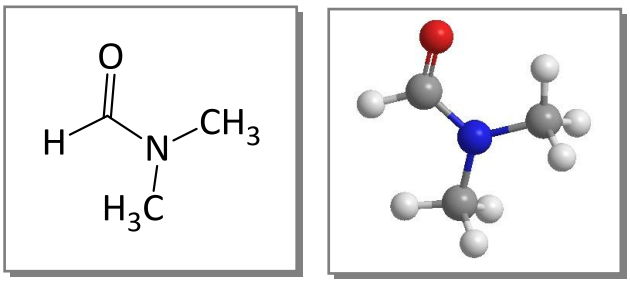

Figure 9.6 - Chemical structure of DMF (dimethylformamide), (O, red; N, blue; C, grey; and H, white).

Infrared spectroscopy was performed to see whether the DMF molecule could be identified in the (as received) PIM-1 material (see Figure 9.7). Subsequent IR analysis was also performed on samples that had been outgassed at 140 and 220 °C. The former (140 °C), is the degas temperature where it was believed all the solvent to have been removed; and the latter (220 °C), is the temperature above which DMF is known to be desorbed from porous materials,[381] and where the TGA showed complete desorption (Figure 9.4). The infrared spectrum of the as received PIM-1 showed the expected stretches, IR (cm^{-1}): ν = 2950, 2918, 2858 (C-H), 2237 (CN), 1710 (C=O), 1603 (C-C Ar), 1263, 1007 (C-O). The peaks around 1441 cm^{-1} could be the bend associated with numerous C-C bonds. Carbon-oxygen double bonds typically show IR stretches in the range, 1700 to 1730 cm^{-1}.[382] The as received PIM-1 material did have a peak around 1710 cm^{-1} which can be attributed to C=O from DMF. Interestingly the same peak was not observed from the two outgassed (140 and 220 °C) samples (see Figure 9.8). DMF is also known to show weak stretches at around 1100 and 1400 cm^{-1}, however, these peaks are masked by that of the fingerprint region of the polymer.

Additionally, there are no broad bands from 3300 to 3600 cm^{-1} in any of the three samples. These would have indicated O-H groups and hence the presence of water molecules. We can therefore assume that this material does not adsorb water from the atmosphere. There is also little change in the fingerprint region of the spectra between the samples, indicating that the bonds associated with the C-H stretches remain unaffected by the heat treatment.

Raman spectroscopy was also performed on the degassed PIM-1. This is displayed in Appendix B.

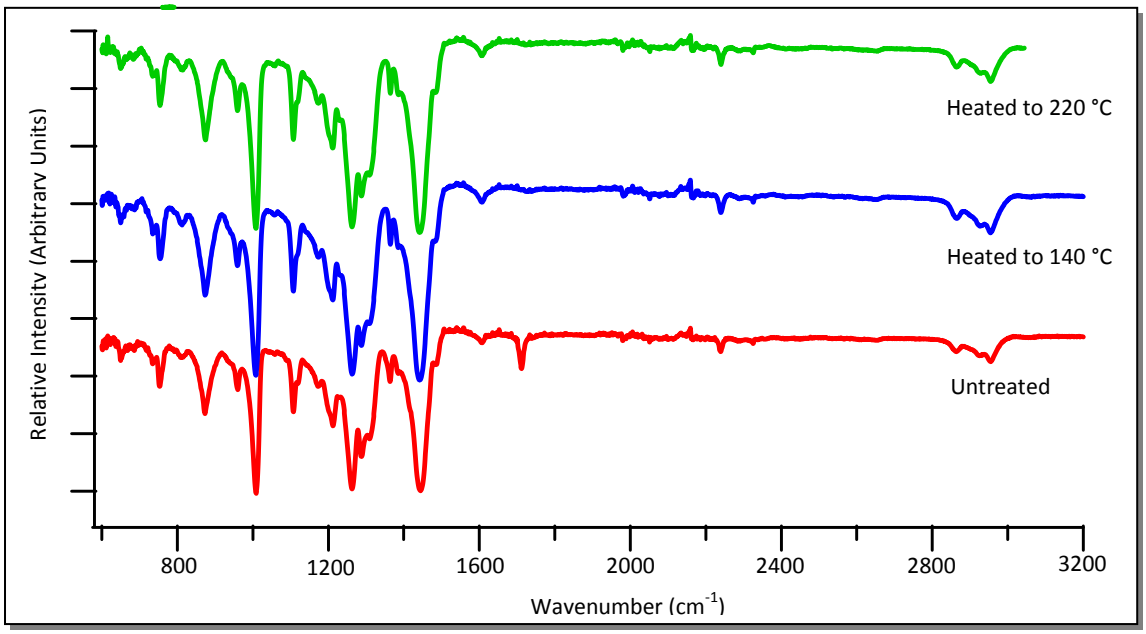

Figure 9.7 - Infrared Spectroscopy of three PIM-1 samples, at RT, from 600 to 3200 cm^{-1}. Sample 1 was as received (untreated), Samples 2 and 3 were heated to 140 and 220 °C, respectively in UHV for ca. 1000 minutes.

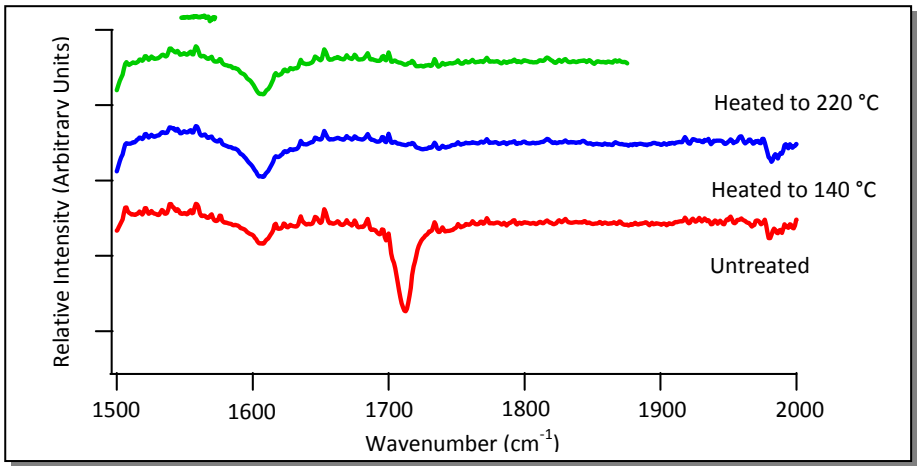

Figure 9.8 - Infrared Spectroscopy of three PIM-1 samples, as shown in Figure 9.7, from 1500 to 2000 cm^{-1}.

9.3.2. Gas Adsorption

9.3.2.1. Nitrogen

PIM-1 showed fairly significant nitrogen uptake at low relative pressures ($p/p_0 < 0.1$), which is consistent with microporous materials. The isotherm does not appear to be of Type I in the IUPAC classification, which would have been expected for the physisorption of gases in microporous materials. Instead of forming a plateau, PIM-1 continues to adsorb nitrogen above the relative pressure of 0.1, where it increases to a total of 474 $cm^3\ g^{-1}$ (STP) (21.2 $mmol\ g^{-1}$), at $p/p_0 = 1$. The gradient in the adsorption

isotherm has not been reported for crystalline porous materials such as zeolites.[152] The significant hysteresis between the adsorption and desorption cycles (as presented in Figure 9.9) could be a result of the non-crystallinity of the material, hence allowing structural movement with increasing pressure. It could also be a result of the polymer containing a substantial quantity of mesopores.

A least squares linear regression was performed in order to calculate the apparent surface area using the nitrogen adsorption isotherm. The linear section between 0.05 and 0.02 p/p_0 was taken to give a BET surface area of 760.7 ± 4.8 $m^2 g^{-1}$ which is close to previously reported values of 760 $m^2 g^{-1}$ for the same material.[296] The Langmuir surface area was calculated to be 881.8 ± 7.6 $m^2 g^{-1}$ using the adsorption data up to 0.02 p/p_0.

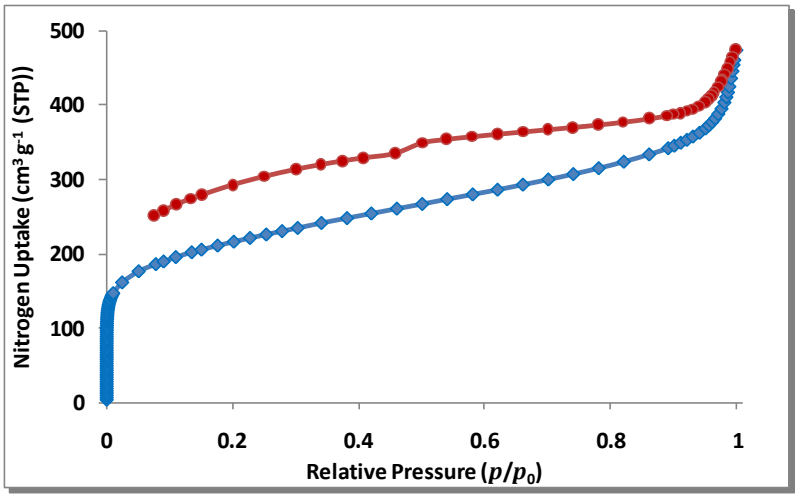

Figure 9.9 - Nitrogen adsorption (♦) and desorption (●) of PIM-1 against relative pressure at 77 K.

The Horváth-Kawazoe (HK) method was used to analyse the low-pressure nitrogen adsorption data to calculate a pore size distribution for PIM-1 (see Figure 9.10). The analysis confirmed the lack of a distinct pore size, and the presence and distribution of pore sizes was biased towards pores in the range around 0.6 to 0.7 nm. This distribution of pore sizes was expected due to the amorphous nature of the material, and could be used to explain the slope of the nitrogen adsorption isotherm and the hysteresis between the adsorption and desorption, as some of the pores may only be accessible at higher relative pressures of nitrogen at 77 K.

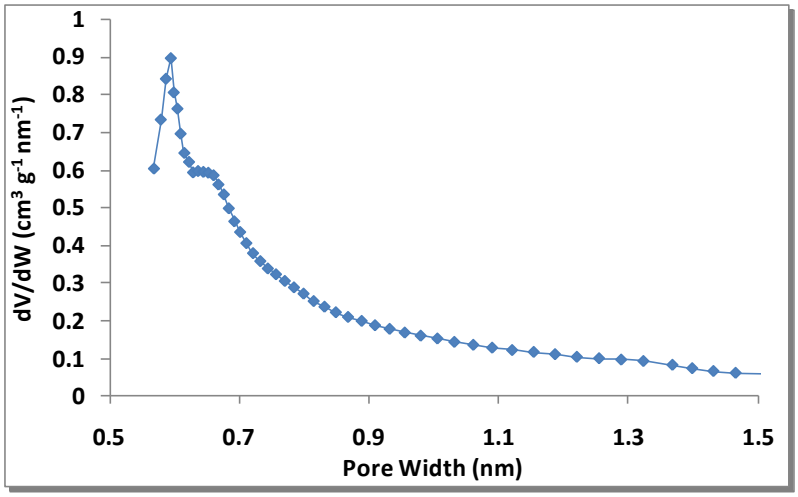

Figure 9.10 - Micropore size distribution for PIM-1 based on the Horváth-Kawazoe (slit pore) analysis of low pressure nitrogen adsorption data (shown in Figure 9.9) showing that the major contribution to porosity is from pores that are less than 1 nm in diameter.

Several additional calculations were used to determine the micropore size distribution of the PIM-1 material, including the Dubinin-Astakhov (DA), Ross Oliver (RO), Horváth-Kawazoe Cheng Yang (HK-CY), and the Ross Oliver cylindrical and spherical methods, which can be seen in Figure 9.11. The Horváth-Kawazoe and Ross Oliver methods used the same nitrogen adsorption data, measured using the Micromeritics ASAP 2010. The Dubinin-Astakhov method used nitrogen adsorption data measured using the Hiden IGA-001. Excellent consistency was observed between the HK, DA, HK-CY, and cylindrical RO methods. The standard RO model displays an intense peak centred around a pore width of 0.4 nm. The spherical RO model displays main peak at *ca*. 0.8 nm with a significant shoulder between 0.8 and 0.9 nm. A similar shoulder is present in the HK, HK-CY and cylindrical RO calculations.

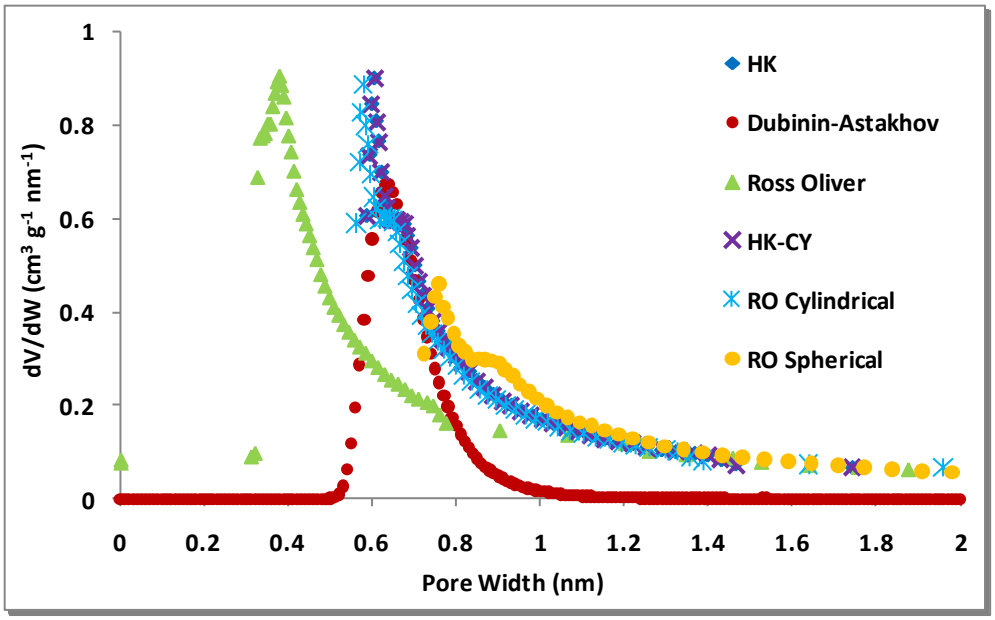

Figure 9.11 - Comparison of the different methods used to calculate the micropore size distribution of PIM-1. The Horváth-Kawazoe and Ross Oliver methods used the same nitrogen adsorption data, measured using the MIcromeretics ASAP 2010. The Dubinin-Astakhov method used nitrogen adsorption data measured using the HIden IGA-001.

Unfortunately, despite the excellent correlation between methods, the pore sizes cannot be measured below around 0.57 nm (for the HK slit pore calculation). This is a result of the instrument not being capable of measuring lower than 7.8×10^{-8} p/p_0. Therefore any pores that are filled below this relative pressure would result in an over exaggeration of the quantity of pores at the measuring limit of the machine. Obviously, any pores that are smaller than the diameter of the nitrogen molecule cannot be detected using this technique.

9.3.2.2. Hydrogen

9.3.2.2.1. Excess Adsorption

The hydrogen sorption isotherm for PIM-1 is shown in Figure 9.12. The material exhibited an excess gravimetric hydrogen uptake of around 1.50 wt.% and 1.30 wt.% at 15 bar and 77 K and 87 K, respectively. A density of 1.25 g cm^{-3} was used for the buoyancy correction, as determined by helium pycnometry at room temperature. The results show that PIM-1 adsorbs a comparable amount of hydrogen to that of zeolites and other porous carbons of similar surface area. The sorption isotherm shows that PIM-1 is fully reversible with almost no hysteresis.

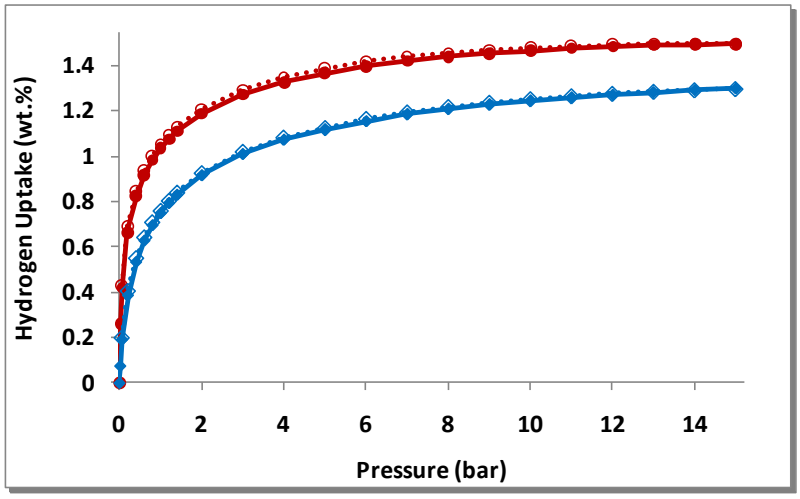

Figure 9.12 - Excess gravimetric hydrogen uptake for PIM-1 at 77 (●) and 87 K (♦) up to 15 bar. Full symbols indicate adsorption, open symbols indicate desorption.

The gravimetric hydrogen storage capacity (7.42 mmol g^{-1}) can be used in conjunction with the density of hydrogen at the triple point (0.077 g cm^{-3}) to calculate the volume of hydrogen adsorbed in the pores. The calculated volume of hydrogen adsorbed in PIM-1 was 0.194 cm^3 g^{-1}, representing a 72% filling of the micropore volume as calculated the BET equation on the nitrogen adsorption isotherm (0.27 cm^3 g^{-1}).

The geometric density of the PIMs can be determined using the measured skeletal density and the calculated micropore volume.[283,290] The Dubinin-Radushkevich equation was extrapolated to $\log^2(p_0/p) = 0$, using the carbon dioxide adsorption isotherm for PIM-1 (at 0 °C) to give a micropore volume of 0.27 cm^3 g^{-1}. This can then be used to calculate the volumetric storage capacity of the PIMs. For PIM-1 this gave a geometric density of 0.93 g cm^{-3} and a volumetric capacity of 14.0 kg m^{-3} at 15 bar and 77 K. However, the packing density of a powder material is unlikely to ever achieve its theoretical density (without being cast in to a crystalline material). Kryuchkov reported that for spherical particles, the packing density would be *ca*. 62% of the theoretical density and for cubic particles this would be *ca*. 52%.[383] Using the tapping method as reported by Jordá-Beneyto *et al*.[114], PIM-1 exhibits a density of 0.48 g cm^{-3}, which is 51% of the geometric density determined above. Using the tapping density, the volumetric capacity of PIM-1 falls to 7.1 kg m^{-3} at 15 bar and 77 K. The bulk density and subsequently, the volumetric storage capacity of PIM-1 could be improved by casting it as a film. However, this process severely reduced the kinetics of the hydrogen uptake by the material at 77 K. Consequently, the low temperature could not be maintained for the duration required to reach an equilibrium hydrogen uptake.

9.3.2.2.2. Empirical Isotherm Equations

The conversion between the measured excess adsorption to the absolute amount adsorbed used equation (3.50), with the assumption that the density of the adsorbed phase is equal to hydrogen at the triple point (0.077 g cm^{-3}), see section 3.6.2.1. The difference between the excess and absolute adsorption at 77 K is presented in Figure 9.13. PIM-1 exhibited an absolute hydrogen uptake of 1.60 and 1.38 wt.% at 15 bar and 77 and 87 K, respectively.

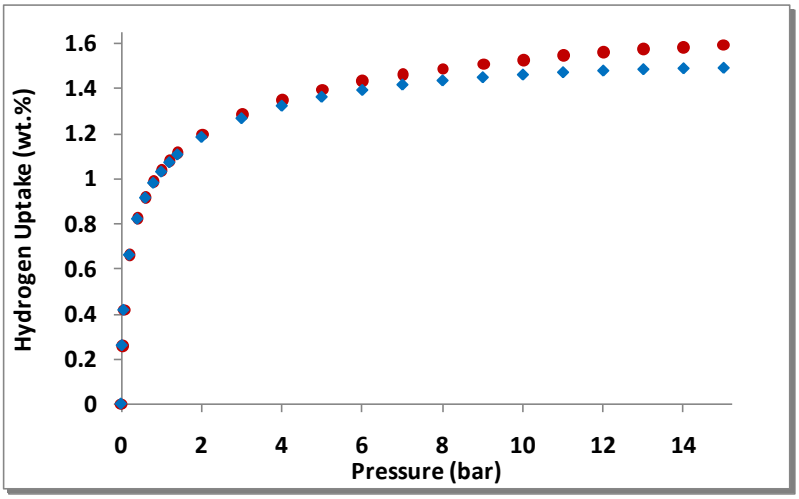

Figure 9.13 - Difference between excess (♦) and absolute (●) hydrogen uptake (wt.%) against pressure (bar) at 77 K using the adsorbed phase density equal to that of hydrogen at the triple point.

The Langmuir plot for PIM-1 at 77 K can be seen in Appendix F. The graph is taken to be linear from 2 to 15 bar, which enables it to be used to calculate the maximum amount adsorbed, n_m; this would be consistent with a plateau for the absolute hydrogen adsorption isotherms. The analysis predicts that PIM-1 will have a maximum hydrogen uptake of 8.40(5) mmol g^{-1}, which equates to 1.69(1) wt.%. Using the pore volume of 0.27 cm g^{-1}, at saturation the adsorbate phase density is estimated to be 0.063 g cm^{-3}; slightly less than that of liquid hydrogen.

The Sips and Tóth empirical isotherm equations were applied to the absolute adsorption isotherm at each temperature. Both equations appear to produce good fits, but residual plots illustrate the differences between the data and the fitted model, as shown in Figure 6.5. The two models produce substantial

differences in their predicted saturation uptakes, which are 2.06(1) and 2.50(6) wt.%, for the Sips and Tóth models, respectively at 77 K.

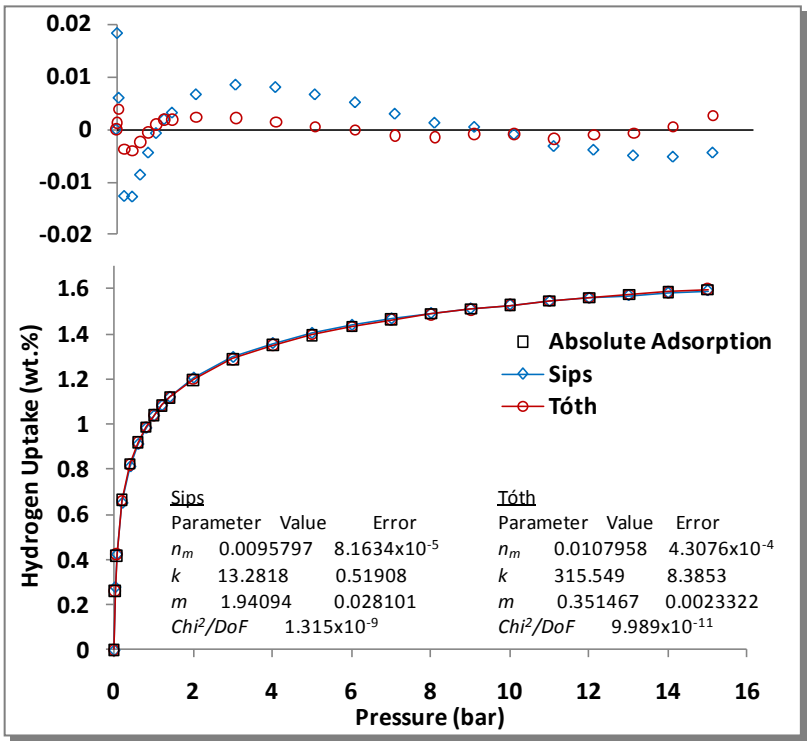

Figure 9.14 - Fitted Sips (◇) and Tóth (○) equations to the absolute hydrogen uptake versus pressure at 77 K up to 15 bar. Residual plots are shown at the top of the figure.

9.3.2.2.3. Enthalpy of Adsorption

9.3.2.2.3.1. Clausius-Clapeyron

The fitted 77 and 87 K absolute adsorption isotherms were used to calculate the enthalpy of adsorption using the Clausius-Clapeyron equation. The enthalpy of adsorption is calculated up to 0.8 wt.% as explained in section 6.2.2.5.4. The analysis shows the reasonably high enthalpies of adsorption for a microporous material that are very similar to NaX and greater than the hypercrosslinked polymers reported by Wood *et al*.[290] The two models give 13.4 and 9.7 kJ mol^{-1}, at the near zero coverage of 0.02 wt.% of hydrogen, for the Sips and Tóth fits, respectively. In fact it is also slightly greater than that reported by Yuan *et al*. for POP-4 (9.0 kJ mol^{-1}).[293] The enthalpies of adsorption decrease sharply with increasing hydrogen uptake, with the two models both giving 6.5 and 6.7 kJ mol^{-1}, at 0.8 wt.%, which are slightly lower that NaX at the same coverage.

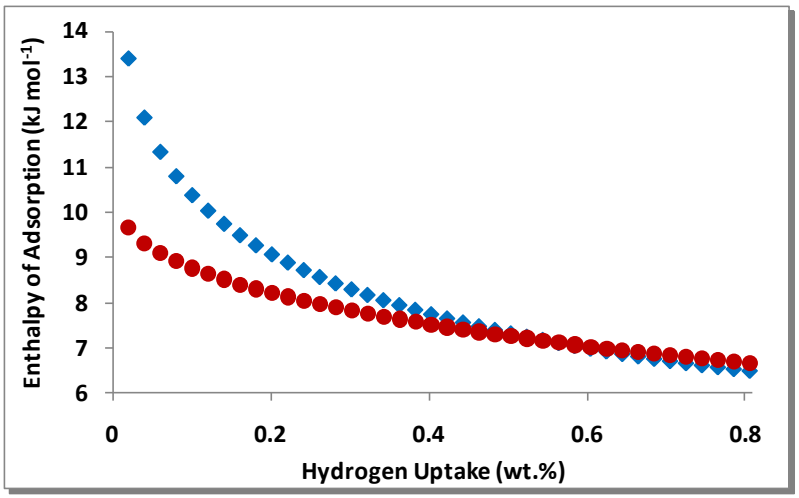

Figure 9.15 - Comparison of the enthalpy of adsorption versus hydrogen uptake for PIM-1, calculated using Clausius-Clapeyron equation (in conjunction with Sips (♦) and Tóth (●) equations fitted to the 77 and 87 K absolute isotherms).

9.3.2.2.3.2. Virial Thermal Type Equation

Equation (3.66) was used to fit the 77 and 87 K isotherms simultaneously. To be consistent with the other materials in this work, values of 6 and 3 were used for the coefficients m and n, respectively. The isosteric enthalpy of adsorption was subsequently calculated according to equation (3.67), as a function of hydrogen uptake which can be seen in Figure 7.13. The analysis gives an isosteric enthalpy of adsorption at zero coverage for PIM-1 of 9.3 kJ mol^{-1}. Despite this value being less than that calculated using the Tóth model, it is still greater that previously reported for other porous organic polymers reported by Yuan *et al*.[293], and it decreases sharply with hydrogen uptake. Unfortunately, Yuan *et al*. did not report the method used to calculate the enthalpy of adsorption. Interestingly, at a hydrogen uptake of 0.8 wt.%, the enthalpy of adsorption is 6.7 kJ mol^{-1}, which is just 0.2 kJ mol^{-1} greater than the Sips model and the same as the Tóth model.

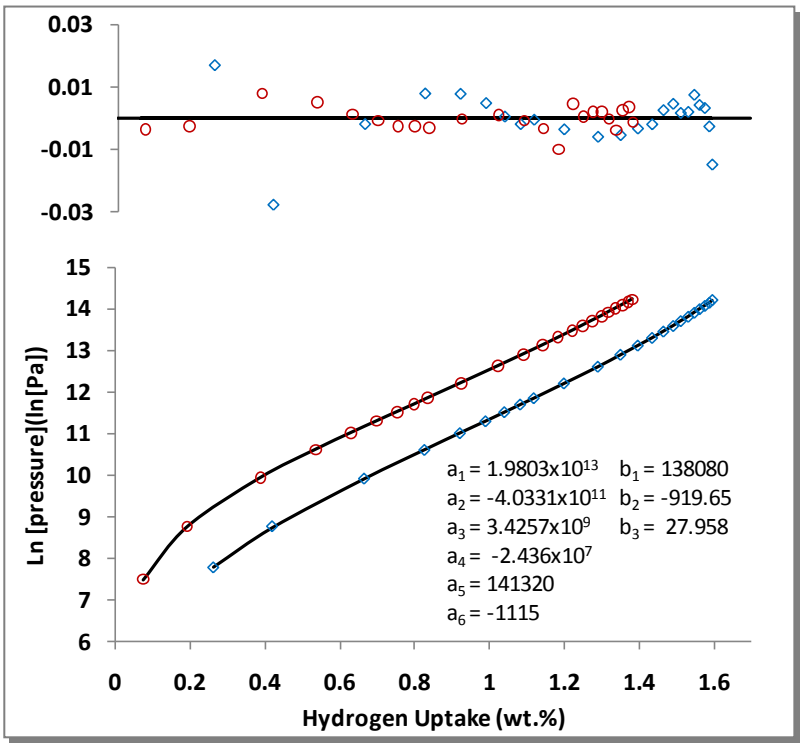

Figure 9.16 - Virial analysis of the hydrogen adsorption data at 77 (◊) and 87 K (O) for PIM-1 to 15 bar. Open symbols display data, whilst the virial plots are indicated by solid lines. Residual plots are shown at the top of the figure.

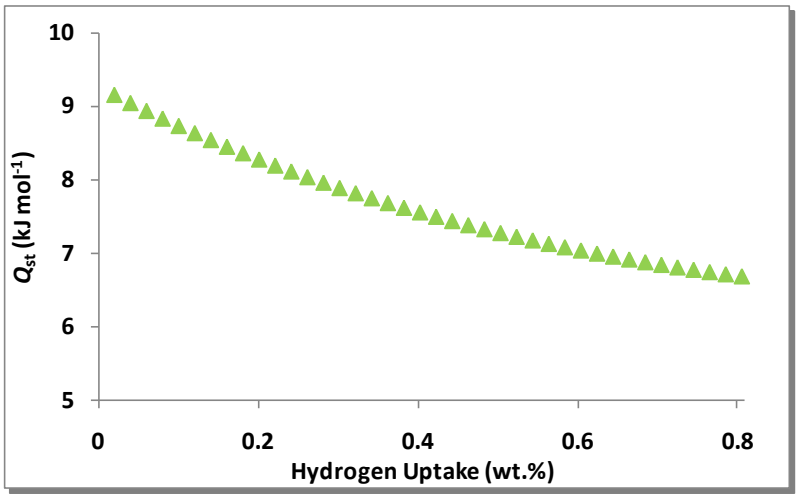

Figure 9.17 - Isosteric enthalpy of adsorption for PIM-1 as a function of hydrogen uptake determined using the Virial type thermal equation with the 77 and 87 K.

Figure 9.18 displays a comparison for the previously determined enthalpies of adsorption with the virial type thermal equation using two temperatures (77 and 87 K). As with the previous materials studied in this investigation, very similar enthalpy of adsorption curves were observed for the Tóth and Virial equations. The Sips model appears to overestimate the enthalpy of adsorption at low surface coverage,

however all three fitting models produced similar values by the time the hydrogen uptake reaches 0.8 wt.%.

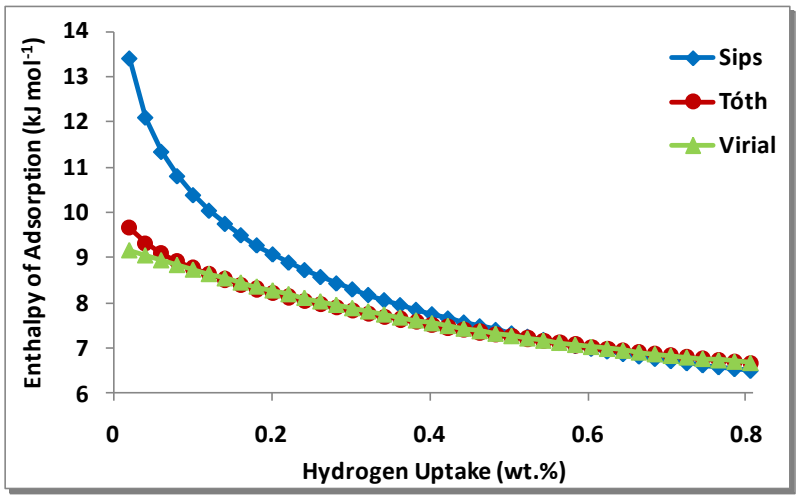

Figure 9.18 - A comparison of the isosteric enthalpy of adsorption for PIM-1 as a function of hydrogen uptake using different fitting methods in conjunction with data generated at 77 and 87 K.

The pore size distribution for PIM-1 is consistent with the relatively high enthalpy of adsorption. The decrease from around 9.3 to 6.7 kJ mol^{-1} (from 0.02 to 0.8 wt.%) may also be considered to be consistent with the distribution of pore sizes that are present in PIM-1. This is in comparison to: NaX which only falls from 9.2 to 7.2 kJ mol^{-1}; IRMOF-1 which decreased from around 6.5 to 5.5 kJ mol^{-1}; and Cu-BTC which decreased from 7.2 to 5.9 kJ mol^{-1}. The Takeda 4A porous carbon, which has a smaller pore size distribution than PIM-1 exhibited a drop in the enthalpy of adsorption from 9.9 to 5.9 kJ mol^{-1}, from 0.02 and 0.8 wt.%. Therefore, this rapid decrease in the enthalpy of adsorption is associated with materials containing very small micropores.

9.4. Porphyrin PIM

Hypercrosslinked polymers have been shown to exhibit high specific surface areas, in particular are those synthesised using Friedel-Crafts alkylation of chloromethylated polystyrene or by polymerisation of suitable aromatic monomers.[102,289,290] The first PIMs were typically soluble and not necessarily network polymers. The triptycene monomer offered the attraction of 3-fold symmetry and potentially a more open structure.

9.4.1. Structure and Characterisation

Triptycene is typically synthesised using a Diels-Alder reaction between anthracene and benzene. The triptycene unit (A2) was used as the catechol monomer in the dibenzodioxane formation with a porphyrin molecule that has fluorinated phenyl groups in the *meso*-positions (*meso*-tetrakis(pentafluorophenyl)porphyrin). McKeown *et al*. showed the porphyrin molecule reacted efficiently with the A1 monomer (5,5´,6,6´-tetrahydroxy-3,3,3´,3´-tetramethyl-1,1´-spirobisindane) and exhibited a greater surface area (980 $m^2 g^{-1}$) than PIM-1, which also contained the A1 monomer.[298]

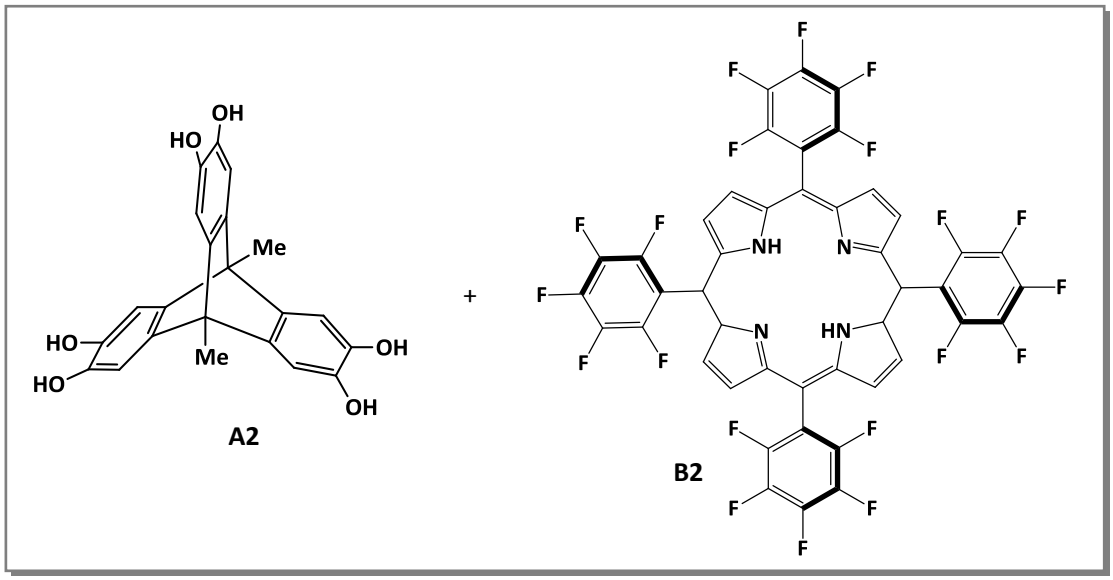

Figure 9.19 - Formation of the insoluble porphyrin-triptycene network PIM synthesised from 9,10-dimethyl-2,3,6,7,12,13-hexahydroxytriptycene (A2) plus meso-tetrakis(pentafluorophenyl)porphyrin (B2) monomer.

The degassing profile gave a mass loss of 3.0% up to 100 °C (in a UHV of *ca*. 10^{-6} mbar) as shown in Figure 9.20.

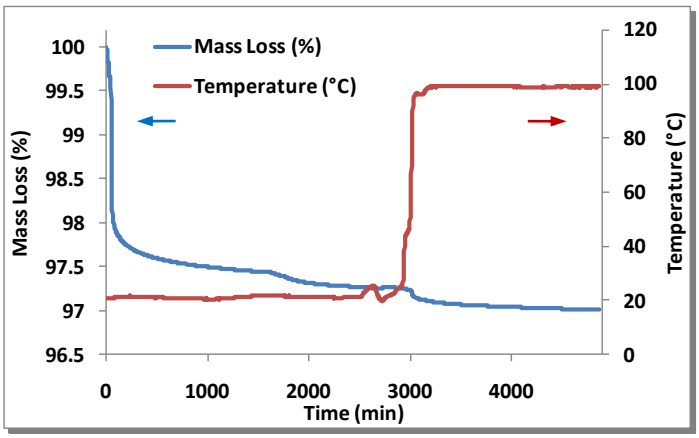

Figure 9.20 - Degassing profiles for the porphyrin-triptycene PIM (A2 + B2) measured on a Hiden IGA-001. A mass loss of ca. 3.0% was observed up to ca. 100 °C.

9.4.2. Gas Adsorption

9.4.2.1. Nitrogen

McKeown *et al*. showed that the porphyrin monomer coupled with 2 equivalents of the spirobisindane (A1) monomer was capable of a nitrogen uptake of *ca*. 220 $cm^3\ g^{-1}$ (STP) (9.8 mmol g^{-1}) at $p/p_0 = 0.1$ and a total nitrogen uptake of *ca*. 400 $cm^3\ g^{-1}$ (STP) (17.8 mmol g^{-1}) at $p/p_0 = 1$.[298] Figure 9.21 illustrates the comparatively superior nitrogen uptake of the porphyrin-triptycene network PIM, which exhibited a nitrogen uptake of *ca*. 370 $cm^3\ g^{-1}$ (STP) (16.5 mmol g^{-1}) at $p/p_0 = 0.1$ and a total nitrogen uptake of *ca*. 635 $cm^3\ g^{-1}$ (STP) (28.3 mmol g^{-1}) at $p/p_0 = 1$. The porphyrin-spirobisindane PIM was reported to have a BET surface area of 980 $m^2\ g^{-1}$.[298] The nitrogen adsorption isotherm (from Figure 9.21) was used to calculate the BET specific surface area of the porphyrin-triptycene PIM. The least squares method was used on the linear section of the BET plots to calculate a surface area of 1419.3 ± 6.7 $m^2\ g^{-1}$, indicating that the triptycene monomer has a significant influence on the BET surface area, possibly due to its 3-dimensoinal symmetry. Linear regression was also used to calculate a Langmuir surface area of 1672.5 ± 15.1 $m^2\ g^{-1}$.

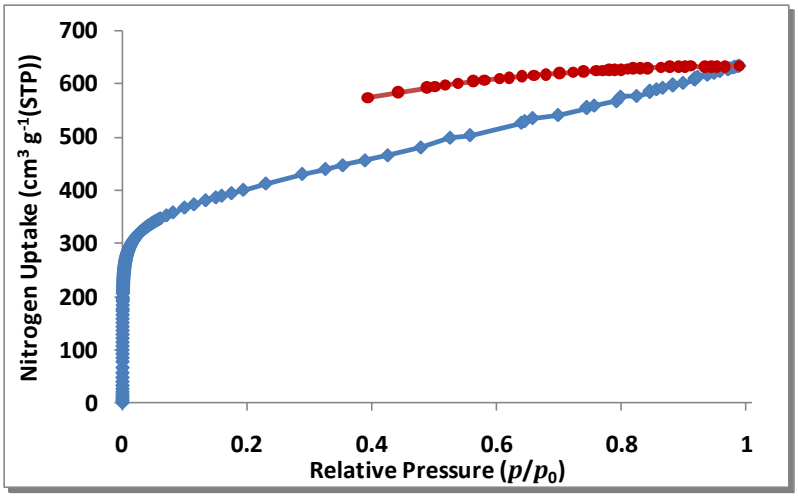

Figure 9.21 - Nitrogen adsorption (♦) and desorption (●) isotherms for the porphyrin-triptycene PIM at 77 K.

9.4.2.2. Hydrogen

9.4.2.2.1. Excess Adsorption

A skeletal density of 1.57 g cm^{-3} was determined by helium pycnometry at room temperature and subsequently used for the buoyancy correction. The hydrogen sorption isotherm for the Porphyrin-PIM is

shown in Figure 9.22. The material exhibited an excess gravimetric hydrogen uptake of 2.55 wt.% and 2.23 wt.% at 20 bar and 77 K and 87 K, respectively. To compare the results to PIM-1, the Porphyrin-PIM had an excess gravimetric hydrogen uptake of 2.48 wt.% and 2.14 wt.% at 15 bar and 77 K and 87 K, respectively.

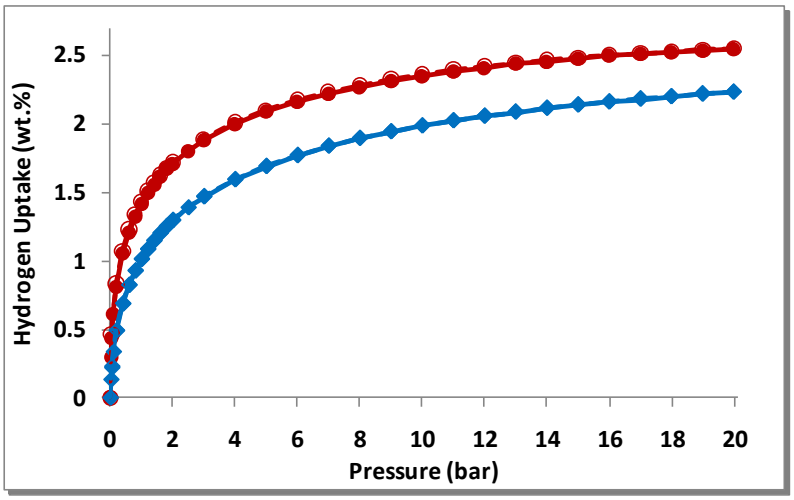

Figure 9.22 - Excess gravimetric hydrogen uptake for Porphyrin-PIM at 77 (●) and 87 K (♦) up to 20 bar. Full symbols indicate adsorption, open symbols indicate desorption.

The gravimetric hydrogen storage capacity (7.42 mmol g^{-1}) can be used in conjunction with the density of hydrogen at the triple point (0.077 g cm^{-3}) to calculate the volume of hydrogen adsorbed in the pores. The calculated volume of hydrogen adsorbed in PIM-1 was 0.331 cm^3 g^{-1}, representing a 66% filling of the micropore volume as calculated by the BET equation on the nitrogen adsorption isotherm (0.50 cm^3 g^{-1}). This micropore volume can also be used to determine the geometric density of the PIMs in conjunction with the measured skeletal density. The geometric density (0.87 g cm^{-3}) can then be used to calculate the (theoretical) volumetric storage capacity of 22.3 kg m^{-3} at 20 bar and 77 K. However, the interparticle void space would also need to be considered for a true volumetric capacity to be determined.

The conversion between the measured excess adsorption to the absolute amount adsorbed used equation (3.50). The Porphyrin-PIM exhibited an absolute hydrogen uptake of 2.78 and 2.41 wt.% at 20 bar and 77 and 87 K, respectively.

The Langmuir plot for Porphyrin-PIM at 77 K can be seen in Appendix F. The graph is taken to be linear from 2 to 20 bar, which enables it to be used to calculate the maximum amount adsorbed, n_m; this would be consistent with a plateau in absolute hydrogen adsorption isotherms. The analysis predicts that

Porphyrin-PIM will have a maximum hydrogen uptake of 14.88(9) mmol g^{-1}, which equates to 2.99(3) wt.%. Using the pore volume of 0.50 cm g^{-1}, at saturation the adsorbate phase density is estimated to be 0.059 g cm^{-3}, slightly less than that of liquid hydrogen.

9.4.2.2.2. Empirical Isotherm Equations

Figure 9.23 illustrates the application of the Sips and Tóth empirical isotherm equations to the absolute adsorption isotherm at 77 K. The residual plot of the fit indicates that neither fit is as close as was observed for PIM-1. The two models produce fairly substantial differences in their predicted saturation uptakes, which are 3.95(5) and 5.34(5) wt.%, for the Sips and Tóth models, respectively at 77 K.

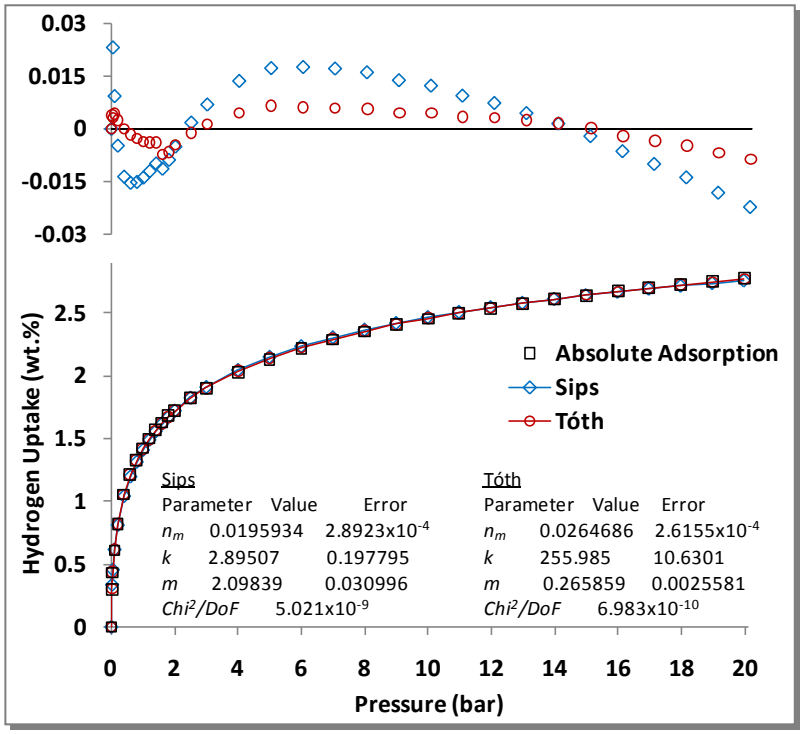

Figure 9.23 - Fitted Sips (◊) and Tóth (○) equations to the absolute hydrogen uptake versus pressure at 77 K up to 20 bar. Residual plots are shown at the top of the figure.

9.4.2.2.3. Enthalpy of Adsorption

9.4.2.2.3.1. Clausius-Clapeyron

The fitted 77 and 87 K absolute adsorption isotherms were used to calculate the enthalpy of adsorption using the Clausius-Clapeyron equation (see Figure 9.24). The enthalpy of adsorption is calculated up to 0.8 wt.% as explained in section 6.2.2.5.4. The two models give 11.9 and 8.4 kJ mol^{-1}, at near zero coverage of 0.02 wt.% of hydrogen, for the Sips and Tóth fits, respectively. This is not quite as high as was

observed by PIM-1 using the same techniques. However, as observed with other microporous materials the enthalpies of adsorption decrease sharply with increasing hydrogen uptake, with the two models both giving 6.08 and 6.04 kJ mol^{-1}, at 0.8 wt.%, which is about 0.5 kJ mol^{-1} lower than was observed for PIM-1.

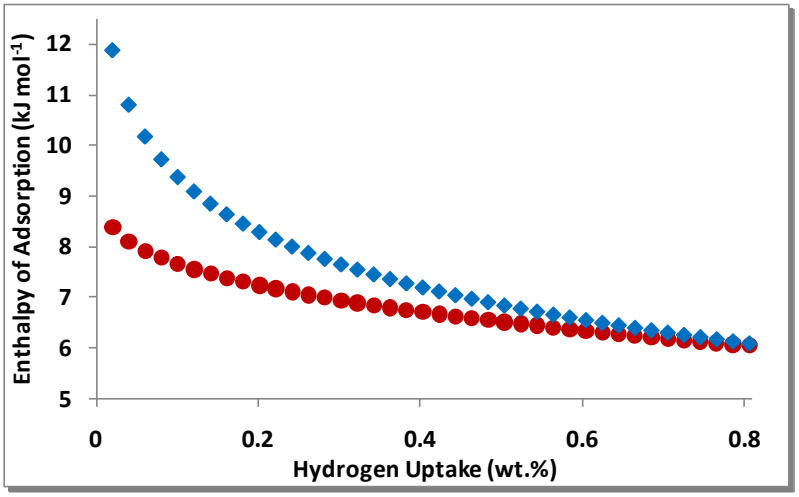

Figure 9.24 - Comparison of the enthalpy of adsorption versus hydrogen uptake for the Porphyrin-PIM, calculated using Clausius-Clapeyron equation (in conjunction with Sips (♦) and Tóth (●) equations fitted to the 77 and 87 K absolute isotherms).

9.4.2.2.3.2. Virial Type Thermal Equation

Equation (3.66) was used to fit the 77 and 87 K isotherms simultaneously using values of 6 and 3 for the coefficients m and n, respectively, as shown in Figure 9.25. The isosteric enthalpy of adsorption was subsequently calculated according to equation (3.67), as a function of hydrogen uptake, which can be seen in Figure 9.26. The analysis produces an isosteric enthalpy of adsorption at zero coverage for the Porphyrin-PIM of 7.6 kJ mol^{-1}. This is very similar to the hypercrosslinked polymers reported by Wood *et al.*[290] Similarly to the Clausius-Clapeyron method, the enthalpy of adsorption calculated using the virial type thermal equation, decreases sharply with increasing hydrogen uptake. At a hydrogen uptake of 0.8 wt.%, the enthalpy of adsorption is 6.1 kJ mol^{-1}, which is exactly between that found by the Sips and Tóth models, respectively (as previously mentioned, at the same hydrogen uptake).

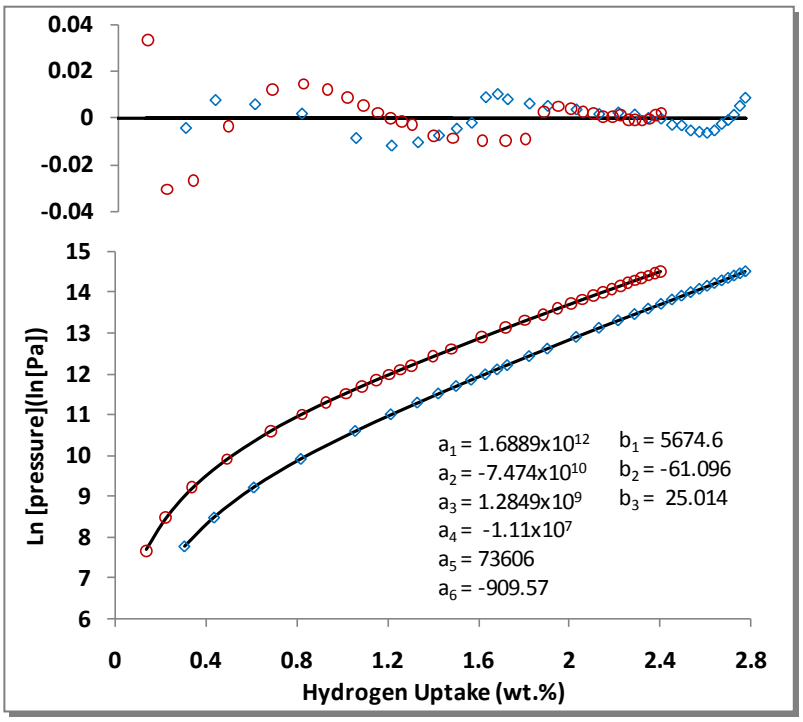

Figure 9.25 - Virial analysis of the hydrogen adsorption data at 77 (◊) and 87 K (○) for Porphyrin-PIM to 20 bar. Open symbols display data, with the solid line indicating the virial plots. Residual plots are shown at the top of the figure.

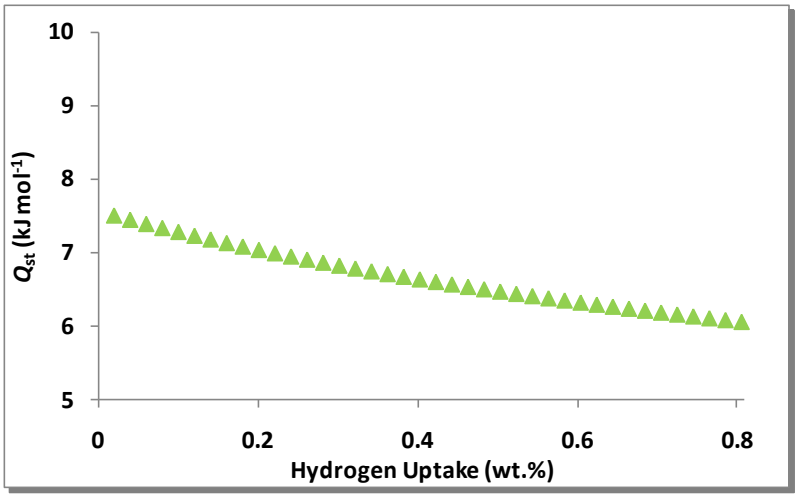

Figure 9.26 - Isosteric enthalpy of adsorption for the Porphyrin-PIM as a function of hydrogen uptake determined using the Virial type thermal equation with the 77 and 87 K.

Figure 9.27 displays a comparison for the previously determined enthalpies of adsorption with the virial type thermal equation using two temperatures (77 and 87 K). Similar enthalpy of adsorption curves were observed for the Tóth and Virial equations at low hydrogen uptake and all three fitting models produced extremely similar values by the time the hydrogen uptake had reached 0.8 wt.%. In fact, the three methods differed by less than 0.1 kJ mol^{-1}.

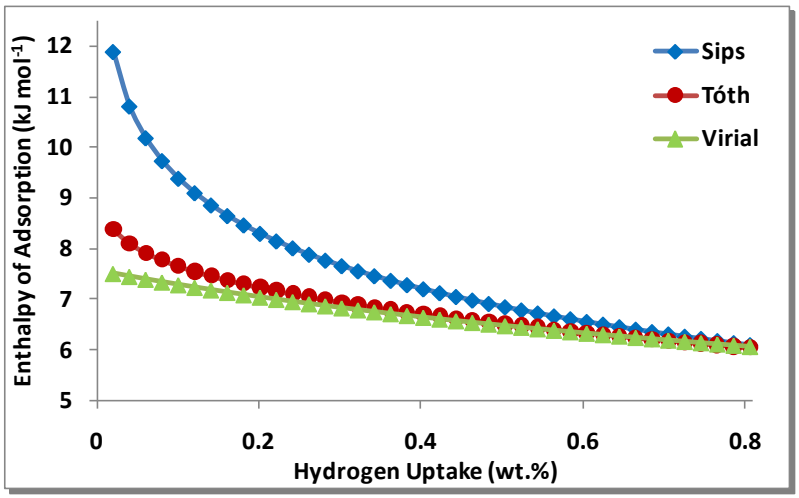

Figure 9.27 - A comparison of the isosteric enthalpy of adsorption for the Porphyrin-PIM as a function of hydrogen uptake using different fitting methods in conjunction with the 77 and 87 K.

9.5. Triptycene-based PIM Series

The porphyrin-triptycene PIM indicated that the triptycene monomer offered increased surface area compared to the spirobisindane monomer, and subsequently illustrated an increase in hydrogen uptake at 77 K. Different triptycene-based monomers were therefore used in conjunction with the B1 monomer as with PIM-1 to assess their impact on surface area and hydrogen uptake.

9.5.1. Structure and Characterisation

As mentioned previously the triptycene molecule is prepared from the anthracene molecule. The anthracene molecule can be prepared with a different substituent attached at each position. These anthracene precursors were used to provide a series of triptycene-based monomers with different alkyl chain groups attached to the bridgehead position (labelled 'R' in Figure 9.28). The triptycene series of PIMs were also synthesised from a catechol and 1,2-difluoro- aryl unit containing monomers as illustrated in Figure 9.28. The 9,10-dialkyl-2,3,6,7,12,13-hexahydroxytriptycene monomer (A2) and 2,3,5,6-tetrafluoroterephthalonitrile (B1) react via a dibenzodioxane formation when mixed with K_2CO_3 and DMF at 80 °C for 24 hours. A range of 9,10-dialkyl-2,3,6,7,12,13-hexahydroxytriptycene monomers (R = Me, Et, *n*-Pr, *i*-Pr, *n*-Bu, *i*-Bu, *t*-Bu, Pe, Oct, Bz) were synthesised via the Diels-Alder reaction. However, surprisingly where R = H, the Diels-Alder reaction was unsuccessful and so a different synthetic procedure was

utilised; a copper (I) bromide mediated reaction of 2,3,6,7,12,13-hexabromotriptycene with sodium methoxide.

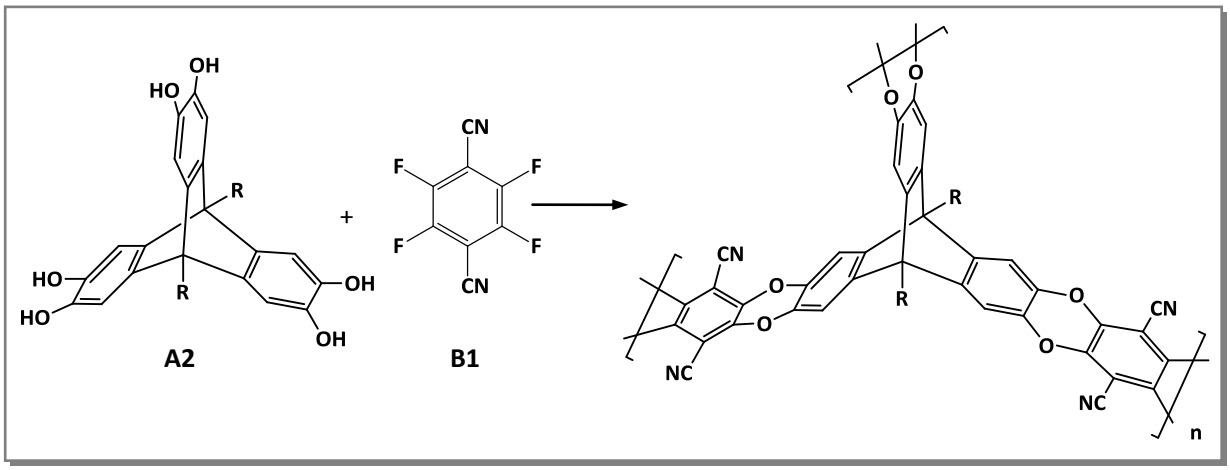

Figure 9.28 - Synthesis of the triptycene-based PIM (Trip(R)-PIM) series. Each monomer was individually prepared before reacting it with the 2,3,5,6-tetrafluoroterephthalonitrile monomer. Reagents and conditions: DMF, 80 °C, 24 hr.

Each of the Trip(R)-PIMs were a yellow/orange insoluble fine powder. Elemental analysis was performed by the synthetic group at the University of Cardiff, who found a lack of residual fluorine (F < 1.0%) which indicated efficient polymerisation (which was the same polymerisation reaction used in the formation of PIM-1). X-ray diffraction of the Trip(R)-PIMs confirmed their amorphicity.

9.5.1.3. Infrared Spectroscopy

The spectra for each member of the Trip(R)-PIM series showed the product material to be consistent with the expected structure of the network polymer. All of the samples were outgassed at 100 °C for *ca*. 1000 minutes before being analysed by infrared spectroscopy. Their spectra were all quite similar and showed no presence of either hydroxyl or carbonyl groups. An example of the assignments was taken from the recent publication in Macromolecules: IR (KBr cm^{-1}): ν = 3060, 3010, 2956, 2870 (C-H), 2235 (CN), 1610 (C-C Ar), 1170 and 1250 (C-O-C).[384] The infrared spectroscopy was performed at the University of Cardiff where each PIM was synthesised before being sent to the University of Birmingham. Raman spectroscopy was also performed on the degassed straight alkyl chain triptycene-based PIMs. This is shown in Appendix B.

9.5.1.4. TGA

Thermogravimetric analysis (performed at the University of Cardiff) of the Trip(R)-PIMs confirmed they did not undergo thermal decomposition up to 400 °C. Examples of the degassing profiles for two Trip(R)-PIMs are displayed in Figure 9.29. The Trip(R)-PIM series typically show a loss of around 3 to 4%.

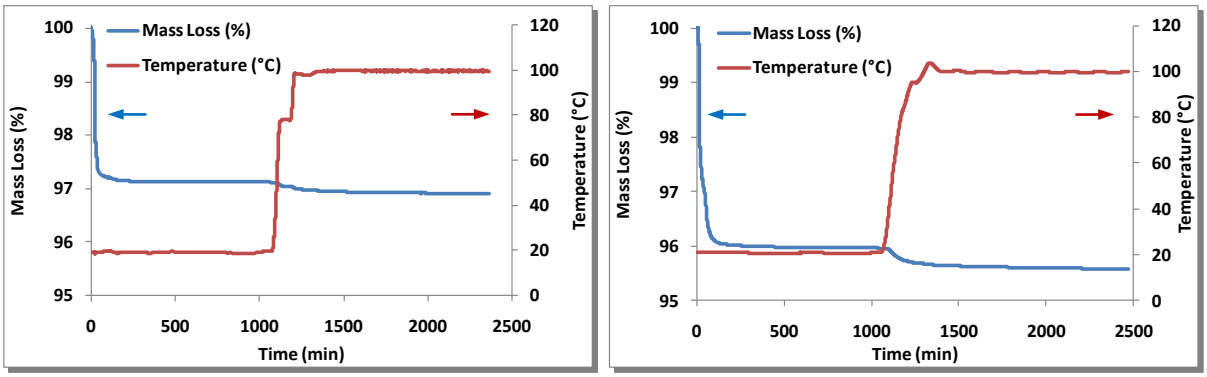

Figure 9.29 - Degassing profiles for the Me- (left) and Bz-substituted (right) Trip(R)-PIMs measured on a Hiden IGA-001. A mass loss of ca. 3 and 4%, respectively, was observed up to ca. 100 °C.

9.5.2. Gas Adsorption

The Trip(Me)-PIM sample was sent to Professor Andrew Cooper's group at the University of Liverpool in order for them to independently verify the nitrogen and hydrogen sorption properties of the material. The group also provided methane adsorption at 0 °C and room temperature.

9.5.2.1. Nitrogen

Nitrogen adsorption was performed at 77 K after being outgassed at 100 to 120 °C for 8 to 12 hours. The series showed impressive nitrogen uptake at low relative pressures ($p/p_0 < 0.1$); the lowest of which was the Trip(Oct)-PIM which showed a similar uptake to that of PIM-1. The most significant difference that can be observed across the series (apart from the absolute uptake values), is the change in shape in the adsorption isotherm as the alkyl group changes. Indeed, the Trip(Oct)-PIM, which contains the long octyl-chain shows an isotherm that is almost Type I in nature (according to the IUPAC classification). Whereas, with a very small alkyl group (as with the Trip(Me)-PIM), nitrogen is continually adsorbed above the relative pressure of 0.1, and in fact rises reasonably sharply up to a total of 945.4 $cm^3\ g^{-1}$ (STP) (42.2 mmol g^{-1}) at a $p/p_0 = 1$. The long alkyl chain containing Trip(R)-PIMs also exhibit less hysteresis than

those which contain short alkyl chains. This suggests that longer chains or more bulky groups restrict the ability of the PIM chains to shift and potentially swell with an increasing pressure of gas rather than being associated with mesopores. The nitrogen adsorption and desorption isotherms can be seen in Figure 9.30 and Figure 9.31, with uptake values being listed in Table 9.1.

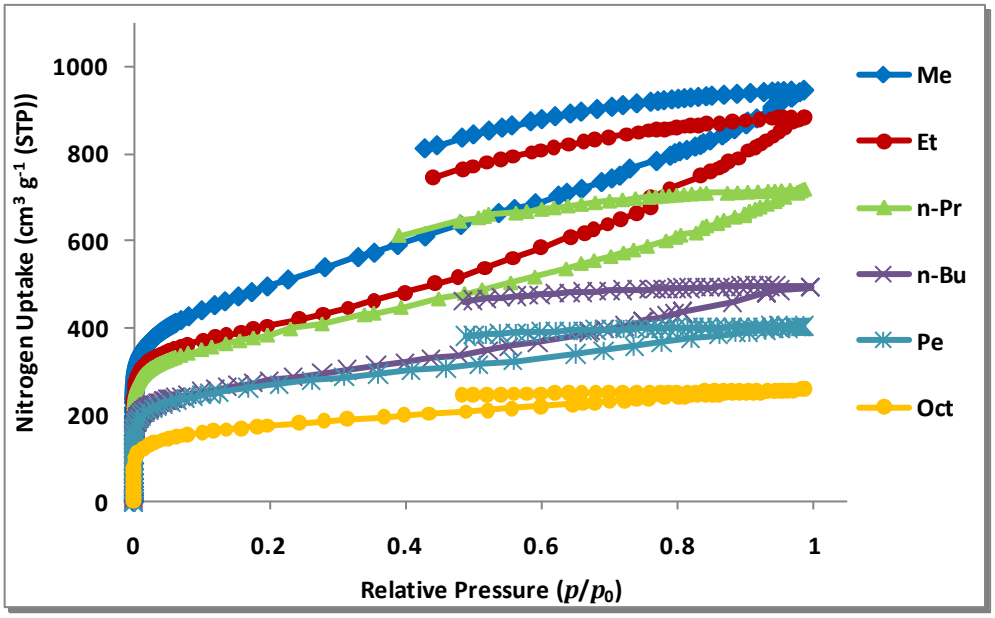

Figure 9.30 - Nitrogen sorption data for the straight chain Trip(R)-PIMs at 77 K.

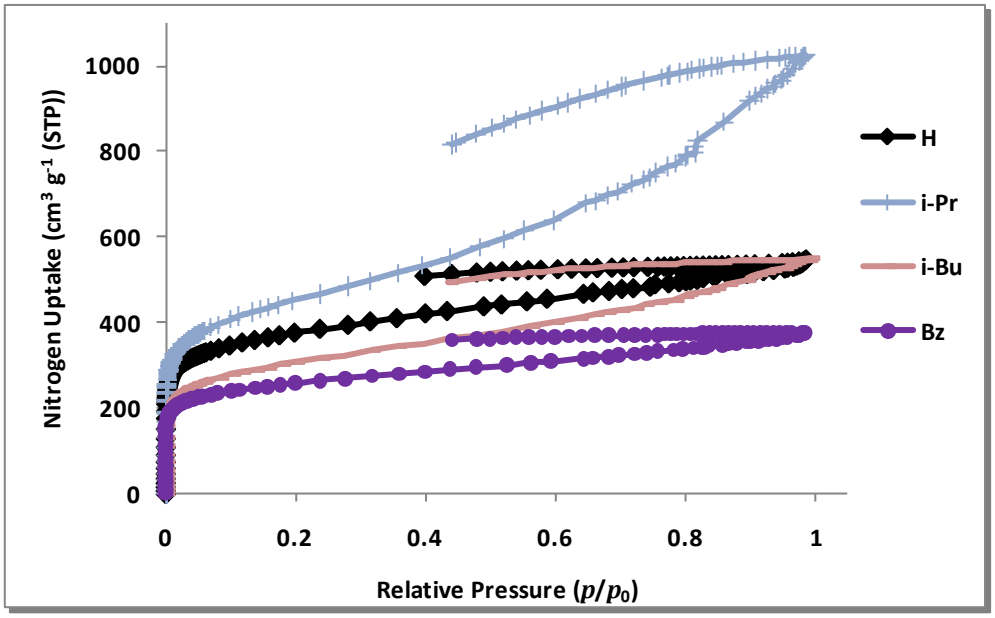

Figure 9.31 - Nitrogen sorption data for the branched chain Trip(R)-PIMs and Trip(H)-PIM, at 77 K.

The nitrogen adsorption isotherm was used to calculate the apparent surface areas of the Trip(R)-PIMs. Least squares linear regression was used between 0.05 and 0.2 p/p_0 to give a BET surface area values, which range from 1759.6 $m^2 g^{-1}$ (for the Trip(Me)-PIM) to 618.1 $m^2 g^{-1}$ (for the Trip(Oct)-PIM); the values are presented in Table 9.1. It is worth noting that the increase in surface area does not completely extend through the series down to R = H, which suggest that the alkyl group alone is of significance in creating microporosity within the structure of the network polymer.

The effect of the branched alkyl chains bring about increased microporosity in comparison to their straight alkyl chain counterpart. This is seen with a greater surface area and overall nitrogen uptake for the Trip(*i*-Pr)-PIMs in comparison with Trip(*n*-Pr)-PIM. The effect (although to a lesser extent) was also observed for the Trip(*i*-Bu)-PIM over Trip(*n*-Bu)-PIM.

Table 9.1 - Nitrogen adsorption data for the Trip(R)-PIMs at 77 K. The surface areas were calculated using the linear region between 0.05 and 0.2 p/p_0 and upto to 0.2 p/p_0 for the BET and Langmuir methods, respectively. Nitrogen uptake values were taken at p/p_0 = 1.

R-group	Surface Area / $m^2 g^{-1}$		Nitrogen uptake /	
	BET	Langmuir	$cm^3 g^{-1}$ (STP)	mmol g^{-1}
H	1315.6 ± 10.9	1592.7 ± 17.6	545.6	24.3
Me	1759.6 ± 5.7	2053.3 ± 28.1	945.4	42.2
Et	1414.2 ± 9.4	1712.3 ± 20.8	884.9	39.5
n-Pr	1343.2 ± 8.4	1617.3 ± 20.0	718.6	32.1
i-Pr	1596.9 ± 11.4	1896.6 ± 24.6	1025.0	45.7
n-Bu	978.0 ± 5.8	1156.9 ± 12.5	494.0	22.0
i-Bu	1074.2 ± 8.0	1300.9 ± 18.3	548.5	24.5
Pe	946.5 ± 7.8	1099.9 ± 15.1	402.9	18.0
Oct	618.1 ± 4.5	754.7 ± 16.6	259.0	11.6
Bz	889.4 ± 8.1	1096.6 ± 11.4	360.9	16.1

The Horváth-Kawazoe (slit pore) method was used to analyse the low-pressure nitrogen adsorption data to calculate a micropore size distribution for Trip(Me)-PIM, shown in Figure 9.32. The analysis confirmed the lack of a distinct pore size, and the presence of a distribution of pore sizes that was biased towards pores in the range around 0.6 to 0.7 nm. Unfortunately, due to equipment problems, additional pore size distributions for this series of triptycene-based PIMs could not be determined.

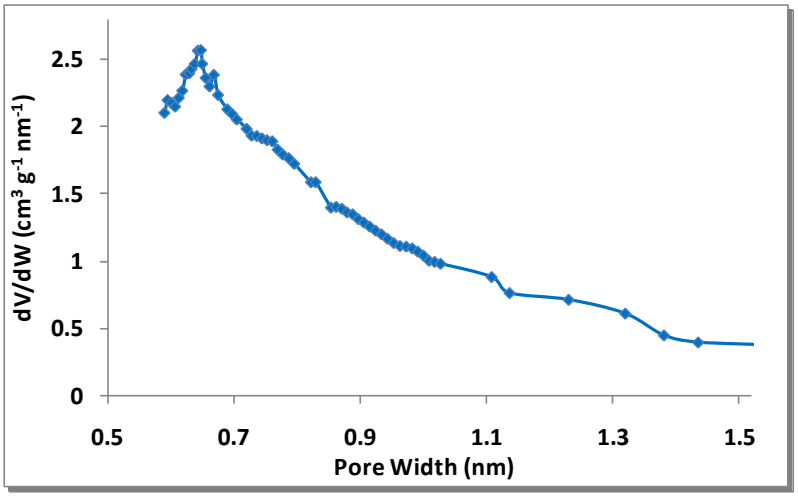

Figure 9.32 - Micropore size distribution for Trip(Me)-PIM based on the Horváth-Kawazoe analysis of low pressure nitrogen adsorption data showing that the major contribution to porosity is from pores that are less than 1 nm in diameter.

9.5.2.2. Hydrogen

9.5.2.2.1. Excess Adsorption

The Trip(R)-PIMs were initially degassed for *ca*. 1000 minutes at room temperature followed by a further 1000 minutes at 100 °C. Although the mass loss had not completely 'levelled-off', previous hydrogen storage measurements had shown that differences in the microgramme range had little effect on the gravimetric hydrogen storage capacity. This, coupled with pressure on equipment time, meant that fully degassing materials was not always possible.

In order to correct the hydrogen sorption data from the effect of buoyancy, helium pycnometry was performed (at room temperature) on the Trip(R)-PIMs to assess their skeletal densities. The analysis was performed after hydrogen sorption measurements so that the material had been degassed prior to pycnometry. The measured densities were determined to be between 1.27 and 1.67 g cm^{-3} (Table 9.2). The increase in alkyl chain length appears to be related to the decrease in network density of the polymer.

The sorption isotherm in Figure 9.33 shows an excess gravimetric hydrogen uptake range of 3.40 wt.% for the Trip(Me)-PIM to 1.29 wt.% for the Trip(Oct)-PIM at 77 K and 18 bar. Figure 9.33 also displays the excess gravimetric hydrogen uptake for the same series of PIMs at 87 K. All of the materials were outgassed again at 100 °C for a further 1000 minutes between hydrogen measurements. The two figures

show a trend of decreasing hydrogen uptake across the homologous series, which seems to correlate with the BET surface areas of the materials (see Table 9.1). Values for the hydrogen uptake at 77 and 87 K, at 1, 10 and 18 bar are given in Table 9.2. All of the triptycene-base PIMs exhibited no hysteresis between the adsorption and desorption isotherms.

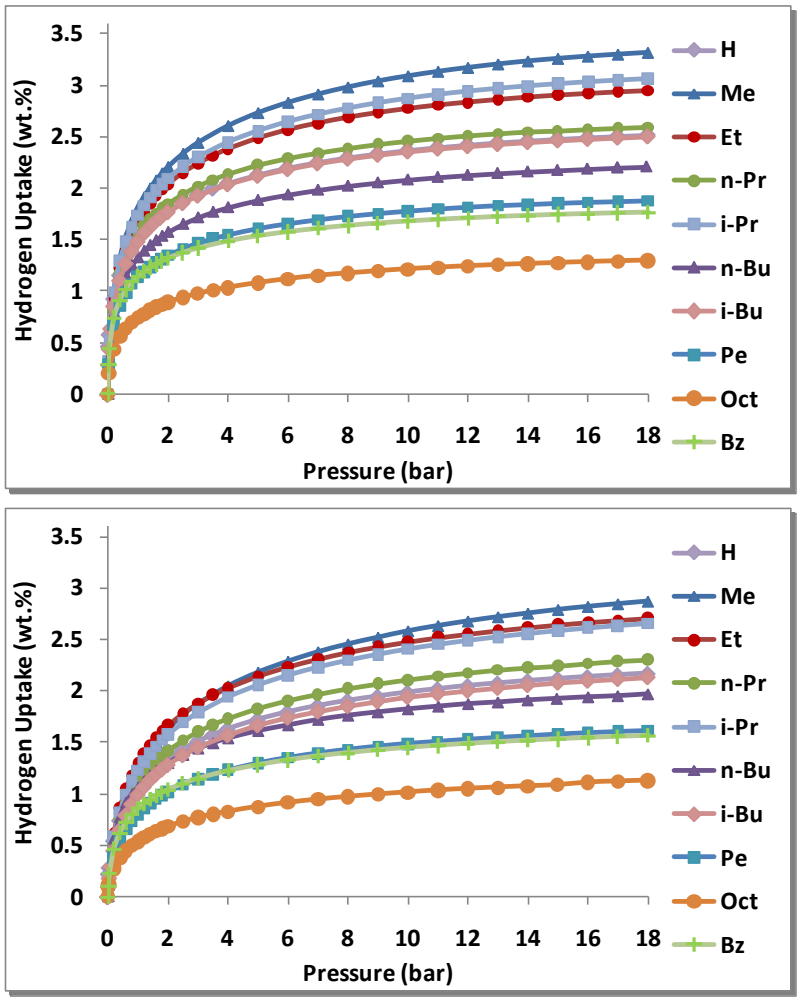

Figure 9.33 - Excess gravimetric hydrogen adsorption isotherms for Trip(R)-PIM series at 77 (top) and 87 K (bottom) up to 18 bar.

Table 9.2 - Excess gravimetric hydrogen adsorption data at 1, 10 and 18 bar, at 77 and 87 K for the Trip(R)-PIMs. The skeletal densities (which were used for the buoyancy correction) were determined by helium pyconometry at room temperature.

R-group	Skeletal Density	Temp.	Hydrogen Uptake					
			1 bar		10 bar		18 bar	
	g cm^{-3}	K	wt.%	*(mmol g^{-1})*	wt.%	*(mmol g^{-1})*	wt.%	*(mmol g^{-1})*
H	1.57	77	1.50	*(7.46)*	2.37	*(11.76)*	2.52	*(12.50)*
		87	1.07	*(5.29)*	1.98	*(9.84)*	2.17	*(10.75)*
Me	1.67	77	1.81	*(8.97)*	3.09	*(15.32)*	3.32	*(16.45)*
		87	1.33	*(6.61)*	2.63	*(13.05)*	2.89	*(14.33)*
Et	1.40	77	1.68	*(8.34)*	2.77	*(13.77)*	2.95	*(14.62)*
		87	1.29	*(6.42)*	2.48	*(12.29)*	2.71	*(13.43)*
n-Pr	1.40	77	1.55	*(7.70)*	2.46	*(12.18)*	2.59	*(12.85)*
		87	1.11	*(5.52)*	2.11	*(10.46)*	2.30	*(11.42)*
i-Pr	1.54	77	1.74	*(8.61)*	2.87	*(14.25)*	3.06	*(15.19)*
		87	1.12	*(5.56)*	2.41	*(11.95)*	2.66	*(13.18)*
n-Bu	1.48	77	1.32	*(6.57)*	2.08	*(10.31)*	2.21	*(10.94)*
		87	1.06	*(5.26)*	1.83	*(9.05)*	1.97	*(9.78)*
i-Bu	1.43	77	1.48	*(7.34)*	2.35	*(11.67)*	2.50	*(12.40)*
		87	0.99	*(4.91)*	1.94	*(9.63)*	2.13	*(10.58)*
Pe	1.48	77	1.13	*(5.63)*	1.78	*(8.81)*	1.88	*(9.31)*
		87	0.80	*(3.97)*	1.49	*(7.38)*	1.61	*(8.00)*
Oct	1.27	77	0.74	*(3.67)*	1.21	*(6.01)*	1.29	*(6.42)*
		87	0.54	*(2.67)*	1.01	*(5.02)*	1.13	*(5.59)*
Bz	1.43	77	1.15	*(5.68)*	1.68	*(8.32)*	1.76	*(8.75)*
		87	0.86	*(4.24)*	1.45	*(7.18)*	1.56	*(7.76)*

Figure 9.34 displays how the linear correlation of hydrogen uptake with the BET specific surface area does not occur at low pressures (e.g. 1 bar) but does correlate at higher pressures (e.g. 18 bar). Chahine's Rule suggests that for every 500 m^2 g^{-1} the maximum hydrogen storage capacity increases by 1 wt.%[162] (represented in Figure 9.34).

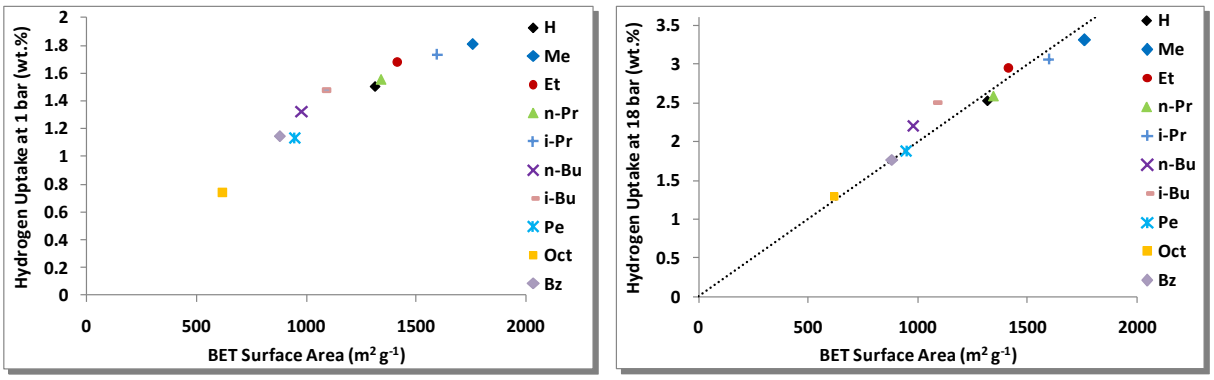

Figure 9.34 - Hydrogen uptake of the Trip(R)-PIMs against BET surface area at 1 (left) and 18 bar (right) at 77 K. The dashed line represents Chahine's rule.[162]

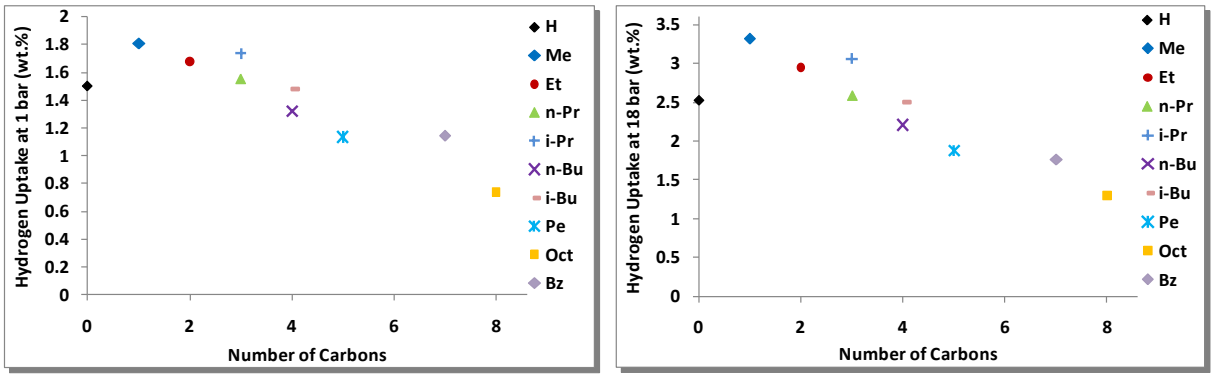

Figure 9.35 - Effect of alkyl group on hydrogen adsorption at 1 (left) and 18 bar (right) at 77 K.

For each Trip(R)-PIM, the amount of hydrogen adsorbed at 10 bar is very similar to the amount of nitrogen adsorbed at low relative pressure (p/p_0 = 0.01), as both values depend upon the number of accessible micropores. By 18 bar, the amount of hydrogen adsorbed was less than the amount of nitrogen adsorbed at p/p_0 = 1. The calculated BET micropore capacities occur just below p/p_0 = 0.1 for all of the Trip(R)-PIMs.

The gravimetric hydrogen storage capacity was used in conjunction with the density of hydrogen at the triple point (0.077 g cm^{-3}) to calculate the volume of hydrogen adsorbed in the pores. Using these volumes (calculated by the BET method), the percentage of the filled pores ranged from 68 to 84%, with the highest being for the triptycene-based PIM with the iso-butyl.

The Langmuir micropore capacities were also calculated. These were about 20% greater than those calculated using the BET method (see Appendix G) and in no case did the concentration of hydrogen (at 18 bar and 77 K) exceed the Langmuir micropore capacity. If these PIMs were capable of swelling under increased hydrogen pressures then the predicted maximum hydrogen capacities would be severely underestimated. If the PIMs were to swell at higher pressures then Type I isotherms would not be observed. Instead, a composite isotherm of Type I and Type IV might be produced (similar to that produced by a material containing micropores and mesopores). This would give a sloping absolute adsorption isotherm with a pronounced hysteresis.

The geometric density of the PIMs can be determined using the measured skeletal density and the calculated micropore volume using the nitrogen adsorption isotherm. This can then be used to calculate

the volumetric storage capacity of the PIMs. For the Trip(Me)-PIM this gave a geometric density of 0.81 g cm^{-3} and (theoretical) volumetric capacity of 27.2 kg m^{-3} at 20 bar and 77 K.

The Trip(Me)-PIM exhibited the highest hydrogen uptake and therefore was used to measure the hydrogen storage capacity at different temperatures, as presented in Figure 9.36. The decrease in hydrogen uptake with increasing temperature is characteristic of porous materials. This is illustrated by plotting hydrogen uptake at different pressures against temperature, (see Figure 9.36).

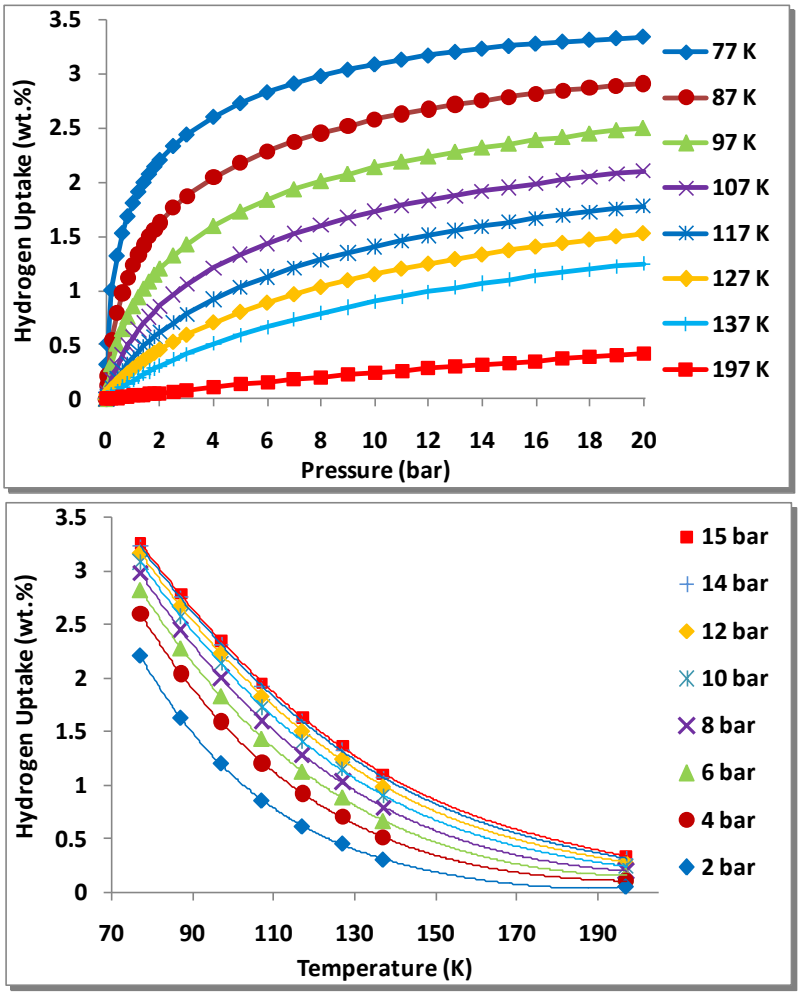

Figure 9.36 - (Top) Variable temperature excess gravimetric isotherms for the Trip(Me)-PIM up to 18 bar. (Bottom) Excess gravimetric hydrogen uptake against temperature at different pressures.

9.5.2.2.2. Absolute Adsorption

The conversion between the measured excess adsorption and the absolute amount adsorbed assumes the density of the adsorbed phase is equal to hydrogen at the triple point (0.077 g cm^{-3}), see section 3.6.2.1. Figure 9.37 displays an example of the difference between the excess and absolute adsorption at

77 K for one of the triptycene-based PIMs. For R = Me, the Trip-PIM exhibited an absolute hydrogen uptake of 3.67 wt.% at 18 bar and 77 K.

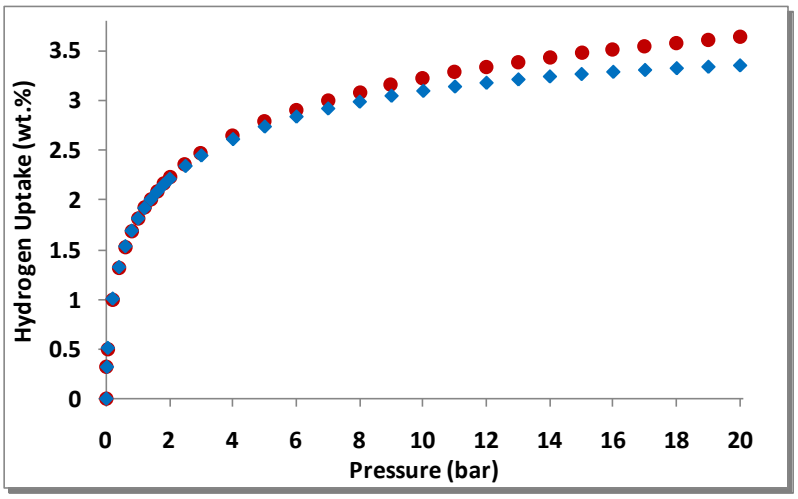

Figure 9.37 - Difference between excess (♦) and absolute (●) hydrogen uptake against pressure up 20 bar at 77 K using the adsorbed phase density of hydrogen at the triple point (0.077 g cm^{-3}).

9.5.2.2.3. The Langmuir Isotherm

The Langmuir plots for the Trip(R)-PIM series can be seen in the Figure 9.38. Least squares linear regression was performed between 2 to 20 bar to calculate a theoretical maximum hydrogen uptake, n_m (see Table 9.3); this would be consistent with a plateau in absolute hydrogen adsorption isotherms. Individual Langmuir plots are shown in Appendix F.

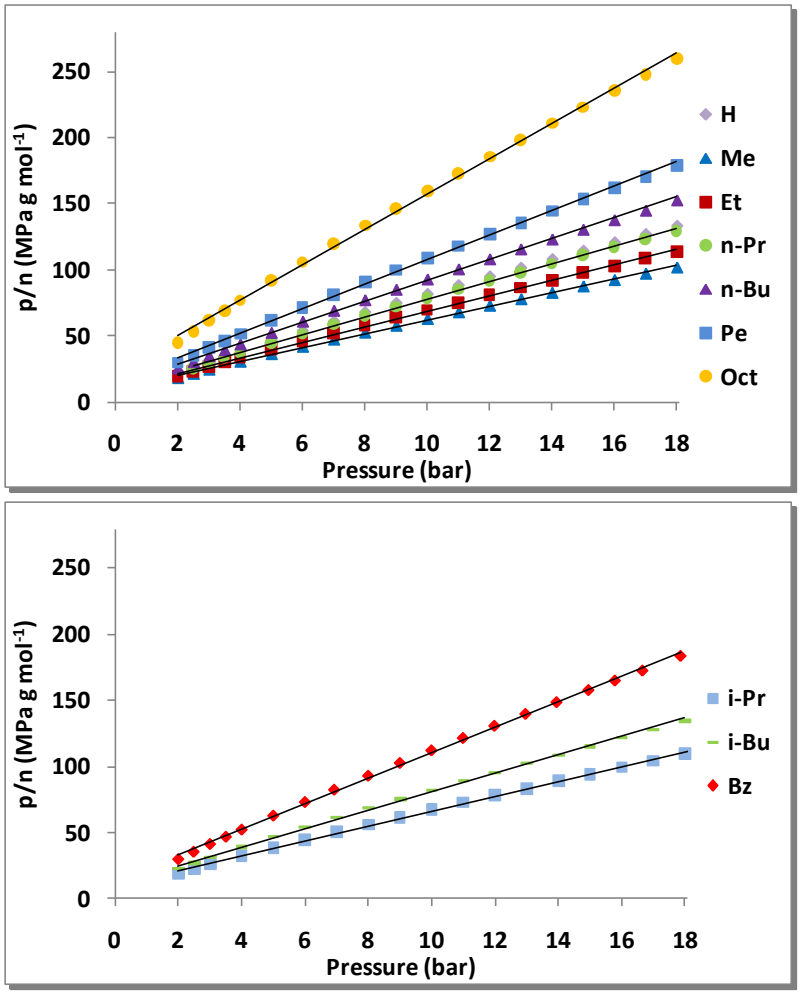

Figure 9.38 - Linearised Langmuir plots for the hydrogen adsorption of the Trip(R)-PIM series at 77 K. Straight chain alkyl groups (top) are separated from branched alkyl groups (bottom) for clarity.

Table 9.3 - Maximum absolute hydrogen uptake as determined by the linearised langmuir equation of the 77 K for the Trip(R)-PIMs. Errors shown are equal to one standard deviation.

R-group	Maximum Hydrogen Uptake (n_m) / wt.%			Maximum Hydrogen Uptake (n_m) / mmol g^{-1}		
H	2.91	±	0.03	14.51	±	0.13
Me	3.90	±	0.04	19.36	±	0.19
Et	3.43	±	0.03	17.03	±	0.14
n-Pr	3.00	±	0.02	14.87	±	0.11
i-Pr	3.58	±	0.03	17.77	±	0.16
n-Bu	2.54	±	0.02	12.58	±	0.11
i-Bu	2.90	±	0.03	14.39	±	0.13
Pe	2.17	±	0.02	10.77	±	0.08
Oct	2.51	±	0.02	7.50	±	0.07
Bz	2.09	±	0.02	10.36	±	0.09

9.5.2.2.4. Empirical Isotherm Equations

The Sips and Tóth empirical isotherm equations were applied to the absolute adsorption isotherm for each triptycene-based PIM, at each measured temperature. Both equations appear to produce good fits for the 77 K isotherm, but residual plots illustrate the differences between the data and the fitted model. An example is shown for the Trip(Me)-PIM in Figure 9.39, residual traces for all of the Trip(R)-PIMs can be found in Appendix E. The residual plots for the Trip(Me)-PIM indicate that the two equations produce an excellent fit to the absolute adsorption isotherm (at 77 K), with both models being within ±0.02, except in the very low pressure region for the Sips model. The Tóth model appears to stick closer to the absolute isotherm across the range. The two models produce fairly significant differences in their predicted saturation uptakes, which are 5.13(4) and 6.08(5) wt.%, for the Sips and Tóth models, respectively at 77 K.

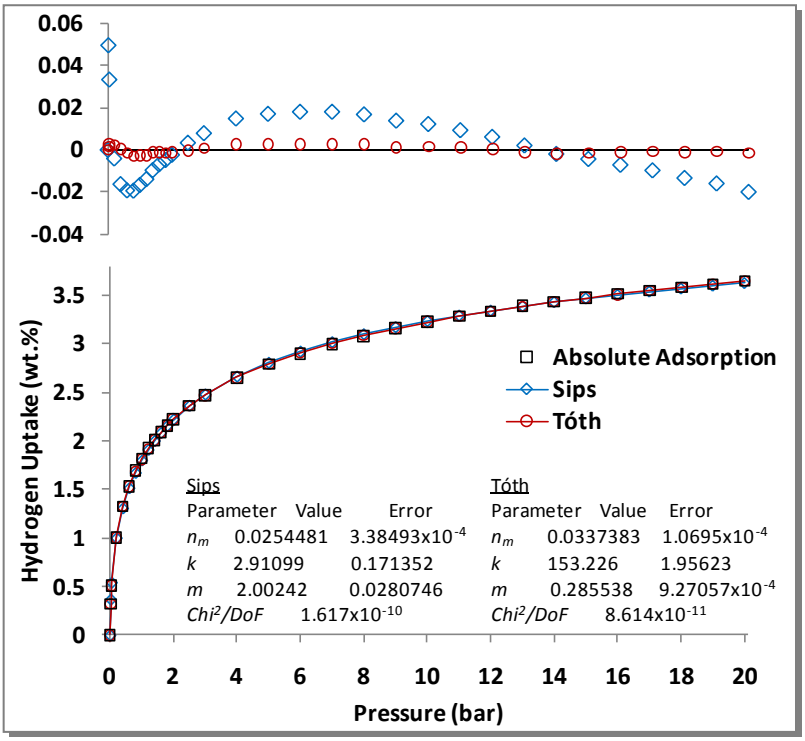

Figure 9.39 - Fitted Sips and Tóth equations to the absolute hydrogen uptake versus pressure at 77 K up to 18 bar for Trip(Me)-PIM. Residual plots are shown at the top of the figure.

9.5.2.2.5. Enthalpy of Adsorption

9.5.2.2.5.3. Clausius-Clapeyron

The fitted 77 and 87 K absolute adsorption isotherms were used to calculate the enthalpy of adsorption using the Clausius-Clapeyron equation. The enthalpy of adsorption is calculated up to 0.8 wt.% as explained in section 6.2.2.5.4. The analysis shows high enthalpies of adsorption for the Trip(H)-PIM with a value of 15.2 and 10.5 kJ mol^{-1}, at the near zero coverage of 0.02 wt.% of hydrogen, for the Sips and Tóth fits, respectively. The enthalpies of adsorption from the Sips model decrease sharply with increasing hydrogen uptake, and begin to converge with the Tóth model by *ca*. 0.8 wt.%. At low hydrogen uptake, the enthalpy of adsorption decreases with increasing alkyl chain length from R = H, to R = *n*-Bu. However, the triptycene-based PIMs that have long or branched alkyl groups display a higher enthalpy of adsorption. Figure 9.40 shows a comparison of the enthalpy of adsorption for the Trip(R)-PIMs after the 77 and 87 K absolute isotherm data was fitted with the Sips and Tóth models, in conjunction with the Clausius-Clapeyron method.

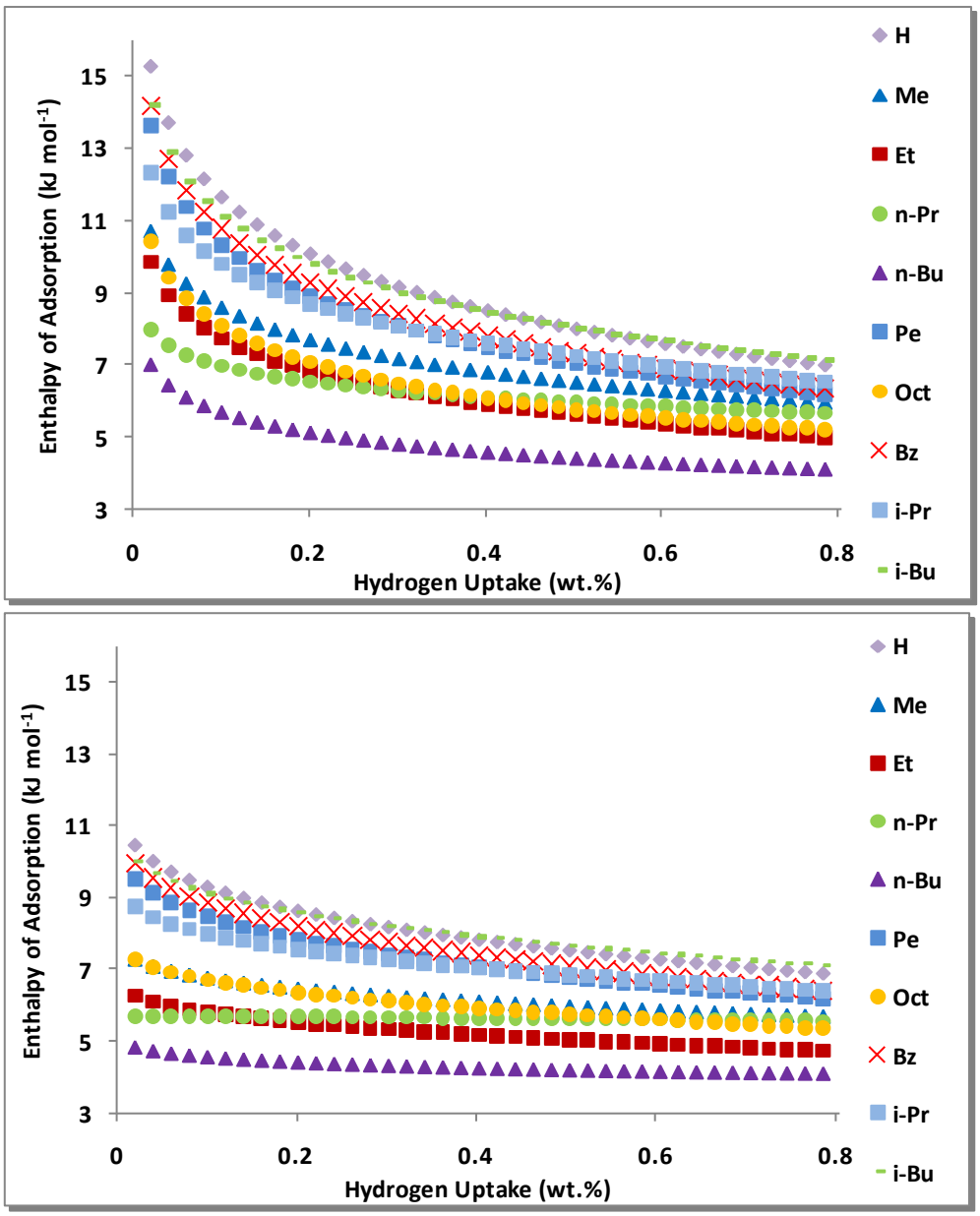

Figure 9.40 - Comparison of the enthalpy of adsorption determined using the Clausius-Clapeyron equation (in conjunction with Sips (top) and the Tóth equations (bottom) fitted to the 77 and 87 K absolute isotherms).

The absolute isotherms, at various temperatures, for Cu-BTC were fitted to both the Sips and Tóth models. The resulting fitted data was plotted as $\ln(p)$ against $1/T$ to produce van't Hoff plots at regular intervals of hydrogen uptake. The gradient of each line was taken, and converted in to a value for the enthalpy of adsorption for that specific amount of hydrogen uptake. Figure 9.41 shows the resulting enthalpy of adsorption against absolute hydrogen uptake, for both the Sips and Tóth models. The standard deviation in the van't Hoff plots was also converted in to a value for enthalpy of adsorption, and

subsequently used as the error at each specific hydrogen capacity. This analysis produced enthalpy of adsorption values of 9.8 and 7.7 kJ mol^{-1} at the near zero coverage of 0.02 wt.% for the Sips and Tóth models, respectively. The enthalpy of adsorption from the Sips model decreases sharply with increasing hydrogen uptake, and becomes close to convergence with the Tóth model by *ca*. 0.8 wt.%. In fact here the Sips and Tóth models produce enthalpies of adsorption values of 6.2 and 6.1 kJ mol^{-1}, respectively, at which point the two values are within the associated error of the other model.

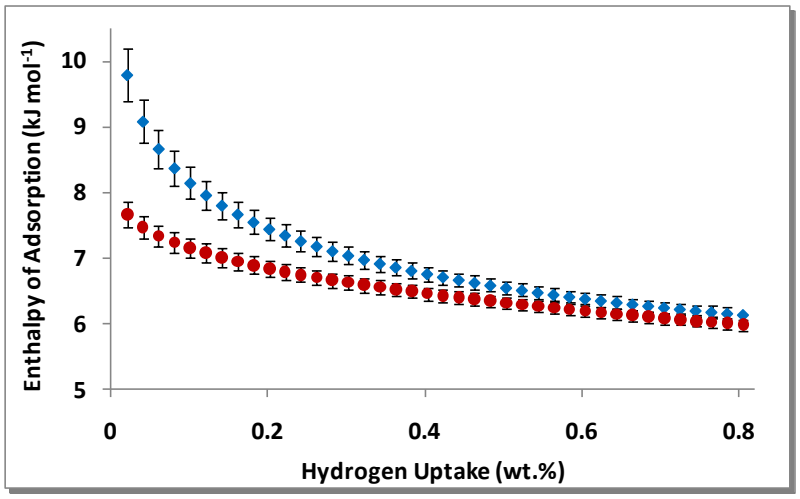

Figure 9.41 - Enthalpy of adsorption versus hydrogen uptake for the Trip(Me)-PIM. Using the Sips (♦) and Tóth (●) models to fit the absolute isotherms (at 77 to 137 K, at 10 K steps). The Clausius-Clapeyron equation and van't Hoff plot were then used to determine the enthalpy of adsorption. Error bars indicate one standard deviation of the van't Hoff plot.

9.5.2.2.5.4. Virial Type Expansion Equation

Figure 9.42 shows the virial plots for the hydrogen adsorption in the triptycene PIM series at 77 K. Least squares linear regression was performed (on the linear section from 0.4 to 5 bar), allowing the A_0 and A_1 values to be determined from the intercepts and gradients respectively (values are given in Table 9.4). The values of the first virial coefficient, A_0, appears to indicate a decreasing adsorbate-adsorbent interaction where the alkyl group increases in size from R = Me. However, the large alkyl groups appear to have strong adsorbate-adsorbent interactions. The Trip(Bz)-PIM shows the least negative A_0 coefficient and therefore highest Henry's law constant (shown in Table 9.4). This is reflected in this material exhibiting the highest enthalpy of adsorption as determined using this technique. For each material, k_H is greater at 77 K than at 87 K, which indicates a stronger adsorbate-adsorbent interaction at the lower

temperature. Equally the adsorbate-adsorbate interactions are stronger at 77 K than 87 K, as indicated by the second virial coefficient A_1. The A_1 parameter increases to larger negative values with the increasing length of the alkyl chain. This indicates an increased adsorbate-adsorbate interaction caused by the increasing steric hindrance of the functional group. This is observed by the different gradients in the Virial plots (see Figure 9.43). This could be related to the increasing pore size, but does show the dependence of the second virial parameter on the functional group.

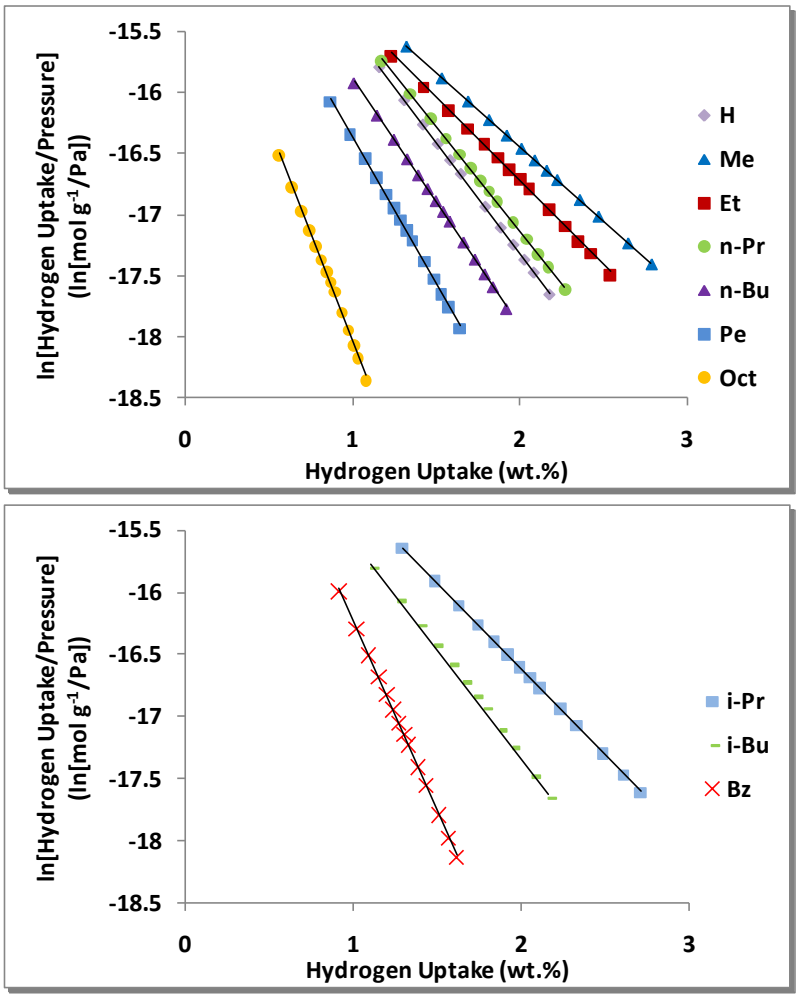

Figure 9.42 - Virial plots for the adsorption of hydrogen in the straight (top) and branched (bottom) Trip(R)-PIM series at 77 K.

The isosteric enthalpies of adsorption, Q_{st}, (shown in Table 9.4) were calculated from the A_0 parameter from the 77 and 87 K data and plotting them against $1/T$ (see Figure 9.43). It is important to note that the Q_{st} values determined here should only be used for guidance and not an accurate indication for the isosteric enthalpy of adsorption due to the small number of temperatures used.

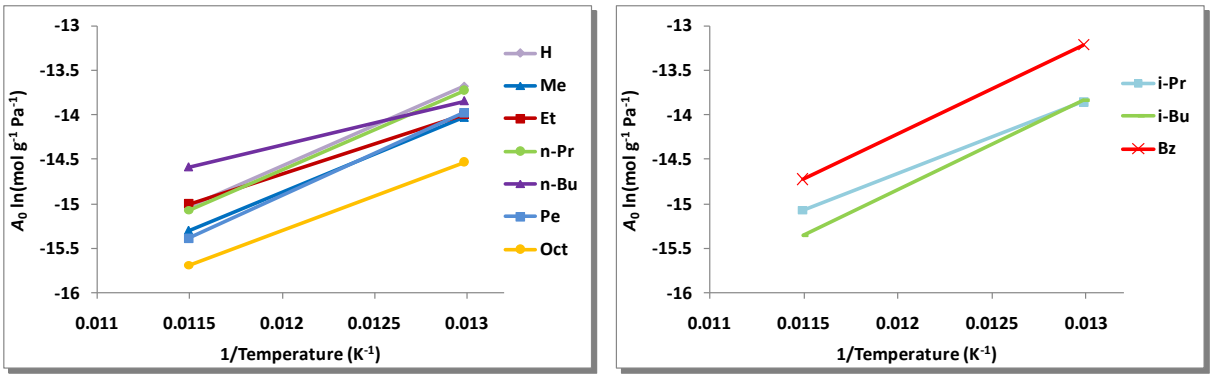

Figure 9.43 - First virial coefficient (A_0) in the Trip(R)-PIM series from the 77 K hydrogen adsorption data.

Table 9.4 - Henry's law constant and Virial parameters A_0 and A_1 for hydrogen adsorption on Trip(R)-PIM series at 77 and 87 K, and the resulting enthalpy of adsorption. The errors shown are equal to one standard deviation. [Errors on the Q_{st} are not given as they are deemed immaterial as only two temperatures were used].

R-group	Temp.	k_H	A_0	A_1	Q_{st}
	K	mol g^{-1} Pa^{-1}	ln(mol g^{-1} Pa^{-1})	g mol^{-1}	kJ mol^{-1}
H	77	1.15E-06	-13.68 ± 0.01	-366.51 ± 1.23	7.6
	87	2.95E-07	-15.04 ± 0.00	-325.91 ± 0.72	
Me	77	8.14E-07	-14.02 ± 0.00	-244.37 ± 0.28	7.1
	87	2.26E-07	-15.30 ± 0.01	-211.09 ± 0.79	
Et	77	8.36E-07	-13.99 ± 0.02	-275.65 ± 2.46	5.6
	87	3.06E-07	-15.00 ± 0.01	-242.12 ± 1.77	
n-Pr	77	1.10E-06	-13.72 ± 0.02	-343.50 ± 1.78	7.5
	87	2.85E-07	-15.07 ± 0.01	-294.35 ± 1.00	
i-Pr	77	9.64E-07	-13.85 ± 0.01	-278.86 ± 0.69	6.8
	87	2.85E-07	-15.07 ± 0.00	-251.61 ± 0.57	
n-Bu	77	9.72E-07	-13.84 ± 0.02	-410.60 ± 2.31	4.1
	87	4.63E-07	-14.58 ± 0.02	-409.82 ± 3.50	
i-Bu	77	9.78E-07	-13.84 ± 0.03	-352.92 ± 3.80	8.5
	87	2.14E-07	-15.36 ± 0.02	-299.16 ± 2.92	
Pe	77	8.53E-07	-13.97 ± 0.02	-483.21 ± 3.74	7.9
	87	2.08E-07	-15.39 ± 0.02	-417.93 ± 3.22	
Oct	77	4.90E-07	-14.53 ± 0.03	-708.39 ± 7.25	6.5
	87	1.53E-07	-15.69 ± 0.01	-658.04 ± 3.98	
Bz	77	1.83E-06	-13.21 ± 0.02	-609.59 ± 3.85	8.4
	87	4.03E-07	-14.72 ± 0.02	-529.19 ± 3.23	

The variable temperature measurements on the Trip(Me)-PIM allowed the virial expansion analysis to be carried out more accurately. Table 9.5 displays the Henry's law constant along with the first and second virial parameters at temperatures from 77 to 137 K, in 10 K steps and then 197 K. The gradient from the

plot of A_0 against $1/T$ (see Figure 9.44) produced an isosteric enthalpy of adsorption of 6.6 ± 0.2 kJ mol^{-1}, compared to 7.1 kJ mol^{-1}, using only the 77 and 87 K absolute isotherm data. This value is significantly different from that which was produced from just two temperatures. The difference could be associated with a higher degree of accuracy or perhaps due to temperature dependence of the isosteric enthalpy of adsorption.[385] The Henry's law constant (which is related to the first virial parameter (K_H=exp(A_0)) is seen to decrease with increasing temperature, which indicates a decrease in adsorbate-adsorbent interaction with in increasing temperature. The second virial parameter is seen to decrease to less negative values with increasing temperature, thus indicating weaker adsorbate-adsorbate interactions.

Table 9.5 - Henry's law constant and virial Parameters A_0 and A_1 for hydrogen adsorption on Trip(Me)-PIM series at various temperatures (77 to 137 K, in 10 K steps and 197 K). The errors shown are equal to one standard deviation.

Temp. K	k_H mol g^{-1} Pa^{-1}	A_0 ln(mol g^{-1} Pa^{-1})	A_1 g mol^{-1}
77	9.58E-07	-13.86 ± 0.027	-257.37 ± 2.043
87	2.57E-07	-15.18 ± 0.023	-224.25 ± 2.163
97	1.12E-07	-16.00 ± 0.021	-213.41 ± 2.490
107	5.09E-08	-16.79 ± 0.010	-197.39 ± 1.465
117	2.68E-08	-17.43 ± 0.003	-181.64 ± 0.592
127	2.38E-08	-17.55 ± 0.102	-238.26 ± 22.460
137	1.05E-08	-18.37 ± 0.031	-178.21 ± 8.705
197	1.42E-09	-20.37 ± 0.001	-114.58 ± 1.000

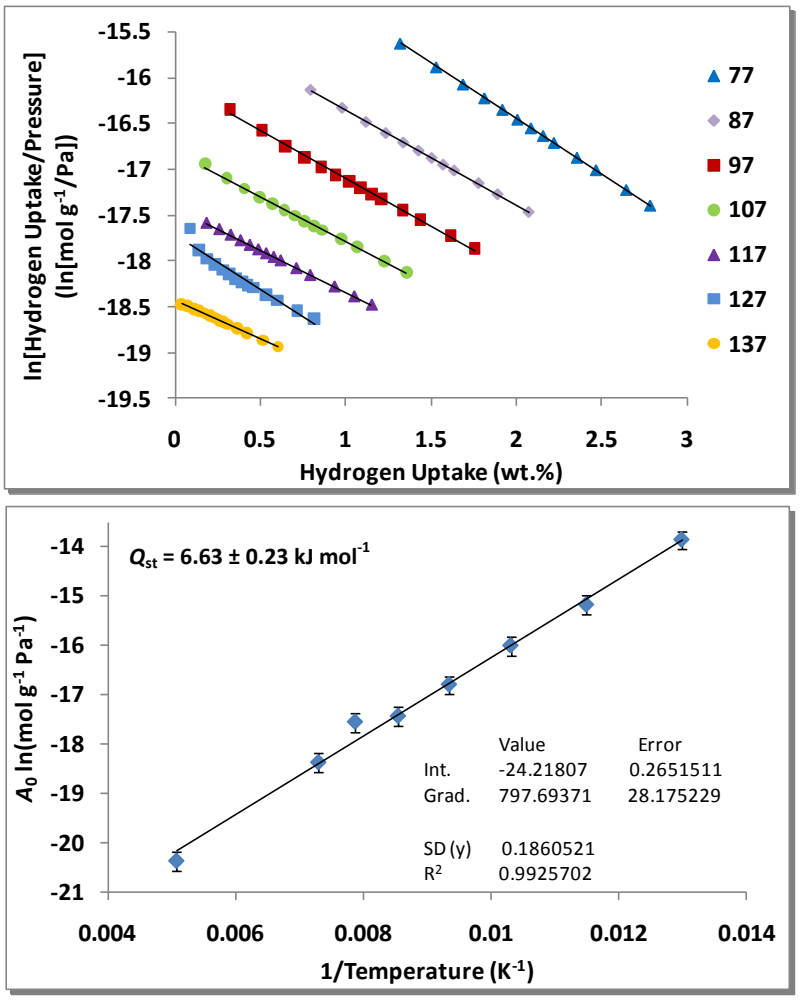

Figure 9.44 - (Left) Virial graphs for the absolute adsorption of hydrogen on Trip(Me)-PIM. (Right) The variation of virial parameter, A_0 with 1/T for the Trip(Me)-PIM (from 77 to 137 K, in 10 K steps, and 197 K).

9.5.2.2.5.5. Virial Type Thermal Equation

Equation (3.66) was used to fit the 77 and 87 K isotherms simultaneously. The equation has no limit to the number of coefficients that can be included, however for consistency, in the results shown below, values of 6 and 3 were used for the *m* and *n* coefficients, respectively. The fit for the Trip(Me)-PIM is shown as an example in Figure 9.45. From the fitting results for all of the Trip(R)-PIM series, the isosteric enthalpy of adsorption can be calculated according to equation (3.67), as a function of hydrogen uptake. Figure 9.46 displays the resulting plots of enthalpy of adsorption against hydrogen uptake (up to 0.8 wt.%).

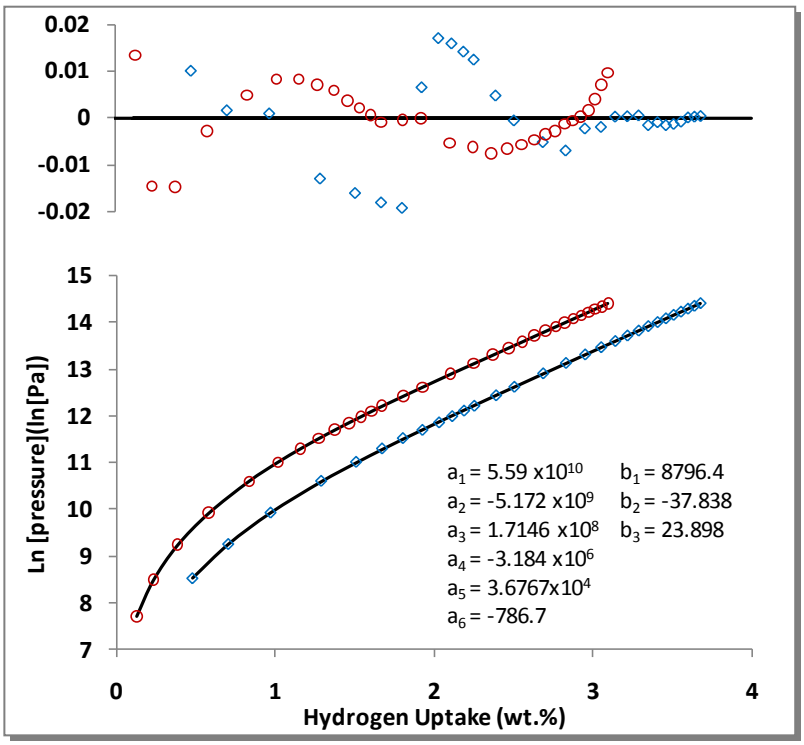

Figure 9.45 - Virial analysis of the hydrogen adsorption at 77 (◊) and 87 K (○) for the Trip(Me)-PIM up to 18 bar. Open symbols display data, whilst the virial plots are indicated by solid lines. Residual plots are shown at the top of the figure.

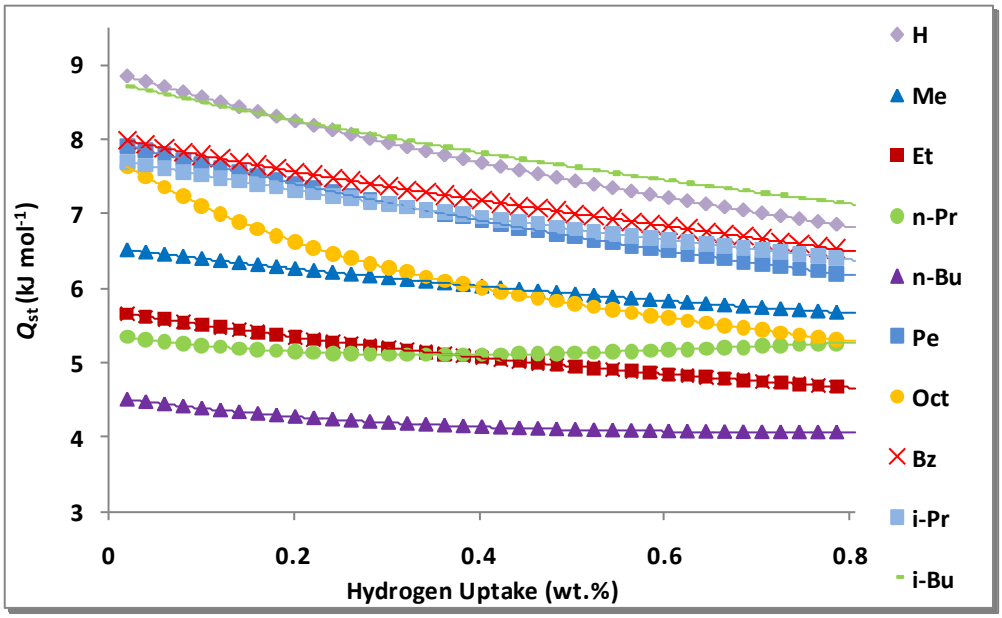

Figure 9.46 - Isosteric enthalpy of adsorption for the Trip(R)-PIM as a function of hydrogen uptake determined using the Virial type thermal equation and the 77 and 87 K data.

The Clausius-Clapeyron equation (in conjunction with the Sips and Tóth models) and virial (thermal equation) methods both produce a range of enthalpy of adsorption values as a function of hydrogen uptake, using just two temperatures. Table 9.6 shows a comparison between these methods at two values

of hydrogen uptake (0.02 and 0.8 wt.%). The comparison indicates that there is good correlation between the Clausius-Clapeyron equation (in conjunction with the Tóth model) and the virial type thermal equation at both 0.02 and 0.08 wt.%. However the Clausius-Clapeyron equation (in conjunction with the Sips model) appears to over-estimate the enthalpy of adsorption at low coverage. The same was made by Furukawa *et al*. when calculating the enthalpy of adsorption for MOF-177.[118] This over-estimation is probably a result of poor fitting to the absolute isotherm data at low surface coverage, which is probably a consequence of the Sips model not reducing to Henry's Law as $p \rightarrow 0$.

Wood *et al*. reported the enthalpy of adsorption for three hypercrosslinked polymers, which ranged from 7.5 kJ mol^{-1} to 6.0 kJ mol^{-1} between 0.1 to 1.1 wt.%.[290] However, the enthalpy of adsorption for the *p*-Dichloroxylene network remained relatively constant between 0.2 to 1.1 wt.% at *ca*. 7.3 kJ mol^{-1}. At low coverage, the Trip(R)-PIMs with R = H and *i*-Bu exhibited greater enthalpies of adsorption than reported by Wood *et al.*[290] Additionally, the triptycene-based PIMs with R = Pe, *i*-Pr, and Bz also displayed higher enthalpies of adsorption than 7.5 kJ mol^{-1} at 0.1 wt.%, however the enthalpy of adsorption for these materials dropped to lower enthalpies compared to the *p*-Dichloroxylene network by 0.8 wt.%.[290]

Table 9.6 - Comparison of the enthalpy of adsorption values obtained for the Trip(R)-PIMs from their respective 77 and 87 K absolute hydrogen adsorption data.

R-group	Enthalpy of adsorption (kJ mol^{-1})					
	Hydrogen Uptake (0.02 wt.%)			Hydrogen Uptake (0.8 wt.%)		
	Clausius-Clapeyron		Virial	Clausius-Clapeyron		Virial
	Sips	Tóth		Sips	Tóth	
H	15.2	10.5	8.9	6.9	6.8	6.8
Me	10.7	7.3	6.5	5.9	5.7	5.7
Et	9.8	6.3	5.7	5.0	4.7	4.6
n-Pr	8.0	5.7	5.4	5.6	5.6	5.3
i-Pr	12.3	8.7	7.7	6.5	6.4	6.4
n-Bu	7.0	4.8	4.5	4.1	4.1	4.1
i-Bu	14.2	10.0	8.7	7.1	7.1	7.1
Pe	13.6	9.5	7.9	6.1	6.2	6.2
Oct	10.4	7.3	7.6	5.2	5.3	5.3
Bz	14.2	10.0	6.5	6.3	6.4	6.5

As the virial thermal equation method does not produce a value for the enthalpy of adsorption for exact hydrogen uptake values, the resulting plot of enthalpy of adsorption versus hydrogen uptake was fitted

with a generic 6-order polynomial equation in Microsoft Excel. The 6-order polynomial equations all had an R-squared values equal to 1; it was then used to calculate the exact enthalpy of adsorption at a specific value of hydrogen uptake, which in this case was 0.02 and 0.8 wt.%.

In general we can see that the bulkier groups (in particular the branched-alkyl groups) exhibit a higher enthalpy of adsorption. This was with the exception of the very small R-groups (H and Me), which also showed relatively high enthalpies of adsorption. Three of the triptycene-based PIMs showed relatively low values across the uptake range examined (Et, *n*-Pr and *n*-Bu).

The Trip(R)-PIMs with smaller straight alkyl chains can pack more efficiently giving smaller pores, but have less structural restrictions and so are capable of moving and hence swelling with increased pressures. The longer straight chain alkyl groups may leave small voids of space between the polymer chains in which hydrogen can diffuse in to and therefore create high enthalpies of adsorption. However, the sheer length of the chain provides too much hindrance for the polymer chains to shift upon the increase in pressure and therefore do not swell to accommodate more guest gas molecules. This correlates with the change in gradient of the nitrogen adsorption isotherms with increasing chain length and also the reduction in the hysteresis from the adsorption to desorption isotherms. The 'medium' length straight chain alkyl groups appear to lie in the middle suggesting they have a more efficient packing whilst the groups are still short enough to allow some swelling. This is reflected in the lowest enthalpy of adsorption begin for the Trip(*n*-Bu)-PIM.

The two triptycene-based PIMs with branched alkyl groups and also the PIM with the benzyl group at the bridgehead position seem to offer a combination of the above properties. These groups appear to separate the polymer chains creating small pores for gas adsorption whilst also allowing for some swelling of the structure.

9.6. Network PIMs

The high surface area found in the polymers containing the triptycene (A2) monomer, resulted in the synthesis of some additional polymers containing this catechol-type monomer. Three 1,2-difluoro- aryl containing (B) monomers were chosen that were hoped to increase the microporosity and the apparent

surface area of the materials. The spirobindane (A1) was also used with the two biphenyl-containing monomers.

9.6.1. Structure and Characterisation

As with the previous groups of PIMs these are formed from a base-mediated aromatic nucleophilic substitution to form rigid linkages between rigid 1,2-dihydroaryl- (catechol) and 1,2-difluoro-aryl unit containing monomers, A and B respectively. A monomers 5,5´,6,6´-tetrahydroxy-3,3,3´,3´-tetramethyl-1,1´-spirobisindane (A1) and 9,10-dimethyl-2,3,6,7,12,13-hexahydroxytriptycene (A2) were used in conjunction with three 2,2'3,3'5,5',6,6'-octafluoro- aryl containing monomers (B3 to B5). Figure 9.47 shows the structures of these monomer units. Figure 9.48 shows an example of the resulting structure from the reaction of an A and B monomer in this group of network-PIMs.

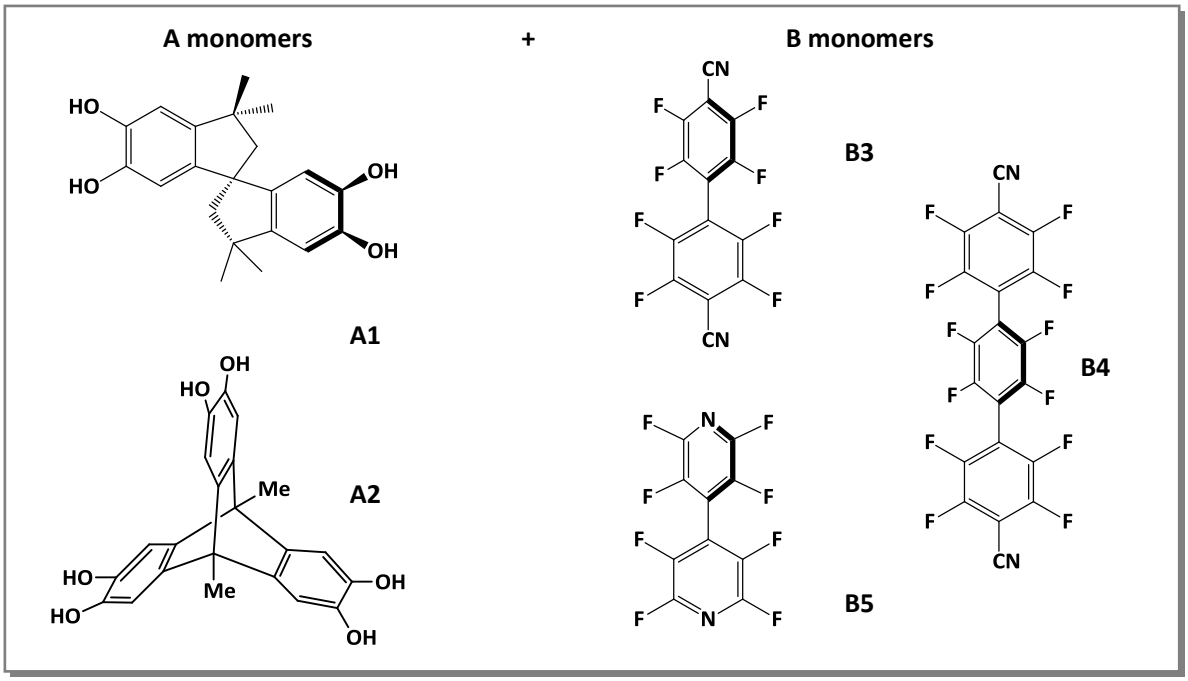

Figure 9.47 - Hydroxylated aromatic monomers (A1 and A2) and fluorinated aromatic monomers (B3 to B5) used for the dioxane-forming polymerisation reaction of the network-PIMs using the typical reagents and conditions. B3 = 2,2'3,3'5,5',6,6'-octafluoro-4,4'-biphenyldicarbonitrile; B4 = 2,2'3,3'5,5',6,6'-octafluoro-4,4'-terphenyldicarbonitrile; B5 = 2,2'3,3'5,5',6,6'-octafluoro-4,4'-bispyridyl.

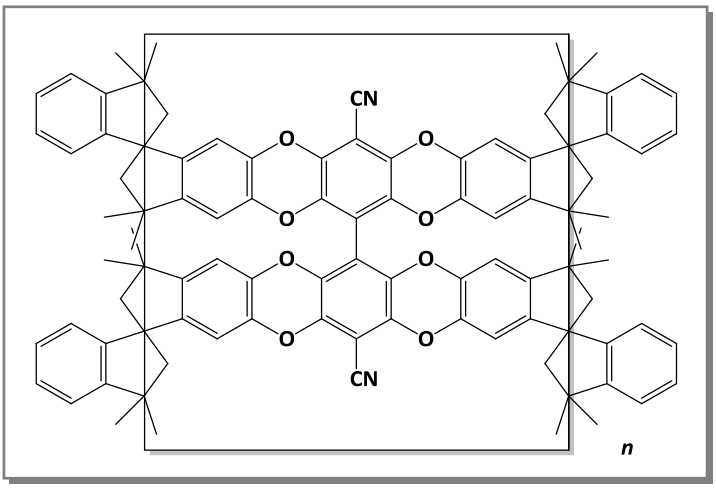

Figure 9.48 - An example of the resulting structure from the base-mediated aromatic nucleophilic substitution to form rigid linkages between monomers A1 and B3.

9.6.1.3. Infrared Spectroscopy

Infrared spectroscopy was performed at the University of Cardiff where the PIM was synthesised. The spectrum for each member of the Trip(R)-PIM series showed the material to be consistent with the expected structure of the network polymer. All of the samples were outgassed at 100 °C for *ca*. 1000 minutes before being analysed by infrared spectroscopy. Their spectra were all quite similar and showed no presence of either hydroxyl or carbonyl groups.

9.6.2. Gas Adsorption

Thermogravimetric analysis of the network PIMs confirmed they did not undergo thermal decomposition up to 400 °C. The network-PIMs exhibited mass losses up to 6%, which occurred by around 100 to 120 °C, therefore this was used as the degassing temperature.

9.6.2.1. Nitrogen

Nitrogen adsorption was performed at 77 K after being outgassed at 100 to 120 °C for 8 to 12 hours. The series of network-PIMs showed impressive nitrogen uptake at low relative pressures ($p/p_0 < 0.1$); with the monomers A2 + B3 and A2 + B5 showing a very similar uptake to the Trip(Me)-PIM. The third network-PIM that contains the A2 monomer displayed a nitrogen uptake slightly lower, but still greater than Trip(Et)-PIM, at $p/p_0 < 0.1$. The two network PIMs containing the A1 monomer both showed greater nitrogen

uptake (at low relative pressures) than PIM-1, which also contains the A1 monomer. The A2 + B4 combination adsorbed the lowest of the three A2 containing PIMs, however it rose sharply at high relative pressures to have the greatest nitrogen uptake at p/p_0 = 1; 784 $cm^3\ g^{-1}$ (STP), *ca.* 35.0 $mmol\ g^{-1}$. This maybe because the larger B monomer allows the polymer structure to swell or it may be because it contains more mesopores.[106] Is it also worth noting that the nitrogen adsorption behaviour of the two network-PIMs containing A2 with B3 and B5 is almost identical, whilst this does not appear to be the case with the A1 monomer.

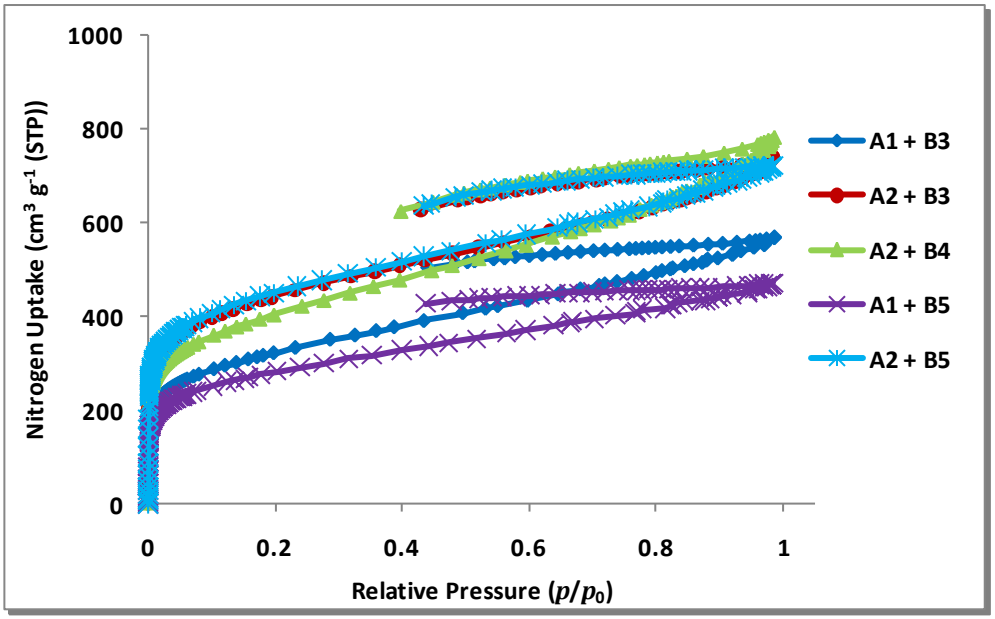

Figure 9.49 - Nitrogen sorption data for the network-PIMs (from A1 and A2 with B3-B5) at 77 K.

The nitrogen adsorption isotherms were used to calculate the BET specific surface areas of the network-PIMs. Linear regression was used on the linear sections of the BET plots in order to calculate apparent surface areas ranging from 1598.7 $m^2\ g^{-1}$ (for A2 + B5) to 1005.3 $m^2\ g^{-1}$ (for A1 + B5). Linear regression was also used to calculate the Langmuir surface areas of these network-PIMs, the values of which are given in Table 9.7 along with the BET surface areas and the nitrogen uptake values at p/p_0 = 1.

Table 9.7 - Nitrogen adsorption data for the Network-PIMs derived from monomers A1 and A2 with B3-B5 at 77 K, including BET and Langmuir apparent surface areas. Nitrogen uptake values were taken at $p/p_0 = 1$.

Monomers	Surface Area; $m^2 g^{-1}$		Nitrogen Uptake	
	BET	Langmuir	$cm^3 g^{-1}$ (STP)	mmol g^{-1}
A1 + B3	1146.8 ± 4.7	1349.5 ± 19.7	569.3	25.4
A2 + B3	1574.5 ± 8.6	1846.1 ± 23.6	741.9	33.1
A2 + B4	1436.3 ± 5.9	1677.6 ± 24.6	784.0	35.0
A1 + B5	1005.3 ± 3.6	1149.7 ± 13.6	471.0	21.0
A2 + B5	1598.7 ± 9.5	1882.4 ± 23.2	722.8	32.2

The Horváth-Kawazoe method was used to analyse the low-pressure nitrogen adsorption data to calculate a pore size distribution for the A1 containing network-PIMs (as illustrated in Figure 9.50). The analysis confirmed the lack of a distinct pore size, and the presence of a distribution of pore sizes that was biased towards pores in the range below 0.65 nm. The pore size distribution for the A1 + B3 network-PIM appeared to show a larger contribution of smaller pores compared to the A1 + B5 network-PIM as a larger peak was observed at the measurement limit of the apparatus (around 0.58 nm).

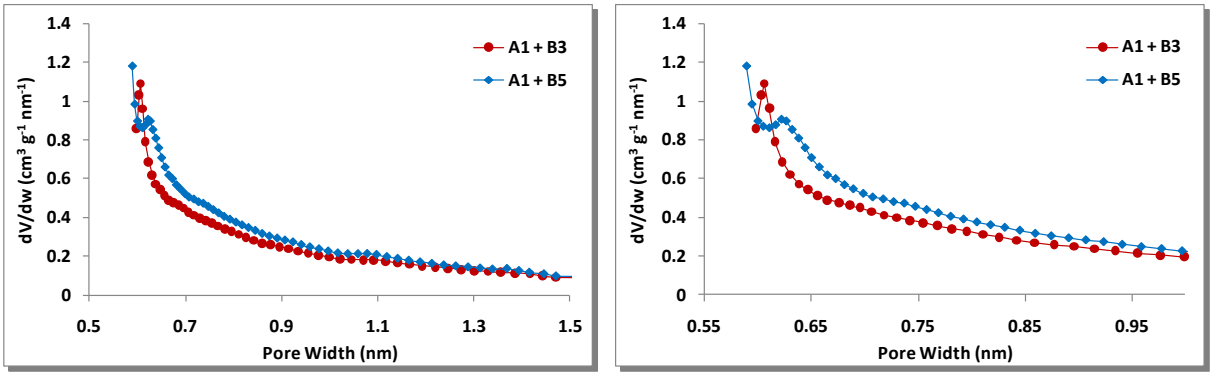

Figure 9.50- Micropore size distribution for A1 containing network-PIMs. The analysis is based on the Horváth-Kawazoe analysis of low pressure nitrogen adsorption data showing that the major contribution to porosity is from pores that are less than 1 nm in diameter.

9.6.2.2. Hydrogen

9.6.2.2.1. Excess Adsorption

The Trip(R)-PIM series initially degassed for *ca*. 1000 minutes at room temperature followed by a further 1000 minutes at 100 °C. Although the mass loss had not completely 'levelled-off', previous hydrogen storage measurements had shown that differences in the microgramme range had little effect on the gravimetric hydrogen storage capacity.

The skeletal densities of the network-PIMs were obtained using helium pycnometry (at room temperature) and subsequently used for buoyancy correction of the hydrogen sorption data. Pycnometry was performed on fully degassed materials. The measured densities are shown in Table 9.8. The network PIMs which contain the A1 monomer, had a lower skeletal density than those that contain the A2 monomer. Whilst the PIMs containing the B5 monomer had both the lowest and highest densities.

The sorption isotherm in Figure 9.51 shows an excess gravimetric hydrogen uptake range of 3.07 wt.% for A2 + B3 to 2.07 wt.% for A1 + B5 at 77 K and 18 bar; although A1 + B3 was only 0.02 wt.% higher at 2.09 wt.% (see Table 9.8), which is within the experimental error of *ca*. 0.05 wt.%. The figure shows that hydrogen uptake generally correlates with the BET surface areas of the materials (see Table 9.7). However, both of the network PIMs which contain the A1 monomer, appear to have almost exactly the same hydrogen adsorption capacities up to 18 bar at 77 K. This can be observed from the isotherms in Figure 9.51 but also from the hydrogen uptake values at 1, 10 and 18 bar (and 77 K) shown in Table 9.8. Additionally, the network-PIM with the highest BET surface area does not exhibit the greatest gravimetric hydrogen storage capacity at 77 K (up to 18 bar). The A2 + B3 network-PIM shows much greater hydrogen uptake at low pressures (< 1 bar) suggesting that it has a greater enthalpy of adsorption in comparison to the other network-PIMS.

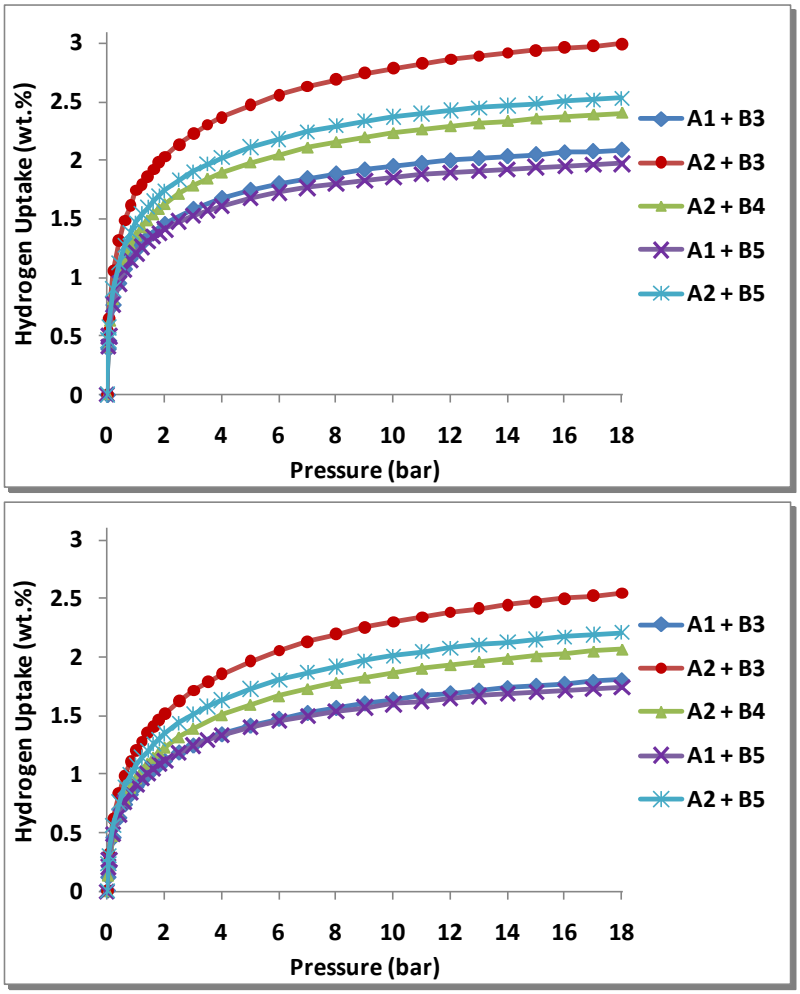

Figure 9.51 - Excess gravimetric hydrogen adsorption data for the Network-PIMs derived from monomers A1 and A2 with B3-B5 at 77 (top) and 87 K (bottom).

Table 9.8 - Skeletal densities as determined by helium pyconometry at room temperature for the network-PIMs using monomers A1 and A2 with B3-B5. Excess gravimetric hydrogen adsorption data for the network-PIMs derived from monomers A1 and A2 with B3-B5 at 77 and 87 K.

Monomers	Skeletal Density	Temp.	Hydrogen Uptake					
			1 bar		10 bar		18 bar	
	g cm^{-3}	K	wt.%	*(mmol g^{-1})*	wt.%	*(mmol g^{-1})*	wt.%	*(mmol g^{-1})*
A1 + B3	1.33	77	1.23	*(6.11)*	1.95	*(9.67)*	2.09	*(10.36)*
		87	0.89	*(4.42)*	1.64	*(8.13)*	1.81	*(8.96)*
A2 + B3	1.55	77	1.74	*(8.64)*	2.79	*(13.83)*	3.00	*(14.86)*
		87	1.20	*(5.95)*	2.30	*(11.42)*	2.55	*(12.63)*
A2 + B4	1.65	77	1.35	*(6.72)*	2.23	*(11.06)*	2.40	*(11.93)*
		87	0.97	*(4.79)*	1.87	*(9.28)*	2.07	*(10.27)*
A1 + B5	1.29	77	1.21	*(5.99)*	1.85	*(9.20)*	1.97	*(9.77)*
		87	0.91	*(4.50)*	1.60	*(7.94)*	1.75	*(8.66)*
A2 + B5	1.72	77	1.47	*(7.27)*	2.37	*(11.76)*	2.53	*(12.55)*
		87	1.07	*(5.32)*	2.01	*(9.97)*	2.21	*(10.97)*

The gravimetric hydrogen storage capacity was used in conjunction with the density of hydrogen at the triple point (0.077 g cm^{-3}) to calculate the volume of hydrogen adsorbed in the pores. Using these volumes (as calculated by the BET method), the percentage of the filled pores ranged from 58 to 72%, with A1+B5 and A2+B5 network PIMs being at either end of the range. The skeletal densities and micropore volumes provided geometric densities that were then used to calculate (theoretical) volumetric capacities. These ranged from 17.5 to 24.9 kg m^{-3} at 20 bar and 77 K, with the two extremes being A1 + B5 and A2 + B3 network PIMs, respectively.

The conversion between the measured excess adsorption and the absolute amount adsorbed also assumes the density of the adsorbed hydrogen at the triple point (0.077 g cm^{-3}), see section 3.6.2.1.

9.6.2.2.2. The Langmuir Isotherm

The Langmuir plots for the network-PIMs can be seen in the Figure 9.52. Least squares linear regression was performed between 2 and 18 bar to calculate a theoretical maximum hydrogen uptake, n_m (see Table 9.9); this would be consistent with a plateau in absolute hydrogen adsorption isotherms. Individual Langmuir plots are shown in Appendix F.

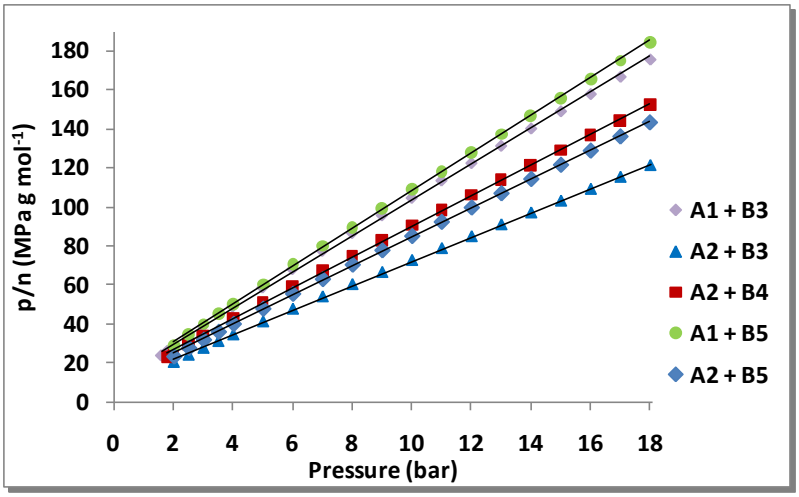

Figure 9.52 - Linearised Langmuir plots for the hydrogen adsorption of the network-PIMs at 77 K.

Table 9.9 - Maximum absolute hydrogen uptake as determined by the linearised Langmuir equation of the 77 K for the network-PIMs. The errors shown are equal to one standard deviation.

Monomers	Maximum Hydrogen Uptake (n_m)	
	wt.%	mmol g^{-1}
A1 + B3	2.20 ± 0.01	10.92 ± 0.06
A2 + B3	3.21 ± 0.02	15.92 ± 0.08
A2 + B4	2.54 ± 0.02	12.61 ± 0.11
A1 + B5	2.07 ± 0.02	10.28 ± 0.08
A2 + B5	2.70 ± 0.02	13.37 ± 0.09

9.6.2.2.3. Empirical Isotherm Equations

The Sips and Tóth empirical isotherm equations were applied to the absolute adsorption isotherm for each network-PIM, at each measured temperature. Both equations appear to produce good fits for the 77 K isotherm, but residual plots illustrate the differences between the data and the fitted model. An example is shown for the A2 + B6 PIM in Figure 9.53, residual traces for all of the Trip(R)-PIMs can be found in Appendix E. The residual plots for the A2 + B3 PIM indicate that the two equations produce a very good fit to the absolute adsorption (at 77 K). Both models are within ±0.04 of the absolute adsorption. The Sips model remaining closer to the absolute isotherm across the range. Both models appear to have one anomalous point. This suggests that the equivalent raw data point is somewhat erroneous. The two models produce fairly significant differences in their predicted saturation uptakes: 4.02(3) and 4.93(9) wt.%, for the Sips and Tóth models, respectively at 77 K.

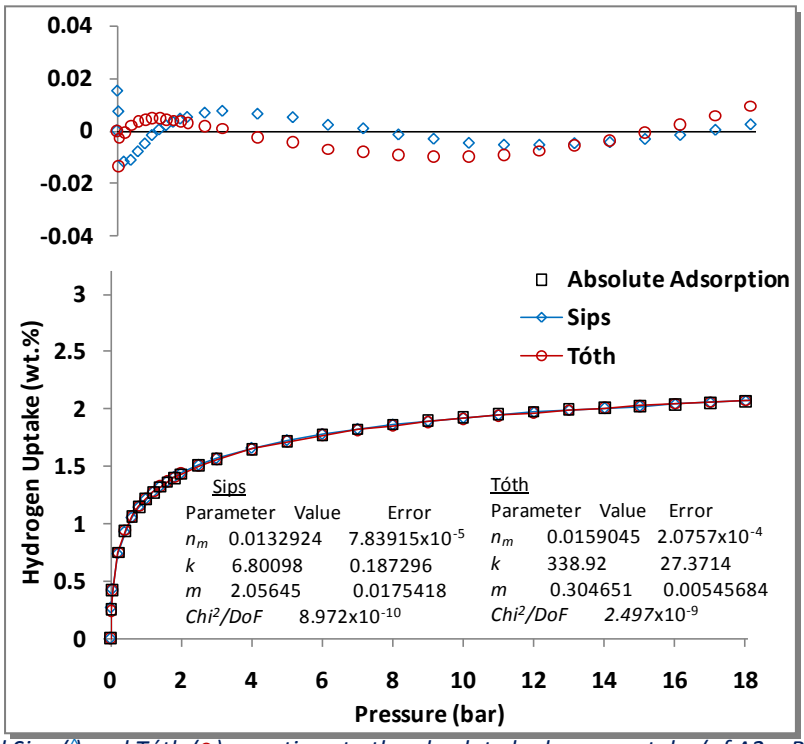

Figure 9.53 - Fitted Sips (◇) and Tóth (○) equations to the absolute hydrogen uptake (of A2 + B3) against pressure at 77 K up to 15 bar. Residual plots are shown at the top of the figure.

9.6.2.2.4. Enthalpy of Adsorption

9.6.2.2.4.1. Clausius-Clapeyron

The fitted 77 and 87 K absolute adsorption isotherms were used to calculate the enthalpy of adsorption using the Clausius-Clapeyron equation (see Figure 9.54). The enthalpy of adsorption is calculated up to 0.8 wt.% as explained in section 6.2.2.5.4.The analysis shows that the PIMs containing the B6 monomer have a higher enthalpy of adsorption at low coverage. With the A1 + B3 combination decreasing rapidly with increasing wt.%, compared to the other B6 containing network-PIM. The three other network-PIMs display very similar enthalpies of adsorption, with the A2 + B4 PIM exhibiting the lowest value at low hydrogen uptake. The A2 + B3 network-PIM was found to exhibit the greatest enthalpy of adsorption at near zero coverage (0.02 wt.% H_2) with both the Sips and Tóth models (14.0 and 9.5 kJ mol^{-1}, respectively).

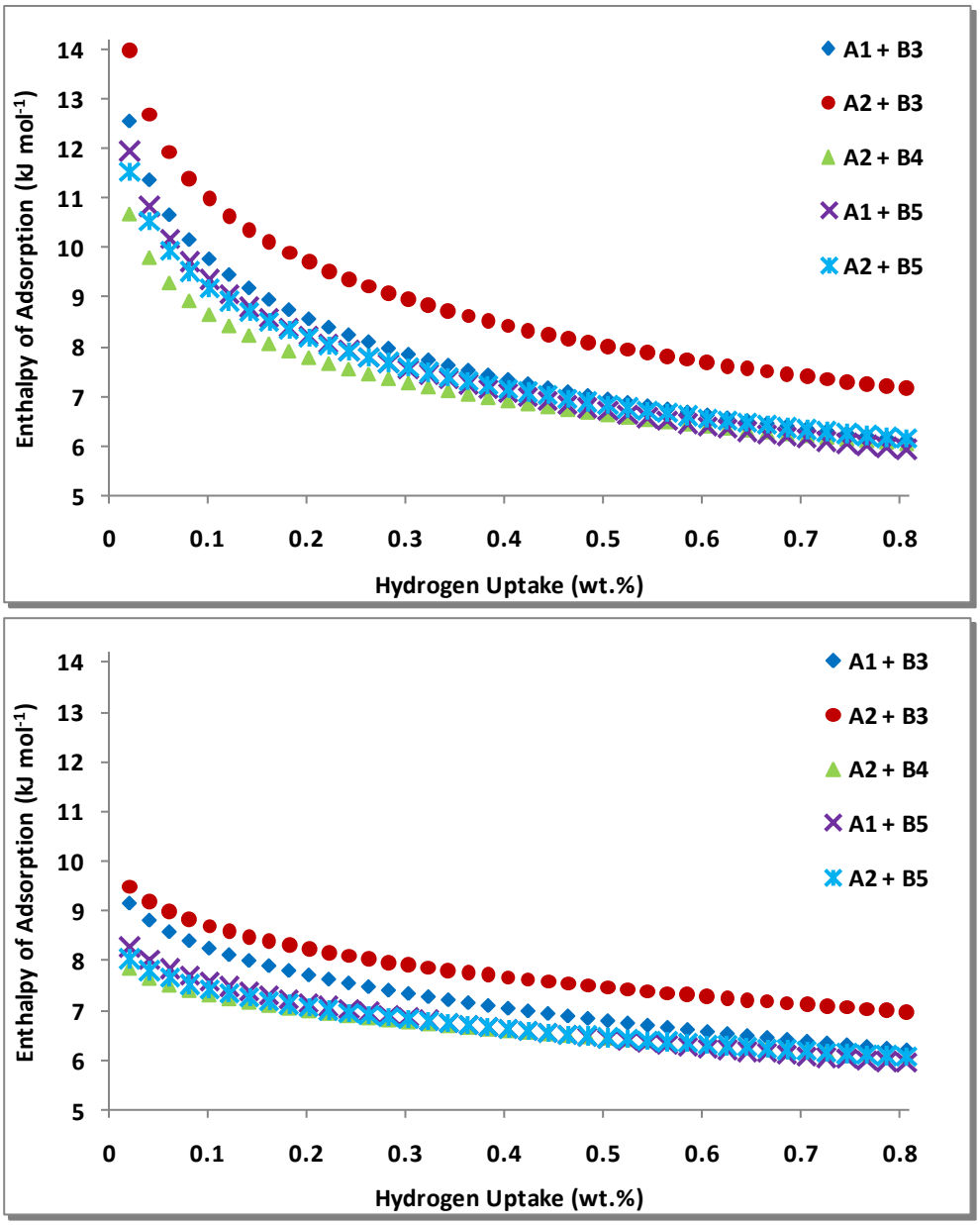

Figure 9.54 - Comparison of the enthalpy of adsorption determined using the Clausius-Clapeyron equation (in conjunction with Sips (top) and the Tóth equations (bottom) fitted to the 77 and 87 K absolute isotherms).

9.6.2.2.4.2. Virial Type Expansion Equation

Figure 9.55 shows the virial plots for the hydrogen adsorption in the network-PIMs at 77 K. Least squares linear regression was performed (on the linear section from 0.4 to 5 bar), allowing for the determination A_0 and A_1 values from the intercepts and gradients respectively, the values for which are shown in Table 9.10. The Henry's law constant (which is related to the first virial parameter (K_H=exp(A_0)) indicates that the A1 + B5 has the strongest adsorbent-adsorbate interaction. However, all of the network-PIMs show very similar A_0 coefficients at both 77 and 87 K. This is illustrated in Figure 9.55 by the gradient of the A_0

coefficients as a function of $1/T$. For each material, k_H is greater at 77 K than at 87 K, which indicates a stronger adsorbate-adsorbent interaction at the lower temperature. Equally the adsorbate-adsorbate interactions are stronger at 77 K than 87 K, as indicated by the A_1 parameter. The isosteric enthalpies of adsorption, Q_{st}, (shown in Table 9.10) were calculated from the A_0 parameter from the 77 and 87 K data and plotting them against $1/T$ (see Figure 9.55). The Q_{st} are similar to those calculated by the Clausius-Clapeyron method, but do not appear to represent the enthalpy of adsorption at zero coverage. It is important to note that the Q_{st} values determined here should only be used for guidance and not an accurate indication for the isosteric enthalpy of adsorption due to the limited number of temperatures used.

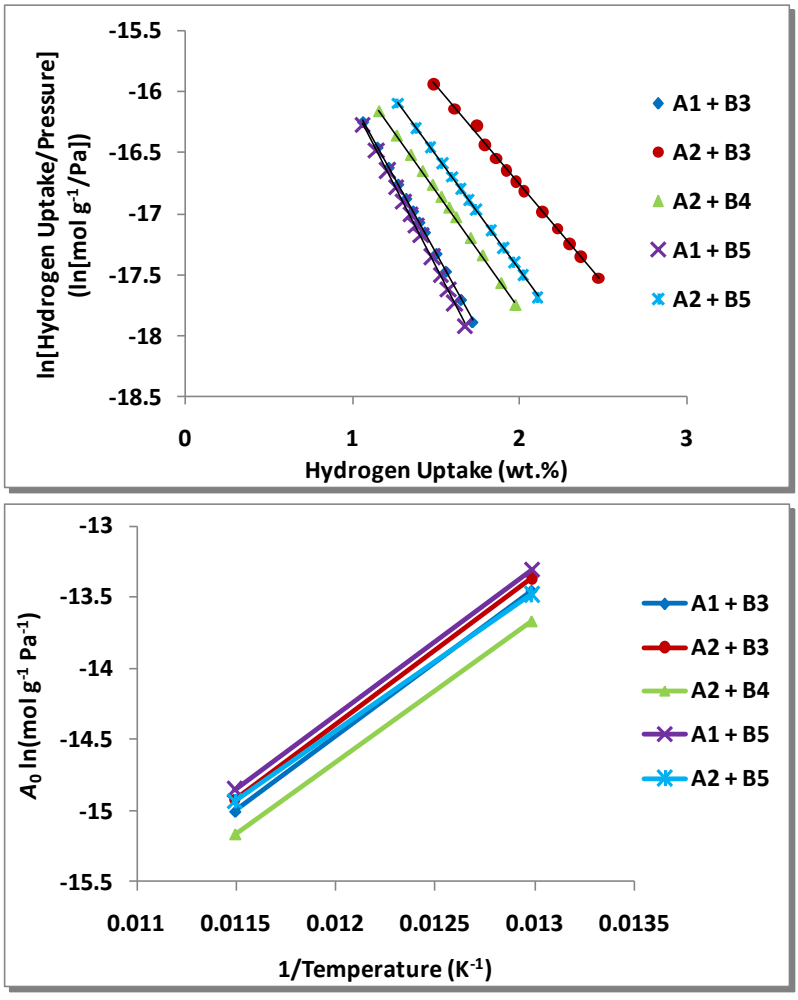

Figure 9.55 - Virial plots for the adsorption of hydrogen(Left) and the first virial coefficient (A_0) in the network-PIMs (Right) at 77 K.

Table 9.10 - Henry's law constant and Virial parameters A_0 and A_1 for hydrogen adsorption on the network-PIMs at 77 and 87 K, and the resulting enthalpy of adsorption. The errors shown are equal to one standard deviation. [Errors on the Q_{st} are not given as they are deemed immaterial as only two temperatures were used].

R-group	Temp.	k_H	A_0	A_1	Q_{st}
	K	mol g^{-1} Pa^{-1}	ln(mol g^{-1} Pa^{-1})	g mol^{-1}	kJ mol^{-1}
A1 + B3	77	1.44E-06	-13.45 ± 0.04	-527.15 ± 4.82	8.66
	87	3.07E-07	-15.00 ± 0.01	-437.79 ± 1.87	
A2 + B3	77	1.57E-06	-13.37 ± 0.03	-344.52 ± 2.93	8.66
	87	3.29E-07	-14.93 ± 0.00	-289.64 ± 0.54	
A2 + B4	77	1.16E-06	-13.67 ± 0.04	-425.10 ± 4.57	8.36
	87	2.58E-07	-15.17 ± 0.01	-350.59 ± 1.31	
A1 + B5	77	1.67E-06	-13.31 ± 0.06	-566.37 ± 8.21	8.61
	87	3.65E-07	-14.82 ± 0.02	-468.45 ± 3.74	
A2 + B5	77	1.40E-06	-13.48 ± 0.04	-409.62 ± 4.48	8.09
	87	3.26E-07	-14.94 ± 0.00	-343.43 ± 0.60	

9.6.2.2.4.3. Virial Type Thermal Equation

Equation (3.66) was used to fit the 77 and 87 K isotherms simultaneously. As per previous materials studied in this work, values of m = 6 and n = 3, were used in the equation. The fit for the A1 + B3 network-PIM is shown as an example in Figure 9.56. From the fitting results for all of the Trip(R)-PIM series, the isosteric enthalpy of adsorption can be calculated according to equation (3.67), as a function of hydrogen uptake. Figure 9.57 shows the resulting plots of enthalpy of adsorption against hydrogen uptake (up to 0.8 wt.%).

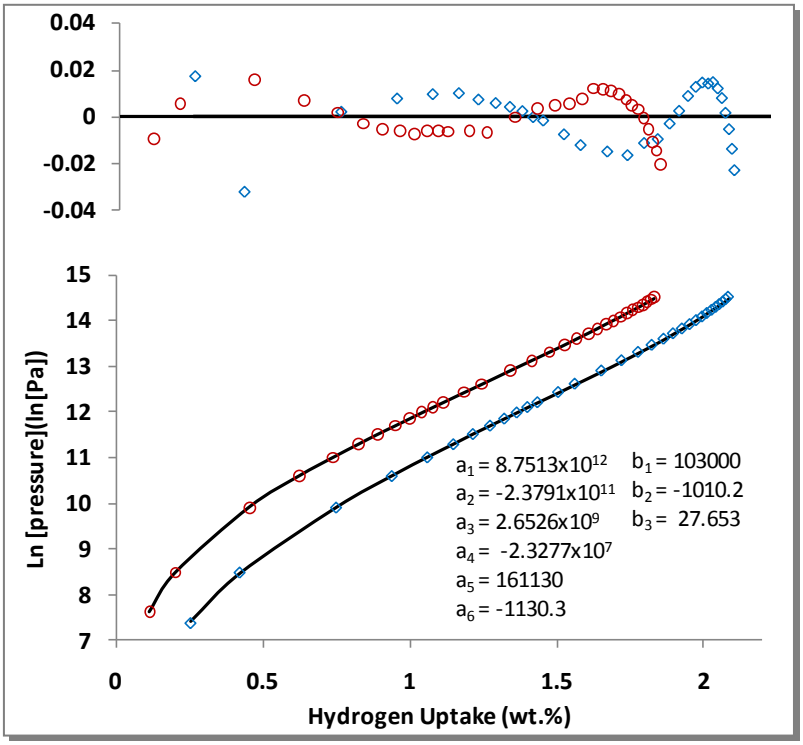

Figure 9.56 - Virial analysis of the hydrogen adsorption at 77 (◊) and 87 K (○) for the network PIM (A1 + B3) to 20 bar. Data is indicated by open shapes, with the solid lines indicating the virial plots. Residual plots are shown at the top of the figure.

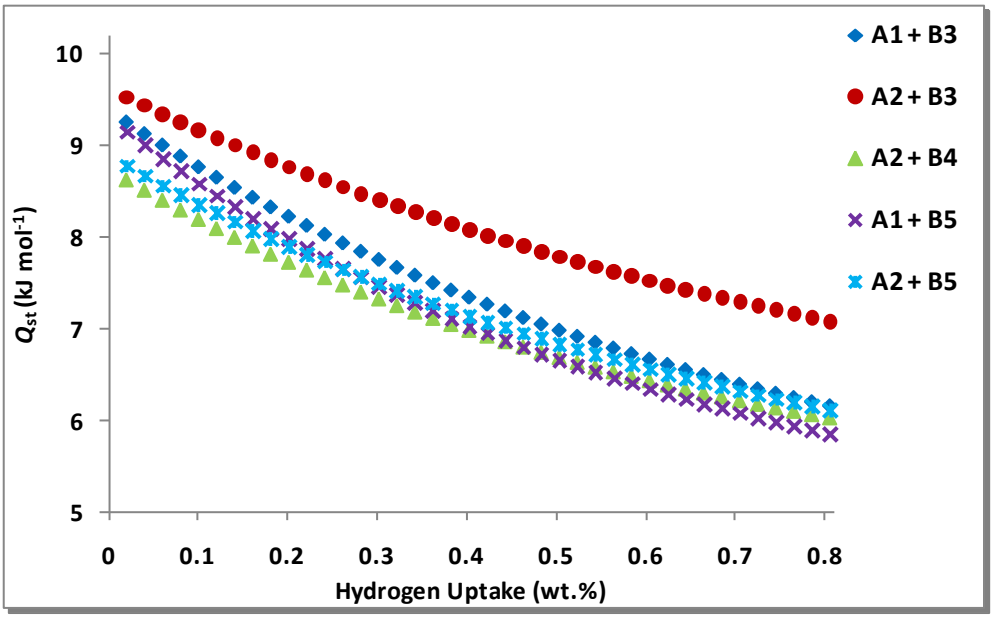

Figure 9.57 - Isosteric enthalpy of adsorption for the network PIMs as a function of hydrogen uptake. Calculated using the Virial type thermal equation and two isotherms at 77 and 87 K.

All of the network-PIMs display greater enthalpies of adsorption than the hypercrosslinked polymers reported by Wood *et al.*[290] at low pressures (using the Clausius-Clapeyron equation). As with previous porous materials, the enthalpy of adsorption appears to be overestimated when fitted with the Sips equation, however the Tóth and Virial fits show good correlation. In fact the two equations are within *ca*. 0.1 kJ mol^{-1} for both of the B6 containing PIMs, as displayed in Table 9.11.

Table 9.11 - Comparison of the enthalpy of adsorption values obtained for the network-PIMs from their respective 77 and 87 K absolute hydrogen adsorption data.

Monomers	Enthalpy of adsorption (kJ mol^{-1})					
	Hydrogen Uptake (0.02 wt.%)			Hydrogen Uptake (0.8 wt.%)		
	Clausius-Clapeyron		Virial	Clausius-Clapeyron		Virial
	Sips	Tóth		Sips	Tóth	
A1 + B3	12.6	9.2	9.3	6.1	6.2	6.2
A2 + B3	14.0	9.5	9.5	7.2	7.0	7.1
A2 + B4	10.7	7.9	8.6	6.0	6.1	6.0
A1 + B5	12.0	8.3	9.2	5.9	5.9	5.9
A2 + B5	11.5	8.0	8.8	6.1	6.1	6.1

The B6 monomer displayed the highest enthalpy of adsorption for both A monomers at low hydrogen uptake. The larger B7 monomer exhibits the lowest enthalpy of adsorption. It is worth noting that this is not directly comparable with the large R-groups in the triptycene-based PIMs, as these were attached (in the 3rd dimension) to the triptycene monomer at the bridgehead position. Here the large molecule bonds to the 1,2-dihydroaryl- (catechol) unit.

The difference between the enthalpy of adsorption from the A1 and A2 monomers in these network-PIMs are relatively similar. However, PIM-1 and the triptycene-based series all contain the same B monomer. In order to draw a comparison, the Trip(Me)-PIM should be used as the A2 monomer in these network-PIMs as they also contain the methyl group at the bridgehead position of the triptycene unit. The heat adsorption for the combination of A1 + B1 was significantly higher than for A2 + B1.

9.7. Macromolecule PIM

The triptycene monomer has shown that it offers PIMs which have a greater surface area, and subsequently have a greater hydrogen uptake at 77 K in comparison to the spirobisindane monomer.

Larger triptycene-based catechol monomers were synthesised to see whether the larger polymer units create a more open structure whilst maintaining the ultramicroporosity observed in previous triptycene-based PIMs.

9.7.1. Structure and Characterisation

A triptycene-based macromolecule was synthesised from two successive dioxane-formation reactions. The first used 2,3-dihydroxytriptycene (A3) with 2,2'3,3'5,5',6,6'-octafluoro-4,4'-biphenyldicarbonitrile (B3), the product of which was then reacted with 9,10-dimethyl-2,3,6,7,12,13-hexahydroxytriptycene (A2) to form the macromolecule-polymer.

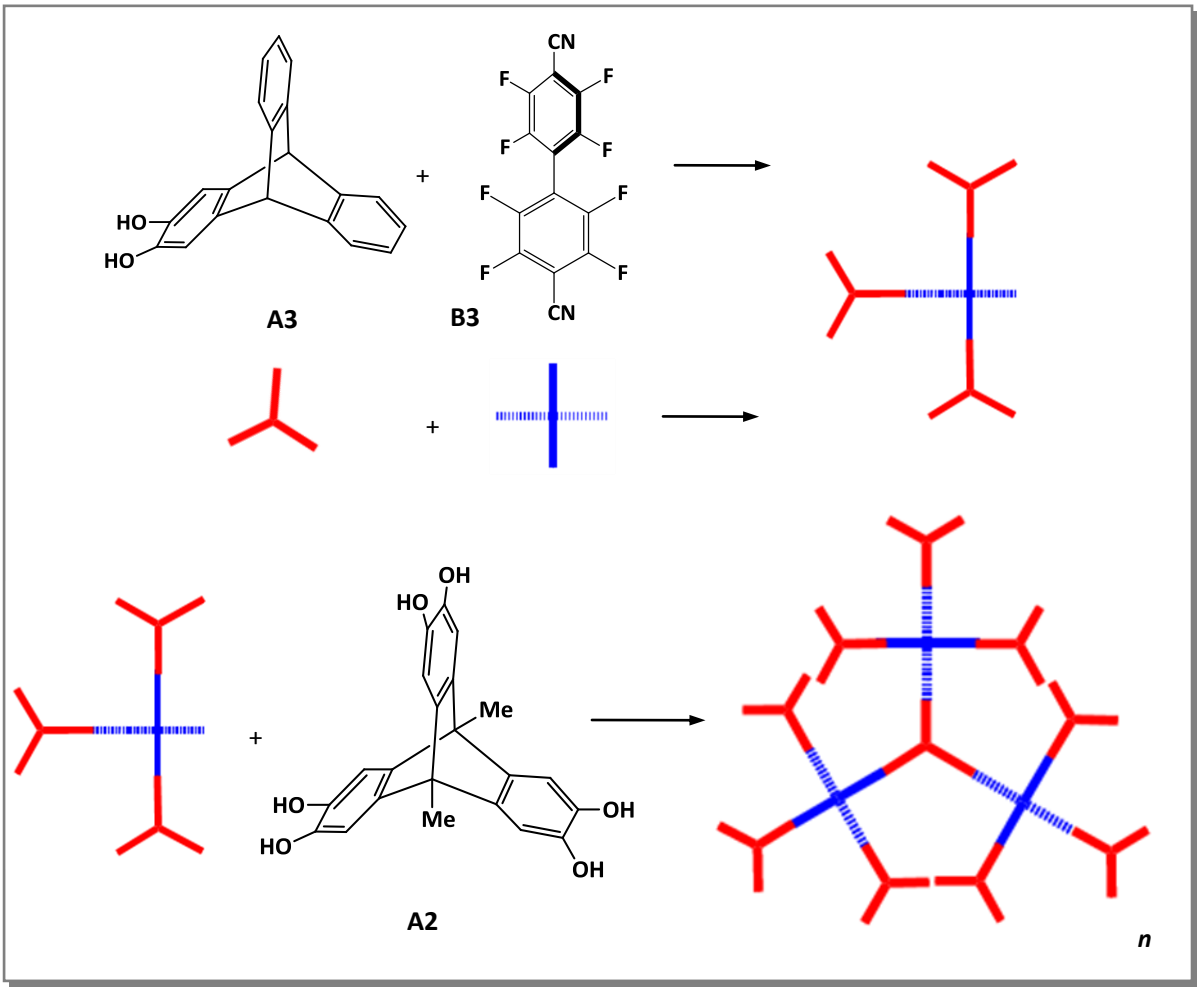

Figure 9.58 - Formation of the triptycene-based macromolecule utilising two dioxane formation reactions using monomers A3 with B3 and then A2 with typical reagents and conditions.

Thermogravimetric analysis of the triptycene-based macromolecule PIMS confirmed they did not undergo thermal decomposition up to 400 °C. The majority of the mass loss was observed on increasing the temperature up to 100 °C, this temperature was therefore used for degassing. The degassing profiles for the triptycene-based macromolecule PIM showed a mass loss of *ca*. 1.0%, up to 100 °C.

9.7.2. Gas Adsorption

9.7.2.1. Nitrogen

Nitrogen adsorption was performed at 77 K after being degassed at 100 °C for 800 minutes. The triptycene-based macromolecule PIM shows a comparable nitrogen uptake to the Trip(Oct)-PIM at low relative pressure ($p/p_0 < 0.1$). The nitrogen uptake has a dramatic increase in uptake at $p/p_0 > 0.9$ leading to final nitrogen uptake of 394 $cm^3\ g^{-1}$ (STP), *ca*. 17.6 mmol g^{-1} (see Figure 9.59). A very similar increase (above $p/p_0 > 0.9$) was also observed by Weber *et al*. for their PIMs.[297] A similar (less dramatic) increase was also observed for PIM-1.

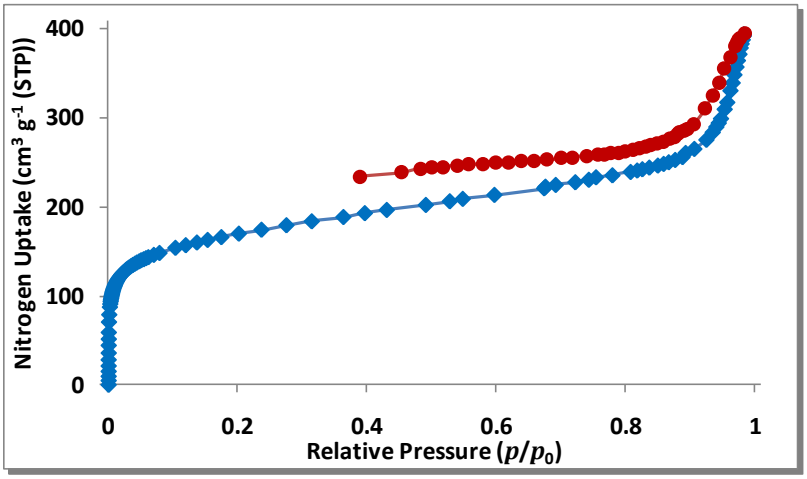

Figure 9.59 - Nitrogen adsorption (♦) and desorption (●) isotherms for the triptycene-based macromolecule PIM at 77 K.

The nitrogen adsorption isotherm was used to calculate the BET and Langmuir specific surface areas of the triptycene-based macromolecule PIM. Least squares linear regression was performed on the linear section of the respective plots to give a specific surface area. The macromolecule PIM exhibited BET and Langmuir surface areas of 607.3 ± 3.2 and 707.8 ± 10.4 $m^2\ g^{-1}$, respectively.

9.7.2.2. Hydrogen

9.7.2.3. Excess Adsorption

The macromolecule PIM was initially degassed for *ca*. 1000 minutes at room temperature followed by a further 1000 minutes at 100 °C. The macromolecule PIMs was found to have a skeletal density of 1.37 g cm^{-3}, which is comparable to the other PIMs. These values were obtained from helium pycnometry (at room temperature) and subsequently used for the buoyancy correction of the hydrogen sorption data. The materials had been degassed prior to the pycnometry measurements.

The initial hydrogen uptake of the triptycene-based macromolecule was 0.95 wt.% at 1 bar and 77 K. The hydrogen uptake at 10 bar is greater than the micropore capacity as calculated from the nitrogen adsorption data using the BET method. However, even at 18 bar, the hydrogen uptake does not exceed the micropore capacity as calculated using the Langmuir method, which is consistent with the other PIMs. It can be observed in Figure 9.60, that the excess gravimetric hydrogen isotherm at 77 K reaches saturation (1.40 wt.%) at 18 bar and then begins to slowly decrease. This is not however observed for the 87 K isotherm. Unfortunately, only the Trip(Oct)-PIM (of the triptycene containing PIMs), exhibits a lower hydrogen uptake than the triptycene-macromolecule PIM at 18 bar and 77 and 87 K. The Trip(Oct)-PIM exhibited an excess gravimetric uptake of 1.29 and 1.13 wt.% at the same temperature and pressure.

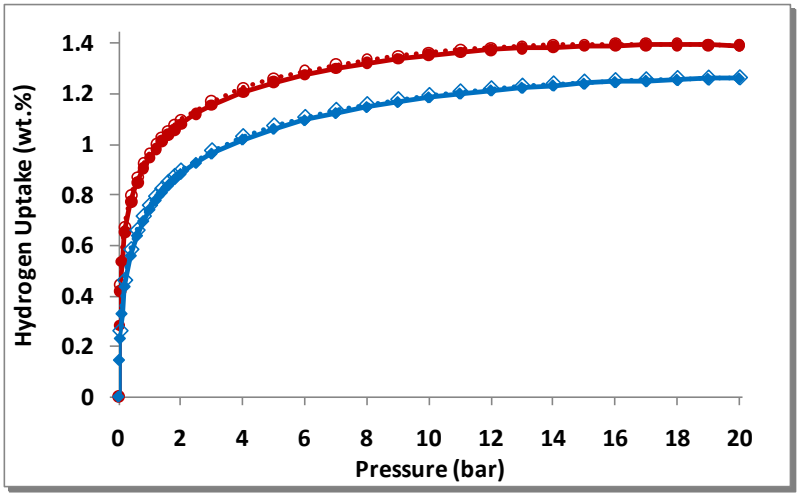

Figure 9.60 - Excess gravimetric hydrogen uptake for the triptycene-based macromolecule PIM at 77 (●) and 87 K (♦) up to 20 bar. Full symbols indicate adsorption, open symbols indicate desorption.

The gravimetric hydrogen storage capacity was used in conjunction with the density of hydrogen at the triple point (0.077 g cm^{-3}) to calculate the volume of hydrogen adsorbed in the pores. Using this volume (0.22 cm^3 g^{-1}), 82% of the (BET) pore volumes were filled. The skeletal densities and micropore volumes provided a geometric density of 1.05 g cm^{-3}. This translated in to a (theoretical) volumetric capacity of 14.7 kg m^{-3}, at 18 bar and 77 K.

The conversion between the measured excess adsorption to the absolute amount adsorbed used equation (3.50) with the assumption that the density of the adsorbed phase is equal to hydrogen at the triple point (0.077 g cm^{-3}), see section 3.6.2.1. The triptycene-macromolecule exhibited an absolute hydrogen uptake of 1.52 and 1.38 wt.% at 20 bar and 77 and 87 K, respectively.

The Langmuir plot for triptycene-macromolecule PIM at 77 K is shown in Appendix F. The graph is taken to be linear from 2 to 20 bar, which enables it to be used for calculating the maximum amount adsorbed, n_m; this would be consistent with a plateau for the absolute hydrogen adsorption isotherms. The analysis predicts that PIM-1 will have a maximum hydrogen uptake of 7.95(4) mmol g^{-1}, which equates to 1.60(1) wt.%. Using the pore volume of 0.22 cm g^{-1}, at saturation the adsorbate phase density is estimated to be 0.073 g cm^{-3}, slightly less than that of hydrogen at the triple point.

9.7.2.4. Empirical Isotherm Equations

The Sips and Tóth empirical isotherm equations were applied to the absolute adsorption isotherm at each temperature. Both equations appear to produce good fits, but residual plots illustrate the small differences between the data and the fitted models (see Figure 9.61). The Tóth model appears to be heading away from the experimental data at higher pressures compared to the Sips model. The two models produce fairly substantial differences in their predicted saturation uptakes, which are 2.06(2) and 2.57(4) wt.%, for the Sips and Tóth models, respectively at 77 K. Both these values are very similar to those predicted for PIM-1, which were 2.06(1) and 2.50(6) wt.%, for the Sips and Tóth models, respectively at 77 K.

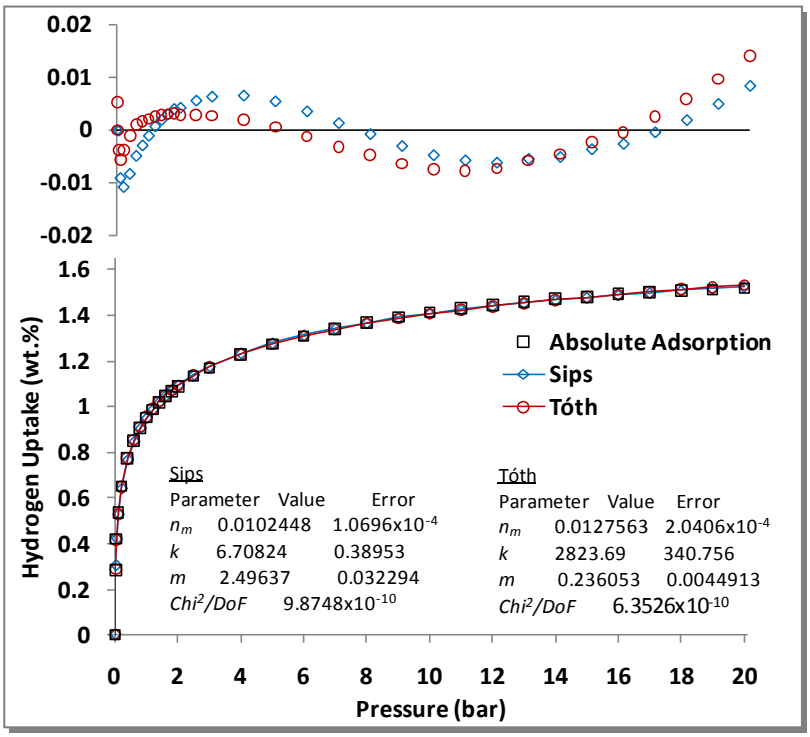

Figure 9.61 - Fitted Sips (◊) and Tóth (○) equations to the absolute hydrogen uptake versus pressure at 77 K up to 20 bar. Residual plots are shown at the top of the figure.

9.7.2.5. Enthalpy of Adsorption

9.7.2.5.1. Clausius-Clapeyron

The fitted 77 and 87 K absolute adsorption isotherms were used to calculate the enthalpy of adsorption using the Clausius-Clapeyron equation. The enthalpy of adsorption is calculated up to 0.8 wt.% as explained in section 6.2.2.5.4. The two models gave 15.2 and 10.6 kJ mol^{-1}, at the near zero coverage of 0.02 wt.% of hydrogen, for the Sips and Tóth fits, respectively. These are the highest values recorded for any of the PIMs in this investigation. The enthalpies of adsorption decrease sharply with increasing hydrogen uptake, with the two models both giving 5.7 and 5.8 kJ mol^{-1}, at 0.8 wt.% (see Figure 9.62).

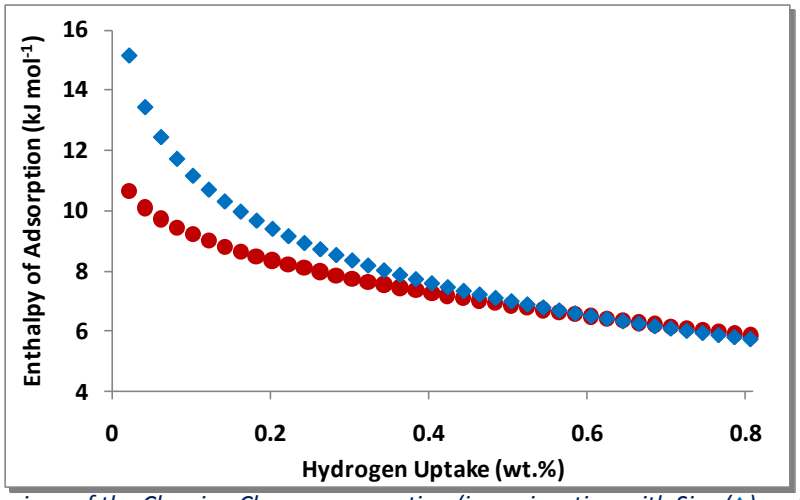

Figure 9.62 - Comparison of the Clausius-Clapeyron equation (in conjunction with Sips (♦) and the Tóth (●) equations fitted to the 77 and 87 K absolute isotherms).

9.7.2.5.2. Virial Type Thermal Equation

Equation (3.66) was used to fit the 77 and 87 K isotherms simultaneously. To be consistent with the other materials in this work, values of 6 and 3 were used for the coefficients m and n, respectively. The isosteric enthalpy of adsorption was subsequently calculated according to equation (3.67), as a function of hydrogen uptake, shown in Figure 9.63. The analysis produced an isosteric enthalpy of adsorption at zero coverage for the triptycene-macromolecule PIM of 9.8 kJ mol^{-1}. This was the highest for any of the amorphous PIMs in this investigation (using this method of determination). The enthalpy of adsorption decreased to 5.9 kJ mol^{-1} at 0.8 wt.% hydrogen, which is in good agreement with the Clausius-Clapeyron equation used previously.

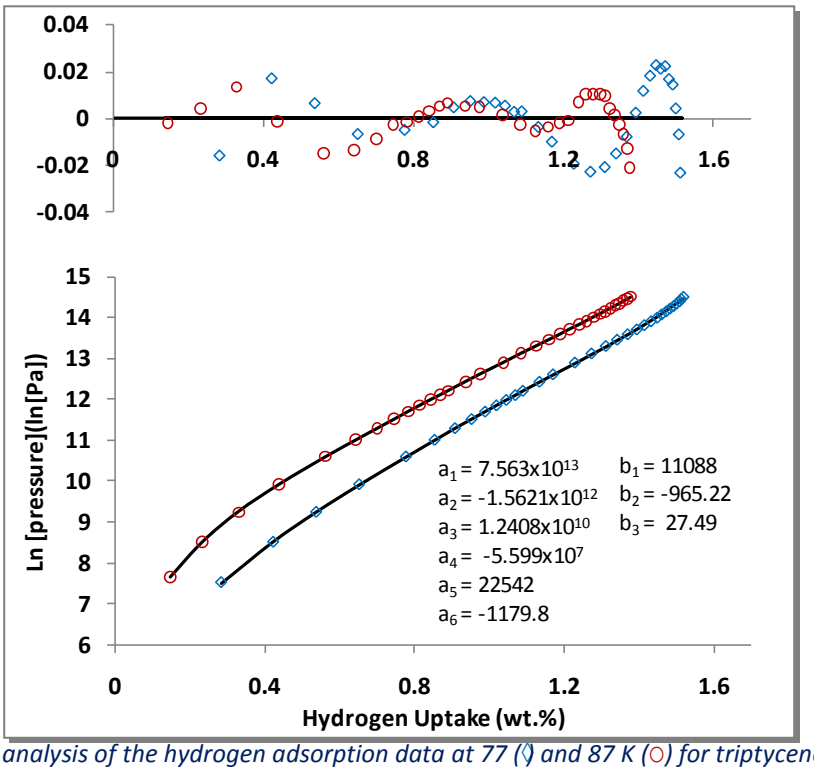

Figure 9.63 - Virial analysis of the hydrogen adsorption data at 77 (◊) and 87 K (○) for triptycene-based macromolecule to 20 bar. Open symbols display data, whilst the virial plots are indicated by solid lines. Residual plots are shown at the top of the figure.

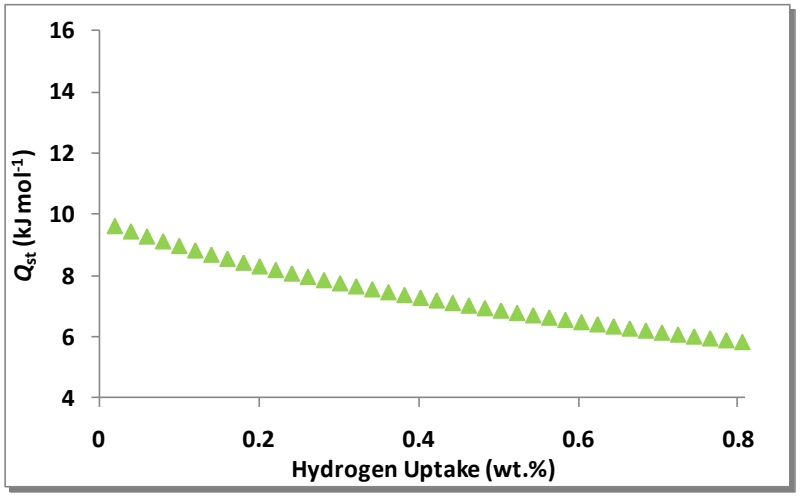

Figure 9.64 - Isosteric enthalpy of adsorption for triptycene-based macromolecule as a function of hydrogen uptake determined using the Virial type thermal equation with the 77 and 87 K.

Figure 9.65 displays a comparison for the previously determined enthalpies of adsorption with the virial type thermal equation using two temperatures (77 and 87 K). As with the previous materials studied in this investigation, very similar enthalpy of adsorption curves were observed for the Tóth and Virial equations. The Sips model appeared to overestimate the enthalpy of adsorption at low surface coverage,

however all three fitting models produced similar values by the time the hydrogen uptake had reached 0.8 wt.%.

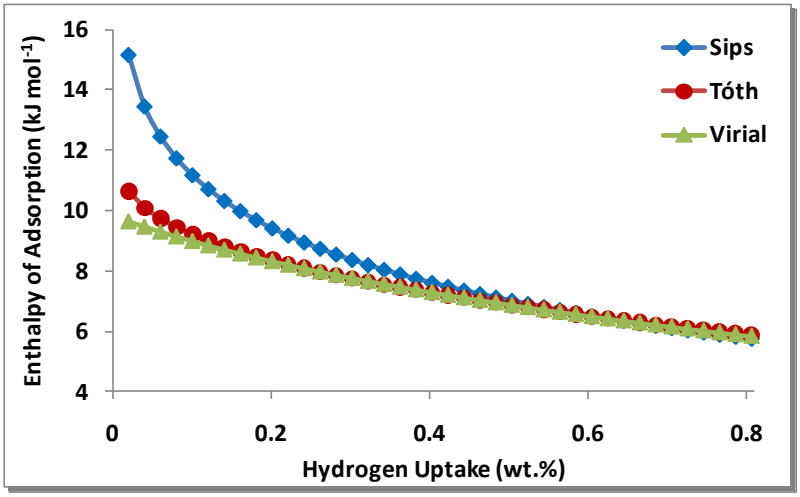

Figure 9.65 - A comparison of the isosteric enthalpy of adsorption for triptycene-based macromolecule as a function of hydrogen uptake using different fitting methods in conjunction with data generated at 77 and 87 K.

9.8. Organic Microporous Crystal

Porous crystals derived from organic compounds have been shown to host gas molecules and solvents as recently shown in COFs by El-Kaderi *et al.*[274] Colleagues at the University of Cardiff searched the Cambridge Structural Database (CSD) for a microporous crystalline material with a low calculated density (< 0.9 g cm^{-3}) and which was composed of rigid aromatic molecules. The crystal structure formed by 3,3',4,4'-tetra(trimethylsilylethynyl)biphenyl (TMS) looked particularly intriguing due to its apparent microporous structure having a resemblance to that of a typical zeolite.

9.8.1. Structure and Characterisation

The structure which was obtained from 3,3',4,4'-tetra(trimethylsilylethynyl)biphenyl has the cubic space group Pn3-n and a large unit cell (a = 29.575(2) Å) which incorporates 24 molecules of TMS (one of which is illustrated in Figure 9.66).

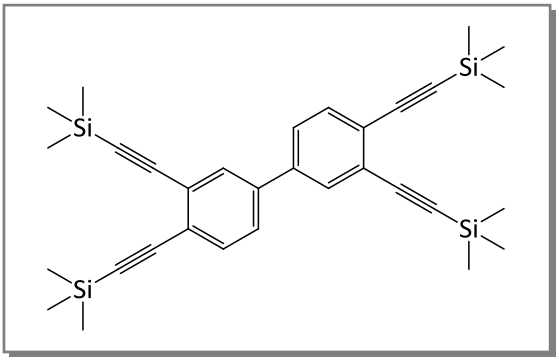

Figure 9.66 - The molecular structure of 3,3',4,4'-tetra(trimethylsilylethynyl)biphenyl (TMS).

Single-crystal XRD confirmed the structure they had synthesised was that which was reported in the CSD. TGA of a freshly synthesised sample showed a mass loss of 7%, which was attributed to the guest solvent molecule. ^{1}H NMR confirmed that the included molecule was hexane and that it was present in the crystal at a ratio of one molecule of hexane to two of TMS.[386] These techniques were performed at the University of Cardiff prior to the material being sent to the University of Birmingham for hydrogen sorption analysis.

Raman spectroscopy was used to observe any vibrational or rotational modes of the organic crystal (see Figure 9.67). The 785 nm (near infrared) laser was used to minimise fluorescence from the sample. A strong C≡C stretch is observed at 2160 cm^{-1}. Modes associated with aromatic C-C bonds were observed at 1600 cm^{-1}. Other relatively strong peaks around 1300 cm^{-1} were associated with CH_3. The Si-C modes exist in the fingerprint region. The assignments were made with reference to the work reported on 1,1-bis(trimethylsilylethynyl)cyclopropane by Trætteberg *et al*.[387]

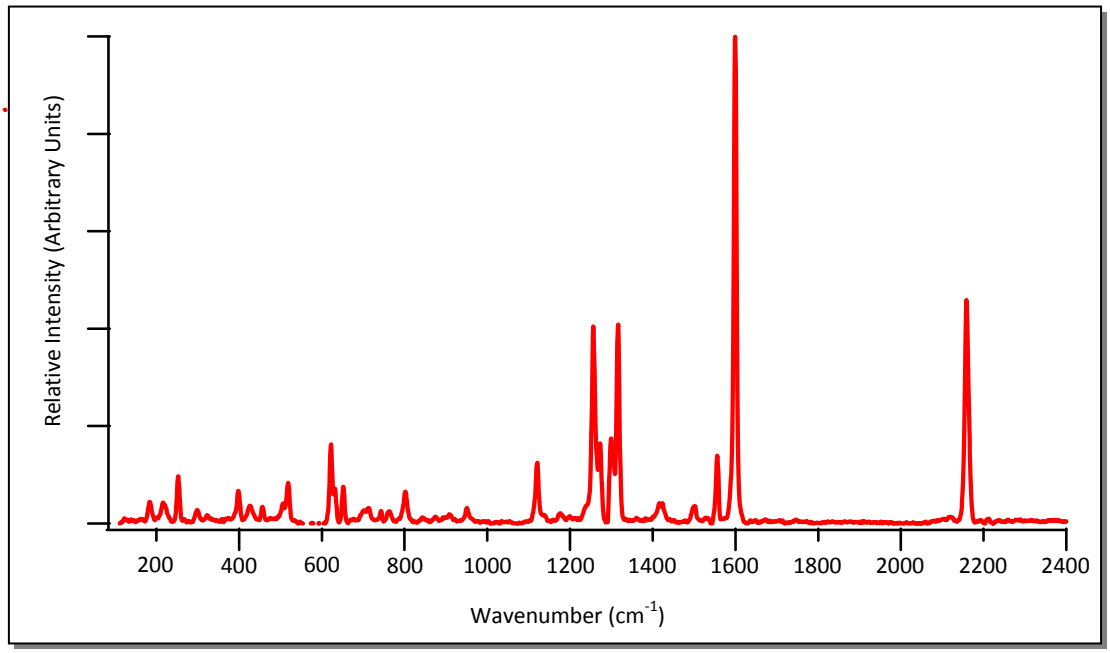

Figure 9.67 - Raman Spectroscopy of the Organic Crystal at room temperature using 785 nm laser from 100 to 2400 cm^{-1}.

9.8.2. Gas Adsorption

9.8.2.1. Nitrogen

Nitrogen adsorption was performed at 77 K after being outgassed at 50 °C for 1000 minutes. The low degassing was required due materials relatively low melting temperature. The evacuated crystal showed reasonable nitrogen uptake at a relative pressure of 74 $cm^3\ g^{-1}$ (STP) at $p/p_0 = 0.1$ (which equates to *ca.* 3.3 mmol g^{-1}). The isotherm appears to be of Type I in the IUPAC classification, which would be expected for the physisorption of gases in to a crystalline microporous material. Linear regression was used on the low-pressure adsorption isotherm to calculate BET and Langmuir surface areas of 264.6 ± 6.1 and 322.7 ± 3.3 $m^2\ g^{-1}$, respectively. This is slightly less than was automatically determined by the Beckman Coulter 3100 Surface Area Analyzer (278 $m^2\ g^{-1}$), and which was subsequently reported by Msayib *et al.*[386] The single point method was used to obtain the total pore volume of 0.16 $cm^3\ g^{-1}$ (at $p/p_0 = 1$). Unfortunately, this is less than each of the micropore volumes for PIMs reported in this work.

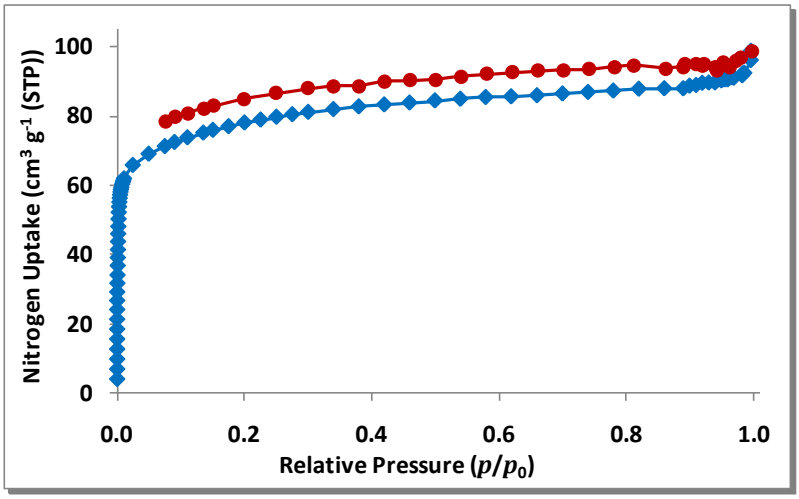

Figure 9.68 - Nitrogen adsorption (♦) and desorption (●) against relative pressure at 77 K.

Further analysis of the low-pressure region (< 0.005 p/p_0) reveals the filling of two different micropores. This is illustrated in Figure 9.69 where it can be observed that the material possesses two different sized pores. This correlates with the crystal structure which has channels of 0.4 and 1.1 nm. Unfortunately, the pore size of the smaller of the two channels cannot currently be measured by this technique due to its inability to measure lower relative pressures. However, it is displayed as a distorted peak around 0.6 nm.

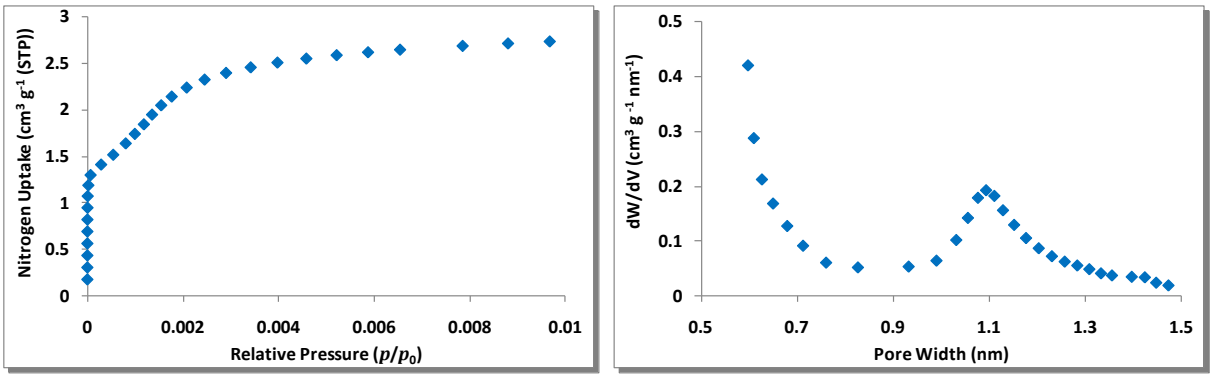

Figure 9.69 - (Left) Low relative pressure region of the nitrogen adsorption isotherm at 77 K. (Right) Pore size distribution calculated from the low pressure nitrogen adsorption data using the Horváth-Kawazoe method.

9.8.2.2. Hydrogen

9.8.2.2.1. Excess Adsorption

The TMS-based crystal was initially degassed for *ca*. 1000 minutes at room temperature followed by a further 1000 minutes at 50 °C. Helium pycnometry was used to determine a skeletal density 0.95 g cm^{-3}, which was close to the calculated crystal density of 0.83 g cm^{-3}. The former value was used for the buoyancy correction of the hydrogen sorption data. The crystal exhibited an excess hydrogen uptake of

0.50 wt.% (2.49 mmol g^{-1}) at and 1 bar and 77 K before rising to 0.86 wt.% (4.25 mmol g^{-1}) at 10 bar. Despite the relatively low hydrogen storage capacity, there are very few other published reports on the hydrogen sorption properties of an organic compound that forms a microporous crystal. In fact the only other material found, which was based on dipeptide crystals, exhibited just 0.45 wt.% (2.2 mmol g^{-1}) at 10 bar and 77 K.[388]

It can be observed from Figure 9.70, that the excess gravimetric hydrogen isotherm at 77 K reaches saturation at 16 bar and then begins to decrease. This is not however observed in the 87 K isotherm, meaning that the two isotherms begin to come closer together at higher pressures. This effect is comparable to the work reported for IRMOF-1 and ZIF-8 by Zhou *et al.*[117] However, that study was performed at much higher pressures and lower temperatures.

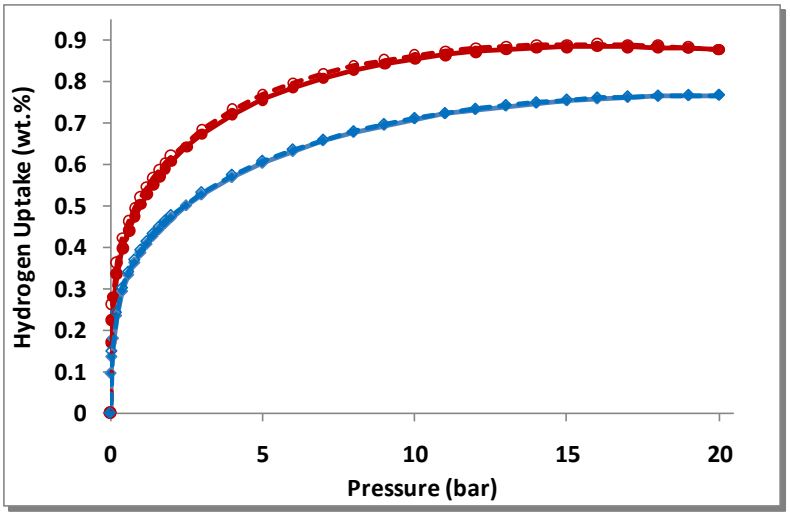

Figure 9.70 - Excess gravimetric hydrogen sorption isotherms for the TMS-based organic crystal at 77 (●) and 87 K (♦) up to 20 bar. Closed and open symbols indicate adsorption and desorption isotherms, respectively.

The gravimetric hydrogen storage capacity (4.39 mmol g^{-1}) was used in conjunction with the density of hydrogen at the triple point (0.077 g cm^{-3}), to calculate the volume of hydrogen adsorbed in the organic crystal (0.115 cm^3 g^{-1}). This corresponded to a filling of 122% of the micropore volume (as calculated using the BET method). The Langmuir micropore volume was calculated to be 0.115 cm^3 g^{-1}, using this value, the pore filling corresponds to 100% of the micropore volume. However, the hydrogen uptake corresponds to 72% of the total pore volume (0.16 cm^3 g^{-1}) of the organic crystal, which is comparable to the other

microporous materials in this study. The Dubinin-Radushkevich equation was extrapolated to $\log^2(p_0/p) = 0$, on carbon dioxide adsorption (at 0 °C) to give a micropore volume of 0.103 $cm^3\ g^{-1}$.

The conversion between the measured excess adsorption to the absolute amount adsorbed used equation (3.50. The Organic Crystal exhibited an absolute hydrogen uptake of 1.06 and 0.92 wt.% at 20 bar and 77 and 87 K, respectively.

9.8.2.2.2. The Langmuir Isotherm

The Langmuir plot for the TMS-based microporous crystal at 77 K is shown in Appendix F. The graph is taken to be linear from 2 to 20 bar, which enables it to be used for calculating the maximum amount adsorbed, n_m; this would be consistent with a plateau in absolute hydrogen adsorption isotherms. The analysis predicts that the Organic Crystal will have a maximum hydrogen uptake of 5.15(2) mmol g^{-1}, which equates to 1.04(1) wt.%. Using the pore volume of 0.16 cm g^{-1}, at saturation the adsorbate phase density is estimated to be 0.065 g cm^{-3}, slightly less than that of liquid hydrogen.

9.8.2.2.3. Empirical Isotherm Equations

Figure 9.71 illustrates the application of the Sips and Tóth empirical isotherm equations to the absolute adsorption isotherm at 77 K. The residual plot of the fit indicates that neither fit is as close as that observed for the PIMs, with distinct differences around 10 and 20 bar. The two models produce fairly substantial differences in their predicted saturation uptakes, which are 1.72 ± 0.12 and 3.09 ± 0.64 wt.%, for the Sips and Tóth models, respectively at 77 K.

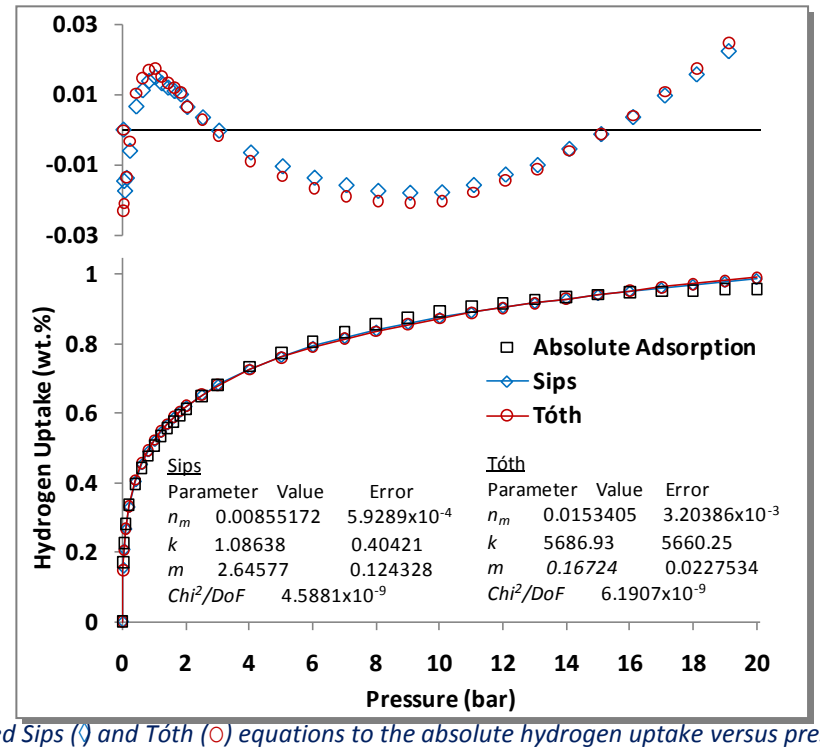

Figure 9.71 - Fitted Sips (◊) and Tóth (○) equations to the absolute hydrogen uptake versus pressure at 77 K up to 20 bar. Residual plots are shown at the top of the figure.

9.8.2.2.4. Enthalpy of Adsorption

9.8.2.2.4.1. Clausius-Clapeyron

The fitted 77 and 87 K absolute adsorption isotherms were used to calculate the enthalpy of adsorption using the Clausius-Clapeyron equation (see Figure 9.72). The enthalpy of adsorption is calculated up to 0.8 wt.% as explained in section 6.2.2.5.4. The two models give a value of 9.83 and 6.98 kJ mol^{-1}, at near zero coverage (0.02 wt.% H_2), for the Sips and Tóth fits, respectively. This is not quite as high as was observed by the Takeda 4A porous carbon, which had a pore size in the range 0.3 to 0.5 m, using the same techniques. The lower enthalpy of adsorption determined here may be a result of the smaller pore having a low relative ratio to the large pore (which has a diameter of 1.1 nm).

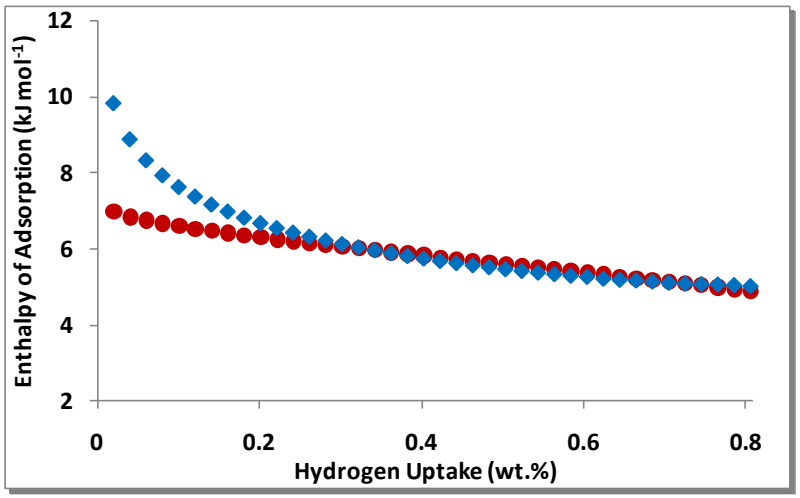

Figure 9.72 - Comparison of the Clausius-Clapeyron equation (in conjunction with Sips (♦) and the Tóth (●) equations fitted to the 77 and 87 K absolute isotherms).

9.8.2.2.4.2. Virial Type Thermal Equation

Equation (3.66) was used to fit the 77 and 87 K isotherms simultaneously using values of 6 and 3 for the coefficients m and n, respectively. The isosteric enthalpy of adsorption was subsequently calculated according to equation (3.67), as a function of hydrogen uptake (shown in Figure 9.74). The analysis produced an isosteric enthalpy of adsorption at zero coverage of 12.0 kJ mol^{-1}, which was *ca*. 2 kJ mol^{-1} higher than that observed for the carbon material.

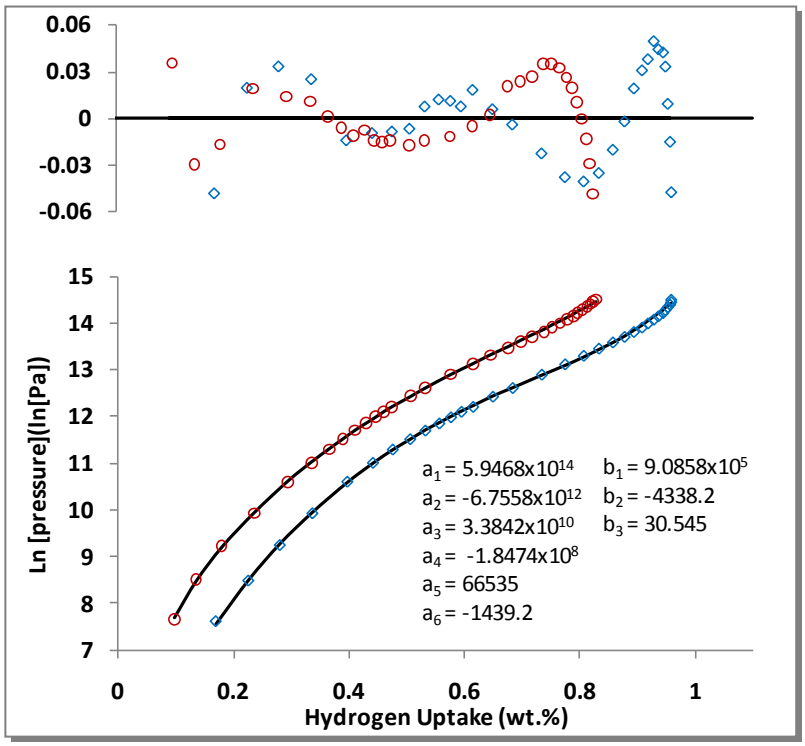

Figure 9.73 - Virial analysis of the hydrogen adsorption at 77 (◊) and 87 K (○) for Organic Crystal to 20 bar. Open symbols display data, with the solid lines indicating the virial plots. Residual plots are shown at the top of the figure.

The observed upturn in the enthalpy of adsorption at around 0.6 wt.% is likely to be due to the convergence of the 77 and 87 K isotherms at higher pressures. In this region, the adsorbate-adsorbate interactions are likely to have a strong effect on the determined enthalpy of adsorption value. If only the low pressure region of the isotherms are considered, the enthalpy of adsorption should not be taken above around 0.5 wt.% for this sample, at this point the 77 K isotherm was equal to a pressure of 1 bar. The enthalpy of adsorption is only shown above this point for this material in order to be comparable with other materials reported in this investigation.

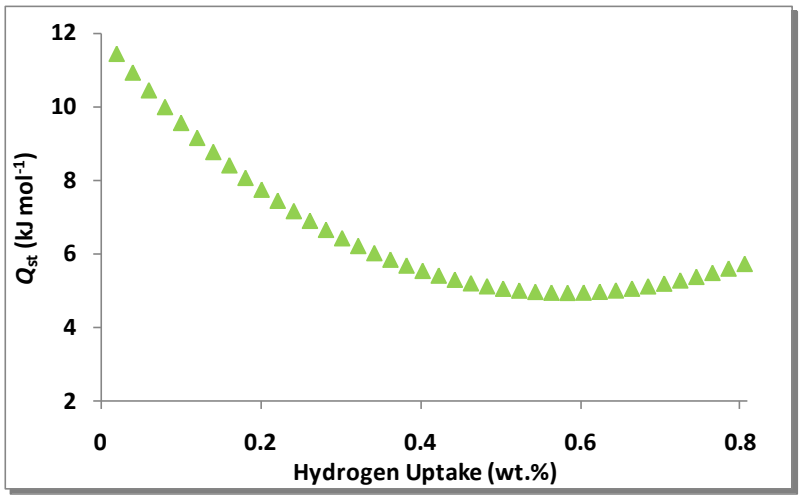

Figure 9.74 - Isosteric enthalpy of adsorption for the TMS-based microporous crystal as a function of hydrogen uptake determined using the Virial type thermal equation with the 77 and 87 K.

Figure 9.75 displays a comparison for the previously determined enthalpies of adsorption with the virial type thermal equation using two temperatures (77 and 87 K). The enthalpy of adsorption curves produced by the Clausius-Clapeyron equation are quite different to the values determined using the virial type thermal equation. This expected to be a result of the poorer fitting from both the Sips and Tóth equations as discussed above. However, due to the lack of hydrogen uptake by the organic crystal, there are very few data points less than 0.2 wt.%. This means that the multi-parameter virial type thermal equation may be subject to increased errors in this low uptake region, due to it having no physical meaning in relation to gas adsorption, which is in contrast to the empirical isotherms.

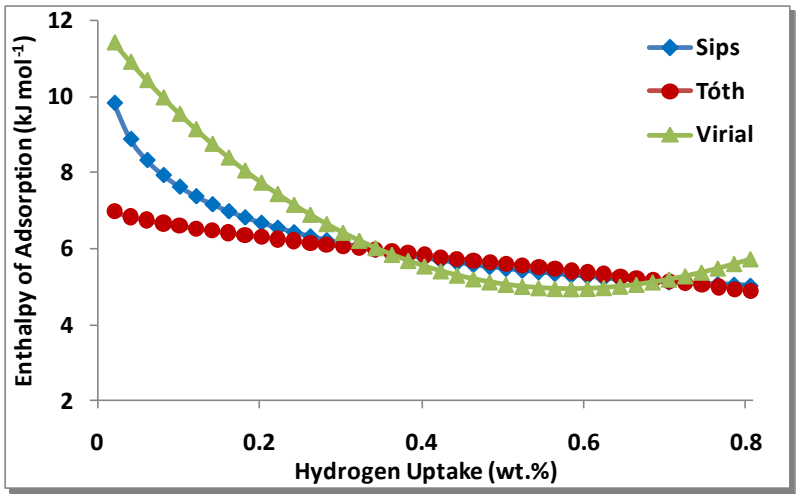

Figure 9.75 - A comparison of the isosteric enthalpy of adsorption for the Organic Crystal as a function of hydrogen uptake using different fitting methods in conjunction with the 77 and 87 K.

9.9. PIM Processing

9.9.1. Carbon Dioxide

Carbon dioxide adsorption (at 0 °C) can be used to determine the micropore volume using the Dubinin-Radushkevich equation. The CO_2 adsorption isotherm (at 0 °C) for PIM-1, for a few of the triptycene-based PIMs (R = Me, Et and *i*-Pr) and the organic crystal are shown in Figure 9.76. PIM-1 exhibits an uptake of 46.7 $cm^3\ g^{-1}$ (STP), which equates to *ca*. 2 mmol g^{-1} at 700 mbar. The three Trip-PIMs showed an uptake of 101.5, 89.0 and 80.8 $cm^3\ g^{-1}$ (STP), *ca*. 4.5, 4.0 and 3.6 mmol g^{-1} at the same temperature and pressure. As expected from the previous gas sorption experiments, the organic crystal exhibited the lowest uptake of carbon dioxide, 20.7 $cm^3\ g^{-1}$ (STP), *ca*. 0.9 mmol g^{-1}. The calculated micropore volumes using this technique have been previously reported in this work.

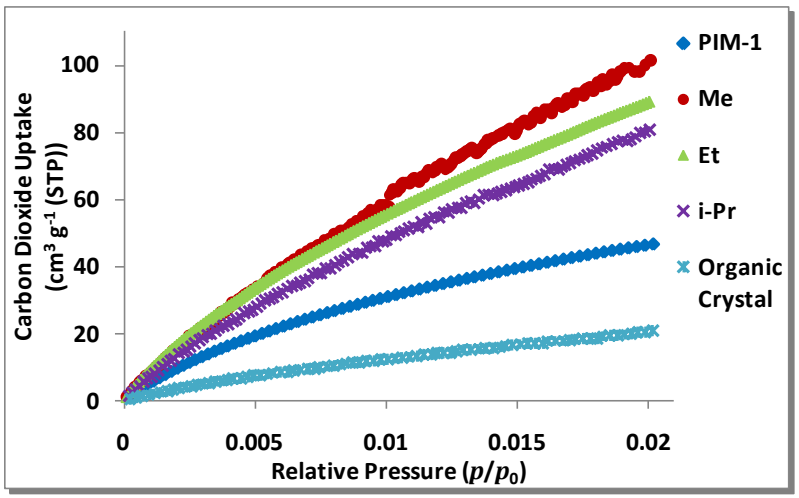

Figure 9.76 - Carbon dioxide adsorption against relative pressure at 0 °C, up to 700 mbar.

9.9.2. PIM Processing using Gaseous Carbon Dioxide

The effect of processing the PIMs was assessed using solvents such as supercritical carbon dioxide. Initially, a sample of PIM-1 was loaded on to the IGA and degassed in the same way as described previously before a hydrogen sorption measurement was performed at 77 K. The sample was then subjected to carbon dioxide (for several days at 18 bar) before a second hydrogen sorption measurement was performed at 77 K. A short degas of 20 minutes was performed (at room temperature) between the carbon dioxide and hydrogen measurements. This process was carried out twice with the same conditions on two portions of the same batch of PIM-1. The resulting hydrogen sorption isotherms are displayed in

Figure 9.77. After being subjected to carbon dioxide, the hydrogen uptake increase from 1.47 to 1.57 wt.% (at 8 bar and 77 K), representing a 7% increase in hydrogen storage capacity. On the second run, the hydrogen uptake rose from 1.48 to 1.58 wt.% (at 8 bar and 77 K).

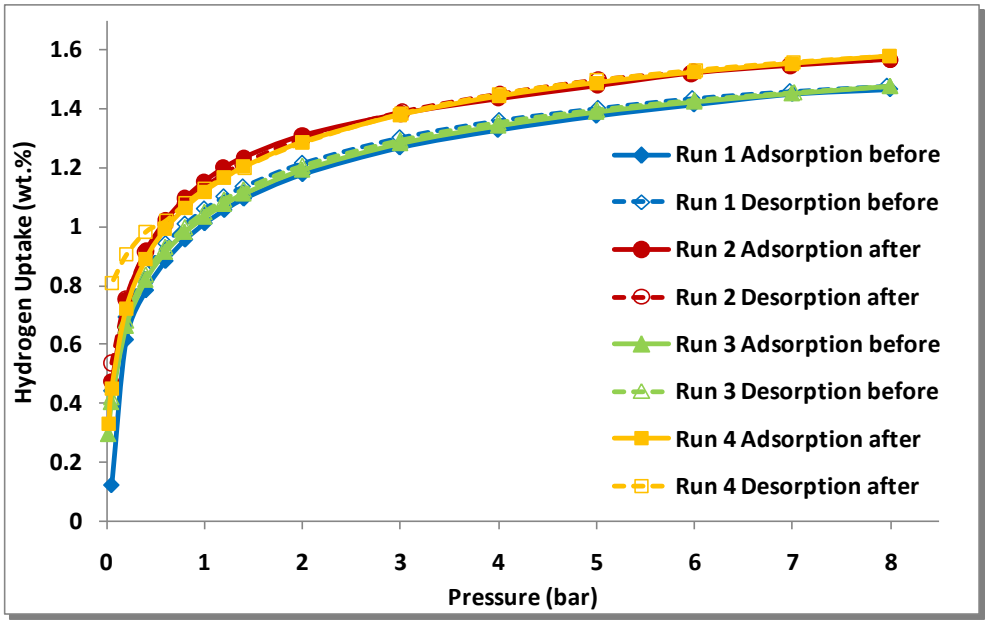

Figure 9.77 - Excess gravimetric hydrogen adsorption and desorption isotherms for PIM-1 at 77 K up to 8 bar, before and after being subjected to carbon dioxide at room temperature up to 18 bar for several days. Runs 1 and 2 were on the first sample, Runs 3 and 4 were on the second sample of PIM-1.

Around 300 mg of a separate portion (of the same batch) of PIM-1 was subjected to supercritical carbon dioxide (at 100 °C and 100 bar) for 2 hours. The sample was then transferred to the IGA in order to perform the hydrogen sorption measurements. The sample was evacuated for 20 minutes prior to the hydrogen sorption measurements (at 77 K). The initial hydrogen run after the supercritical CO_2 displayed a substantial increase in hydrogen uptake at relatively low pressures, which remained present up to 18 bar. At 8 bar, the hydrogen uptake was 1.81 wt.%, which is an increase of 0.35 wt.% from the measurements displayed in Figure 9.77, representing an increase of 24%. At 20 bar and 77 K, the excess gravimetric hydrogen storage capacity was 1.95 wt.%. The hydrogen isotherm was run for a second and third time after the supercritical CO_2 to assess the cyclability of the extra capacity. Unfortunately, the observed increase was not maintained. On the second and third runs, the hydrogen uptake was 1.56 and 1.54 wt.% at 8 bar. Interestingly, this is very close to the improvement observed after processing in gaseous CO_2 at 18 bar. At 20 bar, the hydrogen uptake was 1.70 and 1.68 wt.%.

As illustrated in Figure 9.77 and Figure 9.78, all the isotherms before and after treatment with carbon dioxide exhibited little to no hysteresis from the adsorption to desorption isotherms.

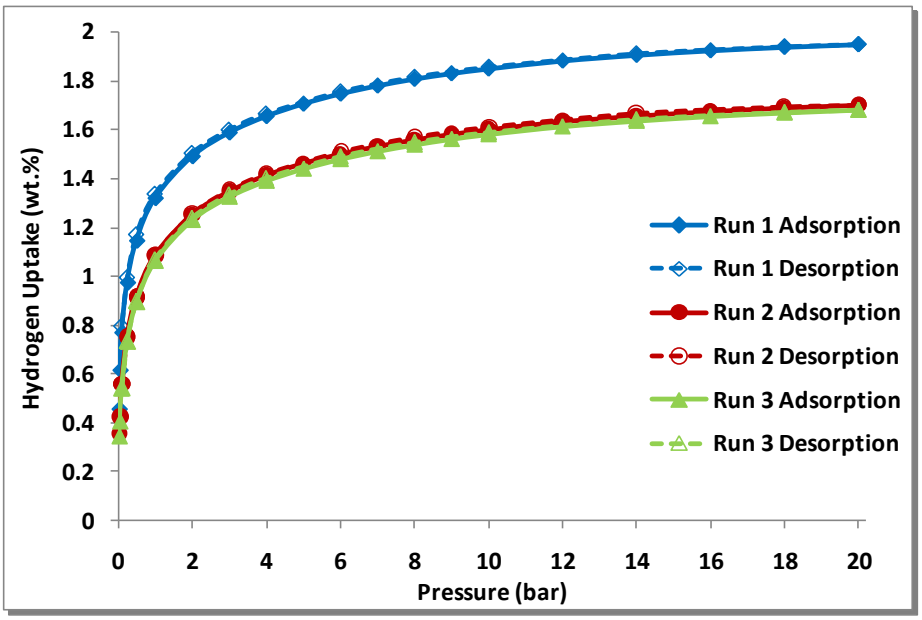

Figure 9.78 - Excess gravimetric hydrogen adsorption and desorption isotherms for PIM-1 at 77 K up to 20 bar. before and after being subjected to supercritical carbon dioxide at 100 °C and 100 bar for 2 hours.

Performing a carbon dioxide treatment in this manner (i.e. externally from the IGA) also rules out the possibility of residual carbon dioxide being present in the hydrogen gas stream of the IGA and that 'artificially' increases the hydrogen uptake.

Raman spectroscopy and TGA-MS were performed to assess whether any carbon dioxide remained inside the pores of PIM-1. Neither techniques showed any evidence that CO_2 was still present, see Figure 9.79 and Figure 9.80. The Raman spectra suggest that the treatment with supercritical CO_2 did not alter the structure of the PIM.

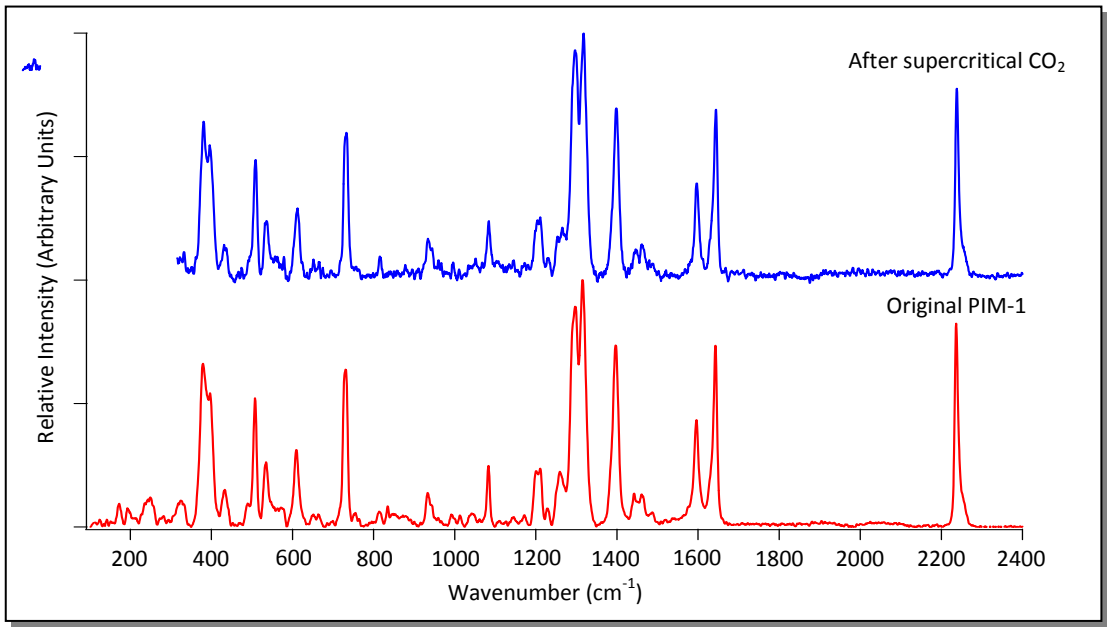

Figure 9.79 - Raman Spectroscopy of PIM-1 at room temperature, before and after supercritical CO_2 treatment using 785 nm laser from 100 to 2400 cm^{-1}.

Using TGA the same mass loss that was previously shown for PIM-1, was not observed here. This suggests that the supercritical CO_2 removes residual solvent from within the pores in the same way as degassing.[389,390] However, it is important to note that in order for the carbon dioxide to become supercritical it needs to be heated above the critical point; in this case the sample was heated to 100 °C. The TGA also displays the thermal stability of PIM-1 up to around 430 °C, above which it begins to decompose. The mass spectrometer indicates a loss of water as the temperature is increased, with a peak in the loss of both water and nitrogen upon thermal decomposition (see Figure 9.80).

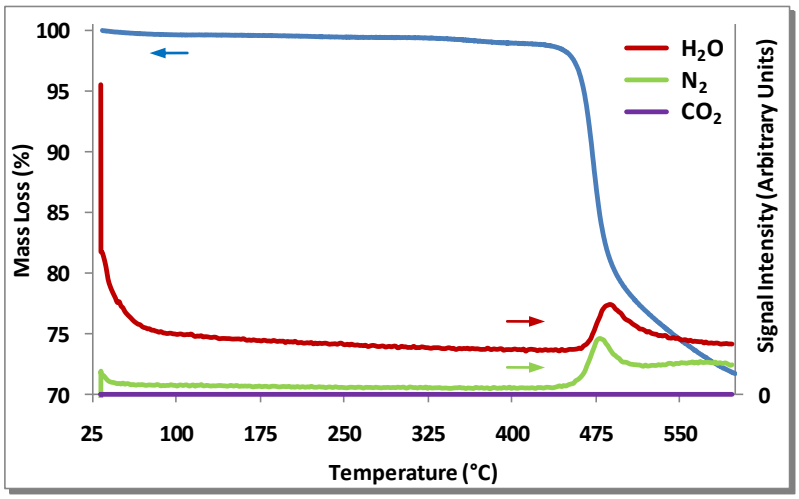

Figure 9.80 - TGA-MS for PIM-1 after being subjected to supercritical CO_2.

The process by which the treatment with gaseous CO_2 alters the PIMs to induce an increase in hydrogen uptake is unclear. Further work is required to investigate this effect.

9.10. Chapter Summary

This chapter reports the structural and gas adsorption properties for several Polymers of Intrinsic Microporosity (PIMs). PIM-1 was first in a series of soluble PIMs, however, the introduction of larger monomers resulted in the PIMs being insoluble. By using the triptycene molecule as the catechol monomer it was found that larger surface areas and an increased hydrogen storage capacity could be produced, in comparison to the spirobisindane monomer.

A series of triptycene-based network PIMs that possess different alkyl groups attached to their bridgehead positions were investigated to observe their effect. It was shown that gas adsorption can be controlled by varying the length of the straight chain and by branching the alkyl units. This lead to BET and Langmuir surface areas of 618 to 1760 $m^2 g^{-1}$, and 754 to 2053 $m^2 g^{-1}$, respectively. The shorter (e.g., R = Me) or branched (e.g., R = *i*-Pr) alkyl chains provided materials with a greater gas adsorption capacity and an ability to swell (as observed by the sloping adsorption on the nitrogen sorption isotherms). Whereas the longer alkyl chains (e.g., R = Oct) exhibited less gas uptake and nitrogen isotherms that were closer to being Type I in nature (according to the IUPAC classification). The triptycene-based PIM with the methyl substituent displayed the greatest excess gravimetric hydrogen uptake at both 1 and 18 bar and 77 K; 1.81 and 3.32 wt.%, respectively. This relatively high uptake was almost matched by the triptycene-based PIM with the branched iso-propyl substituent and also the network PIM with the A2 + B3 monomers, which both exhibited excess gravimetric hydrogen uptake values of 1.74 wt.% at 1 bar and then 3.09 and 3.00 wt.% at 18 bar and 77 K, respectively.

Using the Clausius-Clapeyron equation with the Tóth fitted absolute hydrogen adsorption isotherms at 77 and 87 K, the triptycene-based PIM with the H substituent exhibited the highest enthalpy of adsorption at low hydrogen uptake (10.45 kJ mol^{-1}). However, this high enthalpy of adsorption dropped to 8.85 kJ mol^{-1} using the virial thermal type equation. Using this virial equation, the A2 + B3 network PIM exhibited the highest enthalpy of adsorption at 0.02 wt.%; 9.53 kJ mol^{-1}.

There appears to be a compromise for the PIMs between the potential for large gas uptake and high enthalpies of adsorption. This was shown by the triptycene-based PIMs, where the shorter alkyl chain PIMs had greater nitrogen and hydrogen uptake, but lower enthalpies of adsorption relative to the triptycene-based PIMs with longer alkyl chained substituents. It would be advantageous to design new PIMs similar to the A2 + B3 network PIM which exhibited both high enthalpies of adsorption and large gas uptake.

Since there is a lack of any exposed metal sites (or indeed any metal ions) in PIMs, it would be expected that the enthalpy of adsorption is solely due to dispersive interactions brought about by the close proximity of the pore walls. This means that the larger macromolecule type PIMs are likely to block the microporosity by filling space created by the rigid organic framework. This potentially produces smaller pores with a lower micropore volume. For example, in the triptycene-based PIM series, where the larger alkyl chains have higher enthalpies of adsorption and lower gas uptake.

The majority of the PIMs also exhibited large hysteresis in the nitrogen sorption isotherms, which is probably related to swelling of the polymer network. The PIMs with a large polymer unit displayed less hysteresis which indicates less swelling as a result of greater steric hindrance. Unfortunately, hydrogen adsorption does not give rise to a similar effect under the conditions used in this investigation. Comparing the micropore capacity from the nitrogen adsorption and the hydrogen uptake, it is expected that swelling might occur at higher pressures, once the hydrogen capacity fills the micropore volume.

The volumetric hydrogen storage capacities were determined using the calculated micropore volumes from the nitrogen adsorption isotherms, and the measured skeletal densities. For the Trip(Me)-PIM this gave a geometric density of 0.81 g cm^{-3} and volumetric capacity of 27.2 kg m^{-3} at 20 bar and 77 K. This was the largest volumetric capacity of the PIMs reported in this investigation.

Chapter 10

GENERAL DISCUSSION

The surface texture and the structure of the adsorbent play a crucial role in the physisorption of gases, and by optimizing these properties an enhancement of their adsorption potential can be achieved. The best candidates for storing hydrogen in the molecular form are highly porous nanostructured materials. Among these it is possible to distinguish four main classes: zeolites, carbon materials, metal-organic frameworks (MOFs), and porous polymers.

Despite the application of the BET method to microporous materials being rather crude, a large apparent BET surface area is still regarded as a key property for a high hydrogen storage capacity at low temperatures via physisorption. It's success is probably due to the ease to which the "area" that the method provides, can be easily imagined.[109] Purely microporous materials often have a Type I isotherm with a horizontal plateau that provides the micropore capacity. However this is rarely observed, and instead composite isotherms of either Type I and Type II or Type I and Type IV are more typical. The first combination would be a result of micropores and external surface and the second would be a result of micropores and mesopores. An additional problem lies with non-crystalline materials, where a degree of pore swelling can be mistaken for either external surface or mesopores, or both. The correlation between the BET surface area and some porous materials from the literature was illustrated in Chapter 4. Figure 10.1 displays the correlation between the BET surface area (as determined by nitrogen adsorption at 77 K) with the excess gravimetric hydrogen storage capacity (at 77 K and 15 bar) of all the microporous materials reported in this work. Chahine's Rule suggests that for every 500 $m^2 g^{-1}$ the maximum hydrogen storage capacity increases by 1 wt.%.[162] Panella *et al*. measured a series of carbon-based materials and found a correlation of 0.96 wt.% for every 500 $m^2 g^{-1}$.[196] Using all of the materials in this investigation this correlation was found to be 0.99 wt.% for every 500 $m^2 g^{-1}$, with this value dropping to 0.94 wt.% using just the PIMs. The BET surface areas used for the two MOF materials (in Figure 10.1), were reported by

Panella *et al.*[231], however the correlation between to the hydrogen uptake and surface area suggest that for Cu-BTC, the BET surface area should be closer to 2000 $m^2 g^{-1}$. A BET surface area of 1507 $m^2 g^{-1}$ was reported by Rowsell and Yaghi.[134]

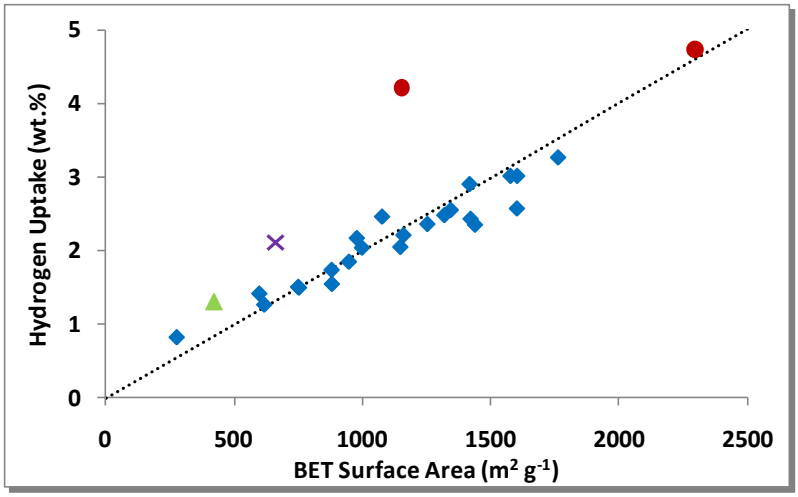

Figure 10.1 - Correlation between the BET surface area and the hydrogen storage capacity (at 15 bar and 77 K) of the microporous materials measured and reported in this work. Carbon (▲), NaX (✕), MOFs (●), and PIMs (♦). The dashed line represents Chahine's rule.[162]

The accuracy of measuring the hydrogen storage capacity of microporous materials relies on several factors, some of which were mentioned in Chapter 3. Besides the obvious problems such as equipment calibration and gas purity; reaching equilibrium and adequate degassing have also been shown to provide a source of substantial errors. Indeed for a volumetric system the "dry mass" of the adsorbent is typically only measured once (either before or after the adsorption study). This can lead to substantial errors in the storage capacity measured if impurities are introduced during sample transfer or measurement.

One of the interesting findings of this project was the difference in degassing times between different materials. Zeolitic materials for example typically desorbed in less than 1000 minutes at the optimum temperature; whereas the metal-organic frameworks took more than 1500 minutes. This is assumed to be due in part to the different impurities (such as solvents and water), which are present in the pores of each material. It was not possible to fully degas the metal-organic frameworks after 1500 minutes; however the rate of mass loss at this point was less than 0.01 mg per hour. It was not possible to degas the materials for longer durations due to time constraints on the equipment, and it had been shown that longer times had little effect on the hydrogen capacity recorded. However this did introduce an issue

when measuring several isotherms back to back. On occasions it was necessary to degas the materials in between measuring two isotherms, if for example it was thought that impurities has been introduced into the gas line (e.g. due to changing gas cylinders). A new dry mass had to be recorded for each isotherm on degassing otherwise not all of the isotherms would start from zero, due to small changes in the degassed condition of the sample. Although the changes in dry mass had a relatively small impact on overall hydrogen capacity, they could have a larger effect on the enthalpy of adsorption values recorded.

This was not found to be such a problem with either the carbon material, NaX or the PIMs. For example the Trip(Me)-PIM was found to repeatedly return to the same dry mass (within *ca*. 20 μg). Figure 10.2 shows a comparison of the excess and absolute hydrogen adsorption for some porous materials. The effect of the surface area can be seen with IRMOF-1 displaying the greatest hydrogen uptake at 15 bar and 77 K.

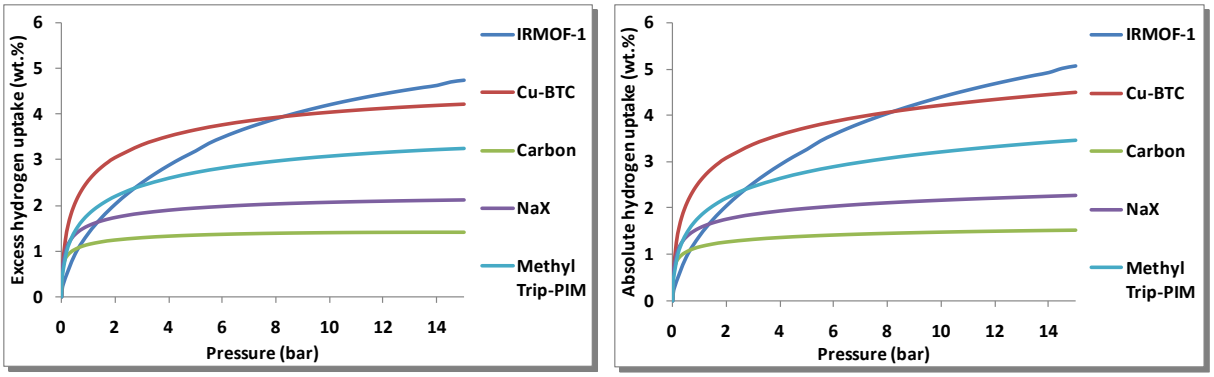

Figure 10.2 - Gravimetric excess (left) and absolute (right) isotherms for some of the porous materials measured at 77 K up to 15 bar hydrogen. The adsorbate phase density was assumed to be equal to that of hydrogen at the triple point (0.077 g cm^{-3}).

It is interesting to compare the hydrogen weight percentage of different materials over a given pressure range. However, if information is required on the curve shape of the isotherm or on how close a material is to saturation at a given pressure then fractional coverage should be plotted against relative pressure. The curve shape of an isotherm plotted in this manner would illustrate the differences in the heterogeneity of different adsorbents, because a heterogeneous surface uptakes more adsorptive, at the same relative equilibrium pressure, as a homogeneous surface with the same overall capacity.[59] A problem occurs when the measured temperature is in the supercritical region of the phase diagram. In

this region, the gas does not saturate to form a liquid, regardless of the temperature or pressure. Unfortunately, for hydrogen, the critical point is 32.97 K and 12.9 bar, and the typical measurement temperature for porous materials is 77 K. As there will not actually be a physical saturation vapour pressure above the critical temperature, then using a "pseudo saturation vapour pressure" might be the best option in order to define a reference pressure, despite it having no physical meaning.

Schmitz *et al*. made similar attempts to "normalise" the excess adsorption isotherms in order to compare their shapes.[191] However, they chose to normalise at an uptake value at just 20 bar, suggesting that each material was fully saturated at this pressure. Unfortunately, measurements at higher pressures by workers such as Kaye *et al*.[147] proved this normalisation to be entirely erroneous. In this work, equation (3.50) was used to calculate the absolute hydrogen uptake using the measured excess quantities. The absolute hydrogen adsorption isotherms (which are Type I) were then fitted using empirical equations such as the Sips and Tóth equations. The two equations can return maximum hydrogen uptake values (complete saturation) as well as the hydrogen storage capacity at any pressure (below saturation). Whilst these values are likely to have fairly large errors attached to them (due to such a small region of the isotherm being used for the fitting), they do prove useful for allowing trends to be observed between different types of microporous materials. For instance, these saturation values can be used to plot fractional coverage against pressure (see Figure 10.5).

Additionally, the predicted hydrogen saturation values can be used to estimate the adsorbate phase density, given a known pore volume (see Table 10.1).[128,132] Despite the Tóth model providing a more accurate fit to the absolute adsorption isotherm, the adsorbate densities are greater than the density of solid hydrogen, which is unlikely to be correct. However, the adsorbate densities produced by the Sips model show a remarkable correlation with the triple point density of hydrogen (0.077 g cm^{-3})[128,132], with four of the five microporous materials chosen for comparison (in Table 10.1). The notably low adsorbate phase density estimated by both the Sips and Tóth models for the activated carbon material suggests the total pore volume reported by Grande *et al*. and Moyer *et al*. could be incorrect. However, both groups in addition to Zlotea *et al*., reported a micropore volume of 0.17 cm^3 g^{-1}.[360,361,363] Additionally, the results of

the round-robin test reported by Silvestre-Albero *et al*. gave micropore volumes (using nitrogen adsorption at 77 K) in the range 0.14 to 0.17 $cm^3 g^{-1}$ and mesopores volumes in the range 0.00 to 0.11 $cm^3 g^{-1}$.[359] Combining these values gave a total pore volume which is remarkably close to the predicted total pore volume using the triple point density of hydrogen and the (Sips) calculated hydrogen saturation value for the carbon material, 0.24 $cm^3 g^{-1}$. This actually provides excellent correlation with the pore volume that was predicted using the extended Tóth equation, 0.253 and 0.257 $cm^3 g^{-1}$, for the 77 and 87 K excess isotherm respectively. The MOFs and zeolites (in theory) only contain micropores, whereas the carbon and PIMs are likely to contain some mesopores which have an influence on the "total" pore volume.

Table 10.1 - Estimation of the adsorbate phase density using the predicted (absolute hydrogen) saturation values and the total pore volume.

Material	Predicted Saturation Value (wt.%)		Estimated Adsorbate Phase Density (g cm^{-3})		Pore Volume ($cm^3 g^{-1}$)
	Sips	Tóth	Sips	Tóth	
IRMOF-1	9.33	12.43	0.078	0.104	1.19 [85]
Cu-BTC	5.77	6.69	0.077	0.089	0.75 [134]
Carbon	1.87	2.06	0.039	0.043	0.48 [361,363]
NaX	2.84	3.28	0.079	0.091	0.36 [162,366]
Methyl Trip-PIM	5.13	6.08	0.081	0.108	0.63

In a similar process the maximum hydrogen adsorption can be converted to a volume of the adsorbate using the triple point density of hydrogen, which then shows good correlation to the reported pore volumes of the microporous materials. These correlations between the predicted maximum hydrogen capacity, adsorbate density and pore volume are also consistent with the modelling work performed by Frost *et al*. on MOF materials.[355]

The conclusions of their work revealed three distinct adsorption regimes with the amount adsorbed correlating to the enthalpy of adsorption at low pressures, the apparent surface area at intermediate pressures and the accessible pore volume at high pressures. They compared MOFs of similar topologies and found for those materials, that the low-pressure regime was in the order of 1 bar, the intermediate pressure was in the order of 30 bar and the high-pressure region was in the order of 120 bar. Frost *et al*.

also stated that these regimes would occur at very different pressures for materials with different topologies and surface chemistry.[355] However, they should occur at similar relative pressures.

The correlation between the maximum hydrogen uptake and the accessible pore volume is illustrated in Figure 10.3. The value predicted by the Sips model shows excellent correlation, whereas the Tóth model appears to have overestimated the maximum hydrogen uptake for IRMOF-1 in comparison to the other four materials. This overestimation is probably due to fitting model only being applied to the adsorption isotherm at low to intermediate pressures. Ideally, the hydrogen adsorption would be measured at higher pressures before a fitting function is used to predict the maximum hydrogen uptake.

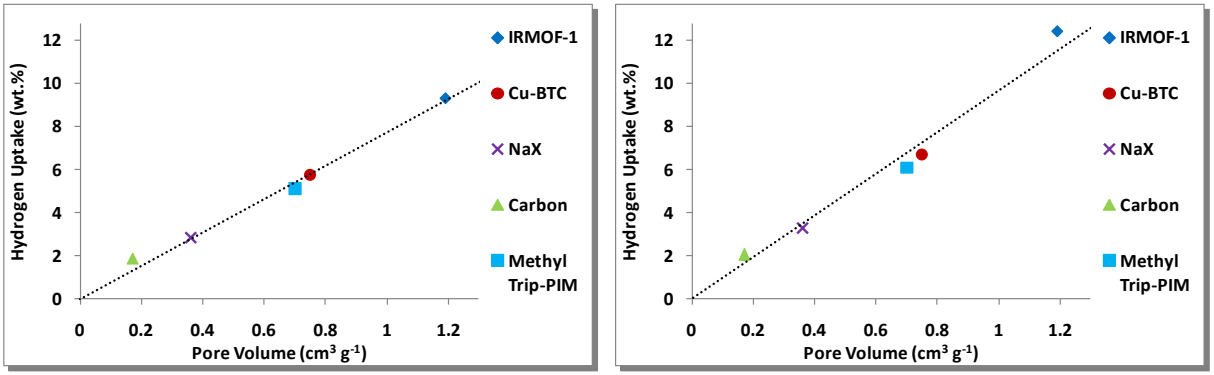

Figure 10.3 - Predicted maximum hydrogen uptake using the Sips (left) and Tóth (right) against pore volume for some microporous materials. The dashed line indicates the line of best fit, which has a gradient of 7.75 and 9.74 wt.% per 1.0 cm^3 g^{-1} for the Sips and Tóth models, respectively. The micropore volume (0.17 cm^3 g^{-1}) was used for the Takeda 4A porous carbon, as this was suspected to be more accurate than the total pore volume.

Thomas previously reported the variation of hydrogen storage capacity with the micropore volume of different types of porous adsorbents.[71,127] Figure 10.4 shows the relationship between the hydrogen uptake at 100 bar and at saturation as predicted by the Sips equation at 77 K, with the (BET) micropore volume of the PIMs measured in this work. The maximum density of the adsorbed phase is often regarded as the density of liquid hydrogen at 20.28 K (0.0708 g cm^{-3}) or the density of hydrogen at the triple point at 13.8 K (0.077 g cm^{-3}). These are represented by dashed lines in Figure 10.4.

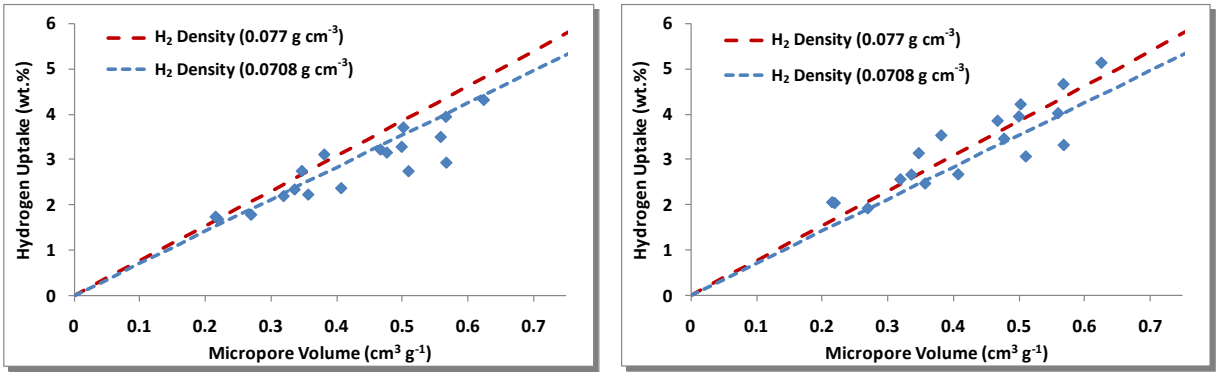

Figure 10.4 - Predicted hydrogen uptake at 100 bar (left) and the maximum (right) using the Sips equation against the micropore volume for the PIMs measured in this work. The two dashed lines represent the density of liquid hydrogen (- -) at 20.28 K (0.0708 g cm^{-3}) and the density of hydrogen at the triple point (–) at 13.8 K (0.077 g cm^{-3}). The micropore volume was calculated using the BET equation on the nitrogen adsorption isotherm at 77 K.

Due to problems of comparing the absolute amount of hydrogen adsorption against the absolute pressure of the bulk phase; comparisons are often made using the fractional coverage. Figure 10.5 displays this comparison using both the Sips and Tóth models to predict the value for complete coverage. The effect of the enthalpy of adsorption is shown by the steepness of the curves. Indeed, the activated carbon material exhibits the steepest curve shape and has the highest enthalpy of adsorption regardless of the number of isotherms used (at different temperatures) and the method of fitting (see Figure 10.6). The opposite was also observed, with IRMOF-1 exhibiting the shallowest curve shape and the lowest enthalpy of adsorption. NaX also displays a steep curve and high enthalpy of adsorption compared to both Cu-BTC and the Trip(Me)-PIM.

The predicted maximum amounts of hydrogen adsorption suggest that hydrogen isotherms of Cu-BTC and the methyl-based triptycene PIM should be more comparable with each other. However even this direct comparison is difficult due to the inevitable difference in pressure at which saturation would occur.

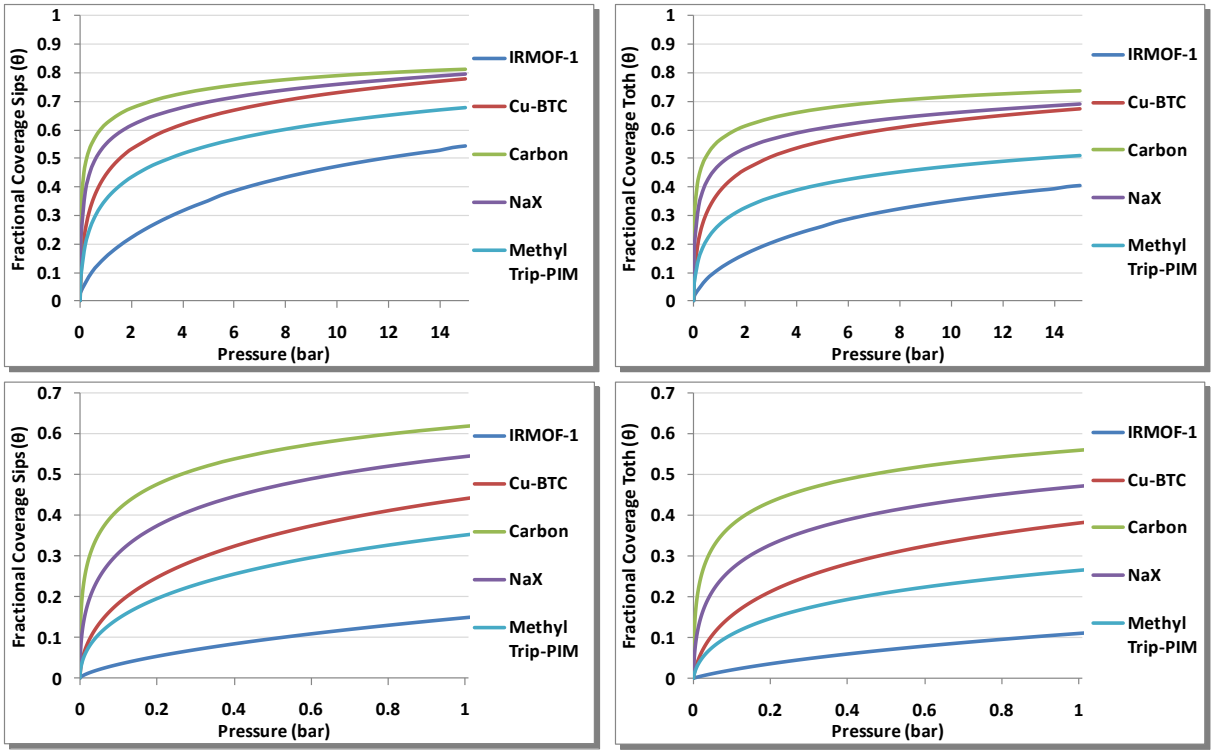

Figure 10.5 - Comparison of fractional coverage versus pressure for some porous materials using the fitted data from the Sips (left) and Tóth equation (right). The maximum saturation uptake value from each respective equation was used as the value for complete coverage. The absolute data was taken at 77 K up to 15 bar (top) and 1 bar (bottom).

As mentioned before, the fitting equations can be used to predict the hydrogen storage capacity at any particular pressure. This is useful for comparing materials where higher pressures could not be measured experimentally. Table 10.2 displays the hydrogen storage capacities of a range of different materials discussed in this work. The gravimetric hydrogen storage capacities were extrapolated (to 100 bar) from the absolute fitted data (using the Sips equation).

The skeletal densities that were stated in previous chapters, and the micropore volumes of each material were used to calculate the geometric densities. This was then used to estimate the volumetric storage capacity from the gravimetric capacity. A similar method to this was also employed by Wong-Foy *et al*.[47] for a series of MOF materials; Hu *et al*. for mesoporous and microporous Ti oxides, as well as an activated carbon material[391]; and Wood *et al*. for hypercrosslinked polymers.[290] Wong-Foy *et al*. reported excess volumetric capacities at 77 K for IRMOF-1 and Cu-BTC of 30.8 and 29.0 kg m^{-3} at 45 and 77 bar,

respectively. The authors converted the gravimetric capacity to a volumetric capacity using crystallographic densities of 0.590 and 0.879 g cm^{-3}.[47]

Using the gravimetric values reported by Wong-Foy *et al*.[47] (at the same pressure mentioned above) and the same technique utilised in this work (with geometric densities of 0.589 and 0.792 g cm^{-3}), the two MOF materials exhibited volumetric capacities of 31.8 and 26.3 kg m^{-3}, respectively. The differences observed here are likely to be a result of the authors using the crystallographic density. In fact, if the density reported by Wong-Foy *et al*.[47] for Cu-BTC is used 0.879 g cm^{-3}, then the volumetric capacity becomes 29.2 kg m^{-3}. Therefore this suggests the method for converting the gravimetric capacity to a volumetric capacity used in this work, is applicable.

Kaye *et al*. reported substantially higher excess gravimetric capacities for IRMOF-1, 7.1 wt.% at saturation 40 bar). This resulted in an absolute uptake of 10.0 wt.% at 100 bar, which the authors converted this to a volumetric capacity of 66 kg m^{-3}.[147] The extrapolated values for IRMOF-1 measured in work (shown in Table 10.2) are much lower due to the relatively low hydrogen uptake observed for this material up to 20 bar.

IRMOF-1 has the lowest geometric density as a result of its greater pore volume, this results in a volumetric capacity that is not much greater than Cu-BTC, despite having a greater gravimetric capacity by almost 2 wt.% at 100 bar. The skeletal density of the Takeda 4A porous carbon was very close to that of pure carbon (2.2 g cm^{-3}).[360] Kelly and Fuller reported the crystal density of zeolite NaX to be 1.43 g cm^{-3}, which is slightly more than was observed in this work. Unfortunately, no volumetric capacities for the carbon material could be found. However, the value of 23.82 kg m^{-3}, is consistent with values for other activated carbons reported by Langmi.[152] Additionally, Langmi reported excess volumetric hydrogen storage capacities for a range of zeolite materials at 15 bar and 77 K. These were in the range of 21 to 31 kg m^{-3}, which is also consistent with that for NaX reported in this work. The methyl Trip-PIM exhibited the lowest skeletal density of the different materials examined here. But with a lower pore volume in comparison to Cu-BTC, the geometric density is greater. Geometric densities for some hypercrosslinked polymers were reported by Tsyurupa *et al*. and Wood *et al*. (using the same method used in this work) to

be in the range 0.71 to 0.91 g cm^{-3}, which correlates well with the methyl Trip-PIM.[283,290] However, Tsyurupa *et al*. did not report any hydrogen uptake values, and Wood *et al*. did not convert their gravimetric capacities to volumetric capacities.[283,290] The volumetric capacity of other microporous polymers in the literature could not be found. Despite having a gravimetric capacity almost twice that of NaX, the methyl Trip-PIM exhibits a volumetric capacity that is only *ca*. 3 kg m^{-3} higher at 100 bar and 77 K. This is a result of its lower geometric density.

Table 10.2 - Hydrogen storage properties for some microporous materials. The gravimetric and volumetric capacities represent the absolute adsorption at 100 bar as calculated using the Sips equation. PIM-1 and AX-21 are also included for comparison.[391]

Material	Geometric Density (g cm^{-3})	Skeletal Density (g cm^{-3})	Gravimetric Capacity (wt.%)	Volumetric Capacity (kg m^{-3})
IRMOF-1	0.59	1.97	7.13	42.00
Cu-BTC	0.79	1.95	5.23	41.41
NaX	1.32	2.50	2.45	32.19
Carbon	1.42	2.16	1.67	23.82
Methyl Trip-PIM	0.81	1.67	4.33	35.21
PIM-1	0.93	1.25	1.79	16.70
AX-21	0.33	2.10	11.96	39.23

The Sips model has consistently been found to overestimate the enthalpy of adsorption at low hydrogen uptake, which has been attributed to poor fitting of the equation to the absolute hydrogen isotherm in that region. This was assumed to be a result of this equation not reducing to Henry's Law as the pressure tends towards zero. The Tóth model has been shown to provide a closer fit to the absolute adsorption isotherm and is therefore believed to produce more accurate enthalpy of adsorption values (particularly at low hydrogen uptake). The different fitting functions also produce different maximum hydrogen uptake values. If this value is then used as 'complete coverage', the enthalpy of adsorption can be plotted against fractional coverage. The differences in maximum uptake as well as the differences in goodness-of-fit (produced by each model), produce very different values for the enthalpy of adsorption at the same absolute value of hydrogen uptake. Figure 10.6 displays the isosteric enthalpy of adsorption for the different microporous materials. The same general trend between the different materials is illustrated by both the Sips and Tóth models and also by plotting them as a function of both absolute uptake and fractional coverage. Both models also indicate that the enthalpy of adsorption values decrease to within

the range 4 to 7 kJ mol^{-1} at higher hydrogen uptake, which is typical for dispersive van der Waals interactions. The enthalpy of adsorption is important at these higher values of hydrogen uptake when considering the usable capacity and the pressures used in practical applications.

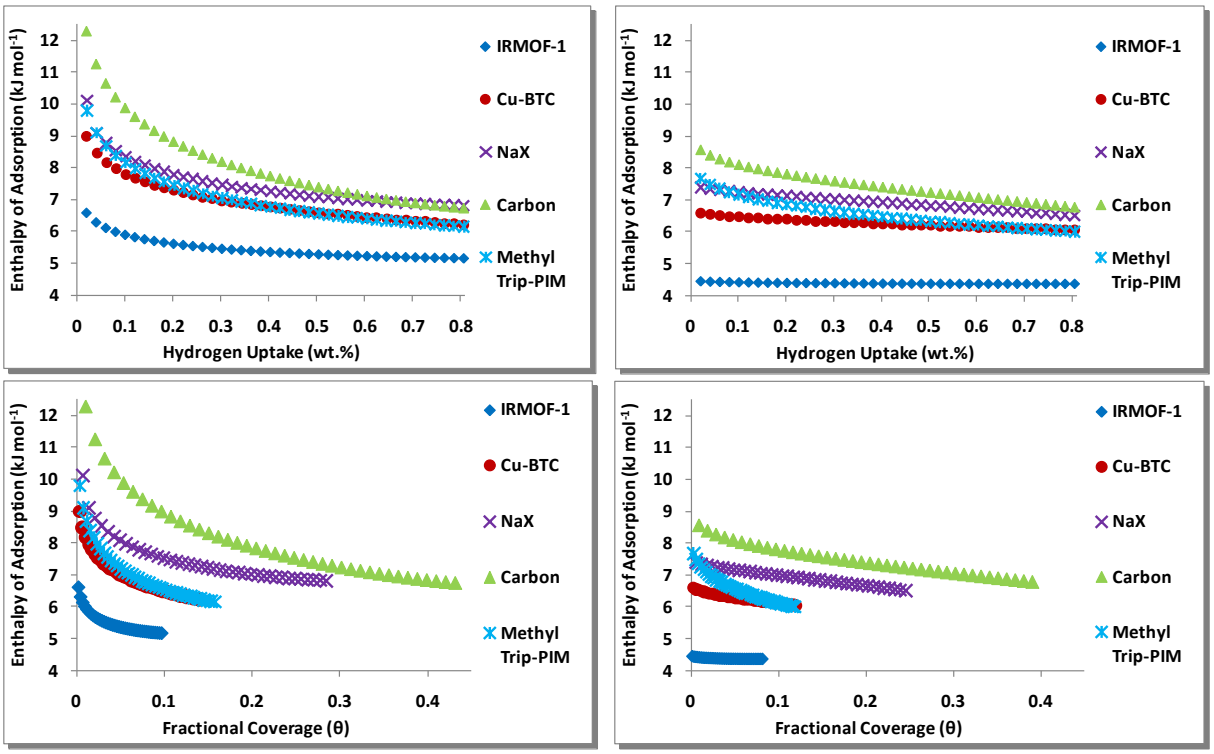

Figure 10.6 - Isosteric enthalpies of adsorption against hydrogen uptake (top) and fractional coverage (bottom) for some porous materials using absolute isotherms from multiple temperatures and the Clausius-Clapeyron (van't Hoff plot) method after the data was fitted using the Sips (left) and Tóth equations (right).

Figure 10.7 displays the correlation between the isosteric enthalpy of adsorption and the pore size for these materials. The plot indicates that smaller pores sizes tend to provide higher isosteric enthalpies of adsorption. The correlation is not linear, particularly with respect to NaX and Cu-BTC. This suggests that the extraframework cations in the NaX and the exposed metal sites in Cu-BTC also play a role in influencing the adsorbate-adsorbent interaction. [218,253]

In zeolites, the presence of strong electrostatic fields within the zeolite intracrystalline channels and cavities are created by the extraframework cations (this case Na^+ ions).[152,218,368] These interactions act in addition to the dispersive van der Waals interactions that are believed to be present in porous materials such as activated carbons.

In Cu-BTC, the hydrogen molecule is small enough to enter the aperture of the triangular window (0.41 nm) in the small secondary pore. Using Thermal Desorption Spectroscopy (TDS) Panella *et al*. concluded that the hydrogen adsorbed in these pores preferentially over the adsorption in the main channel.[308] However, Rowsell and Yaghi,[134] reported that the open metal sites point inwards from the larger pores which Peterson *et al*. reported as being the preferential adsorption site in Cu-BTC.[252] In fact, Peterson *et al*. used neutron powder diffraction to study deuterium sorption in Cu-BTC. They found that almost 95% of the deuterium molecules were adsorbed on to the exposed metal sites up to 0.5 wt.% uptake. This reduced to less than 92% by 0.98 wt.% at which point the remaining 8% of deuterium molecules were adsorbed in the small side pockets.[252] It is important to note that the adsorption sites on the metal centres lie within the pores which is likely to reduce the effect of pore size significantly at 0.02 wt.% (see Figure 10.7).

The problem with then definitively comparing the pore sizes of Cu-BTC and the methyl Trip-PIM is: firstly, the Cu-BTC materials contains exposed metal sites which are believed to attract more molecular hydrogen at lower pressures, meaning that pore size is not solely responsible for the enthalpy of adsorption; and secondly, the pore size for the PIM is based upon nitrogen adsorption at 77 K and not on crystallographic data (due to its amorphicity). This technique suffers from being incapable of measuring pores less than *ca*. 0.6 nm in diameter, due to the restriction of the equipment at very low relative pressures. Therefore any adsorption at lower relative pressures than the equipment can measure will be incorrectly displayed as larger pores. The pore sizes for the PIMs could be compared to those calculated using DFT methods to check for consistency.[290,392] Finally, the PIMs have the potential to swell, allowing for most guest molecules with increased gas pressure. This means that the pore that begins to adsorb at low pressures may be of a greater size (and volume) at higher pressures.

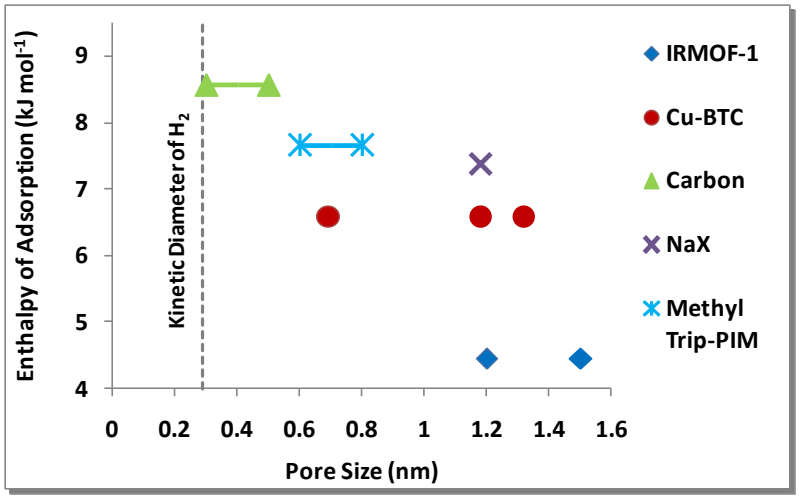

Figure 10.7 - Isosteric enthalpy of adsorption versus pore size for the measured porous materials using the Clausius-Clapeyron (van't Hoff plot) method in conjunction with the Tóth fitting models. The dashed line represents the kinetic diameter for molecular hydrogen (0.289 nm).

It is very unlikely that a porous based (hydrogen) fuel tank will operate at 77 K. Maintaining a whole storage system at a constant 77 K is close to impossible using liquid nitrogen as the cooling source, even if a vacuum superinsulated tank with minimal conduction paths to ambient temperatures, were used. Despite the majority of physisorption materials have relatively low enthalpies of hydrogen adsorption, removing even a small amount of heat during the refuelling process is difficult at cryogenic temperatures and requires substantial quantities of liquid nitrogen from an external source. Exacerbating this problem further is the low thermal conductivity of microporous materials, and hence throughout the storage system. This means that they are likely to be operated at slightly higher temperatures (for example, 100 K).[342]

For materials with a higher enthalpy of adsorption, this doesn't necessarily decrease the usable capacity by too great a degree. The usable capacity is the difference between the maximum pressure that the storage tank, can is used and the pressure that the fuel cell operates (see Figure 10.8). As mentioned in Chapter 1, PEM fuel cells typically operate between 1 and 3 bar,[5,14,18] although some studies use slightly higher operating pressures such as 8 bar as reported by Ahluwalia and Peng.[342]

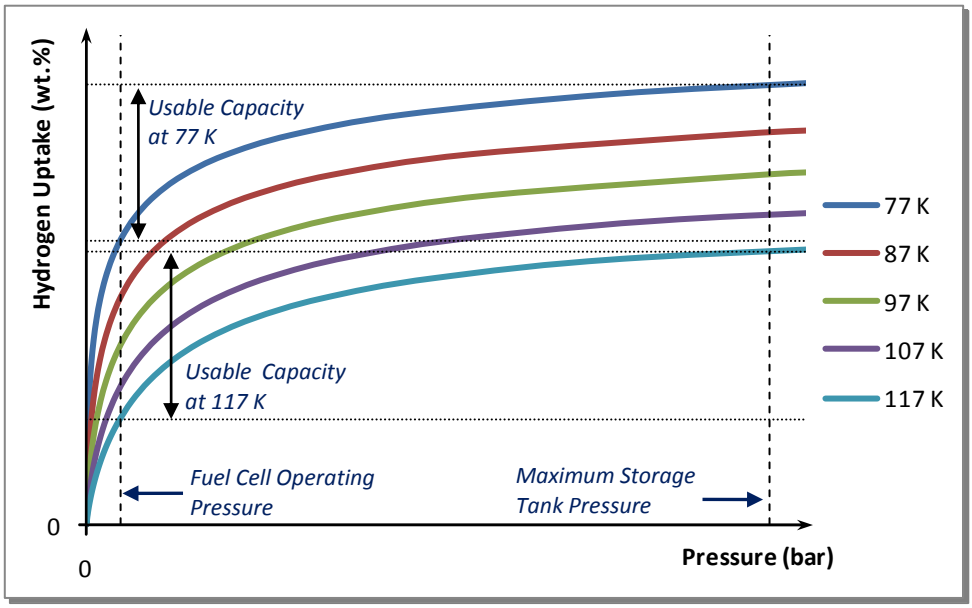

Figure 10.8 - Extrapolated absolute hydrogen storage capacities using the Sips equation for the methyl-substituted triptycene-based PIM from 77 to 117 K, in 10 K steps.

Table 10.3 contains the absolute hydrogen storage capacity at 15 bar at both 77 and 117 K, to display the effect of warming the material by 40 K. The table also contains the usable capacity of five porous adsorbents at both 77 and 117 K. Here, the usable capacity is calculated by assuming a tank pressure of 15 bar and an operational back-pressure of 2 bar. The differences between the absolute and usable capacity as a function of temperature are displayed in Figure 10.9.

IRMOF-1, which has the lowest enthalpy of adsorption, exhibits the greatest decrease usable capacity (> 50%) in between 77 and 117 K. The carbon material exhibited the greatest enthalpy of adsorption and this observed almost a 40% increase in usable capacity over the same temperature range. However, the relatively low storage capacity of the carbon and high enthalpy of adsorption means that the majority of the hydrogen is adsorbed below 2 bar. The temperature dependence on the absolute and usable capacities for these materials is illustrated in Figure 10.9.

Table 10.3 - Absolute hydrogen storage capacities at 15 bar and 77 K and together with the usable hydrogen storage capacities assuming a tank pressure of 15 bar and the operational back-pressure of 2 bar. The effect of warming the system by 40 K up to 117 K is also displayed.

Material	Absolute Capacity at 15 bar (wt.%)		Usable Capacity from 15 to 2 bar (wt.%)	
	77 K	117 K	77 K	117 K
IRMOF-1	4.86	1.80	3.00	1.32
Cu-BTC	4.50	2.56	1.43	1.60
Carbon	1.52	1.06	0.26	0.36
NaX	2.27	1.55	0.53	0.71
Methyl Trip-PIM	3.47	1.72	1.25	1.10

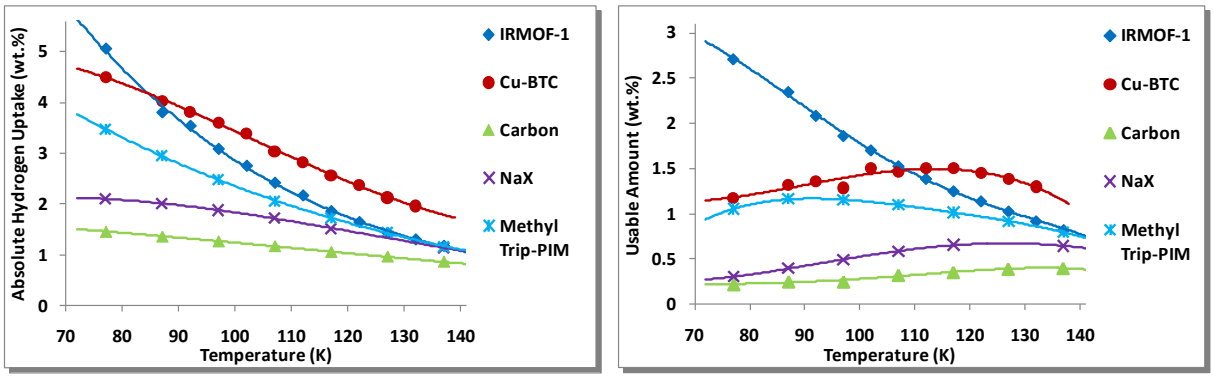

Figure 10.9 - (Left) Comparison of the absolute hydrogen capacity versus temperature for some porous materials. (Right) Comparison of the usable absolute hydrogen capacity versus temperature for some porous materials. The usable range was taken from 2 to 15 bar. The adsorbate phase density was assumed to be equal to that of hydrogen at the triple point (0.077 g cm^{-3}).

Unfortunately, in this work, measuring the hydrogen storage properties at elevated pressures and low temperatures has not been possible. Therefore, in order to evaluate the benefits, regarding the usable capacity, of increasing the pressure from 15 to 100 bar; the absolute hydrogen storage capacity at 100 bar was calculated using the Sips equation. Whilst this extrapolation is known not to be completely accurate, it does allow for trends to be observed. Table 10.4 shows that the usable capacity for these materials increases by about approximately 1 wt.% from 15 to 100 bar at both 77 and 117 K (*ca.* 2 wt.% for IRMOF-1).

Table 10.4 - Calculated absolute hydrogen storage capacities at 100 bar and 77 K and together with the usable hydrogen storage capacities assuming a tank pressure of 100 bar and the operational back-pressure of 2 bar. The effect of warming the system by 40 K up to 117 K is also displayed. The Sips equation was used to calculate the absolute hydrogen storage capacity at 100 bar.

Material	**Calculated Absolute Capacity at 100 bar (wt.%)**		**Usable Capacity from 100 to 2 bar (wt.%)**	
	77 K	**117 K**	**77 K**	**117 K**
IRMOF-1	7.13	3.86	5.27	3.38
Cu-BTC	5.23	3.65	2.15	2.69
Carbon	1.87	1.27	0.41	0.57
NaX	2.55	1.85	0.80	1.40
Methyl Trip-PIM	4.33	2.70	2.10	2.08

Chapter 11

CONCLUSIONS AND FUTURE WORK

11.1. Conclusions

This work studied the physisorption of molecular hydrogen in microporous materials, with particular attention given to microporous polymers. Physisorption occurs as a result of the weak van der Waals interactions that occur between a gas or a liquid and the surface of a solid. As no chemical bonding occurs during the adsorption of hydrogen, the process boasts rapid sorption kinetics and complete reversibility, making it an attractive method for hydrogen storage applications.

11.1.1. Gas Sorption Measurements

As there have been many inaccurate reports of high hydrogen storage capacities, the first objective of this work was to determine the accuracy of the gas sorption equipment that was to be used. This was performed using a standard commercial microporous carbon material, which was provided as part of a round-robin test by the E.C. Framework 6 NESSHY (Novel Efficient Solid Storage for Hydrogen) project. Eleven partners of the round-robin test showed results for measurements at 77 K for the porous carbon. The results ranged from 1.2 to 2 wt.% up to 20 bar at 77 K, and were further dispersed with increasing pressure. The curve shapes of the isotherms also differed significantly, with increasing pressure. It would appear that even when guidelines are provided for the way a porous sample is measured, significant errors can still occur highlighting the difficulties of measuring this class of material. There appeared to be a concentration of isotherms around 1.4 wt.%, which was within the error of the measurement performed in this work, 1.4 ± 0.1 wt.% up to 10 bar. Therefore, indicating that the measurement performed in this work is an accurate reflection of the hydrogen capacity in this sample.

The likely sources of error include equipment calibration purity, equilibration times and adequate degassing times. A standard degassing regime was outlined in the round-robin exercise, which would not be appropriate for all equipment. For example a Sievert's type system that typically contains small bore pipes will take longer to degas than an IGA system, which has large bore pipes. One of the interesting findings of this project was the difference in degassing times between different materials, with the MOFs requiring significantly longer periods of time for degassing. After which small losses of mass were still being observed. This is thought to be as a result of the different solvents used in synthesising the MOF materials.

11.1.2. Isotherm Fitting Equations

The pressure composition isotherms were corrected for buoyancy using the skeletal density for each material as determined using helium pycnometry. As the isotherms are not measured at perfectly spaced intervals of hydrogen uptake, it was necessary to fit the isotherms to an appropriate function in order to deduce the corresponding pressure, at each temperature. Two empirical equations (Sips and Tóth) were used in addition to a multi-parameter virial equation. The excess isotherms were converted to absolute isotherms, utilising the assumption that the density of the adsorbate is equal to that of hydrogen at the triple point, before fitting. The empirical isotherms were fitted using the nonlinear least-squares Levenberg-Marquardt algorithm. Generally, both empirical equations exhibited acceptable fits to the absolute adsorption isotherm. However, the Tóth equation appeared to produce a closer fit, especially in the low-pressure region. This was attributed to the fact that the Sips equation does not reduce to Henry's law at zero coverage. Using the micropore volume and the hydrogen saturation calculated using the Sips equation, the adsorbate density at saturation was found to be very similar to that of hydrogen at the triple point.

11.1.3. Isosteric Enthalpy of Adsorption

The isosteric enthalpies of adsorption for hydrogen in porous materials are typically calculated using data generated for just two temperatures, 77 and 87 K. A newly developed liquid nitrogen cryostat was installed during this project and used to measure pressure composition isotherms at several temperatures between 77 and 137 K. This not only provided a range of isotherms to calculate the isosteric enthalpies of adsorption but also allowed for usable capacities to be determined over a range of temperatures. The cryostat was shown to be accurate to within ± 0.1 °C.

The resulting isosteric enthalpies of adsorption, determined using the Clausius-Clapeyron equation with temperatures from 77 to 137 K, were found to be consistently lower than values using just 77 and 87 K isotherms for the carbon, zeolite and the two MOFs. At near zero coverage, the enthalpy of adsorption was lower, and decreased less rapidly with increasing hydrogen uptake. The reasons for the differences are still unclear. It could be that by using multiple temperatures, a more accurate assessment of the isosteric enthalpy of adsorption can be achieved particularly at low surface coverage where the higher temperature isotherms are shallower. It could also be a result of a temperature dependence of the enthalpy of adsorption.

Using the Clausius-Clapeyron equation in conjunction with the Sips model has consistently been found to overestimate the enthalpy of adsorption at low hydrogen uptake. This has been attributed to poor fitting of the equation to the absolute hydrogen isotherm in that region. This was assumed to be a result of this equation not reducing to Henry's Law as the pressure tends towards zero. The Tóth model has been shown to provide a closer fit to the absolute adsorption isotherm and is therefore believed to produce more accurate enthalpy of adsorption values (particularly at low hydrogen uptake).

Generally there was good agreement in the enthalpy of adsorption curves between the Clausius-Clapeyron equation in conjunction with the Tóth model and the Virial type thermal equation, using two temperatures, 77 and 87 K. However, on occasion significant differences were observed. Therefore, performing both methods might prove to be beneficial accurately determining the isosteric enthalpy of adsorption.

11.1.4. Polymers of Intrinsic Microporosity

One of the aims of this project was to fully characterise the gas sorption properties of this novel class of materials. A series of microporous polymers were synthesised (by our project partners at the Universities of Cardiff and Manchester), with the aim of maximising the available surface area, whilst optimising the pore size to increase the enthalpy of adsorption.

Generally, the polymers of intrinsic microporosity were seen to follow Chahine's rule, which predicts a linear correlation of hydrogen adsorption capacity, at 77 K, with surface area. The gas adsorption properties such as surface area, hydrogen storage capacity and micropore volume were found to be controllable using different monomers. This was particularly apparent in the series of network PIMs based on the triptycene monomers, that possess different alkyl groups attached to their bridgehead positions. The apparent BET and Langmuir surface areas ranged from 618 to 1760 $m^2 g^{-1}$ and 755 to 2053 $m^2 g^{-1}$, respectively. The shorter straight chain (e.g. methyl) and branched (e.g. iso-propyl) alkyl groups produced PIMs with larger micropore volumes, which is believed to be reasonable for the increased hydrogen capacity for these materials. The longer more bulky alkyl groups appeared to reduce the micropore volumes of these network PIMs resulting in lower gas adsorption capacities, but increased the enthalpy of adsorption. Therefore suggesting a trade-off between gas sorption capacity and enthalpy of adsorption.

A micropore size distribution for a the Trip(Me)-PIM, calculated from the low pressure region of nitrogen adsorption isotherm using the Horváth-Kawazoe (slit-pore) confirmed the lack of a distinct pore size, and the presence of a distribution of pore sizes that was biased towards pores in the range around 0.6 to 0.7 nm.

The PIMs exhibit a sloping adsorption and pronounced hysteresis in the nitrogen sorption isotherms. The extension of the hysteresis back down to a low relative pressure suggests that it is caused by mesoporosity, as the hysteresis would close at a higher relative pressure. The hysteresis could also be a result of: swelling of the materials with increased pressures; the restricted access of the nitrogen molecules due to constricted pore openings; or a combination of both.

11.1.5. Comparison of Different Types of Microporous Materials

Of all of the materials measured in this investigation, the two MOFs exhibited the largest gravimetric storage capacities; 4.86 and 4.50 wt.% at 77 K and 15 bar, respectively for IRMOF-1 and Cu-BTC. The highest hydrogen storage capacity displayed by a PIM was the triptycene-based PIM with R = methyl, which was 3.26 wt.% at 77 K and 15 bar. The iso-propyl triptycene-based PIM also displayed good hydrogen uptake, 3.01 wt.% at 77 K and 15 bar. The zeolite NaX and Takeda CMS 4A carbon material exhibited 2.12 and 1.42 wt.% at 77 K and 15 bar. These hydrogen storage capacities are consistent with both the apparent surface areas and the micropore volumes.

The enthalpy of adsorption at low hydrogen coverage was found to follow a general trend with pore size, with higher enthalpies of adsorption exhibited by materials with smaller pore sizes. However, both zeolite NaX and Cu-BTC exhibited higher enthalpies of adsorption than may have been expected by the effect of pore size alone. This is likely to be due to the influence from electrostatic forces as a result of extraframework cations within the cavities and exposed metal sites, respectively.

Of all of the materials measured, the triptycene-based macromolecule PIM exhibited the highest enthalpy of adsorption with the Tóth and Virial type thermal equation giving 10.6 and 9.8 kJ mol^{-1} at 0.02 wt.%. This was closely followed by the triptycene-based PIMs with hydrogen and the iso-butyl group attached at the bridgehead position. These PIMs exhibit a enthalpy of adsorption of 10.5 and 10.0 kJ mol^{-1} for the Tóth and 8.9 and 8.7 kJ mol^{-1} at 0.02 wt.% using the Virial-type thermal equation, respectively.

11.1.6. Practical Considerations

Materials that exhibit higher enthalpy of adsorption values have been shown to lead to retain more of their hydrogen capacity with increasing temperature. In fact, for materials with high enthalpies of adsorption, the usable capacity was actually observed to increase from 77 to 117 K. This is important for practical applications where the whole system is unlikely to be held at 77 K.

The usable capacity of IRMOF-1, which exhibited highest hydrogen uptake and the lowest enthalpy of adsorption, was shown to decrease by more than 50% between 77 and 117 K. Whereas the usable capacity of the Takeda 4A porous carbon, which has the lowest hydrogen uptake and the highest enthalpy of adsorption, increased by almost 40% over the same temperature range. In choosing a material for a practical application one would have to first know the working pressures (minimum and maximum) of the store, and the likely temperature-range. If a store was to function at relatively low pressures and temperatures over 100 K, then it may be more appropriate to choose a material with a small pore size, with a higher enthalpy of adsorption and lower capacity at 77 K (such as the Takeda 4A porous carbon from this work). However if a store was to work at high pressure and below 100 K then a high surface area material with larger pores, a low enthalpy of adsorption and a high capacity at 77 K is likely to be more suitable (such as IRMOF-1).

At present a significant amount of cooling is required to provide a significant hydrogen capacity in porous materials. It is likely that a practical store would run at < 150 K. It has been estimated that an adsorption enthalpy of around 20 kJ mol^{-1} would be required to make a porous material suitable to use at ambient temperatures. A large apparent surface area and accessible pore volume are required for an adsorbent to be capable of a high hydrogen storage density. The findings in this investigation suggest that there is a trade-off between gas sorption capacity and enthalpy of adsorption where dispersive van der Waals interactions dominate adsorption. This is likely to be a consequence of small pore sizes resulting in small pore volumes. The additional adsorbate-adsorbent interactions created by the exposed metal centres can be utilised to increase the enthalpy of adsorption whilst also exhibiting substantial hydrogen storage capacities. It seems unlikely, that the optimal enthalpy of adsorption will be achieved by simply reducing the pore size of the material.

11.2. Future Work

Across the different types of porous materials, the isosteric enthalpy of adsorption has been shown to have a general trend with pore size. Further pore size distribution analysis is required in order to determine whether this is also true for the PIMs. The limitations of gas sorption techniques in determining pore sizes below *ca*. 0.6 nm means that an alternative technique is required. This may be possible using Transmission Electron Microscopy. Due to the soft nature of the PIMs, the technique would require a protective layer (of *ca*. 100 nm) of platinum or tungsten to be deposited across a selected area of *ca*. 20 μm using an SEM focused ion beam. ^{129}Xe NMR spectroscopy can also be used as an alternative to gas sorption techniques to assess the pore size of the PIMs. Whilst the lower limit of this technique is not known, it could be used to confirm, or refute the pore size distribution analysis calculated from gas adsorption techniques.

The maximum amount of hydrogen that is capable of being stored by a porous material is limited by the density of the adsorbed hydrogen within the pores and the total accessible pore volume. However, too large a pore volume reduces the bulk density, which reduces the volumetric hydrogen storage capacity. In order to develop the hydrogen storage capacity of PIMs, further investigation is required in to different types of monomers, possibly with multiple sites of contortion.

In addition to a large micropore volume, a high packing density is required to reach high volumetric hydrogen storage capacities in porous materials. Therefore, finding a practical solution to determine the bulk density of the PIMs is needed to truly assess their capabilities as hydrogen adsorbents. PIM-1 for example, is soluble in polar aprotic solvents and can be cast into films (of *ca*. 60 μm). Finding ways to increase the thickness of these films could improve the packing density. It may be possible to press the porous polymers into a compact. However, the effect on the hydrogen storage capacity, of applying an external pressure to compress the PIMs would have to be ascertained.

The pore swelling that was observed in the nitrogen adsorption isotherms was not observed in the hydrogen pressure composition isotherms below 20 bar. Assessing the high-pressure adsorption of the

PIMs at 77 K could be performed using a manometric Sievert's type system. By comparing the concentration of hydrogen uptake to the calculated micropore capacity (determined from the nitrogen adsorption), it is believed that higher pressures of hydrogen could lead to similar pore swelling effects. This may then lead to significant increases to their hydrogen storage capacity. If the PIMs do swell, at high gas pressures, this may cause problems with a polymer compact.

The processing effects of supercritical carbon dioxide and other solvents such as methanol require further investigation. It is currently unknown how different pressures, temperatures and exposure time of supercritical carbon dioxide affect the improvement of hydrogen storage capacity. More detailed analysis is required to establish the effect of each variable.

It has been clear that dispersive van der Waals interactions are not sufficient to reach the previously suggested optimum enthalpy of adsorption (of *ca*. 20 kJ mol^{-1}) required for any type of porous material to have an adequate hydrogen storage capacity at ambient temperatures. Therefore, it seems apparent that the adsorption enthalpy needs to be increased by other interactions such as electrostatic or quadrupole-quadrupole. One possible method that could be used to achieve this is doping with cations. In order to achieve a substantial gravimetric hydrogen storage capacity, a lightweight ion such as lithium, beryllium or boron would be best. A metal ion that is capable of coordinating multiple hydrogen molecules would be more beneficial in increasing the enthalpy of adsorption. For zeolites the charge-to-volume ratio was found to be important for the electrostatic interactions, which increase as univalent exchangeable cations are replaced by divalent and trivalent ones. With this in mind ions such as Mg^{2+} and Al^{3+} should also be considered.

Performing pressure-composition-temperature isotherms over range of different temperatures allows for the isosteric enthalpy of adsorption to be calculated more accurately compared to using just two

temperatures. However, further investigation is required in order to obtain a better understanding of the temperature dependence of the isosteric enthalpy of adsorption.

Analysis by such equations as the Dubinin type, could give some useful information regarding the temperature dependence of the isosteric enthalpy of adsorption. If the temperature dependence can be accurately determined it should be possible to predict hydrogen adsorption isotherms at different temperatures other than those measured.

Alternative techniques for calculating the enthalpy of adsorption should be explored in order to see whether they correlate with the values calculated from measuring hydrogen adsorption isotherms at different temperatures. Variable temperature Raman spectroscopy could be performed in a similar fashion to the previously reported VTIR spectroscopy. This technique can also be used to determine the enthalpy of adsorption of hydrogen for specific sites. Low temperature thermal desorption spectroscopy might also prove to be important, especially if results from the technique can be quantified, thus producing specific binding energies.

Appendix A

POWDER X-RAY DIFFRACTION – NaX

Table A.1 - Comparison of the observed and calculated 2θ values for the Zeolite NaX. Calculated values were determined using Chekcell in conjunction with the lattice parameter and space group reported by Olsen.[364]

hkl	Observed 2θ	Calculated 2θ	Difference
111	6.119	6.112	0.007
022	9.995	9.989	0.006
311	11.73	11.719	0.012
313	15.42	15.421	-0.001
115	18.39	18.407	-0.017
044	20.038	20.055	-0.017
315	20.997	20.984	0.012
602	22.459	22.451	0.008
533	23.276	23.289	-0.014
622	23.57	23.563	0.008
246	26.646	26.634	0.011
535	27.367	27.352	0.015
733	29.184	29.186	-0.001

POWDER X-RAY DIFFRACTION – IRMOF-1

Table A.2 - Comparison of the observed and calculated 2θ values for the IRMOF-1 (BASF) material. Calculated values were determined using Chekcell in conjunction with the lattice parameter and space group reported by Li et al. and Rowsell and Yaghi.[227,375]

hkl	Observed 2θ	Calculated 2θ	Difference
002	6.855	6.844	0.011
022	9.688	9.684	0.004
113	11.341	11.361	-0.020
004	13.740	13.712	0.028
313	14.946	14.949	-0.003
024	15.325	15.340	-0.015
224	16.797	16.814	-0.017
115	17.811	17.842	-0.031
044	19.426	19.439	-0.012
513	20.347	20.339	0.008
006	20.603	20.630	-0.027
335	22.580	22.571	0.009
155	24.621	24.611	0.010
246	25.803	25.809	-0.006
137	26.493	26.504	-0.011
733	28.290	28.279	0.011
555	29.961	29.957	0.005

Table A.3 - Comparison of the observed and calculated 2θ values for the IRMOF-1 (BASF) material after exposure to air. Calculated values were determined using Chekcell in conjunction with the lattice parameter and space group reported by Rosi et al. for the MOF-69C material.[377] *The two remaining peaks still present from the ideal structure are not included.*

hkl	Observed 2θ	Calculated 2θ	Difference
101	8.852	8.845	0.007
-103	14.766	14.762	0.004
-223	15.724	15.686	0.038
202	17.717	17.743	-0.027
-321	19.26	19.306	-0.046
-223	19.692	19.67	0.021
-331	23.553	23.552	0.002
-332	23.967	23.993	-0.026
331	26.185	26.175	0.010
-515	26.676	26.68	-0.004
-243	28.752	28.756	-0.004
224	29.875	29.886	-0.011

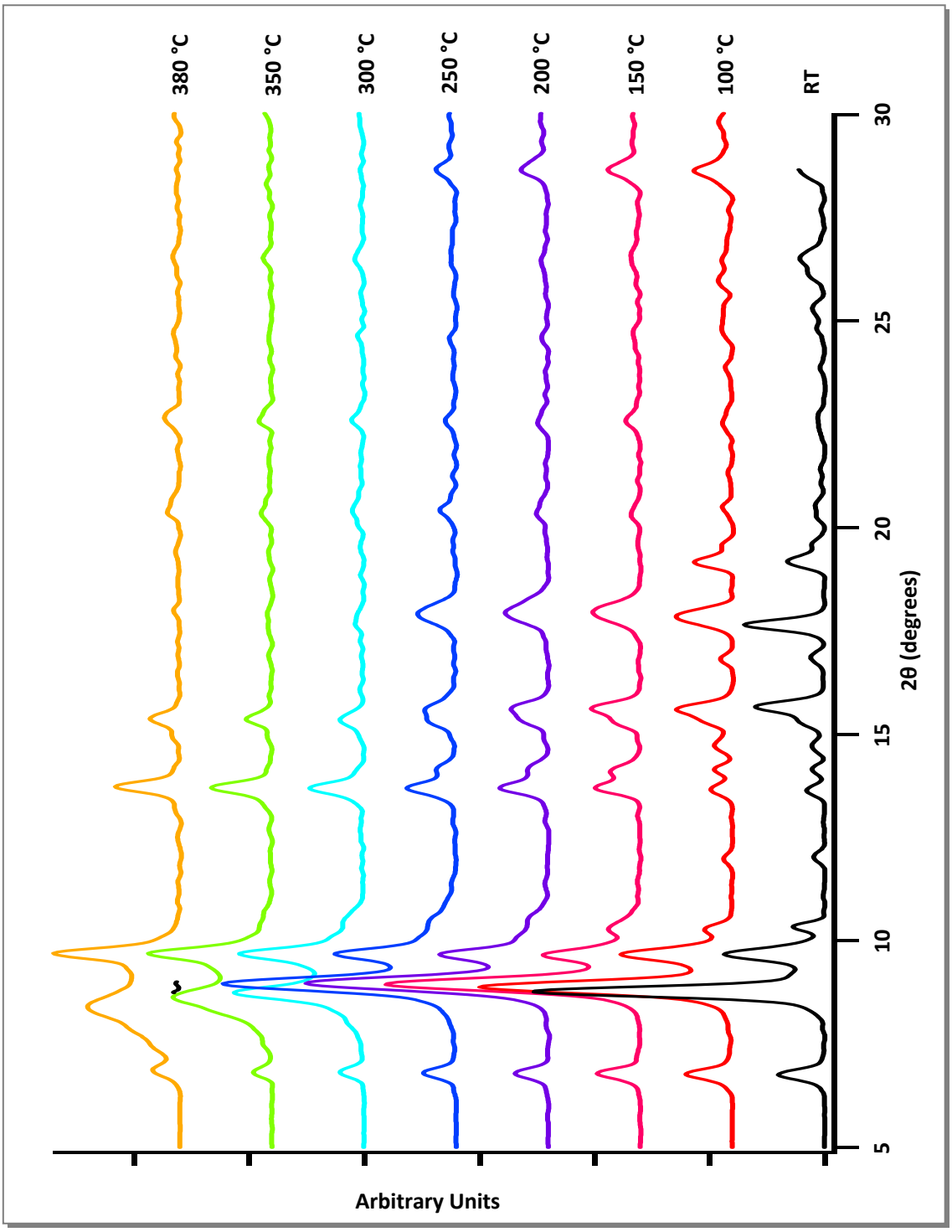

Figure A.1 - Variable temperature in-situ powder XRD pattern for IRMOF-1 after exposure to air. Heated at a rate of 2 K minute^{-1} under flowing helium at a rate of 100 ml minute^{-1} at 2.5 bar.

POWDER X-RAY DIFFRACTION – Cu-BTC

Table A.4 - Comparison of the observed and calculated 2θ values for the Cu-BTC material. Calculated values were determined using Chekcell in conjunction with the lattice parameter and space group reported by Chui et al. [249]

hkl	Observed 2θ	Calculated 2θ	Difference
002	6.699	6.718	-0.020
022	9.501	9.507	-0.006
113	11.154	11.152	0.001
222	11.646	11.650	-0.004
004	13.446	13.460	-0.014
313	14.674	14.674	0.000
024	15.071	15.057	0.014
224	16.507	16.504	0.003
333	17.520	17.513	0.008
044	19.092	19.079	0.013
424	20.261	20.249	0.012
206	21.377	21.356	0.021
226	22.418	22.412	0.006
444	23.410	23.422	-0.012
515	24.154	24.154	0.000
246	25.332	25.329	0.003
535	26.022	26.010	0.012
733	27.741	27.751	-0.010
066	28.766	28.789	-0.023
715	29.389	29.396	-0.006

Appendix B

RAMAN SPECTROSCOPY

PIM-1

Raman spectroscopy was used to observe any vibrational or rotational modes of the degassed PIM-1 structure (see Figure B.1). The 785 nm (near infrared) laser was used to minimise fluorescence from the sample. Very weak C-H vibrational modes can be observed in the region between 2850 to 2930 cm^{-1}. A strong C≡N vibrational mode exists at 2237 cm^{-1}, which corresponds exactly to that which was observed in the infrared spectra. Modes associated with aromatic C-C bonds are observed at 1597 and 1643 cm^{-1}. The ether groups (C-O-C) were observed at 1299 and 1316 cm^{-1}. Other peaks were observed in the fingerprint region which are typical of an organic molecule.

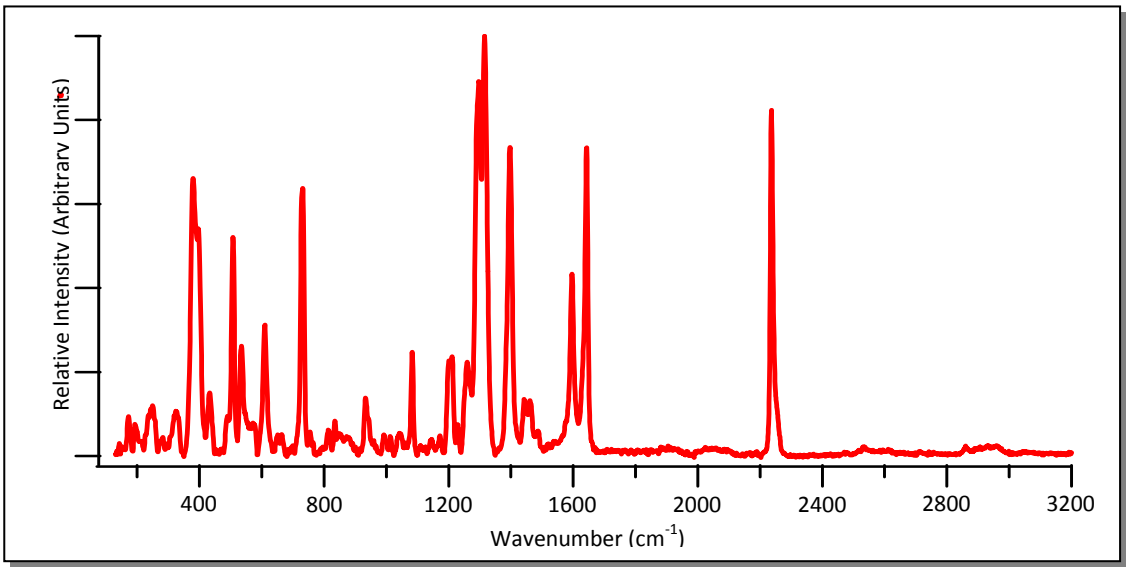

Figure B.1 - Raman Spectroscopy of PIM-1 at room temperature using 785 nm laser from 100 to 3200 cm^{-1}.

Triptycene-Based PIM Series

Raman spectroscopy was used to observe any vibrational or rotational modes of the triptycene-based PIMs with aliphatic chains at the bridgehead position (see Figure B.2). The 785 nm (near infrared) laser was used to minimise fluorescence from the sample. A strong C≡N vibrational mode exists at 2235 cm^{-1} in all samples. This corresponds exactly to that which was observed in the infrared spectra. Modes associated with aromatic C-C bonds are seen at 1600 and 1645 cm^{-1}. The ether groups (C-O-C) are seen at

1310 and 1330 cm^{-1}. Other peaks that are observed in the fingerprint region are typical of an organic molecule.

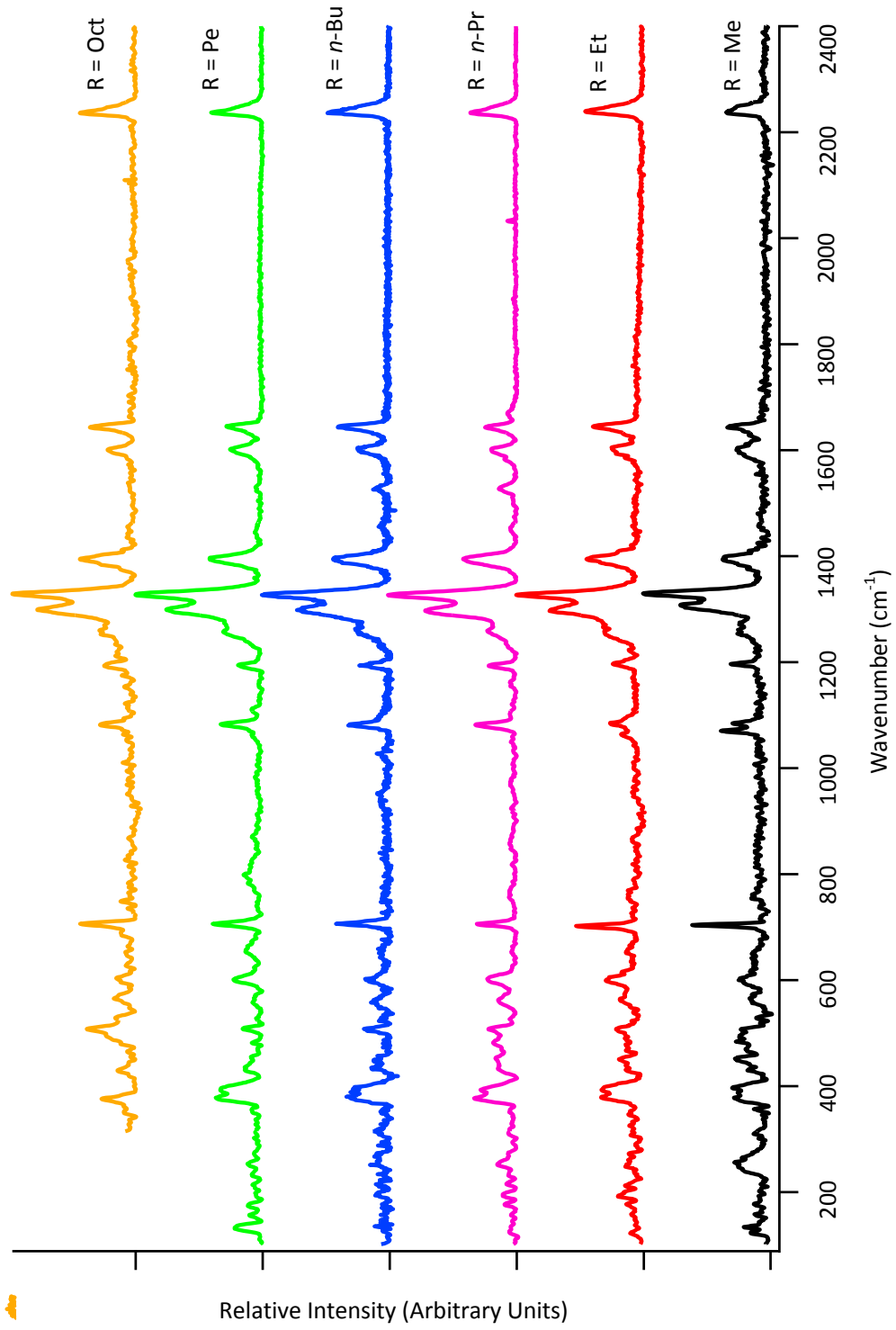

Figure B.2 - Raman spectroscopy of the triptycene-based PIMs, with straight alkyl chains at the bridgehead position. Spectra were taken at room temperature in air, using the 785 nm laser.

Appendix C

HELIUM PYCNOMETRY CONSISTENCY

Helium pycnometry was performed on the porous materials to assess the skeletal density. Three different portions of the degassed PIM-1 material were measured on the Micromeretics (AccuPyc II 1340) pycnometer system to check for consistency in results given with PIM materials. An average skeletal density of 1.25 g cm^{-3} was determined as shown in Table C.1.

Table C.1 - Skeletal density as determined by helium pyconometry at room temperature for the PIM-1 powder.

Run No.	Mass / g	Volume / cm^3	Density / g cm^{-3}
1	0.093	0.074	1.257
2	0.100	0.080	1.250
3	0.097	0.078	1.244
Average	***	***	1.250

Appendix D

ABSOLUTE ADSORPTION IN POROUS SOLIDS

Nomenclature

V_s	=	solid (skeletal volume)
V_a	=	adsorbate phase volume
V_p	=	accessible pore volume
ρ_B	=	bulk gas phase density
$\rho_B(p,T)$	=	bulk gas phase density at pressure p and temperature T
V_c	=	control or displacement (total displaced) volume
m	=	experimentally detected mass of adsorbent
m_s	=	mass of solid
ρ_s	=	solid phase density
m_a	=	mass of adsorbate phase
ρ_a	=	adsorbate phase density
m_e	=	excess adsorption

$$m_s = V_s \rho_s$$

where

$$\rho_s = \frac{m_s}{V_s}$$

$$m_a = V_a \rho_a$$

where

$$\rho_a = \frac{m_a}{V_a}$$

Mass Balance Equations

$$m = m_s + m_a - \rho_B V_C \qquad (D.1)$$

$V_C = V_s + V_a$ and so

$$m = m_s + m_a - \rho_B (V_s + V_a) \qquad (D.2)$$

$\therefore$

$$m = m_s + m_a - \rho_B V_s - \rho_B V_a \qquad (D.3)$$

$m_s = V_s \rho_s$ and $m_a = V_a \rho_a$

$$m = V_s\rho_s + V_a\rho_a - \rho_B V_s - \rho_B V_a \quad (D.4)$$

and so $$m = V_s(\rho_s - \rho_B) + V_a(\rho_a - \rho_B) \quad (D.5)$$

rearranging equation (D.3) gives $$m_a = m - m_s + \rho_B V_s + \rho_B V_a \quad (D.6)$$

The surface excess quantity is the difference between the total amount of adsorbate present in the adsorbed layer and that which would be present in the layer if it had the same density as the bulk gas phase, at the particular measurement temperature and pressure.

$\therefore$ $$m_e = m_a - \rho_B V_a \quad (D.7)$$

By combining equations (D.6) and (D.7)

$$m_e = m - m_s - \rho_B V_s \quad (D.8)$$

$V_s = m_s/\rho_s$ and $\therefore$

$$m_e = m - m_s + \rho_B\left(\frac{m_s}{\rho_s}\right) \quad (D.9)$$

$\therefore$ $$m_e = m - m_s\left(1 - \frac{\rho_B}{\rho_s}\right) \quad (D.10)$$

As $m_a = V_a\rho_a$ equation (D.7) can also be written as

$$m_e = \rho_a V_a - \rho_B V_a \quad (D.11)$$

Or $$m_e = V_a(\rho_a - \rho_B) \quad (D.12)$$

$V_a = m_a/\rho_a$ and $\therefore$ $$m_e = \frac{m_a}{\rho_a}(\rho_a - \rho_B) \quad (D.13)$$

$\therefore$ $$m_e = m_a - m_a\left(\frac{\rho_B}{\rho_a}\right) \quad (D.14)$$

and so $$m_e = m_a\left(1 - \frac{\rho_B}{\rho_a}\right) \quad (D.15)$$

rearranging equation (D.7) gives $$m_a = m_e + \rho_B V_a \quad (D.16)$$

And $\therefore$ rearranging equation (D.15) gives $$m_a = \frac{m_e}{\left(1 - \frac{\rho_B}{\rho_a}\right)} \quad (D.17)$$

EXCESS TO ABSOLUTE ADSORPTION

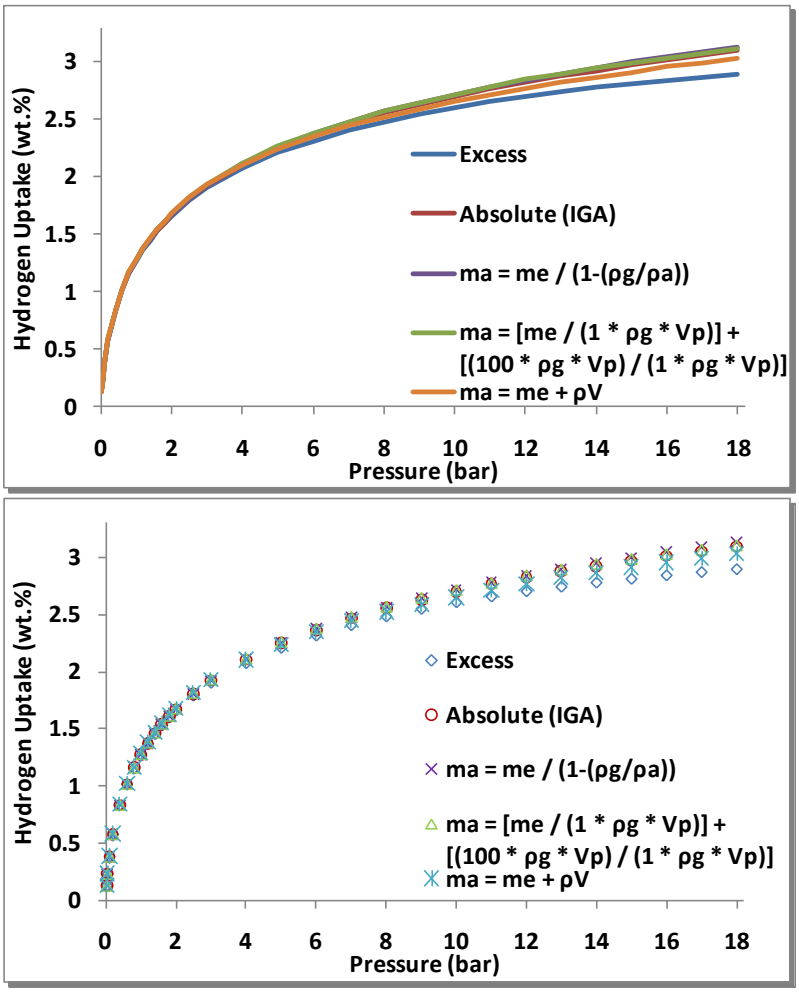

Figure D.1 - A comparison between the excess hydrogen adsorption and the absolute adsorption as determined by different methods. The first and second method utilise the same equation (D.17), however "Absolute (IGA)" is performed within the Hiden IGA-001 software. The third method uses equation (D.18), which was reported by Lin et al. [121] *and is shown here simply for comparison. The fourth method reported by Murata et al.* [124] *and Richard et al.* [123] *uses equation (D.16).*

$$m_a = \left(\frac{m_e}{1 + \rho_H V_P}\right) + \left(\frac{100 + \rho_H V_P}{1 + \rho_H V_P}\right) \qquad (D.18)$$

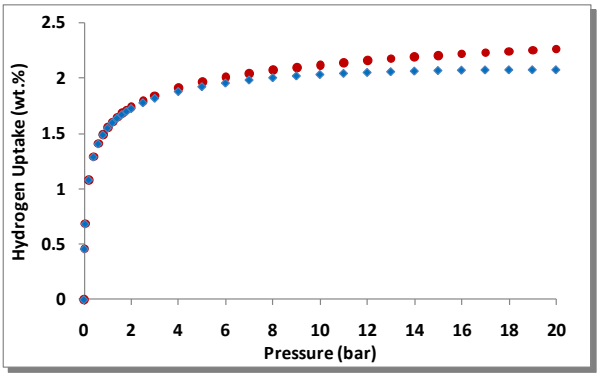

Figure D.2 - Difference between excess (♦) and absolute (●) hydrogen uptake (wt.%) for NaX against pressure (bar) at 77 K using the adsorbed phase density of hydrogen at the triple point.

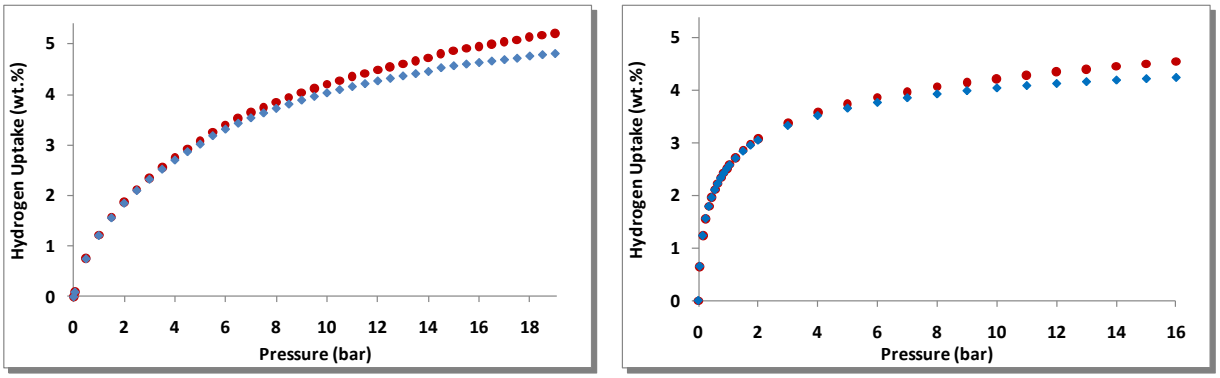

Figure D.3 - Difference between excess (♦) and absolute (●) hydrogen uptake (wt.%) for IRMOF-1 (left) and Cu-BTC (right) against pressure (bar) at 77 K using the adsorbed phase density of hydrogen at the triple point.

Appendix E

SIPS AND TÓTH FITTING EQUATIONS

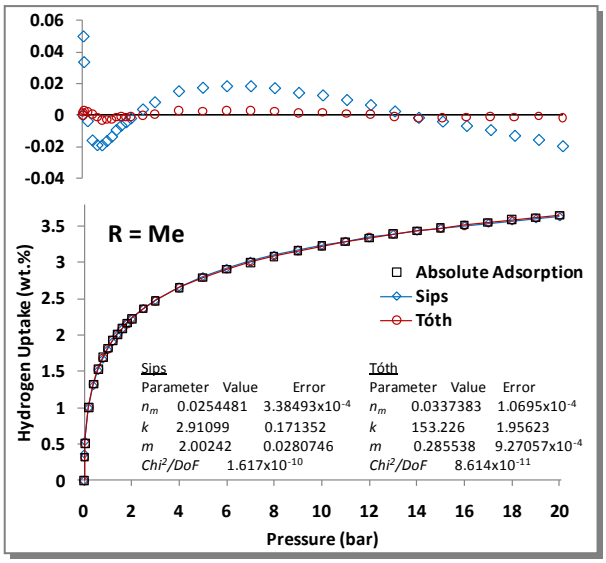

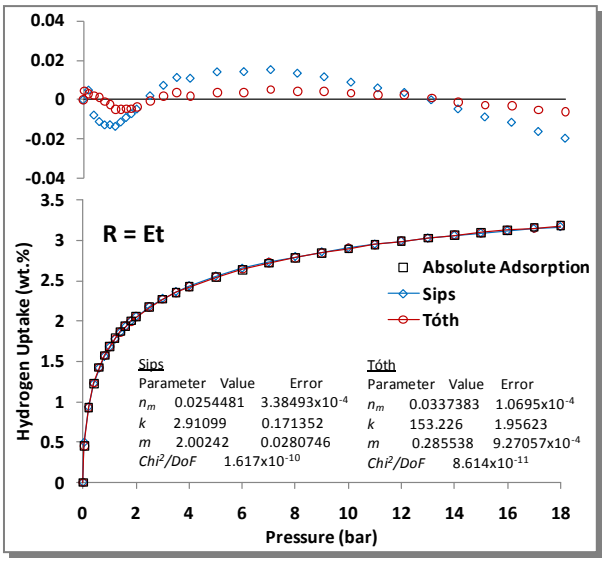

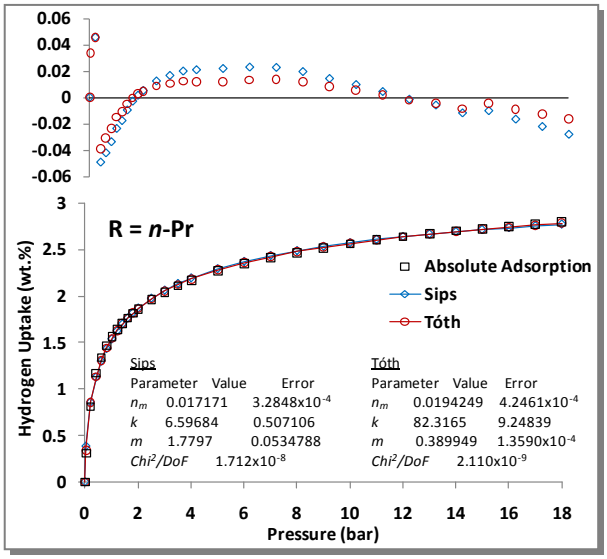

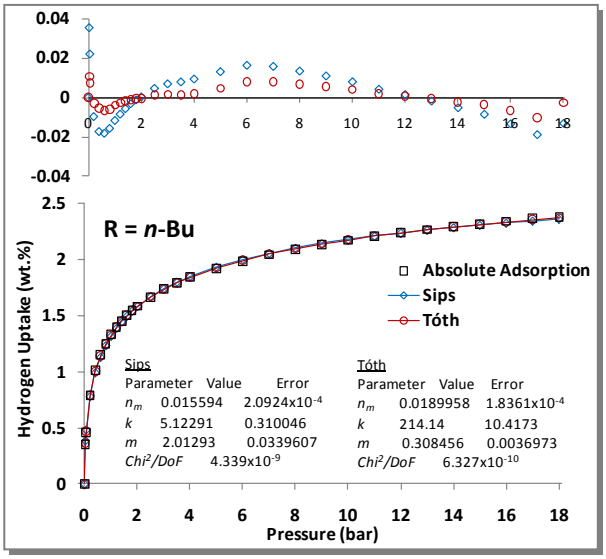

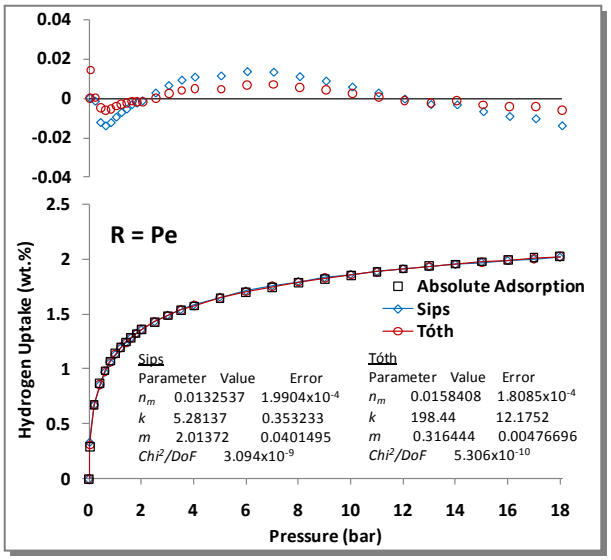
R = Pe
Absolute Adsorption
Sips
Tóth
Hydrogen Uptake (wt.%)
Pressure (bar)
Sips
Parameter Value Error
n_m 0.0132537 1.9904x10^{-4}
k 5.28137 0.353233
m 2.01372 0.0401495
Chi^2/DoF 3.094x10^{-9}
Tóth
Parameter Value Error
n_m 0.0158408 1.8085x10^{-4}
k 198.44 12.1752
m 0.316444 0.00476696
Chi^2/DoF 5.306x10^{-10}

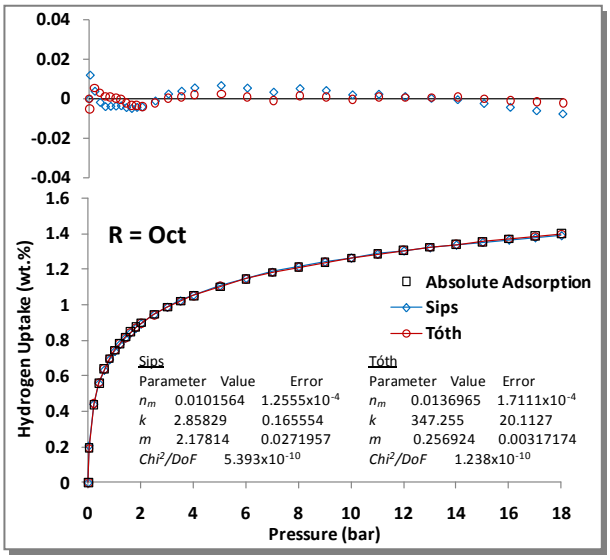
R = Oct
Absolute Adsorption
Sips
Tóth
Hydrogen Uptake (wt.%)
Pressure (bar)
Sips
Parameter Value Error
n_m 0.0101564 1.2555x10^{-4}
k 2.85829 0.165554
m 2.17814 0.0271957
Chi^2/DoF 5.393x10^{-10}
Tóth
Parameter Value Error
n_m 0.0136965 1.7111x10^{-4}
k 347.255 20.1127
m 0.256924 0.00317174
Chi^2/DoF 1.238x10^{-10}

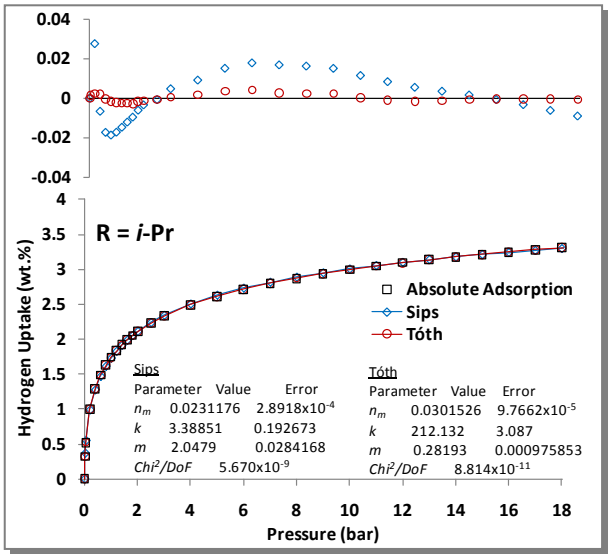
R = *i*-Pr
Absolute Adsorption
Sips
Tóth
Hydrogen Uptake (wt.%)
Pressure (bar)
Sips
Parameter Value Error
n_m 0.0231176 2.8918x10^{-4}
k 3.38851 0.192673
m 2.0479 0.0284168
Chi^2/DoF 5.670x10^{-9}
Tóth
Parameter Value Error
n_m 0.0301526 9.7662x10^{-5}
k 212.132 3.087
m 0.28193 0.000975853
Chi^2/DoF 8.814x10^{-11}

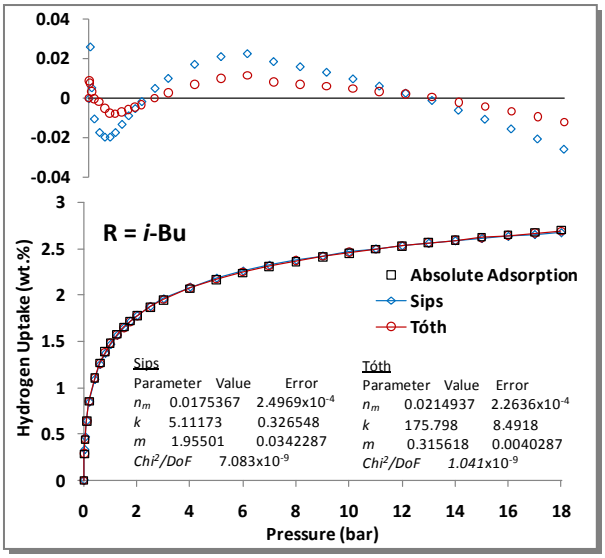
R = *i*-Bu
Absolute Adsorption
Sips
Tóth
Hydrogen Uptake (wt.%)
Pressure (bar)
Sips
Parameter Value Error
n_m 0.0175367 2.4969x10^{-4}
k 5.11173 0.326548
m 1.95501 0.0342287
Chi^2/DoF 7.083x10^{-9}
Tóth
Parameter Value Error
n_m 0.0214937 2.2636x10^{-4}
k 175.798 8.4918
m 0.315618 0.0040287
Chi^2/DoF *1.041*x10^{-9}

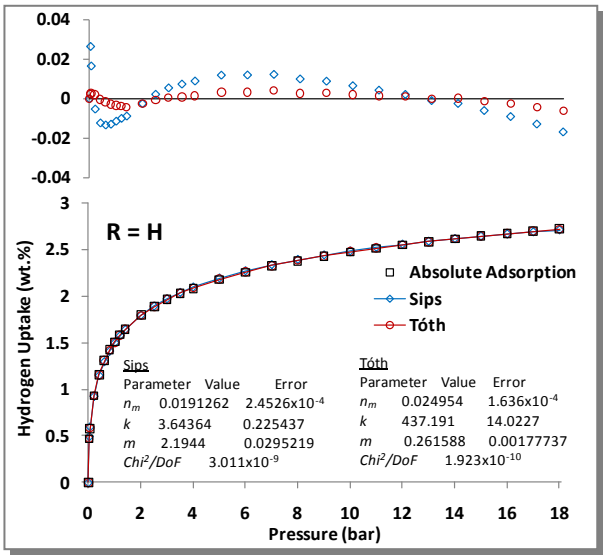
R = H
Absolute Adsorption
Sips
Tóth
Hydrogen Uptake (wt.%)
Pressure (bar)
Sips
Parameter Value Error
n_m 0.0191262 2.4526x10^{-4}
k 3.64364 0.225437
m 2.1944 0.0295219
Chi^2/DoF 3.011x10^{-9}
Tóth
Parameter Value Error
n_m 0.024954 1.636x10^{-4}
k 437.191 14.0227
m 0.261588 0.00177737
Chi^2/DoF 1.923x10^{-10}

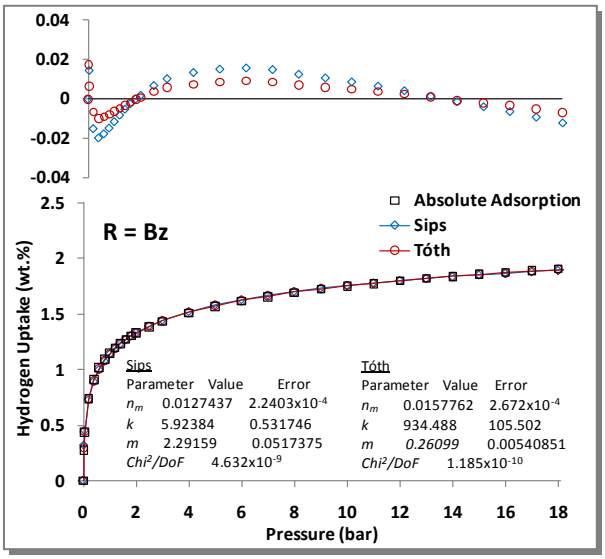
R = Bz
Absolute Adsorption
Sips
Tóth
Hydrogen Uptake (wt.%)
Pressure (bar)
Sips
Parameter Value Error
n_m 0.0127437 2.2403x10^{-4}
k 5.92384 0.531746
m 2.29159 0.0517375
Chi^2/DoF 4.632x10^{-9}
Tóth
Parameter Value Error
n_m 0.0157762 2.672x10^{-4}
k 934.488 105.502
m *0.26099* 0.00540851
Chi^2/DoF 1.185x10^{-10}

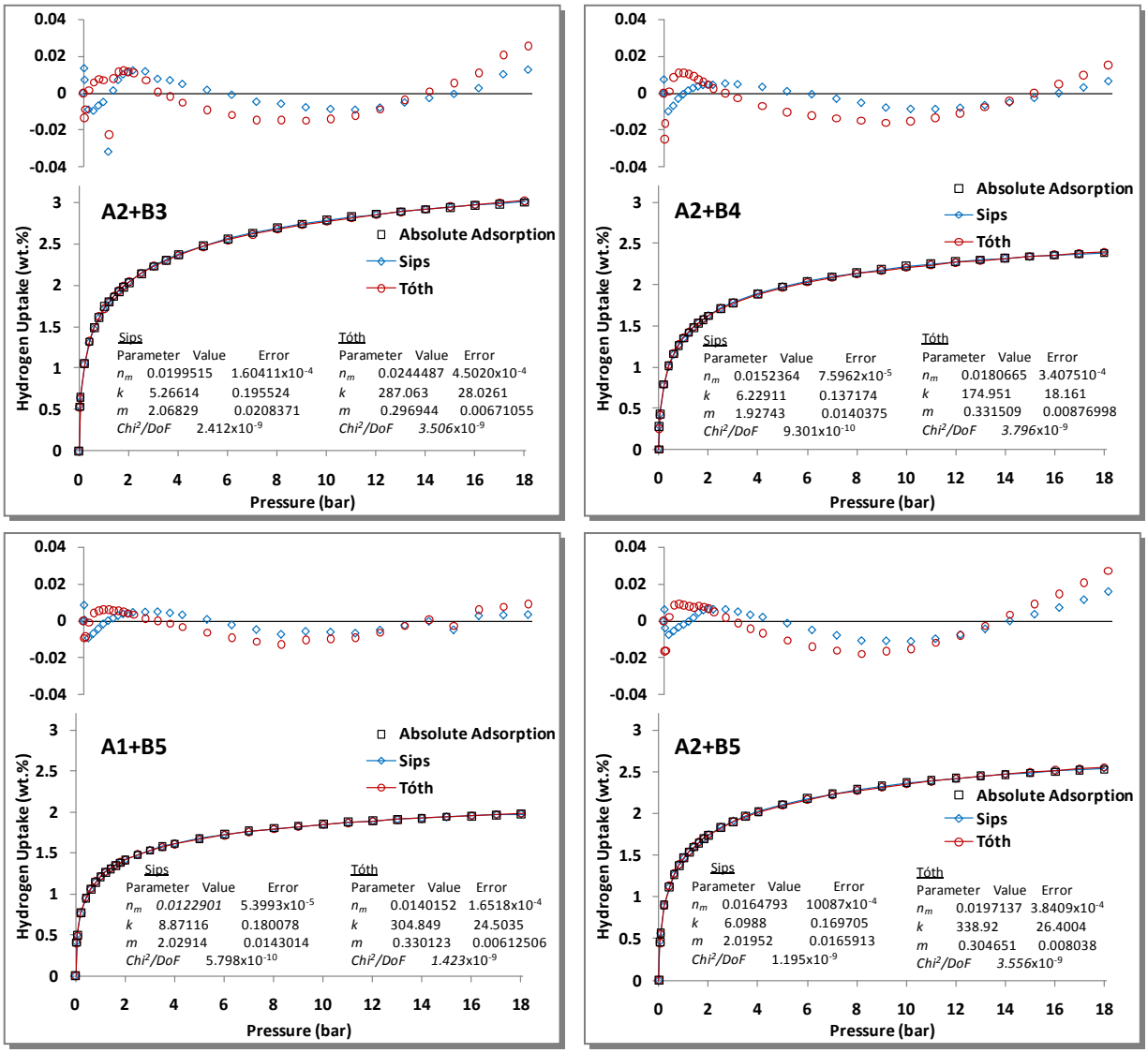

Figure E.1 - Fitted Sips (◇) and Tóth (○) equations to the absolute hydrogen uptake of the Triptycene-based PIMs and Network PIMs, against pressure up to 18 bar at 77 K.

Appendix F

LINEARISED LANGMUIR PLOTS

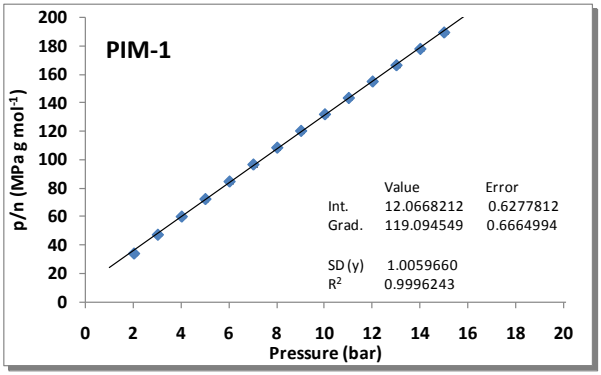

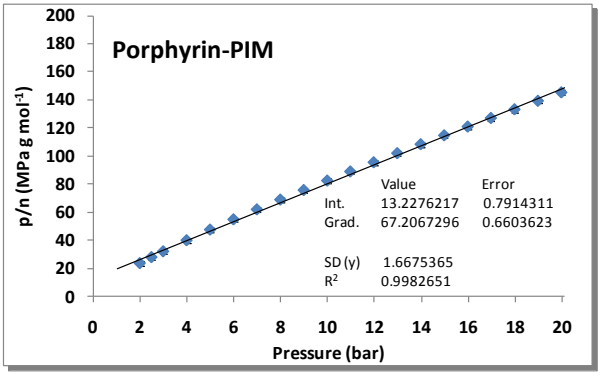

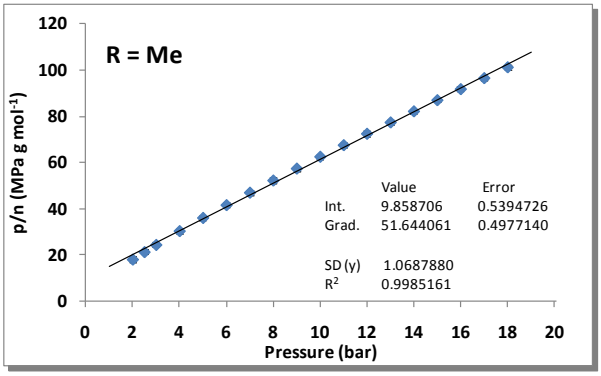

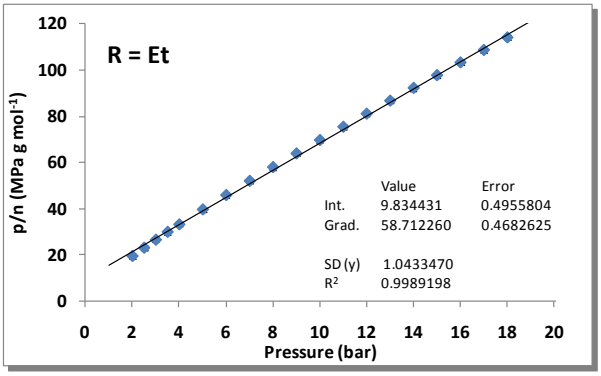

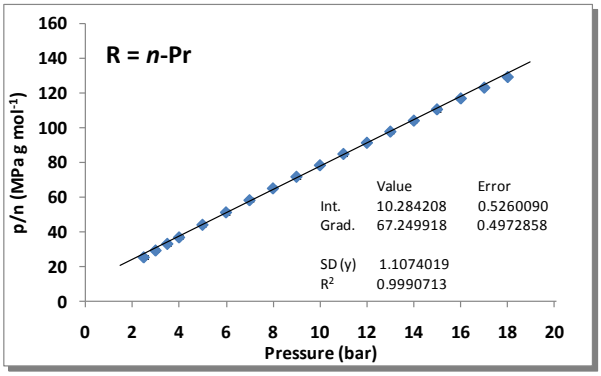

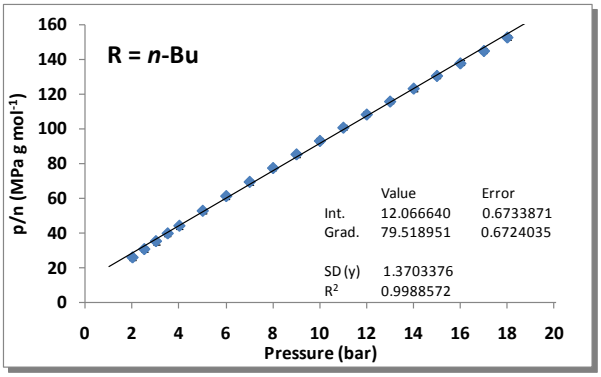

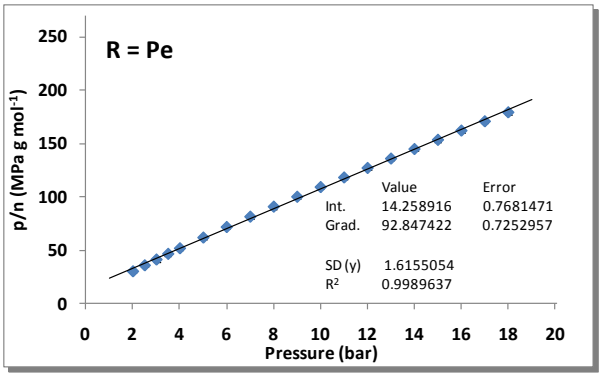
R = Pe
p/n (MPa g mol-1)
Pressure (bar)
Value Error
Int. 14.258916 0.7681471
Grad. 92.847422 0.7252957
SD (y) 1.6155054
R2 0.9989637

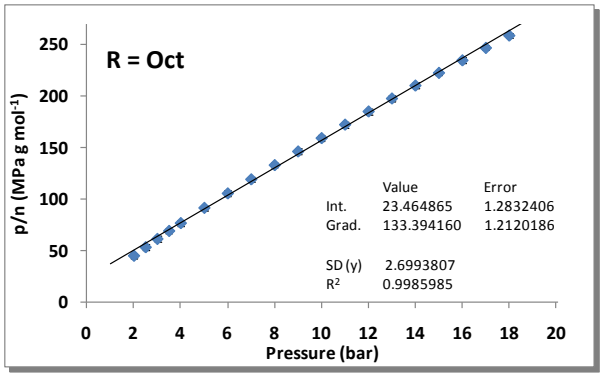
R = Oct
p/n (MPa g mol-1)
Pressure (bar)
Value Error
Int. 23.464865 1.2832406
Grad. 133.394160 1.2120186
SD (y) 2.6993807
R2 0.9985985

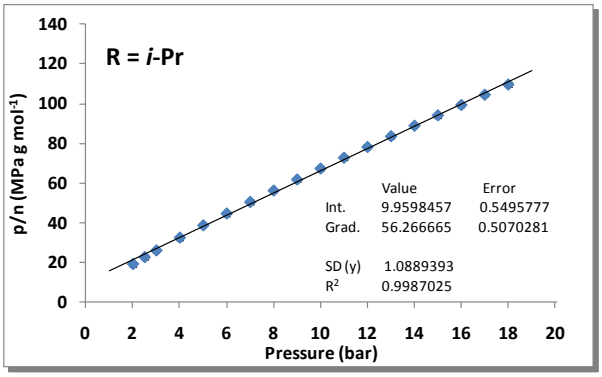
R = i-Pr
p/n (MPa g mol-1)
Pressure (bar)
Value Error
Int. 9.9598457 0.5495777
Grad. 56.266665 0.5070281
SD (y) 1.0889393
R2 0.9987025

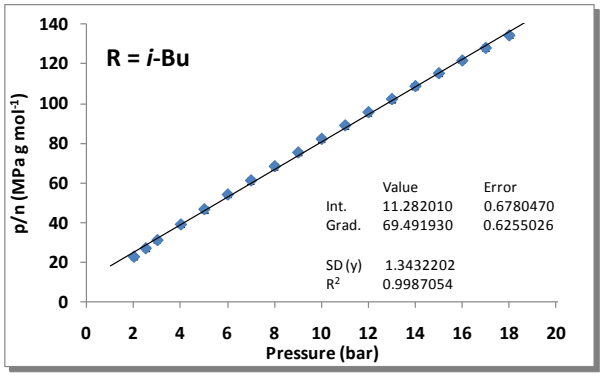
R = i-Bu
p/n (MPa g mol-1)
Pressure (bar)
Value Error
Int. 11.282010 0.6780470
Grad. 69.491930 0.6255026
SD (y) 1.3432202
R2 0.9987054

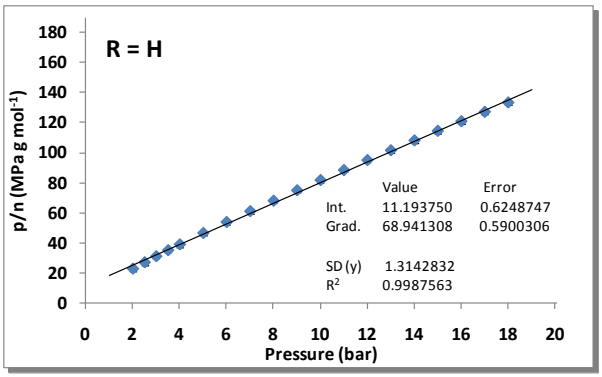
R = H
p/n (MPa g mol-1)
Pressure (bar)
Value Error
Int. 11.193750 0.6248747
Grad. 68.941308 0.5900306
SD (y) 1.3142832
R2 0.9987563

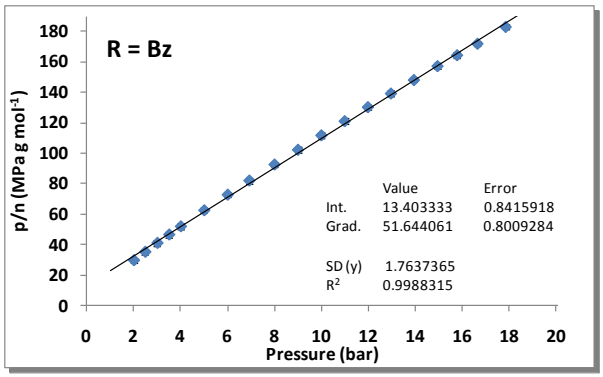
R = Bz
p/n (MPa g mol-1)
Pressure (bar)
Value Error
Int. 13.403333 0.8415918
Grad. 51.644061 0.8009284
SD (y) 1.7637365
R2 0.9988315

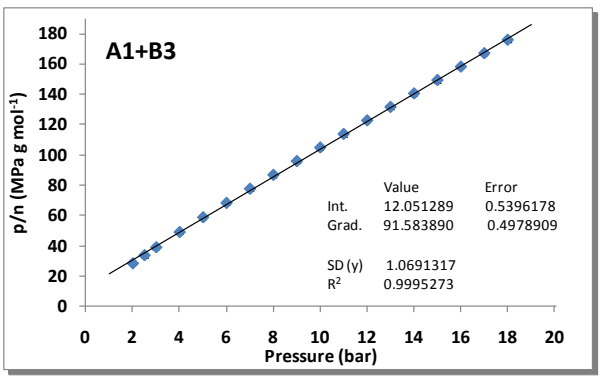
A1+B3
p/n (MPa g mol-1)
Pressure (bar)
Value Error
Int. 12.051289 0.5396178
Grad. 91.583890 0.4978909
SD (y) 1.0691317
R2 0.9995273

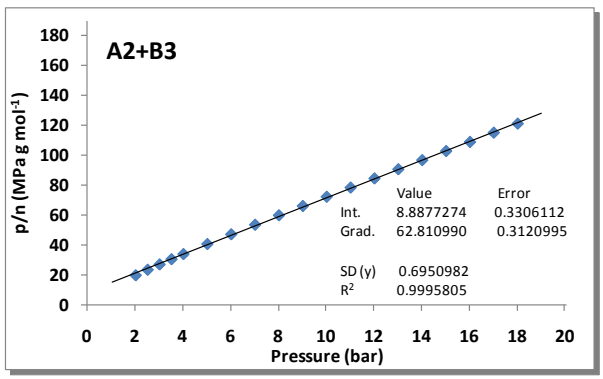
A2+B3
p/n (MPa g mol-1)
Pressure (bar)
Value Error
Int. 8.8877274 0.3306112
Grad. 62.810990 0.3120995
SD (y) 0.6950982
R2 0.9995805

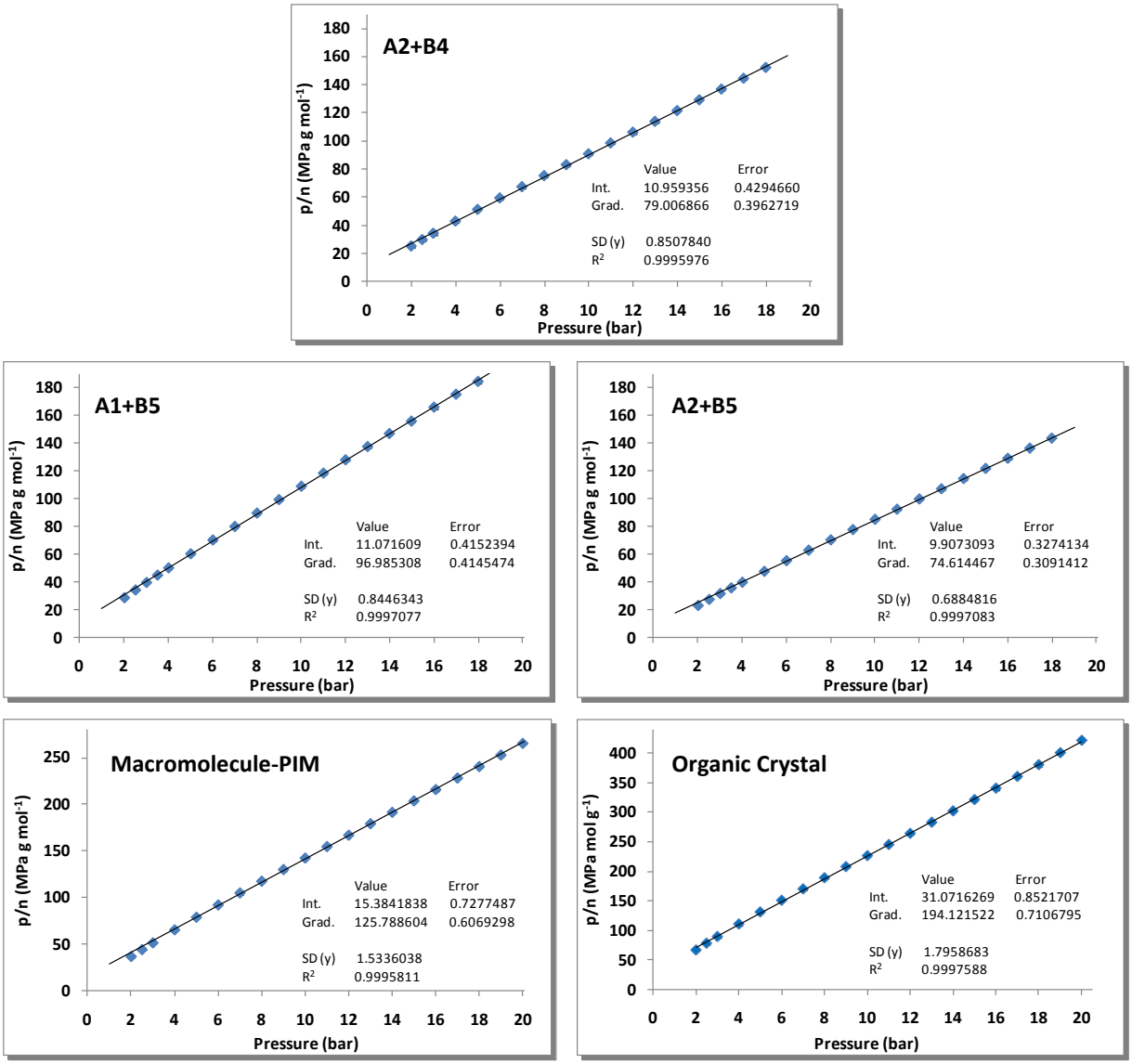

Figure F.1 - Linearised Langmuir plot for the hydrogen adsorption at 77 K from 2 bar.

Appendix G

VIRIAL THERMAL TYPE EQUATION

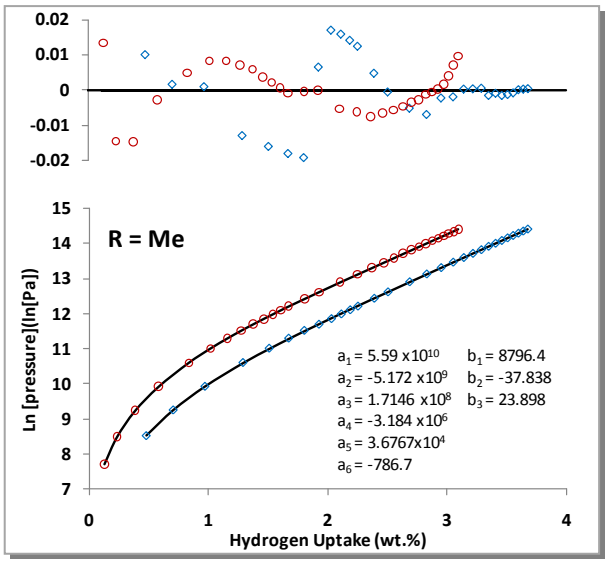

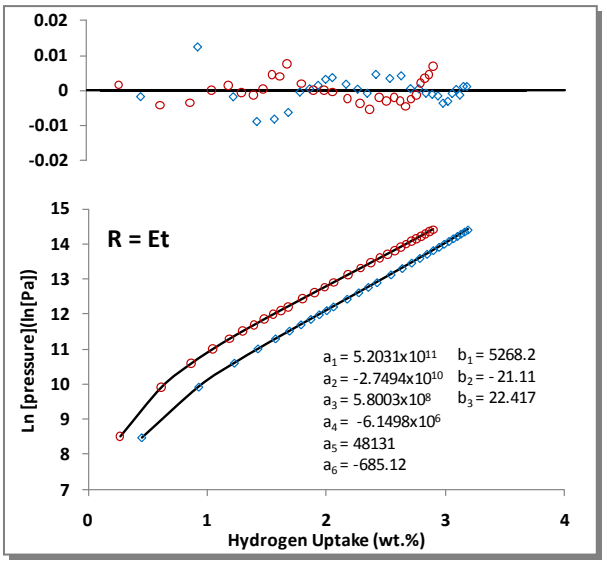

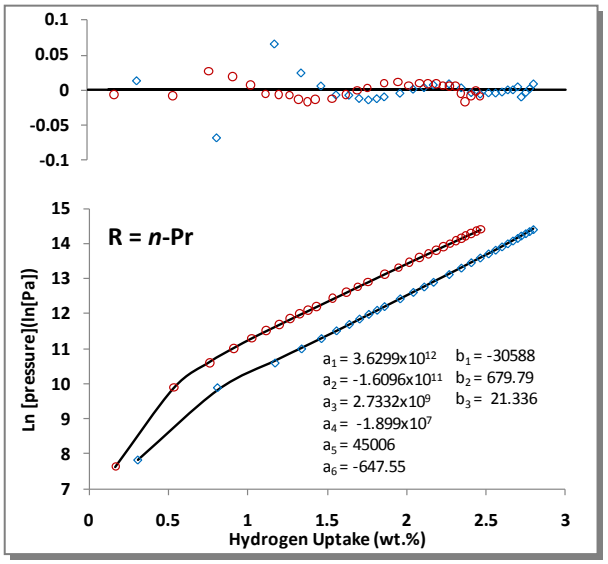

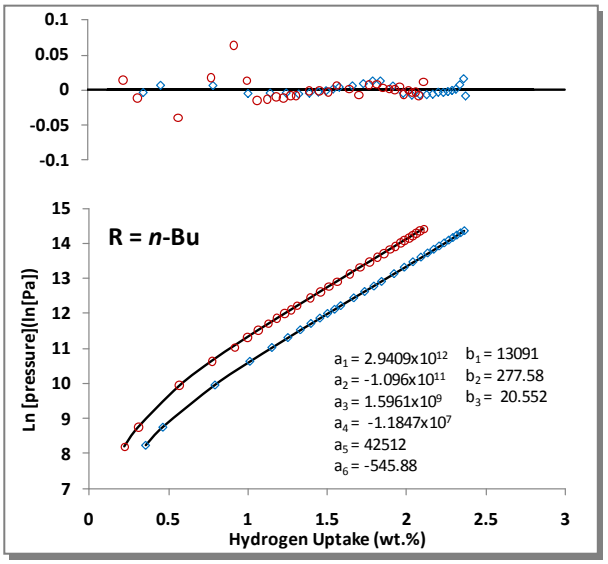

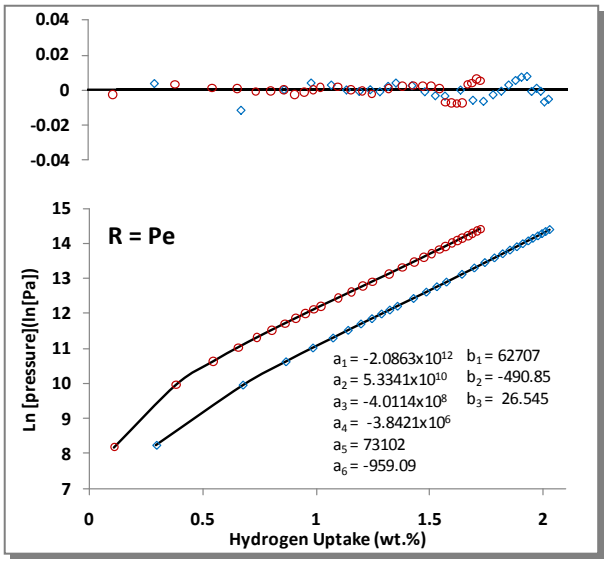
R = Pe
a_1 = -2.0863x10^12 b_1 = 62707
a_2 = 5.3341x10^10 b_2 = -490.85
a_3 = -4.0114x10^8 b_3 = 26.545
a_4 = -3.8421x10^6
a_5 = 73102
a_6 = -959.09
Ln [pressure](ln[Pa])
Hydrogen Uptake (wt.%)

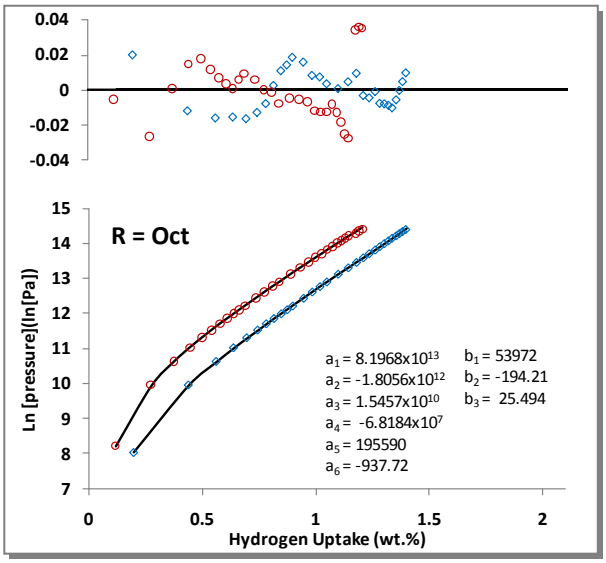
R = Oct
a_1 = 8.1968x10^13 b_1 = 53972
a_2 = -1.8056x10^12 b_2 = -194.21
a_3 = 1.5457x10^10 b_3 = 25.494
a_4 = -6.8184x10^7
a_5 = 195590
a_6 = -937.72
Ln [pressure](ln[Pa])
Hydrogen Uptake (wt.%)

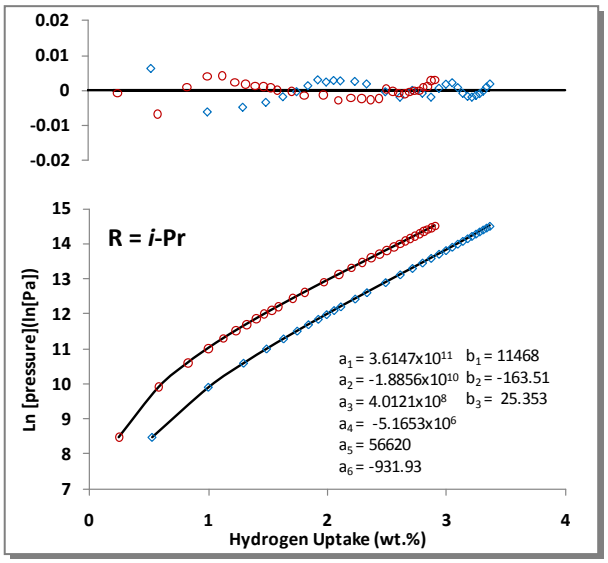
R = *i*-Pr
a_1 = 3.6147x10^11 b_1 = 11468
a_2 = -1.8856x10^10 b_2 = -163.51
a_3 = 4.0121x10^8 b_3 = 25.353
a_4 = -5.1653x10^6
a_5 = 56620
a_6 = -931.93
Ln [pressure](ln[Pa])
Hydrogen Uptake (wt.%)

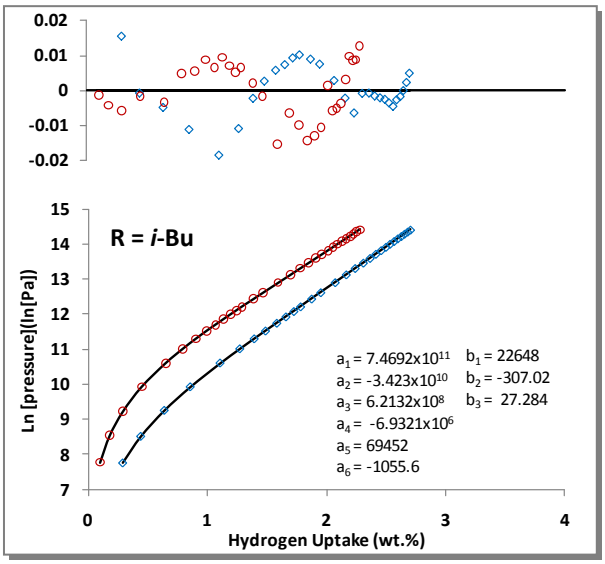
R = *i*-Bu
a_1 = 7.4692x10^11 b_1 = 22648
a_2 = -3.423x10^10 b_2 = -307.02
a_3 = 6.2132x10^8 b_3 = 27.284
a_4 = -6.9321x10^6
a_5 = 69452
a_6 = -1055.6
Ln [pressure](ln[Pa])
Hydrogen Uptake (wt.%)

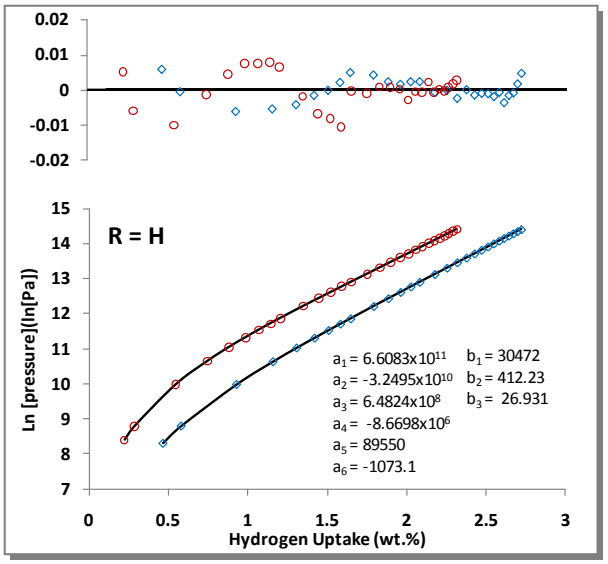
R = H
a_1 = 6.6083x10^11 b_1 = 30472
a_2 = -3.2495x10^10 b_2 = 412.23
a_3 = 6.4824x10^8 b_3 = 26.931
a_4 = -8.6698x10^6
a_5 = 89550
a_6 = -1073.1
Ln [pressure](ln[Pa])
Hydrogen Uptake (wt.%)

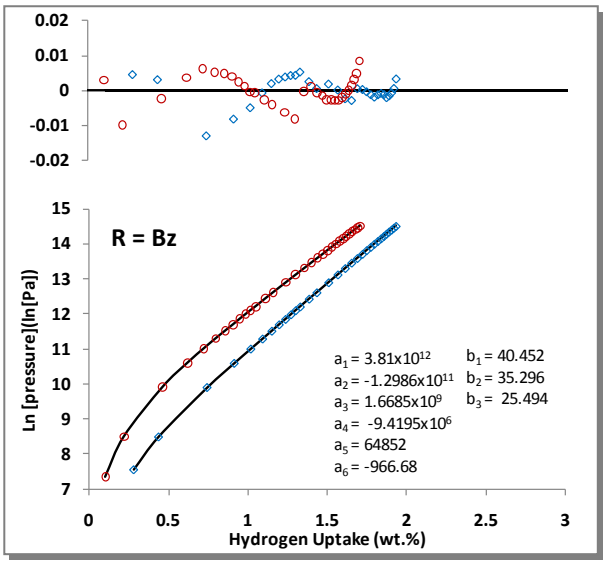
R = Bz
a_1 = 3.81x10^12 b_1 = 40.452
a_2 = -1.2986x10^11 b_2 = 35.296
a_3 = 1.6685x10^9 b_3 = 25.494
a_4 = -9.4195x10^6
a_5 = 64852
a_6 = -966.68
Ln [pressure](ln[Pa])
Hydrogen Uptake (wt.%)

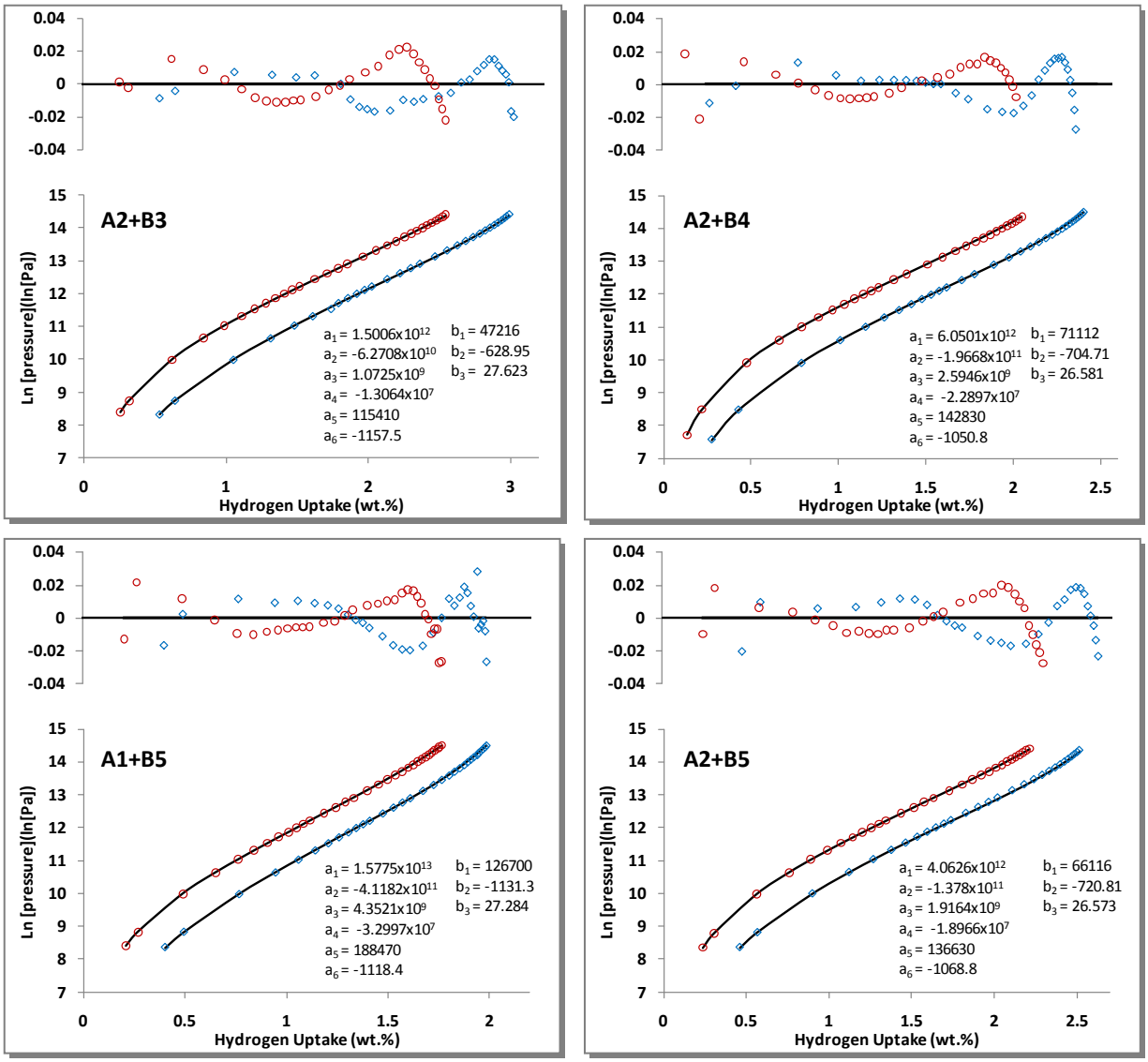

Figure G.1 - Hydrogen adsorption isotherms at 77 (◊) and 87 K (○) for the PIMs plotted as ln(p) against hydrogen uptake. Data is shown by open shapes, virial plots are shown by solid lines. Residual plots can be seen at the top.

Equation (3.66) was used to fit the 77 and 87 K isotherms simultaneously). The equation has no limit to the number of coefficients that can be included, previous researchers have found that values of $m \leq 6$ and $n \leq 3$, were enough to appreciably reduce the χ^2 goodness-of-fit for their range of microporous MOF materials.[134] The isosteric enthalpy of adsorption was subsequently calculated according to equation (3.67), as a function of hydrogen uptake.

Appendix H

NITROGEN ADSORPTION DATA

Table H.1 - Nitrogen adsorption data as measured using the Beckman Coulter 3100 Surface Area Analyzer at 77 K. Micropore capacities were considered to be equal to the monolayer capacities determined using the BET and Langmuir equations, using the adsorption data between 0.05 and 0.2 p/p_0 and up to p/p_0 = 0.2, respectively. The micropore volumes were determined from each respective micropore capacity utilising the assumption of that the density of the adsorbate is equal to that of liquid nitrogen at it's boiling point (0.808 g cm^{-3}).

PIM	Nitrogen uptake				Micropore capacity				Micropore Volume	
	p/p_0 = 0.01		p/p_0 = 0.1		BET		Langmuir		BET	Langmuir
	$cm^3\ g^{-1}$ (STP)	mmol g^{-1}	$cm^3\ g^{-1}$ (STP)	mmol g^{-1}	$cm^3\ g^{-1}$ (STP)	mmol g^{-1}	$cm^3\ g^{-1}$ (STP)	mmol g^{-1}	$cm^3\ g^{-1}$	$cm^3\ g^{-1}$
PIM-1	146.7	6.5	195.4	8.7	174.8	7.8	202.6	9.0	0.27	0.31
Porphyrin	288.7	12.9	366.8	16.4	326.1	14.5	384.3	17.1	0.50	0.59
H	278.3	12.4	349.0	15.6	302.3	13.5	365.9	16.3	0.47	0.57
Me	334.1	14.9	439.6	19.6	404.3	18.0	471.8	21.0	0.63	0.73
Et	300.2	13.4	369.7	16.5	324.9	14.5	393.4	17.6	0.50	0.61
n-Pr	283.1	12.6	348.9	15.6	308.6	13.8	371.6	16.6	0.48	0.57
i-Pr	314.3	14.0	406.4	18.1	366.9	16.4	435.7	19.4	0.57	0.67
n-Bu	199.8	8.9	251.7	11.2	224.7	10.0	265.8	11.9	0.35	0.41
i-Bu	222.8	9.9	278.8	12.4	246.8	11.0	298.9	13.3	0.38	0.46
Pe	197.2	8.8	243.9	10.9	217.5	9.7	252.7	11.3	0.34	0.39
Oct	118.1	5.3	158.1	7.1	142.0	6.3	173.4	7.7	0.22	0.27
Bz	197.3	8.8	239.5	10.7	206.6	9.2	252.0	11.2	0.32	0.39

A1 + B6	213.6	9.5	287.0	12.8	263.5	11.8	310.1	13.8	0.41	0.48
A2 + B6	301.0	13.4	399.6	17.8	361.7	16.1	424.2	18.9	0.56	0.66
A2 + B7	270.7	12.1	359.9	16.1	330.0	14.7	385.4	17.2	0.51	0.60
A1 + B8	191.0	8.5	252.1	11.2	231.0	10.3	264.1	11.8	0.36	0.41
A2 + B8	309.1	13.8	406.8	18.2	367.3	16.4	432.5	19.3	0.57	0.67
A3 + B1	177.3	7.9	228.2	10.2	202.2	9.0	242.3	10.8	0.31	0.37
A4 + B6 + A2	113.5	5.1	154.1	6.9	139.5	6.2	162.6	7.3	0.22	0.25
Organic Crystal	61.9	2.8	73.7	3.3	60.8	2.7	74.1	3.3	0.09	0.11

References

1. Dell, R. M. and Rand, D. A. J., *Energy Storage - A Key Technology for Global Energy Sustainability.* Journal of Power Sources, 2001. **100**(1-2): p. 2-17.
2. Koroneos, C., Dompros, A., Roumbas, G., and Moussiopoulos, N., *Life Cycle Assessment of Hydrogen Fuel Production Processes.* International Journal of Hydrogen Energy, 2004. **29**(14): p. 1443-1450.
3. Züttel, A., *Hydrogen Storage Methods.* Naturwissenschaften, 2004. **91**(4): p. 157-172.
4. Spath, P. L., Lane, J. M., Mann, M. K., and Amos, W. A., *Update of Hydrogen from Biomass - Determination of the Delivered Cost of Hydrogen*, in *NREL Milestone Report*. 2000, U.S. Department of Energy - Hydrogen Program.
5. Department of Energy, U. S. *Multi-Year Research, Development and Demonstration Plan - Planned Program Activities for 2005-2015*. Hydrogen, Fuel Cells & Infrastructure Technologies Program 2007 Hydrogen Production, Storage, and Fuel Cells, Last Updated April 2009 [cited 29/07/2010]; Available from: http://www1.eere.energy.gov/hydrogenandfuelcells/mypp/.
6. Lackner, K. S., *A Guide to CO_2 Sequestration.* Science, 2003. **300**(5626): p. 1677-1678.
7. Turner, J. A., *Sustainable Hydrogen Production.* Science, 2004. **305**(5686): p. 972-974.
8. Holladay, J. D., Hu, J., King, D. L., and Wang, Y., *An Overview of Hydrogen Production Technologies.* Catalysis Today, 2009. **139**(4): p. 244-260.
9. Anderson, D. and Leach, M., *Harvesting and Redistributing Renewable Energy: On the Role of Gas and Electricity Grids to Overcome Intermittency Through the Generation and Storage of Hydrogen.* Energy Policy, 2004. **32**(14): p. 1603-1614.
10. Quakernaat, J., *Hydrogen in a Global Long-Term Perspective.* International Journal of Hydrogen Energy, 1995. **20**(6): p. 485-492.
11. Czernik, S., French, R., Feik, C., and Chronet, E., *Production of Hydrogen by Reforming Biomass Pyrolysis Liquids and Natural Gas.* Fuel Chemistry Division Preprints, 2002. **47**(1): p. 372.
12. Czernik, S., French, R., Feik, C., and Chornet, E., *Hydrogen by Catalytic Steam Reforming of Liquid Byproducts from Biomass Thermoconversion Processes.* Industrial & Engineering Chemistry Research, 2002. **41**(17): p. 4209-4215.
13. Hawkes, F. R., Dinsdale, R., Hawkes, D. L., and Hussy, I., *Sustainable Fermentative Hydrogen Production: Challenges for Process Optimisation.* International Journal of Hydrogen Energy, 2002. **27**(11-12): p. 1339-1347.
14. Léon, A. and Hahn, R., *Hydrogen Technology*. Green Energy and Technology. 2008: Springer Berlin Heidelberg. p. 687.
15. Pollet, B. G., *Hydrogen and Fuel Cells: For a Low Carbon Future* Platinum Metals Review, 2009. **53**(2): p. 78-85.
16. Schlapbach, L. and Züttel, A., *Hydrogen-Storage Materials for Mobile Applications.* Nature, 2001. **414**(6861): p. 353-358.
17. Schlapbach, L., *Technology: Hydrogen-Fuelled Vehicles.* Nature, 2009. **460**(7257): p. 809-811.
18. Barbir, F., *PEM Fuel Cells: Theory and Practise*. 2005, London, UK: Elsevier Academic Press. p. 433.
19. Department of Energy, U. S. *DOE Targets for On-Board Hydrogen Storage Systems for Light-Duty Vehicles*. Current R&D Focus is on 2015 Targets with Potential to Meet Ultimate Targets 2009 Last Updated February 2009 [cited 11/09/2009]; Available from: http://www1.eere.energy.gov/hydrogenandfuelcells/storage/pdfs/targets_onboard_hydro_storage.pdf.
20. Dillich, S. *2009 DOE Hydrogen Program & Vehicle Technologies Program*. Merit Review and Peer Evaluation Meeting 2009 [cited 10/09/2009]; Available from: http://www.hydrogen.energy.gov/ http://www.hydrogen.energy.gov/pdfs/review09/st_0_dillich.pdf.
21. Ustinov, E. A., Do, D. D., Herbst, A., Staudt, R., and Harting, P., *Modeling of Gas Adsorption Equilibrium over a Wide Range of Pressure: A Thermodynamic Approach Based on Equation of State.* Journal of Colloid and Interface Science, 2002. **250**(1): p. 49-62.

22. Züttel, A., *Materials for Hydrogen Storage.* Materials Today, 2003. **6**(9): p. 24-33.
23. Harris, I. R., Book, D., Anderson, P. A., and Edwards, P. P., *Hydrogen Storage: The Grand Challenge.* Fuel Cell Review, 2004. **1**: p. 17-23.
24. Bossel, U. and Eliasson, B. *Energy and the Hydrogen Economy*. 2003 [cited 02/09/2010]; Available from: www.methanol.org http://www.methanol.org/pdf/HydrogenEconomyReport2003.pdf.
25. National Institute of Standards and Technology. *Chemistry WebBook: (Thermophysical Properties of Fluid Systems)*. [cited 01/06/2010]; Available from: http://webbook.nist.gov/chemistry/fluid/.
26. Flynn T.M., *A Liquefaction of Gases*. 7th ed. McGraw-Hill Encyclopedia of Science & Technology, 7th ed. . Vol. 10. 1992, New York: McGraw-Hill.
27. van Vucht, J. H., Kuijpers, F. A., and Bruning, H. C. A. M., *Reversible Room-Temperature Absorption of Large Quantities of Hydrogen by Intermetallic Compounds.* Philips Research Reports, 1970. **25**: p. 133-140.
28. Reilly, J. J. and Wiswall, R. H., *Formation and Properties of Iron Titanium Hydride.* Inorganic Chemistry, 1974. **13**(1): p. 218-222.
29. Reilly, J. J. and Sandrock, G. D., *Hydrogen Storage in Metal Hydrides.* Scientific American, 1980. **242**(2): p. 98-104.
30. Dantzer, P., *Properties of Intermetallic Compounds Suitable for Hydrogen Storage Applications.* Materials Science and Engineering A, 2002. **329-331**: p. 313-320.
31. Sakintuna, B., Lamari-Darkrim, F., and Hirscher, M., *Metal Hydride Materials for Solid Hydrogen Storage: A Review.* International Journal of Hydrogen Energy, 2007. **32**(9): p. 1121-1140.
32. Khrussanova, M., Terzieva, M., Peshev, P., Konstanchuk, I., and Ivanov, E., *Hydriding Kinetics of Mixtures Containing Some 3d-Transition Metal-Oxides and Magnesium.* Zeitschrift Fur Physikalische Chemie Neue Folge, 1989. **164**: p. 1261-1266.
33. Dornheim, M., Doppiu, S., Barkhordarian, G., Boesenberg, U., Klassen, T., Gutfleisch, O., and Bormann, R., *Hydrogen Storage in Magnesium-Based Hydrides and Hydride Composites.* Scripta Materialia, 2007. **56**(10): p. 841-846.
34. Eberle, U., Felderhoff, M., and Schuth, F., *Chemical and Physical Solutions for Hydrogen Storage.* Angewandte Chemie-International Edition, 2009. **48**(36): p. 6608-6630.
35. Vajo, J. J., Skeith, S. L., and Mertens, F., *Reversible Storage of Hydrogen in Destabilized $LiBH_4$.* Journal of Physical Chemistry B, 2005. **109**(9): p. 3719-3722.
36. Orimo, S., Nakamori, Y., Kitahara, G., Miwa, K., Ohba, N., Towata, S., and Züttel, A., *Dehydriding and Rehydriding Reactions of $LiBH_4$.* Journal of Alloys and Compounds, 2005. **404**: p. 427-430.
37. Bogdanovic, B. and Schwickardi, M., *Ti-Doped Alkali Metal Aluminium Hydrides as Potential Novel Reversible Hydrogen Storage Materials.* Journal of Alloys and Compounds, 1997. **253**: p. 1-9.
38. Bogdanovic, B., Brand, R. A., Marjanovic, A., Schwickardi, M., and Tolle, J., *Metal-Doped Sodium Aluminium Hydrides as Potential New Hydrogen Storage Materials.* Journal of Alloys and Compounds, 2000. **302**(1-2): p. 36-58.
39. Zaluska, A., Zaluski, L., and Ström-Olsen, J. O., *Sodium Alanates for Reversible Hydrogen Storage.* Journal of Alloys and Compounds, 2000. **298**(1-2): p. 125-134.
40. Beattie, S. D. and McGrady, G. S., *Hydrogen Desorption Studies of $NaAlH_4$ and $LiAlH_4$ by In-Situ Heating in an ESEM.* International Journal of Hydrogen Energy, 2009. **34**(22): p. 9151-9156.
41. Okada, Y., Sasaki, E., Watanabe, E., Hyodo, S., and Nishijima, H., *Development of Dehydrogenation Catalyst for Hydrogen Generation in Organic Chemical Hydride Method.* International Journal of Hydrogen Energy, 2006. **31**(10): p. 1348-1356.
42. Docter, A. and Lamm, A., *Gasoline Fuel Cell Systems.* Journal of Power Sources, 1999. **84**(2): p. 194-200.
43. Ersoz, A., Olgun, H., and Ozdogan, S., *Reforming Options for Hydrogen Production from Fossil Fuels for PEM Fuel Cells.* Journal of Power Sources, 2006. **154**(1): p. 67-73.
44. Palo, D. R., Dagle, R. A., and Holladay, J. D., *Methanol Steam Reforming for Hydrogen Production.* Chemical Reviews, 2007. **107**(10): p. 3992-4021.

45. zur Megede, D., *Fuel Processors for Fuel Cell Vehicles.* Journal of Power Sources, 2002. **106**(1-2): p. 35-41.
46. Hatanaka, T., Hasegawa, N., Kamiya, A., Kawasumi, M., Morimoto, Y., and Kawahara, K., *Cell Performances of Direct Methanol Fuel Cells with Grafted Membranes.* Fuel, 2002. **81**(17): p. 2173-2176.
47. Wong-Foy, A. G., Matzger, A. J., and Yaghi, O. M., *Exceptional H_2 Saturation Uptake in Microporous Metal-Organic Frameworks.* Journal of the American Chemical Society, 2006. **128**(11): p. 3494-3495.
48. Gregg, S. J. and Sing, K. S. W., *Adsorption, Surface Area and Porosity*. 1982: Academic Press Inc. (London) Ltd. p. 303.
49. Lennard-Jones, J. E., *Processes of Adsorption and Diffusion on Solid Surfaces.* Transactions of the Faraday Society, 1932. **28**: p. 0333-0358.
50. Rouquerol, F., Rouquerol, J., and Sing, K. S. W., *Adsorption by Powders and Porous Solids: Principles, Methodology and Applications*. 1999, London: Academic Press. p. 467.
51. Anderson, P. J. and Horlock, R. F., *Heats of Argon Adsorption on Microporous Magnesium Oxide Powders.* Transactions of the Faraday Society, 1969. **65**(553P): p. 251-258.
52. Everett, D. H. and Powl, J. C., *Adsorption in Slit-Like and Cylindrical Micropores in Henrys Law Region - Model for Microporosity of Carbons.* Journal of the Chemical Society-Faraday Transactions I, 1976. **72**: p. 619-636.
53. Kitagawa, S., Kitaura, R., and Noro, S., *Functional Porous Coordination Polymers.* Angewandte Chemie-International Edition, 2004. **43**(18): p. 2334-2375.
54. Dubinin, M. M., *The Potential Theory of Adsorption of Gases and Vapors for Adsorbents with Energetically Nonuniform Surfaces.* Chemical Reviews, 1960. **60**(2): p. 235-241.
55. Everett, D. H., *IUPAC Manual of Symbols and Terminology for Physicochemical Quantities and Units, Appendix II: Definitions, Terminology and Symbols in Colloid and Surface Chemistry.* Pure and Applied Chemistry, 1972. **31**(4): p. 577-638.
56. Brunauer, S., Deming, L. S., Deming, W. E., and Teller, E., *On a Theory of the van der Waals Adsorption of Gases.* Journal of the American Chemical Society, 1940. **62**(7): p. 1723-1732.
57. Sing, K. S. W., Everett, D. H., Haul, R. A. W., Moscou, L., Pierotti, R. A., Rouquerol, J., and Siemieniewska, T., *Reporting Physisorption Data for Gas Solid Systems with Special Reference to the Determination of Surface-Area and Porosity (Recommendations 1984).* Pure and Applied Chemistry, 1985. **57**(4): p. 603-619.
58. Wang, K., Qiao, S., and Hu, X., *Study of Isosteric Heat of Adsorption and Activation Energy for Surface Diffusion of Gases on Activated Carbon using Equilibrium and Kinetics information.* Separation and Purification Technology, 2004. **34**(1-3): p. 165-176.
59. Tóth, J., *Adsorption: Theory, Modelling, and Analysis*. Surfactant Science Series, ed. Hubbard A. T. Vol. 107. 2002, New York: Marcel Dekker Inc. p. 878.
60. Freundlich, H., *Colloid & Capillary Chemistry* 1926: London: Methuen. p. 883.
61. McBain, J. W., *The Sorption of Gases and Vapours by Solids*. 1932, London: George Routledge & Sons, Ltd. p. 577.
62. Rudzinski, W. and Everett, D. H., *Adsorption of Gases on Heterogeneous Surfaces*. 1992: Academic Press, London. p. 578.
63. Do, D. D., *Adsorption Analysis: Equilibria and Kinetics*, ed. Yang, R. T. Vol. 2. 1998, London: Imperial College London. p. 892.
64. Langmuir, I., *The Adsorption of Gases on Plane Surfaces of Glass, Mica and Platinum.* Journal of the American Chemical Society, 1918. **40**(9): p. 1361-1403.
65. Seifi, M., Ross, D. K., Riley, D. J., and Morrison, I., *The Dependence of the Hydrogen Sorption Capacity of Single-Walled Carbon Nanotubes on the Concentration of Catalyst.* Carbon, 2009. **47**(14): p. 3184-3191.
66. Ye, Y., Ahn, C. C., Witham, C., Fultz, B., Liu, J., Rinzler, A. G., Colbert, D., Smith, K. A., and Smalley, R. E., *Hydrogen Adsorption and Cohesive Energy of Single-Walled Carbon Nanotubes.* Applied Physics Letters, 1999. **74**(16): p. 2307-2309.

67. McCarty, R. D., *Hydrogen: Its Technology and Implications*, ed. Cox, K. E. and Williamson, K. D. Vol. 3, Hydrogen Properties. 1975, Cleveland, Ohio: CRC Press, Inc. p. 321.
68. Sips, R., *On the Structure of a Catalyst Surface.* Journal of Chemical Physics, 1948. **16**(5): p. 490-495.
69. Sips, R., *On the Structure of a Catalyst Surface 2.* Journal of Chemical Physics, 1950. **18**(8): p. 1024-1026.
70. Papageorgiou, S. K., Katsaros, F. K., Kouvelos, E. P., Nolan, J. W., Le Deit, H., and Kanellopoulos, N. K., *Heavy Metal Sorption by Calcium Alginate Beads from Laminaria Digitata.* Journal of Hazardous Materials, 2006. **137**(3): p. 1765-1772.
71. Thomas, K. M., *Adsorption and Desorption of Hydrogen on Metal-Organic Framework Materials for Storage Applications: Comparison with other Nanoporous materials.* Dalton Transactions, 2009(9): p. 1487-1505.
72. Malek, A. and Farooq, S., *Comparison of Isotherm Models for Hydrocarbon Adsorption on Activated Carbon.* AIChE Journal, 1996. **42**(11): p. 3191-3201.
73. Tóth, J., *Uniform Interpretation of Gas/Solid Adsorption.* Advances in Colloid and Interface Science, 1995. **55**: p. 1-239.
74. Walton, K. S., Abney, M. B., and LeVan, M. D., *CO_2 Adsorption in Y and X Zeolites Modified by Alkali Metal Cation Exchange.* Microporous and Mesoporous Materials, 2006. **91**(1-3): p. 78-84.
75. Wang, Y. and LeVan, M. D., *Adsorption Equilibrium of Carbon Dioxide and Water Vapor on Zeolites 5A and 13X and Silica Gel: Pure Components.* Journal of Chemical and Engineering Data, 2009. **54**(10): p. 2839-2844.
76. Walton, K. S., Cavalcante, C. L., and LeVan, M. D., *Adsorption of Light Alkanes on Coconut Nanoporous Activated Carbon.* Brazilian Journal of Chemical Engineering, 2006. **23**(4): p. 555-561.
77. Wang, Y. and LeVan, M. D., *Adsorption Equilibrium of Binary Mixtures of Carbon Dioxide and Water Vapor on Zeolites 5A and 13X.* Journal of Chemical and Engineering Data, 2010. **55**(9): p. 3189-3195.
78. Schindler, B. J., Buettner, L. C., and LeVan, M. D., *Transition to Henry's Law in Ultra-Low Concentration Adsorption Equilibrium for n-Pentane on BPL Activated Carbon.* Carbon, 2008. **46**(10): p. 1285-1293.
79. Pierce, C., Wiley, J. W., and Smith, R. N., *Capillarity and Surface Area of Charcoal.* Journal of Physical and Colloid Chemistry, 1949. **53**(5): p. 669-683.
80. Dubinin, M. M., Zaverina, E. D., and Timofeeva, D. P., *Sorbtsiya I Struktura Aktivnykh Uglei .6. Strukturnye Tipy Aktivnykh Uglei.* Zhurnal Fizicheskoi Khimii, 1949. **23**(10): p. 1129-1140.
81. Dubinin, A. M. M., *A Study of the Porous Structure of Active Carbons Using a Variety of Methods.* Quarterly Reviews, 1955. **9**(2): p. 101-114.
82. Polanyi, M., *Theories of the Adsorption of Gases. A General Survey and Some Additional Remarks. Introductory Paper to Section III.* Transactions of the Faraday Society, 1932. **28**: p. 0316-0332.
83. Jaroniec M., *Fifty years of the theory of the volume filling of micropores* Adsorption, 1997. **3**: p. 187-188.
84. Dubinin, M. M., *Physical Adsorption of Gases and Vapors in Micropores*. Progress in Surface and Membrane Science, ed. Cadenhead, D. A., Danielli, J. F., and Rosenberg, M. D. Vol. 9. 1975: Academic Press, Inc. (London) Ltd. p. 1-70.
85. Poirier, E. and Dailly, A., *Investigation of the Hydrogen State in IRMOF-1 from Measurements and Modeling of Adsorption Isotherms at High Gas Densities.* Journal of Physical Chemistry C, 2008. **112**(33): p. 13047-13052.
86. Amankwah, K. A. G. and Schwarz, J. A., *A Modified Approach for Estimating Pseudo-Vapor Pressures in the Application of the Dubinin-Astakhov Equation.* Carbon, 1995. **33**(9): p. 1313-1319.
87. Dubinin, M. M., *Fundamentals of the Theory of Adsorption in Micropores of Carbon Adsorbents - Characteristics of Their Adsorption Properties and Microporous Structures.* Carbon, 1989. **27**(3): p. 457-467.
88. Dubinin, M. M. and Astakhov, V. A., *Description of Adsorption Equilibria of Vapors on Zeolites over Wide Ranges of Temperature and Pressure.* Molecular Sieve Zeolites - II, 1970. **102**: p. p. 69-85.
89. Hutson, N. D. and Yang, R. T., *Theoretical Basis for the Dubinin-Radushkevich (D-R) Adsorption Isotherm Equation.* Adsorption-Journal of the International Adsorption Society, 1997. **3**(3): p. 189-195.

90. Yang, R. T., *Adsorbents: Fundamentals and Applications*. 2003, Hoboken, New Jersey: John Wiley & Sons, Inc. p. 410.
91. Barrett, E. P., Joyner, L. G., and Halenda, P. P., *The Determination of Pore Volume and Area Distributions in Porous Substances .1. Computations from Nitrogen Isotherms.* Journal of the American Chemical Society, 1951. **73**(1): p. 373-380.
92. Stoeckli, H. F., *On the Theoretical Foundation of the Dubinin-Astakhov Equation.* Carbon, 1981. **19**(4): p. 325-326.
93. Benham, M., *BET Surface Area and Pore Size Distribution Analysis Guide*, in *Operating Guidelines*. 2003, Hiden Isochema Ltd: Warrington, U.K. p. 21.
94. Dubinin, M. M., *Water-Vapor Adsorption and the Microporous Structures of Carbonaceous Adsorbents.* Carbon, 1980. **18**(5): p. 355-364.
95. Roper, M. G. and Broom, D. P., *The Determination of the Pore Size Distribution of an Activated Carbon using Dubinin-Astakhov Analysis of CO_2 Adsorption at 273 K*, in *Application Note 126*. 2009, Hiden Isochema Ltd: Warrington, U.K. p. 6.
96. Sams, J. R., Constabaris, G., and Halsey, G. D., *2nd Virial Coefficients of Neon, Argon, Krypton and Xenon with a Graphitized Carbon Black.* Journal of Physical Chemistry, 1960. **64**(11): p. 1689-1696.
97. Horváth, G. and Kawazoe, K., *Method for the Calculation of Effective Pore-Size Distribution in Molecular-Sieve Carbon.* Journal of Chemical Engineering of Japan, 1983. **16**(6): p. 470-475.
98. Webb, P. A. and Orr, C., *Analytical Methods in Fine Particle Technology*. 1997, Norcross, GA.: Micromeritics Inc. p. 325.
99. Kaminsky, R. D., Maglara, E., and Conner, W. C., *A Direct Assessment of Mean-Field Methods of Determining Pore-Size Distributions of Microporous Media from Adsorption-Isotherm Data.* Langmuir, 1994. **10**(5): p. 1556-1565.
100. Kruk, M., Jaroniec, M., and Choma, J., *Comparative Analysis of Simple and Advanced Sorption Methods for Assessment of Microporosity in Activated Carbons.* Carbon, 1998. **36**(10): p. 1447-1458.
101. Valladares, D. L., Reinoso, F. R., and Zgrablich, G., *Characterization of Active Carbons: The Influence of the Method in the Determination of the Pore Size Distribution.* Carbon, 1998. **36**(10): p. 1491-1499.
102. Lee, J. Y., Wood, C. D., Bradshaw, D., Rosseinsky, M. J., and Cooper, A. I., *Hydrogen Adsorption in Microporous Hypercrosslinked Polymers.* Chemical Communications, 2006(25): p. 2670-2672.
103. Saito, A. and Foley, H. C., *Curvature and Parametric Sensitivity in Models for Adsorption in Micropores.* AIChE Journal, 1991. **37**(3): p. 429-436.
104. Cheng, L. S. and Yang, R. T., *Improved Horváth-Kawazoe Equations Including Spherical Pore Models for Calculating Micropore Size Distribution.* Chemical Engineering Science, 1994. **49**(16): p. 2599-2609.
105. Cheng, L. S. and Yang, R. T., *Predicting Isotherms in Micropores for Different Molecules and Temperatures from a Known Isotherm by Improved Horváth-Kawazoe Equations.* Adsorption-Journal of the International Adsorption Society, 1995. **1**(3): p. 187-196.
106. Lowell, S., Shields, J. E., Thomas, M. A., and Thommes, M., *Characterization of Porous Solids and Powders: Surface Area, Pore Size, and Density*. 4th ed. Particle Technology Series. 2004, Dordrecht: Kluwer Academic. p. 347.
107. Brunauer, S., Emmett, P. H., and Teller, E., *Adsorption of Gases in Multimolecular Layers.* Journal of the American Chemical Society, 1938. **60**(2): p. 309-319.
108. Walton, K. S. and Snurr, R. Q., *Applicability of the BET Method for Determining Surface Areas of Microporous Metal-Organic Frameworks.* Journal of the American Chemical Society, 2007. **129**(27): p. 8552-8556.
109. Rouquerol, J., Llewellyn, P., and Rouquerol, F., *Is the BET Equation Applicable to Microporous Adsorbents?*, in *Studies in Surface Science and Catalysis*. 2007, Elsevier. p. 49-56.
110. Sandrock, G., *A Panoramic Overview of Hydrogen Storage Alloys from a Gas Reaction Point of View.* Journal of Alloys and Compounds, 1999. **293**: p. 877-888.
111. Broom, D. P. *Hydrogen Sorption Measurements on Potential Storage Materials: Experimental Methods & Measurement Accuracy*. 2008 [cited 03/11/2009]; Available from: http://ie.jrc.ec.europa.eu/ http://ie.jrc.ec.europa.eu/publications/scientific_publications/2008/EUR23242EN.pdf.

112. Garberoglio, G., Skoulidas, A. I., and Johnson, J. K., *Adsorption of Gases in Metal Organic Materials: Comparison of Simulations and Experiments.* Journal of Physical Chemistry B, 2005. **109**(27): p. 13094-13103.

113. Zubizarreta, L., Jagiello, J., Arenillas, A., Ania, C. O., Parra, J. B., and Pis, J. J., *Optimizing H_2 Volumetric Storage Capacity of Carbon Materials for Mobile Applications*, in *Characterisation of Porous Solids VIII*, Kaskel, S., Llewellyn, P., Rodríguez-Reinoso, F., and Seaton, N. A., Editors. 2009, Royal Soc Chemistry: Cambridge, U.K. p. 134-141.

114. Jordá-Beneyto, M., Lozano-Castelló, D., Suárez-García, F., Cazorla-Amorós, D., and Linares-Solano, Á., *Advanced Activated Carbon Monoliths and Activated Carbons for Hydrogen Storage.* Microporous and Mesoporous Materials, 2008. **112**(1-3): p. 235-242.

115. Sircar, S., *Measurement of Gibbsian Surface Excess.* AIChE Journal, 2001. **47**(5): p. 1169-1176.

116. Sircar, S., *Gibbsian surface excess for gas adsorption - Revisited.* Industrial & Engineering Chemistry Research, 1999. **38**(10): p. 3670-3682.

117. Zhou, W., Wu, H., Hartman, M. R., and Yildirim, T., *Hydrogen and Methane Adsorption in Metal-Organic Frameworks: A High-Pressure Volumetric Study.* Journal of Physical Chemistry C, 2007. **111**(44): p. 16131-16137.

118. Furukawa, H., Miller, M. A., and Yaghi, O. M., *Independent Verification of the Saturation Hydrogen Uptake in MOF-177 and Establishment of a Benchmark for Hydrogen Adsorption in Metal-Organic Frameworks.* Journal of Materials Chemistry, 2007. **17**(30): p. 3197-3204.

119. Poirier, E. and Dailly, A., *Thermodynamics of Hydrogen Adsorption in MOF-177 at Low Temperatures: Measurements and Modelling.* Nanotechnology, 2009. **20**(20): p. 204006

120. Zhou, L., Zhou, Y. P., Li, M., Chen, P., and Wang, Y., *Experimental and Modeling Study of the Adsorption of Supercritical Methane on a High Surface Activated Carbon.* Langmuir, 2000. **16**(14): p. 5955-5959.

121. Lin, X., Telepeni, I., Blake, A. J., Dailly, A., Brown, C. M., Simmons, J. M., Zoppi, M., Walker, G. S., Thomas, K. M., Mays, T. J., Hubberstey, P., Champness, N. R., and Schröder, M., *High Capacity Hydrogen Adsorption in Cu(II) Tetracarboxylate Framework Materials: The Role of Pore Size, Ligand Functionalization, and Exposed Metal Sites.* Journal of the American Chemical Society, 2009. **131**(6): p. 2159-2171.

122. Lemmon, E. W., Huber, M. L., and McLinden, M. O., *NIST Standard Reference Database 23: Reference Fluid Thermodynamic and Transport Properties-REFPROP, Version 9.0*, National Institute of Standards and Technology, Standard Reference Data Program, Gaithersburg, 2010.

123. Richard, M. A., Bénard, P., and Chahine, R., *Gas Adsorption Process in Activated Carbon Over a Wide Temperature Range Above the Critical Point. Part 1: Modified Dubinin-Astakhov Model.* Adsorption-Journal of the International Adsorption Society, 2009. **15**(1): p. 43-51.

124. Murata, K., El-Merraoui, M., and Kaneko, K., *A New Determination Method of Absolute Adsorption Isotherm of Supercritical Gases Under High Pressure with a Special Relevance to Density-Functional Theory Study.* Journal of Chemical Physics, 2001. **114**(9): p. 4196-4205.

125. Fletcher, A. J., Uygur, Y., and Thomas, K. M., *Role of Surface Functional Groups in the Adsorption Kinetics of Water Vapor on Microporous Activated Carbons.* Journal of Physical Chemistry C, 2007. **111**(23): p. 8349-8359.

126. Payne, H. K., Sturdevant, G. A., and Leland, T. W., *Improved 2-Dimensional Equation of State to Predict Adsorption of Pure and Mixed Hydrocarbons.* Industrial & Engineering Chemistry Fundamentals, 1968. **7**(3): p. 363-374.

127. Thomas, K. M., *Hydrogen Adsorption and Storage on Porous Materials.* Catalysis Today, 2007. **120**(3-4): p. 389-398.

128. Zhao, X. B., Xiao, B., Fletcher, A. J., and Thomas, K. M., *Hydrogen Adsorption on Functionalized Nanoporous Activated Carbons.* Journal of Physical Chemistry B, 2005. **109**(18): p. 8880-8888.

129. Steele, W. A., *Physical Interaction of Gases with Crystalline Solids 2. 2-Dimensional Second and Third Virial-Coefficients.* Surface Science, 1973. **39**(1): p. 149-175.

130. Pan, H. H., Ritter, J. A., and Balbuena, P. B., *Examination of the Approximations used in Determining the Isosteric Heat of Adsorption from the Clausius-Clapeyron Equation.* Langmuir, 1998. **14**(21): p. 6323-6327.

131. Moellmer, J., Celer, E. B., Luebke, R., Cairns, A. J., Staudt, R., Eddaoudi, M., and Thommes, M., *Insights on Adsorption Characterization of Metal-Organic Frameworks: A Benchmark Study on the Novel soc-MOF.* Microporous and Mesoporous Materials, 2010. **129**(3): p. 345-353.

132. Zhao, X. B., Villar-Rodil, S., Fletcher, A. J., and Thomas, K. M., *Kinetic Isotope Effect for H_2 and D_2 Quantum Molecular Sieving in Adsorption/Desorption on Porous Carbon Materials.* Journal of Physical Chemistry B, 2006. **110**(20): p. 9947-9955.

133. Cole, J. H., Everett, D. H., Marshall, C. T., Paniego, A. R., Powl, J. C., and Rodríguez-Reinoso, F., *Thermodynamics of High Temperature Adsorption of Some Permanent Gases by Porous Carbons.* Journal of the Chemical Society-Faraday Transactions I, 1974. **70**: p. 2154-2169.

134. Rowsell, J. L. C. and Yaghi, O. M., *Effects of Functionalization, Catenation, and Variation of the Metal Oxide and Organic Linking Units on the Low-Pressure Hydrogen Adsorption Properties of Metal-Organic Frameworks.* Journal of the American Chemical Society, 2006. **128**(4): p. 1304-1315.

135. Czepirski, L. and Jagiello, J., *Virial-Type Thermal Equation of Gas Solid Adsorption.* Chemical Engineering Science, 1989. **44**(4): p. 797-801.

136. Dinca, M., Dailly, A., Liu, Y., Brown, C. M., Neumann, D. A., and Long, J. R., *Hydrogen Storage in a Microporous Metal-Organic Framework with Exposed Mn^{2+} Coordination Sites.* Journal of the American Chemical Society, 2006. **128**(51): p. 16876-16883.

137. Blach, T. P. and Gray, E. M., *Sieverts apparatus and methodology for accurate determination of hydrogen uptake by light-atom hosts.* Journal of Alloys and Compounds, 2007. **446**: p. 692-697.

138. Poirier, E., Chahine, R., Tessier, A., and Bose, T. K., *Gravimetric and Volumetric Approaches Adapted for Hydrogen Sorption Measurements with In Situ Conditioning on Small Sorbent Samples.* Review of Scientific Instruments, 2005. **76**(5): p. 055101-1-6.

139. Dillon, A. C., Jones, K. M., Bekkedahl, T. A., Kiang, C. H., Bethune, D. S., and Heben, M. J., *Storage of Hydrogen in Single-Walled Carbon Nanotubes.* Nature, 1997. **386**(6623): p. 377-379.

140. Chen, P., Wu, X., Lin, J., and Tan, K. L., *High H_2 Uptake by Alkali-Doped Carbon Nanotubes under Ambient Pressure and Moderate Temperatures.* Science, 1999. **285**(5424): p. 91-93.

141. Chambers, A., Park, C., Baker, R. T. K., and Rodriguez, N. M., *Hydrogen Storage in Graphite Nanofibers.* Journal of Physical Chemistry B, 1998. **102**(22): p. 4253-4256.

142. Lamari-Darkrim, F., Malbrunot, P., and Tartaglia, G. P., *Review of Hydrogen Storage by Adsorption in Carbon Nanotubes.* International Journal of Hydrogen Energy, 2002. **27**(2): p. 193-202.

143. Yang, R. T., *Hydrogen Storage by Alkali-Doped Carbon Nanotubes-Revisited.* Carbon, 2000. **38**(4): p. 623-626.

144. Broom, D. P., *The Accuracy of Hydrogen Sorption Measurements on Potential Storage Materials.* International Journal of Hydrogen Energy, 2007. **32**(18): p. 4871-4888.

145. Robens, E., Krebs, K. F., Meyer, K., Unger, K. K., and Dabrowski, A., *Progress in the Standardisation of Particle and Surface Characterisation.* Colloids and Surfaces a-Physicochemical and Engineering Aspects, 2002. **208**(1-3): p. 253-257.

146. Avraham, I., Danon, A., and Koresh, J. E., *Study of Carbon Molecular Sieve Fibres by Atmospheric TPD-MS of H_2O, CO and CO_2.* Journal of the Chemical Society-Faraday Transactions, 1998. **94**(13): p. 1869-1874.

147. Kaye, S. S., Dailly, A., Yaghi, O. M., and Long, J. R., *Impact of Preparation and Handling on the Hydrogen Storage Properties of $Zn_4O(1,4\text{-Benzenedicarboxylate})_3$ (MOF-5).* Journal of the American Chemical Society, 2007. **129**(46): p. 14176-14177.

148. British Standards Institution, *Determination of the Specific Surface Area of Powders - Part 1: BET Method of Gas Adsorption for Solids (Including Porous Materials)*. 1996, (ISO 9277:1995).

149. Broom, D. P. and Moretto, P., *Accuracy in Hydrogen Sorption Measurements.* Journal of Alloys and Compounds, 2007. **446**: p. 687-691.

150. Zhou, L. and Zhou, Y. P., *Determination of Compressibility Factor and Fugacity Coefficient of Hydrogen in Studies of Adsorptive Storage.* International Journal of Hydrogen Energy, 2001. **26**(6): p. 597-601.

151. Leachman, J. W., Jacobsen, R. T., Penoncello, S. G., and Lemmon, E. W., *Fundamental Equations of State for Parahydrogen, Normal Hydrogen, and Orthohydrogen.* Journal of Physical and Chemical Reference Data, 2009. **38**(3): p. 721-748.

152. Langmi, H. W., *Zeolites as an Alternative to Carbons in Hydrogen Storage for Large Scale Stationary Applications, PhD Thesis* in *Department of Metallurgy and Materials*. 2004, University of Birmingham, U.K. p. 285.

153. Malbrunot, P., Vidal, D., Vermesse, J., Chahine, R., and Bose, T. K., *Adsorbent Helium Density Measurement and its Effect on Adsorption Isotherms at High Pressure.* Langmuir, 1997. **13**(3): p. 539-544.

154. Neimark, A. V. and Ravikovitch, P. I., *Calibration of Pore Volume in Adsorption Experiments and Theoretical Models.* Langmuir, 1997. **13**(19): p. 5148-5160.

155. Chahine, R. and Bose, T. K., *Low-Pressure Adsorption Storage of Hydrogen.* International Journal of Hydrogen Energy, 1994. **19**(2): p. 161-164.

156. Nützenadel, C., Züttel, A., and Schlapbach, L., *Electrochemical Storage of Hydrogen in Carbon Single Wall Nanotubes*, in *Electronic Properties of Novel Materials - Science and Technology of Molecular Nanostructures*, Kuzmany, H., Fink, J., Mehring, M., and Roth, S., Editors. 1999, Amer Inst Physics: Melville. p. 462-465.

157. Liu, C., Fan, Y. Y., Liu, M., Cong, H. T., Cheng, H. M., and Dresselhaus, M. S., *Hydrogen Storage in Single-Walled Carbon Nanotubes at Room Temperature.* Science, 1999. **286**(5442): p. 1127-1129.

158. Fan, Y. Y., Liao, B., Liu, M., Wei, Y. L., Lu, M. Q., and Cheng, H. M., *Hydrogen Uptake in Vapor-Grown Carbon Nanofibers.* Carbon, 1999. **37**(10): p. 1649-1652.

159. Orimo, S., Majer, G., Fukunaga, T., Zuttel, A., Schlapbach, L., and Fujii, H., *Hydrogen in the Mechanically Prepared Nanostructured Graphite.* Applied Physics Letters, 1999. **75**(20): p. 3093-3095.

160. Strobel, R., Jorissen, L., Schliermann, T., Trapp, V., Schutz, W., Bohmhammel, K., Wolf, G., and Garche, J., *Hydrogen Adsorption on Carbon Materials.* Journal of Power Sources, 1999. **84**(2): p. 221-224.

161. Murray, L. J., Dinca, M., and Long, J. R., *Hydrogen Storage in Metal-Organic Frameworks.* Chemical Society Reviews, 2009. **38**(5): p. 1294-1314.

162. Chahine, R. and Bose, T. K., *Characterization and Optimization of Adsorbents for Hydrogen Storage.* Hydrogen Energy Progress XI, Proceedings of the 11th World Hydrogen Energy Conference, 1996. **2**: p. 1259-1263.

163. Texier-Mandoki, N., Dentzer, J., Piquero, T., Saadallah, S., David, P., and Vix-Guterl, C., *Hydrogen Storage in Activated Carbon Materials: Role of the Nanoporous Texture.* Carbon, 2004. **42**(12-13): p. 2744-2747.

164. Jordá-Beneyto, M., Suárez-García, F., Lozano-Castelló, D., Cazorla-Amorós, D., and Linares-Solano, Á., *Hydrogen Storage on Chemically Activated Carbons and Carbon Nanomaterials at High Pressures.* Carbon, 2007. **45**(2): p. 293-303.

165. Popov, V. N., *Carbon Nanotubes: Properties and Application.* Materials Science & Engineering R-Reports, 2004. **43**(3): p. 61-102.

166. Iijima, S., *Helical Microtubules of Graphitic Carbon.* Nature, 1991. **354**: p. 56-58.

167. Thess, A., Lee, R., Nikolaev, P., Dai, H. J., Petit, P., Robert, J., Xu, C. H., Lee, Y. H., Kim, S. G., Rinzler, A. G., Colbert, D. T., Scuseria, G. E., Tomanek, D., Fischer, J. E., and Smalley, R. E., *Crystalline Ropes of Metallic Carbon Nanotubes.* Science, 1996. **273**(5274): p. 483-487.

168. Venkateswaran, U. D., Masica, D. L., Sumanasekera, G. U., Furtado, C. A., Kim, U. J., and Eklund, P. C., *Diameter Dependent Wall Deformations During the Compression of a Carbon Nanotube Bundle.* Physical Review B, 2003. **68**(24): p. 241406, 1-4.

169. Sato, M., Shima, H., and Iiboshi, K., *Core-Tube Morphology of Mutliwall Carbon Nanotubes.* International Journal of Modern Physics B, 2009: p. 1-7.

170. Chen, Y., Shaw, D. T., Bai, X. D., Wang, E. G., Lund, C., Lu, W. M., and Chung, D. D. L., *Hydrogen Storage in Aligned Carbon Nanotubes.* Applied Physics Letters, 2001. **78**(15): p. 2128-2130.

171. Dillon, A. C. and Heben, M. J., *Hydrogen Storage using Carbon Adsorbents: Past, Present and Future.* Applied Physics a-Materials Science & Processing, 2001. **72**(2): p. 133-142.

172. Baughman, R. H., Zakhidov, A. A., and de Heer, W. A., *Carbon Nanotubes - The Route Toward Applications.* Science, 2002. **297**(5582): p. 787-792.

173. Latroche, M., Surble, S., Serre, C., Mellot-Draznieks, C., Llewellyn, P. L., Lee, J. H., Chang, J. S., Jhung, S. H., and Férey, G., *Hydrogen Storage in the Giant-Pore Metal-Organic Frameworks MIL-100 and MIL-101.* Angewandte Chemie-International Edition, 2006. **45**(48): p. 8227-8231.

174. Dinca, M., Dailly, A., Tsay, C., and Long, J. R., *Expanded Sodalite-Type Metal-Organic Frameworks: Increased Stability and H_2 Adsorption Through Ligand-Directed Catenation.* Inorganic Chemistry, 2008. **47**(1): p. 11-13.

175. Li, Y. Q., Xie, L., Liu, Y., Yang, R., and Li, X. G., *Favorable Hydrogen Storage Properties of M(HBTC)(4,4 '-bipy)center dot 3DMF (M = Ni and Co).* Inorganic Chemistry, 2008. **47**(22): p. 10372-10377.

176. Kesanli, B., Cui, Y., Smith, M. R., Bittner, E. W., Bockrath, B. C., and Lin, W. B., *Highly Interpenetrated Metal-Organic Frameworks for Hydrogen Storage.* Angewandte Chemie-International Edition, 2005. **44**(1): p. 72-75.

177. Dailly, A., Vajo, J. J., and Ahn, C. C., *Saturation of Hydrogen Sorption in Zn Benzenedicarboxylate and Zn Naphthalenedicarboxylate.* Journal of Physical Chemistry B, 2006. **110**(3): p. 1099-1101.

178. Fang, Q. R., Zhu, G. S., Xue, M., Zhang, Q. L., Sun, J. Y., Guo, X. D., Qiu, S. L., Xu, S. T., Wang, P., Wang, D. J., and Wei, Y., *Microporous Metal-Organic Framework Constructed from Heptanuclear Zinc Carboxylate Secondary Building Units.* Chemistry - A European Journal, 2006. **12**(14): p. 3754-3758.

179. Wang, Y., Cheng, P., Chen, J., Liao, D. Z., and Yan, S. P., *A Heterometallic Porous Material for Hydrogen Adsorption.* Inorganic Chemistry, 2007. **46**(11): p. 4530-4534.

180. Züttel, A., Sudan, P., Mauron, P., Kiyobayashi, T., Emmenegger, C., and Schlapbach, L., *Hydrogen Storage in Carbon Nanostructures.* International Journal of Hydrogen Energy, 2002. **27**(2): p. 203-212.

181. Takagi, H., Hatori, H., Soneda, Y., Yoshizawa, N., and Yamada, Y., *Adsorptive Hydrogen Storage in Carbon and Porous Materials.* Materials Science and Engineering B-Solid State Materials for Advanced Technology, 2004. **108**(1-2): p. 143-147.

182. Nijkamp, M. G., Raaymakers, J., van Dillen, A. J., and de Jong, K. P., *Hydrogen Storage using Physisorption - Materials Demands.* Applied Physics a-Materials Science & Processing, 2001. **72**(5): p. 619-623.

183. Lim, K. L., Kazemian, H., Yaakob, Z., and Daud, W. R. W., *Solid-State Materials and Methods for Hydrogen Storage: A Critical Review.* Chemical Engineering & Technology, 2010. **33**(2): p. 213-226.

184. Marsh, H. and Rodríguez-Reinoso, F., *Activated Carbon*. First Edition ed. 2006: Elsevier. p. 536.

185. Tam, M. S. and Antal, M. J., *Preparation of Activated Carbons from Macadamia Nut Shell and Coconut Shell by Air Activation.* Industrial & Engineering Chemistry Research, 1999. **38**(11): p. 4268-4276.

186. Lu, Y., *Laboratory Studies on Devolatilization and Char Oxidation under PFBC Conditions. 1. Volatile Release and Char Reactivity.* Energy & Fuels, 1996. **10**(2): p. 348-356.

187. Kumar, M. and Gupta, R. C., *Influence of Carbonization Conditions and Wood Species on Carbon Dioxide Reactivity of Resultant Wood Char Powder.* Fuel Processing Technology, 1994. **38**(3): p. 223-233.

188. Pastor-Villegas, J., Valenzuela-Calahorro, C., and Gomez-Serrano, V., *Preparation of Activated Carbon from Rockrose Char. Influence of Activation Temperature.* Biomass and Bioenergy, 1994. **6**(6): p. 453-460.

189. Rodríguez-Reinoso, F., Molina-Sabio, M., and González, M. T., *The Use of Steam and CO_2 as Activating Agents in the Preparation of Activated Carbons.* Carbon, 1995. **33**(1): p. 15-23.

190. Stoeckli, H. F., *Microporous Carbons and Their Characterization - the Present State-of-the-Art.* Carbon, 1990. **28**(1): p. 1-6.

191. Schmitz, B., Muller, U., Trukhan, N., Schubert, M., Férey, G., and Hirscher, M., *Heat of Adsorption for Hydrogen in Microporous High-Surface-Area Materials.* Chemphyschem, 2008. **9**(15): p. 2181-2184.

192. Innes, R. W., Fryer, J. R., and Stoeckli, H. F., *On the Correlation between Micropore Distribution Obtained from Molecular Probes and from High-Resolution Electron-Microscopy.* Carbon, 1989. **27**(1): p. 71-76.

193. Rios, R. V. R. A., Silvestre-Albero, J., Sepúveda-Escribano, A., Molina-Sabio, M., and Rodríguez-Reinoso, F., *Kinetic Restrictions in the Characterization of Narrow Microporosity in Carbon Materials.* The Journal of Physical Chemistry C, 2007. **111**(10): p. 3803-3805.

194. Schwarz, J. A., *Hydrogen Storage on Activated Carbons*, in *Energy Authority - Final Report 94-20*. 1994, Department of Chemical Engineering and Materials Science, Syracuse University. p. 37.

195. Budd, P. M., Ghanem, B., Msayib, K., McKeown, N. B., and Tattershall, C., *A Nanoporous Network Polymer Derived from Hexaazatrinaphthylene with Potential as an Adsorbent and Catalyst Support.* Journal of Materials Chemistry, 2003. **13**(11): p. 2721-2726.

196. Panella, B., Hirscher, M., and Roth, S., *Hydrogen adsorption in different carbon nanostructures.* Carbon, 2005. **43**(10): p. 2209-2214.

197. Kyotani, T., Nagai, T., Inoue, S., and Tomita, A., *Formation of New Type of Porous Carbon by Carbonization in Zeolite Nanochannels.* Chemistry of Materials, 1997. **9**(2): p. 609-615.

198. Yang, Z. X., Xia, Y. D., and Mokaya, R., *Enhanced hydrogen storage capacity of high surface area zeolite-like carbon materials.* Journal of the American Chemical Society, 2007. **129**(6): p. 1673-1679.

199. Rodríguez-Mirasol, J., Cordero, T., Radovic, L. R., and Rodríguez, J. J., *Structural and Textural Properties of Pyrolytic Carbon formed within a Microporous Zeolite Template.* Chemistry of Materials, 1998. **10**(2): p. 550-558.

200. Johnson, S. A., Brigham, E. S., Ollivier, P. J., and Mallouk, T. E., *Effect of Micropore Topology on the Structure and Properties of Zeolite Polymer Replicas.* Chemistry of Materials, 1997. **9**(11): p. 2448-2458.

201. Barata-Rodrigues, P. M., Mays, T. J., and Moggridge, G. D., *Structured Carbon Adsorbents from Clay, Zeolite and Mesoporous Aluminosilicate Templates.* Carbon, 2003. **41**(12): p. 2231-2246.

202. Su, F. B., Zhao, X. S., Lv, L., and Zhou, Z. C., *Synthesis and Characterization of Microporous Carbons Templated by Ammonium-form Zeolite Y.* Carbon, 2004. **42**(14): p. 2821-2831.

203. Bénard, P. and Chahine, R., *Determination of the Adsorption Isotherms of Hydrogen on Activated Carbons Above the Critical Temperature of the Adsorbate Over Wide Temperature and Pressure Ranges.* Langmuir, 2001. **17**(6): p. 1950-1955.

204. Langmi, H. W., Book, D., Walton, A., Johnson, S. R., Al-Mamouri, M. M., Speight, J. D., Edwards, P. P., Harris, I. R., and Anderson, P. A., *Hydrogen Storage in Ion-Exchanged Zeolites.* Journal of Alloys and Compounds, 2005. **404**: p. 637-642.

205. Langmi, H. W., Walton, A., Al-Mamouri, M. M., Johnson, S. R., Book, D., Speight, J. D., Edwards, P. P., Gameson, I., Anderson, P. A., and Harris, I. R., *Hydrogen Adsorption in Zeolites A, X, Y and RHO.* Journal of Alloys and Compounds, 2003. **356**: p. 710-715.

206. Smart, L. and Moore, E., *Solid State Chemistry: An Introduction*. 1st ed. 1992, London: Chapman & Hall. p. 292.

207. Smart, L. and Moore, E., *Solid State Chemistry: An Introduction*. 3rd ed. 2005, Boca Raton: Taylor & Francis Group. p. 407.

208. Park, K. S., Ni, Z., Cote, A. P., Choi, J. Y., Huang, R. D., Uribe-Romo, F. J., Chae, H. K., O'Keeffe, M., and Yaghi, O. M., *Exceptional Chemical and Thermal Stability of Zeolitic Imidazolate Frameworks.* Proceedings of the National Academy of Sciences of the United States of America, 2006. **103**(27): p. 10186-10191.

209. Baerlocher, C., McCusker, L. B., and Olsen, D. H., *Atlas of Zeolite Frameworks*. 6th ed. 2007, Amsterdam: Elsevier. p. 398.

210. Zhao, X. B., Xiao, B., Fletcher, A. J., Thomas, K. M., Bradshaw, D., and Rosseinsky, M. J., *Hysteretic Adsorption and Desorption of Hydrogen by Nanoporous Metal-Organic Frameworks.* Science, 2004. **306**(5698): p. 1012-1015.

211. Richard, V., Favre, E., Tondeur, D., and Nijmeijer, A., *Experimental Study of Hydrogen, Carbon Dioxide and Nitrogen Permeation Through a Microporous Silica Membrane.* Chemical Engineering Journal, 2001. **84**(3): p. 593-598.

212. Li, J. and Wu, E. D., *Adsorption of Hydrogen on Porous Materials of Activated Carbon and Zeolite NaX Crossover Critical Temperature.* Journal of Supercritical Fluids, 2009. **49**(2): p. 196-202.

213. Jhung, S. H., Yoon, J. W., Lee, S., and Chang, J. S., *Low-Temperature Adsorption/Storage of Hydrogen on FAU, MFI, and MOR Zeolites with Various Si/Al Ratios: Effect of Electrostatic Fields and Pore Structures.* Chemistry - A European Journal, 2007. **13**(22): p. 6502-6507.

214. Stéphanie-Victoire, F., Goulay, A. M., and de Lara, E. C., *Adsorption and Coadsorption of Molecular Hydrogen Isotopes in Zeolites. 1. Isotherms of H_2, HD, and D_2 in NaA by Thermomicrogravimetry.* Langmuir, 1998. **14**(25): p. 7255-7259.

215. Arean, C. O., Palomino, G. T., and Carayol, M. R. L., *Variable Temperature FT-IR Studies on Hydrogen Adsorption on the Zeolite (Mg,Na)-Y.* Applied Surface Science, 2007. **253**(13): p. 5701-5704.

216. Arean, C. O., Delgado, M. R., Palomino, G. T., Rubio, M. T., Tsyganenko, N. M., Tsyganenko, A. A., and Garrone, E., *Thermodynamic Studies on Hydrogen Adsorption on the Zeolites Na-ZSM-5 and K-ZSM-5.* Microporous and Mesoporous Materials, 2005. **80**(1-3): p. 247-252.

217. Palomino, G. T., Bonelli, B., Arean, C. O., Parra, J. B., Carayol, M. R. L., Armandi, M., Ania, C. O., and Garrone, E., *Thermodynamics of Hydrogen Adsorption on Calcium-exchanged Faujasite-type Zeolites.* International Journal of Hydrogen Energy, 2009. **34**(10): p. 4371-4378.

218. Pirngruber, G. D., Raybaud, P., Belmabkhout, Y., Cejka, J., and Zukal, A., *The Role of the Extra-Framework Cations in the Adsorption of CO_2 on Faujasite Y.* Physical Chemistry Chemical Physics, 2010. **12**(41): p. 13534-13546.

219. Kazansky, V. B., Jentoft, F. C., and Karge, H. G., *First Observation of Vibration-Rotation Drift Spectra of Para- and Ortho-Hydrogen Adsorbed at 77 K on LiX, NaX and CsX Zeolites.* Journal of the Chemical Society-Faraday Transactions, 1998. **94**(9): p. 1347-1351.

220. Li, J. R., Kuppler, R. J., and Zhou, H. C., *Selective Gas Adsorption and Separation in Metal-Organic Frameworks.* Chemical Society Reviews, 2009. **38**(5): p. 1477-1504.

221. Lee, J., Farha, O. K., Roberts, J., Scheidt, K. A., Nguyen, S. T., and Hupp, J. T., *Metal-Organic Framework Materials as Catalysts.* Chemical Society Reviews, 2009. **38**(5): p. 1450-1459.

222. Czaja, A. U., Trukhan, N., and Muller, U., *Industrial Applications of Metal-Organic Frameworks.* Chemical Society Reviews, 2009. **38**(5): p. 1284-1293.

223. O'Keeffe, M., *Design of MOFs and Intellectual Content in Reticular Chemistry: A Personal View.* Chemical Society Reviews, 2009. **38**(5): p. 1215-1217.

224. Yaghi, O. M., O'Keeffe, M., Ockwig, N. W., Chae, H. K., Eddaoudi, M., and Kim, J., *Reticular Synthesis and the Design of New Materials.* Nature, 2003. **423**(6941): p. 705-714.

225. Eddaoudi, M., Kim, J., Rosi, N., Vodak, D., Wachter, J., O'Keeffe, M., and Yaghi, O. M., *Systematic Design of Pore Size and Functionality in Isoreticular MOFs and their Application in Methane Storage.* Science, 2002. **295**(5554): p. 469-472.

226. Rosi, N. L., Eckert, J., Eddaoudi, M., Vodak, D. T., Kim, J., O'Keeffe, M., and Yaghi, O. M., *Hydrogen Storage in Microporous Metal-Organic Frameworks.* Science, 2003. **300**(5622): p. 1127-1129.

227. Rowsell, J. L. C., Spencer, E. C., Eckert, J., Howard, J. A. K., and Yaghi, O. M., *Gas Adsorption Sites in a Large-Pore Metal-Organic Framework.* Science, 2005. **309**(5739): p. 1350-1354.

228. Panella, B., Hirscher, M., Putter, H., and Muller, U., *Hydrogen Adsorption in Metal-Organic Frameworks: Cu-MOFs and Zn-MOFs Compared.* Advanced Functional Materials, 2006. **16**(4): p. 520-524.

229. Dybtsev, D. N., Chun, H., and Kim, K., *Rigid and Flexible: A Highly Porous Metal-Organic Framework with Unusual Guest-Dependent Dynamic Behavior.* Angewandte Chemie-International Edition, 2004. **43**(38): p. 5033-5036.

230. Sun, D. F., Ke, Y. X., Collins, D. J., Lorigan, G. A., and Zhou, H. C., *Construction of Robust Open Metal-Organic Frameworks with Chiral Channels and Permanent Porosity.* Inorganic Chemistry, 2007. **46**(7): p. 2725-2734.

231. Panella, B. and Hirscher, M., *Hydrogen Physisorption in Metal-Organic Porous Crystals.* Advanced Materials, 2005. **17**(5): p. 538-541.

232. Sabo, M., Henschel, A., Froede, H., Klemm, E., and Kaskel, S., *Solution Infiltration of Palladium into MOF-5: Synthesis, Physisorption and Catalytic Properties.* Journal of Materials Chemistry, 2007. **17**(36): p. 3827-3832.

233. Hafizovic, J., Bjorgen, M., Olsbye, U., Dietzel, P. D. C., Bordiga, S., Prestipino, C., Lamberti, C., and Lillerud, K. P., *The inconsistency in adsorption properties and powder XRD data of MOF-5 is rationalized by framework interpenetration and the presence of organic and inorganic species in the nanocavities.* Journal of the American Chemical Society, 2007. **129**(12): p. 3612-3620.

234. Younglove, B. A., *Thermo-Physical Properties of Fluids. 1- Argon, Ethylene, Para-Hydrogen, Nitrogen, Nitrogen Trifluoride, and Oxygen.* Journal of Physical and Chemical Reference Data, 1982. **11**: p. 1-353.

235. Saha, D. P., Wei, Z. J., and Deng, S. G., *Hydrogen Adsorption Equilibrium and Kinetics in Metal-Organic Framework (MOF-5) Synthesized with DEF Approach.* Separation and Purification Technology, 2009. **64**(3): p. 280-287.

236. Sillar, K., Hofmann, A., and Sauer, J., *Ab Initio Study of Hydrogen Adsorption in MOF-5.* Journal of the American Chemical Society, 2009. **131**(11): p. 4143-4150.

237. Rowsell, J. L. C. and Yaghi, O. M., *Strategies for Hydrogen Storage in Metal-Organic Frameworks.* Angewandte Chemie-International Edition, 2005. **44**(30): p. 4670-4679.

238. Férey, G., Latroche, M., Serre, C., Millange, F., Loiseau, T., and Percheron-Guegan, A., *Hydrogen Adsorption in the Nanoporous Metal-Benzenedicarboxylate M(OH)(O_2C-C_6H_4-CO_2) (M = Al^{3+}, Cr^{3+}), MIL-53.* Chemical Communications, 2003(24): p. 2976-2977.

239. Bordiga, S., Vitillo, J. G., Ricchiardi, G., Regli, L., Cocina, D., Zecchina, A., Arstad, B., Bjorgen, M., Hafizovic, J., and Lillerud, K. P., *Interaction of Hydrogen with MOF-5.* Journal of Physical Chemistry B, 2005. **109**(39): p. 18237-18242.

240. Sumida, K., Hill, M. R., Horike, S., Dailly, A., and Long, J. R., *Synthesis and Hydrogen Storage Properties of $Be_{12}(OH)_{12}$(1,3,5-benzenetribenzoate)$_4$.* Journal of the American Chemical Society, 2009. **131**(42): p. 15120-15121.

241. Davies, R. P., Less, R. J., Lickiss, P. D., and White, A. J. P., *Framework Materials Assembled from Magnesium Carboxylate Building Units.* Dalton Transactions, 2007(24): p. 2528-2535.

242. Senkovska, I. and Kaskel, S., *Solvent-Induced Pore-Size Adjustment in the Metal-Organic Framework [Mg_3(ndc)$_3$(dmf)$_4$] (ndc = naphthalenedicarboxylate).* European Journal of Inorganic Chemistry, 2006(22): p. 4564-4569.

243. Loiseau, T., Lecroq, L., Volkringer, C., Marrot, J., Férey, G., Haouas, M., Taulelle, F., Bourrelly, S., Llewellyn, P. L., and Latroche, M., *MIL-96, A Porous Aluminum Trimesate 3D structure Constructed from a Hexagonal Network of 18-Membered Rings and μ_3-oxo-Centered Trinuclear Units.* Journal of the American Chemical Society, 2006. **128**(31): p. 10223-10230.

244. Férey, G., Serre, C., Mellot-Draznieks, C., Millange, F., Surble, S., Dutour, J., and Margiolaki, I., *A Hybrid Solid with Giant Pores Prepared by a Combination of Targeted Chemistry, Simulation, and Powder Diffraction.* Angewandte Chemie-International Edition, 2004. **43**(46): p. 6296-6301.

245. Férey, G., Mellot-Draznieks, C., Serre, C., Millange, F., Dutour, J., Surble, S., and Margiolaki, I., *A Chromium Terephthalate-Based Solid with Unusually Large Pore Volumes and Surface Area.* Science, 2005. **309**(5743): p. 2040-2042.

246. Rowsell, J. L. C., Millward, A. R., Park, K. S., and Yaghi, O. M., *Hydrogen Sorption in Functionalized Metal-Organic Frameworks.* Journal of the American Chemical Society, 2004. **126**(18): p. 5666-5667.

247. Furukawa, H., Ko, N., Go, Y. B., Aratani, N., Choi, S. B., Choi, E., Yazaydin, A. O., Snurr, R. Q., O'Keeffe, M., Kim, J., and Yaghi, O. M., *Ultrahigh Porosity in Metal-Organic Frameworks.* Science, 2010. **329**(5990): p. 424-428.

248. Lin, X., Jia, J. H., Zhao, X. B., Thomas, K. M., Blake, A. J., Walker, G. S., Champness, N. R., Hubberstey, P., and Schröder, M., *High H_2 Adsorption by Coordination-Framework Materials.* Angewandte Chemie-International Edition, 2006. **45**(44): p. 7358-7364.

249. Chui, S. S. Y., Lo, S. M. F., Charmant, J. P. H., Orpen, A. G., and Williams, I. D., *A Chemically Functionalizable Nanoporous Material [Cu_3(TMA)$_2$(H_2O)$_3$]$_n$.* Science, 1999. **283**(5405): p. 1148-1150.

250. Vishnyakov, A., Ravikovitch, P. I., Neimark, A. V., Bulow, M., and Wang, Q. M., *Nanopore Structure and Sorption Properties of Cu-BTC Metal-Organic Framework.* Nano Letters, 2003. **3**(6): p. 713-718.

251. Bordiga, S., Regli, L., Bonino, F., Groppo, E., Lamberti, C., Xiao, B., Wheatley, P. S., Morris, R. E., and Zecchina, A., *Adsorption Properties of HKUST-1 Toward Hydrogen and Other Small Molecules Monitored by IR.* Physical Chemistry Chemical Physics, 2007. **9**(21): p. 2676-2685.

252. Peterson, V. K., Liu, Y., Brown, C. M., and Kepert, C. J., *Neutron Powder Diffraction Study of D_2 Sorption in Cu_3(1,3,5-benzenetricarboxylate)$_2$.* Journal of the American Chemical Society, 2006. **128**(49): p. 15578-15579.

253. Karra, J. R. and Walton, K. S., *Effect of Open Metal Sites on Adsorption of Polar and Nonpolar Molecules in Metal-organic Framework Cu-BTC.* Langmuir, 2008. **24**(16): p. 8620-8626.

254. Xiao, B., Wheatley, P. S., Zhao, X. B., Fletcher, A. J., Fox, S., Rossi, A. G., Megson, I. L., Bordiga, S., Regli, L., Thomas, K. M., and Morris, R. E., *High-Capacity Hydrogen and Nitric Oxide Adsorption and Storage in a Metal-Organic Framework.* Journal of the American Chemical Society, 2007. **129**(5): p. 1203-1209.

255. Chun, H., Kim, D., Dybtsev, D. N., and Kim, K., *Metal-Organic Replica of Fluorite Built with an Eight-Connecting Tetranuclear Cadmium Cluster and a Tetrahedral Four-Connecting Ligand.* Angewandte Chemie-International Edition, 2004. **43**(8): p. 989-992.

256. Dinca, M., Yu, A. F., and Long, J. R., *Microporous Metal-Organic Frameworks Incorporating 1,4-Benzeneditetrazolate: Syntheses, Structures, and Hydrogen Storage Properties.* Journal of the American Chemical Society, 2006. **128**(27): p. 8904-8913.

257. Dinca, M. and Long, J. R., *Hydrogen Storage in Microporous Metal-Organic Frameworks with Exposed Metal Sites.* Angewandte Chemie-International Edition, 2008. **47**(36): p. 6766-6779.

258. Choi, H. J., Dinca, M., and Long, J. R., *Broadly Hysteretic H_2 Adsorption in the Microporous Metal-Organic Framework Co(1,4-Benzenedipyrazolate).* Journal of the American Chemical Society, 2008. **130**(25): p. 7848-7850.

259. Walton, K. S., Millward, A. R., Dubbeldam, D., Frost, H., Low, J. J., Yaghi, O. M., and Snurr, R. Q., *Understanding Inflections and Steps in Carbon Dioxide Adsorption Isotherms in Metal-Organic Frameworks.* Journal of the American Chemical Society, 2008. **130**(2): p. 406-407.

260. Maji, T. K., Mostafa, G., Matsuda, R., and Kitagawa, S., *Guest-Induced Asymmetry in a Metal-Organic Porous Solid with Reversible Single-Crystal-to-Single-Crystal Structural Transformation.* Journal of the American Chemical Society, 2005. **127**(49): p. 17152-17153.

261. Llewellyn, P. L., Bourrelly, S., Serre, C., Filinchuk, Y., and Férey, G., *How Hydration Drastically Improves Adsorption Selectivity for CO_2 Over CH_4 in the Flexible Chromium Terephthalate MIL-53.* Angewandte Chemie-International Edition, 2006. **45**(46): p. 7751-7754.

262. Yang, C., Wang, X. P., and Omary, M. A., *Fluorous Metal-Organic Frameworks for High-Density Gas Adsorption.* Journal of the American Chemical Society, 2007. **129**(50): p. 15454-15455.

263. Natarajan, S. and Mahata, P., *Metal-Organic Framework Structures - How closely are they related to Classical Inorganic Structures?* Chemical Society Reviews, 2009. **38**(8): p. 2304-2318.

264. Banerjee, R., Furukawa, H., Britt, D., Knobler, C., O'Keeffe, M., and Yaghi, O. M., *Control of Pore Size and Functionality in Isoreticular Zeolitic Imidazolate Frameworks and their Carbon Dioxide Selective Capture Properties.* Journal of the American Chemical Society, 2009. **131**(11): p. 3875-3877.

265. Huang, X. C., Lin, Y. Y., Zhang, J. P., and Chen, X. M., *Ligand-Directed Strategy for Zeolite-Type Metal-Organic Frameworks: Zinc(II) Imidazolates with Unusual Zeolitic Topologies.* Angewandte Chemie-International Edition, 2006. **45**(10): p. 1557-1559.

266. Banerjee, R., Phan, A., Wang, B., Knobler, C., Furukawa, H., O'Keeffe, M., and Yaghi, O. M., *High-Throughput Synthesis of Zeolitic Imidazolate Frameworks and Application to CO_2 Capture.* Science, 2008. **319**(5865): p. 939-943.

267. Zhou, M., Wang, Q., Zhang, L., Liu, Y. C., and Kang, Y., *Adsorption Sites of Hydrogen in Zeolitic Imidazolate Frameworks.* Journal of Physical Chemistry B, 2009. **113**(32): p. 11049-11053.

268. Hayashi, H., Cote, A. P., Furukawa, H., O'Keeffe, M., and Yaghi, O. M., *Zeolite A Imidazolate Frameworks.* Nature Materials, 2007. **6**(7): p. 501-506.

269. Nouar, F., Eubank, J. F., Bousquet, T., Wojtas, L., Zaworotko, M. J., and Eddaoudi, M., *Supermolecular Building Blocks (SBBs) for the Design and Synthesis of Highly Porous Metal-Organic Frameworks.* Journal of the American Chemical Society, 2008. **130**(6): p. 1833-1835.

270. Buser, H. J., Schwarzenbach, D., Petter, W., and Ludi, A., *The Crystal Structure of Prussian Blue: $Fe_4[Fe(CN)_6]_3.xH_2O$.* Inorganic Chemistry, 1977. **16**(11): p. 2704-2710.

271. Chapman, K. W., Southon, P. D., Weeks, C. L., and Kepert, C. J., *Reversible Hydrogen Gas Uptake in Nanoporous Prussian Blue Analogues.* Chemical Communications, 2005(26): p. 3322-3324.

272. Kaye, S. S. and Long, J. R., *Hydrogen Storage in the Dehydrated Prussian Blue Analogues $M_3[Co(CN)_6]_2$ (M = Mn, Fe, Co, Ni, Cu, Zn).* Journal of the American Chemical Society, 2005. **127**(18): p. 6506-6507.

273. Kaye, S. S. and Long, J. R., *The Role of Vacancies in the Hydrogen Storage Properties of Prussian Blue Analogues.* Catalysis Today, 2007. **120**(3-4): p. 311-316.

274. El-Kaderi, H. M., Hunt, J. R., Mendoza-Cortes, J. L., Cote, A. P., Taylor, R. E., O'Keeffe, M., and Yaghi, O. M., *Designed Synthesis of 3D Covalent Organic Frameworks.* Science, 2007. **316**(5822): p. 268-272.

275. Klontzas, E., Tylianakis, E., and Froudakis, G. E., *Hydrogen Storage in 3D Covalent Organic Frameworks. A Multiscale Theoretical Investigation.* Journal of Physical Chemistry C, 2008. **112**(24): p. 9095-9098.

276. Han, S. S., Furukawa, H., Yaghi, O. M., and Goddard, W. A., *Covalent Organic Frameworks as Exceptional Hydrogen Storage Materials.* Journal of the American Chemical Society, 2008. **130**(35): p. 11580-11581.

277. Furukawa, H. and Yaghi, O. M., *Storage of Hydrogen, Methane, and Carbon Dioxide in Highly Porous Covalent Organic Frameworks for Clean Energy Applications.* Journal of the American Chemical Society, 2009. **131**(25): p. 8875-8883.

278. Davankov, V. A., Rogozhin, S. V., and Tsyurupa, M. P., *Macronet Polystyrene Structures for Ionites and Methods of Producing Same.* United States Patent and Trademark Office, 3 729 457, 1973.

279. McKeown, N. B., Budd, P. M., and Book, D., *Microporous Polymers as Potential Hydrogen Storage Materials.* Macromolecular Rapid Communications, 2007. **28**(9): p. 995-1002.

280. McKeown, N. B., Budd, P. M., Msayib, K. J., Ghanem, B. S., Kingston, H. J., Tattershall, C. E., Makhseed, S., Reynolds, K. J., and Fritsch, D., *Polymers of Intrinsic Microporosity (PIMs).* Chemistry - A European Journal, 2005. **11**(9): p. 2610-2620.

281. Budd, P. M., Butler, A., Selbie, J., Mahmood, K., McKeown, N. B., Ghanem, B., Msayib, K., Book, D., and Walton, A., *The Potential of Organic Polymer-Based Hydrogen Storage Materials.* Physical Chemistry Chemical Physics, 2007. **9**(15): p. 1802-1808.

282. Pastukhov, A. V., Tsyurupa, M. P., and Davankov, V. A., *Hypercrosslinked Polystyrene: A Polymer in a Non-Classical Physical State.* Journal of Polymer Science Part B-Polymer Physics, 1999. **37**(17): p. 2324-2333.

283. Tsyurupa, M. P. and Davankov, V. A., *Porous Structure of Hypercrosslinked Polystyrene: State-Of-The-Art Mini-Review.* Reactive & Functional Polymers, 2006. **66**(7): p. 768-779.

284. Tsyurupa, M. P. and Davankov, V. A., *Hypercrosslinked Polymers: Basic Principle of Preparing the New Class of Polymeric Materials.* Reactive & Functional Polymers, 2002. **53**(2-3): p. 193-203.

285. Davankov, V. A. and Tsyurupa, M. P., *Structure and Properties of Hypercrosslinked Polystyrene - the 1st Representative of a New Class of Polymer Networks.* Reactive Polymers, 1990. **13**(1-2): p. 27-42.

286. Davankov, V. A. and Tsyurupa, M. P., *Structure and Properties of Porous Hypercrosslinked Polystyrene Sorbents Styrosorb.* Pure and Applied Chemistry, 1989. **61**(11): p. 1881-1888.

287. Davankov, V. A., Rogozhin, S. V., and Tsyurupa, M. P., *Macronet Polysterene Structures for Ionites and Methods of producing same*, Office, U. S. P. a. T., Editor. 1971: United States. p. 3.

288. Sidorov, S. N., Bronstein, L. M., Davankov, V. A., Tsyurupa, M. P., Solodovnikov, S. P., Valetsky, P. M., Wilder, E. A., and Spontak, R. J., *Cobalt Nanoparticle Formation in the Pores of Hyper-Cross-Linked Polystyrene: Control of Nanoparticle Growth and Morphology.* Chemistry of Materials, 1999. **11**(11): p. 3210-3215.

289. Ahn, J. H., Jang, J. E., Oh, C. G., Ihm, S. K., Cortez, J., and Sherrington, D. C., *Rapid Generation and Control of Microporosity, Bimodal Pore Size Distribution, and Surface Area in Davankov-Type Hyper-Cross-Linked Resins.* Macromolecules, 2006. **39**(2): p. 627-632.

290. Wood, C. D., Tan, B., Trewin, A., Niu, H. J., Bradshaw, D., Rosseinsky, M. J., Khimyak, Y. Z., Campbell, N. L., Kirk, R., Stockel, E., and Cooper, A. I., *Hydrogen Storage in Microporous Hypercrosslinked Organic Polymer Networks.* Chemistry of Materials, 2007. **19**(8): p. 2034-2048.

291. Germain, J., Frechet, J. M. J., and Svec, F., *Hypercrosslinked Polyanilines with Nanoporous Structure and High Surface Area: Potential Adsorbents for Hydrogen Storage.* Journal of Materials Chemistry, 2007. **17**(47): p. 4989-4997.

292. Germain, J., Svec, F., and Frechet, J. M. J., *Preparation of Size-Selective Nanoporous Polymer Networks of Aromatic Rings: Potential Adsorbents for Hydrogen Storage.* Chemistry of Materials, 2008. **20**(22): p. 7069-7076.

293. Yuan, S. W., Dorney, B., White, D., Kirklin, S., Zapol, P., Yu, L. P., and Liu, D. J., *Microporous Polyphenylenes with Tunable Pore Size for Hydrogen Storage.* Chemical Communications, 2010. **46**(25): p. 4547-4549.

294. Budd, P. M., Ghanem, B. S., Makhseed, S., McKeown, N. B., Msayib, K. J., and Tattershall, C. E., *Polymers of Intrinsic Microporosity (PIMs): Robust, Solution-Processable, Organic Nanoporous Materials.* Chemical Communications, 2004(2): p. 230-231.

295. Budd, P. M., McKeown, N. B., and Fritsch, D., *Free Volume and intrinsic Microporosity in Polymers.* Journal of Materials Chemistry, 2005. **15**(20): p. 1977-1986.

296. McKeown, N. B., Gahnem, B., Msayib, K. J., Budd, P. M., Tattershall, C. E., Mahmood, K., Tan, S., Book, D., Langmi, H. W., and Walton, A., *Towards Polymer-Based Hydrogen Storage Materials: Engineering Ultramicroporous Cavities within Polymers of Intrinsic Microporosity.* Angewandte Chemie-International Edition, 2006. **45**(11): p. 1804-1807.

297. Weber, J., Su, O., Antonietti, M., and Thomas, A., *Exploring Polymers of Intrinsic Microporosity-Microporous, Soluble Polyamide and Polyimide.* Macromolecular Rapid Communications, 2007. **28**(18-19): p. 1871-1876.

298. McKeown, N. B., Hanif, S., Msayib, K., Tattershall, C. E., and Budd, P. M., *Porphyrin-Based Nanoporous Network Polymers.* Chemical Communications, 2002(23): p. 2782-2783.

299. Ghanem, B. S., Msayib, K. J., McKeown, N. B., Harris, K. D. M., Pan, Z., Budd, P. M., Butler, A., Selbie, J., Book, D., and Walton, A., *A Triptycene-Based Polymer of Intrinsic Microposity that Displays Enhanced Surface Area and Hydrogen Adsorption.* Chemical Communications, 2007(1): p. 67-69.

300. Hirscher, M., Panella, B., and Schmitz, B., *Metal-Organic Frameworks for Hydrogen Storage.* Microporous and Mesoporous Materials, 2010. **129**(3): p. 335-339.

301. Poirier, E. and Dailly, A., *On the Nature of the Adsorbed Hydrogen Phase in Microporous Metal-Organic Frameworks at Supercritical Temperatures.* Langmuir, 2009. **25**(20): p. 12169-12176.

302. Poirier, E., Chahine, R., Bénard, P., Lafi, L., Dorval-Douville, G., and Chandonia, P. A., *Hydrogen Adsorption Measurements and Modeling on Metal-Organic Frameworks and Single-Walled Carbon Nanotubes.* Langmuir, 2006. **22**(21): p. 8784-8789.

303. Yanik, R., *Calculations of Isosteric Heats of Adsorption of Neon and Hydrogen Adsorbed on Charcoal in the Temperature Range 22-90 K.* Vacuum, 1996. **47**(2): p. 205-207.

304. Purewal, J., *Hydrogen Adsorption by Alkali Metal Graphite Intercalation Compounds, PhD Thesis*. 2010, California Institute of Technology: Pasadena, California. p. 212.

305. Sircar, S., *Heat of Adsorption on Heterogeneous Adsorbents.* Applied Surface Science, 2005. **252**(3): p. 647-653.

306. Bénard, P. and Chahine, R., *Storage of Hydrogen by Physisorption on Carbon and Nanostructured Materials.* Scripta Materialia, 2007. **56**(10): p. 803-808.

307. Sircar, S., *Excess Properties and Thermodynamics of Multicomponent Gas-Adsorption.* Journal of the Chemical Society-Faraday Transactions I, 1985. **81**: p. 1527-1540.

308. Panella, B., Hones, K., Muller, U., Trukhan, N., Schubert, M., Putter, H., and Hirscher, M., *Desorption Studies of Hydrogen in Metal-Organic Frameworks.* Angewandte Chemie-International Edition, 2008. **47**(11): p. 2138-2142.

309. Panella, B., Hirscher, M., and Ludescher, B., *Low-Temperature Thermal-Desorption Mass Spectroscopy Applied to Investigate the Hydrogen Adsorption on Porous Materials.* Microporous and Mesoporous Materials, 2007. **103**(1-3): p. 230-234.

310. Lochan, R. C. and Head-Gordon, M., *Computational Studies of Molecular Hydrogen Binding Affinities: The Role of Dispersion Forces, Electrostatics, and Orbital Interactions.* Physical Chemistry Chemical Physics, 2006. **8**(12): p. 1357-1370.

311. Lochan, R. C., Khaliullin, R. Z., and Head-Gordon, M., *Interaction of Molecular Hydrogen with Open Transition Metal Centers for Enhanced Binding in Metal-Organic Frameworks: A Computational Study.* Inorganic Chemistry, 2008. **47**(10): p. 4032-4044.

312. Wu, C. H., *Binding-Energies of LiH_2 and LiH_2^+ and the Ionization-Potential of LiH_2.* Journal of Chemical Physics, 1979. **71**(2): p. 783-787.

313. Kaye, S. S. and Long, J. R., *Hydrogen Adsorption in Dehydrated Variants of the Cyano-Bridged Framework Compounds $A_2Zn_3[Fe(CN)_6]_2.xH_2O$ (A = H, Li, Na, K, Rb).* Chemical Communications, 2007(43): p. 4486-4488.

314. Spencer, E. C., Howard, J. A. K., McIntyre, G. J., Rowsell, J. L. C., and Yaghi, O. M., *Determination of the Hydrogen Absorption Sites in Zn_4O(1,4-benzenedicarboxylate) by Single Crystal Neutron Diffraction.* Chemical Communications, 2006(3): p. 278-280.

315. Chen, B., Zhao, X., Putkham, A., Hong, K., Lobkovsky, E. B., Hurtado, E. J., Fletcher, A. J., and Thomas, K. M., *Surface Interactions and Quantum Kinetic Molecular Sieving for H_2 and D_2 Adsorption on a Mixed Metal-Organic Framework Material.* Journal of the American Chemical Society, 2008. **130**(20): p. 6411-6423.

316. Belof, J. L., Stern, A. C., Eddaoudi, M., and Space, B., *On the Mechanism of Hydrogen Storage in a Metal-Organic Framework Material.* Journal of the American Chemical Society, 2007. **129**(49): p. 15202-15210.

317. Sun, D. F., Ma, S. Q., Ke, Y. X., Collins, D. J., and Zhou, H. C., *An Interweaving MOF with High Hydrogen Uptake.* Journal of the American Chemical Society, 2006. **128**(12): p. 3896-3897.

318. Ma, S. Q., Sun, D. F., Ambrogio, M., Fillinger, J. A., Parkin, S., and Zhou, H. C., *Framework-Catenation Isomerism in Metal-Organic Frameworks and its Impact on Hydrogen Uptake.* Journal of the American Chemical Society, 2007. **129**(7): p. 1858-1859.

319. Somorjai, G. A., *The Surface Science of Heterogeneous Catalysis.* Surface Science, 1994. **299**(1-3): p. 849-866.

320. Christmann, K., Ertl, G., and Pignet, T., *Adsorption of Hydrogen on a Pt(111) Surface.* Surface Science, 1976. **54**(2): p. 365-392.

321. Christmann, K. and Ertl, G., *Interaction of Hydrogen with Pt(111): The Role of Atomic Steps.* Surface Science, 1976. **60**(2): p. 365-384.

322. Olsen, R. A., Kroes, G. J., and Baerends, E. J., *Atomic and Molecular Hydrogen Interacting with Pt(111).* Journal of Chemical Physics, 1999. **111**(24): p. 11155-11163.

323. Pasteur, A. T., DixonWarren, S. J., Ge, Q., and King, D. A., *Dynamics of Hydrogen Dissociation on Pt(100): Steering, Screening and Thermal Roughening Effects.* Journal of Chemical Physics, 1997. **106**(21): p. 8896-8904.

324. Gee, A. T., Hayden, B. E., Mormiche, C., and Nunney, T. S., *The Role of Steps in the Dynamics of Hydrogen Dissociation on Pt(533).* Journal of Chemical Physics, 2000. **112**(17): p. 7660-7668.

325. Khoobiar, S., *Particle to Particle Migration of Hydrogen Atoms on Platinum-Alumina Catalysts from Particle to Neighboring Particles.* Journal of Physical Chemistry, 1964. **68**(2): p. 411-412.

326. Lueking, A. D. and Yang, R. T., *Hydrogen Spillover to Enhance Hydrogen Storage - Study of the effect of Carbon Physicochemical Properties.* Applied Catalysis A: General, 2004. **265**(2): p. 259-268.

327. Wang, L. F. and Yang, R. T., *New Sorbents for Hydrogen Storage by Hydrogen Spillover - A Review.* Energy & Environmental Science, 2008. **1**(2): p. 268-279.

328. Cheng, H. S., Chen, L., Cooper, A. C., Sha, X. W., and Pez, G. P., *Hydrogen Spillover in the Context of Hydrogen Storage using Solid-State Materials.* Energy & Environmental Science, 2008. **1**(3): p. 338-354.

329. Lueking, A. and Yang, R. T., *Hydrogen Spillover from a Metal Oxide Catalyst onto Carbon Nanotubes - Implications for Hydrogen Storage.* Journal of Catalysis, 2002. **206**(1): p. 165-168.

330. Lueking, A. D. and Yang, R. T., *Hydrogen Spillover to Enhance Hydrogen Storage - Study of the Effect of Carbon Physicochemical Properties.* Applied Catalysis a-General, 2004. **265**(2): p. 259-268.

331. Yang, F. H., Lachawiec, A. J., and Yang, R. T., *Adsorption of Spillover Hydrogen Atoms on Single-Wall Carbon Nanotubes.* Journal of Physical Chemistry B, 2006. **110**(12): p. 6236-6244.

332. Lueking, A. D., Yang, R. T., Rodriguez, N. M., and Baker, R. T. K., *Hydrogen Storage in Graphite Nanofibers: Effect of Synthesis Catalyst and Pretreatment Conditions.* Langmuir, 2004. **20**(3): p. 714-721.

333. Ramachandran, S., Ha, J. H., and Kim, D. K., *Hydrogen Storage Characteristics of Metal Oxide Doped Al-MCM-41 Mesoporous Materials.* Catalysis Communications, 2007. **8**(12): p. 1934-1938.

334. Lachawiec, A. J., Qi, G. S., and Yang, R. T., *Hydrogen Storage in Nanostructured Carbons by Spillover: Bridge-Building Enhancement.* Langmuir, 2005. **21**(24): p. 11418-11424.

335. Li, Y. W. and Yang, R. T., *Hydrogen Storage on Platinum Nanoparticles Doped on Superactivated Carbon.* Journal of Physical Chemistry C, 2007. **111**(29): p. 11086-11094.

336. Li, Y. W. and Yang, R. T., *Hydrogen Storage in Low Silica Type X Zeolites.* Journal of Physical Chemistry B, 2006. **110**(34): p. 17175-17181.

337. Li, Y. W. and Yang, R. T., *Significantly Enhanced Hydrogen Storage in Metal-Organic Frameworks Via Spillover.* Journal of the American Chemical Society, 2006. **128**(3): p. 726-727.

338. Li, Y. W. and Yang, R. T., *Hydrogen Storage in Metal-Organic Frameworks by Bridged Hydrogen Spillover.* Journal of the American Chemical Society, 2006. **128**(25): p. 8136-8137.

339. Li, Y. and Yang, R. T., *Gas Adsorption and Storage in Metal-Organic Framework MOF-177.* Langmuir, 2007. **23**(26): p. 12937-12944.

340. Li, Y. W., Yang, F. H., and Yang, R. T., *Kinetics and Mechanistic Model for Hydrogen Spillover on Bridged Metal-Organic Frameworks.* Journal of Physical Chemistry C, 2007. **111**(8): p. 3405-3411.

341. Li, Y. W. and Yang, R. T., *Hydrogen Storage in Metal-Organic and Covalent-Organic Frameworks by Spillover.* AIChE Journal, 2008. **54**(1): p. 269-279.

342. Ahluwalia, R. K. and Peng, J. K., *Automotive Hydrogen Storage System using Cryo-Adsorption on Activated Carbon.* International Journal of Hydrogen Energy, 2009. **34**(13): p. 5476-5487.

343. Nandi, M., Sarkar, M., Sarkar, K., and Bhaumik, A., *3D-Hexagonal Mesoporous Silica Having Exceptional H_2 Adsorption Capacity.* Journal of Physical Chemistry C, 2009. **113**(16): p. 6839-6844.

344. Parra, J. B., Ania, C. O., Arenillas, A., Rubiera, F., Palacios, J. M., and Pis, J. J., *Textural Development and Hydrogen Adsorption of Carbon Materials from PET Waste.* Journal of Alloys and Compounds, 2004. **379**(1-2): p. 280-289.

345. Pang, J. B., Hampsey, J. E., Wu, Z. W., Hu, Q. Y., and Lu, Y. F., *Hydrogen Adsorption in Mesoporous Carbons.* Applied Physics Letters, 2004. **85**(21): p. 4887-4889.

346. Chun, H., Dybtsev, D. N., Kim, H., and Kim, K., *Synthesis, X-Ray Crystal Structures, and Gas Sorption Properties of Pillared Square Grid Nets Based on Paddle-Wheel Motifs: Implications for Hydrogen Storage in Porous Materials.* Chemistry - A European Journal, 2005. **11**(12): p. 3521-3529.

347. Chen, B. L., Ockwig, N. W., Millward, A. R., Contreras, D. S., and Yaghi, O. M., *High H_2 Adsorption in a Microporous Metal-Organic Framework with Open Metal Sites.* Angewandte Chemie-International Edition, 2005. **44**(30): p. 4745-4749.

348. Dietzel, P. D. C., Panella, B., Hirscher, M., Blom, R., and Fjellvag, H., *Hydrogen Adsorption in a Nickel Based Coordination Polymer with Open Metal Sites in the Cylindrical Cavities of the Desolvated Framework.* Chemical Communications, 2006(9): p. 959-961.

349. Schimmel, H. G., Kearley, G. J., Nijkamp, M. G., Visserl, C. T., de Jong, K. P., and Mulder, F. M., *Hydrogen Adsorption in Carbon Nanostructures: Comparison of Nanotubes, Fibers, and Coals.* Chemistry - A European Journal, 2003. **9**(19): p. 4764-4770.

350. Schimmel, H. G., Nijkamp, G., Kearley, G. J., Rivera, A., de Jong, K. P., and Mulder, F. M., *Hydrogen Adsorption in Carbon Nanostructures Compared.* Materials Science and Engineering B-Solid State Materials for Advanced Technology, 2004. **108**(1-2): p. 124-129.

351. Germain, J., Fréchet, J. M. J., and Svec, F., *Nanoporous Polymers for Hydrogen Storage.* Polymeric Materials: Science & Engineering, 2007. **97**: p. 272-273.

352. Wood, C. D., Tan, B., Trewin, A., Su, F., Rosseinsky, M. J., Bradshaw, D., Sun, Y., Zhou, L., and Cooper, A. I., *Microporous Organic Polymers for Methane Storage.* Advanced Materials, 2008. **20**(10): p. 1916-1921.

353. Yuan, S. W., Kirklin, S., Dorney, B., Liu, D. J., and Yu, L. P., *Nanoporous Polymers Containing Stereocontorted Cores for Hydrogen Storage.* Macromolecules, 2009. **42**(5): p. 1554-1559.

354. Vuong, T. and Monson, P. A., *Monte Carlo Simulation Studies of Heats of Adsorption in Heterogeneous Solids.* Langmuir, 1996. **12**(22): p. 5425-5432.

355. Frost, H., Duren, T., and Snurr, R. Q., *Effects of Surface Area, Free Volume, and Heat of Adsorption on Hydrogen Uptake in Metal-Organic Frameworks.* Journal of Physical Chemistry B, 2006. **110**(19): p. 9565-9570.

356. Lowell, S., Shields, J., Charalambous, G., and Manzione, J., *Adsorbate Cross-Sectional Area as a Function of the BET C Constant.* Journal of Colloid and Interface Science, 1982. **86**(1): p. 191-195.

357. FP6 Integrated Project NESSHY. *Novel Efficient Solid Storage for Hydrogen*. [cited 01/12/2010]; Available from: www.nesshy.net.

358. Krutyeva, M., Grinberg, F., Furtado, F., Galvosas, P., Kärger, J., Silvestre-Albero, A., Sepulveda-Escribano, A., Silvestre-Albero, J., and Rodríguez-Reinoso, F., *Characterization of Carbon Materials with the Help of NMR Methods.* Microporous and Mesoporous Materials, 2009. **120**(1-2): p. 91-97.

359. Silvestre-Albero, J., Sepúlveda-Escribano, A., Rodríguez-Reinoso, F., Kouvelos, V., Pilatos, G., Kanellopoulos, N. K., Krutyeva, M., Grinberg, F., Kaerger, J., Spjelkavik, A. I., Stocker, M., Ferreira, A., Brouwer, S., Kapteijn, F., Weitkamp, J., Sklari, S. D., Zaspalis, V. T., Jones, D. J., de Menorval, L. C., Lindheimer, M., Caffarelli, P., Borsella, E., Tomlinson, A. G., Linders, M. J. G., Tempelman, J. L., and Bal, E. A., *Characterization Measurements of Common Reference Nanoporous Materials by Gas Adsorption (Round Robin Tests)*, in *Characterisation of Porous Solids VIII*, Kaskel, S., Llewellyn, P., Rodríguez-Reinoso, F., and Seaton, N. A., Editors. 2009, RSC Publishing: Cambridge. p. 9-16.

360. Zlotea, C., Moretto, P., and Steriotis, T., *A Round Robin Characterisation of the Hydrogen Sorption Properties of a Carbon Based Material.* International Journal of Hydrogen Energy, 2009. **34**(7): p. 3044-3057.

361. Grande, C. A., Silva, V., Gigola, C., and Rodrigues, A. E., *Adsorption of Propane and Propylene onto Carbon Molecular Sieve.* Carbon, 2003. **41**(13): p. 2533-2545.

362. Marquardt, D. W., *An Algorithm for Least-Squares Estimation of Nonlinear Parameters.* Journal of the Society for Industrial and Applied Mathematics, 1963. **11**(2): p. 431-441.

363. Moyer, J. D., Gaffney, T. R., Armor, J. N., and Coe, C. G., *Defining Effective Microporosity in Carbon Molecular Sieves.* Microporous Materials, 1994. **2**(4): p. 229-236.

364. Olson, D. H., *The Crystal-Structure of Dehydrated NaX.* Zeolites, 1995. **15**(5): p. 439-443.

365. Joshi, U. D., Joshi, P. N., Tamhankar, S. S., Joshi, V. P., Idage, B. B., Joshi, V. V., and Shiralkar, V. P., *Influence of the Size of Extraframework Monovalent Cations in X-Type Zeolite on Their Thermal Behavior.* Thermochimica Acta, 2002. **387**(2): p. 121-130.

366. Breck, D. W., *Zeolite Molecular Sieves: Structure, Chemistry, and Uses*. 1973, New York: Wiley. p. 771.

367. Grigor'eva, A. S., Vorotyntsev, V. M., Konakhovich, N. F., Mokhort, N. A., and Kirichek, L. M., *Optimization of the Pharmacological Efficiency of Methamphetamine for Local Application.* Pharmaceutical Chemistry Journal, 1997. **31**(4): p. 170-172.

368. Reguera, E., *Materials for Hydrogen Storage in Nanocavities: Design criteria.* International Journal of Hydrogen Energy, 2009. **34**(22): p. 9163-9167.

369. Kelly, J. F. and Fuller, O. M., *Evaluation of a Method for Investigating Sorption and Diffusion in Porous Solids.* Industrial & Engineering Chemistry Fundamentals, 1980. **19**(1): p. 11-17.

370. Saha, D. P. D., Deng, S. G., and Yang, Z. G., *Hydrogen Adsorption on Metal-Organic Framework (MOF-5) Synthesized by DMF Approach.* Journal of Porous Materials, 2009. **16**(2): p. 141-149.

371. Tranchemontagne, D. J., Hunt, J. R., and Yaghi, O. M., *Room Temperature Synthesis of Metal-Organic Frameworks: MOF-5, MOF-74, MOF-177, MOF-199, and IRMOF-0.* Tetrahedron, 2008. **64**(36): p. 8553-8557.

372. Li, J., Cheng, S., Zhao, Q., Long, P., and Dong, J., *Synthesis and Hydrogen-Storage Behavior of Metal-Organic Framework MOF-5.* International Journal of Hydrogen Energy, 2009. **34**(3): p. 1377-1382.
373. Mueller, U., Schubert, M., Teich, F., Puetter, H., Schierle-Arndt, K., and Pastre, J., *Metal-Organic Frameworks - Prospective Industrial Applications.* Journal of Materials Chemistry, 2006. **16**(7): p. 626-636.
374. Son, W. J., Kim, J., Kim, J., and Ahn, W. S., *Sonochemical Synthesis of MOF-5.* Chemical Communications, 2008(47): p. 6336-6338.
375. Li, H., Eddaoudi, M., O'Keeffe, M., and Yaghi, O. M., *Design and synthesis of an exceptionally stable and highly porous metal-organic framework.* Nature, 1999. **402**(6759): p. 276-279.
376. Huang, L. M., Wang, H. T., Chen, J. X., Wang, Z. B., Sun, J. Y., Zhao, D. Y., and Yan, Y. S., *Synthesis, Morphology Control, and Properties of Porous Metal-Organic Coordination Polymers.* Microporous and Mesoporous Materials, 2003. **58**(2): p. 105-114.
377. Rosi, N. L., Kim, J., Eddaoudi, M., Chen, B. L., O'Keeffe, M., and Yaghi, O. M., *Rod packings and metal-organic frameworks constructed from rod-shaped secondary building units.* Journal of the American Chemical Society, 2005. **127**(5): p. 1504-1518.
378. Calleja, G., Botas, J. A., Orcajo, M. G., and Sanchez-Sanchez, M., *Differences Between the Isostructural IRMOF-1 and MOCP-L Porous Adsorbents.* Journal of Porous Materials, 2010. **17**(1): p. 91-97.
379. Alcañiz-Monge, J., Trautwein, G., Pérez-Cadenas, M., and Román-Martínez, M. C., *Effects of Compression on the Textural Properties of Porous Solids.* Microporous and Mesoporous Materials, 2009. **126**(3): p. 291-301.
380. Schlichte, K., Kratzke, T., and Kaskel, S., *Improved Synthesis, Thermal Stability and Catalytic Properties of the Metal-Organic Framework Compound $Cu_3(BTC)_2$.* Microporous and Mesoporous Materials, 2004. **73**(1-2): p. 81-88.
381. Cho, S. H., Ma, B. Q., Nguyen, S. T., Hupp, J. T., and Albrecht-Schmitt, T. E., *A Metal-Organic Framework Material that Functions as an Enantioselective Catalyst for Olefin Epoxidation.* Chemical Communications, 2006(24): p. 2563-2565.
382. Jones, M., *Organic Chemistry*. 2nd ed, ed. Wisnovsky, J. 2000, New York,: W. W. Norton & Company, Inc. p. 1316.
383. Kryuchkov, Y. N., *Bulk Density of Powder Materials.* Glass and Ceramics, 1997. **54**(5-6): p. 157-158.
384. Ghanem, B. S., Hashem, M., Harris, K. D. M., Msayib, K. J., Xu, M. C., Budd, P. M., Chaukura, N., Book, D., Tedds, S., Walton, A., and McKeown, N. B., *Triptycene-Based Polymers of Intrinsic Microporosity: Organic Materials That Can Be Tailored for Gas Adsorption.* Macromolecules, 2010. **43**(12): p. 5287-5294.
385. Huang, Y., *The Temperature Dependence of Isosteric Heat of Adsorption on the Heterogeneous Surface.* Journal of Catalysis, 1972. **25**(1): p. 131-138.
386. Msayib, K. J., Book, D., Budd, P. M., Chaukura, N., Harris, K. D. M., Helliwell, M., Tedds, S., Walton, A., Warren, J. E., Xu, M. C., and McKeown, N. B., *Nitrogen and Hydrogen Adsorption by an Organic Microporous Crystal.* Angewandte Chemie-International Edition, 2009. **48**(18): p. 3273-3277.
387. Trætteberg, M., Khaikin, L. S., Grikina, O. E., Kozhushkov, S. I., and de Meijere, A., *The Structure and Spectra of 1,1-Bis(trimethylsilylethynyl)-Cyclopropane: A Priori Calculated Force Field and Vibrational Effects.* Journal of Molecular Structure, 2002. **641**(1): p. 41-60.
388. Comotti, A., Bracco, S., Distefano, G., and Sozzani, P., *Methane, Carbon Dioxide and Hydrogen Storage in Nanoporous Dipeptide-Based Materials.* Chemical Communications, 2009(3): p. 284-286.
389. Nelson, A. P., Farha, O. K., Mulfort, K. L., and Hupp, J. T., *Supercritical Processing as a Route to High Internal Surface Areas and Permanent Microporosity in Metal-Organic Framework Materials.* Journal of the American Chemical Society, 2009. **131**(2): p. 458-460.
390. Cooper, A. I., *Polymer Synthesis and Processing Using Supercritical Carbon Dioxide.* Journal of Materials Chemistry, 2000. **10**(2): p. 207-234.
391. Hu, X., Skadtchenko, B. O., Trudeau, M., and Antonelli, D. M., *Hydrogen Storage in Chemically Reducible Mesoporous and Microporous Ti Oxides.* Journal of the American Chemical Society, 2006. **128**(36): p. 11740-11741.

392. Germain, J., Hradil, J., Frechet, J. M. J., and Svec, F., *High Surface Area Nanoporous Polymers for Reversible Hydrogen Storage.* Chemistry of Materials, 2006. **18**(18): p. 4430-4435.

Publications

Nitrogen and Hydrogen Adsorption by an Organic Microporous Crystal

Msayib, K. J., Book, D., Budd, P. M., Chaukura, N., Harris, K. D. M., Helliwell, M., Tedds, S., Walton, A., Warren, J. E., Xu, M. C., and McKeown, N. B.

Angewandte Chemie-International Edition, 2009. **48**(18): p. 3273-3277.

Triptycene-Based Polymers of Intrinsic Microporosity: Organic Materials That Can Be Tailored for Gas Adsorption

Ghanem, B. S., Hashem, M., Harris, K. D. M., Msayib, K. J., Xu, M. C., Budd, P. M., Chaukura, N., Book, D., Tedds, S., Walton, A., and McKeown, N. B.

Macromolecules, 2010. **43**(12): p. 5287-5294.

Characterisation of Porous Hydrogen Storage Materials: Carbons, Zeolites, MOFs and PIMs

Tedds, S., Walton, A., and Book, D.

Accepted to Faraday Discussion 151: Hydrogen Storage Materials. (2011). DOI:10.1039/C0FD00022A.

Poster Presentations

Polymers of Intrinsic Microporosity (PIMs) for Hydrogen Storage

Tedds, S., Walton, A., McKeown, N. B. Ghanem, B. S., Budd, P., and Book, D.

MH2008, International Symposium on Metal-Hydrogen Storage Systems, Reykjavik, Iceland (2008)

Porous Hydrogen Storage Materials

Tedds, S., Walton, A., and Book, D.

SSH-IP, Workshop on Solid Storage of Hydrogen – International Perspectives, Crete, Greece (2009)

Characterisation of Porous Hydrogen Storage Materials: Carbons, Zeolites, MOFs and PIMs

Tedds, S., Walton, A., and Book, D.

MOF2010, Metal-Organic Frameworks, Marseille, France (2010*)*